mathematics

Special Issue Reprint

Mathematical Modeling and Data Science for Biology and Medicine

Edited by
Takashi Suzuki

mdpi.com/journal/mathematics

MDPI

Mathematical Modeling and Data Science for Biology and Medicine

Mathematical Modeling and Data Science for Biology and Medicine

Guest Editor

Takashi Suzuki

MDPI

Basel • Beijing • Wuhan • Barcelona • Belgrade • Novi Sad • Cluj • Manchester

Guest Editor
Takashi Suzuki
Center for Mathematical
Modeling and Data Science
Osaka University
Osaka
Japan

Editorial Office
MDPI AG
Grosspeteranlage 5
4052 Basel, Switzerland

This is a reprint of the Special Issue, published open access by the journal *Mathematics* (ISSN 2227-7390), freely accessible at: https://www.mdpi.com/si/mathematics/Math_Modeling_Data_Sci_Biol_Med.

For citation purposes, cite each article independently as indicated on the article page online and as indicated below:

Lastname, A.A.; Lastname, B.B. Article Title. *Journal Name* **Year**, *Volume Number*, Page Range.

ISBN 978-3-7258-4647-4 (Hbk)
ISBN 978-3-7258-4648-1 (PDF)
https://doi.org/10.3390/books978-3-7258-4648-1

Contents

About the Editor

Takashi Suzuki

Takashi Suzuki has been a Professor at Osaka University since 1995, where he is affiliated with the Center for Mathematical Modeling and Data Science (MMDS) since 2017. He specializes in analysis, applied analysis, and mathematical sciences, with research interests in nonlinear partial differential equations, numerical methods, inverse problems, and mathematical modeling in cell biology. He earned his B.S. (1976), M.S. (1978), and Ph.D. (1981) from The University of Tokyo. His academic career began as an Assistant Professor at The University of Tokyo (1978–1986), followed by a promotion to Lecturer (1986–1988) at the same institution. He then served as an Associate Professor at Tokyo Metropolitan University (1988–1993) before becoming a Professor at Ehime University (1993–1995). His work spans theoretical and applied mathematics, contributing significantly to PDEs, numerical analysis, and interdisciplinary applications in biological modeling.

mathematics

MDPI

Editorial

Preface to Special Issue "Mathematical Modeling and Data Science for Biology and Medicine"

Takashi Suzuki

Center for Mathematical Modeling and Data Science, Osaka University, Osaka 560-8531, Japan; suzuki@sigmath.es.osaka-u.ac.jp

This Special Issue, titled "Mathematical Modeling and Data Science for Biology and Medicine", aims to highlight the development and growing application of mathematical models and data science in medicine, as well as their role in enhancing the understanding and clinical management of various diseases. The ten articles included in this Issue explore a diverse array of topics, such as cell differentiation, blood flow, tumor growth under virotherapy, chemotherapy treatment sequences for triple-negative locally advanced breast cancer, incidence-dependent management strategies against an SEIRS epidemic, important measures for the prevention and control of the COVID-19 epidemic, invadopodia formation in cancer cells, fitting parameters for multi-exponential diffusion-weighted MRI, and oncolytic virotherapy. These studies employ a variety of mathematical tools, including graph theory, transport equation, systems of ordinary differential equations, systems of nonlinear diffusion equations, free boundary problems, center manifold theory, and optimization techniques, to model a wide range of biological processes. In addition, medical applications are presented based on their mathematical analyses and numerical simulations. Through these articles, readers will gain valuable insight into the latest trends and applications of mathematical modeling in medicine.

The first contribution introduces a similarity network-based approach to investigate the role of interacting single-cell histone modifications. High-resolution peak counting is shown to be an effective method for constructing per-gene profiles of histone modification marks. The second contribution focuses on the theoretical analysis of the effects of boundary conditions on the solutions of a one-dimensional hemodynamic system. The author extends the applicability of analytical methods in the simulation of blood flow, highlighting the influence of boundary conditions. The third contribution presents a mathematical model, based on ordinary differential equations, to examine the spatially homogenous state of tumor growth under virotherapy. Derived from a partial differential equation (PDE) system, the model is used to analyze the time evolution of the tumor radius and its implications for tumor progression. The fourth contribution studies triple-negative locally advanced breast cancer and underscores the regions exhibiting the most sustained variation in the tumor's cellular population. The fifth contribution showcases a model for the prevention and control of COVID-19, integrating healthcare and medical detection with big data information technology to monitor epidemic trends throughout the entire course of the outbreak. The sixth contribution introduces a mathematical model of an individual cell to simulate invadopodia formation in a three-dimensional domain. The model is formulated using the Stefan problem approach, where the free boundary of the membrane is determined. The subsequent contribution develops a mathematical model to study the impact of epidemic dynamics on non-pharmaceutical interventions. Specifically, an SEIRS epidemic model with reinfection is used to illustrate the results, with an application to

the COVID-19 pandemic. The eighth contribution examines the airborne and physical transmission of COVID-19 within a simple heuristic framework designed to inform public policy decisions. The ninth contribution utilizes diffusion-weighted MRI and compares different methods for multi-exponential analysis of the diffusion signal in the kidneys. The final contribution explores the impact of Allee effects on tumor cell growth through the mathematical modeling of oncological virotherapy. The authors employ an epidemiological model integrating linear and logistic growth, applying different Allee effects to observe their influence on the dynamics of virus–tumor interaction.

The Guest Editor extends his sincere appreciation to all the authors for their valuable contributions to this Special Issue. He is also deeply grateful to the reviewers for their insightful and professional evaluation reports, which have significantly enhanced the quality of the submitted manuscripts. Furthermore, he acknowledges the excellent collaboration with the publisher, the outstanding assistance of the MDPI associate editors, and the significant support of the Managing Editor of this Special Issue, Ms. Helene Hu.

Conflicts of Interest: The author declares no conflicts of interest.

List of Contributions:

1. Baccini, F.; Bianchini, M.; Geraci, F. Graph-Based Integration of Histone Modification Profiles. *Mathematics* **2022**, *10*, 1842. https://doi.org/10.3390/math10111842.
2. Krivovichev, G. On the Effects of Boundary Conditions in One-Dimensional Models of Hemodynamics. *Mathematics* **2022**, *10*, 4058. https://doi.org/10.3390/math10214058.
3. Yang, C.; Wang, J. Modeling and Analyzing Homogeneous Tumor Growth under Virotherapy. *Mathematics* **2023**, *11*, 360. https://doi.org/10.3390/math11020360.
4. López-Alvarenga, J.; Minzoni-Alessio, A.; Olvera-Chávez, A.; Cruz-Pacheco, G.; Chimal-Eguia, J.; Hernández-Ruíz, J.; Álvarez-Blanco, M.; Bautista-Hernández, M.; Quispe-Siccha, R. A Mathematical Model to Optimize the Neoadjuvant Chemotherapy Treatment Sequence for Triple-Negative Locally Advanced Breast Cancer. *Mathematics* **2023**, *11*, 2410. https://doi.org/10.3390/math11112410.
5. Nguyen-Huu, T.; Auger, P.; Moussaoui, A. On Incidence-Dependent Management Strategies against an SEIRS Epidemic: Extinction of the Epidemic Using Allee Effect. *Mathematics* **2023**, *11*, 2822. https://doi.org/10.3390/math11132822.
6. Zhu, C.; Zhu, J.; Shao, J. Epidemiological Investigation: Important Measures for the Prevention and Control of COVID-19 Epidemic in China. *Mathematics* **2023**, *11*, 3027. https://doi.org/10.3390/math11133027.
7. Ramlee, M.; Loling Othman, N.; Suzuki, T. Invadopodia Formation in Cancer Cell: The Mathematical and Computational Modelling Based on Free Boundary Problem. *Mathematics* **2023**, *11*, 3044. https://doi.org/10.3390/math11143044.
8. Dieguez, G.; Batistela, C.; Piqueira, J. Controlling COVID-19 Spreading: A Three-Level Algorithm. *Mathematics* **2023**, *11*, 3766. https://doi.org/10.3390/math11173766.
9. Jasse, J.; Wittsack, H.; Thiel, T.; Zukovs, R.; Valentin, B.; Antoch, G.; Ljimani, A. Toward Optimal Fitting Parameters for Multi-Exponential DWI Image Analysis of the Human Kidney: A Simulation Study Comparing Different Fitting Algorithms. *Mathematics* **2024**, *12*, 609. https://doi.org/10.3390/math12040609.
10. Hernández-López, E.; Wang, J. A Mathematical Perspective on the Influence of Allee Effects in Oncolytic Virotherapy. *Mathematics* **2025**, *13*, 744. https://doi.org/10.3390/math13050744.

mathematics

MDPI

Article

Graph-Based Integration of Histone Modification Profiles

Federica Baccini [1,2,*], Monica Bianchini [3] and Filippo Geraci [2,*]

[1] Department of Computer Science, University of Pisa, 56127 Pisa, Italy
[2] Institute for Informatics and Telematics, CNR, 56124 Pisa, Italy
[3] Department of Information Engineering and Mathematics, University of Siena, 53100 Siena, Italy; monica@diism.unisi.it
* Correspondence: federica.baccini@phd.unipi.it (F.B.); filippo.geraci@iit.cnr.it (F.G.)

Abstract: In this work, we introduce a similarity-network-based approach to explore the role of interacting single-cell histone modification signals in haematopoiesis—the process of differentiation of blood cells. Histones are proteins that provide structural support to chromosomes. They are subject to chemical modifications—acetylation or methylation—that affect the degree of accessibility of genes and, in turn, the formation of different phenotypes. The concentration of histone modifications can be modelled as a continuous signal, which can be used to build single-cell profiles. In the present work, the profiles of cell types involved in haematopoiesis are built based on all the major histone modifications (i.e., H3K27ac, H3K27me3, H3K36me3, H3K4me1, H3K4me3, H3K9me3) by counting the number of peaks in the modification signals; then, the profiles are used to compute modification-specific similarity networks among the considered phenotypes. As histone modifications come as interacting signals, we applied a similarity network fusion technique to integrate these networks in a unique graph, with the aim of studying the simultaneous effect of all the modifications for the determination of different phenotypes. The networks permit defining of a graph-cut-based separation score for evaluating the homogeneity of subgroups of cell types corresponding to the myeloid and lymphoid phenotypes in the classical representation of the haematopoietic tree. Resulting scores show that separation into myeloid and lymphoid phenotypes reflects the actual process of haematopoiesis.

Keywords: histone modifications; omics integration; graph cut; haematopoiesis

MSC: 92-08

1. Introduction

Histones are basic proteins which bind tightly to DNA in the nuclei of eukaryotic cells. According to the 'beads-on-a-string' model [1], they combine into octamers to form nucleosomes, the basic units around which DNA wraps to form chromatin. The nucleosomes, in turn, bind together to form a chain structure that constitutes the backbone of the three-dimensional arrangement of chromosomes.

Some residues of histone proteins, namely lysines and arginines, represent possible targets for post-translational modifications, such as methylation and acetylation [2]. Moreover, particular patterns of histone modifications are interpreted as a code specifying for genetic functions [3,4]. Although parts of the working principles of this code are being investigated, most of it still represents a puzzle for biologists, as well as a computational challenge for bioinformaticians. However, the existence of an intrinsic relationship between the three-dimensional structure of chromosomes, gene accessibility and gene expression has been highlighted [5]. Consequently, histone modifications emerge as fundamental epigenetic agents for the development of different cell phenotypes. The advent of the cost-effective *ChIP-seq* technology [6] that combines chromatin immunoprecipitation and massively parallel sequencing, and the consequent large availability of data, have made it possible to read the traces of all the histone modifications of the genome [7]. Accordingly,

several institutions—which came together to form the International Human Epigenome Consortium (IHEC) (https://ihec-epigenomes.org/) [8]—have teamed up to generate huge databases of such epigenetic markers.

In this paper, we show how histone modification traces can be turned into whole-genome profiles. This is achieved by identifying and counting high-resolution peaks (steep local maxima with sizes as small as a hundred bps) in the histone modification signal. The obtained profiles show behaviour that resembles that of gene expression, with only a small fraction of genes exhibiting relevant activity (relatively high peak counts), and the vast majority being silent. Indeed, the existence of a tight relationship between histone modifications and transcription has been deeply investigated, and quantitative models to predict the expression level of genes from histone modification levels have been derived. It is well-known, in fact, that histone modification levels and gene expression are highly correlated, while only a small number of histone modifications are necessary to accurately predict gene expression [5,9,10]. Consequently, it is possible to borrow methods from differential expression analysis to extract knowledge from histone modification profiles (see, for example, [11]). In particular, the proposed model integrates the information contained in all the histone modification signals involved in haematopoiesis (see https://epigenomesportal.ca/ihec/grid.html?build=2020-10&assembly=4&cellTypeCategories=1, accessed on 23 March 2022). This choice is based on the observation that a single modification may not be able to capture the complexity of epigenetics, since a phenotype is the result of the combination of contrasting contributions—promotion or repression—of several modifications [12].

Initially, the information contained in each histone modification is treated separately, constructing a dissimilarity network of cell types; then, all the networks are integrated using a similarity network fusion technique [13,14]. This integration model is suitable for several applications, including that of clustering a population of cell types into homogeneous groups. Nevertheless, if the sought sub-populations are unknown, it could be useful to compare alternative partitions of the population into subgroups rather than performing clustering. Following this idea, we define a score to quantitatively evaluate the plausibility of a graph bipartition into two subgroups of vertices. The combination of the integration model with the evaluation score for graph bipartitions is then tested by considering a hypothesis on the biological process of haematopoiesis, i.e., the process of the formation of all blood cells from a common progenitor. Specifically, we tested the classical hypothesis on the existence of two main subpopulations of cell types in haematopoiesis, namely the lymphoid and myeloid cells [15]. Figure 1 depicts an outline of the proposed methodology.

The paper is organised as follows. In Section 2, the adopted method is described. In Section 3, the experimental analysis and the obtained results are presented. A discussion of the methodology and the results is offered in Section 4. Finally, some conclusions are given in Section 5.

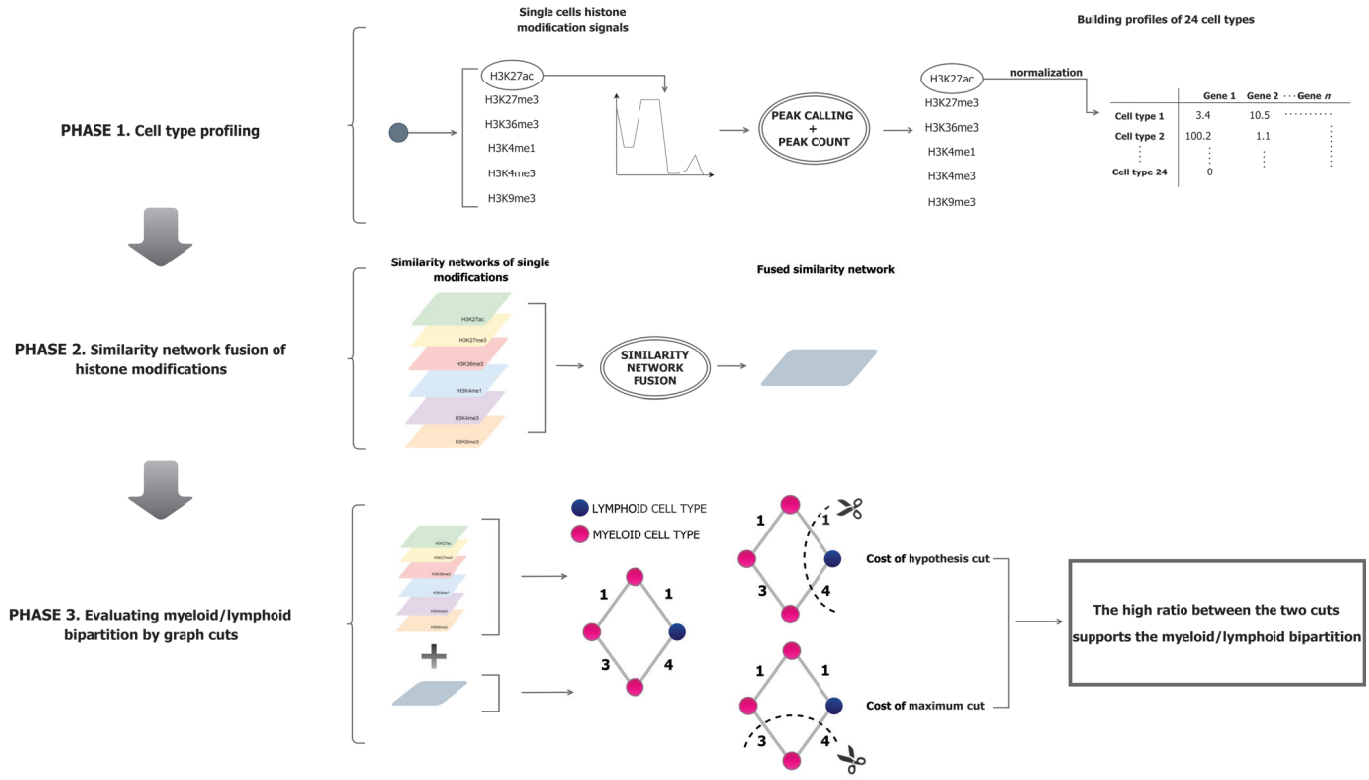

Figure 1. Scheme of the proposed methodology. In Phase 1, histone modification profiles of cell types are built by counting peaks in the modification signal. In Phase 2, a similarity network of cell types is computed for each histone modification; the networks are then fused by using a similarity network [14]. In Phase 3, a graph-cut-based approach is introduced to evaluate the bipartition of the networks into myeloid and lymphoid cell types.

2. Materials and Methods

A histone modification track has the form of a continuous signal. The signal is obtained after a first phase of ChIP-sequencing by associating each nucleotide of the DNA sequence with the number of reads of the modifier covering it [7]. In this section, we first show how to detect and count peaks in these signals in order to build the histone modification profiles of a cell. Moreover, we describe how cell-type profiles from different histone modifications can be organised into a network-based setup and then integrated into a unique, comprehensive graph. Finally, we propose a graph-cut-based hypothesis testing scheme for evaluating graph bipartitions.

2.1. Peak Calling

Let $X = \{x_1, \ldots, x_n\}$ be the histone modification track of a sample cell X, where the value x_i corresponds to the number of supporting reads covering genomic position i. Intuitively, a peak is a contiguous region around a local maximum in track X. More specifically, the peak region consists of two monotone curves leading to a point whose value is the highest within a neighbourhood of points. From this informal definition, two free parameters can be derived to define a peak: (i) its height and (ii) its width. Despite being simple in principle, these two parameters make finding peaks complicated. Indeed, different settings, as well as appropriate algorithms, may be required for specific applications. For instance, setting large surrounding areas is equivalent to seeking large peaks (low-resolution peaks), which are suitable for the identification of genomic sites involved in histone modification. This is the case, for example, of Sole-Search [16], the peak detection algorithm used at IHEC [8]. On the other hand, searching for small peaks (high-resolution peaks) is more appropriate for quantification. Since the first step of this analysis

aims at quantifying the number of peaks in a histone modification track, we design an algorithm to identify high resolution peaks (with resolution on the order of a few bps).

Let $X_h = \{\hat{x}_1, \ldots, \hat{x}_{n/h}\}$ be a transformation of profile X at resolution h, where $\hat{x}_i = mean([x_{hi}, \ldots, x_{(h+1)i-1}])$. Let $R(X_h) = \{r_1, \ldots, r_m\}$ ($m \leq n/h$) be a compact representation of X_h, where consecutive pairs $\hat{x}_i$ and $\hat{x}_{i+1}$ are merged if $\hat{x}_i = \hat{x}_{i+1}$. An element r_i is eligible as a peak if it satisfies, at least, the conditions $r_i > r_{i-1}$ and $r_i > r_{i+1}$. The representation of a histone modification track X_h with $R(X_h)$ allows us to consider all the maxima as candidate peaks independent of their width. Thence, in order for a point r_i to be a real peak, two additional features are required. First, the signal increase has to be steep enough. Second, the candidate r_i has to be compared with its background. To this end, as a background we use the interval $I(r_i) = [\alpha, \beta]$, where α and β are integer numbers such that $\alpha < i < \beta$ and $r_{\alpha-1} = 0$, $r_{\beta+1} = 0$, and $r_j \neq 0 \; \forall j \in [\alpha < i < \beta]$, while the peak intensity is computed as the Z-score of r_i, where:

$$z(r_i) = \frac{r_i - \mu(I(r_i))}{\sigma(I(r_i))}, \tag{1}$$

$\mu()$ denotes the mean, and $\sigma()$ is the standard deviation of the signal distribution over the interval $I()$. The Z-score defined in Equation (1) does not depend on the scale of the histone modification signal and has the advantage of being interpretable as a sort of fold change. Consequently, a peak can be defined as a genomic locus where the score $z()$ is higher than a user-defined threshold (set to 2 in our experiments).

2.2. Normalisation

After the peak-calling step, we proceed by counting the number of peaks for each gene. Peak counting, as many other quantification tasks from NGS data, is influenced by sequencing depth. Indeed, in order for a peak to be individuated, it has to be endowed with a consistent number of supporting reads. This generally happens easily with strong signals, while it requires high coverage for weaker signals. Counts per million (CPM) and reads per kilobase per million [17] (RPKM) are two widespread normalisation methods used in the field of RNA-seq to mitigate the effect of sequencing productivity. Both methods leverage on the acceptable assumption that the overall amount of signals (in this case, peaks) per sample is roughly constant. The main difference between CPM and RPKM is that the latter is based on the additional assumption that the molar concentration of RNA is constant. Consequently, the number of reads per gene is proportional to gene length. In the context of this work, CPM and RPKM assume slightly different semantics. CPM is based on the hypothesis that a cell phenotype is determined only by the presence of a high concentration of a histone modification signals. It is therefore an absolute measure of concentration of histone modification peaks inside a gene. In contrast, RPKM is a relative measure, as it relies on the idea that the determination of a cell phenotype depends on the distribution of the number of peaks along the gene. Hence, in the latter case, it is assumed that a high concentration of histone modifications is not sufficient in itself to produce a phenotype, but rather must be spread along the gene.

Due to the lack of evidence to support a model based on the absolute concentration of histone modifications or relative concentration, both CPM and RPKM are tested in our experiments.

2.3. Cell-Type Expression Profiles

The IHEC data portal [8] makes a variable number of different samples available for a given cell type. Such redundant information can be exploited to build a unique profile for each phenotype, which, in turn, has the effect of mitigating possible bias due to the intrinsic variability of samples. In this work, this is achieved by taking the average of the per-gene contributions of profiles of the same cell type.

Similarly to gene expression, it is reasonable to assume that most genes do not contribute to a phenotype of interest because they are expressed constantly or not at all. In a framework where the computation of similarity/distance between phenotypes is required, the effect of these genes would be that of pushing the ratio between the two nearest and the two furthest elements towards 1. Consequently, it would be complicated to look for differentiated subgroups of phenotypes. Since we are interested in computing similarities/distances between different cell types, a strategy for filtering out those genes is required. Nevertheless, it is difficult to establish a priori a cutoff threshold to filter out infrequently expressed genes, as genes with similar profiles could be excluded only on the basis of a negligible distance from the threshold. In order to solve this issue, we choose to cluster genes, and to interpret each cluster centroid as representing all the group members. In this way, a whole cluster is either retained or filtered out based on the profile of its centroid. In this work, the clustering of genes is performed using the k-means algorithm, and the centroids are initialised using the Lloyd procedure [18] (the implementation is available via the R [19] function **kmeans**). The number of clusters k is set to 50 (thanks to a raw grid search based on the elbow method [20]) to ensure high within-cluster homogeneity, which is required for removing or retaining genes with similar profiles. Finally, we set a conservative threshold for filtering out clusters of genes with constant or no expression [21]. More precisely, a cluster is retained only if the maximum value of its centroid is higher than the lowest 10% of the expression interval.

2.4. Profile Integration

Histone modifications exert their effects directly by influencing the overall structure of chromatin, promoting or inhibiting gene accessibility. As a result, a phenotype can be seen as a combination of all the contributions of the single modifications. Based on this observation, we present a strategy that integrates the information of similarities/dissimilarities between profiles of cell types coming from several modifications into a unique similarity/dissimilarity network. In order to perform profile integration, the *Similarity Network Fusion* (SNF) [14] algorithm (the software can be downloaded in R or MATLAB versions at http://compbio.cs.toronto.edu/SNF/SNF/Software.html, accessed on 23 March 2022) is exploited. The input to SNF consists of a set of similarity networks, one for each histone modification, characterised by the same set of vertices (cell types). Then, by applying a cross-diffusion process (CrDP) [13], SNF outputs a unique weighted similarity graph with the same set of nodes as the original networks. In brief, the algorithm iteratively updates the single similarity networks by promoting (i) strong links, which are not necessarily present in all the networks, and (ii) weak links that are shared by all the networks. Then, at the final iteration step, the contributions of the single networks are averaged to define a unique similarity graph. The resulting network can therefore give information on how multiple variables determine similarities among cell types.

2.5. Hypothesis Testing

The model described in Section 2.4 is applied to graphs where nodes are cell types, and edges are weighted with a similarity value between pairs of cell types. With the aim of studying how to divide the nodes of these graphs into two homogeneous groups, we define a notion of separation by using graph cuts. A sensible bipartition of a similarity network should have low-weighted edges between the two distinct sets and relatively higher-weighted edges within the groups. Thus, the cost of a cut constitutes quantitative information on the level of separation of the graph components. In line with this observation, it is possible to define a score that is proportional to the degree of separation between two groups, a task easier to carry out with dissimilarity graphs. Dissimilarities can be easily computed starting from similarities. For example, a dissimilarity weight can be obtained by first converting similarities into Z-scores and then inverting them with respect to the mean.

Applying a cut to a dissimilarity network is not in itself sufficient to determine the goodness of a network bipartition. In fact, a lower and an upper bound on the cost of a cut induced by a partition must be introduced. In principle, setting the lower and the upper bound as the costs, respectively, of the minimum and the maximum cut might be a reasonable choice. However, the two scores are highly dependent on the weight values and the graph topology. Therefore, they do not represent a good solution when scores obtained for different graphs have to be compared. In order to get rid of these scaling problems, the separation measure can be converted into a scale-free score as follows:

$$S(h) = \frac{\lambda(h) - \min_{c \in C(G)} \lambda(c)}{\max_{c \in C(G)} \lambda(c) - \min_{c \in C(G)} \lambda(c)}, \tag{2}$$

where $C(G)$ denotes the set of all possible graph cuts of graph G, $\lambda()$ denotes the cost function of a cut, and h is the cut induced by the bipartition to be evaluated (referred to as the hypothesis cut). The score $S(h)$ takes on values in the range $[0, 1]$ and reaches its maximum when the cost of the hypothesis cut reaches that of the maximum cut on G (the similarities between vertices of the same group are high and those among vertices of different groups are low). Computation of the maximum cut represents a major issue for computing $S(h)$. Indeed, while exact algorithms for computing the minimum cut exist [22,23], computation of the maximum cut is known to be an NP-complete [24] problem. However, heuristic solutions can be adopted to find the solution.

In this work, the maximum cut approach is implemented in the R environment following the *Greedy Cut Algorithm* proposed in [25]. As for the min-cut, we use the R function `min_cut` from the **igraph** package, which is an implementation of the algorithm proposed in [26].

In our experiments, the score is tested on dissimilarity networks of cell types with the aim of studying if two subpopulations appear to have substantially different phenotypes.

3. Results

3.1. Dataset

The experimental analysis is conducted by using whole-genome histone modification profiles from a collection of cell samples involved in haematopoiesis (the complex differentiation process that starts from stem cells and gives origin to all types of blood cells).

The data come from the 2020-10 release by the *Blueprint project* (https://www.blueprint-epigenome.eu/), and are available at the *International Human Epigenome Consortium* (IHEC) [8] data portal (https://epigenomesportal.ca/ihec/). The dataset consists of 1254 samples of 35 distinct cell types, each registering six modification marks on histone H3. The marks are identified by the Roadmap Epigenome Mapping Centers (http://www.roadmapepigenomics.org/). More specifically, the histone modifications include mono and tri-methylation of lysine 4 (H3K4me1 and H3K4me3), tri-methylation of lysine 9, 27 and 36 (H3K9me3, H3K27me3 and H3K36me3), and acetylation of lysine 27 (H3K27ac). The pre-processed data and the code to perform the analysis are available at https://gitlab.com/gbi1/gbi-of-histone-modifications/, accessed on 23 March 2022.

Since the similarity network fusion method requires all the single modification networks to have the same nodes, we limit our tests to the subset of cell types for which all the histone modification marks are available. Moreover, profiles associated with unhealthy samples are removed, because a pathological state could alter a cell phenotype and would introduce some bias into our analysis. With this filtering, the dataset considered consists of 810 samples partitioned in 24 distinct cell types involved in haematopoiesis (see Table 1, which collects the number of samples of each cell type showing a particular histone modification, for details). As we are interested in studying the plausibility of the distinction into myeloid and lymphoid lineages in haematopoiesis (see Figure 2), where all the cell types are labelled according to their corresponding lineage. As shown in Table 1, 13 cell types belong to the myeloid lineage, and the remaining 11 belong to the lymphoid one.

Table 1. Origin, lineage and number of samples for each cell type and histone modification. The whole dataset consists of 810 samples from the 24 cell types involved in haematopoiesis.

Cell Type	Origin	Lineage	H3K27ac	H3K27me3	H3K36me3	H3K4me1	H3K4me3	H4K9me3
Alternatively activated macrophage	Blood	Myeloid	7	7	7	7	7	7
Band-form neutrophil	Bone marrow	Myeloid	3	3	3	3	4	3
CD14-positive, CD16-negative classical monocyte	Blood	Myeloid	14	9	6	10	9	8
CD34-negative, CD41-positive, CD42-positive megakaryocyte cell	Blood	Myeloid	2	2	3	3	3	2
CD38-negative naive B cell	Blood	Lymphoid	4	5	6	5	7	7
CD4-positive, alpha-beta T cell	Blood	Lymphoid	9	9	9	9	9	9
CD8-positive, alpha-beta T cell	Blood	Lymphoid	6	5	5	5	5	5
Central memory CD4-positive, alpha-beta T cell	Blood	Lymphoid	1	1	1	1	2	1
Class switched memory B cell	Blood	Lymphoid	3	3	2	3	3	3
Cytotoxic CD56-dim natural killer cell	Blood	Lymphoid	4	4	4	5	6	5
Effector memory CD8-positive, alpha-beta T cell	Blood	Lymphoid	2	1	2	2	3	3
Endothelial cell of umbilical vein (proliferating)	Blood	Lymphoid	2	2	2	2	2	2
Endothelial cell of umbilical vein (resting)	Blood	Lymphoid	1	2	2	2	2	2
Erythroblast	Blood	Myeloid	2	2	2	2	2	2
Inflammatory macrophage	Blood	Myeloid	8	8	9	7	8	9
Macrophage	Blood	Myeloid	14	7	7	13	14	8
Mature eosinophil	Blood	Myeloid	2	2	2	2	2	2
Mature neutrophil	Blood	Myeloid	15	13	13	13	13	13
Monocyte	Blood	Myeloid	36	22	3	28	28	15
Naive B cell	Blood	Lymphoid	8	8	9	7	8	8
Neutrophilic metamyelocyte	Bone marrow	Myeloid	3	3	3	3	4	3
Neutrophilic myelocyte	Bone marrow	Myeloid	3	3	3	3	4	3
Plasma cell	Bone marrow	Lymphoid	3	3	3	3	3	3
Segmented neutrophil of bone marrow	Bone marrow	Myeloid	3	3	3	3	4	3
Total			155	127	109	141	152	126

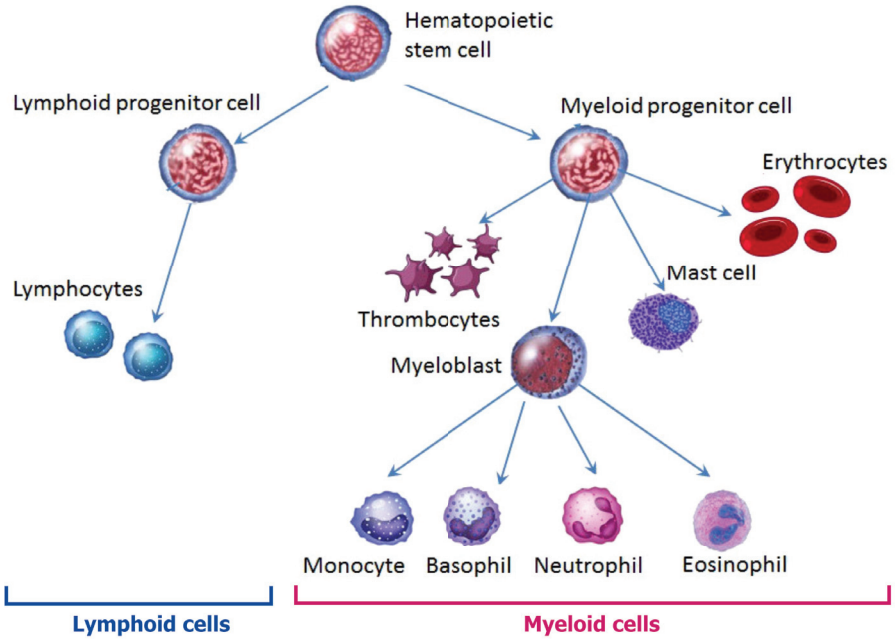

Figure 2. A simplified representation of the classical model of the haematopoietic tree, where the lymphoid and myeloid lineages are highlighted in blue and orange, respectively.

3.2. Histone Signal Distribution

The first step of the experiments is dedicated to the analysis of histone modification signals along the genome. As stated in Section 2.3, whole-genome profiles of cell types are built by quantifying the number of peaks for each gene in the histone modification signal. In this phase, we investigate the possibility that a (relatively) high signal intensity of a histone modification is registered only in a fraction of genes. This hypothesis arises from the observation that in gene expression profiles, most genes are either constantly expressed or not expressed at all [27,28]. Consequently, if whole-genome histone modification profiles follow this behaviour, classical differential expression analysis techniques could be borrowed for processing histone signals.

We experimentally verify this hypothesis by comparing the distribution of the number of peaks per gene (see Figure 3 for a graphical representation) of the profiles of different cell types for each histone modification with the expected distributions of gene expression counts derived from the literature [27,28]. Figure 3 highlights that, as happens in RNA-seq experiments, very low or no signal is registered for the large majority of genes. Indeed, the vast majority of genes have counts equal to 0 or lower than 5. Interestingly, this behaviour appears to be independent of the type of modification.

Therefore, observation of the signal distribution opens up the use of standard differential gene expression normalisation methods for processing histone modification marks. These methods, in turn, can be exploited to perform feature selection in the experiments. Following this idea, each cell type profile is normalised using CPM and RPKM normalisation. Experiments are conducted in the R environment [19] by using the R functions `cpm` and `rpkm` from the **edgeR** package. Subsequently, a feature selection procedure is performed following the strategy described in Section 2.3. Feature selection is applied to both normalisations of the data, with the effect of retaining (i) genes with a consistent number of peaks and (ii) genes with well-differentiated values across samples. In Table 2, the number of features (genes) retained after feature selection is reported. Table 2 shows that out of 21,987 quantified genes, only a fraction are active. In particular, by using RPKM, thus requiring the signal intensity to be proportional to the gene length, the number of active genes is rather small (independent of the histone modification mark). Moreover, RPKM filters many more genes than CPM. This result suggests that there are a number of long genes with enough histone modification marks to be retained after CPM, but with a

sufficient concentration of marks to also be retained after RPKM. Finally, by inspecting the number of genes retained after the application of both normalisation methods (see the last column of Table 2), we observe that few genes are retained after RPKM and filtered out by CPM. This suggests that such genes have small peaks, which emerge because of their short length.

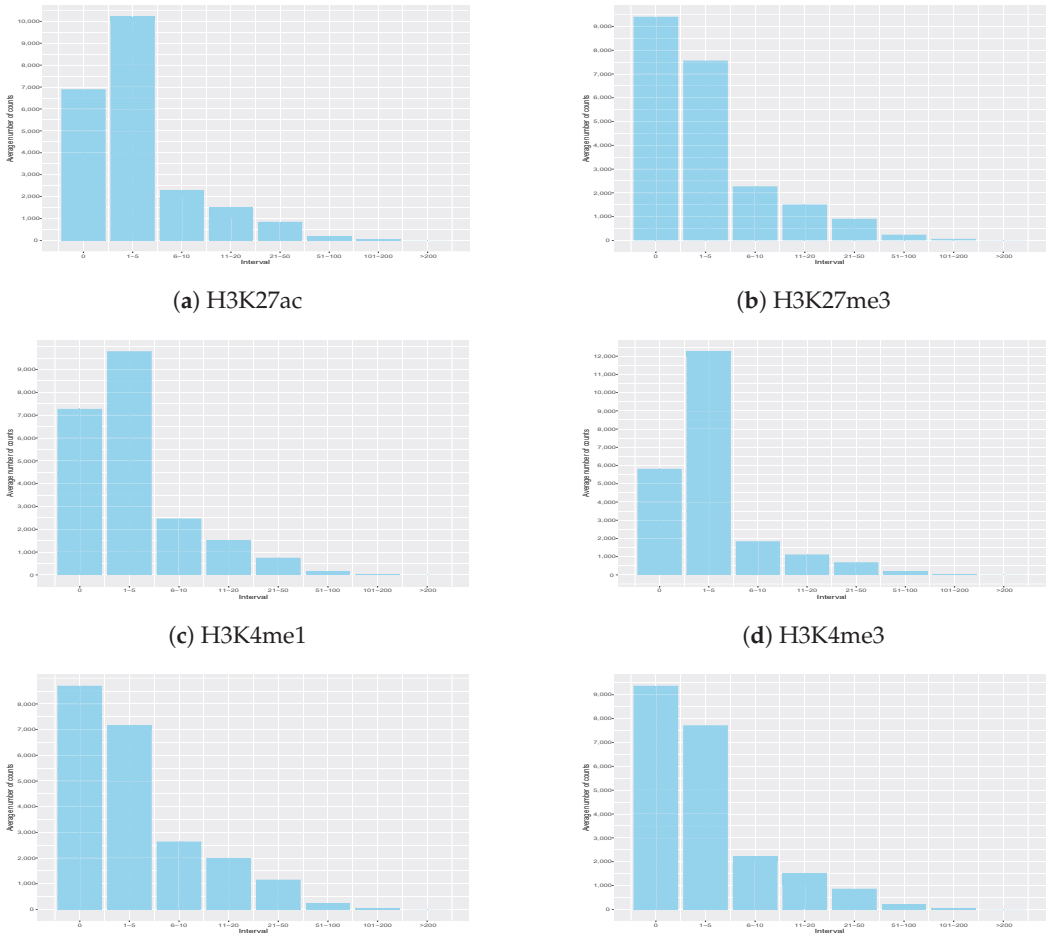

(**a**) H3K27ac (**b**) H3K27me3

(**c**) H3K4me1 (**d**) H3K4me3

(**e**) H3K36me3 (**f**) H3K9me3

Figure 3. Distribution of the signal intensity of the histone modification profiles. The histograms show that most of the genes have no or poorly detectable signal intensity (i.e., lower than 10) while the signal is remarkably high only in a fraction of genes along each sample.

Table 2. The number of genes retained after feature selection using CPM and RPKM normalisation, respectively. In the last column, the number of genes retained by both normalisation methods are reported, showing that almost all the genes retained by RPKM are also maintained by CPM.

Modification	CPM	RPKM	INTERSECTION
H3K27ac	5655	481	340
H3K27me3	5294	235	184
H3K36me3	6062	369	264
H3K4me1	7309	248	206
H3K4me3	5627	235	189
H3K9me3	5295	383	280

3.3. Phenotype Separation Evaluation

In view of evaluating the network integration and the hypothesis testing scheme presented in Sections 2.4 and 2.5, the profiles from the six histone modifications are used to define similarity networks among cell types. The similarity measure is defined as in [14]. Then, the six resulting similarity networks are integrated into a unique graph using Similarity Network Fusion [14] (SNF). The application of SNF requires three parameters: K, T and μ. K denotes the number of neighbours to consider in the K-Nearest Neighbours algorithm exploited by SNF, T is the number of iteration of the Cross Diffusion Process, and μ is a scaling parameter used in the iterative computation of the similarity matrices. In our experiments, we set their values to 5, 10 and 0.3, respectively.

Subsequently, the six similarity networks (corresponding to the six histone modifications analysed) and the results from SNF are turned into dissimilarity networks to test the hypothesis evaluation model described in Section 2.5. For the single-modification networks, edges between cell types are weighted with the normalised squared Euclidean distance between pairs of cell types (in the range $[0, 1]$). For the network resulting from fusion, dissimilarities are computed as follows: First, the Z-score of each similarity weight is computed. Then, the Z-scores are inverted with respect to the mean to obtain a dissimilarity weight.

We choose to test the model for evaluating the separation of each graph into two subgroups of cell types belonging to two distinct lineages in the classic haematopoietic tree [15]. Figure 2 shows a simplified representation of a classical scheme of haematopoiesis, which imposes a strict binary distinction between the myeloid and lymphoid lineages at the first differentiation step. However, recent studies [29,30] have highlighted that this model is a simplification of the real haematopoietic process. Indeed, they admit the existence of some mechanisms allowing myeloid progenitor cells to differentiate into cells belonging to the lymphoid component and vice versa. Consequently, it is interesting to exploit our hypothesis testing model for quantitatively evaluating the separation of the networks of cell types into the components induced by the two lineages.

If the graphical model fits the hypothesis, a cut separating myeloid and lymphoid cell types in each dissimilarity graph would tend to mostly remove edges with a high dissimilarity score. If we allow the possibility that some lower-weighted edges can also be removed, the separation score is expected to be close to (but less than) 1.

Indeed, the results depicted in Figure 4 report a score near 1 for all the networks. In addition, Figure 4 shows that scores obtained using CPM-based normalisation are higher than those obtained using RPKM, even if the gap is not remarkable. This suggests that in order to trigger a certain phenotype, histone modification signals do not have to be spread uniformly along a gene, but it is enough to have them in sufficient concentration. However, although the scores are high, there is still margin to believe that the model shown in Figure 2 may not be the only mechanism describing haematopoiesis.

Finally, from the results of the single-histone modification networks (Figure 4), it emerges that the six histone modifications almost equally contribute to the haematopoietic branch at the first level. This result is enforced by the high score obtained in the SNF network.

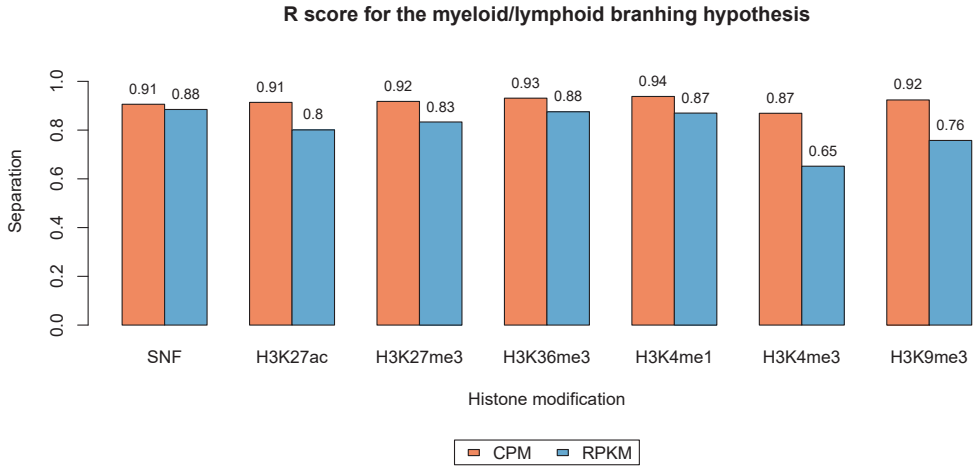

Figure 4. Barplot of the results of hypothesis testing for each modification network and for the network resulting from the fusion process (denoted SNF). The x-axis is labelled according to the different similarity networks. "SNF" refers to the network obtained after the fusion process. The y-axis contains the value of the separation score obtained after applying the graph cuts to the networks. For each network, the separation score is described by two coloured bars, distinguishing results obtained after CPM- or RPKM-based normalisation.

4. Discussion

Histone modifications are complex signals that are not yet fully understood. It is known that an increase/decrease in the concentration of such signals has an impact on gene expression. Furthermore, we know that the presence of large peaks in the signal wave is associated with loci involved in a histone modification [16]. In our experiments, the possibility of using high-resolution peaks to quantify per-gene histone modifications was investigated. In this framework, we studied the distribution of high-resolution peaks across the genome, showing that they behave similarly to gene expression profiles. More specifically, it can be observed, analogous to what happens for gene expression, that only a small fraction of genes have a significant signal intensity. Following this idea, we normalised the histone modification profiles of cells by using CPM and RPKM normalisations. Both methods were tested on our data since the use of a specific normalisation requires different interpretation of signal behaviour. Indeed, CPM measures signal concentration. Accordingly, differences in phenotypes are activated with a sufficient change in the amount of signal in a gene, regardless of the signal distribution. This is consistent with the idea that histone modifications merely have the role of starting/stopping transcription. On the contrary, RPKM is a measure of signal distribution. It is based on the assumption that a significant change in the phenotype is triggered only when a high quantification of the signal is uniformly spread along the genome. In this case, histone modifications would have the role of making the entire gene sequence accessible/hidden to facilitate/prevent transcription.

The results reported in Figure 3 and Table 2 show that, similar to gene expression, in most cases the signal (the number of peaks) is almost absent. This is especially evident using RPKM normalisation. Indeed, after feature selection only a few genes are retained. This indicates the presence of long genes having a high enough number of peaks to pass the filtering threshold for CPM but not RPKM. However, as the intersections of the genes retained with CPM and RPKM show, the opposite phenomenon is also present. In fact, there are short genes whose peak concentration is not sufficient to pass CPM filtering but that have signal distribution exceeding that of RPKM. A further inspection of Table 2 also reveals that the number of active genes is quite constant for all the histone modification types. Although further investigation is required for a correct biological interpretation of this result, no histone modification signal appears to play a dominant role in the regulation

of gene expression. Accordingly, the displayed phenotype comes from the combination of the single modifications. As an example, in the imprinted genes, both the H3K4me3 open chromatin mark and the H3K9me3 compact chromatin mark are present at the promoter site [31].

Based on this observation, we used the SNF method [14] to integrate all the histone modification signals into a unified similarity network among phenotypes. The resulting network, shown in Figure 5, is a graph in which the nodes correspond to cell types and edges are weighted with a similarity score between pairs of cell types. Edge thickness is proportional to the similarity score between connected cell types, so that thicker edges connect cells with similar profiles. The similarity networks of the single histone modifications can be found in the Supplementary Material (Figures S1–S6). Supplementary Material are numbered according to the order in which the modifications are reported in Table 2. All the networks are plotted with the Gephi software [32] using the ForceAtlas2 visualisation algorithm [32]. From observation of the single-modification networks and the fused network, it emerges that strong and common links are promoted by similarity network fusion, as expected. As an example, in Figure 5 cells of the innate immune system (neutrophils, monocytes, macrophages, eosinophils) are tightly linked. This is coherent with the presence of strong links (high similarity scores) among those cells in most of the single modification networks. Another observation regards the strong link in Figure 5 between the "endothelial cell of umbilical vein (proliferating)" and "effector memory CD8-positive, alpha-beta T cell". The similarity score between these two cell types is not very high in the single-modification networks (it is slightly higher in Supplementary Figure S4, representing H3K4me1), but it has a similar value in all the networks. This common link is therefore enhanced by the fusion procedure. Overall, the fused network is a good representation of the combination of the single networks, thus giving an overview of the simultaneous effect of histone modifications in haematopoietic cell differentiation.

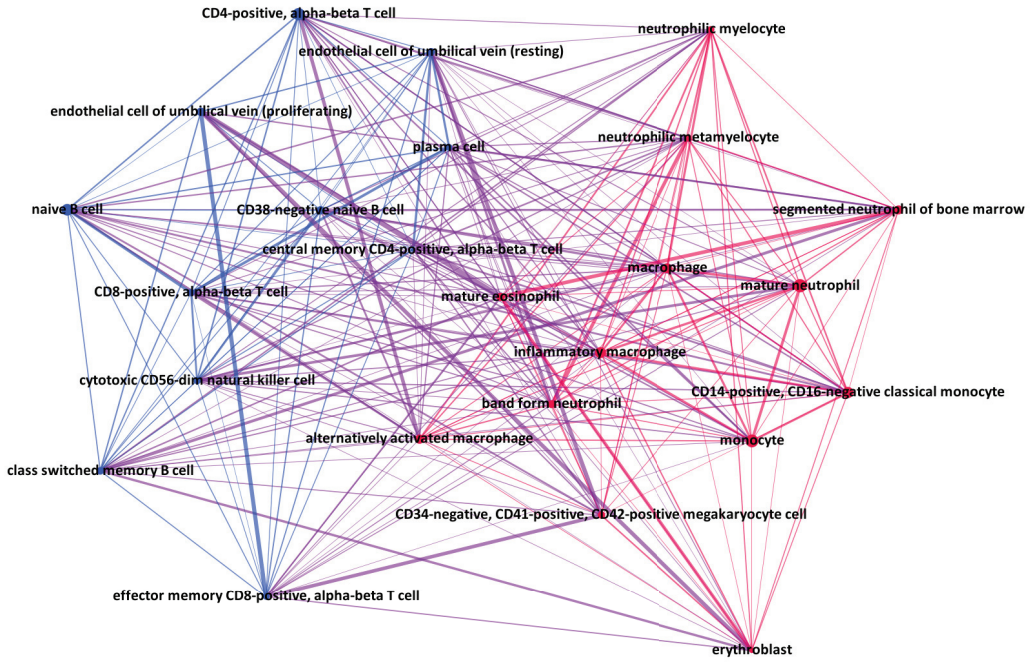

Figure 5. Similarity network of cell types obtained after applying the SNF method. Nodes are coloured according to the classical hypothesis on haematopoiesis: pink nodes correspond to cells labelled as "myeloid"; blue nodes correspond to cells labelled as "lymphoid". Edge thickness is proportional to the similarity score between connected cell types.

The SNF network and the similarity networks of the single histone modifications are exploited for the application of the proposed hypothesis testing model. In order to apply this model, the similarity scores were turned into dissimilarities. The hypothesis testing scheme was then applied to the resulting networks for testing a hypothesis on the biological process of haematopoiesis. More specifically, we evaluated the separation induced on the graphs by differentiation into myeloid and lymphoid lineages, i.e., the first split in the classical haematopoietic tree (see Figure 2). In the ideal case, the cost of the graph cut that partitions the SNF network into the two groups corresponding to the two lineages should be maximum. Indeed, the weights of edges between cell types of the same lineage should be stronger (equivalently, the dissimilarity score should be lower) than those between cell types of different lineages. The results reported in Figure 4 show that the partition separating myeloid and lymphoid cell types is nearly best-case. This indicates that the classic myeloid/lymphoid differentiation branching is a reasonable approximation of the haematopoietic process. However, the same results leave room for concluding that this model in not accurate enough to capture the complexity of haematopoiesis. Interestingly, by applying the hypothesis testing model to the single histone modification graphs, we found that all the signals approximate the classical model with comparable scores. This, once again, can be considered confirmation of the hypothesis that all histone modification marks cooperate for the development of the displayed phenotype.

Overall, the experiments have proven that histone modification marks can be quantified using high resolution peaks. This quantification behaves similarly to gene expression, with only a few genes containing a noticeable number of peaks. Moreover, the analysis of dissimilarity networks between 24 cell types belonging to the haematopoietic tree has shown a close relationship between a given phenotype and a profile of the modification marks. This opens for exploitation differential analysis tools to identify genes involved in a phenotype of interest.

5. Conclusions

Histone modifications are complex signals which regulate gene expression by modifying the three-dimensional structure of chromatin. By consequence, genes become more or less accessible for transcription. The complexity of these signals makes their mining very difficult.

In this paper, we have shown that high-resolution peak counting (down to a few bps) is a reasonable approach to build per-gene profiles of histone modification marks. Experimental analysis of the signals of six histone modifications belonging to 24 cell types highlights that these profiles follow a similar distribution to that of gene expression. The relevance of the peak-based analysis of histone profiles was validated by computationally assessing the classic lymphoid/myeloid differentiation at the first level of the haematopoietic tree. Indeed, our experiments confirm that the classic haematopoietic model fairly approximates the biological process, although suggesting that it does not completely capture its complexity.

In addition to the contribution on the specific topic of haematopoiesis, our work constitutes an advance in epigenetics by providing a framework for analysing histone modification data. Indeed, the signal distribution of histone modification profiles allows the use of standard differential expression techniques to identify genes whose modifications are involved in a given phenotype.

Finally, the proposed graph-based methodology can be easily applied to other application domains where hypotheses on the separation of a population into subgroups must be evaluated.

Supplementary Materials: The following supporting information can be downloaded at: https://www.mdpi.com/article/10.3390/math10111842/s1. The similarity networks of the single histone modifications.

Author Contributions: Data curation, F.B.; Methodology, F.G.; Software, F.B.; Supervision, M.B.; Writing—original draft, F.B., M.B. and F.G. All authors have read and agreed to the published version of the manuscript.

Funding: This research received no external funding.

Institutional Review Board Statement: Not applicable.

Informed Consent Statement: Not applicable.

Data Availability Statement: The data used to build epigenetic profiles of cells are available in the 2020-10 release at the *International Human Epigenome Consortium (IHEC)* [8]. They can be downloaded from https://epigenomesportal.ca/ihec/, accessed on 23 March 2022. The pre-processed data and the code to perform the analysis of the paper are available at https://gitlab.com/gbi1/gbi-of-histone-modifications/, accessed on 23 March 2022.

Acknowledgments: The authors would like to thank Pietro Liò for his useful advice and suggestions.

Conflicts of Interest: The authors declare no conflict of interest.

References

1. Hizume, K.; Yoshimura, S.H.; Takeyasu, K. Linker histone H1 per se can induce three-dimensional folding of chromatin fiber. *Biochemistry* **2005**, *44*, 12978–12989. [CrossRef] [PubMed]
2. Peterson, C.L.; Laniel, M.A. Histones and histone modifications. *Curr. Biol.* **2004**, *14*, R546–R551. [CrossRef] [PubMed]
3. Jenuwein, T.; Allis, C.D. Translating the histone code. *Science* **2001**, *293*, 1074–1080. [CrossRef] [PubMed]
4. Kimura, H. Histone modifications for human epigenome analysis. *J. Hum. Genet.* **2013**, *58*, 439–445. [CrossRef]
5. Karlić, R.; Chung, H.R.; Lasserre, J.; Vlahoviček, K.; Vingron, M. Histone modification levels are predictive for gene expression. *Proc. Natl. Acad. Sci. USA* **2010**, *107*, 2926–2931. [CrossRef]
6. Mardis, E.R. ChIP-seq: Welcome to the new frontier. *Nat. Methods* **2007**, *4*, 613–614. [CrossRef]
7. O'Geen, H.; Echipare, L.; Farnham, P.J. Using ChIP-seq technology to generate high-resolution profiles of histone modifications. In *Epigenetics Protocols*; Springer: Berlin/Heidelberg, Germany, 2011; pp. 265–286.
8. Bujold, D.; Morais, D.A.d.; Gauthier, C.; Côté, C.; Caron, M.; Kwan, T.; Chen, K.C.; Laperle, J.; Markovits, A.N.; Pastinen, T.; et al. The International Human Epigenome Consortium Data Portal. *Cell Syst.* **2016**, *3*, 496–499.E2. [CrossRef]
9. Lawrence, M.; Daujat, S.; Schneider, R. Lateral Thinking: How Histone Modifications Regulate Gene Expression. *Trends Genet.* **2016**, *32*, 42–56. [CrossRef]
10. Bannister, A.; Kouzarides, T. Regulation of chromatin by histone modifications. *Cell Res.* **2011**, *21*, 381–395. [CrossRef]
11. Pepke, S.; Wold, B.; Mortazavi, A. Computation for ChIP-seq and RNA-seq studies. *Nat. Methods* **2009**, *6*, S22–S32. [CrossRef]
12. Vaissière, T.; Sawan, C.; Herceg, Z. Epigenetic interplay between histone modifications and DNA methylation in gene silencing. *Mutat. Res. Mutat. Res.* **2008**, *659*, 40–48. [CrossRef] [PubMed]
13. Wang, B.; Jiang, J.; Wang, W.; Zhou, Z.H.; Tu, Z. Unsupervised metric fusion by cross diffusion. In Proceedings of the 2012 IEEE Conference on Computer Vision and Pattern Recognition, Providence, RI, USA, 16–21 June 2012; pp. 2997–3004. [CrossRef]
14. Wang, B.; Mezlini, A.; Demir, F.; Fiume, M.; Tu, Z.; Brudno, M.; Haibe-Kains, B.; Goldenberg, A. Similarity network fusion for aggregating data types on a genomic scale. *Nat. Methods* **2014**, *11*, 333–337. [CrossRef] [PubMed]
15. Prchal, J.T.; Throckmorton, D.W.; Carroll, A.J.; Fuson, E.W.; Gams, R.A.; Prchal, J.F. A common progenitor for human myeloid and lymphoid cells. *Nature* **1978**, *274*, 590–591. [CrossRef] [PubMed]
16. Blahnik, K.R.; Dou, L.; O'Geen, H.; McPhillips, T.; Xu, X.; Cao, A.R.; Iyengar, S.; Nicolet, C.M.; Ludäscher, B.; Korf, I.; et al. Sole-Search: An integrated analysis program for peak detection and functional annotation using ChIP–seq data. *Nucleic Acids Res.* **2010**, *38*, e13. [CrossRef] [PubMed]
17. Mortazavi, A.; Williams, B.A.; McCue, K.; Schaeffer, L.; Wold, B. Mapping and quantifying mammalian transcriptomes by RNA-Seq. *Nat. Methods* **2008**, *5*, 621. [CrossRef]
18. Lloyd, S. Least squares quantization in PCM. *IEEE Trans. Inf. Theory* **1982**, *28*, 129–137. [CrossRef]
19. R Core Team. *R: A Language and Environment for Statistical Computing*; R Foundation for Statistical Computing: Vienna, Austria, 2017.
20. Thorndike, R.L. Who belongs in the family? *Psychometrika* **1953**, *18*, 267–276. [CrossRef]
21. Tritchler, D.; Parkhomenko, E.; Beyene, J. Filtering genes for cluster and network analysis. *BMC Bioinform.* **2009**, *10*, 193. [CrossRef]
22. Karger, D.R. Global Min-cuts in RNC, and Other Ramifications of a Simple Min-Cut Algorithm. In Proceedings of the SODA, Austin, TX, USA, 25–27 January 1993; Volume 93, pp. 21–30.
23. Ford, L.R.; Fulkerson, D.R. Maximal flow through a network. *Can. J. Math.* **1956**, *8*, 399–404. [CrossRef]

24. Karp, R.M. Reducibility among combinatorial problems. In *Complexity of Computer Computations*; Springer: Berlin/Heidelberg, Germany, 1972; pp. 85–103.
25. Bansal, V.; Bafna, V. HapCUT: An efficient and accurate algorithm for the haplotype assembly problem. *Bioinformatics* **2008**, *24*, i153–i159. [CrossRef]
26. Stoer, M.; Wagner, F. A simple min-cut algorithm. *J. ACM (JACM)* **1997**, *44*, 585–591. [CrossRef]
27. Church, B.V.; Williams, H.T.; Mar, J.C. Investigating skewness to understand gene expression heterogeneity in large patient cohorts. *BMC Bioinform.* **2019**, *20*, 1–14. [CrossRef] [PubMed]
28. De Torrenté, L.; Zimmerman, S.; Suzuki, M.; Christopeit, M.; Greally, J.M.; Mar, J.C. The shape of gene expression distributions matter: How incorporating distribution shape improves the interpretation of cancer transcriptomic data. *BMC Bioinform.* **2020**, *21*, 1–18. [CrossRef] [PubMed]
29. Alberti-Servera, L.; von Muenchow, L.; Tsapogas, P.; Capoferri, G.; Eschbach, K.; Beisel, C.; Ceredig, R.; Ivanek, R.; Rolink, A. Single-cell RNA sequencing reveals developmental heterogeneity among early lymphoid progenitors. *EMBO J.* **2017**, *36*, 3619–3633. [CrossRef]
30. Perié, L.; Duffy, K.R.; Kok, L.; de Boer, R.J.; Schumacher, T.N. The branching point in erythro-myeloid differentiation. *Cell* **2015**, *163*, 1655–1662. [CrossRef]
31. Mikkelsen, T.S.; Ku, M.; Jaffe, D.B.; Issac, B.; Lieberman, E.; Giannoukos, G.; Alvarez, P.; Brockman, W.; Kim, T.K.; Koche, R.P.; et al. Genome-wide maps of chromatin state in pluripotent and lineage-committed cells. *Nature* **2007**, *448*, 553–560. [CrossRef]
32. Jacomy, M.; Venturini, T.; Heymann, S.; Bastian, M. ForceAtlas2, a continuous graph layout algorithm for handy network visualization designed for the Gephi software. *PLoS ONE* **2014**, *9*, e98679. [CrossRef]

mathematics

MDPI

Article

On the Effects of Boundary Conditions in One-Dimensional Models of Hemodynamics

Gerasim V. Krivovichev

Faculty of Applied Mathematics and Control Processes, Saint Petersburg State University, 7/9 Universitetskaya Nab., 199034 Saint Petersburg, Russia; g.krivovichev@spbu.ru

Abstract: The paper is devoted to the theoretical analysis of the effects of boundary conditions on the solutions of the system of one-dimensional (1D) hemodynamics. The integral inequalities, which realize the energy inequalities for the solutions of initial-boundary-value problems, are obtained. It is demonstrated that the unphysical unbounded solutions can take place for the case of bounded functions from boundary conditions. For the periodic boundary conditions, the integral estimation illustrates the correct behavior of the solution. For this case of boundary conditions, the effective Fourier method for the analytical solution is proposed. The analytical solutions, obtained by this approach, can be used for the comparison of different 1D blood-flow models. The results obtained in the paper allow for an the alternatively view of the stated boundary conditions and can explain some problems, which can arise in numerical simulations. They expand the possibilities of the application of analytical methods in the field of blood-flow simulation. The results can be useful for the specialists on blood-flow modeling.

Keywords: blood flow; one-dimensional model; boundary conditions

MSC: 76Z05; 35F46

1. Introduction

Nowadays, the mathematical models of blood flow are widely used in applied medical investigations as a powerful tool for the prediction of the results of surgeries and different vascular defects (such as stenoses and aneurysms) [1,2]. For the simulation of processes in large vascular systems, 1D models are widely used in practice [3,4]. These models are obtained by the averaging of the Navier—Stokes equations on the vessel cross-section [5–7]. As a result, the model based on the hyperbolic nonlinear system of 1D equations on the cross-sectional area and flow rate (or mean velocity) is constructed. These models can be coupled with 0D and 3D models [8], and the obtained results are close to the averaged solutions of 3D models [9].

From the physical viewpoint, blood is considered as an incompressible viscous fluid [10]. In most works, the viscosity of blood is described by the Newtonian model with the proper representation of the velocity profile [5,7,8,11]. However, in many works [12–19] the viscosity is ignored, and blood is considered as an inviscid fluid. This approximation can be used for the case of large arteries and veins, where the viscosity is not as important as it is in small vessels.

In recent decades, 1D models have been used for the simulation of many processes in physiology and medicine. For example, they have been applied to the simulation of system partial hepatectomy [3]; brain hemodynamics predictions [6,20]; the simulation of flow in large arteries [9] and near bifurcations [8]; the modelling of flows in systems with stenosed vessels [21]; the analysis of blood-flow effects on cerebrospinal fluid dynamics [22]; the analysis of flows in tapered vessels [23]; and the simulation of flows in arterial systems [24–26]. It must be noted that the results of the simulations are close to

the results of the experiments (e.g., see [24,25]). Unfortunately, according to the nonlinear nature of the main equations, the different problems for such models in the general case can be solved only numerically. However, analytical methods are also actual in qualitative investigations of 1D hemodynamics because they can be used for the analysis of the qualitative properties of the solution (such as stability, dispersion, dissipation, etc.); for the comparison of different rheological models of blood; and for providing an effective tool for testing programs, which implement the algorithms of numerical methods [27].

The presented paper is devoted to the analytical investigation of possible qualitative properties of the solutions of 1D models of blood flow. It must be noted that investigations of this kind are presented in a relatively small number of works. For example, in the papers of Ashmetkov et al. [28,29], the linearized system for pressure and velocity is considered, and the method for the obtaining of analytical solutions, based on the reflection of waves, is proposed. Paquerot and Remoissenet [30] present a nonlinear model for the description of pressure-wave propagation in arteries. The model leads to the solution of the Boussinesq-type scalar equation. The one-soliton and two-soliton solutions, obtained by the Hirota method, are analyzed. Ilyin in [31] construct the model, based on the inviscid Burgers equation, and apply the method of characteristics for the solution of an initial-boundary-value problem on the semi-infinite interval in order to obtain the nonlinear pressure–velocity relations. Canic et al. [7] present the proof of the theorem, which provides the condition of the existence of a smooth global solution of a nonlinear conservative law system, and provide the conditions for the shock formation. The recent work [32] is devoted to the analysis of the well-posedness of the system of 1D equations in a network in the case of the vessels with viscoelastic properties. The conditions of the existence and uniqueness of the maximal strong solution are obtained, such as the stability estimations.

In the presented paper, we try to expand the field of application of analytical methods in the analysis of 1D blood-flow models and to demonstrate that the problems for linearized 1D system of inviscid hemodynamics can have physically irrelevant (unbounded) solutions for the physically relevant (bounded) boundary conditions. It is demonstrated that for the periodic conditions, this problem is not observed. For this case of boundary conditions, the simple and effective Fourier method is proposed.

The paper has the following structure. In Section 2, the mathematical model and problem statement are presented. In Section 3, the integral estimations of the solution in cases of different boundary conditions are obtained. Some concluding remarks are made in Section 4.

2. Model

The 1D model of the inviscid blood flow in a distensible vessel with impermeable walls is based on the averaged incompressibility condition and momentum equation [6,31]:

$$\frac{\partial A}{\partial t}+\frac{\partial Q}{\partial z}=0, \quad \frac{\partial Q}{\partial t}+\frac{\partial}{\partial z}\left(\frac{Q^2}{A}\right)+\frac{A}{\rho}\frac{\partial P}{\partial z}=0, \tag{1}$$

where t is a time, z is a cylindrical coordinate, $A(t,z)$ is the cross-sectional area, $Q(t,z)$ is the flow rate ($Q=AU$, where U is the mean axial velocity), $P(t,z)$ is the pressure, and ρ is a constant density.

System (1) is closed by the equation-of-state $P=P(A)$. In the case of the arteries, the following equation is used [6,9]:

$$P-P_{ext}=P_d+\frac{\beta}{A_d}(\sqrt{A}-\sqrt{A_d}), \tag{2}$$

where P_{ext} is the external pressure; P_d and A_d are the diastolic pressure and cross-sectional area; $\beta=\frac{4}{3}\sqrt{\pi}Eh$, where E is the Young's modulus; and h is the vessel wall thickness. In the paper, the case of constant values of P_d, A_d, E, and h is considered.

After the substitution of (2) into (1), the following system is obtained:

$$\frac{\partial A}{\partial t}+\frac{\partial Q}{\partial z}=0,\quad \frac{\partial Q}{\partial t}+\frac{\partial}{\partial z}\left(\frac{Q^2}{A}\right)+\gamma\sqrt{A}\frac{\partial A}{\partial z}=0, \tag{3}$$

where $\gamma=\frac{\beta}{2\rho A_d}$.

Let the following dimensionless variables be introduced:

$$\tilde{z}=\frac{z}{L_c},\quad \tilde{t}=\frac{t}{T_c},\quad \tilde{A}=\frac{A}{A_c},\quad \tilde{P}=\frac{P}{\rho U_c^2},\quad \tilde{Q}=\frac{Q}{A_c U_c}, \tag{4}$$

where L_c, T_c, A_c, U_c are the characteristic length, time, cross-sectional area, and velocity. The value of L_c is considered as a vessel length, U_c can be estimated by the maximal wave speed, T_c is computed from L_c and U_c, and A_c can be estimated, for example, from the diastolic cross-sectional radius. The tilde sign in (4) will be ignored in the text below.

After the substitution of (4) into (3), the following equations are obtained:

$$\frac{\partial A}{\partial t}+\frac{\partial Q}{\partial z}=0,\quad \frac{\partial Q}{\partial t}+\frac{\partial}{\partial z}\left(\frac{Q^2}{A}\right)+\xi\sqrt{A}\frac{\partial A}{\partial z}=0, \tag{5}$$

where $\xi=\gamma\frac{\sqrt{A_c}}{U_c^2}$.

The interesting results on the solutions of the initial-boundary-value problems for (5) can be demonstrated for the linearized version of this system. For the linearization, we represent the solution of (5) as $A=\overline{A}+a(t,z)$, $Q=\overline{Q}+q(t,z)$, where $(\overline{A},\overline{Q})$ is the constant steady-state solution of (5), and $a(t,z)$, $q(t,z)$ are the small perturbations, as their first derivatives.

The linearized version of (5) is written as

$$\frac{\partial a}{\partial t}+\frac{\partial q}{\partial z}=0,\quad \frac{\partial q}{\partial t}+d_1\frac{\partial a}{\partial z}+d_2\frac{\partial q}{\partial z}=0, \tag{6}$$

where

$$d_1=\xi\sqrt{\overline{A}}-\frac{\overline{Q}^2}{\overline{A}^2},\quad d_2=\frac{2\overline{Q}}{\overline{A}}.$$

It must be noted that the speed of sound is presented as [9]: $c=\sqrt{\frac{\beta}{2\rho A_d}}A^{\frac{1}{4}}$. So, $c^2=\gamma\sqrt{A}$, and in the dimensionless variables it is written as $c^2=\xi\sqrt{A}$. At the same time, $\overline{U}=\overline{Q}/\overline{A}$. The blood flow in physiological conditions is realized when $|U|<c$ [33], so the coefficient d_1 in (6) is strictly positive.

Let the single blood vessel, corresponding to the spatial interval $z\in[0,l]$ be considered, and the following initial and boundary conditions are stated for (6):

$$a(0,z)=\varphi(z),\quad q(0,z)=\psi(z), \tag{7}$$

$$\delta_1 a(t,0)+\delta_2 q(t,0)=\chi_1(t),\quad \beta_1 a(t,l)+\beta_2 q(t,l)=\chi_2(t), \tag{8}$$

where δ_1, δ_2, β_1, β_2 are the known coefficients, and $\delta_1^2+\delta_2^2\neq 0$, $\beta_1^2+\beta_2^2\neq 0$, and $\varphi(z)$, $\psi(z)$, $\chi_1(t)$, $\chi_2(t)$ are the known functions, which are smooth enough. To ensure the smoothness of solution in $C^1([0,+\infty)\times[0,l])$, the following compatibility conditions are imposed:

$$\delta_1\varphi(0)+\delta_2\psi(0)=\chi_1(0),\quad \beta_1\varphi(l)+\beta_2\psi(l)=\chi_2(0),$$

$$\delta_2 d_1\varphi'(0)+(\delta_1+\delta_2 d_2)\psi'(0)=-\dot{\chi}_1(0),\quad \beta_2 d_1\varphi'(l)+(\beta_1+\beta_2 d_2)\psi'(l)=-\dot{\chi}_2(0).$$

The physiologically adequate solutions of (6)–(8) are expected to be bounded at $\{(t,z)$: $t \in [0,+\infty), z \in [0,l]\}$:

$$\max_{z\in[0,l]}(|a(t,z)|,|q(t,z)|) \le C = const, t \to +\infty. \quad (9)$$

As it will be demonstrated in Section 3, for the bounded and physically relevant functions $\chi_1(t)$ and $\chi_2(t)$, the situation, when the realistic condition (9) is not realized, can be observed.

3. Results

In this section, the integral inequalities, which provide the energy estimates of the solutions of (6)–(8), are obtained in order to demonstrate that the condition (9) can be broken.

Let we rewrite the system (6) in the matrix-vector form:

$$\frac{\partial \mathbf{u}}{\partial t} + \mathbf{A}\frac{\partial \mathbf{u}}{\partial z} = \mathbf{0},$$

where $\mathbf{u} = (a,q)^T$. Matrix $\mathbf{A}$ has two real eigenvalues:

$$\lambda_{1,2} = \frac{d_2 \pm \sqrt{d_2^2 + 4d_1}}{2}.$$

As can be seen, $\lambda_1 > 0$ and $\lambda_2 < 0$. Without the loss of generality, let the case of $\overline{U} > 0$ be considered, so $d_2 > 0$, and we obtain that $\lambda_1 > |\lambda_2|$.

The matrix $\mathbf{A}$ can be presented as $\mathbf{A} = \mathbf{R\Lambda L}$, where $\mathbf{\Lambda}$ is the diagonal matrix of eigenvalues and $\mathbf{L}$, $\mathbf{R}$ are the matrices of left and right eigenvectors of $\mathbf{A}$, respectively.

Theorem 1. *Let the linear function $p(z)$ be presented as*

$$p(z) = p(0)\frac{l-z}{l} + p(l)\frac{z}{l}, \quad (10)$$

where $p(0) > 0$, $p(l) > 0$ and the following inequalities are realized:

$$|p(0)e_1| \le \frac{1}{2}, \quad \left|\frac{e_2}{p(l)}\right| \le \frac{1}{2}, \quad (11)$$

where

$$e_1 = \frac{\delta_1 R_{12} + \delta_2 R_{22}}{\delta_1 R_{11} + \delta_2 R_{21}}, \quad e_2 = \frac{\beta_1 R_{11} + \beta_2 R_{21}}{\beta_1 R_{12} + \beta_2 R_{22}},$$

where R_{ij} are the components of matrix $\mathbf{R}$.

Then, the following inequality takes place:

$$\int_0^l \left(p^2(z)\Big(L_{11}a(t,z) + L_{12}q(t,z)\Big)^2 + \Big(L_{21}a(t,z) + L_{22}q(t,z)\Big)^2\right)dz \le$$

$$\exp(\Lambda t)\int_0^l \left(p^2(z)\Big(L_{11}\varphi(z) + L_{12}\psi(z)\Big)^2 + \Big(L_{21}\varphi(z) + L_{22}\psi(z)\Big)^2\right)dz +$$

$$2\lambda_1 \exp(\Lambda t)\int_0^t \left(p^2(0)\frac{\chi_1^2(\tau)}{(\delta_1 R_{11} + \delta_2 R_{21})^2} + \frac{\chi_2^2(\tau)}{(\beta_1 R_{12} + \beta_2 R_{22})^2}\right)d\tau, \quad (12)$$

where

$$\Lambda = \frac{2\lambda_1 |p(l) - p(0)|}{l \min(p(0), p(l))},$$

and L_{ij} are the components of matrix $\mathbf{L}$.

Proof. We introduce the new variables w_1, w_2 as: $\mathbf{u} = \mathbf{R}\mathbf{w}$, and according to the fact that $\mathbf{L} = \mathbf{R}^{-1}$, system (6) is rewritten as:

$$\frac{\partial w_1}{\partial t} + \lambda_1 \frac{\partial w_1}{\partial z} = 0, \quad \frac{\partial w_2}{\partial t} + \lambda_2 \frac{\partial w_2}{\partial z} = 0, \tag{13}$$

where $w_1 = L_{11}a + L_{12}q$, $w_2 = L_{21}a + L_{22}q$.

The initial and boundary conditions are rewritten as

$$w_1(0,z) = \tilde{\varphi}(z) = L_{11}\varphi(z) + L_{12}\psi(z), \quad w_2(0,z) = \tilde{\psi}(z) = L_{21}\varphi(z) + L_{22}\psi(z),$$

$$w_1(t,0) + e_1 w_2(t,0) = \tilde{\chi}_1(t), \quad w_2(t,l) + e_2 w_1(t,l) = \tilde{\chi}_2(t),$$

where

$$\tilde{\chi}_1(t) = \frac{\chi_1(t)}{\delta_1 R_{11} + \delta_2 R_{21}}, \quad \tilde{\chi}_2(t) = \frac{\chi_2(t)}{\beta_1 R_{12} + \beta_2 R_{22}}.$$

The following new variables are introduced:

$$\overline{w}_1(t,z) = p(z)w_1(t,z), \quad \overline{w}_2(t,z) = w_2(t,z).$$

It must be noted that function $p(z)$ with properties (11) can be selected for any finite values of e_1 and e_2.

So, the Equation (13) are rewritten as

$$\frac{\partial \overline{w}_1}{\partial t} + \lambda_1 \frac{\partial \overline{w}_1}{\partial z} - g(z)\overline{w}_1 = 0, \quad \frac{\partial \overline{w}_2}{\partial t} + \lambda_2 \frac{\partial \overline{w}_2}{\partial z} = 0, \tag{14}$$

where $g(z) = \frac{\lambda_1 p'(z)}{p(z)}$. The initial and boundary conditions are rewritten as

$$\overline{w}_1(0,z) = \overline{\varphi}(z) = p(z)\tilde{\varphi}(z), \quad \overline{w}_2(0,z) = \tilde{\psi}(z), \tag{15}$$

$$\overline{w}_1(t,0) + \bar{e}_1 \overline{w}_2(0,z) = \overline{\chi}_1(t), \quad \overline{w}_2(t,l) + \bar{e}_2 \overline{w}_1(t,l) = \overline{\chi}_2(t), \tag{16}$$

where

$$\bar{e}_1 = e_1 p(0), \quad \bar{e}_2 = \frac{e_2}{p(l)}, \quad \overline{\chi}_1(t) = p(0)\tilde{\chi}_1(t), \quad \overline{\chi}_2(t) = \tilde{\chi}_2(t).$$

We consider some functions $f(z)$, $k(z)$, $h(t)$ and let the following relation take place for $z = a$: $f(a) = -sk(a) + h(t)$, where $s \in \mathrm{R}$. It is easy to demonstrate that $f^2(a) \leq 2h^2(t) + 2s^2k^2(a)$, so $f^2(a) - k^2(a) \leq 2h^2(t) - (1 - 2s^2)k^2(a)$. With the use of this inequality we obtain that

$$\overline{w}_1^2(t,0) - \overline{w}_2^2(t,0) \leq 2\overline{\chi}_1^2(t) - (1 - 2\bar{e}_1^2)\overline{w}_2^2(t,0),$$

and according to the condition $|\bar{e}_1| \leq \frac{1}{2}$ (see (11)), the following inequality can be written:

$$\overline{w}_1^2(t,0) - \overline{w}_2^2(t,0) \leq 2\overline{\chi}_1^2(t), \tag{17}$$

and by the same way, we obtain that

$$\overline{w}_2^2(t,l) - \overline{w}_1^2(t,l) \leq 2\overline{\chi}_2^2(t). \tag{18}$$

It is easy to demonstrate that

$$\frac{\partial}{\partial t}\int_0^l \overline{w}_1^2 dz = -\lambda_1 \overline{w}_1^2\Big|_0^l + 2\int_0^l g\overline{w}_1^2 dz, \quad \frac{\partial}{\partial t}\int_0^l \overline{w}_2^2 dz = -\lambda_1 \overline{w}_2^2\Big|_0^l.$$

So, the following inequality is written:

$$\frac{\partial}{\partial t}\int\limits_0^l(\overline{w}_1^2+\overline{w}_2^2)dz=-\lambda_1\overline{w}_1^2\big|_0^l-\lambda_2\overline{w}_2^2\big|_0^l+2\int\limits_0^l g\overline{w}_1^2dz=-\lambda_1\overline{w}_1^2\big|_0^l+$$

$$|\lambda_2|\overline{w}_2^2\big|_0^l+2\int\limits_0^l g\overline{w}_1^2dz\le\lambda_1(\overline{w}_2^2-\overline{w}_1^2)\big|_0^l+2\int\limits_0^l g\overline{w}_1^2dz.$$

From (17), (18) we obtain that

$$\frac{\partial}{\partial t}\int\limits_0^l(\overline{w}_1^2+\overline{w}_2^2)dz\le 2\lambda_1(\overline{\chi}_1^2(t)+\overline{\chi}_2^2(t))+2\int\limits_0^l g\overline{w}_1^2dz.$$

With the use of the expression for $p(z)$ and the integral mean value theorem, the following inequality can be obtained:

$$2\int\limits_0^l g\overline{w}_1^2dz\le\Lambda\int\limits_0^l\overline{w}_1^2dz.$$

So, the following estimation takes place:

$$\frac{\partial}{\partial t}\int\limits_0^l(\overline{w}_1^2+\overline{w}_2^2)dz\le 2\lambda_1(\overline{\chi}_1^2(t)+\overline{\chi}_2^2(t))+\Lambda\int\limits_0^l(\overline{w}_1^2+\overline{w}_2^2)dz. \tag{19}$$

After the integration of (19) in time, we obtain the following inequality:

$$\frac{\partial}{\partial t}\int\limits_0^l(\overline{w}_1^2+\overline{w}_2^2)dz\le\exp(\Lambda t)\int\limits_0^l(\overline{\varphi}^2(z)+\overline{\psi}^2(z))dz+$$

$$2\lambda_1\exp(\Lambda t)\int\limits_0^t(\overline{\chi}_1^2(\tau)+\overline{\chi}_2^2(\tau))d\tau,$$

and from this inequality, after returning to the variables a and q, we can obtain (12). □

So, as we can see, according to (12), the problem (6)–(8) can have solutions, which are unbounded at $t\to+\infty$, even though the bounded functions $\chi_1(t)$ and $\chi_2(t)$ are considered, and the physically relevant condition (9) may not be realized.

3.1. Case of Boundary Conditions for q

It must be noted that for the special classes of boundary conditions, the integral extimations, which are different from (12), can be obtained. LWe consider system (6) with initial conditions (7) and the following boundary conditions:

$$q(t,0)=q_1(t),\quad q(t,l)=q_2(t). \tag{20}$$

Theorem 2. *Let $q_1(t)$, $q_2(t)\in C^1[0,+\infty)$. Then, the following integral inequality takes place:*

$$\int\limits_0^l\Big(a^2(t,z)+\frac{1}{d_1}\Big(q(t,z)-\frac{1}{l}(q_2(t)z-q_1(t)(z-l))\Big)^2\Big)dz\le$$

$$2\int_0^l \Big(\varphi^2(z)+\frac{1}{d_1}\Big(\psi(z)-\frac{1}{l}(q_2(0)z-q_1(0)(z-l))\Big)^2\Big)dz+\frac{2t}{l}\int_0^t (q_2(\tau)-q_1(\tau))^2 d\tau+$$

$$\frac{2t}{d_1 l^2}\int_0^t\int_0^l (d_2(q_2(\tau)-q_1(\tau))+\dot{q}_2(\tau)z-\dot{q}_1(\tau)(z-l))^2 dz d\tau. \tag{21}$$

Proof. The new function, which satisfies the boundary condition (20), is introduced:

$$\mathcal{Q}(t,z)=q(t,z)-\frac{1}{l}(q_2(t)z-q_1(t)(z-l)).$$

So, the system (6) is rewritten as

$$\frac{\partial a}{\partial t}+\frac{\partial \mathcal{Q}}{\partial z}=F(t),\quad \frac{\partial \mathcal{Q}}{\partial t}+d_1\frac{\partial a}{\partial z}+d_2\frac{\partial \mathcal{Q}}{\partial z}=G(t,z), \tag{22}$$

where

$$F(t)=\frac{q_1(t)-q_2(t)}{l},\quad G(t,z)=\frac{d_2(q_1(t)-q_2(t))-(\dot{q}_2(t)z-\dot{q}_1(t)(z-l))}{l}.$$

System (22) is considered with the following initial and boundary conditions:

$$a(0,z)=\varphi(z),\quad \mathcal{Q}(0,z)=\zeta(z),\quad \mathcal{Q}(t,0)=\mathcal{Q}(t,l)=0,$$

where $\zeta(z)=\psi(z)-\frac{q_2(0)z-q_1(0)(z-l)}{l}$. So, the inhomogeneous system (22) with the homogeneous boundary conditions for $\mathcal{Q}(t,z)$ is considered. According to the Duhamel's principle [34], the solution of this problem can be presented as

$$a(t,z)=\tilde{a}(t,z)+\int_0^t a_\tau(t,z;\tau)d\tau,\quad \mathcal{Q}(t,z)=\tilde{\mathcal{Q}}(t,z)+\int_0^t \mathcal{Q}_\tau(t,z;\tau)d\tau, \tag{23}$$

where $(\tilde{a},\tilde{\mathcal{Q}})$ is the solution of the following problem:

$$\frac{\partial \tilde{a}}{\partial t}+\frac{\partial \tilde{\mathcal{Q}}}{\partial z}=0,\quad \frac{\partial \tilde{\mathcal{Q}}}{\partial t}+d_1\frac{\partial \tilde{a}}{\partial z}+d_2\frac{\partial \tilde{\mathcal{Q}}}{\partial z}=0,\quad t\in(0,+\infty), z\in(0,l), \tag{24}$$

$$\tilde{a}(0,z)=\varphi(z),\quad \tilde{\mathcal{Q}}(t,z)=\zeta(z),$$
$$\tilde{\mathcal{Q}}(t,0)=\tilde{\mathcal{Q}}(t,l)=0, \tag{25}$$

and $(a_\tau,\mathcal{Q}_\tau)$ is the solution of the following problem:

$$\frac{\partial a_\tau}{\partial t}+\frac{\partial \mathcal{Q}_\tau}{\partial z}=0,\quad \frac{\partial \mathcal{Q}_\tau}{\partial t}+d_1\frac{\partial a_\tau}{\partial z}+d_2\frac{\partial \mathcal{Q}_\tau}{\partial z}=0,\quad t\in(\tau,+\infty), z\in(0,l),$$

$$a_\tau(\tau,z;\tau)=F(\tau),\quad \mathcal{Q}_\tau(\tau,z;\tau)=G(\tau,z),\quad \mathcal{Q}_\tau(t,0;\tau)=\mathcal{Q}_\tau(t,l;\tau)=0.$$

We obtain the expression for the time derivative of $\int_0^l(\tilde{a}^2(t,z)+\tilde{\mathcal{Q}}^2(t,z))dz$:

$$\frac{\partial}{\partial t}\int_0^l \tilde{a}^2(t,z)dz=-2\int_0^l \tilde{a}(t,z)\frac{\partial \tilde{\mathcal{Q}}}{\partial z}(t,z)dz=-2\Bigg(\tilde{a}(t,z)\tilde{\mathcal{Q}}(t,z)\Big|_0^l-$$

$$-\int_0^l \tilde{\mathcal{Q}}(t,z)\frac{\partial \tilde{a}}{\partial z}(t,z)dz\Bigg)=-\frac{2}{d_1}\int_0^l \mathcal{Q}(t,z)\frac{\partial \mathcal{Q}}{\partial t}(t,z)dz-\frac{2d_2}{d_1}\int_0^l \tilde{\mathcal{Q}}(t,z)\frac{\partial \tilde{\mathcal{Q}}}{\partial z}(t,z)dz=$$

$$= -\frac{1}{d_1}\frac{\partial}{\partial t}\int\limits_0^l \tilde{\mathcal{Q}}^2(t,z)dz,$$

where the boundary conditions (25) are taken into account.

So, we can obtain the following:

$$\int\limits_0^l \left(\tilde{a}^2(t,z) + \tilde{\mathcal{Q}}^2(t,z)\right)dz = \left(1 - \frac{1}{d_1}\right)\frac{\partial}{\partial t}\int\limits_0^l \tilde{\mathcal{Q}}^2(t,z)dz.$$

After the integration, the following equality is obtained:

$$\int\limits_0^l \left(\tilde{a}^2(t,z) + \frac{1}{d_1}\tilde{\mathcal{Q}}^2(t,z)\right)dz = \int\limits_0^l \left(\varphi^2(z) + \frac{1}{d_1}\zeta^2(z)\right)dz. \tag{26}$$

By the same operations we obtain

$$\int\limits_0^l \left(a_\tau^2(t,z;\tau) + \frac{1}{d_1}\mathcal{Q}_\tau^2(t,z;\tau)\right)dz = F^2(\tau)l + \frac{1}{d_1}\int\limits_0^l G^2(\tau,z)dz. \tag{27}$$

According to Equation (23):

$$\int\limits_0^l a^2(t,z)dz = \int\limits_0^l \left(\tilde{a}^2(t,z) + 2\tilde{a}(t,z)\int\limits_0^t a_\tau(t,z;\tau)d\tau + \left(\int\limits_0^t a_\tau(t,z;\tau)d\tau\right)^2\right)dz.$$

From $\int\limits_0^l \left(\tilde{a}(t,z) - \int\limits_0^t a_\tau(t,z;\tau)d\tau\right)^2 dz \geq 0$ we can obtain

$$2\int\limits_0^l \tilde{a}(t,z)\int\limits_0^t a_\tau(t,z;\tau)d\tau dz \leq \int\limits_0^l \left(\tilde{a}^2(t,z) + \left(\int\limits_0^t a_\tau(t,z;\tau)d\tau\right)^2\right)dz,$$

and the following inequality can be written:

$$\int\limits_0^l a^2(t,z)dz \leq 2\int\limits_0^l \left(\tilde{a}^2(t,z) + \left(\int\limits_0^t a_\tau(t,z;\tau)d\tau\right)^2\right)dz. \tag{28}$$

The same inequality takes place for $\mathcal{Q}(t,z)$.

So, the following estimation is obtained:

$$\int\limits_0^l \left(a^2(t,z) + \frac{1}{d_1}\mathcal{Q}^2(t,z)\right)dz \leq 2\int\limits_0^l \left(\tilde{a}^2(t,z) + \frac{1}{d_1}\tilde{\mathcal{Q}}^2(t,z)\right)dz +$$

$$+2\int\limits_0^l \left(\left(\int\limits_0^t a_\tau(t,z;\tau)d\tau\right)^2 + \frac{1}{d_1}\left(\int\limits_0^t \tilde{\mathcal{Q}}_\tau(t,z;\tau)d\tau\right)^2\right)dz. \tag{29}$$

According to the Cauchy–Schwarz inequality, we obtain

$$\left(\int_0^t a_\tau(t,z;\tau)d\tau\right)^2 \le t\int_0^t a_\tau^2(t,z;\tau)d\tau, \quad \left(\int_0^t \tilde{\mathcal{Q}}_\tau(t,z;\tau)d\tau\right)^2 \le t\int_0^t \tilde{\mathcal{Q}}_\tau^2(t,z;\tau)d\tau.$$

So, the following integral inequality can be obtained from (26)–(29):

$$\int_0^l \left(a^2(t,z)+\frac{1}{d_1}\mathcal{Q}^2(t,z)\right)dz \le 2\int_0^l \left(\varphi^2(z)+\frac{1}{d_1}\zeta^2(z)\right)+2tl\int_0^t F^2(\tau)d\tau+$$

$$+\frac{2t}{d_1}\int_0^l\int_0^t G^2(\tau,z)d\tau dz,$$

and after the return to the function $q(t,z)$ we can see, that inequality (21) is correct. □

As we can see, the last terms in (21) provide the possibility of the time-growing solutions for the bounded physically relevant functions $q_1(t)$ and $q_2(t)$. We construct the simple example, which illustrates this behavior. Let q_1 and q_2 be the constants $q_1 = C_1$, $q_2 = C_2$, $C_1 > C_2$. Let $\psi(z) = Dz + C_1$, where D = $\frac{C_2-C_1}{l} < 0$. Let $\varphi(z) = -\frac{d_2}{d_1}Dz$. This problem has the following solution:

$$q(t,z) = Dz + C_1, \quad a(t,z) = -Dt + \varphi(z).$$

So we can see that constant boundary conditions and bounded initial conditions lead to the unbounded unphysical ($a(t,z) \to +\infty$) solution.

In order to demonstrate the similar behavior in the fully nonlinear model (1), which is widely used in practice, the physiological example on the simulation of blood flow in the part of the human aorta can be considered. For the simulation, the segment Ao. V from aortic model, presented in [9], is chosen. For this case, the variable mechanical properties take place: $A_d = A_d(z)$, $\beta = \beta(z)$. For this vessel, $l = 15.2$ cm, the radius of the inlet cross-section R_{in} is equal to 1.25 cm, and the radius of the outlet cross-section R_{out} is equal to 0.99 cm. The $A_d(z)$ is chosen as

$$A_d(z) = \pi\left(R_{in} + \frac{R_{out}-R_{in}}{l}z\right)^2.$$

The values of β for inlet and outlet cross-sections are computed from the values of the speed of sound, presented in Table IV from [9], and $\beta(z)$ is considered as a linear function: $\beta(z) = \beta_{in} + \frac{\beta_{out}-\beta_{in}}{l}z$.

The following boundary conditions are stated: $Q(t,0) = q_1 = 500$ cm^3/s, $Q(t,l) = q_2 = 300$ cm^3/s, which are close to the typical values of Q from [9]. The initial conditions are stated as

$$A(0,z) = A_d(z), \quad Q(0,z) = \frac{q_2-q_1}{l}z + q_1.$$

The numerical simulations are realized on the time interval from 0 to 1 s. The second-order Lax–Wendroff scheme is used for the computations on the spatial grid with 100 nodes and the time grid with 10,000 nodes. The values of A in the boundary points are computed from the compatibility conditions (for details, see [26]).

In Figure 1, the results of the numerical simulations are presented. As can be seen from the plots of A in the left, middle, and right vessel points, for this type of bounded boundary and the initial conditions, the obtained solutions do not have any physical or physiological meaning because they lead to the unbounded values of A. So, for this practical example we have the same behavior as for the linear theory.

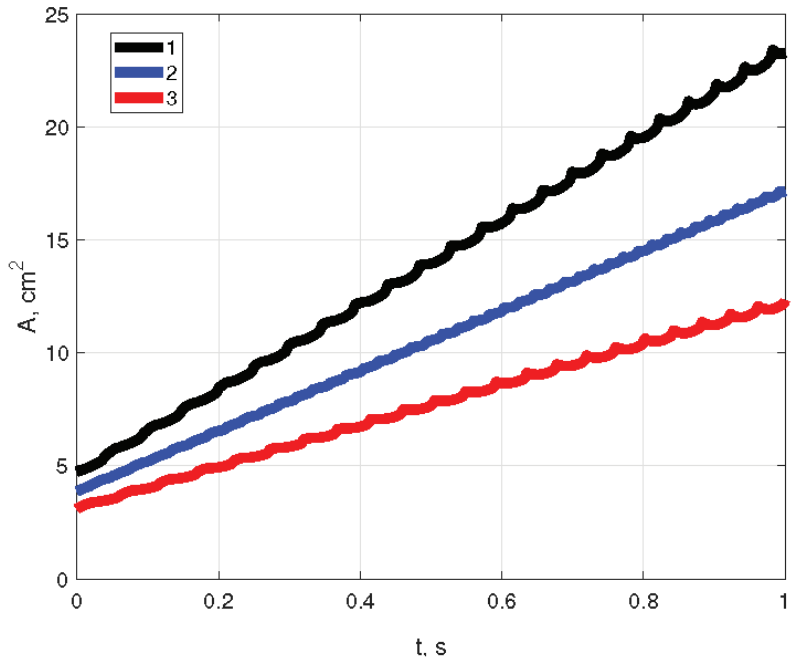

Figure 1. The values of the vascular cross-section in the chosen points: 1—$A(t,0)$; 2—$A(t,l/2)$; and 3—$A(t,l)$.

3.2. Case of Periodic Boundary Conditions

We consider the following periodic boundary conditions for the system (6):

$$a(t,l) = a(t,0), \quad q(t,l) = q(t,0), \tag{30}$$

with the same initial conditions, but it is proposed that $\varphi(l) = \varphi(0)$ and $\psi(l) = \psi(0)$.

3.2.1. Integral Estimation

Theorem 3. *The following equation takes place for the solution of problem* (6), (7), (30)*:*

$$\int_0^l \left(a^2(t,z) + \frac{1}{d_1}q^2(t,z)\right)dz = \int_0^l \left(\varphi^2(z) + \frac{1}{d_1}\psi^2(z)\right)dz, \tag{31}$$

Proof. We obtain the expressions for $\frac{\partial}{\partial t}\int_0^l \left(a^2(t,z) + q^2(t,z)\right)dz$:

$$\frac{\partial}{\partial t}\int_0^l a^2(t,z)dz = -2\int_0^l \tilde{a}(t,z)\frac{\partial \tilde{q}}{\partial z}(t,z)dz = -2\left(a(t,z)q(t,z)\Big|_0^l - \right.$$

$$\left. - \int_0^l q(t,z)\frac{\partial a}{\partial z}(t,z)dz\right) = 2\int_0^l q(t,z)\frac{\partial a}{\partial z}(t,z)dz.$$

$$\frac{\partial}{\partial t}\int_0^l q^2(t,z)dz = 2\int_0^l q(t,z)\frac{\partial q}{\partial z}(t,z)dz = -2\int_0^l q(t,z)\left(d_1\frac{\partial a}{\partial z}(t,z) + d_2\frac{\partial q}{\partial z}(t,z)\right)dz.$$

$$\int_0^l q(t,z)\frac{\partial q}{\partial z}(t,z)dz = q^2(t,z)\Big|_0^l - \int_0^l q(t,z)\frac{\partial q}{\partial z}(t,z)dz,$$

so $\int_0^l q(t,z)\frac{\partial q}{\partial z}(t,z)dz = 0$,

$$d_1 \int_0^l q(t,z)\frac{\partial a}{\partial z}(t,z)dz = -\frac{1}{2}\frac{\partial}{\partial t}\int_0^l q^2(t,z)dz.$$

So, we obtain that

$$\frac{\partial}{\partial t}\int_0^l \Big(a^2(t,z)+q^2(t,z)\Big)dz = 2\int_0^l q(t,z)\frac{\partial a}{\partial z}(t,z)dz - 2d_1\int_0^l q(t,z)\frac{\partial a}{\partial z}(t,z)dz =$$

$$= -\frac{1}{d_1}\frac{\partial}{\partial t}\int_0^l q^2(t,z)dz + \frac{\partial}{\partial t}\int_0^l q^2(t,z)dz.$$

So, the following equation is obtained:

$$\frac{\partial}{\partial t}\int_0^l \left(a^2(t,z)+\frac{1}{d_1}q^2(t,z)\right)dz = 0,$$

and after its integration on t we obtain (31). □

So, for the periodic conditions (30), the condition (9) is realized for any appropriate functions $\varphi(z)$ and $\psi(z)$.

3.2.2. Fourier Method

As is mentioned in the Introduction, the approach to obtain the solution of the initial-boundary-value problem for system (6) in the general form is proposed in [28,29], and it is based on the reflection of waves. In the case of periodic conditions (30), the Fourier method can be easily and effectively used.

Let the solution of system (6) be presented as

$$a(t,z) = \alpha(t)Z(z), \quad q(t,z) = \kappa(t)Z(z). \tag{32}$$

After the substitution of (32) in the first equation of (6), the following relation is obtained:

$$\frac{\dot{\alpha}(t)}{\kappa(t)} = -\frac{Z'(z)}{Z(z)} = -\lambda = const.$$

So, we obtain the following eigenvalue problem:

$$Z'(z) - \lambda Z(z) = 0, \quad Z(0) = Z(l). \tag{33}$$

Problem (33) has the following eigenfunctions and corresponding eigenvalues:

$$Z_m(z) = e^{\frac{2\pi m\mathrm{i}}{l}z}, \quad \lambda_m = \frac{2\pi m\mathrm{i}}{l}, \quad m \in \mathrm{Z}.$$

The solution to the problem with periodic conditions (30) is presented as Fourier expansions on these eigenfunctions:

$$a(t,z) = \sum_{m=-\infty}^{+\infty} \alpha_m(t)e^{\frac{2\pi m\mathrm{i}}{l}z}, \quad q(t,z) = \sum_{m=-\infty}^{+\infty} \kappa_m(t)e^{\frac{2\pi m\mathrm{i}}{l}z}. \tag{34}$$

After the substitution of (34) into (6), the following equations are obtained for $\alpha_m(t)$ and $\kappa_m(t)$:

$$\ddot{\alpha}_m + d_2\lambda_m\dot{\alpha} - d_1\lambda_m^2\alpha_m = 0, \quad \kappa_m = -\frac{\dot{\alpha}_m}{\lambda_m}, \tag{35}$$

for $m \neq 0$.

The solutions of (35) are presented as

$$\alpha_m(t) = C_{1m}e^{\mathrm{i}\frac{\pi m r_1}{l}t} + C_{2m}e^{\mathrm{i}\frac{\pi m r_2}{l}t},$$

where $r_{1,2} = 2\lambda_{1,2}$, and C_{1m} and C_{2m} are the constants. For $m = 0$ we obtain that $\alpha_0(t) = \sigma_0$, $\kappa_0(t) = \sigma_1$, where σ_0 and σ_1 are the constants.

The constants in the expressions for $\alpha_m(t)$ and $\kappa_m(t)$ are defined after the substitution of (34) into initial conditions (7), expanded in the Fourier series on eigenfunctions of (33):

$$\varphi(z) = \sum_{m=-\infty}^{+\infty} \varphi_m e^{\frac{2\pi m\mathrm{i}}{l}z}, \quad \psi(z) = \sum_{m=-\infty}^{+\infty} \psi_m e^{\frac{2\pi m\mathrm{i}}{l}z},$$

where

$$\varphi_m = \frac{1}{l}\int_0^l \varphi(z)e^{-\frac{2\pi m\mathrm{i}}{l}z}dz, \quad \psi_m = \frac{1}{l}\int_0^l \psi(z)e^{-\frac{2\pi m\mathrm{i}}{l}z}dz.$$

After this operation, the following expressions for constants are obtained:

$$C_{1m} = -\frac{2\psi_m + \varphi_m r_2}{r_1 - r_2}, \quad C_{2m} = \frac{r_1\varphi_m + 2\psi_m}{r_1 - r_2}, \quad \sigma_0 = \varphi_0, \quad \sigma_1 = \psi_0.$$

We consider the following example: let $l = 1$, and the initial functions are presented as $\varphi(z) = A_0 + \frac{\sin(2\pi z)}{2}$, $\psi(z) = 0$, where $A_0 \geq 1$. So, we obtain the following values of constants:

$$\sigma_0 = A_0, \quad \sigma_1 = 0, \quad C_{1m} = C_{2m} = 0, \quad m \neq \pm 1,$$

$$C_{11} = \frac{\mathrm{i}r_2}{2(r_1 - r_2)}, \quad C_{21} = -\frac{\mathrm{i}r_1}{2(r_1 - r_2)}, \quad C_{1-1} = -C_{11}, \quad C_{2-1} = -C_{21}.$$

For this example, $a(t,z)$ and $q(t,z)$ are the real functions, written as

$$a(t,z) = A_0 + \frac{1}{2(r_2 - r_1)}(r_2\sin(\pi(2z + r_1t)) - r_1\sin(\pi(2z + r_2t))),$$

$$q(t,z) = \frac{r_1r_2}{2(r_2 - r_1)}(\sin(\pi(2z + r_1t)) - \sin(\pi(2z + r_2t))).$$

4. Discussion and Conclusions

In the presented paper, the author tries to expand the field of application of analytical methods in the simulation of blood flow and to analyze the effects of boundary conditions on the solutions of the linearized system of equations of 1D hemodynamics. The main results can be formulated as follows:

1. The integral estimation (12) for the solution in the case of the general form of the boundary conditions is obtained. As can be seen, the unphysical unbounded solutions can take place for the case of bounded functions $\chi_1(t)$, $\chi_2(t)$.
2. For the case of the boundary conditions on the flow rate, the estimation (21) is obtained, which is more accurate than (12), and it illustrates the similar possible behavior of the solutions.
3. The general theory of the integral inequalities for hyperbolic equations is presented in [35,36]. However, in the presented paper, the more exact estimations are presented for the specific example of the hyperbolic system, where the specific constants in

exponentials are obtained. Moreover, for the boundary conditions only for q, the estimation (21), which is more accurate than the exponential function (the linear function of t), is obtained.
As it is mentioned in [36], the energetic norm is presented by the square of the L_2-norm of the solution. In the left parts of (12), (21), and (32), the integrals, which can be considered as squares of norms of functions, linearly related to the solutions, are presented. So, our estimations can be considered as some kind of energy inequalities for this specific type of hyperbolic system with the appropriate boundary conditions.

4. For the periodic boundary conditions, the exact integral estimation (31) is obtained, which illustrates the correct behavior of the solution—it is bounded at $t \to +\infty$. For this case of boundary conditions, the Fourier method for the analytical solution can be applied. Such analytical solutions can be used for the comparison of different 1D blood-flow models [27].
5. The results obtained in the paper can be useful for the specialists on blood-flow modeling because they allow for an alternative view of the stated boundary conditions and can explain some of the problems that can arise in numerical simulations.
6. In the numerical experiment, where the fully nonlinear model, used in many works, is considered, it is demonstrated that the situation described by the author's theoretical results can be observed in practice, when the bounded initial and boundary conditions lead to the incorrect results from the physical point of view. So, it is important to correctly impose the boundary conditions for the practical predictive simulations. From the medical point of view, this means that the users of the software must choose such conditions carefully because in the opposite case, it can lead to the incorrect results.

Funding: This research received no external funding.

Data Availability Statement: Not applicable.

Acknowledgments: The author wishes to thanks anonymous reviewers for the useful comments and discussion.

Conflicts of Interest: The author declares no conflict of interest.

References

1. Sharifzadeh, B.; Kalbasi, R.; Jahangiri, M.; Toghraie, D.; Karimipour, A. Computer modeling of pulsatile blood flow in elastic artery using a software program for application in biomedical engineering. *Comput. Methods Prog. Biomed.* **2020**, *192*, 105442. [CrossRef] [PubMed]
2. Karimipour, A.; Toghraie, D.; Abdulkareem, L.A.; Alizadeh, A.; Zarringhalam, M.; Karimipour, A. Roll of stenosis severity, artery radius and blood fluid behavior on the flow velocity in the arteries: Application in biomedical engineering. *Med. Hypotheses* **2020**, *144*, 109864. [CrossRef] [PubMed]
3. Audebert, C.; Bucur, C.; Bekheit, M.; Vibert, E.; Vignon-Clementel, I.; Gerbeau, J. Kinetic scheme for arterial and venous blood flow, and application to partial hepatectomy modeling. *Comput. Methods Appl. Mech. Eng.* **2017**, *314*, 102–125. [CrossRef]
4. Marchandise, E.; Willemet, M.; Lacroix, V. A numerical hemodynamic tool for predictive vascular surgery. *Med. Eng. Phys.* **2009**, *31*, 131–144. [CrossRef]
5. Formaggia, L.; Lamponi, D.; Quarteroni, A. One-dimensional models for blood flow in arteries. *J. Eng. Math.* **2003**, *47*, 251–276. [CrossRef]
6. Toro, E.F. Brain venous haemodynamics, neurological diseases and mathematical modelling. A review. *Appl. Math. Comput.* **2015**, *272*, 542–579. [CrossRef]
7. Canic, S.; Kim, E.H. Mathematical analysis of the quasilinear effects in a hyperbolic model blood flow through compliant axi-symmetric vessels. *Math. Methods Appl. Sci.* **2003**, *26*, 1161–1186. [CrossRef]
8. Dobroserdova, T.; Liang, F.; Panasenko, G.; Vassilevski, Y. Multiscale models of blood flow in the compliant aortic bifurcation. *Appl. Math. Lett.* **2019**, *93*, 98–104. [CrossRef]
9. Xiao, N.; Alastruey, J.; Figueroa, C. A systematic comparison between 1-D and 3-D hemodynamics in compliant arterial models. *Int. J. Numer. Methods Biomed. Eng.* **2014**, *30*, 203–231. [CrossRef]
10. Caro, C.G.; Pedley, T.J.; Schroter, R.C.; Seed, W.A. *The Mechanics of the Circulation*, 2nd ed.; Cambridge University Press: Cambridge, UK, 2011.

11. Puelz, C.; Canic, S.; Riviere, B.; Rusin, C.G. Comparison of reduced models for blood flow using Runge—Kutta discontinuous Galerkin methods. *Appl. Numer. Math.* **2017**, *115*, 114–141. [CrossRef]
12. Bertaglia, G.; Caleffi, V.; Valiani, A. Modeling blood flow in viscoelastic vessels: The 1D augmented fluid-structure interaction system. *Comput. Methods Appl. Mech. Eng.* **2020**, *360*, 112772. [CrossRef]
13. Britton, J.; Xing, Y. Well-balanced discontinuous Galerkin methods for the one-dimensional blood flow through arteries model with man-at-eternal-rest and living-man equilibria. *Comput. Fluids* **2020**, *203*, 104493. [CrossRef]
14. Favorskii, A.P.; Tygliyan, M.A.; Tyurina, N.N.; Galanina, A.M.; Isakov, V.A. Computational modeling of the propagation of hemodynamic impulses. *Math. Models Comput. Simul.* **2010**, *2*, 470–481. [CrossRef]
15. Sheng, W.; Zheng, Q.; Zheng, Y. The Riemann problem for a blood-flow model in arteries. *Commun. Comput. Phys.* **2020**, *27*, 227–250. [CrossRef]
16. Spiller, C.; Toro, E.F.; Vazquez-Cendon, M.E.; Contarino, C. On the exact solution of the Riemann problem for blood flow in human veins, including collapse. *Appl. Math. Comput.* **2017**, *303*, 178–189. [CrossRef]
17. Toro, E.F.; Siviglia, A. Flow in collapsible tubes with discontinuous mechanical properties: Mathematical model and exact solutions. *Commun. Comput. Phys.* **2013**, *13*, 361–385. [CrossRef]
18. Toro, E.F.; Muller, L.O.; Siviglia, A. Bounds for wave speeds in the Riemann problem: Direct theoretical estimates. *Comput. Fluids* **2020**, *209*, 104640. [CrossRef]
19. Wang, Z.; Li, G.; Delestre, O. Well-balanced finite difference weighted essentially non-oscillatory schemes for the blood-flow model. *Int. J. Numer. Meth. Fluids* **2016**, *82*, 607–622. [CrossRef]
20. Mohammad, S.; Hessam, B.; Kaveh, L. Physics-informed neural networks for brain hemodynamic predictions using medical imaging. *IEEE Trans. Med. Imaging* **2022**, *41*, 2285–2303.
21. Pfaller, M.R.; Pham, J.; Verma, A.; Pegolotti, L.; Wilson, N.M.; Parker, D.W.; Yang, W.; Marsden, A.L. Automated generation of 0D and 1D reduced-order models of patient-specific blood flow. *Int. J. Numer. Meth. Biomed. Eng.* **2022**, *38*, e3639. [CrossRef]
22. Toro, E.F.; Celant, M.; Zhang, Q.; Contarino, C.; Agarwal, N.; Linninger, A.; Muller, L.O. Cerebrospinal fluid dynamics coupled to the global circulation in holistic setting: Mathematical models,numerical methods and applications. *Int. J. Numer. Meth. Biomed. Eng.* **2022**, *38*, e3532. [CrossRef] [PubMed]
23. Abdullateef, S.; Mariscal-Harana, J.; Khir, A.W. Impact of tapering of arterial vessels on blood pressure,pulse wave velocity, and wave intensity analysis using one-dimensional computational model. *Int. J. Numer. Meth. Biomed. Eng.* **2021**, *37*, e3312. [CrossRef] [PubMed]
24. Matthys, K.S.; Alastruey, J.; Peiro, J.; Khir, A.W.; Segers, P.; Verdonc, P.R.; Parker, K.H.; Sherwin, S.J. Pulse wave propagation in a model human arterial network: Assessment of 1-D numerical simulations against in vitro measurements. *J. Biomech.* **2007**, *40*, 3476–3486. [CrossRef] [PubMed]
25. Alastruey, J.; Khir, A.W.; Matthys, K.S.; Segers, P.; Sherwin, S.J.; Verdonc, P.R.; Parker, K.H.; Peiro, J. Pulse wave propagation in a model human arterial network: Assessment of 1-D visco-elastic simulations against in vitro measurements. *J. Biomech.* **2011**, *44*, 2250–2258. [CrossRef] [PubMed]
26. Krivovichev, G.V. Computational analysis of one-dimensional models for simulation of blood flow in vascular networks. *J. Comput. Sci.* **2022**, *62*, 101705. [CrossRef]
27. Krivovichev, G.V. Comparison of inviscid and viscid one-dimensional models of blood flow in arteries. *Appl. Math. Comput.* **2022**, *418*, 126856. [CrossRef]
28. Ashmetkov, I.V.; Mukhin, S.I.; Sosnin, N.V.; Favorskii, A.P.; Khrulenko, A.B. Analysis and comparison of some analytic and numerical solutions of hemodynamic problems. *Differ. Equ.* **2000**, *36*, 1021–1026. [CrossRef]
29. Ashmetkov, I.V.; Mukhin, S.I.; Sosnin, N.V.; Favorskii, A.P. A boundary value problem for the linearized haemodynamic equations on a graph. *Differ. Equ.* **2004**, *40*, 94–104. [CrossRef]
30. Paquerot, J.-F.; Remoissenet, M. Dynamics of nonlinear blood pressure waves in large arteries. *Phys. Lett. A* **1994**, *194*, 77–82. [CrossRef]
31. Ilyin, O. Nonlinear pressure-velocity waveforms in large arteries, shock waves and wave separation. *Wave Motion* **2019**, *84*, 56–67. [CrossRef]
32. Maity, D.; Raymond, J.-P.; Roy, A. Existence and uniqueness of maximal strong solution of a 1D blood flow in a network of vessels. *Nonl. Anal. Real World Appl.* **2022**, *63*, 103405. [CrossRef]
33. Mukhin, S. I.; Menyailova, M.A.; Sosnin, N.V.; Favorskii, A.P. Analytic study of stationary hemodynamic flows in an elastic vessel with friction. *Differ. Equ.* **2007**, *43*, 1011–1015. [CrossRef]
34. Tikhonov, A.N.; Samarskii, A.A. *Equations of Mathematical Physics*; Dover Publications Inc.: New York, NY, USA, 1990.
35. Godunov, S.K. *The Equations of Mathematical Physics*; Nauka: Moscow, Russia, 1979. (In Russian)
36. Lax, P.D. *Hyperbolic Partial Differential Equations*; AMS: Providence, RI, USA, 2006.

mathematics

MDPI

Article

Modeling and Analyzing Homogeneous Tumor Growth under Virotherapy

Chayu Yang [1] and Jin Wang [2,*]

[1] Department of Mathematics, University of Nebraska-Lincoln, Lincoln, NE 68588, USA
[2] Department of Mathematics, University of Tennessee at Chattanooga, Chattanooga, TN 37403, USA
* Correspondence: jin-wang02@utc.edu

Abstract: We present a mathematical model based on ordinary differential equations to investigate the spatially homogeneous state of tumor growth under virotherapy. The model emphasizes the interaction among the tumor cells, the oncolytic viruses, and the host immune system that generates both innate and adaptive immune responses. We conduct a rigorous equilibrium analysis and derive threshold conditions that determine the growth or decay of the tumor under various scenarios. Numerical simulation results verify our analytical predictions and provide additional insight into the tumor growth dynamics.

Keywords: mathematical oncology; tumor growth; equilibrium points; stability

MSC: 92C50; 37N25

1. Introduction

Tumor virotherapy is a relatively new, yet propitious, strategy in treating cancer [1]. It has shown promising results in preclinical tests and clinical trials for a number of tumor types [2–5]. This therapy makes use of genetically engineered oncolytic viruses that are specific to tumors. Once injected into a tumor, the viruses infect cancer cells, while leaving healthy cells and tissues unharmed. Through the lysis of the infected cells, the viruses replicate and spread within the tumor and continue infecting other cancer cells. There are several distinct advantages of using virotherapy. First, the replication of oncolytic viruses is highly tumor-selective, and, thus, is generally non-pathogenic to normal tissues. Second, the success rate of viral infection is typically high, as viruses can utilize multiple genetic means to attack tumor cells and cause cell lysis. Moreover, viruses can be genetically manipulated to include additional features so as to achieve improved safety and efficacy [6].

A complication involved in the tumor oncolysis process is the response from the host immune system. Once the viruses start attacking tumor cells, the innate immune response is stimulated by the viruses and the infected tumor cells, which tends to limit virus replication and spread, as well as eliminate infected cells. This anti-virus effect of innate immunity has been well observed and documented [7–9]. Recent clinical studies, however, revealed that through the lysis of infected cells, an inflammatory response is induced with the presentation of tumor antigens, which leads to T-cell mediated adaptive immunity against the tumor [6,10]. Thus, the interaction of oncolytic viruses and the immune system contributes to the therapeutic efficacy in two opposite ways: a negative contribution through the anti-virus innate immune response, and a positive contribution through the anti-tumor adaptive immune response.

Ideally, the virotherapy aims to completely remove the tumor cells and the viruses; in the end, though, it is unclear whether such a perfect outcome is realistic. Meanwhile, challenges remain on how to effectively combine the oncolysis and the virus-mediated immunity to ensure the success of the treatment, and how to strategically manipulate

the balance between anti-virus and anti-tumor immune responses to achieve the best outcome [1,6,10]. Theoretical investigations and quantitative analysis, particularly using mathematical modeling, can improve our understanding of tumor virotherapy and provide useful guidelines for clinical studies toward overcoming these challenges.

A number of mathematical models have been published on the study of virotherapy and its impact on tumor growth. Wodarz [11] proposed a model based on ordinary differential equations (ODEs), with two compartments representing the infected and uninfected tumor cell populations where each cell population is assumed to grow in a logistic fashion. The model does not explicitly consider viral dynamics, and a main focus of the work is to explore conditions required for maximum reduction of the tumor load. This model was later extended to a more general formulation [12], and two distinct types of dynamics (representing the success and failure of the treatment, respectively) were found, depending on the spread rate of the viruses. Karev et al. [13] employed a similar modeling framework, but with an emphasis on tumor cell heterogeneity. Novozilov et al. [14] incorporated a ratio-dependent functional response into the model of Wodarz [11], and discussed several possible outcomes of oncolytic virus infection, including no effect on the tumor, stabilization or reduction of the tumor load, and complete elimination of the tumor. Tian [15] analyzed the interaction among the infected tumor cells, uninfected tumor cells, and viruses, also using an ODE model, with a focus on the bifurcation study of the virus replicability measured by the burst size. Wang et al. [16] added a nutrient compartment to a model that includes normal cells, tumor cells, and viruses, and explicitly determined the minimum viral dosage in order for the treatment to be effective. None of these ODE models, however, considered the effects of immune responses and their contribution to the efficacy of the therapy.

Meanwhile, virotherapy models based on partial differential equations (PDEs) have also been used. For example, Wu et al. [17] employed a PDE model to compare the evolution of a tumor under different initial conditions that resulted from three virus-injection strategies. This model was later extended in [18] to incorporate a cytokine-based immune response against the virus-infected tumor cells. In addition, Friedma et al. [19] proposed a reaction-convection-diffusion system to investigate tumor virotherapy in the presence of host innate immune response. Although the PDE models in [18,19] both added a separate equation to represent the effects of the host immune response, they only included the innate immunity and did not consider the adaptive immunity, leading to an incomplete picture for the host immune system dynamics in the course of tumor virotherapy. In a more recent study, Timalsina et al. [20] proposed a PDE modeling framework for tumor virotherapy that incorporates both the innate and adaptive immune responses in the description of the interaction among tumor cells, oncolytic viruses, and host immune systems. Due to the complexity of their PDE system, however, the study in [20] was primarily focused on numerical simulation under a variety of parameter settings, and no mathematical analysis was conducted.

The present paper aims to improve our knowledge of the tumor growth dynamics under virotherapy and the tumor–virus–immunity interaction involved in this process, through a rigorous analysis of an ODE model closely related to the PDE model proposed in [20]. Specifically, we are interested in better understanding the spatially homogeneous state of tumor growth, where theory of differential equations and dynamical systems [21,22] can be applied and a detailed equilibrium analysis can be conducted. The simplified ODE model retains all the variables and the essential temporal dynamical features from the original PDE system. Particularly, it remains as a moving boundary problem where the tumor size changes with time, and the innate and adaptive immune responses are both included. Using this ODE model, we will carefully investigate the complex interaction among tumor cells, oncolytic viruses, and innate and adaptive host immune systems, and derive threshold conditions to quantify the success and failure of the virotherapy.

The remainder of this paper proceeds as follows. In Section 2, we describe our ODE model that depicts the spatially homogeneous state in the course of tumor growth

under virotherapy. In Section 3, we analyze the equilibria of the model and their stability properties, as well as their impact on the growth of the tumor. We present some numerical simulation results in Section 4, and conclude the paper with some discussion in Section 5.

2. Model Formulation

As a starting point, we first present the PDE model proposed in [20] that describes the interaction between the tumor cells, oncolytic viruses, and innate and adaptive host immune responses. This model, formulated as a moving boundary problem, considers a spherical tumor with radial symmetry and consists of the following equations

$$\begin{aligned}
&\frac{\partial X}{\partial t} + \frac{1}{\rho^2}\frac{\partial}{\partial \rho}(\rho^2 UX) = \lambda X - \beta XV - k_2 XZ_2,\\
&\frac{\partial Y}{\partial t} + \frac{1}{\rho^2}\frac{\partial}{\partial \rho}(\rho^2 UY) = \beta XV - k_1 YZ_1 - \delta Y,\\
&\frac{\partial Z_1}{\partial t} + \frac{1}{\rho^2}\frac{\partial}{\partial \rho}(\rho^2 UZ_1) = s_1 YZ_1 - c_1 Z_1,\\
&\frac{\partial Z_2}{\partial t} + \frac{1}{\rho^2}\frac{\partial}{\partial \rho}(\rho^2 UZ_2) = s_2 YZ_2 - c_2 Z_2,\\
&\frac{\partial N}{\partial t} + \frac{1}{\rho^2}\frac{\partial}{\partial \rho}(\rho^2 UN) = k_1 YZ_1 + k_2 XZ_2 + \delta Y - \mu N,\\
&\frac{\partial V}{\partial t} - \frac{D}{\rho^2}\frac{\partial}{\partial \rho}\left(\rho^2 \frac{\partial V}{\partial \rho}\right) = b\delta Y - k_0 Z_1 V - \gamma V,\\
&\frac{1}{\rho^2}\frac{\partial}{\partial \rho}(\rho^2 U) = \lambda X + s_1 YZ_1 + s_2 YZ_2 - c_1 Z_1 - c_2 Z_2 - \mu N,\\
&\frac{dR}{dt} = U(R,t),
\end{aligned} \tag{1}$$

for $t > 0$ and $0 \le \rho \le R(t)$, where t denotes the time and ρ denotes the spatial distance measured from the center of the tumor. The variables $X(\rho,t)$, $Y(\rho,t)$ and $N(\rho,t)$ are the numbers of normal (i.e., not yet infected), infected, and dead tumor cells, respectively; $Z_1(\rho,t)$ and $Z_2(\rho,t)$ are the numbers of the innate and adaptive immune cells, respectively; $V(\rho,t)$ is the number of viruses, and $R(t)$ denotes the moving boundary of the tumor. The motion of all the cells is modeled as a convection process along the radial direction with a velocity $U(\rho,t)$, whereas the motion of the viruses (which are much smaller than cells) is modeled as a diffusion process. Since the total cell density is approximately a constant ($\approx 10^6$ cells/mm^3) [19], with a normalization procedure, it can be assumed that

$$X + Y + Z_1 + Z_2 + N = 1; \tag{2}$$

i.e., each of these variables represents a portion of the total density. In addition, all the parameters involved in this model are described in Table 1.

We will focus on the spatially homogeneous state of tumor growth. To that end, we assume

$$\begin{aligned}
&X = X(t) = \text{density of uninfected tumor cells at time } t,\\
&Y = Y(t) = \text{density of infected tumor cells at time } t,\\
&Z_1 = Z_1(t) = \text{density of innate immune cells at time } t,\\
&Z_2 = Z_2(t) = \text{density of adaptive immune cells at time } t,\\
&N = N(t) = \text{density of dead tumor cells at time } t,\\
&V = V(t) = \text{density of viruses at time } t.
\end{aligned} \tag{3}$$

That is, all the cells and viruses are uniformly distributed over the spatial domain $0 \leq \rho \leq R(t)$ so that each of these density variables only depends on time. Meanwhile, we retain the spatiotemporal dependence of the convective velocity field:

$$U = U(\rho, t) = \text{velocity of cells at distance } \rho \text{ and time } t. \tag{4}$$

However, we remark that if we assume a spatially uniform velocity field $U = U(t)$, it would lead to a stationary tumor with a fixed boundary (i.e., $\frac{dR}{dt} = 0$), which is much easier to analyze but is unrealistic in some sense. A detailed discussion of that scenario is provided in the Appendix A. The spatiotemporal variation of U defined in Equation (4) allows us to study a more realistic and complex tumor with a moving boundary.

With these assumptions, we can manipulate the convection terms in system (1). For example, from the first equation of system (1) we have

$$\frac{1}{\rho^2}\frac{\partial}{\partial \rho}(\rho^2 UX) = X\frac{1}{\rho^2}\frac{\partial}{\partial \rho}(\rho^2 U) = Xf(X, Y, Z_1, Z_2), \tag{5}$$

where

$$f(X, Y, Z_1, Z_2) = (\lambda + \mu)X + (\mu + s_1 Z_1 + s_2 Z_2)Y + (\mu - c_1)Z_1 + (\mu - c_2)Z_2 - \mu. \tag{6}$$

Equation (6) is obtained by adding up the first five equations in system (1) and using the condition (2). Meanwhile, since $V = V(t)$, we have

$$\frac{D}{\rho^2}\frac{\partial}{\partial \rho}\left(\rho^2 \frac{\partial V}{\partial \rho}\right) = 0;$$

i.e., the diffusion term in the virus equation vanishes. In addition, Equation (5) yields

$$\frac{\partial}{\partial \rho}(\rho^2 U) = \rho^2 f(X, Y, Z_1, Z_2).$$

Integrating both sides for ρ yields

$$U(\rho, t) = \frac{\rho}{3} f\big(X(t), Y(t), Z_1(t), Z_2(t)\big), \qquad 0 \leq \rho \leq R. \tag{7}$$

Table 1. Model parameters.

Symbol	Description	Unit
λ	Proliferation rate of tumor cells	h^{-1}
β	Infection rate of viruses	$mm^3\ h^{-1}\ virus^{-1}$
k_1	Killing rate of innate immune response	$mm^3\ h^{-1}\ cell^{-1}$
k_2	Killing rate of adaptive immune response	$mm^3\ h^{-1}\ cell^{-1}$
s_1	Stimulation rate of innate immunity	$mm^3\ h^{-1}\ cell^{-1}$
s_2	Stimulation rate of adaptive immunity	$mm^3\ h^{-1}\ cell^{-1}$
c_1	Clearance rate of innate immune cells	h^{-1}
c_2	Clearance rate of adaptive immune cells	h^{-1}
D	Diffusion coefficient of viruses	$mm^2\ h^{-1}$
b	Burst size of viruses	$virus\ cell^{-1}$
δ	Lysis rate of infected tumor cell	h^{-1}
k_0	Take-up rate of viruses by innate immunity	$mm^3\ h^{-1}\ cell^{-1}$
γ	Clearance rate of viruses	h^{-1}
μ	Removal rate of dead tumor cells	h^{-1}

Thus, we obtain the following ODE system

$$\begin{aligned}
\frac{dX}{dt} &= \lambda X - \beta XV - k_2 XZ_2 - Xf(X,Y,Z_1,Z_2),\\
\frac{dY}{dt} &= \beta XV - k_1 YZ_1 - \delta Y - Yf(X,Y,Z_1,Z_2),\\
\frac{dZ_1}{dt} &= s_1 YZ_1 - c_1 Z_1 - Z_1 f(X,Y,Z_1,Z_2),\\
\frac{dZ_2}{dt} &= s_2 YZ_2 - c_2 Z_2 - Z_2 f(X,Y,Z_1,Z_2),\\
\frac{dV}{dt} &= b\delta Y - k_0 Z_1 V - \gamma V,\\
\frac{dR}{dt} &= \frac{R}{3} f(X,Y,Z_1,Z_2).
\end{aligned} \tag{8}$$

Note that we have dropped the equation for N in the system above. Substituting the expression of f from Equation (6), we may rewrite the first five equations in system (8) as follows:

$$\begin{aligned}
\frac{dX}{dt} &= (\lambda+\mu)X - (\mu - c_1)XZ_1 - (\mu + k_2 - c_2)XZ_2\\
&\quad - (\lambda+\mu)X^2 - \mu XY - \beta XV - s_1 XYZ_1 - s_2 XYZ_2,\\
\frac{dY}{dt} &= \beta XV - (\mu + k_1 - c_1)YZ_1 - (\mu - c_2)YZ_2\\
&\quad - (\delta - \mu)Y - (\lambda+\mu)XY - \mu Y^2 - s_1 Y^2 Z_1 - s_2 Y^2 Z_2,\\
\frac{dZ_1}{dt} &= (\mu - c_1)Z_1 + (s_1 - \mu)YZ_1 - (\mu - c_1)Z_1^2 - (\mu - c_2)Z_1 Z_2\\
&\quad - (\lambda+\mu)XZ_1 - s_1 YZ_1^2 - s_2 YZ_1 Z_2,\\
\frac{dZ_2}{dt} &= (\mu - c_2)Z_2 + (s_2 - \mu)YZ_2 - (\mu - c_1)Z_1 Z_2 - (\mu - c_2)Z_2^2\\
&\quad - (\lambda+\mu)XZ_2 - s_2 YZ_2^2 - s_1 YZ_1 Z_2,\\
\frac{dV}{dt} &= b\delta Y - k_0 Z_1 V - \gamma V.
\end{aligned} \tag{9}$$

Meanwhile, the last equation in system (8) yields

$$R(t) = R(0)\, e^{\frac{1}{3}\int_0^t f(X(\tau),Y(\tau),Z_1(\tau),Z_2(\tau))d\tau}. \tag{10}$$

In what follows, we will focus our attention on the analysis of the equlibria of system (9); each equilibrium represents a steady state in the tumor virotherapy, where the tumor would grow or decay at a constant rate. Ideally, we would hope that the virotherapy can eliminate all the uninfected tumor cells (i.e., X) to ensure a successful outcome. Practically, however, the uninfected tumor cells may or may not be eradicated, yet the tumor could still be effectively controlled in the presence of some level of uninfected tumor cells [19,20]. Thus, in this study we measure the success of the tumor virotherapy by the (exponential) decay of the tumor radius, whose motion is described by Equation (10), at a stable equilibrium. On the other hand, when an equilibrium is unstable, that implies such a steady state cannot be sustained, or may not be reached at all.

3. Equilibrium Analysis

Let the unknowns of system (9) be ordered as (X, Y, Z_1, Z_2, V). Each density variable is non-negative to be biologically meaningful. To facilitate our analysis, we introduce the notations

$$\lambda_\mu = \lambda + \mu,\ \lambda_\delta = \lambda + \delta,\ \lambda_i = \lambda + c_i,\ \mu_i = \mu - c_i,\ \delta_i = \delta - c_i, \quad i = 1,2. \tag{11}$$

We also assume that $\mu_1 > 0$, $\mu_2 > 0$ and $\lambda_2 > k_2$. These assumptions are consistent with the published parameter values in the literature (see, e.g., [18,19]).

3.1. Trivial Equilibria

It is straightforward to observe that there are four simple boundary equilibria (or, trivial equilibria):

$$M_0 = (0,0,0,0,0),\ M_1 = (1,0,0,0,0),\ M_2 = (0,0,0,1,0),\ M_3 = (0,0,1,0,0).$$

By computing the Jacobian matrices associated with these points, we obtain their characteristic polynomials

$$\begin{aligned}
P_0(u) &= (u-\lambda_\mu)(u+\delta-\mu)(u-\mu_1)(u-\mu_2)(u+\gamma),\\
P_1(u) &= (u+\lambda_1)(u+\lambda_2)(u+\lambda_\mu)(u^2+(\lambda_\mu+\lambda_\delta)u+\gamma\lambda_\delta-b\beta\delta),\\
P_2(u) &= (u+k_2-\lambda_2)(u+\delta_2)(u+c_1-c_2)(u+\mu_2)(u+\gamma),\\
P_3(u) &= (u-\lambda_1)(u+\mu_1)(u+k_1+\delta_1)(u+c_2-c_1)(u+k_0+\gamma),
\end{aligned}$$

respectively. Let us define the threshold value of system (9) by

$$\mathcal{R}_0 = \frac{b\delta\beta}{\gamma\lambda_\delta}. \tag{12}$$

The threshold value $\mathcal{R}_0$, which is analogous to the basic reproductive number in an infectious disease model, quantifies the capability that the oncolytic viruses can effectively invade the tumor. Specifically, Equation (12) expresses the threshold value as a ratio of two factors which have opposite effects on the outcome of the virotherapy: the 'positive-effect' factor represented by the product of the viral reproduction rate and infection rate, and the 'negative-effect' factor represented by the virus removal rate and tumor cell reproduction rate.

We then obtain that the equilibrium M_1 is locally asymptotically stable if $\mathcal{R}_0 < 1$ and unstable if $\mathcal{R}_0 > 1$. Biologically, the point M_1 represents a steady state indicating a complete 'failure' of the tumor virotherapy; i.e., uninfected tumor cells occupy 100% of the domain while all other cells and viruses are gone. Our observation here is that when the viral infection/invasion capability is low (such that $\mathcal{R}_0 < 1$), the virotherapy would most likely fail. In that scenario, we have $f(X, Y, Z_1, Z_2) = \lambda$ at the stable equilibrium M_1, so that the tumor radius would exponentially grow at a constant rate $\lambda/3$ based on Equation (10). On the other hand, as long as the threshold value is higher than unity, M_1 becomes unstable which implies that such a state (of complete treatment failure) would not be attained. Meanwhile, the other three equilibria M_0, M_2 and M_3 are always unstable as their characteristic polynomials each has at least one positive root. Each of these three points represents an 'ideal' steady state of the tumor treatment which is free of tumor cells and viruses. Our results show that the tumor growth cannot stabilize at these equilibria regardless of the value of the threshold value, implying that, practically, such a perfect treatment outcome may not be achieved.

3.2. Immunity-Free Equilibria

In addition to these four simple equilibria, system (9) possesses a number of equilibrium points which are more complex in nature. We proceed to first analyze those equilibria that are free of immune cells, i.e., $Z_1 = Z_2 = 0$. We will distinguish two cases, depending on the values of the lysis rate of the infected tumor cells (δ) and the removal rate of the dead tumor cells (μ).

Case 1: $\delta > \mu$.

It is easy to find that there exists a biologically feasible, immunity-free, equilibrium

$$I_0 = (x_0, y_0, 0, 0, v_0) = \left(\frac{(\delta-\mu)\mathcal{R}_0 + \mu}{\mathcal{R}_0(\lambda_\delta \mathcal{R}_0 - \lambda)}, \frac{\lambda_\mu(\mathcal{R}_0-1)}{\mathcal{R}_0(\lambda_\delta \mathcal{R}_0 - \lambda)}, 0, 0, \frac{\lambda_\delta \lambda_\mu (\mathcal{R}_0 - 1)}{\beta(\lambda_\delta \mathcal{R}_0 - \lambda)} \right),$$

if and only if $\mathcal{R}_0 > 1$. The Jacobian matrix at I_0 is

$$J_{I_0} = \begin{bmatrix} -\lambda_\mu x_0 & -\mu x_0 & -(\mu_1 + s_1 y_0)x_0 & -(\mu_2 + k_2 + s_2 y_0)x_0 & -\beta\, x_0 \\ (\frac{b\beta\delta}{\gamma} - \lambda_\mu) y_0 & -\mu y_0 - \frac{b\beta\delta x_0}{\gamma} & -(\mu_1 + k_1 + s_1 y_0) y_0 & -(\mu_2 + s_2 y_0) y_0 & \beta\, x_0 \\ 0 & 0 & \xi_1 & 0 & 0 \\ 0 & 0 & 0 & \xi_2 & 0 \\ 0 & b\delta & -k_0 v_0 & 0 & -\gamma \end{bmatrix},$$

where $\xi_i = \mu_i - \lambda_\mu x_0 + (s_i - \mu) y_0$, $i = 1, 2$. Hence, the characteristic polynomial of J_{I_0} is

$$P_{I_0}(u) = (u - \xi_1)(u - \xi_2)(u^3 + Au^2 + Bu + C),$$

with

$$\begin{aligned} A &= \gamma + \lambda_\delta \mathcal{R}_0 x_0 + \lambda x_0 + \frac{\mu}{\mathcal{R}_0} > 0, \\ B &= (\gamma + \lambda_\delta \mathcal{R}_0 x_0)\left(\lambda x_0 + \frac{\mu}{\mathcal{R}_0} \right) > 0, \\ C &= \gamma \lambda_\mu \lambda_\delta x_0 (\mathcal{R}_0 - 1) > 0. \end{aligned}$$

Let $w = \frac{\lambda_\mu}{\lambda_\delta \mathcal{R}_0 - \lambda}$, then $w \in (0, \lambda_\mu/\delta)$ and $\mathcal{R}_0 = \frac{\lambda w + \lambda_\mu}{\lambda_\delta w}$, $x_0 = \frac{w(\lambda w + \delta - \mu)}{\lambda w + \lambda_\mu}$. Hence,

$$\begin{aligned} A &= \gamma + \delta - \mu + 2\delta w, \\ B &= \delta w(\gamma + \delta - \mu + \delta w), \\ C &= \gamma \lambda_\mu \left(\delta - \mu - \frac{\delta^2 w}{\lambda} + \frac{\mu \lambda_\delta^2 w}{\lambda(\lambda w + \lambda_\mu)} \right). \end{aligned}$$

Consider the following function

$$D(w) = A(w)B(w) - C(w), \quad w \in (0,\ \lambda_\mu/\delta).$$

One can easily verify that $(A(w)B(w))'' > 0$ and $C''(w) < 0$, hence $D''(w) > 0$. In addition, since

$$D(0+) = \gamma \lambda_\mu (\mu - \delta) < 0 < A(\lambda_\mu/\delta -)B(\lambda_\mu/\delta -) = D(\lambda_\mu/\delta -),$$

there exists a $w_* \in (0, \lambda_\mu/\delta)$ such that $D(w) < 0$ for $w \in (0, w_*)$ and $D(w) > 0$ for $w \in (w_*, \lambda_\mu/\delta)$. Hence, if we let $r = \frac{\lambda w_* + \lambda_\mu}{\lambda_\delta w_*} > 1$, then $AB < C$ for $\mathcal{R}_0 \in (r, \infty)$ and $AB > C$ for $\mathcal{R}_0 \in (1,\ r)$. Thus, by Routh–Hurwitz stability criterion, each root of $P_{I_0}(s)$ has a negative real part if and only if $\mathcal{R}_0 \in (1,\ r)$ and $\xi_i < 0, i = 1, 2$. Moreover, $\xi_i < 0$ is equivalent to

$$\mu_i \lambda_\delta \mathcal{R}_0^2 + ((s_i - \delta)\lambda_\mu - \lambda \mu_i)\mathcal{R}_0 - s_i \lambda_\mu < 0.$$

Hence, it is easy to obtain that $1 < \mathcal{R}_0 < R_i$, where

$$R_i = \frac{\sqrt{((s_i - \delta)\lambda_\mu - \lambda\mu_i)^2 + 4 s_i \mu_i \lambda_\delta \lambda_\mu} - ((s_i - \delta)\lambda_\mu - \lambda \mu_i)}{2\mu_i \lambda_\delta}, \quad i = 1, 2.$$

Therefore, we conclude that I_0 is locally asymptotically stable if $1 < \mathcal{R}_0 < \min\{r, R_1, R_2\}$ and unstable if $\mathcal{R}_0 > \min\{r, R_1, R_2\}$. At the point I_0, direct calculation yields

$$f(X, Y, Z_1, Z_2) = \lambda_\mu x_0 + \mu y_0 - \mu = \frac{\lambda_\mu \delta}{\lambda_\delta \mathcal{R}_0 - \lambda} - \mu.$$

Hence, the tumor radius will be exponentially increasing if $\mathcal{R}_0 < 1 + \frac{\lambda\delta}{\mu\lambda_\delta}$, and decreasing if $\mathcal{R}_0 > 1 + \frac{\lambda\delta}{\mu\lambda_\delta}$.

The immunity-free equilibrium I_0 represents a steady state where uninfected tumor cells, infected tumor cells, and viruses co-exist, but both innate and adaptive immune cells vanish. In particular, the density of the infected tumor cells is positive at I_0, indicating some degree of success for the viral invasion into the tumor. Effective control of the tumor, however, depends on the stability of I_0 and the value of $f(X, Y, Z_1, Z_2)$ at that steady state. Consequently, the threshold value has to be in a certain range, i.e., $1 + \frac{\lambda\delta}{\mu\lambda_\delta} < \mathcal{R}_0 < \min\{r, R_1, R_2\}$, to ensure a successful outcome of the tumor virotherapy.

Case 2: $\delta < \mu$.

One can verify that the immunity-free equilibrium I_0 exists if and only if $1 < \mathcal{R}_0 < \frac{\mu}{\mu-\delta}$. Furthermore, $C\left(w\left(\frac{\mu}{\mu-\delta}\right)\right) = 0$ and thus $D\left(w\left(\frac{\mu}{\mu-\delta}\right)\right) > 0$, which implies $\frac{\mu}{\mu-\delta} < r$. Hence, I_0 is locally asymptotically stable if $1 < \mathcal{R}_0 < \min\{\frac{\mu}{\mu-\delta}, R_1, R_2\}$ and thereby the tumor radius would decrease if $1 + \frac{\lambda\delta}{\mu\lambda_\delta} < \mathcal{R}_0 < \min\{\frac{\mu}{\mu-\delta}, R_1, R_2\}$.

When $\mu > \delta$, there is an additional immunity-free equilibrium in the form of

$$E_0 = \left(0, \frac{\mu - \delta}{\mu}, 0, 0, \frac{b\delta(\mu - \delta)}{\gamma\mu}\right),$$

and $-\gamma, \delta - \mu$, $\delta_1 + \frac{(\mu-\delta)s_1}{\mu}, \delta_2 + \frac{(\mu-\delta)s_2}{\mu}$, and $\lambda_\delta\left(1 - \frac{\mu-\delta}{\mu}\mathcal{R}_0\right)$ are all eigenvalues of the Jacobian at E_0. Note that

$$\delta_i + \frac{(\mu - \delta)s_i}{\mu} < 0 \Longleftrightarrow R_i > \frac{\mu}{\mu - \delta}.$$

Hence, E_0 is locally asymptotically stable if $\min\{\mathcal{R}_0, R_1, R_2\} > \frac{\mu}{\mu-\delta}$. This additional equilibrium represents a success of the tumor virotherapy, where only the infected tumor cells and viruses co-exist while the uninfected tumor cells and immune cells all vanish. At E_0, it is straightforward to obtain $f(X, Y, Z_1, Z_2) = -\delta < 0$, i.e., the tumor radius would exponentially decrease to 0.

3.3. Single-Immunity Equilibria

Next, we explore the equilibria of system (9) where one of the immune components (Z_1 and Z_2) may be nonzero. If $Z_1 = 0$ and $XYZ_2V \neq 0$, we can solve the following equations

$$\lambda = \beta V + k_2 Z_2 + f(X, Y, 0, Z_2), \tag{13}$$

$$\beta XV = \delta Y + Y f(X, Y, 0, Z_2), \tag{14}$$

$$s_2 Y = c_2 + f(X, Y, 0, Z_2), \tag{15}$$

$$b\delta Y = \gamma V. \tag{16}$$

Substitute $V = \frac{b\delta}{\gamma}Y$ from Equation (16) to obtain

$$X = \frac{1}{\lambda_\delta \mathcal{R}_0}(s_2 Y + \delta_2), \tag{17}$$

$$Z_2 = \frac{\lambda_2}{k_2} - \frac{\lambda_\delta \mathcal{R}_0 + s_2}{k_2} Y, \tag{18}$$

$$\lambda_\mu X + (s_2 Z_2 - s_2 + \mu)Y + \mu_2(Z_2 - 1) = 0. \tag{19}$$

Substituting Equations (17) and (18) into Equation (19), we obtain a quadratic equation

$$g(Y) := A_2 Y^2 + B_2 Y + C_2 = 0,$$

where

$$\begin{aligned} A_2 =& -\frac{s_2}{k_2}(\lambda_\delta \mathcal{R}_0 + s_2) < 0, \\ B_2 =& \mu + \frac{(\lambda_2 - k_2)s_2}{k_2} + \frac{s_2 \lambda_\mu}{\lambda_\delta \mathcal{R}_0} - \frac{\mu_2}{k_2}(\lambda_\delta \mathcal{R}_0 + s_2), \\ C_2 =& \frac{\delta_2 \lambda_\mu}{\lambda_\delta \mathcal{R}_0} + \frac{(\lambda_2 - k_2)\mu_2}{k_2} > 0. \end{aligned}$$

Since $A_2 C_2 < 0$, then $g(Y) = 0$ has a unique positive solution

$$y_2 = \frac{B_2 + \sqrt{B_2^2 - 4A_2 C_2}}{-2A_2}.$$

In addition, $x_2 = X(y_2) > 0$, $v_2 = V(y_2) > 0$ since $y_2 > 0$, and

$$\begin{aligned} z_2 = Z_2(y_2) > 0 \Longleftrightarrow & y_2 < \frac{\lambda_2}{\lambda_\delta \mathcal{R}_0 + s_2} \\ \Longleftrightarrow & B_2 + \sqrt{B_1^2 - 4A_2 C_2} < \frac{2s_2 \lambda_2}{k_2} \\ \Longleftrightarrow & -A_2 C_2 < \frac{\lambda_2 s_2}{k_2}\left(\frac{\lambda_2 s_2}{k_2} - B_2\right) \\ \Longleftrightarrow & \mu_2 \lambda_\delta \mathcal{R}_0^2 + ((s_2 - \delta)\lambda_\mu - \lambda \mu_2)\mathcal{R}_0 - s_2 \lambda_\mu > 0 \\ \Longleftrightarrow & \mathcal{R}_0 > R_2\,. \end{aligned}$$

Hence, there exists a unique innate-immunity-free equilibrium

$$I_2 = (x_2, y_2, 0, z_2, v_2)$$

if and only if $\mathcal{R}_0 > R_2$.

Similarly, if $Z_2 = 0$ and $XYZ_1V \neq 0$, then

$$\lambda = \beta V + f(X, Y, Z_1, 0), \tag{20}$$

$$\beta XV = Y(k_1 Z_1 + \delta + f(X, Y, Z_1, 0)), \tag{21}$$

$$s_1 Y = c_1 + f(X, Y, Z_1, 0), \tag{22}$$

$$b\delta Y = V(k_0 Z_1 + \gamma). \tag{23}$$

Solve X and Y as functions of Z_1,

$$Y(Z_1) = \frac{\lambda_1(k_0 Z_1 + \gamma)}{s_1(k_0 Z_1 + \gamma) + \gamma\lambda_\delta \mathcal{R}_0}, \tag{24}$$

$$X(Z_1) = \frac{(s_1 Y(Z_1) + k_1 Z_1 + \delta_1)(k_0 Z_1 + \gamma)}{\gamma\lambda_\delta \mathcal{R}_0}, \tag{25}$$

$$\lambda_\mu X + (Z_1 - 1)(s_1 + \mu_1) + \mu Y = 0. \tag{26}$$

Let

$$h(Z_1) = \lambda_\mu X(Z_1) + (Z_1 - 1)(s_1 Y(Z_1) + \mu_1) + \mu Y(Z_1), \quad Z_1 \in [0, 1].$$

One can verify that $Y'(Z_1) > 0$, $Y''(Z_1) = \frac{-2k_0 s_1 Y'(Z_1)}{s_1(k_0 Z_1 + \gamma) + \gamma\lambda_\delta \mathcal{R}_0}$, and thereby

$$\begin{aligned} h''(Z_1) &= \lambda_\mu X''(Z_1) + s_1(2Y'(Z_1) + (Z_1 - 1)Y''(Z_1)) + \mu Y''(Z_1) \\ &> \frac{2k_0 s_1 \lambda_\mu Y'(Z_1)}{s_1(k_0 Z_1 + \gamma) + \gamma\lambda_\delta \mathcal{R}_0} + \frac{2s_1 Y'(Z_1)(s_1\gamma + \gamma\lambda_\delta \mathcal{R}_0 + k_0(s_1 - \mu))}{s_1(k_0 Z_1 + \gamma) + \gamma\lambda_\delta \mathcal{R}_0} \\ &= \frac{2s_1 Y'(Z_1)(s_1\gamma + \gamma\lambda_\delta \mathcal{R}_0 + k_0(s_1 + \lambda))}{s_1(k_0 Z_1 + \gamma) + \gamma\lambda_\delta \mathcal{R}_0} \\ &> 0. \end{aligned}$$

Since $h(1) = \lambda_\mu X(1) + \mu Y(1) > 0$, then $h(Z_1) = 0$ has a unique soultion $z_1 \in (0, 1)$ if $h(0) < 0$; i.e.,

$$\begin{aligned} &\lambda_\mu X(0) - (s_1 Y(0) + \mu_1) + \mu Y(0) < 0 \\ \Longleftrightarrow &\frac{\lambda_\mu}{\lambda_\delta \mathcal{R}_0}(s_1 Y(0) + \delta_1) - (s_1 - \mu)Y(0) - \mu_1 < 0 \\ \Longleftrightarrow &\left(\frac{s_1\lambda_\mu}{\lambda_\delta \mathcal{R}_0} - s_1 + \mu\right)\frac{\lambda_1}{s_1 + \lambda_\delta \mathcal{R}_0} + \frac{\delta_1\lambda_\mu}{\lambda_\delta \mathcal{R}_0} - \mu_1 < 0 \\ \Longleftrightarrow &-\mu_1\lambda_\delta \mathcal{R}_0^2 - ((s_1 - \delta)\lambda_\mu - \lambda\mu_1)\mathcal{R}_0 + s_1\lambda_\mu < 0 \\ \Longleftrightarrow &\mathcal{R}_0 > R_1. \end{aligned}$$

Thus, if $\mathcal{R}_0 > R_1$, system (8) has a unique adaptive-immunity-free equilibrium

$$I_1 = (x_1, y_1, z_1, 0, v_1).$$

Each of the two equilibrium points I_1 and I_2 represents a tumor steady state where uninfected tumor cells, infected tumor cells, viruses, and one type (either innate or adaptive) of immune cells co-exist. Through direct calculation, we find $f(X, Y, Z_1, Z_2) = s_i y_i - c_i$ at I_i, for $i = 1, 2$. Hence, the tumor would grow if $s_i y_i - c_i > 0$ and decay if $s_i y_i - c_i < 0$ at the state I_i ($i = 1, 2$).

3.4. Dual-Immunity Equilibria

Lastly, if both immune components are nonzero at an equilibrium, $Z_1 Z_2 \neq 0$, then $Y = \frac{c_1 - c_2}{s_1 - s_2} := y^*$. Hence, there exists an equilibrium such that $Z_1 Z_2 \neq 0$ only if $\frac{c_1 - c_2}{s_1 - s_2} \in (0, 1)$; i.e.,

$$(c_1 - c_2)(s_1 - s_2) > 0 \quad \text{and} \quad |c_1 - c_2| < |s_1 - s_2|.$$

Let

$$f_0 = s_1 y^* - c_1 = s_2 y^* - c_2 = \frac{s_2 c_1 - s_1 c_2}{s_1 - s_2}. \tag{27}$$

Then we can show that only two equilibrium points can possibly exist under this setting: one which is free of uninfected tumor cells when $f_0 + \delta < 0$, and the other whose

components are all positive (an interior equilibrium) when $f_0 + \delta \geq 0$. We discuss these two cases separately as follows.

Case (i): $f_0 + \delta < 0$.

Through some algebraic manipulation, one can obtain that the first such equilibrium must take the form

$$E_X = \left(0,\ y^*,\ \frac{-f_0-\delta}{k_1},\ 1+\frac{f_0+\delta}{k_1}-\frac{\mu y^*}{f_0+\mu},\ \frac{k_1 b\delta y^*}{k_1\gamma - k_0(f_0+\delta)}\right).$$

The equilibrium E_X exists if and only if

$$(f_0+\mu)(f_0+\delta+k_1) > k_1\mu y^*.$$

This equilibrium represents another steady state of successful tumor virotherapy, where all normal (i.e., uninfected) tumor cells are eliminated. In fact, at E_X we can easily calculate $f(X,Y,Z_1,Z_2) = f_0 < -\delta < 0$, which indicates that the tumor radius would exponentially decrease toward 0.

Case (ii): $f_0 + \delta \geq 0$.

On the other hand, to find the interior equilibrium, we solve the following equations

$$\lambda = \beta V + k_2 Z_2 + f(X,Y,Z_1,Z_2), \tag{28}$$
$$\beta XV = Y(k_1 Z_1 + \delta + f(X,Y,Z_1,Z_2)), \tag{29}$$
$$s_1 Y = c_1 + f(X,Y,Z_1,Z_2), \tag{30}$$
$$s_2 Y = c_2 + f(X,Y,Z_1,Z_2), \tag{31}$$
$$b\delta Y = V(k_0 Z_1 + \gamma), \tag{32}$$

and obtain

$$Y = y^*, \tag{33}$$
$$V(Z_1) = \frac{b\delta y^*}{k_0 Z_1 + \gamma}, \tag{34}$$
$$X(Z_1) = \frac{(k_0 Z_1+\gamma)(k_1 Z_1 + f_0 + \delta)}{\gamma\lambda_\delta \mathcal{R}_0}, \tag{35}$$
$$Z_2 = \frac{1}{k_2}\left(\lambda - f_0 - \frac{\gamma\lambda_\delta \mathcal{R}_0 y^*}{k_0 Z_1+\gamma}\right) := \psi_1(Z_1), \tag{36}$$
$$Z_2 = 1 - Z_1 - \frac{\lambda_\mu X(Z_1) + \mu y^*}{f_0+\mu} := \psi_2(Z_1). \tag{37}$$

Let $\psi(Z_1) = \psi_1(Z_1) - \psi_2(Z_1)$, then the interior equilibrium is determined by the root of $\psi(Z_1) = 0,\ \ Z_1 \in (0,1)$. Note that $\psi(Z_1)$ is an increasing function, hence, there is a unique root $z_1^* \in (0,1)$ if and only if $\psi(0) < 0 < \psi(1)$; i.e.,

$$y^*\lambda_\delta \mathcal{R}_0^2 + \left(f_0 - \lambda + k_2 - \frac{k_2\mu y^*}{f_0+\mu}\right)\mathcal{R}_0 - \frac{k_2\lambda_\mu(f_0+\delta)}{\lambda_\delta(f_0+\mu)} > 0$$

and

$$\frac{\gamma\lambda_\delta y^*\mathcal{R}_0^2}{k_0+\gamma} + \left(f_0 - \lambda - \frac{k_2\mu y^*}{f_0+\mu}\right)\mathcal{R}_0 - \frac{k_2\lambda_\mu(k_0+\gamma)(k_1+f_0+\delta)}{\gamma\lambda_\delta(f_0+\mu)} < 0,$$

These yield

$$R_3 < \mathcal{R}_0 < R_4,$$

where

$$R_3 = \frac{\sqrt{\left(f_0 - \lambda + k_2 - \frac{k_2\mu y^*}{f_0+\mu}\right)^2 + \frac{4y^*k_2\lambda_\mu(f_0+\delta)}{f_0+\mu}} - \left(f_0 - \lambda + k_2 - \frac{k_2\mu y^*}{f_0+\mu}\right)}{2y^*\lambda_\delta},$$

$$R_4 = \frac{\sqrt{\left(f_0 - \lambda - \frac{k_2\mu y^*}{f_0+\mu}\right)^2 + \frac{4y^*k_2\lambda_\mu(k_1+f_0+\delta)}{f_0+\mu}} - \left(f_0 - \lambda - \frac{k_2\mu y^*}{f_0+\mu}\right)}{\frac{2\gamma\lambda_\delta y^*}{k_0+\gamma}}.$$

For the existence of an interior equilibrium in the form of

$$E^* = (x^*, y^*, z_1^*, z_2^*, v^*)$$

with all positive components, it clearly only requires $z_2^* > 0$; i.e., $\mathcal{R}_0 < \frac{(\lambda - f_0)(k_0 z_1^* + \gamma)}{\gamma\lambda_\delta y^*}$ based on Equation (36). Since $z_1^* > 0$, the following condition

$$R_3 < \mathcal{R}_0 < \min\left\{\frac{\lambda - f_0}{\lambda_\delta y^*}, R_4\right\}$$

is sufficient to ensure the existence of E^* where all the tumor cells (uninfected and infected), immune cells, and viruses co-exist and balance each other. If E^* is stable, the success of the tumor treatment at this steady state also depends on the value of f_0 defined in Equation (27): the tumor grows if $f_0 > 0$ and decays if $f_0 < 0$.

4. Numerical Results

We now conduct numerical simulation to verify our analytical results presented in Section 3. Meanwhile, since the stabilities of several equilibria (such as I_1, I_2, E_X and E^*) are challenging to analyze mathematically, our numerical findings will provide useful insight into the system dynamics near these equilibrium points.

The definition and units of all the model parameters are listed in Table 1. We first conduct a numerical simulation using a set of baseline values for these parameters from the literature [19,20], where such parameters have been fitted to experimental data. The simulation results are presented in Figure 1, with the left panel showing the evolution of the density variables (X, Y, Z_1, Z_2, V) and the right panels showing the evolution of the tumor radius R. The parameter values are given in the caption. We observe that shortly after the start of the therapy (i.e., $t = 0$), the tumor radius stops growing and even decreases slightly, indicating that the virotherapy is taking effect. This period lasts about 1.5–2 days, after which the oncolytic virus loses its effectiveness and the tumor starts to grow exponentially. Correspondingly, the density of the uninfected tumor cells first decreases, and then increases to and stabilizes at a level close to 100%, while the density of the viruses decreases to a level near 0 after about 1.5 days. This pattern of tumor evolution is qualitatively consistent with the experimental observations [8,20].

Next, we vary some of these parameters within their biologically feasible ranges to explore the rich dynamics of tumor growth under different settings that represent a range of possible treatment scenarios. For each figure set presented below, the left panel shows the time evolution of the density variables and the right panel depicts the change of the tumor radius with respect to time. The parameter values are specified for each set of results (see the caption of each figure).

Regarding the trivial equilibria studied in Section 3.1, Figure 2 demonstrates that M_1 is locally asymptotically stable when $\mathcal{R}_0 < 1$. In particular, note that the percentage of the uninfected tumor cells (X) is 100% at this steady state. Correspondingly, the tumor radius $R(t)$ is exponentially increasing (in a hypothetic way) with a constant rate once the tumor growth stabilizes at the equilibrium M_1.

For the immunity-free equilibria, Figures 3–6 provide numerical verification of the analytical predictions in Section 3.2. Figures 3 and 4 show that I_0 is locally asymptotically stable when $\delta > \mu$ and $1 < \mathcal{R}_0 < \min\{r, R_1, R_2\}$. At this stable equilibrium, the tumor would grow if $\mathcal{R}_0 < 1 + \frac{\lambda\delta}{\mu\lambda_\delta}$; this is illustrated in Figure 3 where $\mathcal{R}_0 = 1.11 < 1 + \frac{\lambda\delta}{\mu\lambda_\delta} = 1.67$. On the other hand, the tumor would decay if $\mathcal{R}_0 > 1 + \frac{\lambda\delta}{\mu\lambda_\delta}$, as illustrated in Figure 4 where $\mathcal{R}_0 = 3.18 > 1 + \frac{\lambda\delta}{\mu\lambda_\delta} = 2.52$. Figures 5 and 6 illustrate the dynamics associated with I_0 and E_0 when $\mu > \delta$. Figure 5 shows that I_0 is locally asymptotically stable and the tumor radius decreases to 0 when $1 + \frac{\lambda\delta}{\mu\lambda_\delta} = 1.25 < \mathcal{R}_0 = 1.50 < \frac{\mu}{\mu-\delta} = 1.75$. Note also that the percentage of the uninfected tumor cells is pretty low (10%) at this steady state. Figure 6 shows that E_0 is locally asymptotically stable when $\mathcal{R}_0 > \frac{\mu}{\mu-\delta}$, and in this case, $f(X, Y, Z_1, Z_2) = -\delta$, thereby the tumor radius is exponentially decreasing to 0.

Concerning the single-immunity equilibria analyzed in Section 3.3, Figures 7 and 8 depict the local stabilities of I_1 and I_2, respectively. At the equilibrium point I_i, the tumor growth rate is determined by $f(X, Y, Z_1, Z_2) = s_i y_i - c_i$ for $i = 1, 2$. With the parameter setting in Figure 7, $s_1 y_1 - c_1 = 2 > 0$, and with that in Figure 8, $s_2 y_2 - c_2 = 1 > 0$. Thus, the tumor radius is exponentially increasing in each case. We note that the levels of the uninfected tumor cells remain very high (more than 70%) for both steady states. In contrast, Figure 9 shows that at the equilibrium I_2 the tumor radius is decreasing to 0, where $s_2 y_2 - c_2 = -0.3 < 0$ and where the uninfected tumor cells are only about 35%.

Regarding the dual-immunity equilibria investigated in Section 3.4, Figure 10 illustrates that when the equilibrium E_X exists and is stable, the tumor radius $R(t)$ at that state will decay and approach 0, where $f(X, Y, Z_1, Z_2) = f_0 < -\delta < 0$. In addition, if there is a stable interior equilibrium E^*, then the tumor radius at E^* would also be decreasing to 0 if $f_0 < 0$. This is verified in Figure 11, where $-\delta \leq f_0 = -0.18 < 0$.

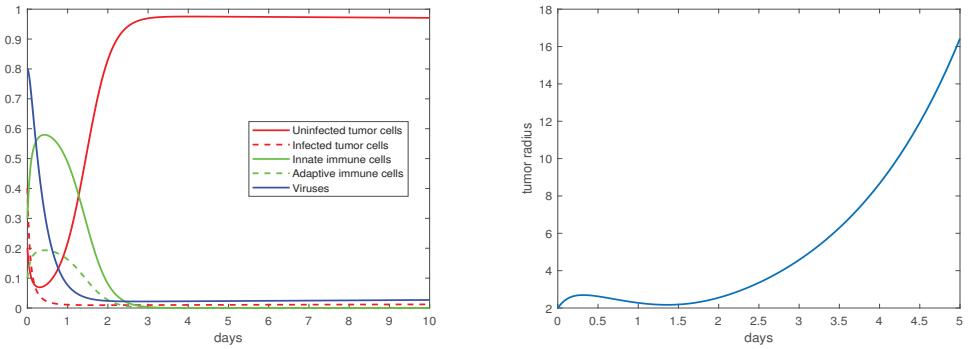

Figure 1. Simulation results for the base scenario. The values of the the parameters are: $\lambda = 2$, $\beta = 3.5$, $k_1 = 2$, $k_2 = 2$, $s_1 = 56$, $s_2 = 56$, $c_1 = 2$, $c_2 = 2$, $\delta = 5.6$, $k_0 = 1$, $\gamma = 2.5$, $\mu = 2.1$, $b = 1$.

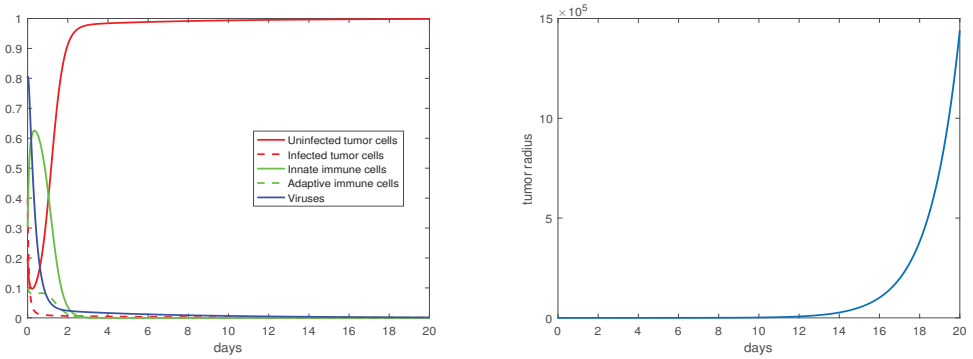

Figure 2. The equilibrium $M_1 = (1, 0, 0, 0, 0)$ is asymptotically stable and the tumor radius is exponentially increasing when $\mathcal{R}_0 = 0.93 < 1$. The values of the the parameters are: $\lambda = 2$, $\beta = 3.5$, $k_1 = 1$, $k_2 = 2, s_1 = 60$, $s_2 = 20$, $c_1 = 2$, $c_2 = 1, \delta = 10$, $k_0 = 1.5, \gamma = 2.5, \mu = 2.5$, $b = 0.8$.

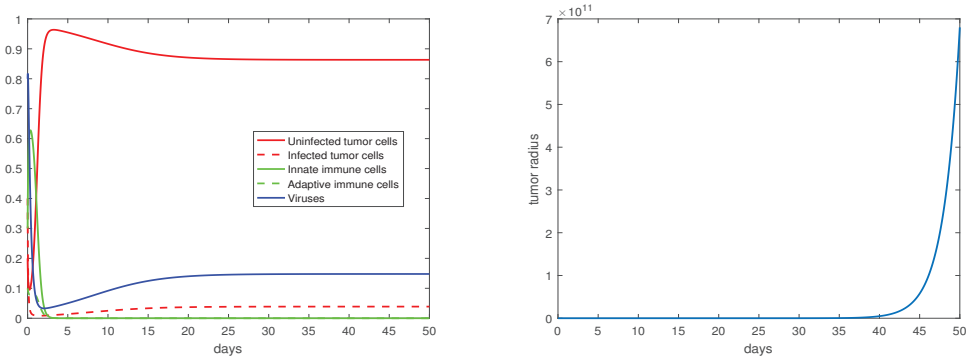

Figure 3. The equilibrium $I_0 = (0.86, 0.04, 0, 0, 0.15)$ is asymptotically stable and the tumor radius is exponentially increasing when $\delta > \mu$ and $\mathcal{R}_0 = 1.11 < \min\{r = 6.05, R_1 = 1.17, R_2 = 1.36\}$. The values of the parameters are: $\lambda = 2,\ \beta = 3.5,\ k_1 = 1,\ k_2 = 2, s_1 = 60,\ s_2 = 20,\ c_1 = 2,\ c_2 = 1,$ $\delta = 10,\ k_0 = 1.5, \gamma = 2.5, \mu = 2.5,\ b = 0.95$.

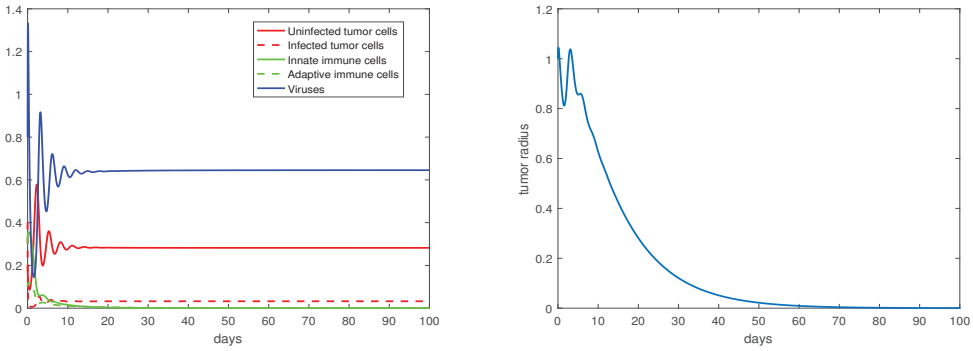

Figure 4. The equilibrium $I_0 = (0.28, 0.03, 0, 0, 0.65)$ is asymptotically stable and the tumor radius is exponentially decreasing when $\delta > \mu$ and $\mathcal{R}_0 = 3.18 < \min\{r = 6.05, R_1 = 4.42, R_2 = 3.60\}$. The values of the parameters are: $\lambda = 2,\ \beta = 3.5,\ k_1 = 1,\ k_2 = 2, s_1 = 22,\ s_2 = 21,\ c_1 = 1.1,\ c_2 = 1,$ $\delta = 20,\ k_0 = 1.5, \gamma = 2.5, \mu = 1.2,\ b = 2.5$.

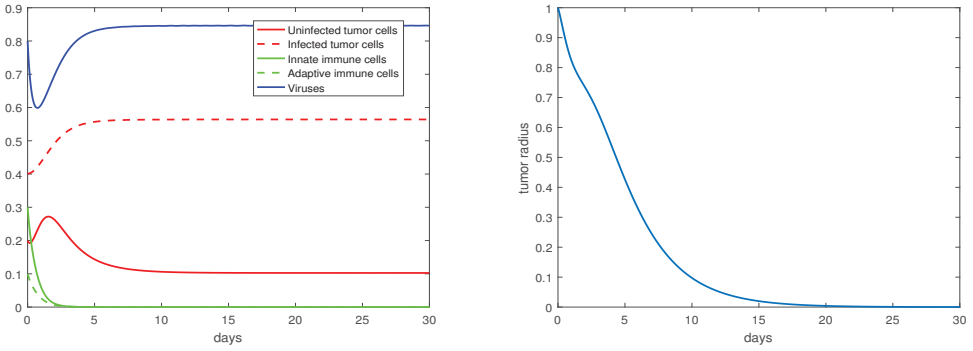

Figure 5. The equilibrium $I_0 = (0.10, 0.56, 0, 0, 0.84)$ is asymptotically stable and the tumor radius is exponentially decreasing when $\delta < \mu$ and $1 < \mathcal{R}_0 = 1.50 < \min\{\frac{\mu}{\mu-\delta} = 1.75, R_1 = 2.06, R_2 = 1.85\}$. The values of the parameters are: $\lambda = 2,\ \beta = 3.5,\ k_1 = 1,\ k_2 = 2, s_1 = 2,\ s_2 = 1.5,\ c_1 = 3,\ c_2 = 2.5,$ $\delta = 1.5,\ k_0 = 1.5, \gamma = 2.5, \mu = 3.5,\ b = 2.5$.

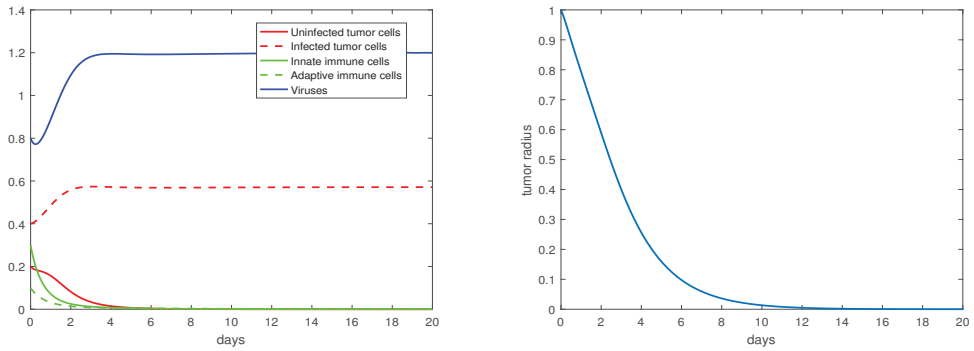

Figure 6. The equilibrium $E_0 = (0, 0.57, 0, 0, 1.20)$ is asymptotically stable and the tumor radius is exponentially decreasing when $\delta < \mu$ and $\min\{\mathcal{R}_0 = 2.10, R_1 = 2.06, R_2 = 1.85\} > \frac{\mu}{\mu-\delta} = 1.75$. The values of the parameters are: $\lambda = 2,\ \beta = 3.5,\ k_1 = 1,\ k_2 = 2, s_1 = 2,\ s_2 = 1.5,\ c_1 = 3,\ c_2 = 2.5,$ $\delta = 1.5,\ k_0 = 1.5, \gamma = 2.5, \mu = 3.5,\ b = 3.5.$

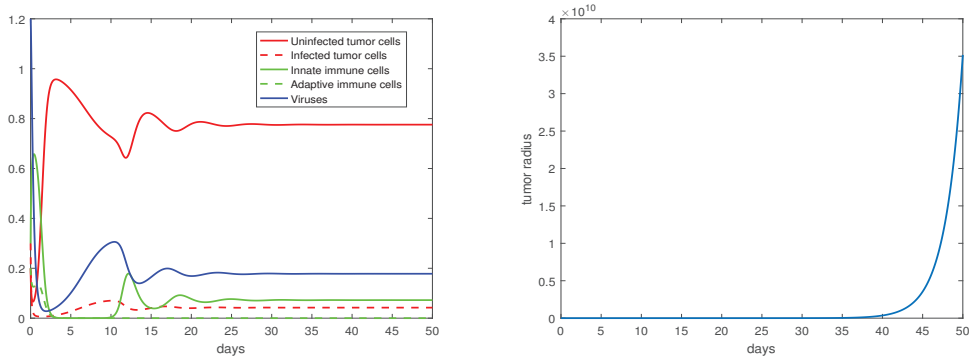

Figure 7. The equilibrium $I_1 = (0.75, 0.05, 0.05, 0, 0.23)$ is asymptotically stable and the tumor radius is exponentially increasing when $\mathcal{R}_0 = 1.28 > R_1 = 1.12$. The values of the parameters are: $\lambda = 2,\ \beta = 3.5,\ k_1 = 1,\ k_2 = 2, s_1 = 80,\ s_2 = 20,\ c_1 = 2,\ c_2 = 1, \delta = 10,\ k_0 = 1.5, \gamma = 2.5,$ $\mu = 2.5,\ b = 1.1.$

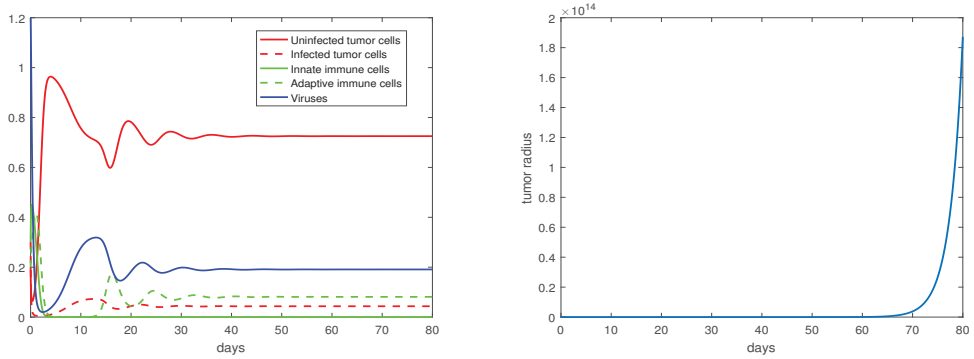

Figure 8. The equilibrium $I_2 = (0.73, 0.04, 0, 0.08, 0.19)$ is asymptotically stable and the tumor radius is exponentially increasing when $\mathcal{R}_0 = 1.28 > R_2 = 1.14$. The values of the parameters are: $\lambda = 2,\ \beta = 3.5,\ k_1 = 1,\ k_2 = 2, s_1 = 60,\ s_2 = 50,\ c_1 = 2,\ c_2 = 1, \delta = 10,\ k_0 = 1.5, \gamma = 2.5,$ $\mu = 2.5,\ b = 1.1.$

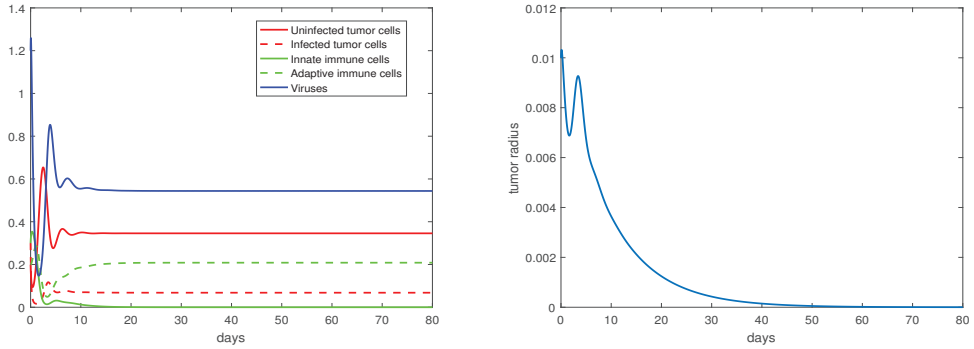

Figure 9. The equilibrium $I_2 = (0.35, 0.08, 0, 0.21, 0.55)$ is asymptotically stable and the tumor radius is exponentially decreasing when $\mathcal{R}_0 = 2.33 > R_2 = 1.67$. The values of the parameters are: $\lambda = 2,\ \beta = 3.5,\ k_1 = 1,\ k_2 = 2, s_1 = 20,\ s_2 = 10,\ c_1 = 2,\ c_2 = 1, \delta = 10,\ k_0 = 1.5, \gamma = 2.5,$ $\mu = 2.5,\ b = 2.$

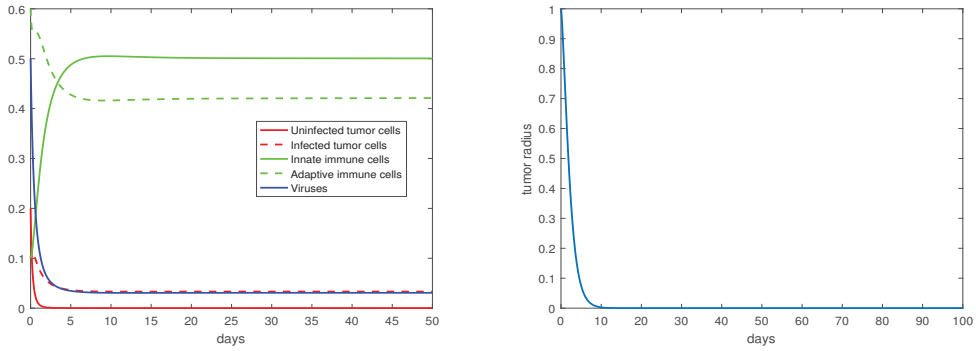

Figure 10. The equilibrium $E_X = (0, 0.03, 0.5, 0.42, 0.03)$ is asymptotically stable and the tumor radius is exponentially decreasing when $\mathcal{R}_0 = 1.2$. The values of the parameters are: $\lambda = 2,\ \beta = 3.5,\ k_1 = 1,\ k_2 = 9.3, s_1 = 30,\ s_2 = 15,\ c_1 = 3,\ c_2 = 2.5, \delta = 1.5,\ k_0 = 1.5, \gamma = 2.5,$ $\mu = 2.5,\ b = 2.$

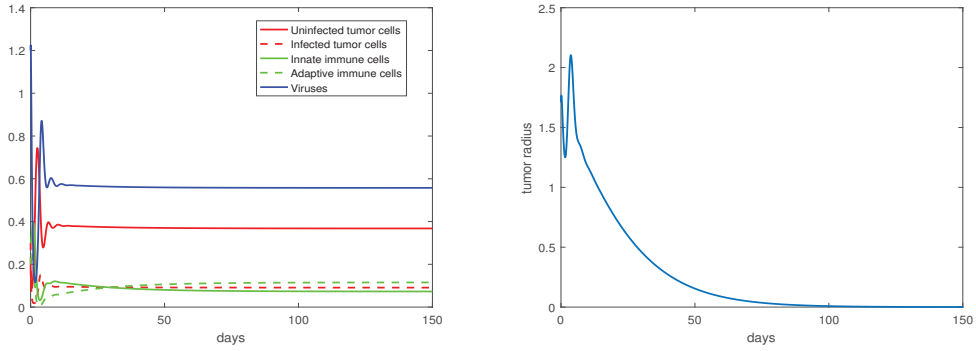

Figure 11. The equilibrium $E^* = (0.38, 0.09, 0.1, 0.082, 0.57)$ is asymptotically stable and the tumor radius is exponentially decreasing when $R_3 = 2.05 < \mathcal{R}_0 = 2.24 < \min\{\frac{\lambda - f_0}{\lambda_\delta y^*} = 2.4, R_4 = 5.84\}$. The values of the parameters are: $\lambda = 2,\ \beta = 3.5,\ k_1 = 1,\ k_2 = 9.3, s_1 = 9,\ s_2 = 20,\ c_1 = 1,\ c_2 = 2,$ $\delta = 8,\ k_0 = 1.5, \gamma = 2.5, \mu = 2.5,\ b = 2.$

5. Discussion

We have presented an ODE model to describe the spatially homogeneous state of tumor growth under virotherapy. This model, derived and simplified from the PDE system (1), enables us to conduct a detailed analysis on the time evolution of the tumor radius and the various equilibrium points, their stability properties, and their impact on tumor growth.

Our model describes the process of tumor growth as a moving boundary problem. The threshold value $\mathcal{R}_0$ introduced in our analysis represents the capability that the oncolytic viruses can effectively invade the tumor. When $\mathcal{R}_0 < 1$, for example, the stability of the equilibrium M_1 and the exponential increase of the tumor radius at M_1 indicate a failure of the tumor treatment due to the insufficient invasion capability of the viruses. Consequently, $\mathcal{R}_0 > 1$ provides a necessary condition for effective viral invasion, though the eventual outcome of the tumor therapy would be determined by the specific dynamical properties at an equilibrium and the associated tumor growth rate. When $\mathcal{R}_0$ is above unity, both the number of the equilibrium points and the complexity of the dynamics increase. In general, each equilibrium represents a steady state, and the tumor growth dynamics near such a steady state are shaped by the interaction among the uninfected and infected tumor cells, the innate and adaptive immune cells, and the viruses. Although the dynamical behaviors for some of the equilibria (I_1, I_2, E_X and E^*) have not been fully resolved analytically, our numerical simulation results provide helpful insight into their stability and connection to the growth rate of the tumor.

Our results show that the threshold value $\mathcal{R}_0$ can be used to as an indicator regarding the chance of success for tumor virotherapy. The value of $\mathcal{R}_0$ can be modified by genetically manipulating the viruses; for example, increasing the burst size b (which leads to a larger $\mathcal{R}_0$) is an effective strategy to improve the efficacy of the virotherapy [19]. From the modeling perspective, the higher $\mathcal{R}_0$ is, the better outcome the therapy might achieve. From the practical point of view, however, it is not possible to increase $\mathcal{R}_0$ in an arbitrary manner. Meanwhile, high value of $\mathcal{R}_0$ might come at the price of some side effects of the tumor treatment, such as harming normal body tissues surrounding the tumor [19]. Our analysis and simulation results show that the virotherapy can achieve a success for relatively low $\mathcal{R}_0$ (for example, between 1 and 2), as long as we can push the solution orbit into the basin of attraction for one of those stable equilibrium points where the associated tumor growth rate is negative. These findings could provide useful guidelines for the design of practical virotherapy protocols to improve the rate of success for tumor treatment.

It is known that some tumors (such as melanoma, kidney cancer, and lung cancer) are likely to trigger a strong adaptive immune response and are commonly referred to as "hot tumors", while some other tumors (such as glioblastoma, prostate cancer, and breast cancer) are able to suppress the adaptive immune response and are commonly referred to as "cold tumors". Our model could offer useful insight into the treatment of these two types of tumors. In particular, the parameter k_2 in our model measures the rate of fighting cancerous cells due to the adaptive immune response. Our results suggests that an increased value of k_2 could improve the performance of the tumor therapy, as shown in Figures 10 and 11 where the tumor radius quickly decays and approaches 0. This parameter represents the T-cell infiltration rate in practical tumor treatment. In fact, many therapeutic strategies have been proposed to increase the T-cell infiltration rate so as to possibly turn a cold tumor into a hot tumor [23].

Our model can be naturally extended to include other approaches for tumor treatment, such as chemotherapy and radiation therapy. The combination of these different treatment options could potentially achieve a better performance than using a single therapy, and the mathematical model could help to quantify and predict the treatment outcome. In addition, the current model does not take into account potential mutations of the oncolytic viruses. This could be an interesting direction for our future modeling effort.

Tumor growth is a highly complex process that involves rich temporal and spatial dynamics. This paper is focused on the temporal growth dynamics of the tumor and related equilibrium analysis, without considering the spatial heterogeneity. It may be important to mathematically investigate the spatial heterogeneity of tumor growth in some situations, and a few quantitative studies have been performed in this direction (see, e.g., [24,25]). These models are generally simpler than the PDE model (1), though their analytical tools might be generalized to handle more complex tumor models such as (1).

Author Contributions: Conceptualization, J.W.; Methodology, C.Y. and J.W.; Formal analysis, C.Y.; Investigation, C.Y. and J.W.; Writing—original draft, C.Y. and J.W.; Writing—review & editing, J.W. All authors have read and agreed to the published version of the manuscript.

Funding: This research was partially funded by the National Science Foundation grant numbers 1951345 and 1913180.

Data Availability Statement: Not applicable.

Conflicts of Interest: The authors declare no conflict of interest.

Appendix A. Homogeneous State with a Fixed Boundary

With the assumption in (3), if we additionally assume that the velocity field is spatially uniform; i.e., $U = U(t)$, then we have

$$U(t)\frac{\partial}{\partial \rho}(\rho^2) = \rho^2 f\big(X(t), Y(t), Z_1(t), Z_2(t)\big).$$

This yields $U(t) \equiv 0$ and $f(X, Y, Z_1, Z_2) \equiv 0$. Consequently, we obtain $\frac{dR}{dt} = 0$, and the tumor would be stationary with a fixed boundary under this setting.

As a result, we obtain the following ODE system

$$\begin{aligned}
\frac{dX}{dt} &= \lambda X - \beta XV - k_2 XZ_2,\\
\frac{dY}{dt} &= \beta XV - k_1 YZ_1 - \delta Y,\\
\frac{dZ_1}{dt} &= s_1 YZ_1 - c_1 Z_1,\\
\frac{dZ_2}{dt} &= s_2 YZ_2 - c_2 Z_2,\\
\frac{dV}{dt} &= b\delta Y - k_0 Z_1 V - \gamma V.
\end{aligned} \tag{A1}$$

To simplify the notation, let us define

$$R_0 = \frac{\gamma\lambda}{b\beta\delta}. \tag{A2}$$

Clearly, the system (A1) has a trivial equilibrium $Q_0 = (0, 0, 0, 0, 0)$ and an immunity-free equilibrium $Q_1 = (\frac{\gamma}{b\beta}, R_0, 0, 0, \frac{\lambda}{\beta})$. Based on their Jacobian matrices

$$J_0 = \begin{bmatrix} \lambda & 0 & 0 & 0 & 0\\ 0 & -\delta & 0 & 0 & 0\\ 0 & 0 & -c_1 & 0 & 0\\ 0 & 0 & 0 & -c_2 & 0\\ 0 & b\delta & 0 & 0 & -\gamma \end{bmatrix} \text{ and } J_1 = \begin{bmatrix} 0 & 0 & 0 & -\frac{k_2\gamma}{b\beta} & -\frac{\gamma}{b}\\ \lambda & -\delta & -k_1 R_0 & 0 & \frac{\gamma}{b}\\ 0 & 0 & s_1 R_0 - c_1 & 0 & 0\\ 0 & 0 & 0 & s_2 R_0 - c_2 & 0\\ 0 & b\delta & \frac{-k_0\lambda}{\beta} & 0 & -\gamma \end{bmatrix},$$

their characteristic polynomials are

$$\begin{aligned}
p_0(u) &= (u-\lambda)(u+\delta)(u+c_1)(u+c_2)(u+\gamma),\\
p_1(u) &= (u - s_1R_0 + c_1)(u - s_2R_0 + c_2)(u^3 + (\delta+\gamma)u^2 + \gamma\lambda\delta),
\end{aligned}$$

respectively. Hence, Q_0 and Q_1 are both unstable since λ is a positive eigenvalue for J_0, and the polynomial $u^3 + (\delta + \gamma)u^2 + \gamma\lambda\delta$ has at least one root with positive real part based on the Routh–Hurwitz criterion. In addition, $R_0 < \frac{c_1}{s_1}$ leads to the equilibrium

$$Q_2 = \left(\frac{c_1}{s_1\lambda}(k_1 Z_1 + \delta), \frac{c_1}{s_1}, \frac{\gamma(c_1 - s_1 R_0)}{k_0 s_1 R_0}, 0, \frac{\lambda}{\beta}\right)$$

and $R_0 > \frac{c_2}{s_2}$ leads to the equilibrium

$$Q_3 = \left(\frac{\gamma}{b\beta}, \frac{c_2}{s_2}, 0, \frac{\lambda(s_2 R_0 - c_2)}{k_2 s_2 R_0}, \frac{c_2 b\delta}{s_2\gamma}\right).$$

Their associated characteristic polynomials can be written as follows

$$p_2(u) = \left(u - \frac{c_1 s_2}{s_1} + c_2\right)(u^4 + a_3 u^3 + a_2 u^2 + a_1 u + a_0),$$
$$p_3(u) = \left(u - \frac{c_2 s_1}{s_2} + c_1\right)(u^4 + b_3 u^3 + b_2 u^2 + b_1 u + b_0),$$

where a_i, b_i $(i = 0, 1, 2, 3)$ are constants determined by the parameters in model (A1). One can verify that $a_0 < 0$ and $b_2 = 0$. Hence, Q_2 and Q_3 are both unstable by the Routh–Hurwitz criterion.

Our analysis of this scenario, which represents a spatially homogeneous tumor state with a fixed boundary, shows that all the equilibrium points are unstable. This result implies that a tumor cannot stabilize under such a setting; instead, the tumor size has to change with time in the presence of tumor–virus–immune interaction, leading to the more realistic (and more complex) scenario with a moving tumor boundary.

References

1. Shah, A.C.; Benos, D.; Gillespie, G.Y.; Markert, J.M. Oncolytic viruses: Clinical applications as vectors for the treatment of malignant gliomas. *J. Neurooncol.* **2003**, *65*, 203–226. [CrossRef] [PubMed]
2. Kasuya, H.; Takeda, S.; Nomoto, S.; Nakao, A. The potential of oncolytic virus therapy for pancreatic cancer. *Cancer Gene Ther.* **2005**, *12*, 725–736. [CrossRef] [PubMed]
3. Kirn, D.H.; McCormick, F. Replicating viruses as selective cancer therapeutics. *Mol. Med. Today* **1996**, *2*, 519–527. [CrossRef] [PubMed]
4. Kirn, D.; Hermiston, T.; McCormick, F. ONYX-015: Clinical data are encouraging. *Nat. Med.* **1998**, *4*, 1341–1342. [CrossRef]
5. Parato, K.A.; Senger, D.; Forsyth, P.A.; Bell, J.C. Recent progress in the battle between oncolytic viruses and tumours. *Nat. Rev. Cancer* **2005**, *5*, 965–976. [CrossRef] [PubMed]
6. Chiocca, E.A.; Rabkin, S.D. Oncolytic viruses and their application to cancer immunotherapy. *Cancer Immunol. Res.* **2014**, *2*, 295–300. [CrossRef]
7. Lawler, S.E.; Chiocca, E.A. Oncolytic virus-mediated immunotherapy: A combinatorial approach for cancer treatment. *J. Clin. Oncol.* **2015**, *33*, 2812–2814. [CrossRef]
8. Fulci, G.; Breymann, L.; Gianni, D.; Kurozomi, K.; Rhee, S.S.; Yu, J.; Kaur, B.; Louis, D.N.; Weissleder, E.; Caligiuri, M.A.; et al. Cyclophosphamide enhances glioma virotherapy by inhibiting innate immune responses. *Proc. Natl. Acad. Sci. USA* **2006**, *103*, 12873–12878. [CrossRef]
9. Wein, L.M.; Wu, J.T.; Kirn, D.H. Validation and analysis of a mathematical model of a replication-competent oncolytic virus for cancer treatment: Implications for virus design and delivery. *Cancer Res.* **2003**, *63*, 1317–1324.
10. Melcher, A.; Parato, K.; Rooney, C.M.; Bell, J.C. Thunder and lightning: Immunotherapy and oncolytic viruses collide. *Mol. Ther.* **2011**, *19*, 1008–1016. [CrossRef]
11. Wodarz, D. Viruses as antitumor weapons: Defining conditions for tumor remission. *Cancer Res.* **2001**, *61*, 3501–3507.
12. Komarova, N.L.; Wodarz, D. ODE models for oncolytic virus dynamics. *J. Theor. Biol.* **2010**, *263*, 530–543. [CrossRef] [PubMed]
13. Karev, G.P.; Novozhilov, A.S.; Koonin, E.V. Mathematical modeling of tumor therapy with oncolytic viruses: Effects of parametric heterogeneity on cell dynamics. *Biol. Direct* **2006**, *1*, 30. [CrossRef] [PubMed]
14. Novozhilov, A.S.; Berezovskaya, F.S.; Koonin, E.V.; Karev, G.P. Mathematical modeling of tumor therapy with oncolytic viruses: Regimes with complete tumor elimination within the framework of deterministic models. *Biol. Direct* **2006**, *1*, 6. [CrossRef]
15. Tian, J.P. The replicability of oncolytic virus: Defining conditions on tumor virotherapy. *Math. Biosci. Eng.* **2011**, *8*, 841–860. [PubMed]

16. Wang, Z.; Guo, Z.; Peng, H. A mathematical model verifying potent oncolytic efficacy of M1 virus. *Math. Biosci.* **2016**, *276*, 19–27. [CrossRef]
17. Wu, J.T.; Byrne, H.M.; Kirn, D.H.; Wein, L.M. Modeling and analysis of a virus that replicates selectively in tumor cells. *Bull. Math. Biol.* **2001**, *63*, 731–768. [CrossRef]
18. Wu, J.T.; Kirn, D.H.; Wein, L.M. Analysis of a three-way race between tumor growth, a replication-competent virus and an immune response. *Bull. Math. Biol.* **2004**, *66*, 605–625. [CrossRef]
19. Friedman, A.; Tian, J.P.; Fulci, G.; Chiocca, E.A.; Wang, J. Glioma virotherapy: Effects of innate immune suppression and increased viral replication capacity. *Cancer Res.* **2005**, *66*, 2314–2319. [CrossRef]
20. Timalsina, A.; Tian, J.P.; Wang, J. Mathematical and computational modeling of tumor virotherapy with mediated immunity. *Bull. Math. Biol.* **2017**, *79*, 1736–1758. [CrossRef]
21. Murray, J.D. *Mathematical Biology*, 3rd ed.; Springer: Berlin/Heidelberg, Germany, 2007.
22. Asamoah, J.K.K.; Nyabadza, F.; Jin, Z.; Bonyah, E.; Khan, M.A.; Li, M.Y.; Hayat, T. Backward bifurcation and sensitivity analysis for bacterial meningitis transmission dynamics with a nonlinear recovery rate. *Chaos Solitons Fractals* **2020**, *140*, 110237. [CrossRef]
23. Liu, Y.T.; Sun, Z.J. Turning cold tumors into hot tumors by improving T-cell infiltration. *Theranostics* **2021**, *11*, 5365–5386. [CrossRef] [PubMed]
24. Hinow, P.; Gerlee, P.; McCawley, L.J.; Quaranta, V.; Ciobanu, M.; Wang, S.; Graham, J.M.; Ayati, B.P.; Claridge, J.; Swanson, K.R.; et al. A spatial model of tumor-host interaction: Application of chemotherapy. *Math. Biosci. Eng.* **2009**, *6*, 521–546. [PubMed]
25. Preziosi, L. *Cancer Modelling and Simulation*; Chapman Hall/CRC Press: Boca Raton, FL, USA, 2003.

mathematics

MDPI

Article

A Mathematical Model to Optimize the Neoadjuvant Chemotherapy Treatment Sequence for Triple-Negative Locally Advanced Breast Cancer

Juan C. López-Alvarenga [1], Antonmaria Minzoni-Alessio [2,†], Arturo Olvera-Chávez [2], Gustavo Cruz-Pacheco [2], Juan C. Chimal-Eguia [3], Joselín Hernández-Ruíz [4], Mario A. Álvarez-Blanco [5], María Y. Bautista-Hernández [6] and Rosa M. Quispe-Siccha [7,*]

[1] Population Health & Biostatistics, School of Medicine, University of Texas Rio Grande Valley, Edinburgh, TX 78539, USA
[2] Instituto de Investigaciones en Matemáticas Aplicadas y en Sistemas, Universidad Nacional Autónoma de México, Ciudad de México CP 04510, Mexico
[3] Laboratorio de Ciencias Matemáticas y Computacionales, Centro de Investigación en Computación, Instituto Politécnico Nacional, Ciudad de México CP 07738, Mexico
[4] Servicio de Farmacología Clínica, Hospital General de México "Dr. Eduardo Liceaga", Ciudad de México CP 06726, Mexico
[5] Unidad de Oncología Médica, Servicio de Oncología, Hospital General de México "Dr. Eduardo Liceaga", Ciudad de México CP 06726, Mexico
[6] Unidad de Radio Terapia, Servicio de Oncología, Hospital General de México "Dr. Eduardo Liceaga", Ciudad de México CP 06726, Mexico
[7] Unidad de Investigación y Desarrollo Tecnológico, Hospital General de México "Dr. Eduardo Liceaga", Ciudad de México CP 06726, Mexico
* Correspondence: rosa.quispe@salud.gob.mx
† Deceased on 1 July 2017.

Abstract: Background: Triple-negative locally advanced breast cancer is an aggressive tumor type. Currently, the standard sequence treatment is applied, administering anthracyclines first and then a taxane plus platinum. Clinical studies for all possible treatment combinations are not practical or affordable, but mathematical modeling of the active mitotic cell population is possible. Our study aims to show the regions with the tumor's most substantial cellular population variation by utilizing all possible values of the parameters $\left(\alpha_s^i\right)$ that define the annihilatory drug capacity according to the proposed treatment. Method: A piecewise linear mathematical model was used to analyze the cell population growth by applying four treatments: standard sequences of 21 days (SS21) and 14 days (SS14), administering anthracyclines first, followed by a taxane plus platinum, and inverted sequences of 21 days (IS21) and 14 days (IS14), administering a taxane plus platinum first then anthracyclines. Results: The simulation showed a higher effect of IS14 over SS14 when the rate of drug resistance was larger in the cell population during DNA synthesis (G1 and S) compared to cells in mitosis (G2 and M). However, if the proportion of resistant cells in both populations was equivalent, then treatments did not differ. Conclusions: When resistance is considerable, IS14 is more efficient than SS14, reducing the tumor population to a minimum.

Keywords: mathematical model and simulations; neoadjuvant chemotherapy; triple-negative; locally advanced breast cancer

MSC: 37N25; 92-10; 34C60

1. Introduction

During the last 50 years, different mathematical models have been developed to illustrate how a cancerous tumor's growth begins, its dynamics, and treatments. Some models include the organism's resistance to the different drugs that are usually administered as

the first step to reduce the size of the tumor (neoadjuvant therapy) before the primary treatment, usually consisting of surgery for all types of cancer [1–4] but especially for breast cancer [5–11].

Because breast cancer is one of the most studied pathologies in the world, many efforts have been devoted to understanding the relationships between immune cells, tumor cells, and certain adjuvant treatments [6,12–14]. To cite an example, Jarett et al. [12] discussed the effects of trastuzumab on the overexpression of the HER2 gene, which is characteristic of breast cancer, using a mathematical model and integrating the experimental results [12–14]. Other examples include those where neoadjuvant treatment affects the immune system and its interaction with cancer cells [12,14,15].

When cancer is in its early stages, surgery is performed first and then radiotherapy. Therefore, implementing the reverse sequence (radiotherapy first and later surgery) has been widely ruled out for many cancers. For instance, Lopez-Alonso and Poleszczuk J. et al. [16,17] reversed the traditional treatment (radiotherapy first to induce antitumor immunity and then surgery) for different cancers and evaluated the overall survival (OS) and the disease-free survival (DFS), obtaining better results. We were interested in inquiring if a reverse or different sequence would produce better results compared with a traditional one as a research question.

Triple-negative breast cancer (no expression of estrogen receptor, progesterone receptor, and growth factor 2 receptor (Her2)) represents 20% of breast cancer cases in young women, with early recurrence and dissemination to the viscera and central nervous system. In patients with triple-negative, locally advanced breast cancer (TN-LABC; T3-T4, N1-N3), unlike other molecular subtypes, the complete pathological response (pCR) is a surrogate for more remarkable overall survival and DFS compared with that of patients with residual disease [18,19].

The order of chemotherapy administration before or after surgery may change the outcome. For example, the National Surgical Adjuvant Breast and Bowel Project (NSABP) Study B-18 demonstrated a 13% pCR rate when doxorubicin (DX) (60 mg/m^2) plus cyclophosphamide (CPh) (600 mg/m^2) was administered every 21 days for four cycles during the pre-surgery period. This chemotherapy slightly improved the survival and disease-free time compared with the same chemotherapy administered in the post-surgery period. However, the NSABP Study B-27 later showed that adding docetaxel every 21 days for four cycles after the standard neoadjuvant sequence with DX and CPh increased the pCR to 26% ($p < 0.001$) [20].

Adding carboplatin (CP) to the sequential neoadjuvant chemotherapy scheme increases the probability of the pCR in patients with TN-LABC by 13% [21]. However, other long-term results of randomized phase II studies, CALGB 40603 (Alliance) [22] and GeparSixto [23], showed that CP increases the pCR but does not improve the event-free interval. The low number of patients may explain these controversial findings.

The morphological phenotypes in TN-LABC might determine a low response to systemic therapy in TN-LABC; other poor-prognosis factors are inflammatory carcinoma in individuals older than 40 years and a high proliferation index [24]. Different susceptibilities to treatment depend on their genotype (tumor markers), e.g., basal-like (BL) tumors carrying pathogenic mutations in the BRCA1 gene (57%) or BRCA2 gene (23%) respond to treatment with platinum agents [25]. In a study with 290 patients with TN-LABC, 47% of BL-1 tumors responded to chemotherapy compared with 28% of BL-2 tumors [26]. Additionally, patients with tumors expressing p53 and Ki-67 protein markers treated with taxanes might respond better to neoadjuvant chemotherapy [27,28].

When the tumor's interstitial fluid pressure (IFP) increases, the bioavailability of antineoplastic drugs decreases. Therefore, the drugs do not reach the tumor cells at a sufficient concentration. When paclitaxel (PX) is administered after anthracyclines, the IFP increases. However, PX is administered before anthracyclines. In that case, the IFP decreases [29,30], and the order of the treatment sequence in TN-LABC patients may increase reduction rates and favor increases in complete pathological responses.

Mathematical models help to explain the response probability to treatments and their combinations. The logarithmic death or log-kill is a cancer model with a constant exponential growth fraction per time step. However, the presence of effective cancer drugs also decreases the tumor size by a constant fraction. For example, if a drug eliminates 90% of a tumor cell population and a second drug destroys 90%, in the end, they may eliminate 99% of the tumor cells [31]. A modification to the log-kill is the Norton–Simon hypothesis, which relates the treatment effects to the growth rate and the tumor size [32]. For example, a small tumor with a high growth rate can be eliminated using a particular medication at a specific dose; however, the same drug has a weaker effect on treating tumors of a larger size with a low growth rate.

A piecewise linear mathematical model (PLMM) based on Roe-Dale R. et al. [13] was proposed to analyze four treatment schedules (standard sequence, 21 and 14 days, and inverted sequence, 21 and 14 days) [22]. The novelty of our PLMM is a wide spectrum of growth rates of the active mitotic cell population (AMCP) for treatment sequences and chemotherapy cell resistance.

2. Materials and Methods

Four chemotherapy sequences were described using standard doses of DX, CPh, CP, and PX (defined in Section 2.1); then, the evolution of the AMCP was described using linear ordinary differential equations (ODEs). Finally, we determined which treatment sequence had a higher probability of success for neoadjuvant chemotherapy patients with TN-LABC to reach a maximum tumor reduction that could direct a better pCR and more conservative breast surgeries.

2.1. Standard Doses

The standard dose scheme we used for our model is detailed below:

(a) The DX dose was 60 mg/m^2 body surface area every 21 or 14 days for 4 cycles.

(b) The CPh dose was 600 mg/m^2 body surface area every 21 or 14 days for 4 cycles. The treatment administered every 14 days is proposed by the NCCN guidelines in the United States of America; however, some countries continue administering treatment every 21 days as described in previous studies [20]. The treatment administration every 14 days is associated with unacceptable hematological toxicity. That must be balanced by administering granulocyte colony-stimulating factor (GCSF) [33].

(c) The PX dose was 80 mg/m^2 of body surface area intravenously every week for 12 weeks.

(d) The CP dose was obtained through the Calvert formula, $Dose = (IFG + 25) \times AUC$, where IFG is the glomerular function index or creatinine clearance; this is the volume of fluid filtered per time unit from renal glomerular capillaries into Bowman's capsule, usually measured in milliliters per minute. The IFG varies for each patient. For the CP every three weeks, which was our schedule, the AUC = 6 (6 units equals 6 mg. min/mL), where the AUC is the area under the curve of free plasma carboplatin concentration versus time. This is a method used to reduce toxicity based on renal clearance values calculated using the age and health condition of the patient.

2.2. Standard Sequence of 21-Day Cycle (SS21)

DX plus CPh was administered every 21 days for four cycles during the first phase. In the second phase, PX was issued weekly on days 1, 8, and 15. Moreover, CP was administered on day 1 of each of the four cycles, as shown in Figure 1a.

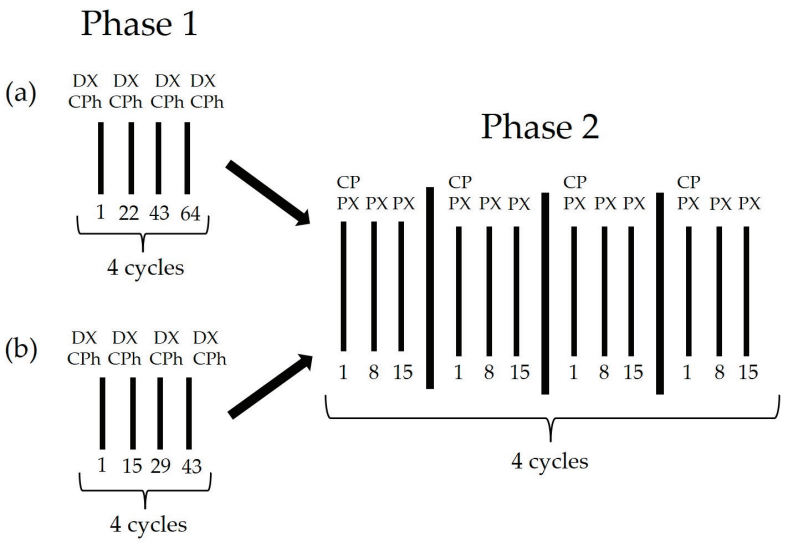

Figure 1. The standard sequence of neoadjuvant chemotherapy treatment for triple-negative locally advanced breast cancer. It starts with phase 1 and finishes with phase 2: (**a**) standard sequence of 21 day cycles (SS21) and (**b**) standard sequence of 14 day cycles (SS14).

2.3. Standard Sequence of 14-Day Cycle (SS14)

The chemotherapy sequence was the same as the standard dose but with a DX and CPh administration every 14 days for four cycles, as shown in Figure 1b.

Neoadjuvant therapy with SS21 (Figure 1a) is considered a safe and efficient option for treating TN-LABC. However, because this therapy can induce drug resistance [34], treatment with SS14 (Figure 1b) prevents the repopulation of tumor cells but at the cost of higher toxicity. Therefore, GCSF was administered in patients with breast cancer receiving neoadjuvant chemotherapy per cycle of chemotherapy.

2.4. Inverted Sequence of 21-Day Cycle (IS21)

In the inverted sequence, phase 2 was used as the first treatment; that is, PX was administered on days 1, 8, and 15, and CP on day 1 of each cycle for four cycles. Next, DX and CPh were sequentially administered using standard doses every 21 days, as shown in Figure 2a.

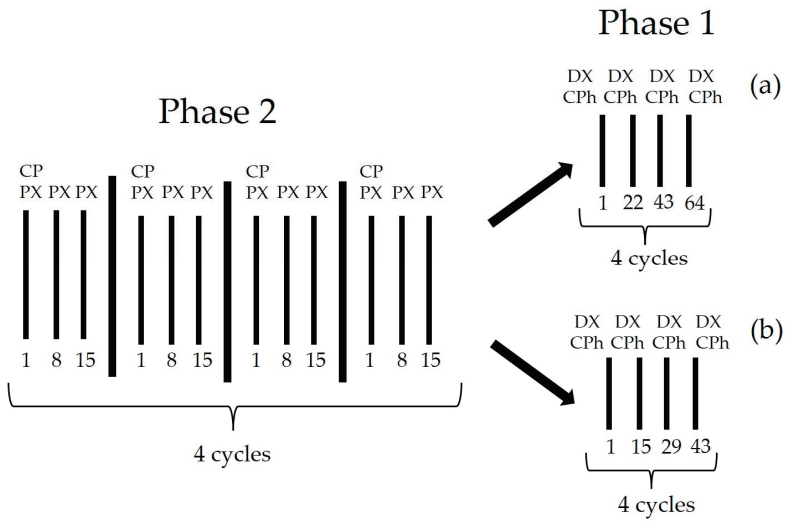

Figure 2. The inverted sequence of neoadjuvant chemotherapy treatment for triple-negative locally advanced breast cancer. It starts with phase 2 and finishes with phase 1: (**a**) inverted sequence of 21 day cycles (IS21) and (**b**) inverted sequence of 14 day cycles (IS14).

2.5. Inverted Sequence of 14-Day Cycle (IS14)

This chemotherapy was identical in dosage to that described above, but DX and CPh were administered every 14 days for four cycles, as shown in Figure 2b.

Treatment was inverted beginning with phase 2, starting with PX treatment, then CP was added on day 1 of each cycle, followed by phase 1, DX plus CPh. This was used to prevent cross-resistance (when acquired resistance induced by a drug treatment results in resistance to other drugs). This significantly increases the possibility of pCR and more conservative breast surgery in TN-LABC patients [21].

2.6. Glossary of Parameters Used in Models

N_i: N_1 and N_2 are the numbers of cells in compartments 1 and 2, respectively.

G0, G1, S, G2, and M are cellular phases: G_1 and S are in compartment N_1, and G_2 and M are in compartment N_2.

λ_i: is the exchange between compartments N_1 and N_2.
α_s^i: is the tumor cell survival proportion after applying drugs s (DX plus CPh).
γ: is the effect of PX on mitosis.
κ_i: represents the portion of susceptible cells resistant because of drug s.
β_s^i: parameter that indicates the decrease in the resistant population.

2.7. Quantitative Model

For the quantitative comparison of the chemotherapy sequencing strategies, we used a dynamic system describing the evolution of the different cell populations that contain the tumor. Based on the PLMM [13], we described the development of cell populations using a linear ODE, including the cancer treatment cycle. Although our model included the primary tumor and possible positive axillary nodes in TN-LABC, both were considered a single tumor volume, and cell proliferation was not limited to a specific geometry. Therefore, the model will not work with metastatic disease because cells spreading to other tissues have higher proliferation rates, and the response to the SS21 treatment was low.

Five phases of the cell cycle were described: quiescent cells (G0), cells that start synthesizing RNA and proteins (G1), DNA synthesis replication (S), proteins and RNA continue to be synthesized (G2), and mitosis (M). The G0 state is not properly part of the division process; thus, this phase was not considered in the PLMM. Instead, phases G1 and S were grouped into the N_1 compartment and phases G2 and M into N_2 (in this study, we defined $N_i,\ i = 1,\ 2$ as the AMCP). The cell cycle followed an exponential growth pattern in each compartment, represented by a first-order ODE system:

$$\frac{dN_1}{dt} = -\lambda_1 N_1 + 2\lambda_2 N_2;\ \frac{dN_2}{dt} = -\lambda_1 N_1 - \lambda_2 N_2 \tag{1}$$

where λ_1 and λ_2 are the rate of exchange between compartments N_1 and N_2, and $2\lambda_2$ represents the M phase of the cell cycle. Under the Norton–Simon hypothesis [32], our model corresponded to the exponential growth phase (that is, we were far from the saturation point where medications have low effectiveness because of the tumor size). Therefore, the matrix representation of Equation (1) is defined as:

$$N = \begin{pmatrix} N_1 \\ N_2 \end{pmatrix} \in \mathbb{R}^2 \tag{2}$$

$$\frac{dN}{dt} = \frac{d}{dt}\begin{pmatrix} N_1 \\ N_2 \end{pmatrix} = \begin{pmatrix} -\lambda_1 & 2\lambda_2 \\ \lambda_1 & -\lambda_2 \end{pmatrix} N = GN;\ G = \begin{pmatrix} -\lambda_1 & 2\lambda_2 \\ \lambda_1 & -\lambda_2 \end{pmatrix} \tag{3}$$

The solution for the whole linear system of the autonomous ODE is given by $exp(G\tau)$. The product of this matrix by the initial condition $N(0)$ provides the value of the population in period τ:

$$N(\tau) = exp(G\tau)N(0) \tag{4}$$

where $exp(G\tau) = \sum_{i=0}^{\infty} \frac{1}{i!}(G\tau)^i$. The growth in the N_1 and N_2 populations depends on parameters λ_1 and λ_2. Determining which value of these parameters corresponds to each subject is challenging. These can change because of numerous circumstances owing to individual differences in the cell proliferation speed (usually measured by the proliferation index Ki-67) [27,28]. Nevertheless, the growth of these cell populations can be estimated by sweeping a values interval of these parameters using clinical knowledge from published studies and comparing the development of the tumor cell population.

2.8. Doxorubicin and Cyclophosphamide Effect

A drug's effect on treatment is described as an instant change in the AMCP when the dose is administered. The application of matrix D_s to population N represents this behavior. The subscript s represents DX and CPh drugs: the type of chemotherapy that inhibits the replication of tumor cells. Following the PLMM, the matrix instantly acts on the N population; the matrix is diagonal because drugs independently modify each population.

$$D_s = \begin{pmatrix} \alpha_s^1 & 0 \\ 0 & \alpha_s^2 \end{pmatrix} \tag{5}$$

Here, α_s^i, i = 1, 2, is the tumor cell survival proportion after applying drug s to AMCPs N_1 and N_2. The cell population affected by drug s in each treatment within period τ is expressed as follows:

$$N(\tau) = D_s exp(G\tau)N(0) \tag{6}$$

The effect of matrix D_s depends on the time it is applied. Figure 3 shows that when D_s is used at different times (τ_1, τ_2, and τ_3), the population change ΔN_i, i = 1, 2 after chemotherapy can be negative, zero, or positive.

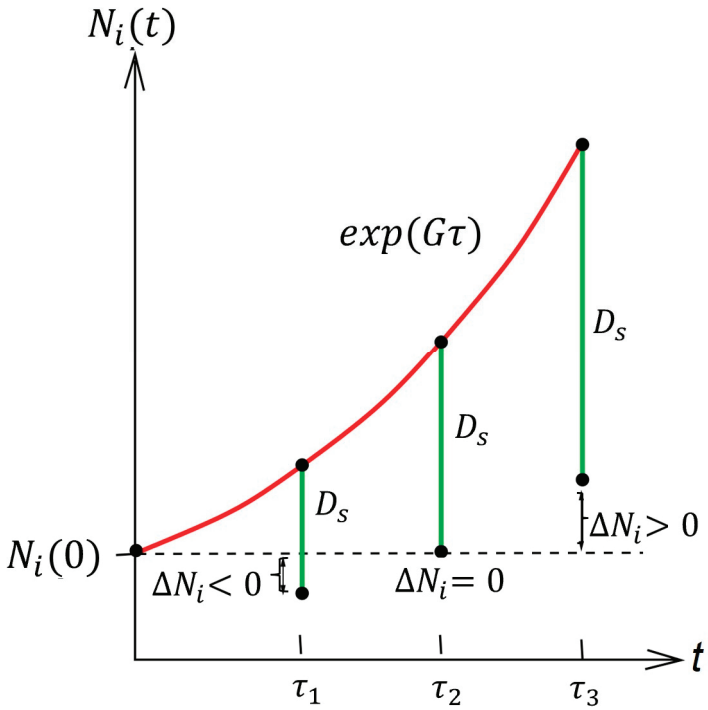

Figure 3. Graphic representation of the AMCP changes ΔN_i, i = 1, 2 in different periods owing to the application of the D_s matrix.

The time interval was limited in size because of the toxicity effect of D_s. Therefore, τ was considered, given this restriction. According to our chemotherapy sequencing model with s drugs, the minimum time interval to prevent toxicity was 14 days, reinforced with the GCSF.

Note that when m doses of drug s are administered, the resulting number of AMCPs is as follows:

$$N(m\tau) = (D_s exp\ (G\tau))(D_s exp\ (G\tau)) \ldots (D_s exp\ (G\tau))N(0)$$

$$N(m\tau) = (D_s exp(G\tau))^m N(0) \tag{7}$$

where $N(m\tau)$ denotes the administration of different chemotherapy sequences by the corresponding matrix multiplication for $\tau_1 = 21-$day and $\tau_2 = 14-$ day cycles (as defined in the chemotherapy sequences in Figures 1 and 2).

2.9. Qualitative Behavior of Paclitaxel

One of the mechanisms of the action of PX is the inhibition of mitotic spindle formation during cell division, blocking the mitosis process. The addition of PX as matrix P, a modification of matrix G, was represented. PX influences the cell cycle growth matrix; therefore, this drug has continuous effects over time during its application.

Therefore, the AMCP N now takes the following form:

$$\frac{dN}{dt} = PN \tag{8}$$

We represented matrix P as follows:

$$P = \begin{pmatrix} -\lambda_1 & \gamma\lambda_2 \\ \lambda_1 & -\lambda_2 \end{pmatrix} \tag{9}$$

where coefficient γ is the effect of PX on mitosis; $\gamma \in [0,\ 2]$ is considered. For $\gamma = 2$, we have cell mitosis; for $\gamma = 1$, a bifurcation point exists; and for $\gamma < 1$, the eigenvalue is negative (see Appendix A) as the tumor size decreases to zero. Therefore, in this case, the effectiveness of PX was sufficient for the tumor to disappear. Additionally, the addition of CP on day 1 of each cycle is shown in Figures 1 and 2, and the action mechanism through which PX destroyed the tumor cells was enhanced, for which the γ value was even more reduced. Therefore, we implemented the CP effect in the mathematical model to increase parameter γ, which was a robust approximation of the effect of CP and PX in each simulation cycle.

We contrasted cell growth for SS21, SS14, IS21, and IS14 of the s drugs, including PX. The results of the combination of chemotherapy with PX are represented in Figure 4. The objective was to minimize the active mitotic cell fraction $N_i(\tau),\ i = 1,\ 2$.

Figure 4a shows that in period τ, exponential growth was such that after applying D_s, it could not return to the initial population state, in which ΔN_i was positive, referring to tumor growth at a slower rate. However, PX could reduce the maximum growth of the $exp(G\tau)$, resulting in a new matrix $exp(P\tau)$, where the effect of chemotherapy reached the objective of reducing the initial population, for which ΔN_i was negative, as shown in Figure 4b. The above demonstrated that the tumor would have been almost or entirely reduced.

When ΔN_i is negative, repeating this chemotherapy process allowed the tumor to be effectively reduced, as shown in Figure 4c, where the reduction is shown after mD_s.

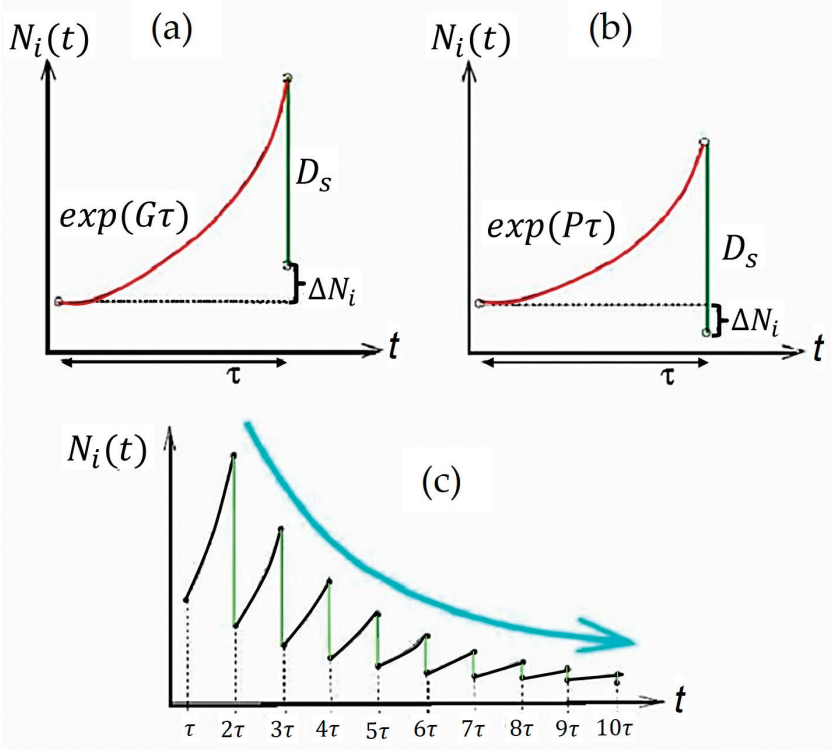

Figure 4. (**a**) The $\exp(G\tau)$ represents the growth earnings of the AMCP N_i, $i = 1, 2$; (**b**) $\exp(P\tau)$ describes the growing loss of the N_i cell population owing to chemotherapy with PX, and (**c**) illustrates the sequential chemotherapy treatment after ten applications at time intervals τ.

2.10. Resistance Model

When the drug resistance effect was incorporated into the model, the cell population was divided into chemotherapy-resistant and susceptible. Furthermore, a pharmacological effect was defined as when a cell group transitions from susceptible to resistant, and such conversion occurred instantly in our simulations. Following the same PLMM scheme, we have $\overline{N}(t)$, the AMCP with a vector of four components, that is, in $\mathbb{R}^4$.

$$\frac{d\overline{N}}{dt} = \begin{pmatrix} G & 0 \\ 0 & G \end{pmatrix} \overline{N}(t) = \widetilde{G}\overline{N}(t) \tag{10}$$

Here, G is as defined in Equation (3), 0 is the null matrix, and $\overline{N}(t)$ is defined as

$$\overline{N}(t) = \begin{pmatrix} N_1^{se} \\ N_2^{se} \\ N_1^{re} \\ N_2^{re} \end{pmatrix} \tag{11}$$

where N_1^{se} and N_2^{se} are the susceptible AMCPs and N_1^{re} and N_2^{re} are the resistant AMCPs. The fundamental matrix of this system is $exp\left(\widetilde{G}\tau\right)$, and the AMCP with the effect of drugs $\widetilde{D}_s$ after period τ is as follows:

$$\overline{N}(\tau) = \widetilde{D}_s exp\left(\widetilde{G}\tau\right)\overline{N}(0) \tag{12}$$

In this case, matrix $\widetilde{D}_s$ represents the population's instantaneous change through the susceptible cell's annihilation by drugs and the cell transformation from susceptible to resistant. Therefore, matrix $\widetilde{D}_s$ takes the following form:

$$\widetilde{D}_s = \begin{pmatrix} (1-k_1)\alpha_s^1 & 0 & 0 & 0 \\ 0 & (1-k_2)\alpha_s^2 & 0 & 0 \\ k_1\alpha_s^1 & 0 & \beta_s^1 & 0 \\ 0 & k_2\alpha_s^2 & 0 & \beta_s^2 \end{pmatrix} \tag{13}$$

where the α_s^i parameters are the same as those described in Section 2.8; parameters β_s^i, where i =1, 2, indicate a decrease in the resistant population (they represent the survival rate after applying drugs s to the N_1 and N_2 AMCPs); and the parameter k_i, where i = 1, 2, represents the rate of cell exchange speed for the susceptible to the resistant population. For example, the resistance model we described in Equation (12) depends on the k_i parameters, where k_1 is the parameter of the N_1 population, and k_2 is the parameter of the N_2 population because of s drugs. As two inputs, $\widetilde{D}_s(3,\ 3) = \widetilde{D}_s(4,\ 4)$, represent the effect of drugs on the resistant cells, and because such cells do not change owing to this effect, their numerical value is equal to 1. Therefore, the matrix of Equation (13) is as follows:

$$\widetilde{D}_S = \begin{pmatrix} (1-k_1)\alpha_S^1 & 0 & 0 & 0 \\ 0 & (1-k_2)\alpha_S^2 & 0 & 0 \\ k_1\alpha_S^1 & 0 & 1 & 0 \\ 0 & k_2\alpha_S^2 & 0 & 1 \end{pmatrix} \tag{14}$$

In the results, Section 3.4 shows the simulations of numerical experiments with resistant and susceptible AMCPs under different parameters.

3. Results

3.1. Growth Rate Simulations of Tumor Cell Population

Figure 5 illustrates the rationale behind the lambda values that we used in our simulations and shows three graphs of the growth rate of the total tumor cell population for parameters $\lambda_i \in [0,\ 0.12]$, i = 1, 2. The unit of λ_i is 1/day. We considered the interval reasonable compared with the possible growth. Using the linear ODE model, we presented the growth rate of the total AMCP (N_f/N_i, where $N_f = N_1(\tau) + N_2(\tau)$ was the final cell population, and $N_i = N_1(0) + N_2(0)$ was the initial AMCP) for end time of $\tau = 25$ days . The purpose of timing was to observe any significant difference in AMCP growth within a time interval.

As shown in the graphs, the population growth rate $(N_1(\tau) + N_2(\tau))/(N_1(0) + N_2(0))$ was relatively homogeneous regarding parameters λ_i. λ_2 was more susceptible to population growth than λ_1 because λ_2 was the parameter that described final active mitosis. The yellow curve represents the λ_i for which $N_f/N_i = 2$ for $\tau = 25$ days. Total tumor doubling time ranged from 60 to 175 days [35–37]; however, our model represented the growth rate of the tumor's AMCP (10% to 20%) [38–41]. Appendix B shows that if the tumor doubling time was 100 days, then the AMCP rate of the tumor should double every 28.9 days. Because only the AMCP was considered in this study, we used a doubling time of 25 days. In these simulations, we used the same initial conditions: $N_1 = 500$ and $N_2 = 300$. Appendix C shows that the results obtained were independent of the initial conditions.

Figure 5 demonstrates the results from homogeneity; parameters $\lambda_1 = 0.1$ and $\lambda_2 = 0.05$ were considered throughout the study to ensure that the active cell fraction duplicated after 25 days. Appendix C shows that the qualitative behavior of the AMCP growth evolution was similar for several parameters because of the linearity of Equation (4).

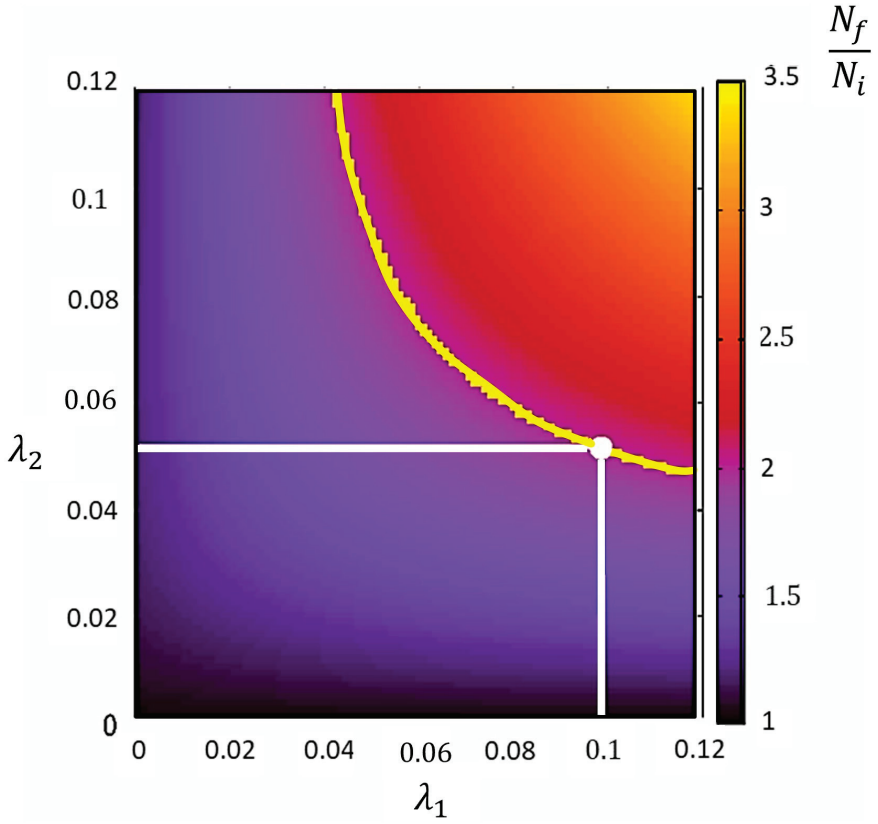

Figure 5. Growth rate simulations of the tumor AMCP for end time $\tau = 25$ days. The color bar represents the rate $N_f/N_i = (N_1(\tau) + N_2(\tau))/(N_1(0) + N_2(0))$. The yellow curve represents the parameters λ_i, $i = 1, 2$ for which $N_f/N_i = 2$ is the tumor duplication.

3.2. Simulations of Effects of Doxorubicin and Cyclophosphamide

To perform a comparative analysis of cell growth, we defined the values of α_s^i for the s drugs. However, because we did not have a specific value for these parameters, we swept the possible oncological values of these parameters, so $\alpha_s^i \in [0,\ 1]$, $i = 1, 2$.

$\alpha_s^i = 1$ indicates that the drug does not affect the cells; $\alpha_s^i = 0$ indicates that the drug annihilates the whole AMCP, as shown in Figure 6. The λ_i of the G matrix parameters and the initial conditions were the same as those chosen in the previous section.

When performing the numeric simulations with the cell cycles, we first let the tumor cell growth evolve with no drug for five days (corresponding to the zero time). We exposed the AMCP to $m = 4$ cycles with s drugs (as shown in Figures 1 and 2). The result of the growth rate with the effect of the s drugs, standard doses (defined in Section 2.1), and $\tau_2 = 14$ days is shown in Figure 6a, where the color bar represents the rate $N_{SS14}\left(t_f\right)/N_{SS14}(0) = \left(N_{(1)SS14}\left(t_f\right) + N_{(2)SS14}\left(t_f\right)\right)/\left(N_{(1)SS14}(0) + N_{(2)SS14}(0)\right)$ for $t_f = m\tau_2 + 5$.

When the sensitivity to medications was high, administering the same dose in a shorter time τ_2 had a benefit up to an intermediate point of $\alpha_s^i \approx 0.5$ values because tumor growth was prevented. Drugs were highly effective in killing tumor cells at low values of α_s^i. AMCP growth was small compared with that shown by the color bar (dark colors) in Figure 6a. Mathematically, reducing each drug period was convenient, not reaching an excessive increase in the dose to avoid intolerable toxicity.

The darkest part (black color) in Figure 6b is diagonal, indicating a more significant reduction in AMCP growth. As expected, SS14 treatment reduced the AMCP more than SS21 treatment, but the values of the medication parameters modulated this reduction α_S^i, whereas those of SS14 produced a better response.

The two simulations showed the importance of drug administration in an optimal period to prevent tumor growth. In addition, the best SS14 treatment used GCSF to prevent high toxicity.

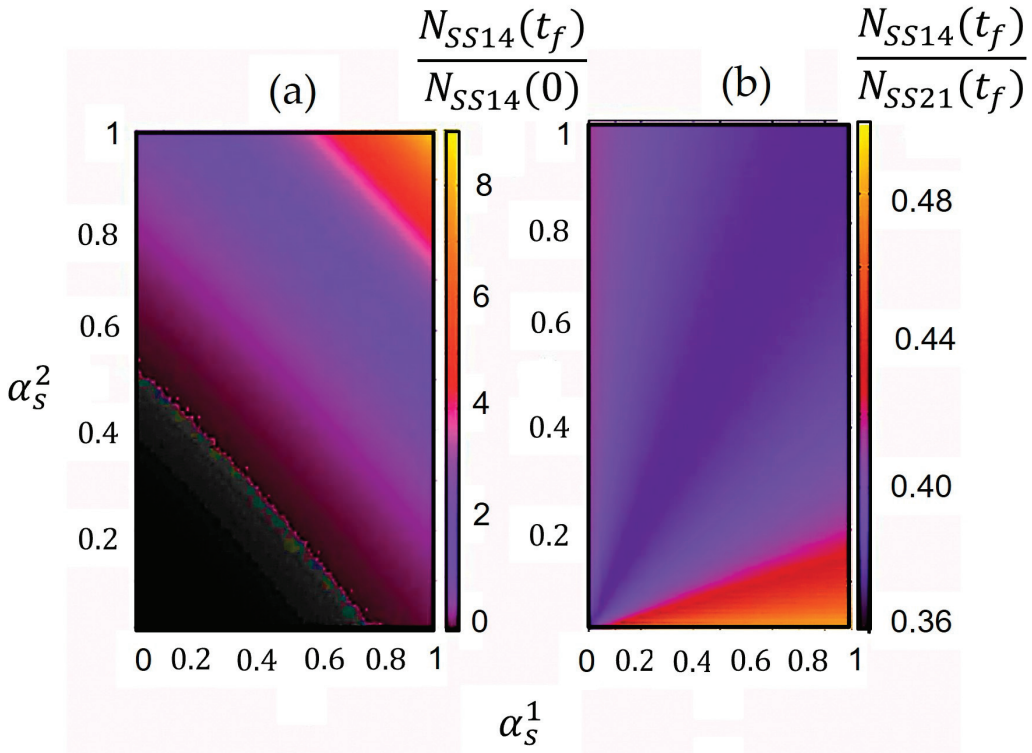

Figure 6. Growth rate simulations of the tumor AMCP with the s (DX + CPh) drug effect: (**a**) $N_{SS14}\left(t_f\right)/N_{SS14}(0) = \left(N_{(1)SS14}\left(t_f\right) + N_{(2)SS14}\left(t_f\right)\right)/\left(N_{(1)SS14}(0) + N_{(2)SS14}(0)\right)$ and (**b**) $N_{SS14}\left(t_f\right)/N_{SS21}\left(t_f\right) = \left(N_{(1)SS14}\left(t_f\right) + N_{(2)SS14}\left(t_f\right)\right)/\left(N_{(1)SS21}\left(t_f\right) + N_{(2)SS21}\left(t_f\right)\right)$, where $\tau_1 = 21$ days and $\tau_2 = 14$ days, and $t_f = m\tau_i + 5$. The color bar represents the tumor AMCP rate.

3.3. Simulations of the Paclitaxel Effect

Figure 7 illustrates the active mitotic cell population (the y-axis represents logarithmic values) for specific α_s^i values as a function of time. The active mitotic cell population (N1 + N2) evolved as a function of λ_i to double this population in 25 days. The growth rate without drugs (red line) was exponential from an initial population of 800 million cells to reach an order of 129,825 million cells after 184 days, which was a doubling approximately every 25 days. Concerning the final cell population after the treatment with SS14, the population was 158 million cells (yellow line followed by dark blue line); after SI14, it was 125 million cells (green line followed by light blue line) after 184 days. SI14 killed the AMCP 21% more effectively than SS14.

Figure 8 shows a comparison of the final AMCP after treatments of SS14 and IS14, doing a complete sweep of the α_s^i interval, using λ_i values to double the AMCP in 25 days.

The simulation results shown in Figure 8a show the difference in the population growth rate between the SS14 and IS14 treatments. In both cases, $\tau_2 = 14 - day$ cycles were considered for s drugs. We chose $\gamma = 1.5$ because it is a common value and is far from the bifurcation point for the cases in which the PX cycle is applied. The final total population result with the SS14 treatment was compared with that of IS14 $\left[N_{SS14}\left(t_f\right)/N_{IS14}\left(t_f\right)\right]$. The final versus initial AMCP growth rate of SS14 $\left[N_{SS14}\left(t_f\right)/N_{SS14}(0)\right]$ is shown in Figure 8b and of IS14 $\left[N_{IS14}\left(t_f\right)/N_{IS14}(0)\right]$ in Figure 7c to compare the growth order. As

in previous simulations, the AMCP evolved without drugs for 5 days and $m = 4$ cycles so that $t_f = m\tau_2 + 5$. Including PX therapy, in four cycles of 15 days (as shown in the second phase in Figure 1 and the first phase in Figure 2), t_f remained equal to $t_f = 4\tau_2 + 4 \times 15 + 5$.

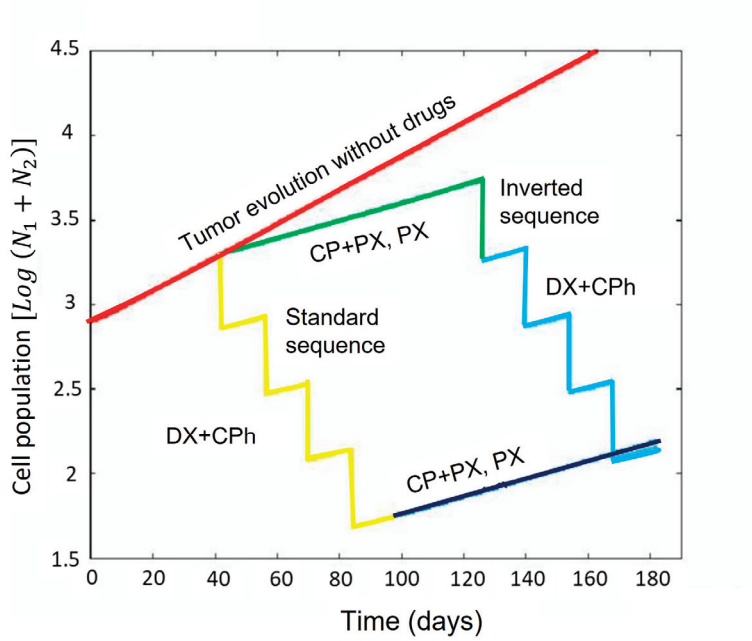

Figure 7. Temporal evolution of the AMCP rate of the tumor during the complete treatment of SS14 and IS14, considering the doubling of this population without treatment at 25 days to the parameter's values: $\alpha_S^1 = 0.9$, $\alpha_S^2 = 0.2$, $\lambda_1 = 0.1$, $\lambda_2 = 0.05$ and $\gamma = 1.5$. The SS14 is represented by a yellow line (DX + CPh) followed by dark blue (CP + PX, PX), and the IS14 by a green line (PX + CP, PX) followed by the light blue line (DX + CPh).

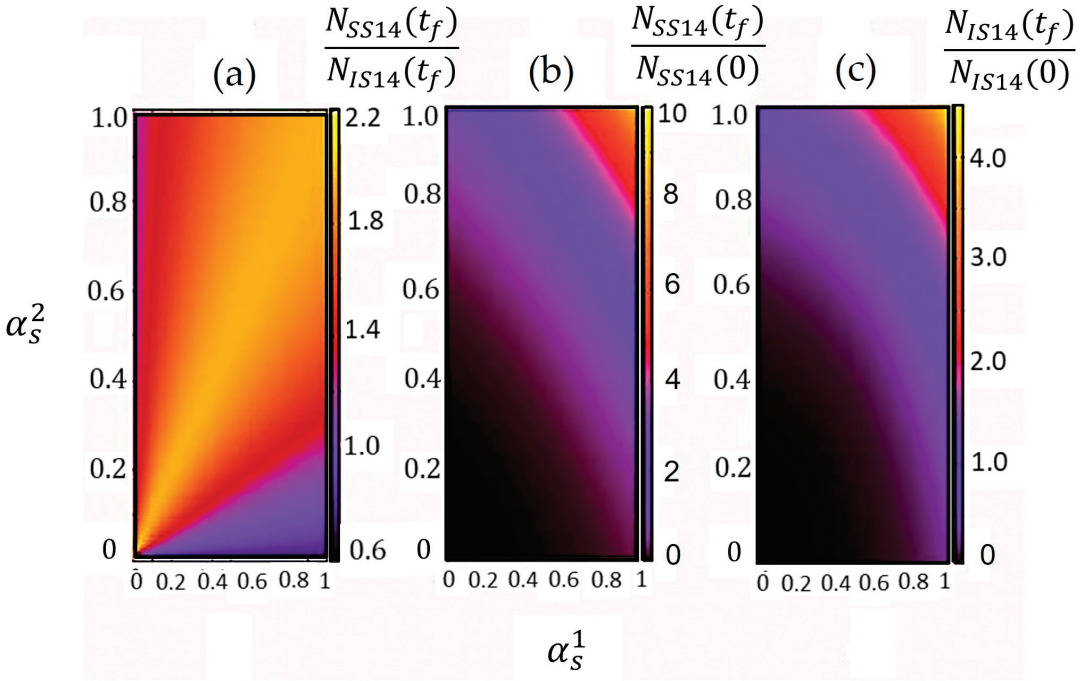

Figure 8. Growth rate simulations of the tumor AMCP with the effect of s (DX + CPh) and PX drugs: (**a**) comparing $\left[N_{SS14}\left(t_f\right)/N_{IS14}\left(t_f\right)\right]$; (**b**) $\left[N_{SS14}\left(t_f\right)/N_{SS14}(0)\right]$, and (**c**) $\left[N_{IS14}\left(t_f\right)/N_{IS14}(0)\right]$, where $t_f = m\tau_2 + 5$ for m = 4 cycles and $\tau_2 = 14$ days. The color bar represents the tumor AMCP rate.

We can see in Figure 8a that by doing the complete sweep over the parameters α_S^1 and α_S^2, the resulting population in SS14 was more significant than that obtained in IS14. Furthermore, the area covered by values α_s^i, corresponded to the greater efficiency of the IS14, whereas the SS14 occupied approximately 90%, which meant that IS14 was more efficient in containing tumor growth. We had a similar behavior if the value of $\tau_1 = 21$ days.

Figure 8b,c shows the tumor growth for SS14 and IS14, respectively. The color level represents how much the tumor grew compared with the initial population. The IS14 treatment, including the PX and CP, was found to be one of the best chemotherapies for patients with TN-LABC. Its population growth was minimal compared with that under the SS14 treatment [22,23,29]. Notably, the toxicity of the therapy had to remain within a specific limit.

3.4. Simulations of Resistance Model

The first simulation group came from an initial AMCP, with $\lambda_1 = 0.1$ and $\lambda_2 = 0.05$, used in Figure 5. As in the previous simulations, the matrix (14) $\alpha_S^i \in [0, 1]$, $i = 1, 2$ parameters represented the drug effects, and the unit intervals were partitioned into 100 equidistant portions. Figure 8 shows the results of five simulations of the tumor population rate with the effect of resistance to s drugs. The color bar corresponds to the final population rate versus the initial population $\left(N_{SS14}^{se}\left(t_f\right) + N_{SS14}^{re}\left(t_f\right)\right) / \left(N_{SS14}^{se}(0) + N_{SS14}^{re}(0)\right)$; the simulation time was $t_f = m\tau + 5 = 4 \times 14 + 5$.

When the plots of Figure 9 were analyzed, we observed homogeneity in the growing proportion of the resistant and susceptible populations as the k_i value increased. The yellow line in the five charts shows that the final population was equal to the initial population, for which it took a value of one; this line separates the areas of the α_S^1 and α_S^2 parameters, where the population increased or decreased. The yellow line in Figure 9d,e represents no growth or a decrease in the active AMCP, closer to the axis origin, indicating that a more aggressive therapy should be chosen to prevent the tumor from becoming resistant to the drug.

In the following numerical experiment, we performed some simulations to compare the efficiency of the standard sequence versus the inverse sequence, considering the effect of s drug resistance. Figure 9 shows the results of the simulations of the growth rate of the final AMCP, SS14 versus IS14 $\left[\left(N_{SS14}^{se}\left(t_f\right) + N_{SS14}^{re}\left(t_f\right)\right) / \left(N_{IS14}^{se}\left(t_f\right) + N_{IS14}^{re}\left(t_f\right)\right)\right]$, for the same simulation time t_f before and k_i values as in Figure 9b–d. The extreme values of k_i in Figure 9a,e were not considered because the smallest value produced almost no change from susceptible to resistant cells. The highest value corresponded to a quick change from susceptible to resistant cells. The values of the parameters ($\lambda_1 = 0.1$ and $\lambda_2 = 0.05$) were the same as the previous simulations, and $\gamma = 1.5$ was the same as that used in Figure 7 in Section 3.3, which was dedicated to PX.

When Figure 10a–c was analyzed for $k_1 = k_2$, we observed that the growth rate of the tumor AMCP for SS14 versus IS14 was similar, with a slight variation, as shown in Figure 10c by the color bar. However, when comparing the $k_1 \neq k_2$ values, a significant difference was observed in the efficiency of the two treatments. The conversion rate from susceptible to resistant cells differed between the N_1 and N_2 populations. Figure 10d–f shows that the performance of the IS14 treatment was more efficient than that of SS14, provided that $k_1 > k_2$. Note that the variation in the population proportion in the color bar is higher than in Figure 10a–c, where rates above one predominated. At the right end of graph (f), we can observe a population below the yellow line.

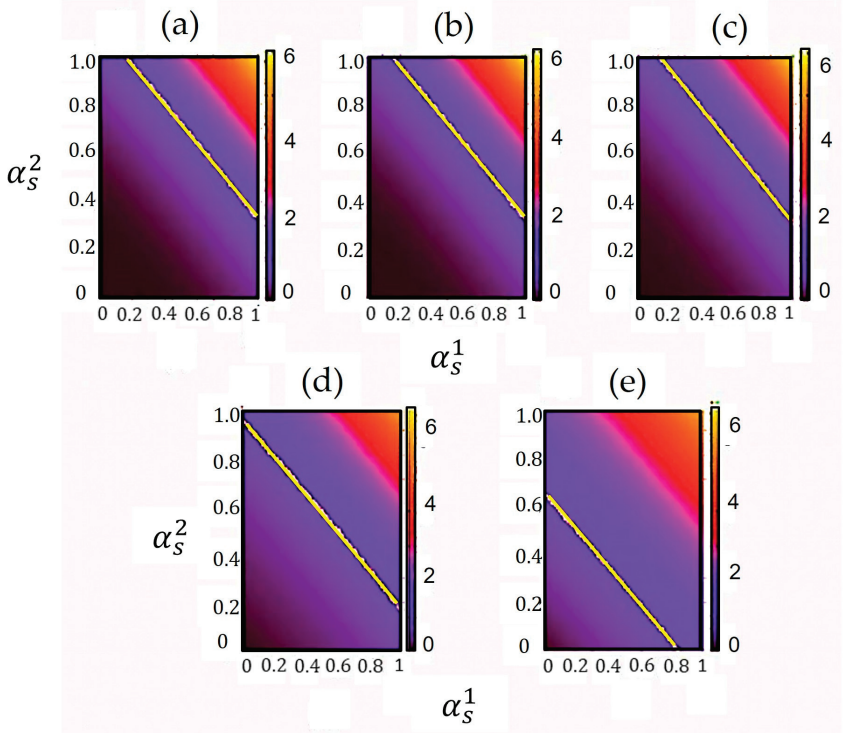

Figure 9. Comparison of tumor AMCP growth rate simulations, with the effect of s drug resistance for $k_1 = k_2$ values: (**a**) 0.0001, (**b**) 0.001, (**c**) 0.01, (**d**) 0.1, and (**e**) 0.3. The color bar represents the proportion of tumor cell populations $\left[\left(N^{se}_{SS14}\left(t_f\right) + N^{re}_{SS14}\left(t_f\right)\right)/\left(N^{se}_{SS14}(0) + N^{re}_{SS14}(0)\right)\right]$, and the yellow line represents the value 1 of the population rate.

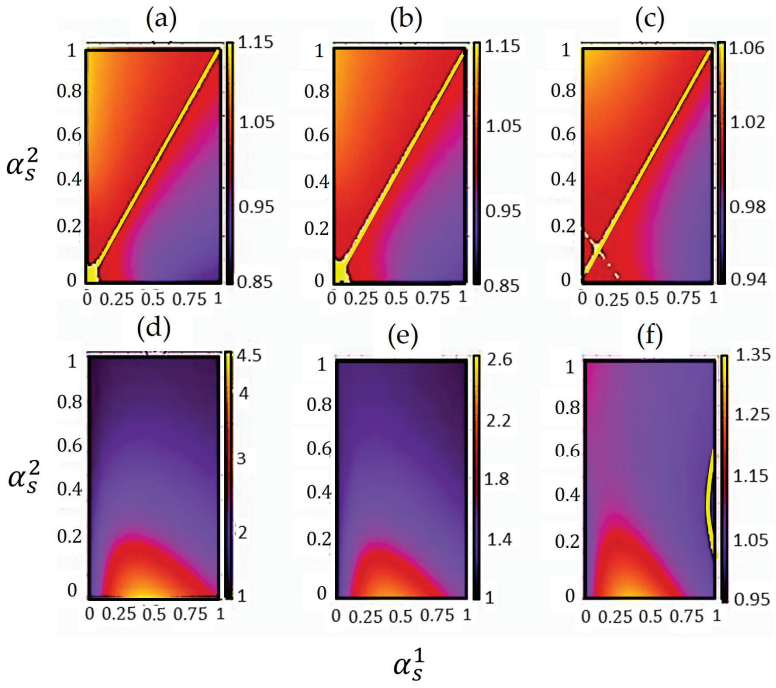

Figure 10. Comparison of the final growth rate simulations of the tumor AMCP, with the effect of the s drug resistance, for $k_1 = k_2$ values: (**a**) 0.001, (**b**) 0.01, and (**c**) 0.1; for $k_1 > k_2$ values: (**d**) $k_1 = 0.1$, $k_2 = 0.01$, (**e**) $k_1 = 0.05$ $k_2 = 0.01$, and (**f**) $k_1 = 0.02$, $k_2 = 0.01$. The color bar represents the final AMCP rate of SS14 versus IS14 $\left[\left(N^{se}_{SS14}\left(t_f\right) + N^{re}_{SS14}\left(t_f\right)\right)/\left(N^{se}_{IS14}\left(t_f\right) + N^{re}_{IS14}\left(t_f\right)\right)\right]$, and the yellow line represents the value 1 of the population rate.

A more detailed analysis of Figure 10 is shown in Figure 11; this figure compares the population growth rate simulations of the tumor cells, SS14 versus IS14, for three cases: $k_1 > k_2$, $k_1 < k_2$, and $k_1 = k_2$ where the exchanges of k_1 and k_2 values were analyzed when they were close.

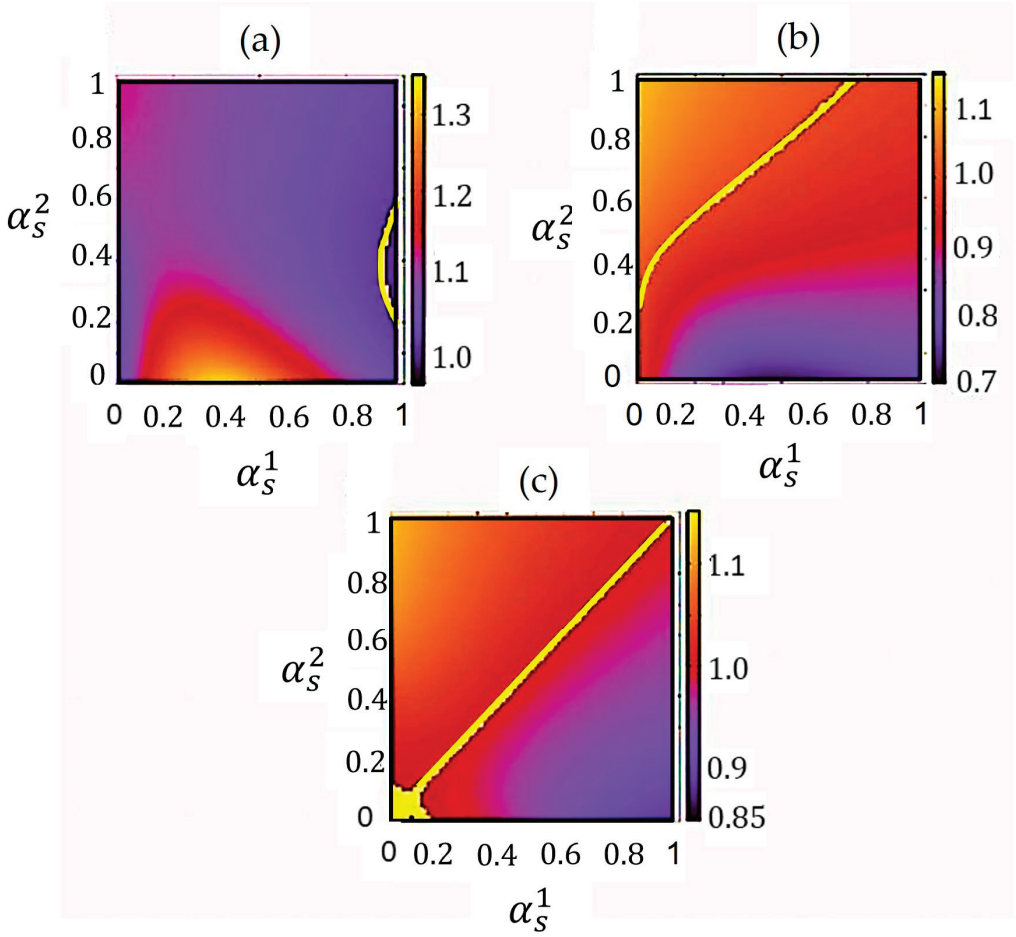

Figure 11. Comparison of the final growth rate simulations of the tumor AMCP with the effect of s drug resistance for values: (**a**) $k_1 > k_2$, $k_1 = 0.02$, and $k_2 = 0.01$; (**b**) $k_1 < k_2$, $k_1 = 0.01$, and $k_2 = 0.02$; and (**c**) $k_1 = k_2 = 0.01$. Color bars represent the final AMCP rate of SS14 versus IS14 $\left[\left(N_{SS14}^{se}\left(t_f\right) + N_{SS14}^{re}\left(t_f\right)\right) / \left(N_{IS14}^{se}\left(t_f\right) + N_{IS14}^{re}\left(t_f\right)\right)\right]$, and the yellow line represents the value 1 of the population rate.

The yellow line represents a value of 1; because the final populations of the SS14 and IS14 treatments were equal, the line shifts to the left when $k_1 < k_2$ and $k_1 = k_2$, respectively. When $k_1 > k_2$, IS14 was more efficient than SS14. On the contrary, the yellow line divides the graph when $k_1 < k_2$, and SS14 was more efficient than IS14. In Figure 11a, the area covered by the highest efficiency of the IS14 treatment is noticeably larger. In Figure 11b, the highest efficiency of SS14 barely exceeded that of IS14, and when $k_1 = k_2$, we could not differentiate which of the two sequences was more efficient. Notably, the results were qualitatively similar for the 21-day cycles.

4. Discussion

In this study, we used a PLMM to describe the parameters that defined the order of four proposed oncological treatments. In addition, a uniform numerical sweep was performed for the parameters $\lambda_i \in [0, 0.12]$ and $\alpha_s^i \in [0, 1]$ to obtain a realistic tumor growth function. This approach produced an extensive qualitative and quantitative vision of the problem to explain the effects of the drugs on the AMCP.

Cancerous tumors actively divide cells during the G2 and M phases (active reproduction phase). In TN-LABC, the AMCP is between 20% and 60% of the tumor mass (43,44), which is used when calculating the doubling time of the tumor. In this study, the simulations of the tumor duplication were obtained for reasonable clinical times, $\tau = 25$ days using the initial conditions of $N_1 = 500$ and $N_2 = 300$, as shown in Figure 5. Appendix C shows that the results obtained were independent of the initial conditions.

The matrix D_s, from Equation (5), represents the annihilating effect of s drugs on the AMCP. The drug effect was considered instantaneous concerning the timescales involved in the AMCP growth evolution. These timescales involved in sudden cell death were compared with the timeframe of AMCP growth without drugs. Proposing the killing effect of the medications as instantaneous was a suitable approximation, as illustrated in Figure 4.

We used a simplified mathematical model based on Roe et al.'s model (16), as mentioned throughout the text. One strength of this analysis were the exhaustive scenarios considered regarding ratios between cell populations and cellular dynamics by rates after treatments. However, one of this model's limitations was using two populations instead of more populations that corresponded to the cell cycle, as Roe et al. did in their model. The AMCPs grouped the G1 (protein and RNA synthesis) and S (replication synthesis) cycles in population N_1 and the G2 (protein and RNA synthesis continues) and M (mitosis) cycles in population N_2; in this process, the state G0 (quiescent cells) was not considered. The reason for grouping the populations this way was that the drugs acted approximately homogeneously on the G1 and S cycles and the G2 and M cycles, which allowed us to handle a limited number of parameters. Although this was a limitation of the model, it was an advantage because we could study the global behavior of the model for a wide range of these parameters. Therefore, we obtained a broad qualitative and quantitative overview of the model.

Regarding the complexity of the tumor, owing to the model representing generic populations at any point in the tumor, by varying the model's parameters, we could explore a wide range of cell types that considered this complexity. In the next phase of the study, we will add the effects of the immune system to the mathematical model.

A randomized phase II trial demonstrated that adding CP to weekly PX followed by DX and CPh significantly increased the pCR rate in stages II-III of TN-LABC [22]. Strategies to reduce the toxicity of sequential neoadjuvant chemotherapy in TN-LABC include adjusting the weekly CP dose, compensated with GCEF [29], adjusting by the age and comorbidity of patients to define the best treatment, determine adequate premedication, and prevent severe adverse reactions to PX.

The findings of Shepherd et al. [22] supported our mathematical model because the authors obtained higher PCR rates (administering first CP plus PX and then DX plus CPh) and provided helpful information for training our mathematical model with the specific parameters λ and α. As a result, our mathematical model was flexible enough to increase prediction accuracy with future adjustments using the poor clinical prognosis features of TN-LABC. These characteristics may include age less than 40 years, tumor size greater than 5 cm, presence of palpable axillary lymph nodes, inflammatory changes in the breast, histological characteristics (high histological grade tumors), and the immunohistochemical characteristics (triple-negative) of elevated Ki67, p53-positivity, and tumor-infiltrating lymphocytes $\geq$30. Comparing the findings of this study with our mathematical model, and we verified the consistency in the results obtained in the clinic, as observed in Figures 7–11, which showed that the IS14 treatment was more efficient than the SS14 treatment.

This type of PLMM swept all values of the computed parameters, helping to examine a wide range of drugs that can be used in clinical trials.

5. Conclusions

The sweep of all parameters λ_i and α_s^i allowed us to visualize the variability in cell growth concerning variations in the amount of drug applied. Here, the inverted treatment sequence outperformed the standard treatment, allowing maximum AMCP and tumor

size reductions. In addition, IS14 was more effective than IS21 but with a higher degree of toxicity; however, this can be compensated for with GCSF because some TN-LABC patients (with the basal-like subtype, BRCA1 gene mutations, p53 and ki-67, inflammatory carcinoma in individuals under 40 years of age, and other tumors with a high proliferation index) will need it, especially those who do not respond to IS21 treatment. The numerical results obtained in this study are consistent with the clinical results referenced in the manuscript. This study provides a complementary approach to that used in the clinic for optimal control.

Author Contributions: This study was carried out by a multidisciplinary team of mathematicians, physicians, and molecular biology experts. A.M.-A., one of the major contributors, passed away on 1 July 2017. He built the matrix coefficients, made the core model, and started the toxicity model. The equations were created and finished by A.O.-C., G.C.-P., J.C.C.-E. and R.M.Q.-S., and simulations were conducted by A.O.-C., M.A.Á.-B. and M.Y.B.-H., who made the clinical analyses and conception of the coefficients' treatment sequences and data model. J.H.-R. made the cell relationship and molecular analysis. The integrated analysis, paper writing, and contribution to the model's conception were performed by J.C.L.-A. and R.M.Q.-S. All authors have read and agreed to the published version of the manuscript.

Funding: This paper was funded by the Hospital General de México "Dr. Eduardo Liceaga" (DI/12/111/04/17) and the Department of Population Health & Biostatistics at the University of Texas Rio Grande Valley.

Data Availability Statement: No new data were created or analyzed in this study.

Acknowledgments: The authors thank the Dirección de Investigación del Hospital General de México "Dr. Eduardo Liceaga" (N° DI/12/111/04/17); COFAA-IPN and EDI-IPN and Leonel Vela, head of the Department of Population Health & Biostatistics, at University Texas Rio Grande Valley for their generous support to publish this paper.

Conflicts of Interest: The authors declare no conflict of interest.

Appendix A

This section develops a mathematical model to explain the PX action on TN-LABC with the BL subtype (12).

We calculated the eigenvalue of the matrix $P = \begin{pmatrix} -\lambda_1 & \gamma\lambda_2 \\ \lambda_1 & -\lambda_2 \end{pmatrix}$ and values of $\gamma\, \epsilon\, [0,\ 2]$, where γ measures PX effectiveness, as defined in Section 2.6. In solving it, we obtained the following spectrum:

$$\rho_{\pm} = \frac{-(\lambda_1 + \lambda_2) \pm \sqrt{(\lambda_1 + \lambda_2)^2 + 4(\gamma - 1)\lambda_1\lambda_2}}{2} \tag{A1}$$

For $\gamma = 1$, the following is obtained:

$$\rho_{\pm} = \begin{cases} 0 \\ -(\lambda_1 + \lambda_2) \end{cases} \tag{A2}$$

For $\gamma = 1$ there is a bifurcation point in the cell population; this means that when $\rho_{\pm} = 0$, the solution is a constant behavior (with no changes), while for $\rho_{\pm} = -(\lambda_1 + \lambda_2)$, the behavior is of exponential decay.

For $\gamma > 1$, we have $D = \sqrt{(\lambda_1 + \lambda_2)^2 + 4(\gamma - 1)\lambda_1\lambda_2} > (\lambda_1 + \lambda_2)$; therefore, an eigenvalue shall be positive, and the other negative; the tumor will grow for almost any initial condition.

For $\gamma < 1$, we have $D = \sqrt{(\lambda_1 + \lambda_2)^2 + 4(\gamma - 1)\lambda_1\lambda_2} < (\lambda_1 + \lambda_2)$. In this case, both eigenvalues are negative, for which the tumor size will decrease to zero. In this case, the PX effectiveness is enough to reduce the tumor.

Appendix B

In TN-LABC, only a fraction of the tumor P_a (AMCP) is in active mitosis, usually between 10% and 20% [38–41], as shown in Figure A1.

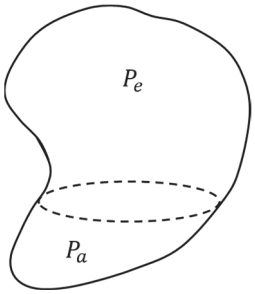

Figure A1. Schematic of a TN-LABC tumor, the active mitotic cell population is P_a, and P_e is the non-mitotic cell population.

However, if we call the tumor P_e, then the active part grows as follows:

$$P_a(T) = P_a(0)e^{\lambda T} \tag{A3}$$

At time T, the complete tumor grows in the form:

$$P_a(T) + P_e = P_a(0)e^{\lambda T} + P_e \tag{A4}$$

Therefore, the time T at which the tumor doubles its total size is:

$$P_a(T) + P_e = 2(P_a(0) + P_e) \tag{A5}$$

Substituting Equation (A4) in (A5), we have:

$$P_a(0)e^{\lambda T} + P_e = 2(P_a(0) + P_e) \tag{A6}$$

Solving T from Equation (A6) gives us the following:

$$e^{\lambda T} = \frac{2P_a(0) + P_e}{P_a(0)}$$

$$T = \frac{1}{\lambda} ln\left(\frac{2P_a(0) + P_e}{P_a(0)}\right) \tag{A7}$$

During this time, the active part of the tumor $P_a(T)$ has grown. Solving Equation (A3) and replacing T, we have:

$$\frac{P_a(T)}{P_a\ (0)} = e^{\lambda T}$$

$$P_a(T) = P_a(0)e^{\lambda(\frac{1}{\lambda} ln(\frac{2P_a(0)+P_e}{P_a(0)}))}$$

$$\frac{P_a(T)}{P_a\ (0)} = \frac{2P_a(0) + P_e}{P_a(0)} \tag{A8}$$

Therefore, the relationship between the doubling times of the active part and the complete tumor is as follows:

$$\frac{\ln(2)}{ln\left(\frac{2P_a(0)+P_e}{P_a(0)}\right)} \tag{A9}$$

For example, if the active part of the tumor is 10%, then $P_a\ (0) = 1$ and $P_e\ (0) = 9$; in this case, the relationship between the doubling time of the active part and the complete tumor is:

$$\frac{\ln(2)}{ln(11)} = 0.289 \tag{A10}$$

If the complete tumor doubles every 100 days, the active part doubles every 28.9 days.

As in this paper, the model only considered the AMCP; for this reason, we used a doubling time of 25 days.

Appendix C

Many simulations presented in this study had arbitrary initial conditions. However, in this appendix, we show that the results obtained in simulations, in general, are independent of the initial conditions taken, mainly because the results only depend on the initial and final AMCP rates.

Because the model is a system of piecewise linear differential equations, then the stability of the system depends solely on the principal eigenvalue p of the fundamental matrix (15), which competes with the damping parameters α_s^i owing to the drug represented in the matrix D_s (Equation (5)). Therefore, $p \times \alpha_s^i > 1$ represents system instability and $p \times \alpha_s^i < 1$ represents system stability.

We considered tumor cell growth without any drug action. The following Equation represents AMCP growth.

$$\overline{N}(\tau) = exp\Big(\widetilde{G}\tau\Big)\overline{N}(0) \tag{A11}$$

where $\overline{N}$ might be in $\mathbb{R}^2$ *or* $\mathbb{R}^4$. The AMCP $\overline{N}(\tau)$ may be approximately expressed as:

$$\|\overline{N}(\tau)\| \ \sim p\|\overline{p}_0\|\langle\overline{N}(0),\ \overline{p}_0\rangle \tag{A12}$$

where p is the most significant eigenvalue of the matrix $exp\Big(\widetilde{G}\tau\Big)$ and $\overline{p}_0$ the corresponding eigenvector, so that:

$$exp\Big(\widetilde{G}\tau\Big)\overline{p}_0 \sim p\overline{p}_0 \tag{A13}$$

We may say that for almost all initial populations, they shall be practically aligned with the final population to $\overline{p}_0$; therefore, the rate between $\|\overline{N}(0)\|$ and $\|\overline{N}(\tau)\|$ in general, is independent of the initial population $\overline{N}(0)$.

We observed that the reason why the PLMM dynamics are determined by p was from the eigenvalues of the matrix of Equation (3), considering that the matrix parameters are $\lambda_1 = \lambda$ and $\lambda_2 = \alpha\lambda$, where α is a coefficient, so that $\alpha\ \epsilon\ [0, \infty)$. Therefore, the matrix spectrum is as follows:

$$\rho_{\pm} = -\frac{(1+\alpha)\lambda}{2}\left(1 \pm \sqrt{1 + 4\alpha/(1+\alpha)^2}\right) \tag{A14}$$

where $\rho_+ > 0$ and $\rho_- < 0$ for $\forall\alpha\ \epsilon\ [0, \infty)$. That is, the origin has hyperbolic point stability, and the rate of the eigenvalues is as follows:

$$\rho_r = \frac{|\rho_-|}{|\rho_+|} = \frac{1 + \sqrt{1 + 4\alpha/(1+\alpha)^2}}{1 - \sqrt{1 + 4\alpha/(1+\alpha)^2}} \tag{A15}$$

Its variation of $\rho_r\ \epsilon\ [5.7, \infty)$, that is, the $|\rho_-| \sim 6|\rho_+|$. This means that the dynamic may be understood as a sudden contraction to the eigenvector corresponding to the positive eigenvalue, and then the entire dynamic develops in this direction. Finally, we indicated that $(N_1,\ N_2)$ in the $\mathbb{R}^2$ first only contains the eigenvector of the positive eigenvalue.

Now, for the standard sequence, when we consider that the tumor is treated with an *n-k* dose of the *s* drug (DX and CF) and for a *k* dose of PX, where $n > k$ and integer numbers, the population dynamic evolves as follows:

$$\overline{N}_a(n\tau) = \left(D_s \exp\left(\overline{G}\tau\right)\right)^{n-k} \left(\exp\left(\widetilde{P}\tau\right)\right)^k \overline{N}(0) \tag{A16}$$

We can approximate the final population magnitude as follows:

$$\|\overline{N}_a(n\tau)\| \sim p^{n-k} q^k \langle \overline{N}(0),\, \overline{q}_0\rangle \langle \overline{p}_0, \overline{q}_0\rangle \tag{A17}$$

where q is the most significant eigenvalue of the matrix $\exp\left(\widetilde{P}\tau\right)$, and $\overline{q}_0$ is its corresponding eigenvector; p is the most significant eigenvalue of the matrix $D_s \exp\left(\overline{G}\tau\right)$, and $\overline{p}_0$ is its corresponding eigenvector.

For the inverted sequence, we have the following:

$$\overline{N}_b(n\tau) = \left(\exp\left(\widetilde{P}\tau\right)\right)^{n-k} \left(D_s \exp\left(\widetilde{G}\tau\right)\right)^k \overline{N}(0) \tag{A18}$$

for which the final population size approximates as follows:

$$\|\overline{N}_b(n\tau)\| \sim \|q^{n-k} p^k \langle \overline{N}(0),\, \overline{p}_0\rangle \langle \overline{p}_0, \overline{q}_0\rangle\| \tag{A19}$$

If we consider that $\langle \overline{N}(0),\, \overline{p}_0\rangle \sim \langle \overline{N}(0),\, \overline{q}_0\rangle$, then the rate between these final populations is approximately:

$$\frac{\|\overline{N}_a\|}{\|\overline{N}_b\|} \sim \frac{p^{n-k} q^k}{p^k q^{n-k}} \cong \left(\frac{p}{q}\right)^{n-2k} \tag{A20}$$

regardless of what the initial population is.

References

1. Shahriyari, L.; Komarova, N.L. Symmetric vs. Asymmetric Stem Cell Divisions: An Adaptation against Cancer? *PLoS ONE* **2013**, *8*, e76195. [CrossRef] [PubMed]
2. Butner, J.D.; Wang, Z.; Elganainy, D.; Al Feghali, K.A.; Plodinec, M.; Calin, G.A.; Dogra, P.; Nizzero, S.; Ruiz-Ramírez, J.; Martin, G.V.; et al. A Mathematical Model for the Quantification of a Patient's Sensitivity to Checkpoint Inhibitors and Long-Term Tumour Burden. *Nat. Biomed. Eng.* **2021**, *5*, 297–308. [CrossRef] [PubMed]
3. Shahriyari, L. Cell Dynamics in Tumour Environment after Treatments. *J. R. Soc. Interface* **2017**, *14*, 20160977. [CrossRef]
4. Chamseddine, I.M.; Rejniak, K.A. Hybrid Modeling Frameworks of Tumor Development and Treatment. *Wiley Interdiscip. Rev. Syst. Biol. Med.* **2020**, *12*, e1461. [CrossRef] [PubMed]
5. McKenna, M.T.; Weis, J.A.; Barnes, S.L.; Tyson, D.R.; Miga, M.I.; Quaranta, V.; Yankeelov, T.E. A Predictive Mathematical Modeling Approach for the Study of Doxorubicin Treatment in Triple Negative Breast Cancer. *Sci. Rep.* **2017**, *7*, 5725. [CrossRef] [PubMed]
6. Mehdizadeh, R.; Shariatpanahi, S.P.; Goliaei, B.; Peyvandi, S.; Rüegg, C. Dormant Tumor Cell Vaccination: A Mathematical Model of Immunological Dormancy in Triple-Negative Breast Cancer. *Cancers* **2021**, *13*, 245. [CrossRef] [PubMed]
7. Solís-Pérez, J.E.; Gómez-Aguilar, J.F.; Atangana, A. A Fractional Mathematical Model of Breast Cancer Competition Model. *Chaos Solitons Fractals* **2019**, *127*, 38–54. [CrossRef]
8. Wodarz, D.; Komarova, N. *Dynamics of Cancer: Mathematical Foundations of Oncology*; World Scientific: Singapore, 2014.
9. Chakrabarti, A.; Verbridge, S.; Stroock, A.D.; Fischbach, C.; Varner, J.D. Multiscale Models of Breast Cancer Progression. *Ann. Biomed. Eng.* **2012**, *40*, 2488–2500. [CrossRef]
10. Abernathy, K.; Abernathy, Z.; Baxter, A.; Stevens, M. Global Dynamics of a Breast Cancer Competition Model. *Differ. Equ. Dyn. Syst.* **2020**, *28*, 791–805. [CrossRef]
11. Knútsdóttir, H.; Pálsson, E.; Edelstein-Keshet, L. Mathematical Model of Macrophage-Facilitated Breast Cancer Cells Invasion. *J. Theor. Biol.* **2014**, *357*, 184–199. [CrossRef]
12. Jarrett, A.M.; Bloom, M.J.; Godfrey, W.; Syed, A.K.; Ekrut, D.A.; Ehrlich, L.I.; Yankeelov, T.E.; Sorace, A.G. Mathematical Modelling of Trastuzumab-Induced Immune Response in an in Vivo Murine Model of HER2+ Breast Cancer. *Math. Med. Biol.* **2019**, *36*, 381–410. [CrossRef] [PubMed]
13. Roe Dale, R.; Isaacson, D.; Kupferschmid, M. A Mathematical Model of Breast Cancer Treatment with CMF and Doxorubicin. *Bull. Math. Biol.* **2011**, *73*, 585–608. [CrossRef] [PubMed]

14. Wei, H.C. Mathematical Modeling of Tumor Growth: The MCF-7 Breast Cancer Cell Line. *Math. Biosci. Eng.* **2019**, *16*, 6512–6535. [CrossRef] [PubMed]
15. Castillo Montiel, E.; Chimal Eguía, J.C.; Tello, J.I.; Piñon Zaráte, G.; Herrera Enríquez, M.; Castell Rodríguez, A.E. Enhancing Dendritic Cell Immunotherapy for Melanoma Using a Simple Mathematical Model. *Theor. Biol. Med Model.* **2015**, *12*, 1–14. [CrossRef]
16. Lopez Alfonso, J.C.; Poleszczuk, J.; Walker, R.; Kim, S.; Pilon Thomas, S.; Conejo Garcia, J.J.; Soliman, H.; Czerniecki, B.; Harrison, L.B.; Enderling, H. Immunologic Consequences of Sequencing Cancer Radiotherapy and Surgery. *JCO Clin. Cancer Inform.* **2019**, *3*, 1–16. [CrossRef]
17. Poleszczuk, J.; Luddy, K.; Chen, L.; Lee, J.K.; Harrison, L.B.; Czerniecki, B.J.; Soliman, H.; Enderling, H. Neoadjuvant Radiotherapy of Early-Stage Breast Cancer and Long-Term Disease-Free Survival. *Breast Cancer Res.* **2017**, *19*, 1–7. [CrossRef]
18. Liedtke, C.; Mazouni, C.; Hess, K.R.; André, F.; Tordai, A.; Mejia, J.A.; Symmans, W.F.; Gonzalez-Angulo, A.M.; Hennessy, B.; Green, M.; et al. Response to Neoadjuvant Therapy and Long-Term Survival in Patients with Triple-Negative Breast Cancer. *J. Clin. Oncol.* **2008**, *26*, 1275–1281. [CrossRef]
19. Huang, M.; O'shaughnessy, J.; Zhao, J.; Haiderali, A.; Cort Es, J.; Ramsey, S.D.; Briggs, A.; Hu, P.; Karantza, V.; Aktan, G.; et al. Association of Pathologic Complete Response with Long-Term Survival Outcomes in Triple-Negative Breast Cancer: A Meta-Analysis. *Cancer Res.* **2020**, *80*, 5427–5434. [CrossRef]
20. Rastogi, P.; Anderson, S.J.; Bear, H.D.; Geyer, C.E.; Kahlenberg, M.S.; Robidoux, A.; Margolese, R.G.; Hoehn, J.L.; Vogel, V.G.; Dakhil, S.R.; et al. Preoperative Chemotherapy: Updates of National Surgical Adjuvant Breast and Bowel Project Protocols B-18 and B-27. *J. Clin. Oncol.* **2008**, *26*, 778–785. [CrossRef]
21. Sikov, W.M.; Berry, D.A.; Perou, C.M.; Singh, B.; Cirrincione, C.T.; Tolaney, S.M.; Kuzma, C.S.; Pluard, T.J.; Somlo, G.; Port, E.R.; et al. Impact of the Addition of Carboplatin and/or Bevacizumab to Neoadjuvant Once-per-Week Paclitaxel Followed by Dose-Dense Doxorubicin and Cyclophosphamide on Pathologic Complete Response Rates in Stage II to III Triple-Negative Breast Cancer: CALGB 40603 (Alliance). *J. Clin. Oncol.* **2015**, *33*, 13–21. [CrossRef]
22. Shepherd, J.H.; Ballman, K.; Mei, Y.; Polley, C.; Campbell, J.D.; Fan, C.; Selitsky, S.; Fernandez Martinez, A.; Parker, J.S.; Hoadley, K.A.; et al. CALGB 40603 (Alliance): Long-Term Outcomes and Genomic Correlates of Response and Survival After Neoadjuvant Chemotherapy with or Without Carboplatin and Bevacizumab in Triple-Negative Breast Cancer. *J. Clin. Oncol.* **2022**, *40*, 1323–1334. [CrossRef] [PubMed]
23. Hahnen, E.; Lederer, B.; Hauke, J.; Loibl, S.; Kröber, S.; Schneeweiss, A.; Denkert, C.; Fasching, P.A.; Blohmer, J.U.; Jackisch, C.; et al. Germline Mutation Status, Pathological Complete Response, and Disease-Free Survival in Triple-Negative Breast Cancer Secondary Analysis of the GeparSixto Randomized Clinical Trial. *JAMA Oncol.* **2017**, *3*, 1378–1385. [CrossRef] [PubMed]
24. Sørlie, T.; Perou, C.M.; Tibshirani, R.; Aas, T.; Geisler, S.; Johnsen, H.; Hastie, T.; Eisen, M.B.; Van De Rijn, M.; Jeffrey, S.S.; et al. Gene Expression Patterns of Breast Carcinomas Distinguish Tumor Subclasses with Clinical Implications. *Proc. Natl. Acad. Sci. USA* **2001**, *98*, 10869–10874. [CrossRef] [PubMed]
25. Atchley, D.P.; Albarracin, C.T.; Lopez, A.; Valero, V.; Amos, C.I.; Gonzalez-Angulo, A.M.; Hortobagyi, G.N.; Arun, B.K. Clinical and Pathologic Characteristics of Patients with BRCA-Positive and BRCA-Negative Breast Cancer. *J. Clin. Oncol.* **2008**, *26*, 4282–4286. [CrossRef]
26. Prat, A.; Fan, C.; Fernández, A.; Hoadley, K.A.; Martinello, R.; Vidal, M.; Viladot, M.; Pineda, E.; Arance, A.; Muñoz, M.; et al. Response and Survival of Breast Cancer Intrinsic Subtypes Following Multi-Agent Neoadjuvant Chemotherapy. *BMC Med.* **2015**, *13*, 1–11. [CrossRef]
27. Kim, T.; Han, W.; Kim, M.K.; Lee, J.W.; Kim, J.; Ahn, S.K.; Lee, H.B.; Moon, H.G.; Lee, K.H.; Kim, T.Y.; et al. Predictive Significance of P53, Ki-67, and Bcl-2 Expression for Pathologic Complete Response after Neoadjuvant Chemotherapy for Triple-Negative Breast Cancer. *J. Breast Cancer* **2015**, *18*, 16–21. [CrossRef]
28. Pan, Y.; Yuan, Y.; Liu, G.; Wei, Y. P53 and Ki-67 as Prognostic Markers in Triplenegative Breast Cancer Patients. *PLoS ONE* **2017**, *12*, e0172324. [CrossRef]
29. Earl, H.M.; Vallier, A.L.; Hiller, L.; Fenwick, N.; Young, J.; Iddawela, M.; Abraham, J.; Hughes-Davies, L.; Gounaris, I.; McAdam, K.; et al. Effects of the Addition of Gemcitabine, and Paclitaxel-First Sequencing, in Neoadjuvant Sequential Epirubicin, Cyclophosphamide, and Paclitaxel for Women with High-Risk Early Breast Cancer (Neo-TAnGo): An Open-Label, 2×2 Factorial Randomised Phase 3 Trial. *Lancet Oncol.* **2014**, *15*, 201–212. [CrossRef]
30. Taghian, A.G.; Abi Raad, R.; Assaad, S.I.; Casty, A.; Ancukiewicz, M.; Yeh, E.; Molokhia, P.; Attia, K.; Sullivan, T.; Kuter, I.; et al. Paclitaxel Decreases the Interstitial Fluid Pressure and Improves Oxygenation in Breast Cancers in Patients Treated with Neoadjuvant Chemotherapy: Clinical Implications. *J. Clin. Oncol.* **2005**, *23*, 1951–1961. [CrossRef]
31. Skipper, H.E. *Laboratory Models: Some Historical Perspective*; Wittes, R.E., Goldin, A., Eds.; American Society of Clinical Oncology: Alexandria, VA, USA, 1986; Volume 70.
32. Norton, L. Cancer Log-Kill Revisited. In *American Society of Clinical Oncology Educational Book*; ASCO Educational Book; American Society of Clinical Oncology: Alexandria, VA, USA, 2014.
33. Citron, M.L.; Berry, D.A.; Cirrincione, C.; Hudis, C.; Winer, E.P.; Gradishar, W.J.; Davidson, N.E.; Martino, S.; Livingston, R.; Ingle, J.N.; et al. Randomized Trial of Dose-Dense versus Conventionally Scheduled and Sequential versus Concurrent Combination Chemotherapy as Postoperative Adjuvant Treatment of Node-Positive Primary Breast Cancer: First Report of Intergroup Trial C9741/Cancer and Leukemia Group B Trial 9741. *J. Clin. Oncol.* **2003**, *21*, 1431–1439. [CrossRef]

34. Lovitt, C.J.; Shelper, T.B.; Avery, V.M. Doxorubicin Resistance in Breast Cancer Cells Is Mediated by Extracellular Matrix Proteins. *BMC Cancer* **2018**, *18*, 41. [CrossRef] [PubMed]
35. Ryu, E.B.; Chang, J.M.; Seo, M.; Kim, S.A.; Lim, J.H.; Moon, W.K. Tumour Volume Doubling Time of Molecular Breast Cancer Subtypes Assessed by Serial Breast Ultrasound. *Eur. Radiol.* **2014**, *24*, 2227–2235. [CrossRef]
36. Nakashima, K.; Uematsu, T.; Takahashi, K.; Nishimura, S.; Tadokoro, Y.; Hayashi, T.; Sugino, T. Does Breast Cancer Growth Rate Really Depend on Tumor Subtype? Measurement of Tumor Doubling Time Using Serial Ultrasonography between Diagnosis and Surgery. *Breast Cancer* **2019**, *26*, 206–214. [CrossRef] [PubMed]
37. Dahan, M.; Hequet, D.; Bonneau, C.; Paoletti, X.; Rouzier, R. Has Tumor Doubling Time in Breast Cancer Changed over the Past 80 Years? A Systematic Review. *Cancer Med.* **2021**, *10*, 5203–5217. [CrossRef] [PubMed]
38. Gerdes, J.; Lelle, R.J.; Pickartz, H.; Heidenreich, W.; Schwarting, R.; Kurtsiefer, L.; Stauch, G.; Stein, H. Growth Fractions in Breast Cancers Determined in Situ with Monoclonal Antibody Ki-67. *J. Clin. Pathol.* **1986**, *39*, 977–980. [CrossRef]
39. Lellé, R.J. In Situ Determination of the Ki-67 Growth Fraction (Ki-67 GF) in Human Tumors (Studies in Breast Cancer). *Acta Histochem. Suppl.* **1990**, *39*, 109–124.
40. Lashen, A.G.; Toss, M.S.; Katayama, A.; Gogna, R.; Mongan, N.P.; Rakha, E.A. Assessment of Proliferation in Breast Cancer: Cell Cycle or Mitosis? An Observational Study. *Histopathology* **2021**, *79*, 1087–1098. [CrossRef]
41. Whitman, J.; Cook, D.; Patel, S.; Munn, L.; Cole, J.A. Accurate Prediction of Tumor Growth and Doubling Times for Triple Negative Breast Cancer (TNBC) Allows for Patient-Specific Assessment of Tumor Aggressiveness. In Proceedings of the American Association for Cancer Research Annual Meeting, Philadelphia, PA, USA, 16–19 September 2022.

mathematics

MDPI

Article

On Incidence-Dependent Management Strategies against an SEIRS Epidemic: Extinction of the Epidemic Using Allee Effect

Tri Nguyen-Huu [1,2,*], Pierre Auger [1] and Ali Moussaoui [3]

[1] UMMISCO, Institut de Recherche Pour le Développement, Sorbonne Université, F-93143 Bondy, France
[2] IXXI, ENS Lyon, 69364 Lyon, France
[3] Laboratoire d'Analyse Non Linéaire et Mathématiques Appliquées, Department of Mathematics, Faculty of Science, University of Tlemcen, Tlemcen 13000, Algeria; al_moussaoui@mail.univ-tlemcen.dz
* Correspondence: tri.nguyen-huu@ird.fr

Abstract: We developed a mathematical model to study the effects of non-pharmaceutical interventions (NPIs) on the dynamics of an epidemic. The level of intervention was assessed as a fraction of the population being isolated and depended on the level of incidence of the epidemic in the population. We performed a mathematical analysis of the model and showed that, depending on the choice of the prevalence-dependent isolation function, it is possible to create new endemic equilibria and to change the stability of the disease-free equilibrium for which the epidemic vanishes. The model was then applied to the case of the COVID-19 pandemic. Several NPI management strategies were considered. In the case of an NPI intensity increasing with the level of infection, it is possible to avoid the initial epidemic peak of great amplitude that would have occurred without intervention and to stabilize the epidemic at a chosen and sufficiently low endemic level. In the case of an NPI intensity decreasing with the level of infection, the epidemic can be driven to extinction by generating an "Allee" effect: when the incidence is below a given level, the epidemic goes extinct whereas, above it, the epidemic will still be able take hold at a lower endemic level. Simulations illustrate that appropriate NPIs could make the COVID-19 vanish relatively fast. We show that, in the context of the COVID-19 pandemic, most countries have not chosen to use the most efficient strategies.

Keywords: SEIRS model; non-pharmaceutical interventions; target endemic level; Allee effect; COVID-19

MSC: 92D30

1. Introduction

We present here a theoretical approach aiming at evaluating the effects of some non-pharmaceutical interventions (NPIs) such as lockdown, social distancing or teleworking in order to limit the number of cases. We discuss their ability to fulfill some requirements such as keeping the number of cases at a level low enough to be managed by hospitals or maintaining a lockdown at a level low enough to avoid consequences that are too damaging to the economy. We are also looking for NPI measures in order to bring about the eradication of the epidemic. In SIRS and SEIRS classical epidemic models, there exist a disease-free equilibrium (DFE) and a single endemic equilibrium (EE) that can be positive depending on the values of the parameters. A basic reproduction number of the epidemic $\mathcal{R}_0$ is defined and represents the number of people infected by a single infectious person during their illness. According to the value of this parameter, there are two cases: either $\mathcal{R}_0$ is smaller than 1 and the epidemic goes extinct, i.e., the DFE is globally stable while the EE does not exist, or the epidemic takes hold, i.e., $\mathcal{R}_0$ is greater than 1, the DFE is unstable and the EE is globally stable.

The aim of this work was to propose NPI protection measures depending on the number of infected people to control and eradicate an epidemic. Therefore, a proportion of

protected people is defined by function $v(I)$. Such infected-dependent protection measures significantly allow for modifying the global phase portrait by creating several endemic equilibria depending on the particular choice of the function $v(I)$. We particularly considered choices of the protection function that allow for bringing about the extinction of the epidemic. In particular, we focused on a class of protection functions that generate an "Allee" effect. The Allee effect is well known in population dynamics and ecology [1]. A commonly accepted definition of the Allee effect is a positive density dependence of the growth rate per capita. More precisely, the demographic Allee effect is the positive relationship between the overall individual fitness and population density. The weak Allee effect keeps the population growth rate quite low but positive at a low density whereas the strong Allee effect induces a negative growth rate below a certain threshold [2,3]. It can generally be observed and has high significance at a low population level, and it is often used to explain tipping points, as a low or negative growth rate may result in the extinction of endangered species. The Allee effect aims at taking into account the difficulties in mating or the absence of cooperative behavior (defense, feeding) between individuals at a low density causing the eradication of the species: panda populations hardly grow, partly because of a very low birthrate; fish stocks may be unable to recover from overfishing. In order to grow, the initial population must be at a sufficiently high density above this threshold. In the case of a harvested population, a high price of the resource due in particular to its scarcity can also induce an Allee effect [4].

Equivalently, such an effect could happen in an epidemiology context, when the number of infected people is too small to start a wave of infection. While an Allee effect is generally not desirable in ecology, creating the conditions of such an effect would be a great asset in order to mitigate an epidemic. A judicious choice of functions $v(I)$ allows for generating two endemic equilibria, one at a low level, denoted EE1, and the other at a higher endemic level, denoted EE2. By analogy, the case where EE1 is unstable while EE2 is stable corresponds to an "Allee" effect. According to the basins of attraction of equilibria, we can create a situation where any initial condition chosen below the level of infection of EE1 can lead to the eradication of the epidemic whereas, for any initial condition above, the epidemic settles and stabilizes in the long term at the level of EE2. In this work, we focused on a class of functions $v(I)$ allowing us to generate such an Allee effect as well as any other class of functions allowing us to cause the extinction of the epidemic.

The article is made up of seven sections. After an introductory part, Section 2 presents a general SEIRS epidemic model with infected-dependent control and a mathematical analysis of the epidemic model, such as the existence of endemic equilibria and stability properties. In Section 3, we discuss the application of the model to the SARS-CoV-2 epidemic. In Section 4, we compare several infection-dependent NPI strategies. Among these, we present a constant level strategy, a strategy used to avoid a large-scale epidemic peak and to stabilize the epidemic at an endemic level low enough to avoid congestion in hospitals and strategies that allow for generating an Allee effect that permits the provoking of the extinction of the epidemic below some endemic threshold. Section 5 is devoted to identifying which strategies have been used against COVID-19. Section 6 presents a discussion of the results with a comparison of the different strategies showing the advantages, limitations and costs of each one. We conclude in Section 7.

2. An SEIRS Model with NPI Depending on the Number of Infected People

In the following model, the population is distributed among four compartments that are almost equivalent to those of a classical SEIRS model: a compartment S with susceptible individuals, a compartment E with exposed individuals, a compartment I with both asymptomatic (infectious without symptoms onset) and pre-symptomatic (infectious before symptoms onset or test) individuals and a compartment R, which contains individuals that have been removed from the infection dynamics, i.e., asymptomatic individuals after recovery, and symptomatic individuals who are assumed to be quarantined as soon as they get aware of their condition (symptoms onset or positive test). We assumed a constant total

population $N = S + E + I + R$ since the time scale of the epidemic is small compared to the one of population growth.

We considered an epidemic focus, such as a country where the epidemic has just started. It is normally necessary to take into account the urban mobility of individuals in the dynamics of the epidemic. We cite the work [5], in which aged structured individuals are supposed to move between their place of residence, workplaces, universities, schools, public places, shopping centers and more places [6,7]. In a previous model [8], we also took into account the daily movements of people between their home and the various places where they are required to move and where they are more or less protected from contact with infectious persons as well as lockdown and protection by masks following the work by [9].

We assumed that individuals can switch between a normal state and a state in which they are removed from the dynamics because of NPI, such as isolation, lockdown or social distancing. Thus, NPIs result in a proportion v of the population being in a state of isolation. For example, an NPI that imposes two days of teleworking per labor week (five days) would result in a proportion $v = 40\%$ of isolated people working from home every day. However, people may be in a different state every day. In the following sections, v will refer to a more general definition of NPI intensity that will not only apply to lockdown or teleworking but also to social distancing or mask wearing by assuming that any measure is equivalent to a percentage of time spent in isolation. It should be noticed that measures such as lockdown, stay-at-home or curfew apply to the whole population independent of their infection status.

Infected individuals follow the natural process of the disease corresponding to a classical SEIRS model, i.e., exposed individuals can become infected after an incubation time $\frac{1}{k}$. Infected individuals are removed after an average time $\frac{1}{\alpha}$, either because they recovered or because they have been tested or are symptomatic and thus quarantined. They lose their immunity after a time $\frac{1}{\gamma}$. The number of newly infected individuals per unit of time for the population in a classical SEIRS model is given by the expression $\beta\frac{SI}{N}$, where β is the transmission rate of the disease for one infectious individual in a population with only susceptible individuals. Since the same NPI rules apply to susceptible and asymptomatic/presymptomatic individuals, only a proportion $1 - v$ of both S and I is involved in the disease transmission. Thus, this expression must be replaced by $\beta\frac{(1-v)S(1-v)I}{N}$. A detailed justification of this formula is presented in Appendix B. Figure 1 illustrates the reduction in the number of infections: without NPI, four infections occur. With NPI, a proportion $v = 0.5$ of the population is isolated (shaded area) and cannot be infected or infect others. Compared to the case without NPI, infections can only occur between two persons outside of the shaded area; thus, the ones with a red cross cannot occur any more. The number of infections is reduced to $(1 - v)^2 = 0.25$ of the original infections.

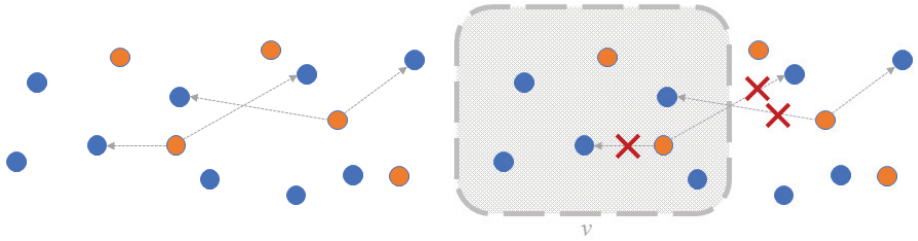

(**a**) Without NPI (**b**) With NPI

Figure 1. Reduction in the number of infections due to NPI. Infected individuals are represented in blue, and symptomatic/presymptomatic in orange. Infections are represented by a gray arrow. Red crosses signal the infections that do not occur anymore due to NPI. (**a**) Without NPI, four infections occur. (**b**) With NPI, a proportion $v = 0.5$ of individuals are isolated (shaded area). The number of infections is reduced to $(1 - v)^2 = 0.25$ of the number of original number of infections.

The modified SEIRS model reads

$$\begin{cases} \frac{dS}{dt} &= -\beta(1-v)^2\frac{SI}{N} + \gamma R, \\ \frac{dE}{dt} &= \beta(1-v)^2\frac{SI}{N} - kE, \\ \frac{dI}{dt} &= kE - \alpha I, \\ \frac{dR}{dt} &= \alpha I - \gamma R. \end{cases} \tag{1}$$

Individuals who present onsets or who have been tested are supposed to be definitively isolated and removed from the dynamics, thus belonging to the removed class R. To summarize, v represents the proportion of isolated individuals for whom the status is unknown, whereas the isolation of individuals who have been recognized as infectious is part of the removal process corresponding to the term αI (see Section 3.2 for more details on α). The parameters are summarized in Table 1.

Table 1. Parameters used in model (1).

Parameter	Interpretation
β	infection rate
k	transfer rate from exposed to infected. $1/k$ is the average incubation duration.
α	$1/\alpha$ is the average time spent in the infectious state.
γ	transfer rate from recovered to susceptible. $1/\gamma$ is the average time before losing immunity.
v	intensity of NPI, measured as the equivalent proportion of the population in isolation.

Now, let us consider the effect of NPI, which depends on the number of infected individuals, i.e., we impose that the proportion of individuals $v(I)$ in state 1 depends on the intensity of the epidemic, i.e., the number of infected individuals I.

Since the dynamics of R can be deduced from the ones of S, E and I, the dynamics are governed by the system

$$\begin{cases} \frac{dS}{dt} &= -\beta(1-v(I))^2\frac{SI}{N} + \gamma(N-S-E-I), \\ \frac{dE}{dt} &= \beta(1-v(I))^2\frac{SI}{N} - kE, \\ \frac{dI}{dt} &= kE - \alpha I. \end{cases} \tag{2}$$

The resulting model is an SEIRS model with a modified transmission rate that reflects the NPI intensity, which changes with the number of infected individuals. One way to derive the previous SEIRS model would also be to consider the version of the baseline confinement model in [8] and to assume that the proportion $v(I)$ of isolated people depends on the number of infected people I. However, the classical SEIRS models can only have one endemic equilibrium, whereas the model with NPI can have several endemic equilibria and different dynamics. The model obtained with constant v is similar to the one in [8]. For the sake of simplicity, we assume that v is a continuous map.

We provide a brief demonstration the properties (existence, uniqueness, positivity and boundedness) of the solutions in Appendix A.

2.1. Disease-Free Equilibria

In mathematical epidemiology, disease-free equilibria (DFE) are defined as equilibria for which no individual is infected by the disease, i.e., $I = E = 0$ in our model. Instability of the DFE usually corresponds to a value of the basic reproduction number $\mathcal{R}_0$ greater than 1 and is associated with the occurrence of an epidemic wave [10]. Equilibria of system (1) verify $\alpha I - \gamma R = 0$, which implies that $R = 0$ at a DFE since $I = 0$. Finally, $S = N - E - I - R = N$, which makes $(N, 0, 0)$ the unique disease-free equilibrium of model (2).

2.2. Endemic Equilibria

Interior endemic equilibria (S^*, E^*, I^*) verify:

$$\begin{cases} \beta(1-v(I^*))^2 \frac{S^*I^*}{N} = \gamma(N - S^* - E^* - I^*), \\ \beta(1-v(I^*))^2 \frac{S^*I^*}{N} = kE^*, \\ kE^* = \alpha I^*. \end{cases} \tag{3}$$

The equilibrium of the susceptible population can be expressed in terms of the infected one:

$$S^* = N - \left(1 + \frac{\alpha}{k} + \frac{\alpha}{\gamma}\right) I^*. \tag{4}$$

The infected population I^* verifies the following expression:

$$\frac{\beta}{N}(1-v(I^*))^2 \left(N - \left(1 + \frac{\alpha}{k} + \frac{\alpha}{\gamma}\right) I^*\right) = \alpha. \tag{5}$$

Let us define the function $\hat{v}$ such that, for $I \geq 0$,

$$\hat{v}(I) = 1 - \frac{1}{\sqrt{\mathcal{R}_0 - \frac{\beta}{N}\left(\frac{1}{\alpha} + \frac{1}{k} + \frac{1}{\gamma}\right) I}}. \tag{6}$$

where $\mathcal{R}_0 = \frac{\beta}{\alpha}$ is the basic reproduction rate of the SEIRS epidemic. We deduce from Equation (5) that, at endemic equilibria, the equality

$$v(I^*) = \hat{v}(I^*) \tag{7}$$

holds. For a given control function v associated with a given set of mitigation measures, the set of endemic equilibria can be determined by finding the solution of Equation (7). In other words, each time that the graph of the chosen function v intersects the function $\hat{v}$, it corresponds to an endemic equilibrium, as will be illustrated in the next section.

The continuous map $\hat{v}$ defined on $[0, I_m]$, where $I_m = \frac{\mathcal{R}_0}{\frac{\beta}{N}\left(\frac{1}{\alpha} + \frac{1}{k} + \frac{1}{\gamma}\right)}$, is monotonously decreasing and intersects the horizontal axis at the classical endemic equilibrium $I_{EE} = \frac{\mathcal{R}_0 - 1}{\frac{\beta}{N}\left(\frac{1}{\alpha} + \frac{1}{k} + \frac{1}{\gamma}\right)}$, $(I_{EE} < I_m)$, reached in the absence of mitigation measures ($v = 0$). We also note that $\hat{v}(0) = 1 - \frac{1}{\sqrt{\mathcal{R}_0}}$. As shown in the following subsection, the disease-free equilibrium (DFE) is stable if and only if $v(0) > 1 - \frac{1}{\sqrt{\mathcal{R}_0}}$.

2.3. Stability Analysis

We now study the dynamics of the SEIRS model by finding the stability of the equilibria (DFE and endemic equilibria). For the sake of simplicity, we assume that v is $\mathcal{C}^1$ around the equilibria. The Jacobian matrix for the SEIRS model (2) reads:

$$J = \begin{pmatrix} -\frac{\beta}{N}(1-v(I))^2 I - \gamma & -\gamma & -\frac{\beta}{N}(1-v(I))^2 S - \gamma + 2\frac{\beta}{N} v'(I)(1-v(I)) IS \\ \frac{\beta}{N}(1-v(I))^2 I & -k & \frac{\beta}{N}(1-v(I))^2 S - 2\frac{\beta}{N} v'(I)(1-v(I)) IS \\ 0 & k & -\alpha \end{pmatrix}. \tag{8}$$

2.3.1. Local Stability of the DFE

For the DFE, $(N, 0, 0)$, the Jacobian reads

$$J_{\text{DFE}} = \begin{pmatrix} -\gamma & -\gamma & -\gamma - \beta(1-v(0))^2 \\ 0 & -k & \beta(1-v(0))^2 \\ 0 & k & -\alpha \end{pmatrix}. \tag{9}$$

We are ensured to find one negative eigenvalue, $\lambda_1 = -\gamma < 0$. We consider the remaining minor matrix J_{MIN}:

$$J_{MIN} = \begin{pmatrix} -k & \beta(1-v(0))^2 \\ k & -\alpha \end{pmatrix}. \tag{10}$$

We find that its trace, $Tr(J_{MIN}) = -k - \alpha$, is negative and that the determinant, $det(J_{MIN}) = k(\alpha - \beta(1-v(0))^2)$, can be positive or negative. It is positive when $v(0) > 1 - \frac{1}{\sqrt{\mathcal{R}_0}}$. Under these conditions, the DFE is locally asymptotically stable and it is possible to generate an Allee effect.

2.3.2. Local Stability for an Endemic Equilibrium

For any interior equilibrium (S^*, E^*, I^*), the Jacobian matrix simplifies by incorporating equilibrium expressions (3):

$$J^* = \begin{pmatrix} -\gamma - \frac{kE^*}{S^*} & -\gamma & -\gamma - \alpha + 2\frac{kv'(I^*)E^*}{(1-v(I^*))} \\ \frac{kE^*}{S^*} & -k & \alpha - 2\frac{kv'(I^*)E^*}{(1-v(I^*))} \\ 0 & k & -\alpha \end{pmatrix}. \tag{11}$$

The characteristic equation reads as follows:

$$\lambda^3 + a_1\lambda^2 + a_2\lambda + a_3 = 0, \tag{12}$$

with:

$$a_1 = \left(\alpha + k + \gamma + \frac{kE^*}{S^*}\right) > 0, \tag{13}$$

$$a_2 = (\alpha + k + \gamma)\frac{kE^*}{S^*} + \gamma(k+\alpha) + 2\frac{k^2v'(I^*)E^*}{(1-v(I^*))}, \tag{14}$$

$$a_3 = 2\frac{\gamma k^2 v'(I^*)E^*}{(1-v(I^*))} + (\alpha\gamma + \gamma k + \alpha k)\frac{kE^*}{S^*} > 0. \tag{15}$$

The Routh–Hurwitz conditions $a_1 > 0$ and $a_3 > 0$ are always verified for a positive interior endemic equilibrium. If $v'(I^*) > 0$, it is easy to check that the last Routh–Hurwitz condition is also verified. Indeed, after simplification, $a_1a_2 > a_3$ reads:

$$\begin{aligned}(\alpha^2 + k^2 + \gamma^2 + \alpha k + \alpha\gamma + k\gamma)\frac{kE^*}{S^*} + (\alpha + k + \gamma)\left(\frac{kE^*}{S^*}\right)^2 \\ + \gamma(k+\alpha)\left(\alpha + k + \gamma + \frac{kE^*}{S^*}\right) + 2k^2\left(\alpha + k + \frac{kE^*}{S^*}\right)\frac{v'(I^*)E^*}{1-v(I^*)} > 0.\end{aligned} \tag{16}$$

It is always verified for a positive endemic equilibrium when $v'(I^*) > 0$. In other words, if the level of protection increases with the number of infected individuals, the endemic equilibrium is stable. It is still true when $v'(I^*) < 0$ and $|v'(I^*)|$ is small. In other cases ($v'(I^*) < 0$ and $|v'(I^*)|$ is larger than a given threshold), the equilibrium is unstable.

As a consequence, the stability of endemic equilibria is independent of the stability of the DFE.

2.4. Numerical Simulations

In the following sections, analytical results are supported by simulations. Simulations were performed in Maple using a Fehlberg fourth–fifth-order Runge–Kutta numerical scheme (RKF45) [11]. For ODE systems in epidemiology, it is important to ensure that the numerical results are accurate and carry the qualitative properties of the solutions. Some studies focused on numerical methods dedicated to epidemiology, such as [12] or [13]. However, like other papers relying mostly on the analytical study of the systems

(equilibria, stability, asymptotic dynamics) such as [14], we do not provide a complete proof of the convergence analysis (consistency, stability), as simulations were used mainly to illustrate the dynamics. All simulations outputs appear to be qualitatively consistent with the analytical results, as well as the numerical values (equilibria). The parameters used in the simulations presented in this article were estimated for the case of the COVID-19 pandemic based on medical and statistical studies and are discussed in Section 3.2, apart for the country population, infection rate β and NPI intensity v, which are country-dependent.

2.5. Sensitivity Analysis

We performed a sensitivity analysis of the model and $\mathcal{R}_0$ with respect to the parameters γ, α, k, ν and β, assuming that ν is a constant parameter. We used the FME package in R for the local sensitivity analysis of variables S, E, I, R and a partial rank correlation coefficient (PRCC) for $\mathcal{R}_0$. Results are shown in Figure 2.

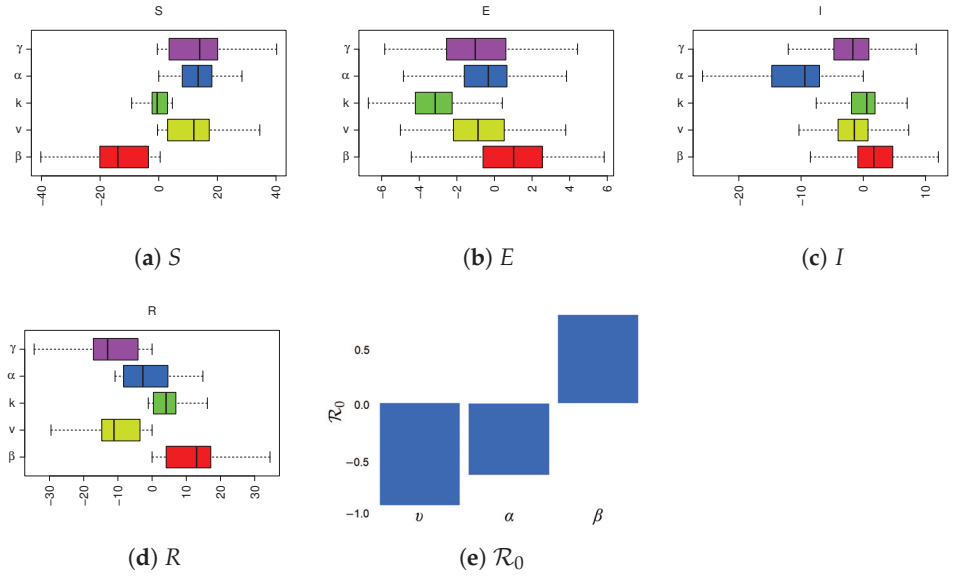

(**a**) S (**b**) E (**c**) I

(**d**) R (**e**) $\mathcal{R}_0$

Figure 2. Sensitivity analysis for (**a**) S, (**b**) E, (**c**) I, (**d**) R and (**e**) $\mathcal{R}_0$, taking into account parameters γ (purple), α (blue), k (green), ν (yellow) and β (red). Parameters values are $\beta = 1.2$, $k = 0.2$, $\alpha = 0.5$, $v = 0.4$ and $\gamma = 1/200$, $N = 100$.

The model is quite sensitive to parameters β, ν, γ and α and, to a lesser extent, to parameter k. This can be explained by the fact that compartment E is only a transition compartment. Indeed, modifying the value of k changes the duration spent in the exposed state and delays the infection dynamics, but does not really change the magnitude of the infection among the population. All other parameters greatly influence the dynamics; hence, a good estimation would be required in order to accurately assess the magnitude of the epidemic. This sensitivity analysis confirms that NPI intensity is a key factor for mitigating the epidemics. On the other hand, its negative influence on R means that NPIs with a higher intensity result in a lower immunity to the disease in the population.

3. Application to the COVID-19 Epidemic

Several approaches have been used to model the COVID-19 pandemic. We propose here to illustrate the model presented in the previous section with the case of COVID-19. The global response to COVID-19 is highly related to behavioral epidemiology since the only measures that were available before the appearance of the vaccine were NPIs, which consist of modifying the habits of the population. Behavioral epidemiology studies how the behavior of individuals and their lifestyle affect their health conditions and influence the dynamics of epidemics. We refer to [15] and more generally [16] as early contributions. It is obvious that the global evolution of the epidemic depends on all the decisions taken by each individual according to the context in which they finds themself and their personal

situation: the age of individuals, their social status, the frequency of their daily trips to sites where the risk of infection is more or less significant, their protective behavior by using masks or even by teleworking and many other multiple aspects regarding their life style. We refer to [5] as an example for the COVID-19 epidemic taking into account different places and ages in China. We also cite a more recent contribution [17], which is a study on the influence of social cohesion and socioeconomic status on health conditions again in China.

This kind of aggregated model remains very simplistic but has the advantages of being able to be handled analytically and, more importantly, to easily exhibit major tendencies. The model that we used here is extremely simple and cannot accurately describe all the aspects of the COVID-19 pandemic. However, it is sufficient for describing the different NPI strategies and estimating at least qualitatively their effect on such a pandemic. Our choice here was to consider the individual behaviors as a single aggregated term of NPI intensity rather than considering the extreme diversity of individual behaviors, as well as a limited number of compartments. Indeed, other compartments such as quarantined, asymptomatic carriers, etc., could also be introduced and would provide a greater accuracy; however, they would only marginally modify the dynamics and would not provide much more useful information regarding the goal of this model, i.e., estimating the qualitative evolution over time of the pandemic in regard to different NPI intensity strategies.

3.1. Background of the COVID-19 Pandemic

The onset of the COVID-19 epidemic was brutal, with very high peaks of contamination leading to the saturation of intensive care units. In the United States, the occupancy rate of intensive care beds reached over 60% in the most populous states and large cities [18]. In France, the number of beds able to accommodate severely ill patients requiring intensive care in hospitals was limited to around 5000 beds and the number of respirators available seemed also insufficient in view of the foreseeable arrival of seriously ill patients. In the absence of any measures, a very significant proportion of the population would have been infected after the epidemic wave. As a result, several governments in the world decided to put in place NPIs such as lockdown, social distancing or teleworking in order to limit the number of cases and keep hospital admissions of seriously ill patients below the hospital capacity threshold. This policy was adopted by many countries and worked with some success and limitations. Regardless, hospitals were under very strong pressure, sometimes leading to the saturation of intensive care units [19] despite such measures. The evaluation of the effects of NPIs is a central question that has been studied in previous works, such as [20] in Italy or in [14], where the authors evaluated how successful the governmental measures were in Rohingya refugee camps.

However, lockdown has had disastrous consequences for the economy, generating waves of unemployment and causing considerable budget deficits for the states, with very serious difficulties for those in need. Some countries have chosen to set up a partial lockdown while maintaining activity or have opted to end the lockdown early enough to limit the disastrous consequences for their economy, especially in Northern Europe. Many countries remain extremely cautious in this area, fearing the occurrence of successive epidemic waves after lockdown. The question of the end of lockdown is therefore crucial and it is important to develop scientific methods allowing us to control this phase by limiting the damage.

NPIs were set up in order to rapidly address problems such as intensive care units overload and hospital pressure. However, they were not specifically thought of as a long-term answer to a long-lasting epidemic (several years) that may be caused by reinfection. It is commonly admitted that immunity usually lasts at least six months, but there is still uncertainty about a possible loss of immunity that would happen later on. As of today, a few cases of reinfection have been reported [21]. In [22], the author spotted that reinfection is possible but the bigger question is "if reinfections are going to happen, how frequently are they happening?". In a preprint, Ward et al. [23] observed a decline in antibodies in UK

patients, which led to the fear of a possible loss of immunity. Furthermore, the appearance of new variants also increases the possibility of reinfection [24,25].

3.2. Dynamics without Protection Measures: Parameters Estimation Based on COVID-19

Much work has been devoted to modeling the COVID-19 epidemic: Refs. [26–28] in China, Refs. [29–31] in Japan and, in Algeria, [32,33]. We also cite [34] in which the authors studied the effects of different quarantine and protection measures on the dynamics of the epidemic with a mathematical model, and [35] for Canada. Only a few works have been devoted to modeling the epidemic in the hypothesis of reinfection, such as [36] or [37].

The question of reinfection quickly rose with the onset of the pandemic, as it was unclear if immunity could be lost [38]. The loss of immunity or the risk of reinfection is an important question in epidemiology, such as for HIV [39]. In the context of COVID-19, few cases of re-infections have been observed [21], but most studies prior to fall 2021 suggested a long-lasting protection ($\geq$90 days [40], $\geq$6 months [41]) but could not totally exclude the possibility of reinfections after a longer time or because of mutations. However, the appearance of new variants shed a light on massive reinfection occurrences. Evidence that variants could elude immune responses was found [24,25]. Several new variants (English, South African, Brazilian, Delta, Omicron) have been able to develop and even replace the original virus. These variants can be more virulent, more contagious and, for some of them, even more resistant to vaccines (see [42] for the Brazilian variant and [43] for UK and South Africa). It has recently been found that the Omicron variant might evade antibodies induced by infection or vaccination [44]. In [45], it was suggested that the relative risk of reinfection has risen to 81%. Long-term reinfections due to new variants or a loss of immunity have become a realistic hypothesis. In this general context, we considered an SEIRS model with the possibility of re-infection in the long term, with a reinfection rate γ. For the COVID-19 epidemic, we used the same general SEIRS model presented in the previous theoretical section. Since it is a highly simplified model that relies on strong assumptions, it may not be suitable for a realistic description or prediction of the current pandemic. However, it can provide useful qualitative information about the evolution of the disease in the context of possible re-infections and about the benefits and disadvantages of different NPI strategies.

Parameters of the model can be estimated from various medical and statistical reports about COVID-19.

As of 2022, though the proportion of asymptomatic carriers is pretty much well known (50% in [46], 40% in the meta-analysis performed in [47]), there is no clear consensus about the role of asymptomatic carriers on the dynamics of the population. Some studies state that more than half of infections are due to asymptomatic carriers [48], whereas other suggest that asymptomatic transmission is marginal or due to a misclassification of presymptomatic cases as asymptomatic [49,50]. Because of those uncertainties, we did not take into account separate compartments for asymptomatic and symptomatic people in this work for the sake of simplicity. Instead, we considered a class I that includes both symptomatic and presymptomatic carriers. Symptomatic carriers were included in the R class since they are supposed to be isolated as soon as they are aware of their condition. For that reason, we did not use a quarantined/isolated class as is often carried out in other approaches, such as in [51], since symptomatic/isolated and healed individuals do not play any role in the transmission of the disease. As a consequence, the average time spent in the infectious class $1/\alpha$ lies somewhere between the average infectious time for presymptomatic carriers $1/\alpha_p$ and the one for asymptomatic carriers $1/\alpha_a$, i.e., $1/\alpha \in [1/\alpha_p, 1/\alpha_a]$. It was found in [52] that infectiousness can occur from 2.3 days (95% CI, 0.8–3.0 days) before symptom onset, with a peak at 0.7 days (95% CI, 0.2–2.0 days) before onset. We estimated a rough lower boundary for $1/\alpha_p \geq 1$. The same study found a significant decline in infectiousness 10 days after onset. Other studies suggest that an infection more than 5 days after symptoms onset is very unlikely [53]. We thus set an upper

boundary for $1/\alpha_a \leq 7.3$. As a consequence, we estimated that the parameter α lies in the interval $[0.13, 1]$.

As a consequence, we chose to set $\alpha = 0.67$ in this model. The model that we obtained does not differ qualitatively from a model with an explicit asymptomatic compartment and provides a similar dynamic, with a marginal quantitative difference. On the contrary, such an approach allows for avoiding the use of too many parameters on which there is much uncertainty, thus following the principle of parsimony. Additional information obtained by using an asymptomatic compartment would not have been useful considering the scope of our study, and it would have come with a much higher prior uncertainty.

Following the estimation of α, we set parameter k to 0.27 day^{-1} since the average duration between infection and symptoms onset is 5.2 days [54].

$\mathcal{R}_0 = \frac{\beta}{\alpha}$ has been estimated as between 2 and 6 for most countries, with most probable values in the range 2–3 [55]. Some other studies suggest even higher values (between 3.5 and 6 [56]). In the following simulation, we decided to set $\beta = 1.2$ in order to obtain $\mathcal{R}_0 = 2.4$. In Section 5, we will estimate β for each case study based on incidence time series obtained from data sources.

It is important to note that estimates of the previous parameters (α, β, k) may be very inaccurate. In the case of COVID-19, one may find inconsistencies about indicators estimations between different studies: they depend on many factors (country, population density, local habits, culture, genetics), may vary in time (seasonal effects, new variants) or may be based on different protocols. Nevertheless, we sought to make a reasonable choice of parameters among those found in the literature. If there may be much uncertainty about the numerical values that we obtained from simulations, the qualitative results are robust despite the inaccuracy of the parameters estimations.

Finally, there is a major uncertainty about parameter γ at the present time. The average duration after which immunity is lost is $1/\gamma$. Values between 60 and 365 were used in [36]. As of today, immunity is assumed to last at the very least 200 days, so we considered several possible values of $1/\gamma$ larger than 200.

Figure 3 compares several dynamics in the total absence of protective measures for a country population of 50,000,000 individuals for different values of γ. In the absence of NPI ($v = 0$), the dynamics follow those of a classical SEIRS model, tending toward the endemic equilibrium with decreasing oscillations. Note that they differ from those of a classical SEIR model without reinfection ($\gamma = 0$, red dashed line curve). In the latter, the epidemic eventually vanishes after one wave of infection. In addition, note that there is very little difference between the first peaks for the different values of γ.

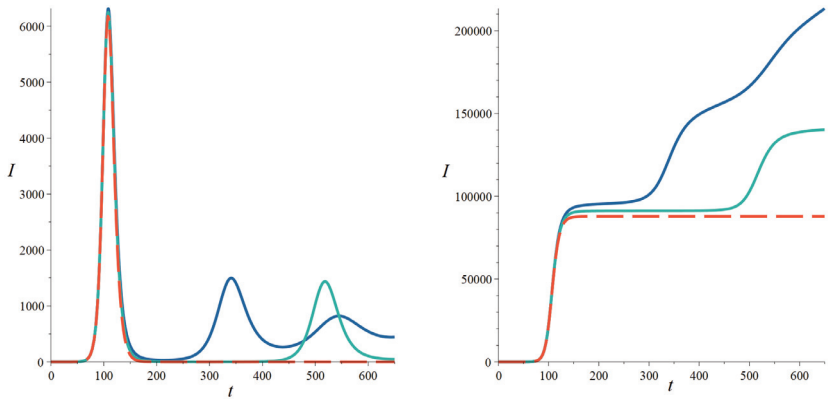

(**a**) Active cases

(**b**) Cumulative cases (including reinfections)

Figure 3. Evolution of the epidemic in the absence of NPI $v = 0$ for $1/\gamma = 200$ (blue), 400 (green) and compared to a model without reinfection ($\gamma = 0$, red dashed curve). (**a**) Active cases per 100,000 (**b**) and cumulative cases per 100,000. The initial conditions are $(S(0) = N - 1, E(0) = 0, I(0) = 1)$. Parameters values are $\beta = 1.2$, $k = 0.27$, $\alpha = 0.67$ and $N = 50{,}000{,}000$.

It is known that, in the absence of any protective measure against the epidemic, a large proportion of the population is infected after the first peak in a proportion ranging from 0.8 to almost the entire population depending on the value of $\mathcal{R}_0$ [28,32,57]. The aim of this work was precisely to show that, by using adequate protective measures, it is possible to greatly limit the level of infection and even to cause the disappearance of the epidemic in a relatively short time.

Figure 3 shows that considering different values for γ leads to the same qualitative dynamics. Despite the large range for γ, the amplitude of the first peak is similar, whereas the second one is shifted in time but has a similar amplitude (Figure 3a). Reinfection naturally causes an infinite growth of the cumulative cases (Figure 3b) that occurs in stages.

The number of active cases I per 100,000 at the equilibrium decreases with $1/\gamma$. However, Figure 3a illustrates that, if no control measures are taken, it remains high for a large range of values. Whatever the value of parameter γ, the first epidemic peak is very high and it is essential to take protective measures to limit the number of cases and even to stop the epidemic quickly.

4. Possible Strategies against an Epidemic with Reinfection

We now present several possible strategies to fight the epidemic when it starts. Based on the mathematical analysis of the general SEIRS model, we considered three main classes of epidemic NPI strategies: a first one consisting of a constant control, a second one stabilizing the epidemic at a sufficiently low target endemic level and a third one aiming at the eradication of the epidemic. In order to compare the various strategies, all simulations in this section used the same set of epidemiological parameters: $\beta = 1.2$, $k = 0.2$, $\alpha = 0.5$ and $\gamma = 1/200$ for a fictional disease and a fictional country with $N = 50{,}000{,}000$ inhabitants. All indicators (I, cumulative cases) are presented for 100,000 individuals to be consistent with indicators found in the literature.

4.1. Strategy 1: Constant Control

We compared some constant control strategies with different intensities v_0, shown in Figure 4. The $\hat{v}(I)$ function is represented in red as in all the following figures.

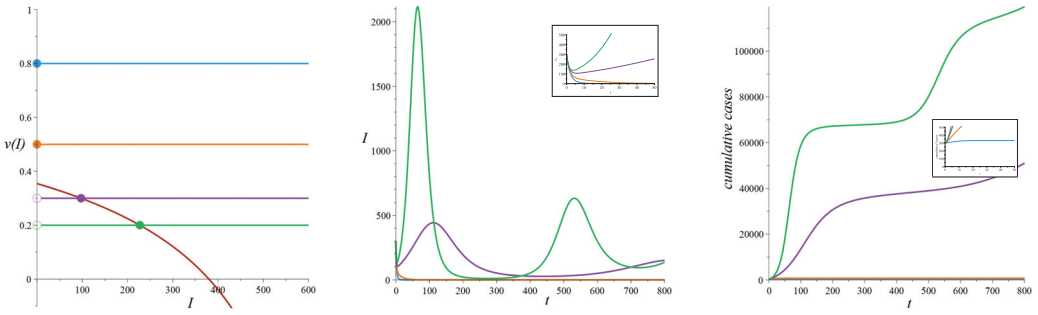

(**a**) Functions v and $\hat{v}$ (**b**) Number of active cases (I) (**c**) Cumulative cases

Figure 4. Comparison of constant control strategies: $v = 0.8$ (blue), $v = 0.5$ (orange), $v = 0.3$ (purple), $v = 0.2$ (green). Parameters values are $\beta = 1.2$, $k = 0.2$, $\alpha = 0.5$ and $\gamma = 1/200$, $N = 50{,}000{,}000$. The initial condition is I(0) = 300 per 100,000. (**a**) Comparison of functions v and $\hat{v}$ (red curve) with stable (solid circles) and unstable (empty circles) equilibria. (**b**) Evolution of the number of active cases I. An insert shows the details of the region $0 < t < 50$. (**c**) Evolution of the number of cumulative cases.

Each intersection with a constant v function defines an endemic equilibrium, which is the case of the purple and green function. Two outcomes are possible. If v_0 is high enough, the epidemic goes extinct (Figure 4b) since the DFE is stable and there is no endemic equilibrium ($v = 0.8$: blue and $v = 0.5$: orange, Figure 4a). The number of active cases per 100,000 falls below 1 in around 80 days for $v = 0.5$ and around 20 days for $v = 0.8$. If v_0 is low, the system tends toward a stable endemic equilibrium since the DFE is unstable ($v = 0.3$: purple and $v = 0.2$: green). In the latter case, the number of active cases I shows

oscillations and stabilizes around the endemic equilibrium. Peaks appear corresponding to different waves of infection. As v_0 increases, the value I^* at the equilibrium gets lower and peaks get lower and more distant in time. The number of cumulative cases keeps increasing as people get reinfected, and its value eventually become larger than the total population.

4.2. Strategy 2: NPI Intensity Increasing with the Number of Cases

This is the most natural strategy since the intensity of measures usually increases with the level of epidemics. Many governments choose to have a light level of social distancing at a low level of incidence and more effective measures at higher levels.

The dynamics present an unstable DFE and a unique endemic equilibrium. To illustrate this, we chose a family of increasing monotonic maps $v(I)$ $v : I \mapsto v_0 I/(I+100)$ for different values of $v_0 = 0.8, 0.5$ and 0.3 (see Figure 5). The intersection with the curve $\hat{v}$ defines a unique endemic equilibrium I^* that is locally asymptotically stable. The value of I^* decreases with v_0: I^* is around 220, 128 and 67 for $v_0 = 0.3, 0.5$ and 0.8, respectively. High values of v_0 lead to a rapid decrease in the epidemic, whereas a low value (purple curve) still allows for large amplitude peaks that may not be manageable by hospitals.

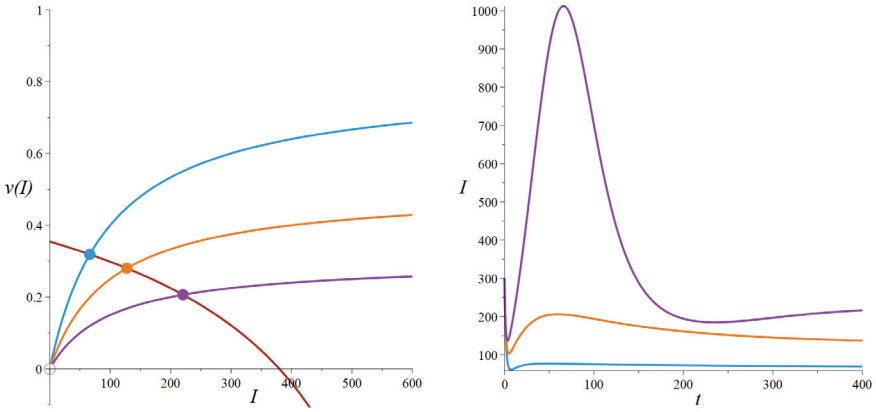

(**a**) Functions v and $\hat{v}$ (**b**) Number of active cases (I)

Figure 5. Comparison of strategies lowering the endemic equilibrium. Chosen functions are $v : I \mapsto v_0 I/(I+100)$, with $v_0 = 0.8$ (blue), $v_0 = 0.5$ (orange) and $v_0 = 0.3$ (purple). Parameters values are $\beta = 1.2$, $k = 0.2$, $\alpha = 0.5$ and $\gamma = 1/200$. The initial condition is I(0) = 300 per 100,000 individuals. (**a**) Comparison of functions v and $\hat{v}$ (red curve) with stable endemic equilibria (solid circles) and an unstable DFE (empty circle). (**b**) Evolution of the number of active cases I per 100,000 individuals.

Since the number of cases decreases with the target endemic level, this strategy may become useful for keeping the epidemic low enough to prevent hospital congestion with a lower level of active cases. Unfortunately, it is not possible to reach the extinction of the epidemic.

4.3. Strategy 3: Seek to Extinguish the Epidemic

A necessary condition to end the epidemic is to have a stable DFE, which requires that $v(0) > \hat{v}(0)$. This requires a high NPI intensity at a low level of cases I, contrary to strategy 2. This can be achieved by using any function $v > \hat{v}$, such as a sufficiently high constant control, as shown previously. A key element in our work is that, since $\hat{v}$ is decreasing, it is much more important to keep v at high levels when I is low than when I is high. Indeed, the extinction of the epidemic can be achieved with a decreasing function, with a low-intensity NPI when I is high and a high-intensity NPI when I is low.

Figure 6 depicts the case of a decreasing control function v (purple curve). Two other control functions (orange and blue) are represented in order to see what would happen if the parameters were misevaluated. More specifically, we chose the following family of piecewise linear maps:

$$v : I \mapsto \begin{cases} v_0\left(1 - \frac{I}{I_{max}}\right) & \text{if } 0 \leq I < I_{max}, \\ 0 & \text{if } I_{max} \leq I. \end{cases} \tag{17}$$

with $v_0 = 0.8$ and $I_{max} = 200$ (blue), 50 (orange) and 500 (purple) (see Figure 6a).

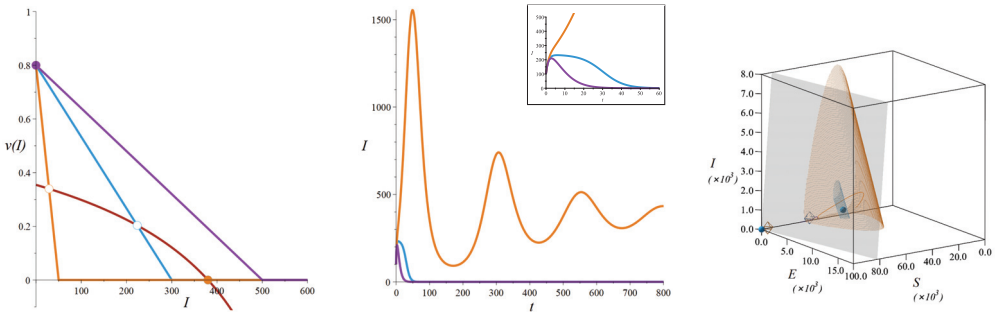

(**a**) Functions v and $\hat{v}$ (**b**) Number of active cases (I) (**c**) Phase portrait

Figure 6. Comparison of control strategies that create an Allee effect. Chosen functions are piecewise linear maps, decreasing from 0.8 to 0 from $I = 0$ to $I = I_{max}$ and equal to 0 elsewhere, with $I_{max} = 300$ (blue), $I_{max} = 50$ (orange) and $I_{max} = 500$ (purple). Parameters values are $\beta = 1.2$, $k = 0.2$, $\alpha = 0.5$ and $\gamma = 1/200$ for a population of 50,000,000 individuals. The initial conditions are $S_0 = 60{,}000$, $E_0 = 800$, $I_0 = 100$ for 100,000 individuals. (**a**) Comparison of functions v and $\hat{v}$ (red curve) with a stable (solid circle) DFE and unstable (empty circles) endemic equilibria. (**b**) Evolution of the number of active cases I. The early dynamics are depicted in insert. (**c**) Phase portrait. Stable equilibria are represented by a solid sphere, and unstable equilibria by a diamond, in colors corresponding to their respective maps v. Surfaces indicate the basin of attractions of the stable endemic equilibrium, the colors corresponding to their respective maps. The gray plane delimits the volume of possible initial conditions ($S + E + I + R \leq N$).

The purple map drives the epidemic to extinction (Figure 6b). Blue and orange maps create a lower unstable endemic equilibrium and a stable endemic equilibrium, generating an "Allee" effect: the lower the incidence, the more difficult it is for the disease can spread. Depending on the initial conditions, the epidemic may disappear or tend toward the high endemic equilibrium. The basins of attraction of the endemic equilibria for the different measures are represented in their respective colors in Figure 6c. Stronger measures lead to a smaller basin of attraction for the endemic equilibrium.

Such a strategy may be less natural since it means higher-intensity measures when I is low than when I is high. However, the intensity is still lower than in strategy 1, and it can provoke the extinction of the epidemic, which cannot be achieved with strategy 2. Furthermore, the extinction of the epidemic occurs in a relatively short time compared to the measures taken by most governments that vary in intensity and have been spread over more than a year.

5. Case of the COVID-19 Pandemic: Estimation of NPI Intensities and Identification of the Strategies Chosen by Several Countries

We estimated the time evolution of NPI intensities $\nu(t)$ for several countries in order to find a match with one of the previous strategies discussed in the previous section. For that purpose, we used incidence (and equivalently the total number of new cases) and hospital admission (if available) data collected from John Hopkins University's Github repository (https://github.com/CSSEGISandData/COVID-19/blob/master/csse_COVID_19_data/csse_COVID_19_time_series/, accessed on 1 March 2023) and Our World in Data (https://ourworldindata.org/COVID-vaccinations, accessed on 1 March 2023).

We simulated the evolution of the incidence using the SEIRS model defined in Section 2 with a time-varying NPI intensity $\nu(t)$. We assumed that, for each country, all parameters except $\nu(t)$ remain constant for the total duration of the simulation. For that reason, we used data time series from February 2020 to no later than October 2021 in order to avoid

the effects of new variants such as *delta* and *omicron* that would make the assumption of a constant β highly irrelevant.

Accordingly to Section 3.2, parameters $\alpha = 0.67, k = 0.26, \gamma = 1/200$ were fixed and estimated based on medical and statistical studies. The country population was extracted from the previous sources, and parameters β and $\nu(t)$ were fitted. Assuming that no NPI has been set up during the initial exponential phase $\nu(t) = 0$, we extracted incidence data between the date with the first reported case and the end of this exponential phase (we assumed that it ends at the first inflection point, which occurs slightly before the peak maximum). We then estimated the last remaining parameter β by fitting the incidence curve obtained from simulations with initial condition $S(0) = N, E(0) = 0, I(0) = 1, R(0) = 0$, with the daily incidence rate provided by data from the previous sources. Using the least square method, we fitted two parameters β and the fictional start date t_0 (theoretical date at which $I(t_0) = 1$).

We then assumed that, after this initial exponential phase, the infection rate β remains constant, but, since NPIs have been set up, $\nu(t)$ now evolves with time. For the sake of simplicity, we considered that the NPI intensity $\nu(t)$ is the same for all the days of a same week. We fitted $\nu(t)$ with the least square method since the number of values of $\nu(t)$ is still large (1 per week), and we used a hill climbing algorithm in order to find the best fit. Finally, we smoothed the results by taking the mean over 7 days.

We then intended to identify the strategies used by comparing the values of ν with the incidence and tried to exhibit a tendency. Since the incidence may be underestimated during the first wave of the epidemic, we also compared ν to the number of admissions in hospitals (when data are available), which is supposed to be a scaled and slightly shifted version of the real incidence curve. It then may provide a more reliable estimation of the real incidence rate up to a multiplicative constant. Moreover, NPIs were often set in order to avoid hospitals and ICUs saturation, which also makes this indicator more relevant than the observed incidence. Figure 7 shows the results obtained for the United Kingdom, France, Germany and New York City. This figure shows the time evolution of new cases, hospitalizations and $\nu(t)$, as well as the phase portraits ν vs. *new cases* and ν vs. *hospitalizations*. Results for a few other countries are shown in Appendix C, Figure A2. Note that we replaced the incidence rate by the number of new cases, which is just a scaled version that is of the same order as the hospitalization number, which makes the figure easier to read.

It appears that the NPI intensity is not highly linearly correlated to new cases or hospitalization, apart from France ($R^2 = 0.40$), which could be associated to strategy 2. For other countries, the value of ν appears to be relatively constant or slightly increasing with the new cases or hospitalizations; hence, they can be associated to strategy 1 or 2. An increase in the NPI intensity around the incidence peaks on the time series confirms that the chosen strategy is more likely to be strategy 2. Other countries shown in the appendix exhibit a constant or slightly increasing tendency, except for Russia, which exhibits a slightly decreasing tendency, which can be considered as constant. For the United Kingdom, ν seems to slightly decrease with the number of cases, but is constant with hospitalizations, which certainly illustrates that hospitalization works better than the measured incidence rate. All those examples illustrate that strategies 1 and 2 appear to be more natural than strategy 3, and thus are chosen by most countries.

We compared those strategies with the ones chosen by two countries that allegedly maintained a very low incidence: New Zealand and Vietnam. New Zealand adopted an elimination strategy in response to COVID-19 ("keep it out, prepare for it, stamp it out") after an initial lockdown from 25 March 2020,which was progressively lifted after 28 April 2020. It included a strong border control of the island, contact tracing and strong public measures. As a continental country, Vietnam imposed a strict border control with a long quarantine for travelers, as well as very localized and strong lockdowns. Both countries experienced a very low incidence level and maintained relatively normal activity at the moment when other countries were struck by incidence peaks (winter 2020–2021).

Incidence and NPI intensity are shown for both countries in Figure 8 (no hospitalization data were available from the previous sources).

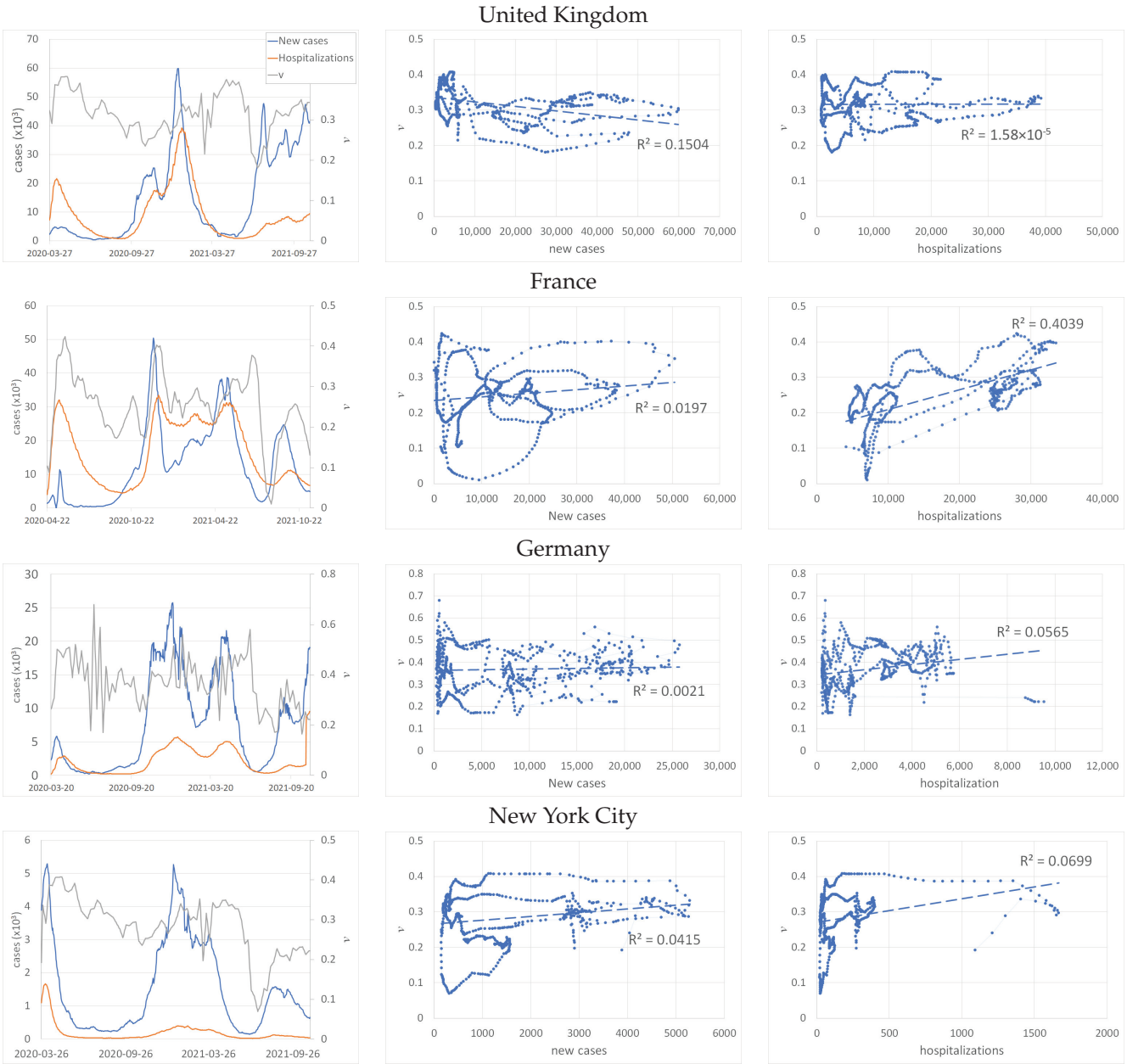

Figure 7. Epidemiological dynamics and NPI strategies for UK, France, Germany and New York City. **Left**: time evolution of the number of new cases, admission to hospitals and NPI intensity ν. **Middle**: phase portrait of NPI intensity ν vs. new cases. **Right**: phase portrait of NPI intensity ν vs. hospitalizations. For each point cloud, linear regression was performed in order to see if a linear relationship could be exhibited.

The NPI intensity seems to be constant or decreasing with the incidence rate, with the highest values reached at very low incidence rates. Incidence peaks do not seem to be associated with stronger measures but are more constant in intensity. For those reasons, our estimation of NPI intensity for those countries seem to be consistent with strategy 3.

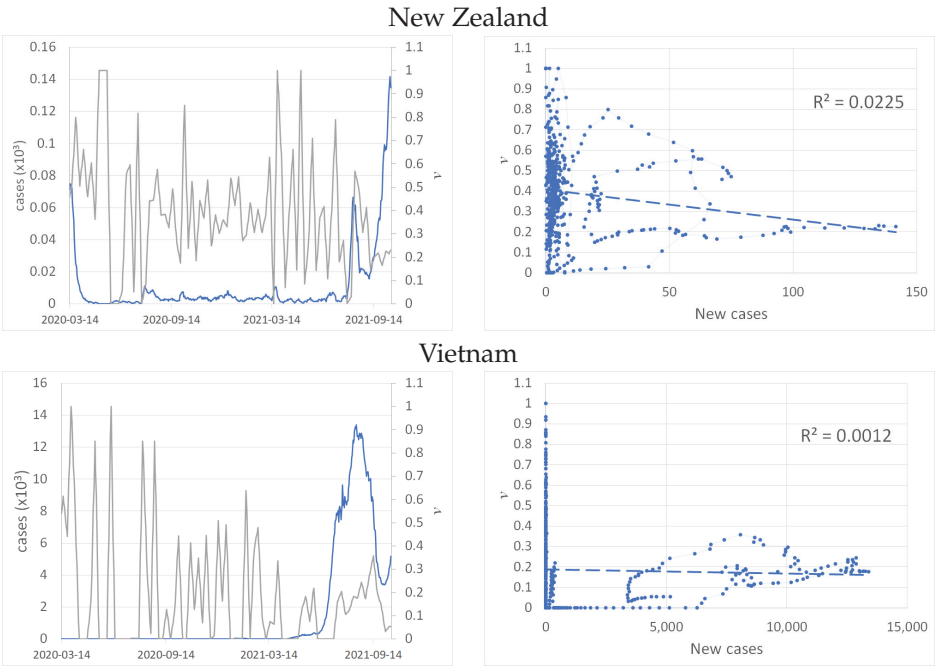

Figure 8. Epidemiological dynamics and NPI strategies for New Zealand and Vietnam. **Left**: time evolution of the number of new cases (blue) and NPI intensity (grey) ν. **Right**: phase portrait of NPI intensity ν vs. new cases and linear regression.

6. Comparison and Discussion of the Effects of Various NPI Strategies on the Dynamics of the Epidemic

We have shown that we can control an epidemic when it starts by imposing a level of NPI that depends on the number of infected persons each day. In the absence of protective measures, a peak of infected cases reaches over 6000 cases per 100,000 and lasts for around 150 days. We now compare the different strategies used to control the epidemic: strategies 1 (blue), 2 (green) and 3 (purple and orange); see Figure 9a. All strategies have the same maximum intensity $v_0 = 0.6$. Blue and purple always cause the epidemic to end since the only equilibrium is the DFE. The green strategy leads to a low endemic equilibrium. The orange strategy leads either to an endemic equilibrium or to the extinction of the epidemic depending on the initial condition (Figure 9b).

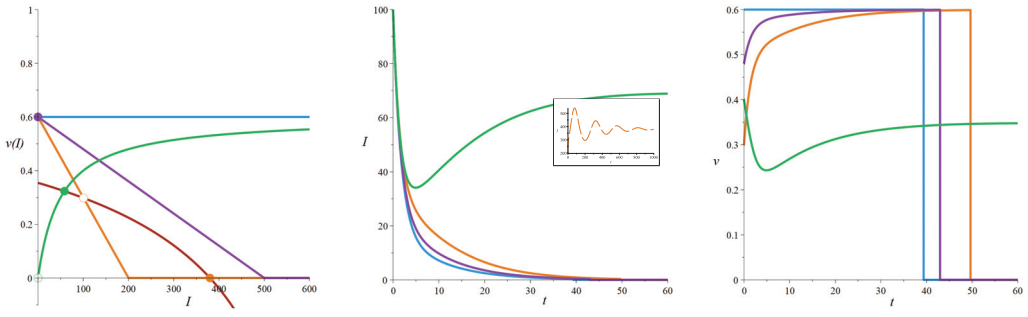

(**a**) Functions v and $\hat{v}$ (**b**) Number of active cases (I) (**c**) NPI intensity v

Figure 9. Comparison of the different NPI strategies: constant control (blue), decreasing function (purple and orange) and lower endemic equilibrium (green). Parameters values are $\beta = 1.2$, $k = 0.2$, $\alpha = 0.5$ and $\gamma = 1/200$ for a population of 50,000,000 individuals. The initial conditions are $I(0) = 100$ per 100,000. (**a**) Comparison of functions v and $\hat{v}$ (red curve) with stable (solid circles) and unstable (empty circles) equilibria. (**b**) Evolution of the number of active cases I. Insert: an additional dynamic for the initial condition $S(0) = 45{,}000, E(0) = 200, I(0) = 800$ for the orange strategy. (**c**) NPI intensity $v(t)$.

The benefit of the orange strategy over the purple one is its lower intensity. This comes along with the risk of the dynamics ending trapped at the endemic equilibrium if the initial condition is unfavorable, i.e., when NPIs are set up too late (insert of Figure 9b).

We set a threshold (here, less than 1 case per 100,000) under which we consider that the epidemic has gone extinct. When the number of cases falls under this threshold, we assume that it is not necessary to maintain any NPI. The duration and the time evolution of NPI intensity is represented in Figure 9c. The green strategy keeps the epidemic at a low level; it requires a moderately intense but never-ending NPI. Strategy 1 (blue, constant $v = 0.6$) is the most effective and has the shortest total NPI duration but may be difficult to implement from the start. It drives the epidemic to extinction in 39 days. It should be noticed that 0.6 already represents a high-intensity NPI, such as a lockdown, that may be difficult to set up in practice or that at least requires some time to be achieved. For the same initial condition, NPIs for purple and orange strategies last 43 and 49 days, respectively. They have the advantage of proposing NPIs with a gradually increasing intensity that reaches the maximum value at the end of the epidemic, which gives health authorities more time to set it up. Overall, their duration seems reasonable compared to the one of the blue strategy.

The analysis of the dynamics of the epidemic for those different strategies allows us to rank their effectiveness, intensity and duration, as shown in Table 2.

Table 2. Comparison of the effectiveness, intensity and duration for the different strategies, for the same maximum intensity.

	Strategy 1	**Strategy 2**	**Strategy 3**
Effectiveness	high	low	high
Intensity	highest	medium	high
Duration	short	very long	short

The effectiveness is clearly higher in strategies 1 and 3 than in 2 since the latter is unable to prevent the endemic equilibrium and put an end to the epidemic by itself. Type 2 strategies do not seem desirable to us because they lead to a permanent endemic state with lasting NPI measures, even if they may allow for limiting the magnitude of an epidemic peak in order to prevent ICU saturation. Strategy 3 combines the advantages of efficiency, a shorter duration and a lower intensity than strategy 1. Based on those findings, it seems more profitable to seek to get rid of the epidemic using a purple or orange strategy (strategy 3). However, it may seem counter-intuitive in the sense that it is necessary to strengthen the NPI intensity as the number of infected persons decreases in order to achieve the eradication of the epidemic in some time frame.

Those strategies have different outcomes in terms of social and economic costs. Strategies 1 and 3 have a short duration but a high intensity, contrary to strategy 2, which has a very long duration and a moderate intensity. NPIs are known to induce much stress and anxiety and, more generally, a decline in mental health [58,59]. We do not discuss this matter here, but there is a need to carefully consider a possible trade-off between the duration and intensity of NPIs.

As shown in the previous section, most countries have adopted strategy 1 (blue) or 2 (green) instead, except for New Zealand and Vietnam. When the health situation worsens, the level of measures is reinforced for some weeks in order to return to a lower level of virus circulation, resulting in successive epidemic waves. In France, three lockdowns have been established. For each lockdown, its intensity has been reduced when the epidemic peak has diminished sufficiently so as not to saturate the hospitals but without maintaining it long enough at a high level to bring about the eradication of the epidemic. These successive confinements have generated astronomical infections and economic costs. Epidemic waves seem to endlessly follow each other unless a vaccination policy can achieve collective immunity. On the contrary, New Zealand and Vietnam maintained a low incidence level and seem to have suffered a lower social and economic cost, except for tourism.

To summarize, our results indicate that lockdowns should be strengthened and absolutely not released when the incidence drops until the epidemic actually ends. Carrying out the contrary leads to a new increase in the number of cases toward an endemic equilibrium.

In our opinion, these epidemic control methods could be used locally for medium-sized cities that can be isolated for a period of at least one to two months by prohibiting or very strictly controlling the entry and exit of people from this city. The application of these classes of strategies would require the use of a significant number of tests allowing for a good estimation of the numbers of infected people at the time when the control must be implemented. It requires properly positioning the various endemic equilibria created by the epidemic control function. In the context of COVID-19, our work suggests that strong, short and early measures are more effective than mild but long-lasting ones. We think that these results may be of interest since some countries such as Israel expect to live permanently with the disease.

7. Conclusions

In this work, we studied an SEIRS epidemic model with reinfection and illustrated the results with an application to the COVID-19 pandemic. We analyzed the effects of several kinds of infection-dependent NPIs on the dynamics of the epidemic and on the characteristics (existence and stability) of disease-free and endemic equilibria. We showed that NPI strategies could be divided into three main classes and highlighted their benefits and drawbacks, such as their ability to put an end to the epidemic, the amplitude and duration of the peaks and the feasibility of the considered measures. We found that constant NPI strategies are effective for extinguishing the epidemic but may be too intense to be practically usable. Strategies with NPI intensity decreasing with the number of cases I may also put an end to the epidemic by creating an Allee effect while being easier to set up. However, they can lead to a large epidemic peak or a (lower) endemic equilibrium instead of extinction if they are not set up carefully. Finally, the most intuitive strategy (NPI intensity increasing with the number of cases) proved to be the least efficient while being unable to put an end to the epidemic.

The key element of our study is that, in the context of the spread of a disease with a loss of immunity, Allee effects do not exist naturally, contrary to what is observed in population ecology. However, while this phenomenon is not desirable in the latter, it appears to be mandatory to end an epidemic, and has to be artificially created using NPIs. In terms of public health, creating an Allee effect would imply setting up early measures with more intensity. Strategies such as type 3 can bring about the extinction of the epidemic and could have important implications for public health policy. They are already in use for animal epidemics: in the case of diseases spreading in farms animals, the decision is often to kill all the animals in a same location. Such policies prevent the disease from spreading at a larger scale but are highly controversial. The situation seems more delicate in the case of human epidemics because even softer policies such as travel restrictions and confinement measures are difficult to impose. However, a more systematic and efficient screening, better information and very localized and short lockdowns may prevent major outbreaks. Many countries decided to use strategies 1 or 2 against COVID-19, as we showed in Section 5, and failed to create an Allee effect. They have been reluctant to set high-intensity NPIs at low virus circulation levels or during the early stages of the pandemic because carrying this out may have been greatly unpopular and a major restriction of liberties, but possibly also because of the financial cost. However, our work suggests that spending money for early prevention, information and screening may reduce the final cost. Even if our results may be considered with care due to the many assumptions that we made in our model, we think that we have provided a good illustration that (1) delaying the response to a problem eventually results in a highest social and economical cost, and (2) people are nevertheless inclined to use that kind of sub-efficient strategy. We believe that such a conclusion holds for other major problems that we are facing nowadays, particularly for the ones related to climate change. We illustrated our model with the case of COVID-19.

However, further investigations on other epidemics would be necessary to identify what strategies are commonly used and to confirm if strategy 3 is the most efficient.

As a perspective, we could study a network of several cities connected by the movement of individuals from one city to another by rail or by plane. It would be interesting to study the coupling of epidemic management methods depending on the number of infected people in the different cities. We refer to [60,61] for disease spread in meta-populations.

In the future, we plan to reconsider our model by considering two compartments for asymptomatic (A) and infectious (I) carriers in a future SEAIRS version. We also plan to improve the realism of the model by explicitly including other factors, such as vaccination, health infrastructures and a more detailed description of social behaviors. We also plan to provide a more detailed study on the economic and social costs of NPIs. However, we hope and are inclined to think that our conclusions obtained through a theoretical approach on the effectiveness of the various strategies can be useful for practical case studies, as density-dependent protection strategies could be used to target a sufficiently low level of endemicity or find a strategy to put an end to the epidemic while considering constraints such as social cost or hospitals capacity.

Author Contributions: Conceptualization, T.N.-H., P.A. and A.M.; methodology, T.N.-H., P.A. and A.M.; software, T.N.-H. and A.M.; formal analysis, T.N.-H., P.A. and A.M.; writing—original draft preparation, T.N.-H. and P.A. All authors have read and agreed to the published version of the manuscript.

Funding: This research received no external funding.

Institutional Review Board Statement: Not applicable.

Informed Consent Statement: Not applicable.

Data Availability Statement: Data sharing not applicable

Conflicts of Interest: The authors declare no conflict of interest.

Abbreviation

The following abbreviation is used in this manuscript:

NPIs Non-Pharmaceutical Interventions

Appendix A. Mathematical Properties of the Model

The demonstrations for the mathematical properties (positivity, boundedness, existence and uniqueness of the solutions) of model (1) are classical. We present here brief demonstrations.

Proposition A1. *The non-negative region $\mathbb{R}^4_+$ is positively invariant for model (1).*

Proof. We consider a solution with an initial condition in $\mathbb{R}^4_+$. Let us assume that $t_m = \sup\{t > 0 : S(t) > 0, E(t) > 0, I(t) > 0, R(t) > 0\}$ exists. Thus, $t_m > 0$, and the inequality $dS/dt \geq -\beta SI/N$ holds on $[0, t_m]$. After using the separation of variables methods and integration, we obtain $S(t_m) \geq S(0)exp\Big(-\beta \int_0^{t_m} I(u)du\Big)$>0. Similarly, we can show that $E(t_m) > 0, I(t_m) > 0$ and $R(t_m) > 0$, which completes the proof. □

Proposition A2. *Solutions of model (1) are bounded.*

Proof. By summing the equations in system (1), we find that $dN/dt = 0$. The total population $N = S + E + I + R$ is constant, which implies that $0 \leq S \leq N$, $0 \leq E \leq N$, $0 \leq I \leq N$ and $0 \leq R \leq N$. This completes the proof. □

Proposition A3. *The initial value problem for model (1) with an initial condition in $\mathbb{R}^4_+$ has a unique maximal solution.*

Proof. The proofs consists of showing that system (1) fulfills the conditions of the Picard–Lindelöf theorem, i.e., that if we rewrite the system as $dX/dt = f(X)$, with $X = (S, E, I, R)$, then f is Lipschitz continuous. This is straightforward, except for the term $g(X) = \beta(1 - v(I))^2 SI/N$. Let us consider the continuous non-negative bounded map $h(I) = \beta(1 - v(I))^2/N$. For two states $X_1 = (S_1, E_1, I_1, R_1)$ and $X_2 = (S_2, E_2, I_2, R_2)$, we have:

$$\begin{aligned} |g(X_2) - g(X_1)| &= |h(I_2)S_2I_2 - h(I_1)S_1I_1| \\ &\leq |h(I_2)S_2I_2 - h(I_1)S_2I_1| + |h(I_1)S_2I_1 - h(I_1)S_1I_1| \\ &\leq S_2|h(I_2)I_2 - h(I_1)I_1| + I_1h(I_1)|S_2 - S_1|, \\ &\leq N|h(I_2)I_2 - h(I_1)I_1| + Nh(I_1)|S_2 - S_1| \\ &\leq N\sup(h)|I_2 - I_1| + Nh(I_1)|S_2 - S_1|, \end{aligned} \tag{A1}$$

$$\begin{aligned} |g(X_2) - g(X_1)| &= |h(I_2)S_2I_2 - h(I_1)S_1I_1| \\ &\leq |h(I_2)S_2I_2 - h(I_2)S_2I_1| + |h(I_2)S_2I_1 - h(I_1)S_2I_1| \\ &\quad + |h(I_1)S_2I_1 - h(I_1)S_1I_1| \\ &\leq h(I_2)S_2|I_2 - I_1| + S_2I_1|h(I_2) - h(I_1)| + I_1h(I_1)|S_2 - S_1| \\ &\leq N\sup(h)|I_2 - I_1| + N^2|h(I_2) - h(I_1)| + N\sup(h)|S_2 - S_1|. \end{aligned} \tag{A2}$$

Map g is then Lipschitz continuous, which completes the proof. □

Appendix B. More Details on the Infection Rate Formula

Deriving an infection model from classic ones such as SIR models may be more complicated than it seems, and the choice of the terms in the equations may be difficult to understand. For that reason, we intend to justify in this appendix the infection rate that we used in our model when isolating a proportion v of the population:

$$\beta(1 - v)^2 \frac{SI}{N}. \tag{A3}$$

Indeed, the term $(1 - v)^2$ may be difficult to understand, and we think it deserves a more detailed explanation. We also provide a numerical illustration of our results by simulating contacts in a population with and without NPIs.

Appendix B.1. Detailed Calculation of the Infection Rate Formula

In the original infection model without NPI, the number of secondary infections per unit of time due to one infected individual is $\beta \frac{S}{N}$ or, more precisely,

$$pc\frac{S}{N}, \tag{A4}$$

where c is the average number of contacts that individuals have per unit of time, p is the probability of infection for each contact and S/N is the proportion of susceptible individuals in the population. Note that, in the classical SIR model, neither the number of the removed individuals R nor their status (isolated or simply immune to the disease) appear in the transmission formula. We remind the main idea behind this formula: an infected individual encounters c others per unit of time. Since only a proportion S/N are susceptible, this makes cS/N potential new cases, and, for each case, infection may occur with a probability p. On average, an infected individual infects pcS/N per unit of time. When summing over all infected individuals, there are, on average, $\beta\frac{SI}{N}$ new cases per unit of time in the population.

Now, let us assume that a proportion v of individuals are isolated regardless of their status (for example, some NPIs may order that non-essential workers stay at home). The proportion of susceptible individuals in the non-isolated population remains unchanged since

$$\frac{(1 - v)S}{(1 - v)N} = \frac{S}{N}, \tag{A5}$$

as well as the probability of infection p. However, the number of contacts is reduced due to isolation since only a proportion $1 - v$ is not isolated. Indeed, since isolated individuals are assumed to be randomly chosen, an average proportion v of one's contact would be isolated. The average number of contacts then drops to $(1 - v)c$. The number of secondary cases due to one infected individual is then

$$p(1 - v)c\frac{S}{N} = (1 - v)\beta\frac{S}{N}, \tag{A6}$$

Finally, the total number of new cases per unit of time is obtained by summing the new cases for each of the $(1 - v)I$ non-isolated infected individuals, and reads

$$(1 - v)^2\beta\frac{SI}{N}. \tag{A7}$$

Note again that even if another isolation status were to be considered, (quarantined, etc.), the formula would be the same according to the reasoning related to Formula (A5).

Appendix B.2. Simulation of Infectious Contacts

In order to provide some numerical support, we designed the following simulations: we considered N individuals with different infectious statuses and set a random graph of contacts between people, such as the average number of contacts per individuals being c. We then computed the number of infectious contacts (contacts between one non-isolated infected and one non-isolated susceptible individual) for different sets of possible statuses (susceptible, infectious, removed or even quarantined) with or without isolating a random fraction v of the individuals. We then compared the results with the estimates provided by the respective expressions (A3) and (A4). We reproduced the simulations with different sets of possible statuses: susceptible and infectious statuses were always considered, but we also introduced a removed class even if the formula does not explicitly refer to it, and a possible quarantined class, which consists of infectious individuals that have been isolated after having received knowledge of their disease. As removed individuals, they do not participate in the disease transmission process. However, removed individuals are considered as cured and immune but may be in contact with other individuals, whereas the quarantined ones are physically isolated from the population.

As illustrated in Figure A1, after isolation, the number of infectious contacts is reduced on average to a quantity $(1 - v)^2$ of the infectious contacts before isolation. As expected, explicitly representing the removed and quarantined does not affect the validity of the formula.

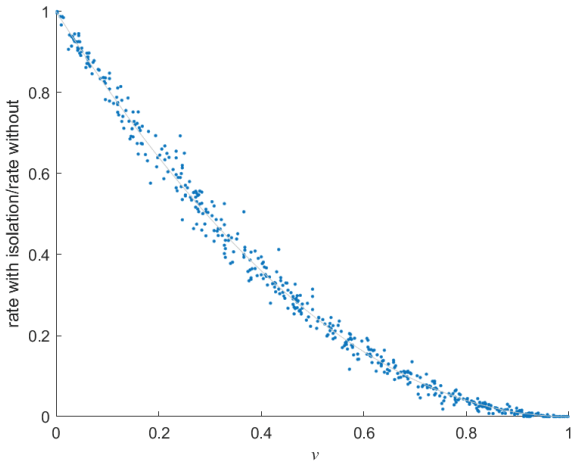

Figure A1. Reduction in the number of infectious contacts due to isolation (left). We performed 500 simulations with a total population of $N = 500$ individuals, which were randomly assigned a susceptible, infectious status (all simulations). For each simulation, we isolated a random proportion v of the population and reported the ratio between the infection rate with isolation and the infection rate without isolation. The point cloud that we obtained approximately fits the curve $(1 - v)^2$ (grey curve).

Appendix C. Illustration for Several Other Countries

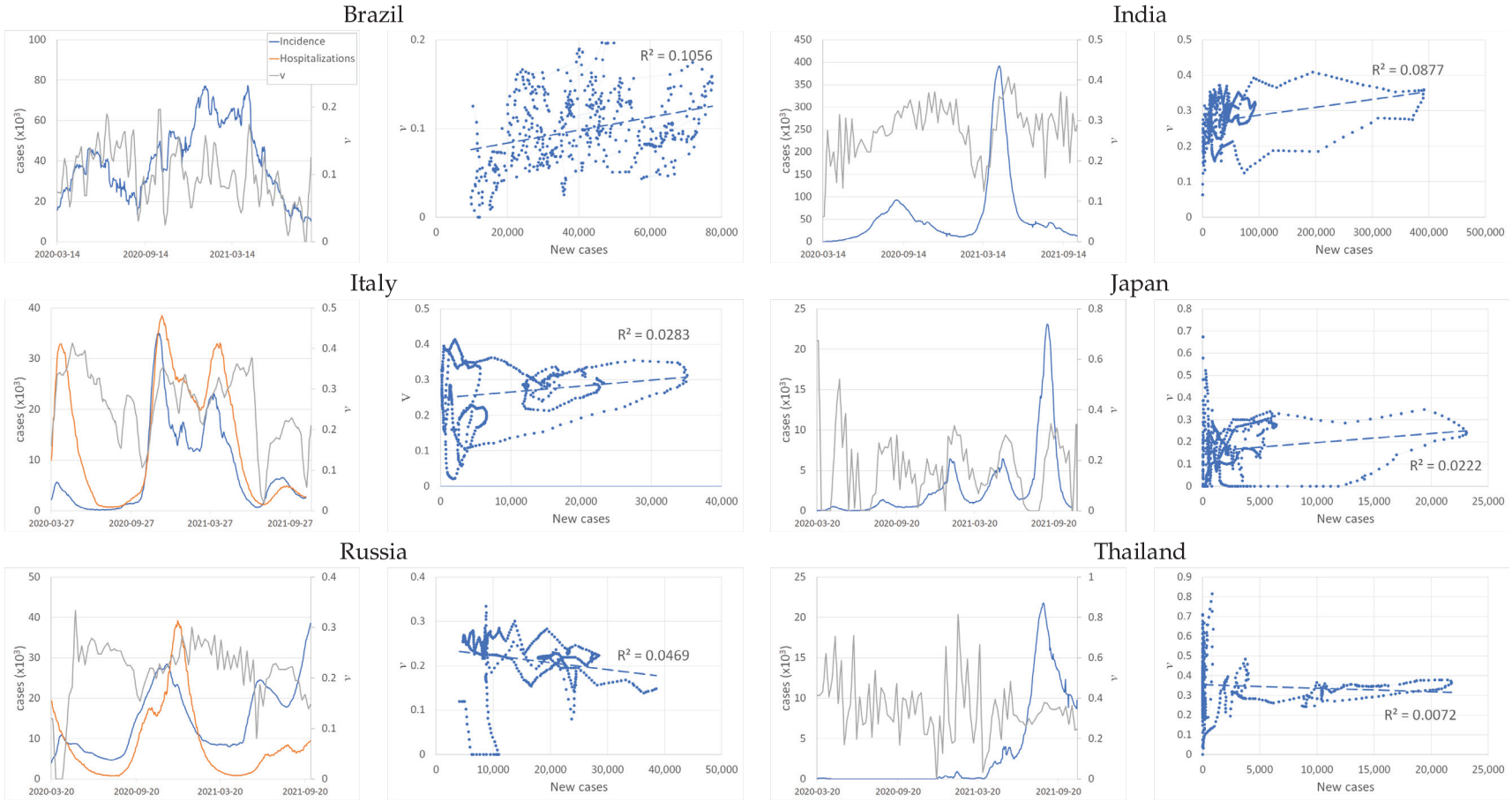

Figure A2. Epidemiological dynamics and NPI strategies for different countries. **Left**: time evolution of the number of new cases, admission to hospitals and NPI intensity ν. **Right**: phase portrait of NPI intensity ν vs. new cases. For the point cloud, linear regression was performed in order to see if a linear relationship could be exhibited.

The Matlab code for this program is available on the GitHub repository https://github.com/tnguyenh/M2AS---COVID-19/ (accessed on 1 June 2023).

References

1. Allee, W.C.; Bowen, E.S. Studies in animal aggregations: Mass protection against colloidal silver among goldfishes. *J. Exp. Zool.* **1932**, *61*, 185–207. [CrossRef]
2. Odum, E.P.; Barrett, G.W. *Fundamentals of Ecology*; Saunders Philadelphia: Philadelphia, PA, USA , 1971.
3. Courchamp, F.; Berec, L.; Gascoigne, J. *Allee Effects in Ecology and Conservation*; OUP Oxford: Singapore, 2008.
4. Holden, M.H.; McDonald-Madden, E. High prices for rare species can drive large populations extinct: The anthropogenic Allee effect revisited. *J. Theor. Biol.* **2017**, *429*, 170–180. [CrossRef] [PubMed]
5. Liu, Y.; Gu, Z.; Xia, S.; Shi, B.; Zhou, X.N.; Shi, Y.; Liu, J. What are the underlying transmission patterns of COVID-19 outbreak? An age-specific social contact characterization. *EClinicalMedicine* **2020**, *22*, 100354. [CrossRef]
6. Xia, S.; Liu, J.; Cheung, W. Identifying the relative priorities of subpopulations for containing infectious disease spread. *PLoS ONE* **2013**, *8*, e65271. [CrossRef] [PubMed]
7. Perkins, T.A.; Paz-Soldan, V.A.; Stoddard, S.T.; Morrison, A.C.; Forshey, B.M.; Long, K.C.; Halsey, E.S.; Kochel, T.J.; Elder, J.P.; Kitron, U.; et al. Calling in sick: Impacts of fever on intra-urban human mobility. *Proc. R. Soc. B Biol. Sci.* **2016**, *283*, 20160390. [CrossRef] [PubMed]
8. Auger, P.; Moussaoui, A. On the Threshold of Release of Confinement in an Epidemic SEIR Model Taking into Account the Protective Effect of Mask. *Bull. Math. Biol.* **2021**, *83*, 25 . [CrossRef] [PubMed]
9. Howard, J.; Huang, A.; Li, Z.; Tufekci, Z.; Zdimal, V.; van der Westhuizen, H.M.; von Delft, A.; Price, A.; Fridman, L.; Tang, L.H.; et al. An evidence review of face masks against COVID-19. *Proc. Natl. Acad. Sci. USA* **2021**, *118*, e2014564118. [CrossRef] [PubMed]
10. van den Driessche, P.; Watmough, J. Reproduction numbers and sub-threshold endemic equilibria for compartmental models of disease transmission. *Math. Biosci.* **2002**, *180*, 29–48. [CrossRef]
11. Fehlberg, E. Klassische Runge-Kutta-Formeln vierter und niedrigerer Ordnung mit Schrittweiten-Kontrolle und ihre Anwendung auf Wärmeleitungsprobleme. *Computing* **1970**, *6*, 61–71. [CrossRef]
12. Shokri, A.; Mehdizadeh Khalsaraei, M.; Molayi, M. Nonstandard Dynamically Consistent Numerical Methods for MSEIR Model. *J. Appl. Comput. Mech.* **2022**, *8*, 196–205. [CrossRef]
13. Khalsaraei, M.M.; Shokri, A.; Ramos, H.; Heydari, S. A positive and elementary stable nonstandard explicit scheme for a mathematical model of the influenza disease. *Math. Comput. Simul.* **2021**, *182*, 397–410. [CrossRef]
14. Kamrujjaman, M.; Mahmud, M.S.; Ahmed, S.; Qayum, M.O.; Alam, M.M.; Hassan, M.N.; Islam, M.R.; Nipa, K.F.; Bulut, U. SARS-CoV-2 and Rohingya Refugee Camp, Bangladesh: Uncertainty and How the Government Took Over the Situation. *Biology* **2021**, *10*, 124. [CrossRef] [PubMed]
15. Bauch, C.; d'Onofrio, A.; Manfredi, P. Behavioral Epidemiology of Infectious Diseases: An Overview. In *Modeling the Interplay between Human Behavior and the Spread of Infectious Diseases*; Springer Science & Business Media: Berlin/Heidelberg, Germany, 2012; pp. 1–19. [CrossRef]
16. Manfredi, P.; D'Onofrio, A. *Modeling the Interplay between Human Behavior and the Spread of Infectious Diseases*; Springer: New York, NY, USA, 2013. [CrossRef]
17. Feng, Z.; Cramm, J.M.; Nieboer, A.P. Associations of Social Cohesion and Socioeconomic Status with Health Behaviours among Middle-Aged and Older Chinese People. *Int. J. Environ. Res. Public Health* **2021**, *18*, 4894. [CrossRef]
18. Centers for Disease Control. 2021. Available online: https://www.cdc.gov/nhsn/covid19/report-patient-impact.html (accessed on 1 March 2023).
19. Trentini, F.; Marziano, V.; Guzzetta, G.; Tirani, M.; Cereda, D.; Poletti, P.; Piccarreta, R.; Barone, A.; Preziosi, G.; Arduini, F.; et al. Pressure on the Health-Care System and Intensive Care Utilization During the COVID-19 Outbreak in the Lombardy Region of Italy: A Retrospective Observational Study in 43,538 Hospitalized Patients. *Am. J. Epidemiol.* **2021**, *191*, 137–146. [CrossRef] [PubMed]
20. Antonini, C.; Calandrini, S.; Stracci, F.; Dario, C.; Bianconi, F. Mathematical Modeling and Robustness Analysis to Unravel COVID-19 Transmission Dynamics: The Italy Case. *Biology* **2020**, *9*, 394. [CrossRef]
21. Ota, M. Will we see protection or reinfection in COVID-19? *Nat. Rev. Immunol.* **2020**, *20*, 351. [CrossRef]
22. Stokel-Walker, C. What we know about COVID-19 reinfection so far. *BMJ* **2021**, *372*, n99. [CrossRef]
23. Ward, H.; Cooke, G.; Atchison, C.; Whitaker, M.; Elliott, J.; Moshe, M.; Brown, J.C.; Flower, B.; Daunt, A.; Ainslie, K.; et al. Declining prevalence of antibody positivity to SARS-CoV-2: A community study of 365,000 adults. *Lancet Reg. Health-Eur.* **2021**, *4*, 100098. [CrossRef]
24. Callaway, E. Fast-spreading COVID variant can elude immune responses. *Nature* **2021**, *589*, 500–501. [CrossRef]
25. Tillett, R.L.; Sevinsky, J.R.; Hartley, P.D.; Kerwin, H.; Crawford, N.; Gorzalski, A.; Laverdure, C.; Verma, S.C.; Rossetto, C.C.; Jackson, D.; et al. Genomic evidence for reinfection with SARS-CoV-2: A case study. *Lancet Infect. Dis.* **2021**, *21*, 52–58. [CrossRef]
26. Adam, D. MODELLING THE PANDEMIC The simulations driving the world's response to COVID-19. *Nature* **2020**, *580*, 316–318. [CrossRef] [PubMed]

27. Kissler, S.M.; Tedijanto, C.; Goldstein, E.; Grad, Y.H.; Lipsitch, M. Projecting the transmission dynamics of SARS-CoV-2 through the postpandemic period. *Science* **2020**, *368*, 860–868. [CrossRef] [PubMed]
28. Bacaër, N. Un modèle mathématique des débuts de l'épidémie de coronavirus en France. *Math. Model. Nat. Phenom.* **2020**, *15*, 29. [CrossRef]
29. Liu, Z.; Magal, P.; Seydi, O.; Webb, G. Understanding unreported cases in the COVID-19 epidemic outbreak in Wuhan, China, and the importance of major public health interventions. *Biology* **2020**, *9*, 50. [CrossRef]
30. Sun, H.; Qiu, Y.; Yan, H.; Huang, Y.; Zhu, Y.; Gu, J.; Chen, S.X. Tracking Reproductivity of COVID-19 Epidemic in China with Varying Coefficient SIR Model. *J. Data Sci.* **2022**, *18*, 455–472. [CrossRef]
31. Kuniya, T. Prediction of the epidemic peak of coronavirus disease in Japan, 2020. *J. Clin. Med.* **2020**, *9*, 789. [CrossRef]
32. Moussaoui, A.; Auger, P. Prediction of confinement effects on the number of COVID-19 outbreak in Algeria. *Math. Model. Nat. Phenom.* **2020**, *15*, 37. [CrossRef]
33. Moussaoui, A.; Zerga, E.H. Transmission dynamics of COVID-19 in Algeria: The impact of physical distancing and face masks. *Aims Public Health* **2020**, *7*, 816. [CrossRef]
34. Kucharski, A.J.; Klepac, P.; Conlan, A.J.; Kissler, S.M.; Tang, M.L.; Fry, H.; Gog, J.R.; Edmunds, W.J.; Emery, J.C.; Medley, G.; et al. Effectiveness of isolation, testing, contact tracing, and physical distancing on reducing transmission of SARS-CoV-2 in different settings: A mathematical modelling study. *Lancet Infect. Dis.* **2020**, *20*, 1151–1160. [CrossRef]
35. Tuite, A.R.; Fisman, D.N.; Greer, A.L. Mathematical modelling of COVID-19 transmission and mitigation strategies in the population of Ontario, Canada. *Cmaj* **2020**, *192*, E497–E505. [CrossRef]
36. Malkov, E. Simulation of coronavirus disease 2019 (COVID-19) scenarios with possibility of reinfection. *Chaos Solitons Fractals* **2020**, *139*, 110296. [CrossRef]
37. Batistela, C.M.; Correa, D.P.; Bueno, Á.M.; Piqueira, J.R.C. SIRSi compartmental model for COVID-19 pandemic with immunity loss. *Chaos Solitons Fractals* **2021**, *142*, 110388. [CrossRef]
38. Costa, A.O.C.; de Carvalho Aragão Neto, H.; Lopes Nunes, A.P.; Dias de Castro, R.; Nóbrega de Almeida, R. COVID-19: Is reinfection possible? *EXCLI J.* **2021**, *20*, 522–536. [CrossRef]
39. Cai, L.; Liu, J.; Chen, Y. Dynamics of an Age-Structured HIV Model with Super-Infection. *Appl. Comput. Math. Int. J.* **2021**, *20*, 257–276.
40. Sheehan, M.M.; Reddy, A.J.; Rothberg, M.B. Reinfection Rates Among Patients Who Previously Tested Positive for Coronavirus Disease 2019: A Retrospective Cohort Study. *Clin. Infect. Dis. Off. Publ. Infect. Dis. Soc. Am.* **2021**, *73*, 1882–1886. [CrossRef] [PubMed]
41. Hanrath, A.T.; Payne, B.A.I.; Duncan, C.J.A. Prior SARS-CoV-2 infection is associated with protection against symptomatic reinfection. *J. Infect.* **2021**, *82*, e29–e30. [CrossRef] [PubMed]
42. Sabino, E.C.E.A. Resurgence of COVID-19 in Manaus, Brazil, despite high seroprevalence. *Lancet* **2021**, *397*, 452–455. [CrossRef]
43. Goddard, A.F.; Patel, M. SARS-CoV-2 variants and ending the COVID-19 pandemic. *Lancet* **2021**, *397*, 952–954.
44. Hoffmann, M.; Krüger, N.; Schulz, S.; Cossmann, A.; Rocha, C.; Kempf, A.; Nehlmeier, I.; Graichen, L.; Moldenhauer, A.S.; Winkler, M.S.; et al. The Omicron variant is highly resistant against antibody-mediated neutralization: Implications for control of the COVID-19 pandemic. *Cell* **2022**, *185*, 447–456.e11. [CrossRef] [PubMed]
45. Ferguson, N. *Report 49: Growth and Immune Escape of the Omicron SARS-CoV-2 Variant of Concern in England*; Technical Report; Imperial College London: London, UK, 2021. [CrossRef]
46. Santé Publique France. 2021. Available online: https://www.santepubliquefrance.fr/dossiers/coronavirus-covid-19/coronavirus-chiffres-cles-et-evolution-de-\la-covid-19-en-france-et-dans-le-monde/articles/covid-19-tableau-de-bord\-de-l-epidemie-en-chiffres (accessed on 26 October 2022).
47. Ma, Q.; Liu, J.; Liu, Q.; Kang, L.; Liu, R.; Jing, W.; Wu, Y.; Liu, M. Global Percentage of Asymptomatic SARS-CoV-2 Infections Among the Tested Population and Individuals With Confirmed COVID-19 Diagnosis: A Systematic Review and Meta-analysis. *JAMA Netw. Open* **2021**, *4*, e2137257. [CrossRef]
48. Johansson, M.A.; Quandelacy, T.M.; Kada, S.; Prasad, P.V.; Steele, M.; Brooks, J.T.; Slayton, R.B.; Biggerstaff, M.; Butler, J.C. SARS-CoV-2 Transmission From People Without COVID-19 Symptoms. *JAMA Netw. Open* **2021**, *4*, e2035057. [CrossRef]
49. Bender, J.K.; Brandl, M.; Höhle, M.; Buchholz, U.; Zeitlmann, N. Analysis of Asymptomatic and Presymptomatic Transmission in SARS-CoV-2 Outbreak, Germany, 2020. *Emerg. Infect. Dis.* **2021**, *27*, 1159–1163. [CrossRef]
50. Luo, L.; Liu, D.; Liao, X.; Wu, X.; Jing, Q.; Zheng, J.; Liu, F.; Yang, S.; Bi, H.; Li, Z.; et al. Contact settings and risk for transmission in 3410 close contacts of patients with COVID-19 in Guangzhou, China: A prospective cohort study. *Ann. Intern. Med.* **2020**, *173*, 879–887. [CrossRef]
51. Martcheva, M. *An Introduction to Mathematical Epidemiology*; Volume 61: Texts in Applied Mathematics; Springer: Boston, MA, USA, 2015. [CrossRef]
52. He, X.; Lau, E.H.; Wu, P.; Deng, X.; Wang, J.; Hao, X.; Lau, Y.C.; Wong, J.Y.; Guan, Y.; Tan, X.; et al. Temporal dynamics in viral shedding and transmissibility of COVID-19. *Nat. Med.* **2020**, *26*, 672–675. [CrossRef]
53. Walsh, K.A.; Spillane, S.; Comber, L.; Cardwell, K.; Harrington, P.; Connell, J.; Teljeur, C.; Broderick, N.; Gascun, C.F.D.; Smith, S.M.; et al. The duration of infectiousness of individuals infected with SARS-CoV-2. *J. Infect.* **2020**, *81*, 847–856. [CrossRef] [PubMed]

54. Lauer, S.A.; Grantz, K.H.; Bi, Q.; Jones, F.K.; Zheng, Q.; Meredith, H.R.; Azman, A.S.; Reich, N.G.; Lessler, J. The incubation period of coronavirus disease 2019 (COVID-19) from publicly reported confirmed cases: Estimation and application. *Ann. Intern. Med.* **2020**, *172*, 577–582. [CrossRef]
55. Hilton, J.; Keeling, M.J. Estimation of country-level basic reproductive ratios for novel Coronavirus (SARS-CoV-2/COVID-19) using synthetic contact matrices. *PLoS Comput. Biol.* **2020**, *16*, e1008031. [CrossRef] [PubMed]
56. Ke, R.; Romero-Severson, E.; Sanche, S.; Hengartner, N. Estimating the reproductive number R0 of SARS-CoV-2 in the United States and eight European countries and implications for vaccination. *J. Theor. Biol.* **2021**, *517*, 110621. [CrossRef] [PubMed]
57. Ferguson, N.M.; Laydon, D.; Nedjati-Gilani, G.; Imai, N.; Ainslie, K.; Baguelin, M.; Bhatia, S.; Boonyasiri, A.; Cucunubá, Z.; Cuomo-Dannenburg, G.; et al. Impact of non-pharmaceutical interventions (NPIs) to reduce COVID-19 mortality and healthcare demand. Imperial College COVID-19 Response Team. *Imp. Coll. COVID-19 Response Team* **2020**, *20*, 77482.
58. Hoffart, A.; Johnson, S.U.; Ebrahimi, O.V. Loneliness and Social Distancing During the COVID-19 Pandemic: Risk Factors and Associations With Psychopathology. *Front. Psychiatry* **2020**, *11*, 589127. [CrossRef]
59. Lüdecke, D.; von dem Knesebeck, O. Decline in Mental Health in the Beginning of the COVID-19 Outbreak Among European Older Adults—Associations With Social Factors, Infection Rates, and Government Response. *Front. Public Health* **2022**, *10*, 844560. [CrossRef] [PubMed]
60. Arino, J.; Van Den Driessche, P. The basic reproduction number in a multi-city compartmental epidemic model. In *Positive Systems*; Springer: Berlin/Heidelberg, Germany, 2003; pp. 135–142.
61. Arino, J.; Van den Driessche, P. Disease spread in metapopulations. *Fields Inst. Commun.* **2006**, *48*, 1–13.

mathematics

MDPI

Article

Epidemiological Investigation: Important Measures for the Prevention and Control of COVID-19 Epidemic in China

Cheng-Cheng Zhu [1], Jiang Zhu [2,*] and Jie Shao [3]

[1] School of Science, Jiangnan University, Wuxi 214122, China; chengchengzhu@jiangnan.edu.cn
[2] School of Mathematics and Statistics, Jiangsu Normal University, Xuzhou 221116, China
[3] School of Business, University of Science and Technology of China, Hefei 230026, China; jieshao@mail.ustc.edu.cn
* Correspondence: jiangzhu@jsnu.edu.cn

Abstract: Based on China's summary of three years of experience and measures in the prevention and control of the COVID-19 epidemic, we have built a COVID-19 prevention and control model integrating health and medical detection, big data information technology to track the trend of the epidemic throughout the whole process, isolation of key epidemic areas, and dynamic prevention and control management throughout the whole process. This model provides a simple, feasible, and theoretically reliable prevention and control model for future large-scale infectious disease prevention and control. The Lyapnov functional method is replaced by the global exponential attractor theory, which provides a new mathematical method for studying the global stability of the multi parameter, multi variable infectious disease prevention and control system. We extracted mathematical methods and models suitable for non-mathematical infectious disease researchers from profound and difficult to understand mathematical theories. Using the results of the global exponential Attractor theory obtained in this paper, we studied the global dynamics of the COVID-19 model with an epidemiological investigation. The results demonstrated that the non-constant disease-free equilibrium is globally asymptotically stable when $\lambda^* < 0$, and the COVID-19 epidemic is persisting uniformly when $\lambda^* > 0$. In order to understand the impact of the epidemiological investigation under different prevention and control stages in China, we compare the control effects of COVID-19 under different levels of epidemiological investigation policies. We visually demonstrate the global stability and global exponential attractiveness of the COVID-19 model with transferors between regions and epidemiological investigation in a temporal-spatial heterogeneous environment with the help of numerical simulations. We find that the epidemiological investigation really has a significant effect on the prevention and control of the epidemic situation, and we can also intuitively observe the relationship between the flow of people (including tourism, shopping, work and so on) and epidemiological investigation policies. Our model is adapted to different stages of prevention and control; the emergency "circuit breaker" mechanism of the model is also consistent with actual prevention and control.

Keywords: global exponentially attracting set; temporal-spatial heterogeneous COVID-19 model; epidemiological investigation

MSC: 35B41; 35K57; 35B35; 37N25; 92D25; 92D30

1. Introduction

The epidemic of novel coronavirus pneumonia has spread around the world for three years [1–5]. As a self-limiting epidemic in a temporal-spatial heterogeneous environment [6], different countries have formulated different prevention and control policies according to their national conditions. For the prevention and control of the COVID-19 epidemic, governments and medical staff have made great efforts in the past three years.

Researchers have also expressed their opinions and proposed many different control methods and prevention strategies. The prevention and control of COVID-19 is different for different countries and regions [7–12]. Akter and Jin [13] propose a Caputo-based fractional compartmental model for the dynamics of the novel COVID-19. Martinez-Fernandez et al. [14] compared Verhulst's, Gompertz's, and SIR models from the point of view of their efficiency to describe the behavior of COVID-19 in Spain. These mathematical models are used to predict the future of the pandemic by first solving the corresponding inverse problems to identify the model parameters in each wave separately, using the observed data in daily cases in the past [15]. In the beginning of the COVID-19 pandemic, universities have experienced unique challenges due to their dual nature as a place of education and residence. Up to now, China has been a country with a very low fatality ratio of COVID-19. The lowest fatality ratio of COVID-19 in the world is due to the strict epidemiological investigation policy of the Chinese government. These epidemiological investigation policies include big data screening, travel reports and national nucleic acid testing. At the beginning of December 2022, the Chinese government made timely adjustments to relax the prevention and control strategy in response to the domestic epidemic spread trend, and canceled the nationwide nucleic acid, travel reports and other epidemiological investigations. The current epidemiological investigation strategy has changed into finding out the base number and situation of key populations, and strengthening health monitoring and early intervention. After the relaxation of epidemiological investigations, there has been a rapid and significant increase in the number of infected people in China. China's epidemiological investigation policy has its own characteristics in global epidemic prevention and control policies. According to data released by the WHO under this type of prevention and control, only 33,144 people in China have died from COVID-19. We believe that the prevention and control strategy of this epidemiological investigation can serve as an experience to learn from, and we can also try this strategy in future outbreaks similar to COVID-19.

The purpose of this article is to study the positive impact of epidemiological investigations on epidemic prevention and control through mathematical modeling methods.

In order to use mathematical theory to analyze the rationality and effectiveness of epidemiological investigation under different prevention and control stages in China, we construct a COVID-19 model with transferors between regions, an epidemiological investigation and a relapse in a temporal-spatial heterogeneous environment. Our model is divided into six compartments, namely susceptible individuals (S), latent patients (L), transferors between regions (T), infected individuals (I), persons under epidemiological investigation (E), temporary restorers (R) and healthy individuals (H). The parameters description and transfer diagram as shown in Table 1 and Figure 1.

Table 1. State variables and parameters of COVID-19 ($SLTEIRH$) model.

Parameter	Description
$\Lambda(x,t)$	Total recruitment scale into this homogeneous social mixing community at location x and time t.
$\beta_i(x,t), i=1,2$	Contact rate at location x and time t.
$\alpha(x,t), \sigma(x,t), \nu_2(x,t)$	Infection rate at location x and time t.
$\delta(x,t)$	Contact rate when moving between regions at location x and time t.
$\gamma(x,t)$	Rate of epidemiological investigation at location x and time t.
$\theta_1(x,t)$	Release rate of epidemiological investigation at location x and time t.
$\theta_2(x,t)$	Complete cure rate at location x and time t.
$\rho(x,t)$	Relapse rate at location x and time t.
$\phi(x,t)$	Per-capita recovery (treatment) rate at location x and time t.
$\omega(x,t)$	Interregional transfer rate of patients with incubation period and asymptomatic infection at location x and time t.
$\nu_1(x,t)$	Asymptomatic infection rate at location x and time t.
$\mu(x,t)$	Natural mortality rate at location x and time t.
$\eta_i(x,t), i=1,2,3$	Fatality ratio at location x and time t.
k	Epidemiological investigation proportions at different stages of prevention and control.

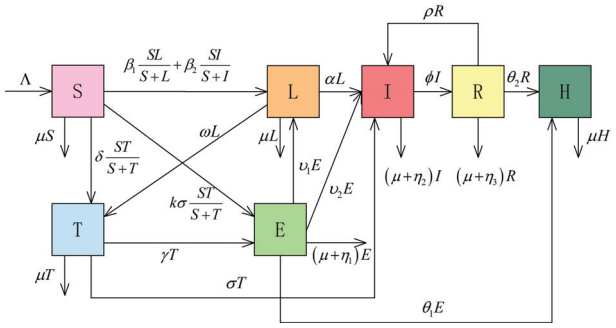

Figure 1. Transfer diagram for the COVID-19 ($SLTEIRH$) model with transferors between regions, epidemiological investigation and relapse in a temporal-spatial heterogeneous environment.

From Figure 1, the following system with the initial-boundary-value conditions is constructed by:

$$
\begin{cases}
\frac{\partial S}{\partial t} = \nabla\cdot(d_S(x)\nabla S) + \Lambda(x,t) - \beta_1(x,t)\frac{SL}{S+L} - \beta_2(x,t)\frac{SI}{S+I} \\
\quad - \delta(x,t)\frac{ST}{S+T} - k\sigma(x,t)\frac{ST}{S+T} - \mu(x,t)S, \\
\frac{\partial L}{\partial t} = \nabla\cdot(d_L(x)\nabla L) + \beta_1(x,t)\frac{SL}{S+L} + \beta_2(x,t)\frac{SI}{S+I} + \nu_1(x,t)E \\
\quad - [\mu(x,t) + \omega(x,t) + \alpha(x,t)]L, \\
\frac{\partial T}{\partial t} = \nabla\cdot(d_T(x)\nabla T) + \delta(x,t)\frac{ST}{S+T} + \omega(x,t)L \\
\quad - [\mu(x,t) + \gamma(x,t) + \sigma(x,t)]T, \\
\frac{\partial E}{\partial t} = \gamma(x,t)T + k\sigma(x,t)\frac{ST}{S+T} \\
\quad - [\mu(x,t) + \eta_1(x,t) + \nu_1(x,t) + \nu_2(x,t) + \theta_1(x,t)]E, \\
\frac{\partial I}{\partial t} = \nabla\cdot(d_I(x)\nabla I) + \alpha(x,t)L + \sigma(x,t)T + \nu_2(x,t)E + \rho(x,t)R \\
\quad - [\mu(x,t) + \eta_2(x,t) + \phi(x,t)]I, \\
\frac{\partial R}{\partial t} = \nabla\cdot(d_R(x)\nabla R) + \phi(x,t)I - [\mu(x,t) + \eta_3(x,t) + \rho(x,t) + \theta_2(x,t)]R, \\
\frac{\partial H}{\partial t} = \nabla\cdot(d_H(x)\nabla H) + \theta_1(x,t)E + \theta_2(x,t)R - \mu(x,t)H, \\
\quad x\in\Omega, t>0, \\
\frac{\partial S}{\partial \mathbf{n}} = \frac{\partial L}{\partial \mathbf{n}} = \frac{\partial T}{\partial \mathbf{n}} = \frac{\partial E}{\partial \mathbf{n}} = \frac{\partial I}{\partial \mathbf{n}} = \frac{\partial R}{\partial \mathbf{n}} = \frac{\partial H}{\partial \mathbf{n}} = 0,\ x\in\partial\Omega, t>0, \\
S(x,0) = S_0(x) \geq 0, L(x,0) = L_0(x) \geq 0, T(x,0) = T_0(x) \geq 0, \\
E(x,0) = E_0(x) \geq 0, I(x,0) = I_0(x) \geq 0, R(x,0) = R_0(x) \geq 0, \\
H(x,0) = H_0(x) \geq 0, x\in\Omega.
\end{cases}
\tag{1}
$$

Here, Ω is a bounded domain in $\mathbb{R}^m (m \geq 1)$ with smooth boundary $\partial\Omega$ (when $m > 1$), $d_S(x), d_L(x), d_T(x), d_I(x), d_R(x), d_H(x) \in \mathbf{C}^1(\Omega)$ are positive, continuous and uniformly bounded diffusion coefficients depending on space.Since most of the people who participated in the epidemiological investigation were quarantined at home or in the hospital, we do not consider the diffusion of them in this article. $\Lambda(x,t), \beta_1(x,t), \beta_2(x,t), \rho(x,t), \nu_1(x,t), \nu_2(x,t), \alpha(x,t), \omega(x,t), \delta(x,t), \sigma(x,t), \theta_1(x,t), \theta_2(x,t), \gamma(x,t), \phi(x,t), \mu(x,t), \eta_1(x,t), \eta_2(x,t)$ and $\eta_3(x,t)$ are bounded and positive Hölder continuous functions on accounting; k represents the proportion of epidemiological investigation of susceptible persons. Neumann boundary conditions $\frac{\partial S}{\partial \mathbf{n}} = \frac{\partial L}{\partial \mathbf{n}} = \frac{\partial T}{\partial \mathbf{n}} = \frac{\partial E}{\partial \mathbf{n}} = \frac{\partial I}{\partial \mathbf{n}} = \frac{\partial R}{\partial \mathbf{n}} = \frac{\partial H}{\partial \mathbf{n}} = 0$ denotes that the change rate on the boundary of the region Ω is equal to 0. It is straightforward to verify that $\frac{SI}{S+I}\left(\frac{SL}{S+L}, \frac{ST}{S+T}\right)$ is a Lipschitz continuous function of S and $I(L,T)$ in the open first quadrant. Therefore, we can extend it to the entire first quadrant by defining it to be zero whenever $S = 0$ or $I = 0$ $(L = 0, T = 0)$. Throughout the paper, we assume that the initial value S_0, L_0, T_0, E_0, I_0 and R_0 are nonnegative continuous functions on $\overline{\Omega}$, and the number of infected individuals is positive, i.e., $\int_\Omega I_0(x)dx > 0$. Specific parameters described in Table 1.

The highlight of this model is to examine the impact of epidemiological investigation on epidemic prevention and control. Epidemiological investigation policies at different stages can be adjusted through the parameter k in the model to achieve the best prevention and control effect. The epidemiological investigation in the model can be understood as a comprehensive compartment including the nucleic acid test, big data monitoring, and even vaccination. Of course, we can also refine compartment E in the process of modeling. However, in addition to increasing the difficulty of mathematical reasoning, this refinement will not have a significant impact on the long-term dynamic behavior of the model. Therefore, it is appropriate for us to select a comprehensive compartment for this epidemic investigation. Taking the spread of the COVID-19 epidemic as the research object, combined with the current development of the COVID-19 epidemic, Yang et al. [16] sorts out the relevant mathematical models for the study of the spread of COVID-19, among which the models based on the SIR model and SEIR model and the mathematical models combined with these two models are mainly selected. Finally, the importance of the reasonable and effective control of parameters and multi-model combined modeling is pointed out forthe future.

The organization of this paper is as follows. In Section 2, we first provide a sufficient condition for the existence of the global exponentially attracting set, which can be more easily applied to specific models. Second, we prove the existence of the system (1), and then we obtain the global stability and persistence of the COVID-19 epidemic with an epidemiological investigation. In Section 3, we simulate the impact of the epidemiological investigation and travel on the prevention and control of COVID-19 in China. By adjusting the proportion of the epidemiological investigation, we simulate the spread of the COVID-19 epidemic under different epidemiological investigations. In Section 4, we provide our conclusions and some discussions.

2. The Effectiveness Analysis of Epidemiological Investigation

Because the structure of the epidemiological investigation model (1) is complex, it contains multiple coupled state variables, and the coefficients are all temporal-spatial heterogeneous except for the spatially heterogeneous diffusion coefficient. It is tedious and difficult to discuss the global stability of system (1) by adopting the usual method of constructing Lyapunov functionals. For these reasons, we need to seek new breakthroughs in methods and find some new methods and means to solve the stability analysis problems of systems with a large number of equations. It is well known that the global attractor theory can discuss the dynamics of dissipative evolutionary systems. However, the existing global attractor and even global exponential attractor theories are all abstract conditions that are esoteric and difficult to understand in mathematical theory. They are difficult to apply directly to actual mathematical models. This seriously hinders the general infectious disease researchers from applying these mathematical theories to understand and discover the laws of disease transmission. Through our previous studies [6,17], we have tried many times to discuss the transmission of some specific diseases with the help of the global attractor theory in infinite-dimensional dynamical systems and have achieved good results. Therefore, we hope to continue these efforts and obtain some more convenient conditions that can be applied directly.

Let $\mathbf{H}$ be Hilbert space; $\mathbf{H}_1 \subset \mathbf{H}$ is a dense and compact inclusion. $A : \mathbf{H}_1 \to \mathbf{H}$ is a symmetrical sectorial operator and all eigenvalues of A are

$$0 > \lambda_1 \geq \lambda_2 \geq \cdots \geq \lambda_k > \ldots, \ \lambda_k \to -\infty \ (k \to \infty), \tag{2}$$

Consider the system of reaction diffusion equations

$$\begin{cases} \frac{du}{dt} = Au + G(t, u), \\ u(0) = u_0. \end{cases} \tag{3}$$

In the following lemma, we provide a sufficient condition to prove the global exponentially attracting set of system (3). This condition is more convenient in terms of computation and workload compared with our previous research results in the verification process of the actual model.

Theorem 1. *Assume that condition (2) holds, and there exists a constant $C > 0$ such that for any bounded set $\mathbf{B}$, there exists a constant $t_{\mathbf{B}} > 0$, such that for $\forall u_0 \in \mathbf{B} \subset \mathbf{H}_1$, the solution $u = u(t, u_0)$ of system (3) satisfies condition*

$$\langle G(t,u), u\rangle_{\mathbf{H}} \leq C, \forall t \geq t_{\mathbf{B}}, \tag{4}$$

then, in the system (3) exists a global exponentially attracting set $\widetilde{\mathcal{A}^*}$; it exponentially attracts any bounded set under the $\mathbf{H}$-norm.

Proof. Assume that $u = u(t, u_0)$ is a solution of the system (3), where $u_0 \in \mathbf{B}$. Then, by the definition of the fractional power subspace generated by sectorial operator A, we can obtain that

$$\begin{aligned} \langle Au + G(t,u), u\rangle_{\mathbf{H}} &= \langle Au, u\rangle_{\mathbf{H}} + \langle G(t,u), u\rangle_{\mathbf{H}} \\ &= -\|u\|^2_{\mathbf{H}_{\frac{1}{2}}} + \langle G(t,u), u\rangle_{\mathbf{H}} \\ &\leq -\|u\|^2_{\mathbf{H}_{\frac{1}{2}}} + C, \forall t \geq t_{\mathbf{B}}. \end{aligned} \tag{5}$$

Since A: $\mathbf{H}_1 \to \mathbf{H}$ is a symmetrical sectorial operator, the eigenvectors $\{e_j\}_{j\in\mathbb{N}}$ corresponding to the eigenvalues $\{\lambda_j\}_{j\in\mathbb{N}}$ are a complete orthonormal base of $\mathbf{H}$. For any $u \in \mathbf{H}$, assume that u can be presented as

$$u = \sum_{i=1}^{\infty} x_i e_i, \|u\|^2_{\mathbf{H}} = \sum_{i=1}^{\infty} x_i^2.$$

In addition, it follows from $\lim\limits_{j\to\infty} \lambda_j = -\infty$ that for any $N > 0$, there is an integral number $J \geq 1$, such that $-N \geq \lambda_j, \forall j \geq J+1$.

Let

$$\mathbf{H}_1^J = span\{e_1, e_2, \ldots, e_J\} \text{ and } \mathbf{H}_2^J = \left(\mathbf{H}_1^J\right)^{\perp}.$$

Then, each $u \in \mathbf{H}$ can be decomposed as

$$\begin{aligned} u &= Pu + (I-P)u := u_1 + u_2, \\ u_1 &= \sum_{i=1}^{J} x_i e_i \in \mathbf{H}_1^J,\ u_2 = \sum_{i=J+1}^{\infty} x_i e_i \in \mathbf{H}_2^J, \end{aligned}$$

where P: $\mathbf{H} \to \mathbf{H}_1^J$ is the projector.

By using the condition (5), there exists positive constants $C > 0$, such that for any bounded set $\mathbf{B} \subset \mathbf{H}_1$, there exists a $t_{\mathbf{B}} > 0$, which satisfies that

$$\frac{1}{2}\frac{d}{dt}\langle u, u\rangle_{\mathbf{H}} = \left\langle \dot{u}, u\right\rangle_{\mathbf{H}} = \langle Au + G(t,u), u\rangle_{\mathbf{H}} \leq -\|u\|^2_{\mathbf{H}_{\frac{1}{2}}} + C.$$

Since $\mathbf{H}_{\frac{1}{2}} \hookrightarrow \mathbf{H}$, there exists $C_1 > 0$, such that

$$\|u\|_{\mathbf{H}_{\frac{1}{2}}} \geq C_1 \|u\|_{\mathbf{H}}, \ \forall u \in \mathbf{H}_{\frac{1}{2}}.$$

Hence,

$$\frac{1}{2}\frac{d}{dt}\|u\|_{\mathbf{H}}^2 \leq -C_1^2\|u\|_{\mathbf{H}}^2 + C,$$

By Gronwall's inequality in differential form Lemma 2.3 of [18], we obtain that

$$\|u\|_{\mathbf{H}}^2 \leq e^{-\alpha t}\|u_0\|_{\mathbf{H}}^2 + \frac{2C}{\alpha}\left(1 - e^{-\alpha t}\right), \tag{6}$$

where $\alpha = 2C_1^2$. Assume that $r > 0$, such that $\frac{2C}{\alpha} < r^2$. Since B is bounded, there exists a constant $K_B > 0$, such that for any $u_0 \in B$, $\|u_0\|_{\mathbf{H}} \leq K_B$. It follows from (6) that if we take t_B big enough, such that $\|u(t,u_0)\|_{\mathbf{H}}^2 = \|\mathcal{Q}(t)u_0\|_{\mathbf{H}}^2 \leq r^2, \forall t \geq t_B$. Hence, $B_r \subset H$ is an absorbing set. Moreover, this implies that

$$\|P\mathcal{Q}(t)u_0\|_{\mathbf{H}} \leq r, \ \forall t \geq t_B.$$

It means that $\{\|P\mathcal{Q}(t)\mathbf{B}\|_{\mathbf{H}}\}_{t\geq t_{\mathbf{B}}}$ is bounded.
It follows that from the inner product of Equation (3) in $\mathbf{H}$ with u_2, we have

$$\begin{aligned}
\frac{1}{2}\frac{d}{dt}\langle u, u_2\rangle_{\mathbf{H}} &= \frac{1}{2}\frac{d}{dt}\langle u_2, u_2\rangle_{\mathbf{H}} = \frac{1}{2}\frac{d}{dt}\langle u, u - u_1\rangle_{\mathbf{H}} \\
&= \frac{1}{2}\frac{d}{dt}\langle u, u\rangle_{\mathbf{H}} - \frac{1}{2}\frac{d}{dt}\langle u_1, u_1\rangle_{\mathbf{H}} \\
&= \left\langle \dot{u}, u\right\rangle_{\mathbf{H}} - \left\langle \dot{u}_1, u_1\right\rangle_{\mathbf{H}} \\
&= \langle Au + G(t,u), u\rangle_{\mathbf{H}} - \left\langle \dot{u}_1, u_1\right\rangle_{\mathbf{H}} \\
&\leq -\|u\|_{\mathbf{H}_{\frac{1}{2}}}^2 + C - \left\langle \dot{u}_1, u_1\right\rangle_{\mathbf{H}}, \forall t \geq t_{\mathbf{B}},
\end{aligned} \tag{7}$$

and

$$\begin{aligned}
\langle Au_2, u_2\rangle_{\mathbf{H}} &= -\|u_2\|_{\mathbf{H}_{\frac{1}{2}}}^2 \\
&= \sum_{i=J+1}^{\infty} \lambda_i x_i^2 \\
&\leq -N\sum_{i=J+1}^{\infty} x_i^2 = -N\|u_2\|_{\mathbf{H}}^2.
\end{aligned} \tag{8}$$

Note that

$$\begin{aligned}
\langle Au, u\rangle_{\mathbf{H}} &= \langle A(u_1+u_2), u_1+u_2\rangle_{\mathbf{H}} \\
&= \langle Au_1, u_1\rangle_{\mathbf{H}} + \langle Au_2, u_2\rangle_{\mathbf{H}} \\
&= -\|u_1\|_{\mathbf{H}_{\frac{1}{2}}}^2 - \|u_2\|_{\mathbf{H}_{\frac{1}{2}}}^2,
\end{aligned}$$

it follows from (7) and (8) that

$$\begin{aligned}
\frac{1}{2}\frac{d}{dt}\langle u_2, u_2\rangle_{\mathbf{H}} &\leq -\|u\|_{\mathbf{H}_{\frac{1}{2}}}^2 + C - \frac{1}{2}\frac{d}{dt}\langle u_1, u_1\rangle_{\mathbf{H}} \\
&\leq -N\|u_2\|_{\mathbf{H}}^2 + C - \frac{1}{2}\frac{d}{dt}\langle u_1, u_1\rangle_{\mathbf{H}}, \forall t \geq t_{\mathbf{B}}.
\end{aligned}$$

By integrating both ends of this inequality, we can obtain that

$$\|u_2\|_{\mathbf{H}}^2 \leq -2N\int_{t_B}^{t}\|u_2\|_{\mathbf{H}}^2 ds + 2C(t - t_B) + \|u(t_B)\|_{\mathbf{H}}^2$$

$$\leq \quad -2N\int_{t_B}^{t}\|u_2\|_{\mathbf{H}}^2 ds + 2C(t-t_B) + r^2.$$

By Gronwall's inequality, we have that

$$\|u_2\|_{\mathbf{H}}^2 \leq e^{-2N(t-t_{\mathbf{B}})}r^2 + \frac{C}{N}\Big(1 - e^{-2N(t-t_{\mathbf{B}})}\Big), \forall t \geq t_{\mathbf{B}}$$

and $N > 0$ is arbitrary. Therefore, N is large enough, such that $\frac{C}{N} < \varepsilon$; then, we deduce that the **Condition (C*)** of [19] holds. Hence, it follows from Theorems 3.3 and 4.1 in [19] that in the system (3) exists a global exponentially attracting set $\widetilde{\mathcal{A}^*}$; it exponentially attracts any bounded set under the **H**-norm. □

From now on, we denote that $\mathbf{H} = \mathbf{L}^2(\Omega)$, $\mathbf{H}_1 = \mathbf{H}_0^1(\Omega) \cap \mathbf{C}^{2,1}(\Omega)$, $\mathbf{H}^7 = \mathbf{H} \times \mathbf{H} \times \mathbf{H} \times \mathbf{H} \times \mathbf{H} \times \mathbf{H} \times \mathbf{H}$ and $\mathbf{H}_1^7 = \mathbf{H}_1 \times \mathbf{H_1} \times \mathbf{H}_1 \times \mathbf{H}_1 \times \mathbf{H}_1 \times \mathbf{H}_1 \times \mathbf{H}_1$. Note that $\mathbf{H}^7$ and $\mathbf{H}_1^7$ are Banach spaces equipped with norm

$$\Big\|(S, L, T, E, I, R)^T\Big\|_{\mathbf{H}^7} := \max\{\|S\|_{\mathbf{H}}, \|L\|_{\mathbf{H}}, \|T\|_{\mathbf{H}}, \|E\|_{\mathbf{H}}, \|I\|_{\mathbf{H}}, \|R\|_{\mathbf{H}}, \|H\|_{\mathbf{H}}\} \tag{9}$$

and

$$\Big\|(S, L, T, E, I, R)^T\Big\|_{\mathbf{H}_1^7} := \max\Big\{\|S\|_{\mathbf{H}_1}, \|L\|_{\mathbf{H}_1}, \|T\|_{\mathbf{H}_1}, \|E\|_{\mathbf{H}_1}, \|I\|_{\mathbf{H}_1}, \|R\|_{\mathbf{H}_1}, \|H\|_{\mathbf{H}_1}\Big\}.$$

For any given continuous function f on $\overline{\Omega} \times (0, +\infty)$, we denote

$$\begin{aligned} f^*(t) &= \sup_{x\in\overline{\Omega}} f(x,t) \text{ and } f_*(t) = \inf_{x\in\overline{\Omega}} f(x,t), \\ f^* &= \sup_{x\in\overline{\Omega}, t>0} f(x,t) \text{ and } f_* = \inf_{x\in\overline{\Omega}, t>0} f(x,t). \end{aligned}$$

By the similar method used in [17], we can prove the following existence, positivity and boundedness of the global solution of the system (1).

Theorem 2. *For each* $(S_0(x), L_0(x), T_0(x), E_0(x), I_0(x), R_0(x), H(x)) \in \mathbf{C}(\overline{\Omega} \times [-\tau, 0])$, *system (1) exists a positive and uniformly bounded global solution* $(S(x,t), L(x,t), T(x,t), E(x,t), I(x,t), R(x,t), H(x,t)) \in \mathbf{C}^{2,1}(\Omega \times (-\tau, \infty))$.

Proof. Since

$$\begin{aligned} A &= (\nabla \cdot (d_S(x)\nabla), \nabla \cdot (d_L(x)\nabla), \nabla \cdot (d_T(x)\nabla), 0, \\ &\quad \nabla \cdot (d_I(x)\nabla), \nabla \cdot (d_R(x)\nabla), \nabla \cdot (d_H(x)\nabla)) \end{aligned}$$

is a symmetrical sectorial operator and all eigenvalues of L are

$$0 > \lambda_1 \geq \lambda_2 \geq \cdots \geq \lambda_K > \ldots, \ \lambda_K \to -\infty \ (K \to \infty),$$

Let

$$\begin{aligned} &G(S, L, T, E, I, R, H) := (g_1(S, L, T, E, I, R, H), g_2(S, L, T, E, I, R, H), \\ &g_3(S, L, T, E, I, R, H), g_4(S, L, T, E, I, R, H), g_5(S, L, T, E, I, R, H) \\ &g_6(S, L, T, E, I, R, H), g_7(S, L, T, E, I, R, H))^T, \end{aligned}$$

where

$$\begin{aligned} g_1(S, L, T, E, I, R, H) &= \Lambda(x,t) - \beta_1(x,t)\frac{SL}{S+L} - \beta_2(x,t)\frac{SI}{S+I} \\ &\quad -\delta(x,t)\frac{ST}{S+T} - k\sigma(x,t)\frac{ST}{S+T} - \mu(x,t)S, \end{aligned}$$

$$\begin{aligned}
g_2(S,L,T,E,I,R,H) &= \beta_1(x,t)\frac{SL}{S+L}+\beta_2(x,t)\frac{SI}{S+I}+\nu_1(x,t)E\\
&\quad -[\mu(x,t)+\omega(x,t)+\alpha(x,t)]L,\\
g_3(S,L,T,E,I,R,H) &= \delta(x,t)\frac{ST}{S+T}+\omega(x,t)L-[\mu(x,t)+\gamma(x,t)+\sigma(x,t)]T,\\
g_4(S,L,T,E,I,R,H) &= \gamma(x,t)T+k\sigma(x,t)\frac{ST}{S+T}\\
&\quad -[\mu(x,t)+\eta_1(x,t)+\nu_1(x,t)+\nu_2(x,t)+\theta_1(x,t)]E,\\
g_5(S,L,T,E,I,R,H) &= \alpha(x,t)L+\sigma(x,t)T+\nu_2(x,t)E+\rho(x,t)R\\
&\quad -[\mu(x,t)+\eta_2(x,t)+\phi(x,t)]I,\\
g_6(S,L,T,E,I,R,H) &= \phi(x,t)I-[\mu(x,t)+\eta_3(x,t)+\rho(x,t)+\theta_2(x,t)]R,\\
g_7(S,L,T,E,I,R,H) &= \theta_1(x,t)E+\theta_2(x,t)R-\mu(x,t)H
\end{aligned}$$

In addition, by means of the differential mean value theorem of multivariate functions and (9),

$$\begin{aligned}
&\|g_1(S_1,L_1,T_1,E_1,I_1,R_1,H_1)-g_1(S_2,L_2,T_2,E_2,I_2,R_2,H_2)\|_{\mathbf{H}}\\
=\;&\Big\|-\beta_1(x,t)\Big(\tfrac{S_1L_1}{S_1+L_1}-\tfrac{S_2L_2}{S_2+L_2}\Big)-\beta_2(x,t)\Big(\tfrac{S_1I_1}{S_1+I_1}-\tfrac{S_2I_2}{S_2+I_2}\Big)\\
&-[\delta(x,t)+k\sigma(x,t)]\Big(\tfrac{S_1T_1}{S_1+T_1}-\tfrac{S_2T_2}{S_2+T_2}\Big)-\mu(x,t)(S_1-S_2)\Big\|_{\mathbf{H}}\\
\le\;&\beta_1^*(t)\|u-v\|_{\mathbf{H}}+\beta_2^*(t)\|u-v\|_{\mathbf{H}}+(\delta^*(t)+k\sigma^*(t))\|u-v\|_{\mathbf{H}}\\
&+\mu^*(t)\|u-v\|_{\mathbf{H}}\\
=\;&\big(\beta_1^*(t)+\beta_2^*(t)+\delta^*(t)+k\sigma^*(t)+\mu^*(t)\big)\|u-v\|_{\mathbf{H}},
\end{aligned}$$

where $u=(S_1,L_1,T_1,E_1,I_1,R_1,H_1), v=(S_2,L_2,T_2,E_2,I_2,R_2,H_2)$. Similarly,

$$\begin{aligned}
&\|g_2(S_1,L_1,T_1,E_1,I_1,R_1,H_1)-g_2(S_2,L_2,T_2,E_2,I_2,R_2,H_2)\|_{\mathbf{H}}\\
\le\;&\big(\beta_1^*(t)+\beta_2^*(t)+\nu_1^*(t)+\mu^*(t)+\alpha^*(t)+\omega^*(t)\big)\|u-v\|_{\mathbf{H}},\\
&\|g_3(S_1,L_1,T_1,E_1,I_1,R_1,H_1)-g_3(S_2,L_2,T_2,E_2,I_2,R_2,H_2)\|_{\mathbf{H}}\\
\le\;&(\delta^*(t)+\omega^*(t)+\gamma^*(t)+\sigma^*(t)+\mu^*(t))\|u-v\|_{\mathbf{H}},\\
&\|g_4(S_1,L_1,T_1,E_1,I_1,R_1,H_1)-g_4(S_2,L_2,T_2,E_2,I_2,R_2,H_2)\|_{\mathbf{H}}\\
\le\;&\big(\gamma^*(t)+k\sigma^*(t)\mu^*(t)+\eta_1^*(t)+\nu_1^*(t)+\nu_2^*(t)+\theta_1^*(t)\big)\|u-v\|_{\mathbf{H}},\\
&\|g_5(S_1,L_1,T_1,E_1,I_1,R_1,H_1)-g_5(S_2,L_2,T_2,E_2,I_2,R_2,H_2)\|_{\mathbf{H}}\\
\le\;&(\alpha^*(t)+\sigma^*(t)+\nu_2^*(t)+\rho^*(t)+\mu^*(t)+\eta_2^*(t)+\phi^*(t))\|u-v\|_{\mathbf{H}},\\
&\|g_6(S_1,L_1,T_1,E_1,I_1,R_1,H_1)-g_6(S_2,L_2,T_2,E_2,I_2,R_2,H_2)\|_{\mathbf{H}}\\
\le\;&(\phi^*(t)+\mu^*(t)+\eta_3^*(t)+\rho^*(t)+\theta_2^*(t))\|u-v\|_{\mathbf{H}},\\
&\|g_7(S_1,L_1,T_1,E_1,I_1,R_1,H_1)-g_7(S_2,L_2,T_2,E_2,I_2,R_2,H_2)\|_{\mathbf{H}}\\
\le\;&\big(\theta_1^*(t)+\theta_2^*(t)+\mu^*(t)\big)\|u-v\|_{\mathbf{H}}.
\end{aligned}$$

If we choose

$$\begin{aligned}
h(t) = \max\{&\beta_1^*(t)+\beta_2^*(t)+\delta^*(t)+k\sigma^*(t)+\mu^*(t),\\
&\beta_1^*(t)+\beta_2^*(t)+\nu_1^*(t)+\mu^*(t)+\alpha^*(t)+\omega^*(t),\\
&\delta^*(t)+\omega^*(t)+\gamma^*(t)+\sigma^*(t)+\mu^*(t),\\
&\gamma^*(t)+k\sigma^*(t)\mu^*(t)+\eta_1^*(t)+\nu_1^*(t)+\nu_2^*(t)+\theta_1^*(t),\\
&\alpha^*(t)+\sigma^*(t)+\nu_2^*(t)+\rho^*(t)+\mu^*(t)+\eta_2^*(t)+\phi^*(t),\\
&\phi^*(t)+\mu^*(t)+\eta_3^*(t)+\rho^*(t)+\theta_2^*(t),\theta_1^*(t)+\theta_2^*(t)+\mu^*(t)\},
\end{aligned}$$

then

$$\begin{aligned}
& \|G(t,u)-G(t,v)\|_{\mathbf{H}^7} \\
= \; & \|(g_1(t,u)-g_1(t,v)),(g_2(t,u)-g_2(t,v)),(g_3(t,u)-g_3(t,v)), \\
& (g_4(t,u)-g_4(t,v)),(g_5(t,u)-g_5(t,v)), \\
& (g_6(t,u)-g_6(t,v)),(g_7(t,u)-g_7(t,v))\|_{\mathbf{H}^7} \\
= \; & \max\{\|g_1(t,u)-g_1(t,v)\|_{\mathbf{H}},\|g_2(t,u)-g_2(t,v)\|_{\mathbf{H}}, \\
& \|g_3(t,u)-g_3(t,v)\|_{\mathbf{H}},\|g_4(t,u)-g_4(t,v)\|_{\mathbf{H}},\|g_5(t,u)-g_5(t,v)\|_{\mathbf{H}}, \\
& \|g_6(t,u)-g_6(t,v)\|_{\mathbf{H}},\|g_7(t,u)-g_7(t,v)\|_{\mathbf{H}}\} \\
\leq \; & h(t)\cdot\|u-v\|_{\mathbf{H}^7}.
\end{aligned}$$

Hence, the Lipschitz condition is well verified. Therefore, by Theorem 11.3.5 of [20] and Theorem 2.3 of [21], we can guarantee that in system (2) exists a global solution

$$(S(x,t),L(x,t),T(x,t),E(x,t),I(x,t),R(x,t),H(x,t))\in\mathbf{C}^{2,1}(\Omega\times(-\tau,\infty)).$$

According to the method in Lemma 2.1 and Theorem 2.2 of the recent paper [18], we can easily obtain the positivity of the global solution of the system (1). Moreover, by a similar proof of our recent Theorem 3.1 of [17], we can prove that the the global solution of the system (1) is bounded. □

Next, we prove the existence of the global exponentially attracting set of system (1) by verifying the condition (4). Then, we obtain the existence of the global exponentially attracting set of the system (1).

Theorem 3. *In system (1) exists a global exponentially attracting set $\mathcal{A}^*$; it exponentially attracts any bounded set in $\mathbf{H}^7$.*

Proof. We first verify condition (4).

$$\begin{aligned}
& \left\langle \begin{array}{c} \Lambda(x,t)-\beta_1(x,t)\frac{SL}{S+L}-\beta_2(x,t)\frac{SI}{S+I} \\ -\delta(x,t)\frac{ST}{S+T}-k\sigma(x,t)\frac{ST}{S+T}-\mu(x,t)S \end{array}, \quad S \right\rangle_{\mathbf{H}} \\
= & \int_\Omega \Lambda(x,t)Sdx-\int_\Omega \beta_1(x,t)\frac{S^2L}{S+L}dx-\int_\Omega \beta_2(x,t)\frac{S^2I}{S+I}dx \\
& -\int_\Omega[\delta(x,t)+k\sigma(x,t)]\frac{S^2T}{S+T}dx-\int_\Omega \mu(x,t)S^2dx \\
\leq & \Lambda^*\int_\Omega Sdx
\end{aligned}$$

$$\begin{aligned}
& \left\langle \begin{array}{c} \beta_1(x,t)\frac{SL}{S+L}+\beta_2(x,t)\frac{SI}{S+I}+\nu_1(x,t)E \\ -[\mu(x,t)+\omega(x,t)+\alpha(x,t)]L \end{array}, \quad L \right\rangle_{\mathbf{H}} \\
= & \int_\Omega \beta_1(x,t)\frac{SL^2}{S+L}dx+\int_\Omega \beta_2(x,t)\frac{SLI}{S+I}dx \\
& +\int_\Omega \nu_1(x,t)ELdx-\int_\Omega[\mu(x,t)+\alpha(x,t)+\delta(x,t)]L^2dx \\
\leq & \beta_1^*\int_\Omega L^2dx+\beta_2^*\int_\Omega LIdx+\nu_1^*\int_\Omega ELdx,
\end{aligned}$$

$$\begin{aligned}
& \left\langle \delta(x,t)\frac{ST}{S+T}+\omega(x,t)L-[\mu(x,t)+\gamma(x,t)+\sigma(x,t)]T, T \right\rangle_{\mathbf{H}} \\
= & \int_\Omega \delta(x,t)\frac{ST^2}{S+T}dx+\int_\Omega \omega(x,t)LTdx \\
& -\int_\Omega[\mu(x,t)+\gamma(x,t)+\sigma(x,t)]T^2dx
\end{aligned}$$

$$
\begin{aligned}
&\leq \delta^* \int_\Omega T^2 dx + \omega^* \int_\Omega LT dx,\\
&\left\langle \begin{array}{c} \gamma(x,t)T + k\sigma(x,t)\frac{ST}{S+T} \\ -[\mu(x,t)+\eta_1(x,t)+\nu_1(x,t)+\nu_2(x,t)+\theta_1(x,t)]E \end{array}, E \right\rangle_{\mathbf{H}}\\
&= \int_\Omega \gamma(x,t)ETdx + \int_\Omega k\sigma(x,t)\frac{SET}{S+T}dx\\
&\quad - \int_\Omega [\mu(x,t)+\eta_1(x,t)+\nu_1(x,t)+\nu_2(x,t)+\theta_1(x,t)]E^2 dx\\
&\leq \gamma^* \int_\Omega ETdx + k\sigma^* \int_\Omega ETdx,\\
&\left\langle \begin{array}{c} \alpha(x,t)L + \sigma(x,t)T + \nu_2(x,t)E + \rho(x,t)R \\ -[\mu(x,t)+\eta_2(x,t)+\phi(x,t)]I \end{array}, I \right\rangle_{\mathbf{H}}\\
&= \int_\Omega \alpha(x,t)LIdx + \int_\Omega \sigma(x,t)ITdx + \int_\Omega \nu_2(x,t)EIdx\\
&\quad + \int_\Omega \rho(x,t)IRdx - \int_\Omega [\mu(x,t)+\eta_2(x,t)+\phi(x,t)]I^2 dx\\
&\quad \leq \alpha^* \int_\Omega LIdx + \sigma^* \int_\Omega ITdx + \nu_2^* \int_\Omega EIdx + \rho^* \int_\Omega IRdx,\\
&\langle \phi(x,t)I - [\mu(x,t)+\eta_3(x,t)+\rho(x,t)+\theta_2(x,t)]R, R\rangle_{\mathbf{H}}\\
&= \int_\Omega \phi(x,t)IRdx - \int_\Omega [\mu(x,t)+\eta_3(x,t)+\rho(x,t)+\theta_2(x,t)]R^2 dx\\
&\leq \phi^* \int_\Omega IRdx,\\
&\langle \theta_1(x,t)E + \theta_2(x,t)R - \mu(x,t)H, H\rangle_{\mathbf{H}}\\
&= \int_\Omega \theta_1(x,t)EHdx + \int_\Omega \theta_2(x,t)RHdx - \int_\Omega \mu(x,t)H^2 dx\\
&\leq \theta_1^* \int_\Omega EHdx + \theta_2^* \int_\Omega RHdx.
\end{aligned}
$$

From Theorem 2, we know the solution of system (1)

$$u = (S(x,t), L(x,t), T(x,t), E(x,t), I(x,t), R(x,t), H(x,t))$$

is uniformly bounded, hence, from above the inner product estimation, we can obtain that there exists a constant $C > 0$, such that

$$\langle G(t,u), u\rangle_{\mathbf{H}^7} \leq C,$$

then condition (4) holds. On the other hand, as we know that

$$
\begin{aligned}
A \quad = \quad & (\nabla\cdot(d_S(x)\nabla), \nabla\cdot(d_L(x)\nabla), \nabla\cdot(d_T(x)\nabla), 0, \nabla\cdot(d_I(x)\nabla),\\
& \nabla\cdot(d_R(x)\nabla), \nabla\cdot(d_H(x)\nabla))
\end{aligned}
$$

is a symmetrical sectorial operator and all eigenvalues of L are

$$0 > \lambda_1 \geq \lambda_2 \geq \cdots \geq \lambda_K > \ldots,\ \lambda_K \to -\infty\ (K \to \infty),$$

therefore, by Theorem 1, we can obtain that system (1) has a global exponentially attracting set $\mathcal{A}^*$. □

After verifying the global exponentially attracting set, we can use our methods in [6,17] similarly to discuss the stability and uniform persistance of the COVID-19 epidemic,

which was intervened upon by an epidemiological investigation. It is clearly observed that system (1) demonstrates a disease-free equilibrium $E^0(x) = (S^0(x), 0, 0, 0, 0, 0, 0)$. Linearize the last six equations of the system (1) at the disease-free equilibrium and let $L = e^{\lambda t}\chi(x), T = e^{\lambda t}\varphi(x), E = e^{\lambda t}\psi(x), I = e^{\lambda t}\xi(x), R = e^{\lambda t}\zeta(x), H = e^{\lambda t}\varrho(x)$; we can obtain the following characteristic equation system (10) corresponding to the last six equations of system (1)

$$\begin{cases} \lambda\Phi(x) = \nabla \cdot (D(x)\nabla\Phi(x)) + M(x,t)\Phi(x), \ x \in \Omega, \\ \frac{\partial\Phi}{\partial \mathbf{n}} = 0, \ x \in \partial\Omega, \end{cases} \tag{10}$$

where $\Phi(x) = (\chi(x), \varphi(x), \psi(x), \xi(x), \zeta(x), \varrho(x))^T$,

$$D(x) = \begin{bmatrix} d_L(x) & 0 & 0 & 0 & 0 & 0 \\ 0 & d_T(x) & 0 & 0 & 0 & 0 \\ 0 & 0 & 0 & 0 & 0 & 0 \\ 0 & 0 & 0 & d_I(x) & 0 & 0 \\ 0 & 0 & 0 & 0 & d_R(x) & 0 \\ 0 & 0 & 0 & 0 & 0 & d_H(x) \end{bmatrix}$$

and

$$\begin{aligned} & M(x,t) \\ = \ & (m_{ij}(x,t)) \\ = \ & \begin{bmatrix} m_{11}(x,t) & 0 & \nu_1(x,t) & \beta_2(x,t) & 0 & 0 \\ \omega(x,t) & m_{22}(x,t) & 0 & 0 & 0 & 0 \\ 0 & \gamma(x,t) + k\sigma(x,t) & m_{33}(x,t) & 0 & 0 & 0 \\ \alpha(x,t) & \sigma(x,t) & \nu_2(x,t) & m_{44}(x,t) & \rho(x,t) & 0 \\ 0 & 0 & 0 & \phi(x,t) & m_{55}(x,t) & 0 \\ 0 & 0 & \theta_1(x,t) & 0 & \theta_2(x,t) & -\mu(x,t) \end{bmatrix}, \end{aligned}$$

where

$$\begin{aligned} m_{11}(x,t) &= \beta_1(x,t) - [\mu(x,t) + \omega(x,t) + \alpha(x,t)], \\ m_{22}(x,t) &= \delta(x,t) - [\mu(x,t) + \gamma(x,t) + \sigma(x,t)], \\ m_{33}(x,t) &= -[\mu(x,t) + \eta_1(x,t) + \nu_1(x,t) + \nu_2(x,t) + \theta_1(x,t)], \\ m_{44}(x,t) &= -[\mu(x,t) + \eta_2(x,t) + \phi(x,t)], \\ m_{55}(x,t) &= -[\mu(x,t) + \eta_3(x,t) + \rho(x,t) + \theta_2(x,t)] \end{aligned}$$

and $m_{ij}(x) \geq 0, i \neq j, x \in \overline{\Omega}$. By the Krein–Rutman theorem, we can obtain that there exists a real principal eigenvalue λ^* of Equation (1) and a corresponding eigenvector $\Phi^*(x) >> 0$ for all $x \in \overline{\Omega}$ in the case of Neumann boundary conditions. Next, we use this principal eigenvalue as a threshold to characterize the spread trend of COVID-19.

Theorem 4. *The following statements are valid.*

(1) If $\lambda^* < 0$, then

$$\begin{aligned} \lim_{t\to\infty} S(x,t) &= S^0(x), \lim_{t\to\infty} L(x,t) = 0, \lim_{t\to\infty} T(x,t) = 0, \\ \lim_{t\to\infty} E(x,t) &= 0, \lim_{t\to\infty} I(x,t) = 0, \lim_{t\to\infty} R(x,t) = 0, \lim_{t\to\infty} H(x,t) = 0 \end{aligned}$$

in **H**, *and hence, the disease-free equilibrium is globally asymptotically stable. In a biological sense, the COVID-19 epidemic can be effectively controlled and will eventually die out.*

(2) If $\lambda^* > 0$, then there exists a endemic equilibrium $(S^*(x), L^*(x), T^*(x), E^*(x), I^*(x), R^*(x), H^*(x))$, such that any solution (S, L, T, E, I, R, H) satisfies

$$\lim_{t\to\infty} S(x,t) = S^*(x), \lim_{t\to\infty} L(x,t) = L^*(x), \lim_{t\to\infty} T(x,t) = T^*(x),$$

$$\begin{aligned}\lim_{t\to\infty} E(x,t) &= E^*(x), \lim_{t\to\infty} I(x,t) = I^*(x), \lim_{t\to\infty} R(x,t) = R^*(x),\\ \lim_{t\to\infty} H(x,t) &= H^*(x)\end{aligned}$$

for $x \in \overline{\Omega}$, and hence, the endemic equilibrium is globally asymptotically stable. In a biological sense, the COVID-19 epidemic continues to coexist with human beings.

Proof.

(1) The proof can be obtained by a similar method in the literature [6,17,22].

(2) Similar to the proof in [6,17], we can obtain that there exists a function $m(x) > 0$ independent of the initial data, such that any solution (S, L, T, E, I, R) satisfies

$$\begin{aligned}\liminf_{t\to\infty} S(x,t) &\geq m(x), \liminf_{t\to\infty} L(x,t) \geq m(x),\\ \liminf_{t\to\infty} T(x,t) &\geq m(x), \liminf_{t\to\infty} E(x,t) \geq m(x),\\ \liminf_{t\to\infty} I(x,t) &\geq m(x), \liminf_{t\to\infty} R(x,t) \geq m(x),\\ \liminf_{t\to\infty} H(x,t) &\geq m(x)\end{aligned} \tag{11}$$

for $x \in \overline{\Omega}$, and hence, the disease persists uniformly. According to the proof of the global exponentially attracting set in [19], it can be observed that global exponentially attracting set $\mathcal{A}^*$ contains the global attractor $\mathcal{A}$. By Theorem A.2.2 of [23], we can obtain that there exists an equilibrium $(S^*(x), L^*(x), T^*(x), E^*(x), I^*(x), R^*(x), H^*(x))$, such that any solution (S, L, T, E, I, R, H) satisfies

$$\begin{aligned}\lim_{t\to\infty} S(x,t) &= S^*(x), \lim_{t\to\infty} L(x,t) = L^*(x),\\ \lim_{t\to\infty} T(x,t) &= T^*(x), \lim_{t\to\infty} E(x,t) = E^*(x),\\ \lim_{t\to\infty} I(x,t) &= I^*(x), \lim_{t\to\infty} R(x,t) = R^*(x),\\ \lim_{t\to\infty} H(x,t) &= H^*(x).\end{aligned} \tag{12}$$

It follows from (11) that the equilibrium is not the disease-free equilibrium and the each limit of (12) is not equal to 0; thus, this equilibrium is the endemic equilibrium. Hence, the endemic equilibrium is globally asymptotically stable. □

3. Effect Simulation of Epidemiological Investigation

Previously, we provided a strict mathematical proof for the long-term dynamic behavior of the model. Although the global attractor theory is a commonly used method in infinite dimensional dynamic systems, the validation conditions we provided in this article are different from the validation methods in other existing conclusions. The validation conditions we provide are more convenient and can be easily used by researchers even for those who are not majoring in mathematics, which is also an innovation of this article. In order to understanding our theoretical results more intuitively, we will simulate the impact of different epidemic investigation strategies on the epidemic. These epidemic investigation strategies really exist during different periods of China's fight against COVID-19. Since we want to simulate the long-term dynamic behavior of COVID-19, we innovatively used 0 as the initial value of the compartments in the program for drawing three-dimensional images and select the month as the unit for the time axis.

3.1. Stability and Persistence of COVID-19 in China under the Dynamic Clearing Policy

Before December 2022, the Chinese government has been strictly implementing the prevention and control policy of dynamic clearing and has achieved remarkable results. With the help of official authoritative data and reasonable estimates, we focus on modeling the impact of the interregional movement and epidemiological investigations on

the prevention and control of COVID-19. According to the policy of the epidemiological investigation, people who live with or have contact with confirmed or asymptomatic infected persons are the objects of the key investigation. Therefore, the proportional coefficient of the epidemiological investigation of returnees from travel should be greater than 1. In addition, compartment H has little effect on the entire disease spreading process; we focus on simulating the changes of the first six compartments. The specific data are shown in Table 2. Part of the data in Table 2 comes from authoritative official data and part comes from reasonable estimates, which are not arbitrary. Our estimate is based on rigorous mathematical calculations [8,24] using actual official published data within a reasonable range.

Table 2. The parameters' description of the COVID-19 epidemic in China.

Parameter	Data Estimated	Data Sources
Λ	8	Calculate
β_1	0.6	Reference [6]
β_2	0.3	Reference [6]
α	0.6	Reference [25]
ω	0.1	Reference [25]
γ	0.7	Reference [25]
ν_1	0.0003	Calculate
ν_2	0.0002	Calculate
θ_1	0.7	Calculate
θ_2	0.8	Calculate
ρ	0.002	Reference [6]
ϕ	0.8	Reference [25]
μ	0.1595	Reference [26]
η_1	0.021	Reference [25]
η_2	0.047	Reference [25]
η_3	0.021	Reference [25]
δ	0.2	Calculate
σ	0.2	Calculate
k	1.7	Calculate
d_S	3	Calculate
d_L	2.5	Calculate
d_T	5	Calculate
d_I	0.3	Reference [22]
d_R	2	Reference [22]

Refering to the data in Table 2 and our system (1), we first simulate the spread trend of the novel coronavirus pneumonia epidemic in China (Figure 2).

The image is a more realistic projection of the current spread of the COVID-19 epidemic in China. From the graph, we can observe that COVID-19 is persistent.

If we choose $\beta_1 = 0.006, \beta_2 = 0.003$ in Table 2, then we can obtain the image in Figure 3. At this time, the disease-free equilibrium is globally asymptotically stable.

3.2. Comparison of Prevention and Control under Different Proportions of Epidemiological Investigation

Our model focuses on an epidemiological investigation and the impact of interregional movement on the prevention and control of COVID-19. Through research, we found that the degree of control of an epidemiological investigation has an impact on people's desire to travel. Close range activities related to life will continue but also decrease accordingly. When the epidemic investigation policy is tightened, people will go out as little as possible. In order to clearly observe the impact of the epidemiological investigation, we design three epidemiological investigation strategies with different levels. By comparison, we can find

that different epidemiological investigations have different effects on COVID-19 prevention and control. First, we focus on the epidemiological investigation of close and sub-close contacts of infected populations. The parameter k in the model represents the proportion of an epidemiological investigation of contact between the susceptible person and the infected person after interregional movement, which essentially describes the scope of the susceptible person, close contact and sub-close contact participating in the epidemiological investigation. We choose $k = 1.7$ and $k = 3$, respectively, to simulate the changes of T, E and I (Figure 4).

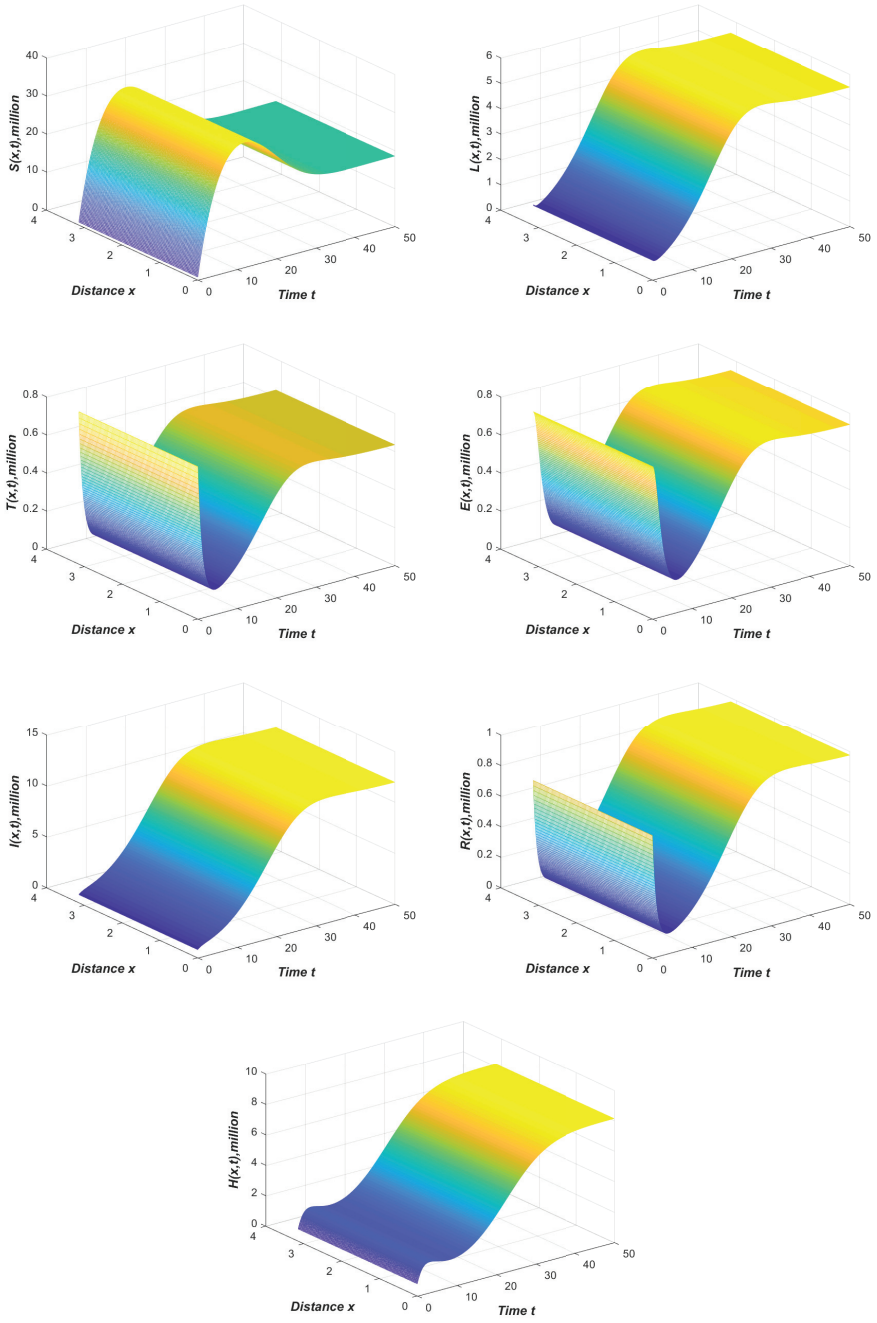

Figure 2. The spread trend of COVID-19 in China.

If the contact rate is very low (for example $\beta_1 = \beta_2 = 10^{-5}$), the probability of susceptible individuals being infected is very low, and the epidemic will disappear.

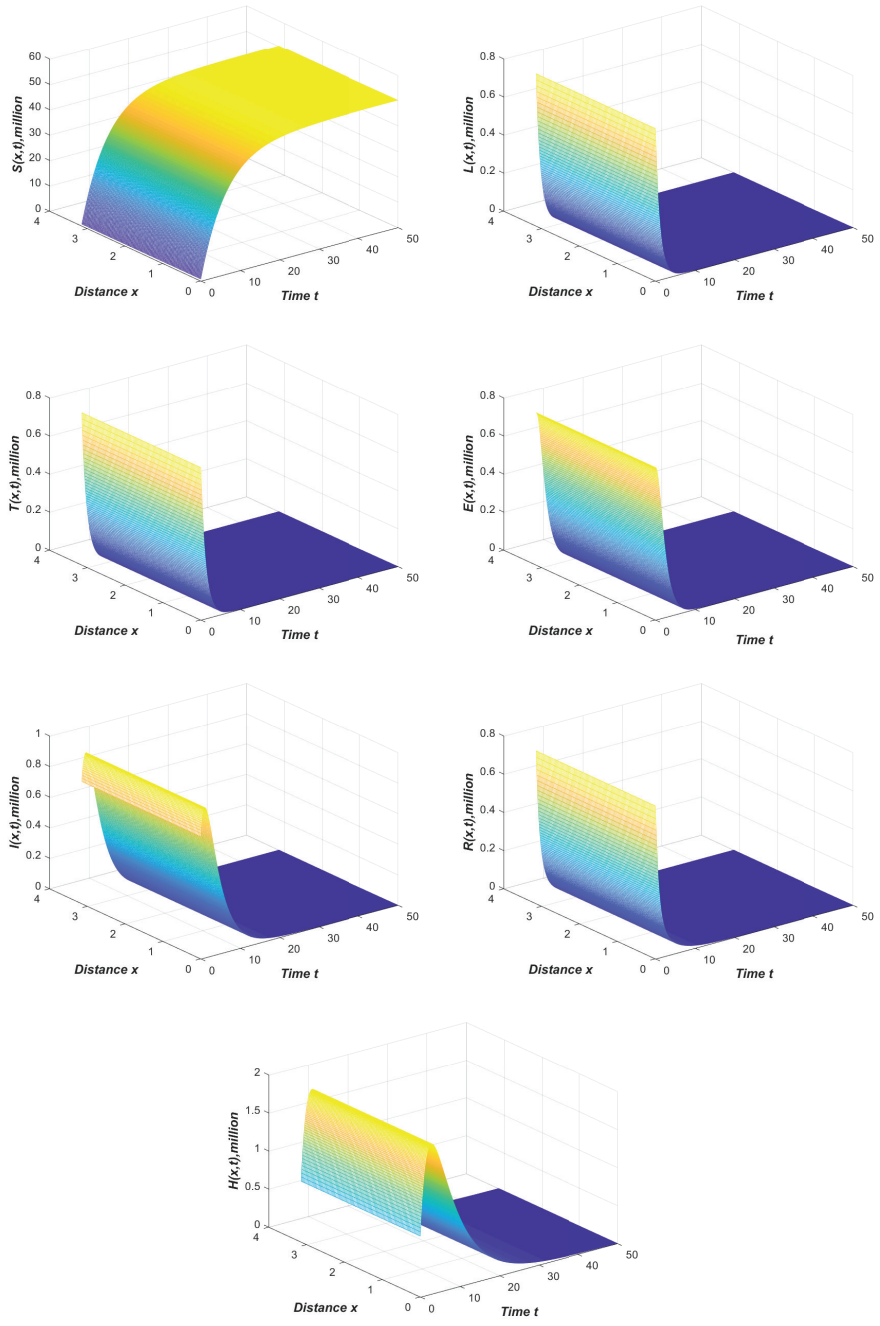

Figure 3. The global stability of disease-free equilibrium of constant coefficient COVID-19 model.

From the Figure 4, we can clearly observe when the scope of the epidemiological investigation expands ($k = 3$), the number of people participating in the epidemiological investigation increases, and strict policies lead to a significant decrease in people transferring between regions. Due to the increase in the proportion of the epidemiological investigation of co-living people, everyone clearly understands that the risk factor of the current epidemic is at a high level; thus, people's desire to go out has decreased significantly. At this stage, everyone can avoid travel unless necessary. On the other hand, expanding testing will also find more infected people.

Next, we examine the epidemiological investigation rate of the population that has moved between regions. We choose $\gamma = 0.3$ and $\gamma = 0.7$, respectively, to simulate the changes of T, E and I (Figure 5).

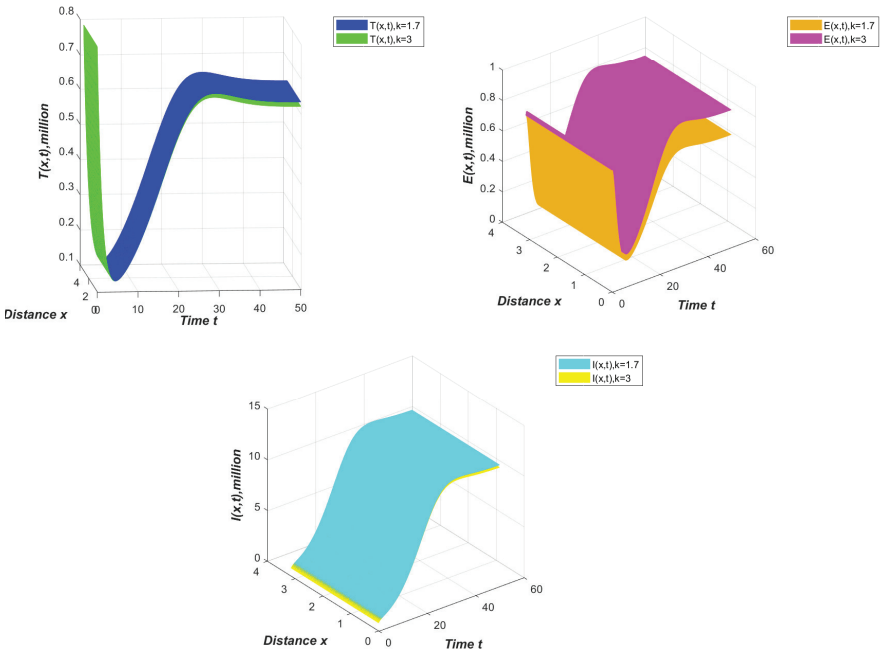

Figure 4. Comparison of compartment T, E and I under $k = 1.7$ and $k = 3$.

From Figure 5, we can find that implementing a strict epidemiological investigation policy can effectively reduce the number of movement between regions, the number of epidemiological investigations and the number of infected people. Strengthening the epidemiological investigation can effectively control the diffusion of COVID-19.

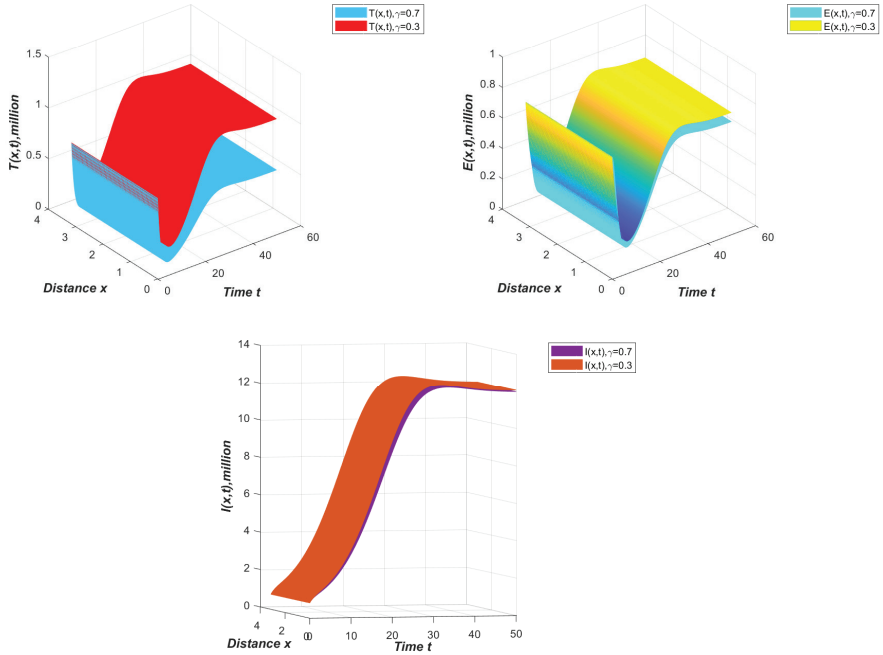

Figure 5. Comparison of compartment T, E and I under $\gamma = 0.3$ and $\gamma = 0.7$.

In Figure 6, while expanding the scope of the epidemiological investigation, we also increased the proportion of the epidemiological investigation. We find that the final effect of this prevention and control policy is similar to Figure 4, because the proportion of the epidemiological investigation of transferors is increased, and the time to find infected people is earlier than that of only expanding the detection scope of the co-living. The strict epidemiological investigation policy shown in Figure 5 has bought more time for the

prevention and control of the epidemic, so that infected persons and close contacts can be detected as early as possible, and the further spread of the epidemic can be controlled. The strict epidemiological investigation in Figure 6 is an important part of the current Chinese government's dynamic clearing policy.

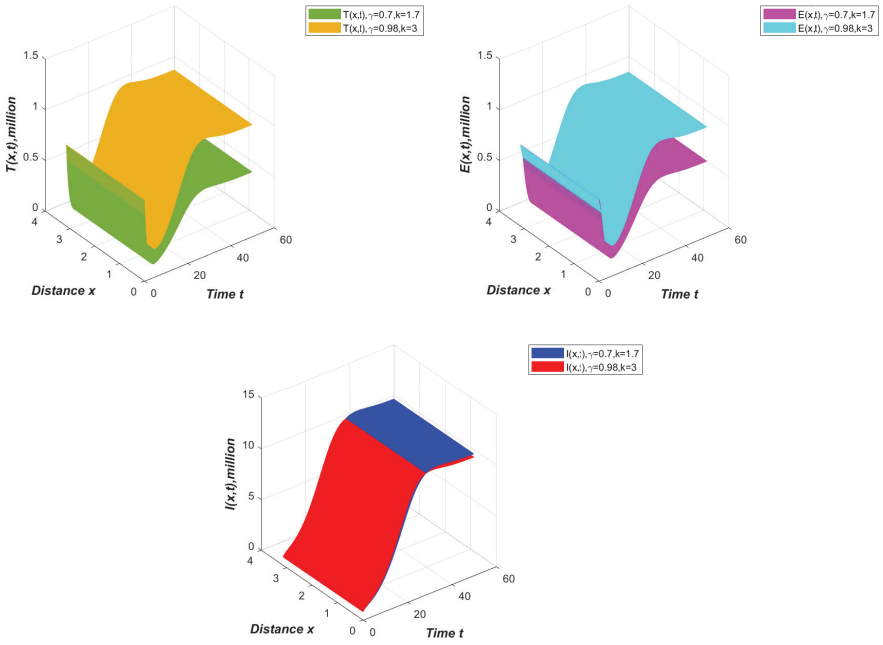

Figure 6. Comparison of compartment T, E and I under different rates of epidemiological investigation.

3.3. Effect of Prevention and Control under Circuit-Breaker Mechanism

In China, the dynamic clearing policy requires that once a confirmed case is found in a certain area, the government will quickly carry out a strict epidemiological investigation, including closure and control management, nucleic acid for all employees, and quarantine and treatment in designated hospitals. The Civil Aviation of China has also introduced stricter prevention and control measures for inbound flights. Once the number of positive passengers exceeds 5, the flight will be grounded. This extremely tight control is also known as a circuit-breaker mechanism. The circuit breaker mechanism is also reflected in our model. Lockdown management and travel restrictions will reduce the travel rate to zero, that is, the parameter $\delta = \omega = 0$ in our model. The centralized quarantine can effectively reduce the contact rate, especially the contact rate with confirmed patients, that is, $\beta_2 = 0$. After considering a strong circuit-breaker mechanism, our model (1) can be evolved, as in Figure 7:

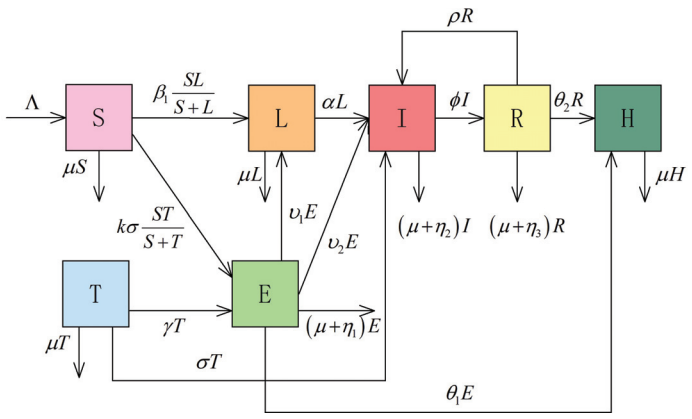

Figure 7. Dynamic clearing COVID-19 model with circuit-breaker mechanism.

The equations corresponding to the evolution model is shown in system (13),

$$\begin{cases} \frac{\partial S}{\partial t} = \nabla \cdot (d_S(x)\nabla S) + \Lambda(x,t) - \beta_1(x,t)\frac{SL}{S+L} - k\sigma(x,t)\frac{ST}{S+T} - \mu(x,t)S, \\ \frac{\partial L}{\partial t} = \nabla \cdot (d_L(x)\nabla L) + \beta_1(x,t)\frac{SL}{S+L} + \nu_1(x,t)E - [\mu(x,t) + \alpha(x,t)]L, \\ \frac{\partial T}{\partial t} = \nabla \cdot (d_T(x)\nabla T) - [\mu(x,t) + \gamma(x,t) + \sigma(x,t)]T, \\ \frac{\partial E}{\partial t} = \gamma(x,t)T + k\sigma(x,t)\frac{ST}{S+T} \\ \quad - [\mu(x,t) + \eta_1(x,t) + \nu_1(x,t) + \nu_2(x,t) + \theta_1(x,t)]E, \\ \frac{\partial I}{\partial t} = \nabla \cdot (d_I(x)\nabla I) + \alpha(x,t)L + \sigma(x,t)T + \nu_2(x,t)E + \rho(x,t)R \\ \quad - [\mu(x,t) + \eta_2(x,t) + \phi(x,t)]I, \\ \frac{\partial R}{\partial t} = \nabla \cdot (d_R(x)\nabla R) + \phi(x,t)I - [\mu(x,t) + \eta_3(x,t) + \rho(x,t) + \theta_2(x,t)]R, \\ \frac{\partial H}{\partial t} = \nabla \cdot (d_H(x)\nabla H) + \theta_1(x,t)E + \theta_2(x,t)R - \mu(x,t)H, \\ \quad x \in \Omega, t > 0, \\ \frac{\partial S}{\partial \mathbf{n}} = \frac{\partial L}{\partial \mathbf{n}} = \frac{\partial T}{\partial \mathbf{n}} = \frac{\partial E}{\partial \mathbf{n}} = \frac{\partial I}{\partial \mathbf{n}} = \frac{\partial R}{\partial \mathbf{n}} = \frac{\partial H}{\partial \mathbf{n}} = 0, \ x \in \partial\Omega, t > 0, \\ S(x,s) = S_0(x,s) \geq 0, L(x,s) = L_0(x,s) \geq 0, T(x,s) = T_0(x,s) \geq 0, \\ E(x,s) = E_0(x,s) \geq 0, I(x,s) = I_0(x,s) \geq 0, R(x,s) = R_0(x,s) \geq 0, \\ H(x,s) = H_0(x,s) \geq 0, x \in \Omega, -\tau \leq s \leq 0. \end{cases} \tag{13}$$

The global dynamic behavior of the model (13) can also be obtained by the method in the previous section.

Combined with the actual COVID-19 epidemic prevention and control, we can find that under the powerful circuit-breaker mechanism, asymptomatic infections and confirmed patients will be quarantined in a centralized manner, and they have no possibility of diffusion at all. Other groups of people in the area will also be in a state of restricted movement due to the sealing policy. They can only move within the community, and the living materials are uniformly distributed by the government. Therefore, the diffusion coefficients in model (13) are all equal to 0 or tend to 0 under the circuit-breaker mechanism. Next, we simulate the model with the circuit-breaker mechanism. Select $\delta = \omega = \beta_2 = 0$, and other data will still use the data in Table 2; then, we obtain Figure 8.

From Figure 8, we can clearly observe that after cutting off contact and travel for the first time, with high-density nucleic acid detection, the effect of epidemic control has been greatly improved. At this time, the model tends to have a disease-free equilibrium and is globally asymptotically stable. Comparing Figure 2, we can find that the other simulated data are identical except for $\delta = \omega = \beta_2 = 0$. However, Figure 2 tends towards the endemic equilibrium. This demonstrates that the circuit-breaker mechanism can control the diffusion of COVID-19 faster and make the disease disappear.

3.4. Epidemic Situation in China after the Opening of Epidemiological Investigation Policy

On 7 December 2022, the Chinese government released the policy of epidemic prevention and control. Epidemiological investigations such as trip codes and all staff nucleic acids were cancelled. In the following month, as many as 70% of Chinese people were infected with COVID-19, and the convalescents began to travel in large numbers. According to the data officially released by China, from 8 December 2022 to 12 December 2023, there were 59,938 deaths related to COVID-19 in hospitals in medical institutions across the country, including 54,435 deaths from underlying diseases combined with COVID-19 infection. The average age of death cases is 80.3 years, and more than 90% of them are accompanied by basic diseases.

If we choose $k = \gamma = \nu_1 = \nu_2 = \theta_1 = \eta_1 = 0$ in system (1), we can simulate the current COVID-19 diffusion trend in China and the state of the people.

By comparing Figure 2 and Figure 9, we can find that the number of people moving between regions has increased significantly since the epidemiological survey was released. Due to the lack of mandatory nucleic acid testing, the number of asymptomatic patients and infected persons has also increased significantly. Because multiple strains of viruses

coexist in China, the number of secondary infections and relapses has also increased dramatically, and the number of completely cured patients has decreased. This comparison just demonstrates that the epidemiological investigation has a very good control over the spread of global infectious diseases. Although COVID-19 is now classified as a Class B infectious disease, an epidemiological investigation is still an effective means to control the epidemic situation when the number of infected people increases sharply due to the virus mutation. Epidemiological investigation can also be used for reference when dealing with other global epidemics in the future.

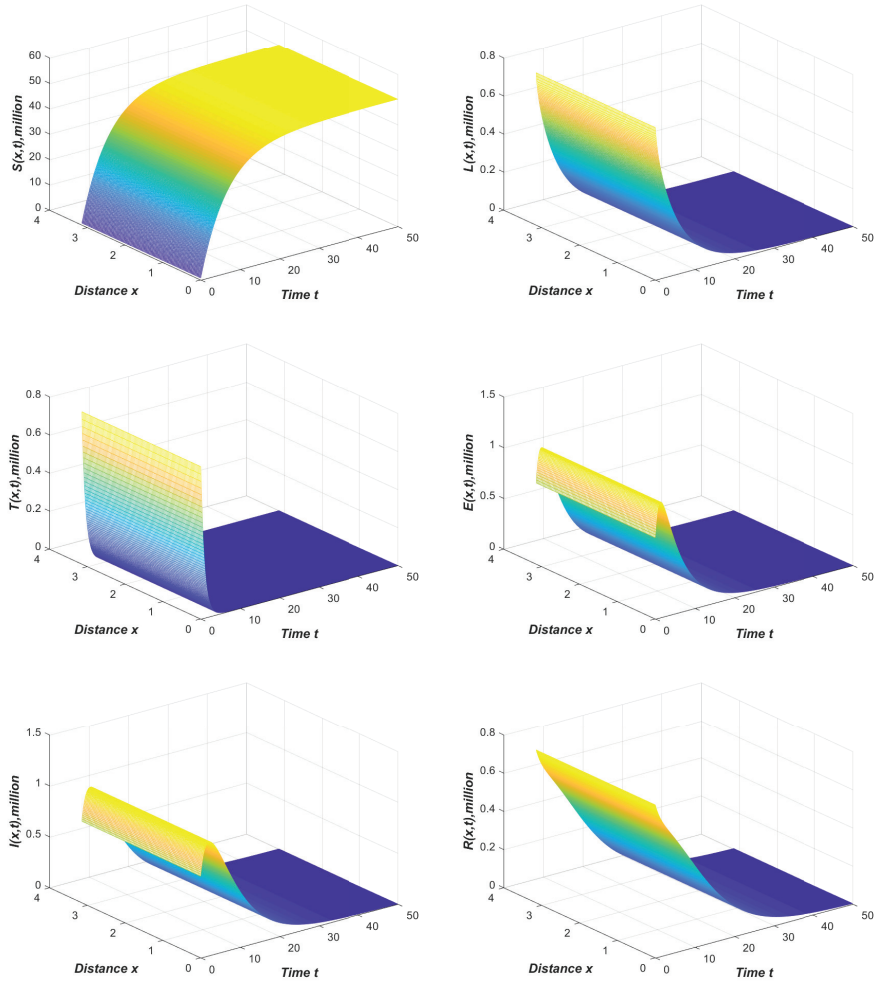

Figure 8. The dynamics of temporal-spatial heterogeneity in COVID-19 epidemic with circuit-breaker mechanism when $\delta = \omega = \beta_2 = 0$.

Based on the previous introduction, we know that in December 2022, the Chinese government cancelled the strategy of conducting epidemic investigations and instead monitored key populations. There has been a surge in social infections. We have compiled the cumulative confirmed cases announced on the official website of the Chinese Health Commission in December (starting on 24 December 2022, the Chinese government no longer released data on a daily basis).

We have listed the data for December 2022 in Table 3.

Comparing the above data with the number of infected individuals simulated by our model, we can draw the following simulation diagram, in which we select the initial value of 30,000 people in the infected person's compartment.

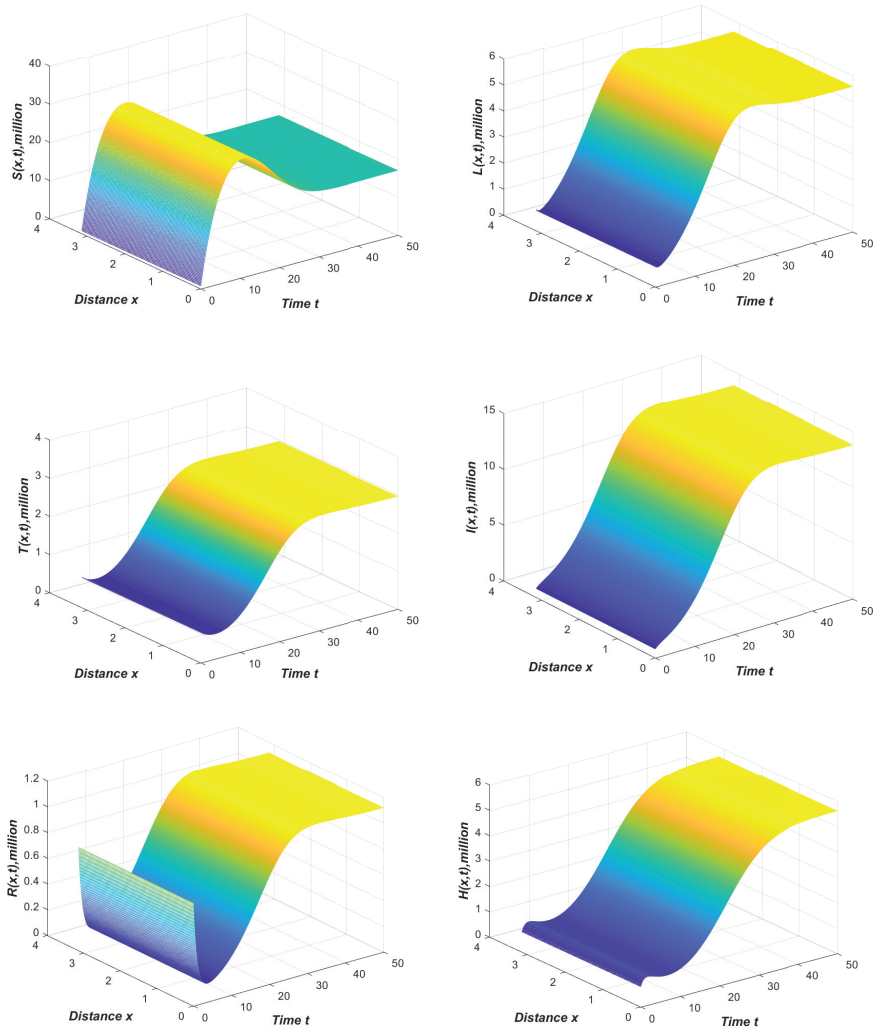

Figure 9. The spread trend of the COVID-19 in China without epidemiological investigation.

Table 3. Total confirmed cases in China from December 1st to December 23rd.

Date	Total Confirmed Cases	Date	Total Confirmed Cases
1 Dec. 2022	327,964	2 Dec. 2022	331,952
3 Dec. 2022	336,165	4 Dec. 2022	340,483
5 Dec. 2022	345,529	6 Dec. 2022	349,938
7 Dec. 2022	354,017	8 Dec. 2022	357,652
9 Dec. 2022	360,734	10 Dec. 2022	363,072
11 Dec. 2022	365,312	12 Dec. 2022	367,627
13 Dec. 2022	369,918	14 Dec. 2022	371,918
15 Dec. 2022	374,075	16 Dec. 2022	376,361
17 Dec. 2022	378,458	18 Dec. 2022	380,453
19 Dec. 2022	383,175	20 Dec. 2022	386,276
21 Dec. 2022	389,306	22 Dec. 2022	393,067
23 Dec. 2022	397,195	24 Dec. 2022	None

From Figure 10, we can observe that the simulation effect of our model is in good agreement with the actual data.

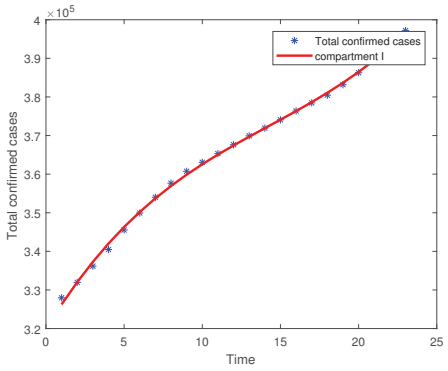

Figure 10. Comparison between official data and compartment simulation.

In the numerical simulation above, we simulated the prevention and control effects of various epidemiological investigations. We summarize the four most important categories as follows:

1. If the data in Table 2 is selected, the endemic equilibrium is globally asymptotically stable.
2. If the contact rate is very low, the disease-free equilibrium is globally asymptotic and stable.
3. If it is a circuit-breaker mechanism, the disease-free equilibrium is globally asymptotic and stable.
4. When opening the epidemiological investigation policy; the endemic equilibrium is globally asymptotically stable.

4. Conclusions

By 2023, the global COVID-19 epidemic has been effectively controlled, but there are still sporadic outbreaks in some countries. In April 2023, India experienced another wave of COVID-19 outbreaks. Experts also predict that China will have a second wave of COVID-19 from May to June 2023. Therefore, daily monitoring and prevention cannot be relaxed. In this paper, we focused on the impact of epidemiological investigation policies on the COVID-19 outbreak. In order to more intuitively demonstrate the practicality of our results, we discuss the impact of the epidemiological investigation on epidemic prevention and control in light of the current spread of the COVID-19 epidemic. Using Theorem 1, we can obtain that system (1) has a global exponentially attracting set $\mathcal{A}^*$, then we prove that the COVID-19 model with travel and an epidemiological investigation persists uniformly and that the model has a global exponentially attracting set. Compared with the results in [17], the condition (4) in this article is easier to verify, and the amount of calculation is much less. Our model covers epidemiological investigations at different stages of the COVID-19 epidemic in China. By selecting appropriate parameters to simulate, we provide intuitive results of various epidemiological investigation policies. Although the current COVID-19 epidemic has achieved good control results, other diseases such as the influenza A virus still pose a threat to human health, and the coronavirus may undergo further mutations in the future. The epidemiological investigation experience accumulated during the COVID-19 epidemic can be applied to the prevention and control of other diseases.

The COVID-19 epidemic in China has been effectively controlled, with occasional recurrences and new cases emerging. Based on the current situation of epidemic prevention and control, it is recommended that the Chinese government strengthen the popularization of public health knowledge. Conduct necessary epidemiological investigations on key populations, such as those entering the epidemic area, newly diagnosed and relapsed individuals and their close contacts, and effectively monitor the variation of domestic strains.

Through research, we find that the global exponential attractor theory is more convenient than the Lyapunov method in discussing the long-term dynamic behavior of multi equation coupled systems, and the verification conditions provided in this paper are conve-

nient for researchers of different research directions. Although the COVID-19 pandemic has become a thing of the past in most countries, epidemiological investigations as a prevention and control strategy can be borrowed from the prevention and control of other diseases.

Author Contributions: Methodology, C.-C.Z., J.Z. and J.S.; Formal analysis, J.Z.; Writing—original draft, C.-C.Z. and J.Z.; Writing—review & editing, C.-C.Z., J.Z. and J.S. All authors have read and agreed to the published version of the manuscript.

Funding: This work was supported by the Natural Science Foundation of Jiangsu Province, China (Grant No. BK20190578).

Data Availability Statement: The data in this article are all public data published on the official websites of the World Health Organization, the Chinese Health Commission and everyone can check them on the corresponding websites.

Conflicts of Interest: The authors declare that they have no competing interests.

References

1. Feng, L.X.; Jing, S.L.; Hu, S.K.; Wang, D.F.; Huo, H.F. Modelling the effects of media coverage and quarantine on the COVID-19 infections in the UK. *Math. Biosci. Eng.* **2020**, *17*, 3618–3636. [CrossRef]
2. Feng, X.; Chen, J.; Wang, K.; Wang, L.; Zhang, F.; Jin, Z.; Zou, L.; Wang, X. Phase-adjusted estimation of the COVID-19 outbreak in South Korea under multi-source data and adjustment measures: A modelling study. *Math. Biosci. Eng.* **2020**, *17*, 3637–3648. [CrossRef]
3. Machado, B.; Antunes, L.; Caetano, C.; Pereira, J.F.; Nunes, B.; Patricio, P.; Morgado, M.L. The impact of vaccination on the evolution of COVID-19 in Portugal. *Math. Biosci. Eng.* **2021**, *19*, 936–952. [CrossRef] [PubMed]
4. Suzuki, A.; Nishiura, H. Transmission dynamics of varicella before, during and after them COVID-19 pandemic in Japan: A modelling study. *Math. Biosci. Eng.* **2022**, *19*, 5998–6012. [CrossRef] [PubMed]
5. Yang, C.; Wang, J. Modeling the transmission of COVID-19 in the USA case study. *Infect. Dis. Model.* **2021**, *6*, 195–211.
6. Zhu, C.C.; Zhu, J. The effect of self-limiting on the prevention and control of the diffuse COVID-19 epidemic with delayed and temporal-spatial heterogeneous. *BMC Infect. Dis.* **2021**, *21*, 1145. [CrossRef]
7. Dai, Y.; Zhang, R.; Jiang, Y.; Jin, H.; Zhao, J.; Guo, A.; Chen, X.; Fan, D.; Yang, L. Infection control management strategy for operating room during COVID-19 pandemic. *Ann. Transl. Med.* **2022**, *10*, 1252. [CrossRef]
8. Luo, X.F.; Feng, S.; Yang, J.; Peng, X.L.; Cao, X.; Zhang, J.; Yao, M.; Zhu, H.; Li, M.Y.; Wang, H.; et al. Nonpharmaceutical interventions contribute to the control of COVID-19 in China based on a pairwise model. *Infect. Dis. Model.* **2021**, *6*, 643–663. [CrossRef]
9. Mbogo, R.W.; Orwa, T.O. SARS-COV-2 outbreak and control in Kenya-Mathematical model analysis. *Infect. Dis. Model.* **2021**, *6*, 370–380 [CrossRef] [PubMed]
10. Sabirli, R.; Koseler, A.; Goren, T. High GRP78 levels in Covid-19 infection: A case-control study. *Life Sci.* **2021**, *265*, 118781. [CrossRef]
11. Tang, K.H.D.; Chin, B.L.F. Correlations between control of COVID-19 transmission and influenza occurrences in Malaysia. *Public Health* **2021**, *198*, 96–101. [CrossRef]
12. Thongtha, A.; Modnak, C. Optimal COVID-19 epidemic strategy with vaccination control and infection prevention measures in Thailand. *Infect. Dis. Model.* **2022**, *7*, 835–855. [CrossRef]
13. Akter, S.; Jin, Z. A fractional order model of the COVID-19 outbreak in Bangladesh. *Math. Biosci. Eng.* **2022**, *20*, 2544–2565. [CrossRef] [PubMed]
14. Martinez-Fernandez, P.; Fernandez-Muniz, Z.; Cernea, A.; Fernandez-Martinez, J.L.; Kloczkowski, A. Three Mathematical Models for COVID-19 Prediction. *Mathematic* **2020**, *17*, 506. [CrossRef]
15. Childs, M.R.; Wong, T.E. Assessing parameter sensitivity in a university campus COVID-19 model with vaccinations. *Infect. Dis. Model.* **2023**, *8*, 374–389. [CrossRef]
16. Yang, H.; Lin, X.; Li, J. A Review of Mathematical Models of COVID-19 Transmission. *Contemp. Math.* **2023**, *4*, 75–98. [CrossRef]
17. Zhu, C.C.; Zhu, J. Spread trend of COVID-19 epidemic outbreak in China: Using exponential attractor method in a spatial heterogeneous SEIQR model. *Math. Biosci. Eng.* **2020**, *17*, 3062–3087. [CrossRef] [PubMed]
18. Zhu, C.C.; Zhu, J.; Liu, X.L. Influence of spatial heterogeneous environment on long-term dynamics of a reaction-diffusion SVIR epidemic model with relapse. *Math. Biosci. Eng.* **2019**, *16*, 5897–5922. [CrossRef]
19. Zhang, J.; Kloeden, P.E.; Yang, M.; Zhong, C.K. Global exponential κ-dissipative semigroups and exponential attraction. *Discrete Contin. Dyn. Syst.* **2017**, *37*, 3487–3502. [CrossRef]
20. Vrabie, I.I. C_0 *Semigroups and Application*; Elsevier Science BV: New York, NY, USA, 2003.
21. Wu, J. *Theory and Applications of Partial Functional Differential Equations*; Applied Mathematical Sciences; Springer: New York, NY, USA, 1996.

22. Zhu, C.C.; Zhu, J. Dynamic analysis of a delayed COVID-19 epidemic with home quarantine in temporal-spatial heterogeneous via global exponential attractor method. *Chaos Solitons Fractals* **2021**, *143*, 110546. [CrossRef]
23. Ma, T.; Wang, S. *Phase Transition Dynamics*; Springer Science+Business Media, LLC.: Berlin, Germany, 2014.
24. Tang, B.; Xia, F.; Bragazzi, N.L.; McCarthy, Z.; Wang, X.; He, S.; Sun, X.; Tang, S.; Xiao, Y.; Wu, J. Lessons drawn from China and South Korea for managing COVID-19 epidemic: Insights from a comparative modeling study. *ISA Trans.* **2022**, *124*, 164–175. [CrossRef] [PubMed]
25. Notification of Pneumonia Outbreak of New Coronavirus Infection. Available online: http://www.nhc.gov.cn; http://en.nhc.gov.cn (accessed on 1 January 2023).
26. World Health Statistics. 2013. Available online: http://www.who.int (accessed on 1 January 2023).

mathematics

MDPI

Article

Invadopodia Formation in Cancer Cell: The Mathematical and Computational Modelling Based on Free Boundary Problem

Muhammad Akmal Ramlee [1,*], Nuha Loling Othman [1,*] and Takashi Suzuki [2]

[1] Faculty of Computer Science and Information Technology, Universiti Malaysia Sarawak, Jalan Datuk Mohd Musa, 94300 Kota Samarahan, Sarawak, Malaysia
[2] Center for Mathematical Modeling and Data Science, Osaka University, 1-3 Machikaneyama-cho, Toyonaka City 560-8531, Osaka, Japan; suzuki@sigmath.es.osaka-u.ac.jp
* Correspondence: muhdakmal.lee@gmail.com (M.A.R.); zzt230c@gmail.com (N.L.O.)

Abstract: We present a mathematical model of an individual cell to expand the simulation of invadopodia formation to a three-dimensional (3D) domain for a more realistic complexity. Simulating invadopodia replication in order for it to be biologically relevant is important since it helps us to understand cancer invasion and metastasis better as well as giving some insight into investigating ways to stop the spread of this fatal disease. Invadopodia formation is formulated using the Stefan problem approach, where the free boundary is characterised by the Stefan free boundary condition, in which the boundary membrane is not known in advance. Level set method is proposed to indicate the behaviour of the cell interface and the motion of the plasma membrane. An enthalpy method (phase-transition problem) is used to describe the cell membrane diffusion. In addition to this, we were able to improve the simulation outcome, giving it a more realistic complexity by using a different simulation technique and domain as well as a different data set. Singularities and instabilities were eliminated. The results that were achieved have the potential to be helpful for novel approaches or to be extended to other methods in the development of a more accurate numerical simulation.

Keywords: invadopodia; individual cell model; free boundary problem; finite element method; Stefan problem; level set method; phase transition; enthalpy

MSC: 92-08; 92-10

1. Introduction

The term cancer encompasses a variety of diseases that are broadly categorised by abnormal cell behaviour which act differently from normal cells due to the gene mutations that alter the normal cellular instructions [1]. Tissue invasion and metastasis are one of the "hallmarks of cancer" [2,3] and the leading cause of death among cancer patients [4]. Invasion of cancer cells is the capacity of the cells to disrupt the basement membrane (BM) and secondary tumours arise when it penetrates the surrounding tissue or extracellular matrix (ECM), also referred to as metastasis.

The key factor in tumour invasion and metastasis is proteolytic deterioration of the ECM [5,6] which are propelled by actin-rich protrusions of the plasma membrane, also called invadopodia [7]. Invadopodia is also called 'invasive feet' as it is most commonly detected on the basal surfaces of invasive cancer cells; invadopodia have the ability to invade through the ECM [8]. The morphology of invadopodia is a small punctuated finger-like protrusion or elongated shapes [9]. According to Saitou et al. [10], cancer cells can form one to ten invadopodia with a lifespan of several tens of minutes to 60 min and a size ranging from 0.05 to 2 μm [11]. Numerous cell biological processes must be coordinated for the formation of invadopodia and the degradation of ECM. The formation of invadopodia and the degradation of ECM require the coordination of numerous cell biological processes. The molecular dynamics and biological phenomena related to invadopodia formation and

ECM degradation are further detailed in [12]. Figure 1 depicts the scheme of invadopodia in invasive cancer cell while Figure 2 shows the role of invadopodia in cancer invasion and metastasis.

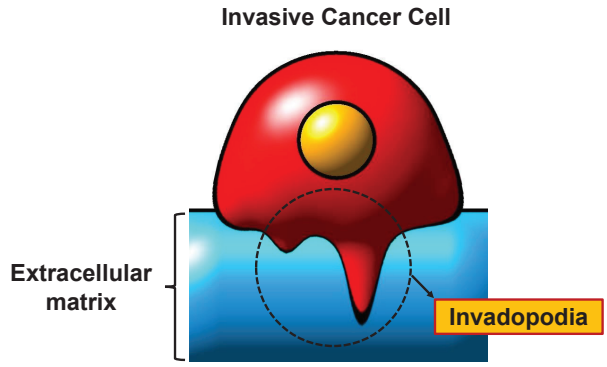

Figure 1. A scheme of invadopodia.

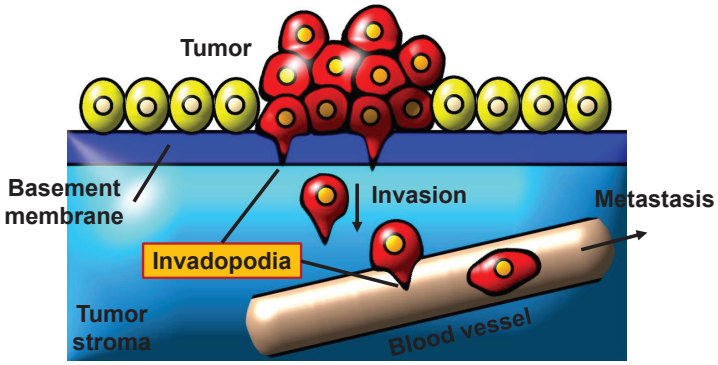

Figure 2. Invadopodia's role in cancer invasion and metastasis.

Over the past decade, numerous studies have been carried out to comprehend the mechanism of tumour growth and cancer invasion from a mathematical point of view using continuous and discrete models, particularly in partial differential equations (PDEs) and ordinary differential equations (ODEs) [13–16]. Some studies have been successful in capturing the structure of cancer at the tissue level [17,18]. At present, the model of cancer cell invasion at the subcellular level (single cell) is of particular interest [9,10,12,19–21], while numerical analysis on the cancer cell invasion model with the free boundary problem was conducted in [22].

Saitou et al. [10] investigated the formation of invadopodia by introducing mathematical models of several fundamental processes. In [10], they analysed the spatio-temporal dynamics of the model in two spatial dimensions by using the numerical computational approach. In their results, the dynamics of the model is explored, particularly in space and time for two spatial dimensions by using the Monte-Carlo approach. This study is extremely significant because it offers new insight on how invadopodia exist in cancer cells. Numerous subsequent studies built on this one by using or modifying the model presented here such as [9,12,19–21].

For instance, ref. [20] investigates a free boundary problem for cell protrusion formation where the aim of the paper is to model the chemical interactions between the cell and its environment during the process of invadopodia formation. They prove the free boundary problem is well-posed. They eventually exhibit the main biological feature that can be accounted for via the model which is the formation of invadopodia. Ref. [9] present a superconvergent second order Cartesian method to solve a free boundary problem with two harmonic phases coupled through the moving interface. The model was proposed to

describe the formation of cell protrusions. The finite difference method (FDM) proposed in this paper consists of second-order discretisation and a new stabilised ghost fluid method.

This paper aims to improve the simulation of invadopodia formation with respect to the previous research of [12] in which the results were simulated in a two-dimensional (2D) domain and an in silico model of an individual cell was presented. Therefore, we simulated our results in a 3D domain for accurate results and conditions where the complexities of simulations are more realistic. Simulating invadopodia formation accurately in order for it to be biologically relevant is important since it helps us to understand cancer invasion and metastasis better, as well as giving some insight into investigating ways to stop the spread of this fatal disease. We note that in the previous work of [12], the simulations demonstrate the existence of singularities and instabilities. For that reason, eliminating the existence of singularities and instabilities is crucial in simulating the results for the solution to be more accurate.

2. Materials and Methods

There are two parts to this section, individual cell model and numerical scheme, in accordance with [12].

2.1. Individual Cell Model

2.1.1. Classical Solution Scheme

This subsection describes the mathematical cell-deformation model that explains the invadopodia-formation process, as depicted in Figure 3. According to [12,20], ECM is in the outer domain of the cell. We define the flux of type 1 matrix metalloproteinase (MT1-MMP) enzymes, denoted by $g(x,t)$. MT1-MMP generates ligands c_* which is a flux-degraded matrix at the cell boundary which then diffuses into the ECM. Ligands will then activate signals that diffuse within the cell when bound to the cell membrane.

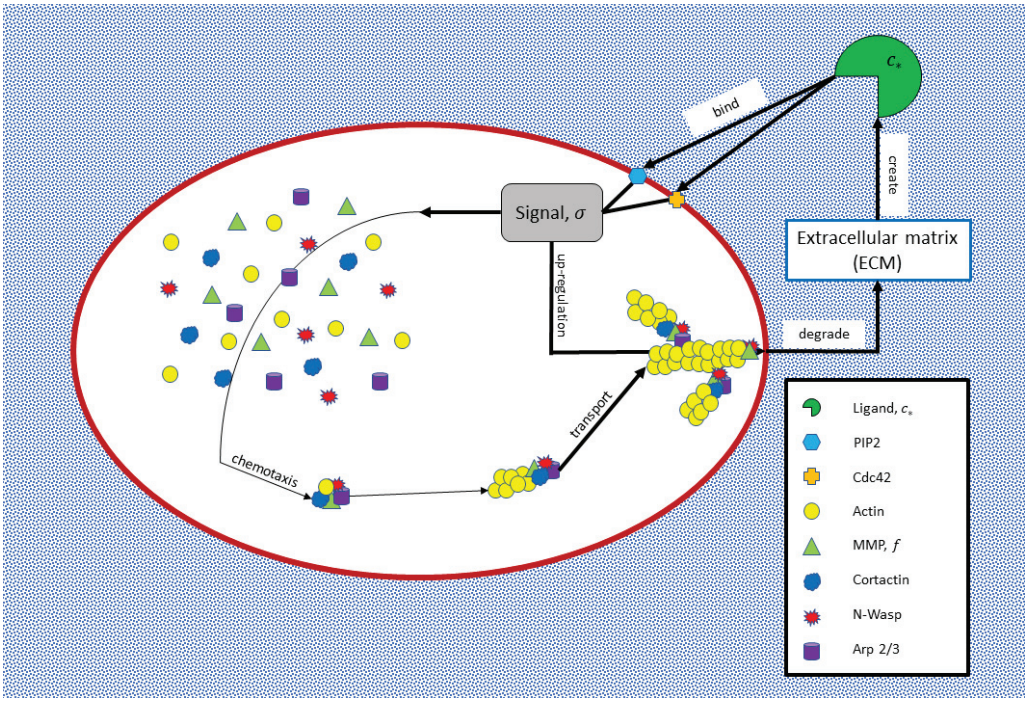

Figure 3. An individual cell model.

The model of a single cell is described by using the Eulerian approach. Let $\psi(x,t)$ be defined across the entire domain Ω to detect the cell membrane. The plasma membrane is define as:

$$\Gamma_t = \{x \in \Omega | \psi(x,t) = 0\}, \tag{1}$$

where Ω is the Lipschitz domain indicating the cancer cell with smooth boundary, $\partial\Omega$, and a particle on the moving interface Γ_t is defined by x.

While the zero level set function, ψ detects the location of the plasma membrane which satisfies:

$$\psi_t(x,t) + v \cdot \nabla\psi(x,t) = 0 \tag{2}$$

which is a smooth level set function, whereas at the interface, v is defined as the velocity of the plasma membrane:

$$v = \gamma_n(\nabla\sigma - \nabla c_*) \quad \text{on} \quad \Gamma_t \tag{3}$$

where γ_n is a positive constant and σ is the signal gradient inside the cell. Keep in mind that it would be impossible for the domain to grow the shape's volume, which can lead to discontinuity, because velocity v is only defined on the boundary. Since the zero level set function takes the plasma membrane into account, velocity extension is defined throughout the entire domain to prevent discontinuity as:

$$\begin{gathered}(\nabla\psi \cdot \nabla)w = 0, \quad \forall x \in \Omega, \quad w \in (x,y) \\ w = v \quad \Gamma\end{gathered} \tag{4}$$

where:

$$v|_{\psi(x,t)=0} = \nabla\sigma|_{\psi(x,t)=0} - \nabla c_*|_{\psi(x,t)=0}.$$

Hence, substituting (3) into (2), we obtain:

$$\psi_t + v \cdot \nabla\psi = 0 \quad \text{on} \quad \Gamma_t. \tag{5}$$

The cell's plasma membrane may shrink or expand. On the plasma membrane, Γ_t and MMPs, f degraded ECM and c and produced an ECM fragment that is ligands. Henceforth, the chemical reactions that occur between ECM and MMPs are derived by:

$$c_t + \nabla \cdot vc = -\kappa_c fc, \qquad c_{*t} + \nabla \cdot vc_* = \kappa_c fc \qquad \text{on} \quad \bigcup_{0<t<T} \Gamma_t \times \{t\} \tag{6}$$

where κ_c is the reaction rate of the diffusion coefficient. Then, f and σ are defined inside the cell as:

$$\begin{aligned}&\sigma_t = d_\sigma \Delta\sigma \quad \text{in} \quad \bigcup_{0<t<T} \omega_n^t \times \{t\}, \qquad \sigma|_{\Gamma_t} = c_* \quad \text{on} \quad \bigcup_{0<t<T} \omega_n^t \times \{t\} \\ &f_t = d_f \Delta f + k_f\sigma - \lambda_f f \quad \text{in} \quad \bigcup_{0<t<T} \omega_n^t \times \{t\}.\end{aligned} \tag{7}$$

Since the density of MMPs does not change during ECM fibre proteinase cutting, it can be concluded that:

$$c_{*t} = d_{c_*}\Delta c_* \quad \text{in} \quad \bigcup_{0<t<T} \omega_c^t \times \{t\}, \qquad \frac{\partial c_*}{\partial \nu} = g \quad \text{on} \quad \bigcup_{0<t<T} \omega_c^t \times \{t\}. \tag{8}$$

We define $\omega_n^t = \{x \in \Omega | \psi(x,t) < 0\} \subset\subset \Omega$ as a one-domain inside cell. Hence:

$$Q_n = \bigcup_{0<t<T} \omega_n^t \times \{t\} \tag{9}$$

and $\omega_c^t = \{x \in \Omega | \psi(x,t) > 0\}$ as an outside cell. Thus:

$$Q_c = \bigcup_{0<t<T} \omega_c^t \times \{t\}. \tag{10}$$

If the solution of $y = y(t)$ to:

$$\frac{dy}{dt} = v(y,t), \qquad y|_{t=s} = x$$

is denoted by $y = U(t,s)x$, then:

$$\frac{D\psi}{Dt} = \psi_t + v \cdot \nabla = -(\nabla \cdot v)\psi.$$

Substituting (9) and (10) into (7), we obtain:

$$\begin{aligned} \sigma_t = d_\sigma \Delta\sigma \quad \text{in} \quad Q_n, \qquad \sigma|_{\Gamma_t} = c_* \quad \text{on} \quad \Gamma \\ f_t = d_f \Delta f + k_f \sigma - \lambda_f f \qquad \text{in} \quad Q_n. \end{aligned} \tag{11}$$

The total mass of conservation of f guarantees, by Liouville's Theorem, that the following derivations on the boundary will be produced:

$$d_f \frac{\partial f}{\partial \nu} + (\nu \cdot v) f = 0 \qquad \text{on} \quad \Gamma = \bigcup_{0<t<T} \Gamma_t \times \{t\}. \tag{12}$$

As the MMPS density at the boundary will not change during cutting through the fiber-proteinases of ECM, it holds that:

$$c_{*t} = d_{c_*} \Delta c_* \quad \text{in} \quad Q_c, \qquad c_*|_{\partial\Omega} = 0, \qquad \frac{\partial c_*}{\partial \nu} = g \quad \text{on} \quad \Gamma. \tag{13}$$

Figure 4 shows a simplified version of the signalling pathways depicted in Figure 3. From Figure 4, the MMP generates ligands on the cell membrane which then diffuses into the ECM as described in (13). Ligands will then activate signals that diffuse within the cell when bound to the cell membrane as in (11). The membrane is then pushed by the interface's normal velocity (3).

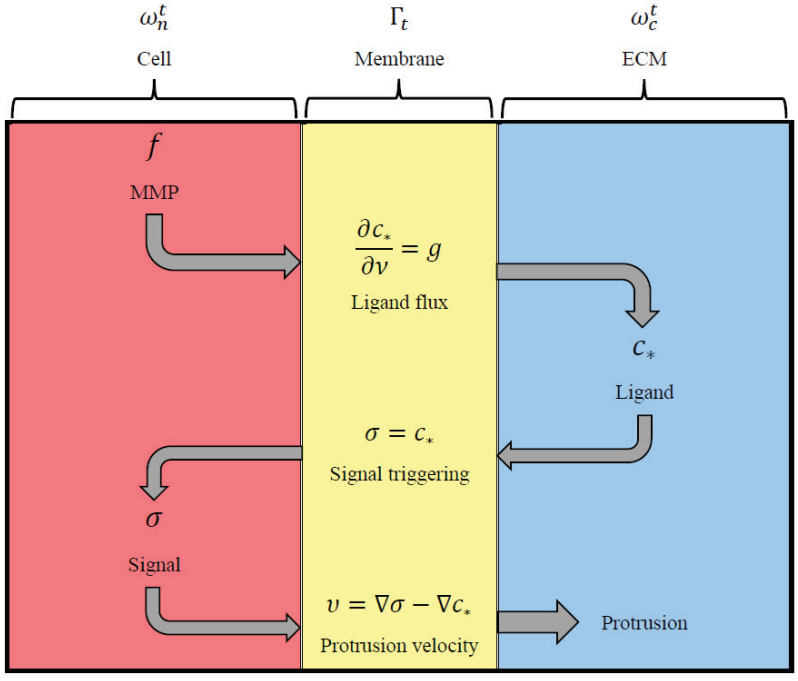

Figure 4. A schematic representation of the molecular interactions.

2.1.2. Free Boundary Problem

In order to simulate the formation of invadopodia, we proposed velocity extension to the entire domain of the cell. The cell model from Figure 3 was simplified, as shown in Figure 5. According to [12,20], when the velocity of protrusion is not imposed, the free boundary problem enables accurate membrane localisation even when it is unknown with respect to the PDE systems. As a result, we used the cell membrane as a free boundary to distinguish between any activity occurring within and outside of cells.

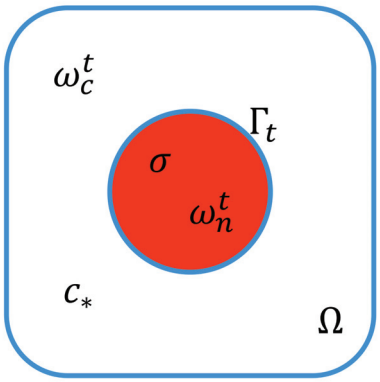

Figure 5. A simple cell model.

Given MT1-MMP at any time on the cell membrane and signal generation for actin polymerisation is represented by:

$$d_\sigma^{-1}\sigma_t = \Delta\sigma \qquad \text{in} \quad Q_n, \qquad \sigma|_{\partial\omega_c^t} = c_* \tag{14}$$

while degradation of ECM is:

$$d_{c_*}^{-1}c_{*t} = \Delta c_* \qquad \text{in} \quad Q_c, \qquad \frac{\partial c_*}{\partial \nu} = 0 \tag{15}$$

where $d > 0$ is a diffusion coefficient. Let $\sigma = c_* = g(x,t)$, considering the cell's primary problem. Define:

$$\theta = \begin{cases} \sigma \text{ in } Q_n = \{\psi < 0\} \\ c_* \text{ in } Q_c = \{\psi > 0\} \end{cases}. \tag{16}$$

Next, define the Stefan condition. Suppose that g is continuous and diffuse where $\pm\psi > 0$ if and only if $\pm g > 0$; it holds that:

$$\theta = g, \qquad \nu = -[\nabla\theta]_-^+. \tag{17}$$

Therefore:

$$\begin{aligned} \gamma_n^{-1}\psi_t &= -\gamma_n^{-1}(v\cdot\nu)\frac{\partial\psi}{\partial\nu} \\ &= \left(\frac{\partial c_*}{\partial\nu} - \frac{\partial\sigma}{\partial\nu}\right)\frac{\partial\psi}{\partial\nu} \\ &= \left[\frac{\partial\theta}{\partial\nu}\right]_-^+\frac{\partial\psi}{\partial\nu} \end{aligned} \tag{18}$$

where $\theta = g = c_*$ on Γ.

2.2. Numerical Scheme

2.2.1. Weak Form Derivation

In this subsection, we will solve the modelling of invadopodia formation and migration of a single cell. Based on the phase-transition formulation, a mathematical model was developed to address these problems. According to [12,23,24], the problems are characterised as time-dependent differential equations with boundary conditions at an unknown interface concerning which it has to be part of the solution. Let $\Omega \subset \mathbb{R}^N$, $N = 1, 2, \ldots$ be a smooth bounded domain and:

$$\begin{aligned} H(u)_t = \Delta u \qquad & \text{in} \quad Q = \Omega \times (0,T) \\ u\,|_{\partial\Omega} = 0, \qquad & u\,|_{t=0} = u_0(x) \end{aligned} \tag{19}$$

where $u = u(x,t)$ represents the temperature distribution and H represents the enthalpy function.

Let $\varphi \in H^1(\Omega)$ be trial function:

$$-\int_\Omega \left(\frac{\partial}{\partial x}\frac{\partial u}{\partial x} + \frac{\partial}{\partial y}\frac{\partial u}{\partial y}\right)\varphi - \int_\Omega H(u)_t\varphi = 0.$$

Using integration by parts:

$$-\int_\Omega \frac{\partial}{\partial x}\left(\varphi\frac{\partial u}{\partial x}\right) + \frac{\partial}{\partial y}\left(\varphi\frac{\partial u}{\partial y}\right) - \left(\frac{\partial u}{\partial x}\frac{\partial \varphi}{\partial x} + \frac{\partial u}{\partial y}\frac{\partial \varphi}{\partial y}\right) - H(u)_t\varphi \; d\Omega = 0$$

Hence:

$$\int_\Omega (\nabla u \cdot \nabla\varphi) - H(u)_t\varphi \; d\Omega - \int_{\partial\Omega} (\nabla u)\cdot\varphi\nu \; d\Omega. \tag{20}$$

2.2.2. Stefan Problems—Phase-Transition Formulation

Generally, Stefan problems is the emergence of smooth boundaries or interfaces between different phases of a substance that result from a phase transformation [12,25]. Therefore, for this research, Stefan problems are involved in the deformation of the cancer cell membrane or interfaces between inner and outer cell domains that arise from the molecular interactions to produce protrusions called invadopodia. Defining the temperature field is represented by Q and its evolution is given by:

$$\begin{aligned} H(u)_t &= \Delta u \qquad\quad \text{in} \quad Q\setminus\Gamma \\ [u]^+_- = 0, &\qquad [H(u)]^+_- = \ell \qquad \text{on} \quad \Gamma \end{aligned} \tag{21}$$

where $\Gamma = \{\Phi = 0\}$. On jump condition Γ, it is taken between the inner and outer cell or otherwise the following holds:

$$\ell v = -\left[k_+\frac{\partial u_+}{\partial \nu} - k_-\frac{\partial u_-}{\partial \nu}\right] \tag{22}$$

where ℓ is the heat transfer of the cell, $k\pm$ are the constant for thermal diffusivities on Ω and ν is the outward normal vector. Setting $\ell \neq 1$, the problem is then simplified into finding $u(x,t)$ as well as Γ_t, such that:

$$v = -\frac{1}{\ell}\left[\frac{\partial u}{\partial \nu}\right]^+_-, \qquad x \in \Gamma. \tag{23}$$

The outward normal vector, ν, is defined by:

$$\nu = \nabla\Phi/|\nabla\Phi| \tag{24}$$

and the curvature term, κ, by:

$$\kappa = \nabla\nu = \nabla\cdot\left(\frac{\nabla\Phi}{|\nabla\Phi|}\right). \tag{25}$$

From (24) and (25), expression v is rewritten as:

$$v = -[\nabla u]\cdot\nu = -[\nabla u]\cdot\left(\frac{\nabla\Phi}{|\nabla\Phi|}\right) \tag{26}$$

where $|\nabla u|$ is the jump taken between two regions—inner and outer cell or otherwise. As a result from (5), we obtained:

$$\Phi_t + v\cdot\nabla\Phi = 0, \qquad v = (v\cdot\nu)\nu \tag{27}$$

where $v\cdot\nu$ is the Stefan condition.

During the process of physical or chemical transformations, Liouville's Theorem of the first volume of enthalpy H between two regions where it must be equal guarantees the total mass of conservation, which is in line with [26].

Based on Theorem 1 (Liouville's Theorem) from [12], the volume of ligands that diffuse outside the cell which then bind to the cell membrane are equal to the volume of signals generated inside the cell to produce invadopodia during the molecular interactions of cell membrane deformation.

2.2.3. Cell Deformation: Free Boundary Conversion

Based on degenerate parabolic equations, we describe the boundary of the cell as free boundary. See details on this in [12]. A cell's phase interfaces may experience sudden shifts during the phase-transition process that happen between the outer and inner cell, which can result in singularities and instabilities. During this process, invadopodia will pierce and move through the complex-appearing collagen walls.

The simulation procedure is carried out in discrete time steps as the phase-transition formulation is built on a time-dependent scheme. Phase transition begins when invadopodia start to break through a cell, a process known as invasion that is easily observed in 2D rather than 3D. Let:

$$\begin{aligned} &H_g(\theta)_t = \Delta\theta \qquad\qquad \text{in} \quad Q = \Omega \times (0,T) \\ &\left.\frac{\partial\theta}{\partial\nu}\right|_{\partial\Omega} = 0, \\ &\theta|_{t=0} = \theta_0(x) \geq 0 \end{aligned} \tag{28}$$

where

$$H_g(\theta) = \begin{cases} \alpha_+\theta + \ell \text{ in } \{\theta > g\} \\ \alpha_-\theta - \ell \text{ in } \{\theta < g\} \end{cases}.$$

We discretise the problem based on Euler time discretisation such that:

$$\begin{aligned} &\frac{\theta^{n+1}}{\delta t} - \nabla\cdot(\kappa\nabla\theta^{n+1}) = f^{n+1} + \frac{\theta^n}{\delta t}, \qquad \text{in} \quad Q = \Omega\times(0,T) \\ &\frac{\partial\theta^{n+1}}{\partial\nu} = 0, \qquad \text{on} \quad \partial\Omega_t \\ &\theta^{n+1}|_{t=0} = \theta_0(x) \geq 0. \end{aligned} \tag{29}$$

2.2.4. Phase-Transition Formulation

For this subsection, the density of signals, ligands and plasma membrane are time-dependent. However, only the plasma membrane is treated as free boundary. From (28), we define enthalpy, $v = H_g(\theta)$ by:

$$f(v) = \begin{cases} \alpha_-^{-1}(v+\ell), & v < \ell \\ 0, & -\ell \leq v \leq \ell \\ \alpha_+^{-1}(v-\ell), & \ell < v \end{cases} \tag{30}$$

if and only if $\theta = f_g(v) + \Delta g$. Based on Theorem 2 in [12]:

$$\begin{aligned} &v_t = \Delta f(v) + \Delta g \qquad\qquad \text{in} \quad Q \\ &\left.\frac{\partial}{\partial\nu}f(v)\right|_{\partial\Omega} = 0 \qquad\qquad \left.\frac{\partial g}{\partial\nu}\right|_{\partial\Omega} = 0 \\ &v|_{t=0} = v_0(x) \geq 0. \end{aligned} \tag{31}$$

Likewise as in Subsection 2.2.3, problem (31) is discretised into:

$$\begin{aligned}
&\frac{v^{n+1}}{\delta t} - \nabla \cdot (\kappa \nabla f^{n+1}) - \nabla \cdot (\kappa \nabla g^{n+1}) = h^{n+1} + \frac{v^n}{\delta t}, && \text{in} \quad Q = \Omega \times (0, T) \\
&\frac{\partial f^{n+1}}{\partial \nu} = 0, \qquad \frac{\partial g^{n+1}}{\partial \nu} = 0 && \text{on} \quad \partial\Omega_t \\
&v^{n+1}\Big|_{t=0} = v_0(x) \geq 0.
\end{aligned} \tag{32}$$

3. Results

To verify the methods, we begin our numerical simulations. We divide our results into two parts: level set method and enthalpy method (phase-transition formulation), where the results obtained will be discussed in Section 4. The PDEs are solved numerically using FreeFem++ (v 4.10) [27] using a P1 finite element method (FEM) and meshes were generated using Gmsh (v 4.9.3) [28].

3.1. Level Set Method

When dealing with moving boundaries, numerical simulations for the free boundary problem of this model encountered significant challenges. Therefore, the level set method is carried out for a single cell model, while the level set approach is used to represent the plasma membrane, in order to overcome the difficulty in dealing with moving boundaries. Let $\psi(\cdot, t) = \psi$ be a smooth level set function, as you may recall from Section 2.

Consider that at the start of the computation there is no signal density. ECM will degrade, create diffused ligands outside of the cell, bind to receptors and generate an internal signal as a result. Inside the cell, signal densities spread and activate actin polymerisation. We defined the boundary data as follows based on (14) and (15):

1. Test 1: $\sigma = c_* = g = 0.01(2 + \sin(2\pi(x+y)^2)\cos(\pi(x+0.5)))$ and level set solution as $\psi = 0.05 \times \sinh((((x-y)^{1/2}) - R)/(\epsilon h)^2)$ where $\epsilon = 5$ and $h = 0.2$.
2. Test 2: Modifications of equations from Test I. $\sigma = c_* = g = 0.01(2 + \sin(4\pi(x+y)^2)\cos(\pi((2x)+0.5)))$ and level set solution as $\psi = 0.05 \times \tanh((((x-y)^{1/2}) - R)/\epsilon h)^2$ where $\epsilon = 5$ and $h = 0.2$.

Figures 6 and 7 illustrate the formation of invadopodia and protrusion at the cell's boundary. Protrusion developed as a result of membrane displacement brought on by the presence of a signal gradient that was sparked by interactions between the membrane and the surrounding ECM.

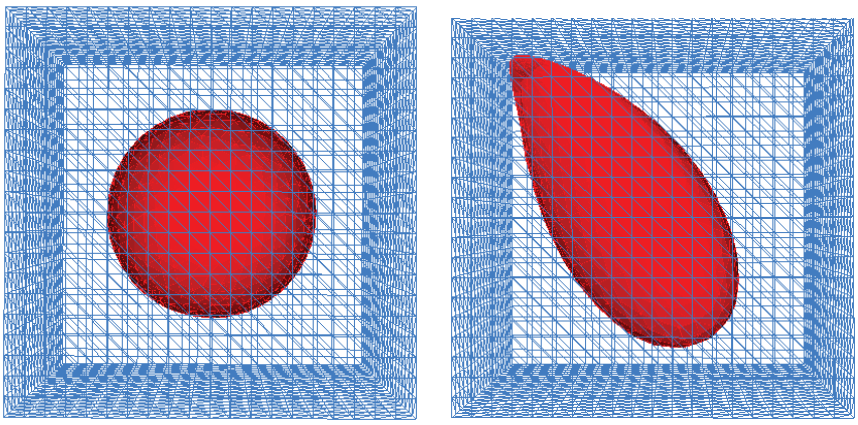

(**a**) (**b**)

Figure 6. *Cont.*

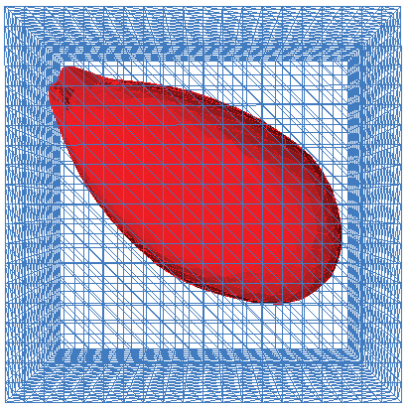

(**c**)

Figure 6. Simulation of invadopodia formation with outer domain (box). (**a**) Initial cell shape. (**b**) Invadopodia formed based on Test 1. (**c**) Invadopodia formed based on Test 2.

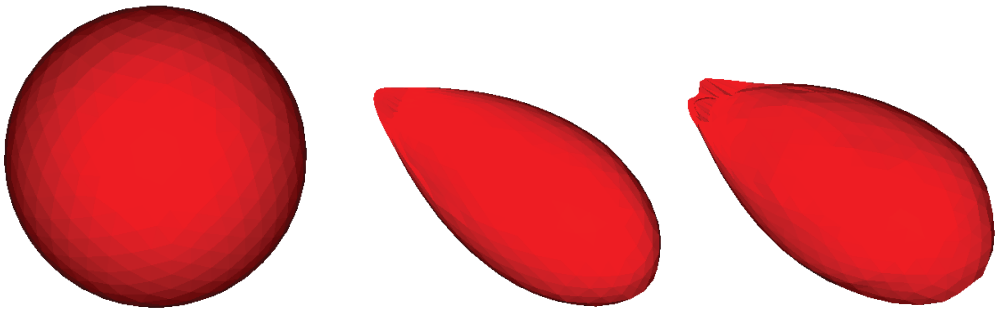

(**a**) (**b**) (**c**)

Figure 7. Simulation of invadopodia formation without outer domain (box). (**a**) Initial cell shape. (**b**) Invadopodia formed based on Test 1. (**c**) Invadopodia formed based on Test 2.

3.2. Enthalpy Method

Phase transition begins when invadopodia start to break through a cell, a process known as invasion. As described previously, the plasma membrane is regarded as a free boundary and is time-dependent in this problem, although the density of signals and ligands does not change over time. Figures 8 and 9 show the invasion of invadopodia and cell migration from Tests 1 and 2 based on (28).

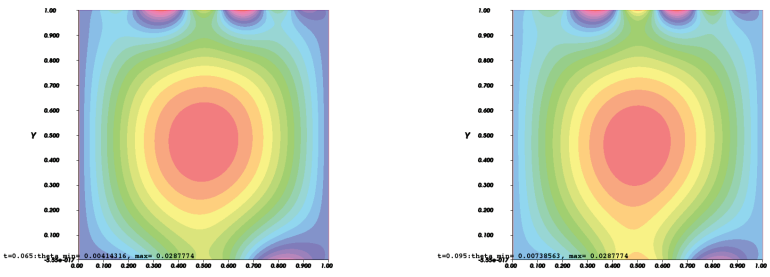

(**a**) (**b**)

Figure 8. *Cont.*

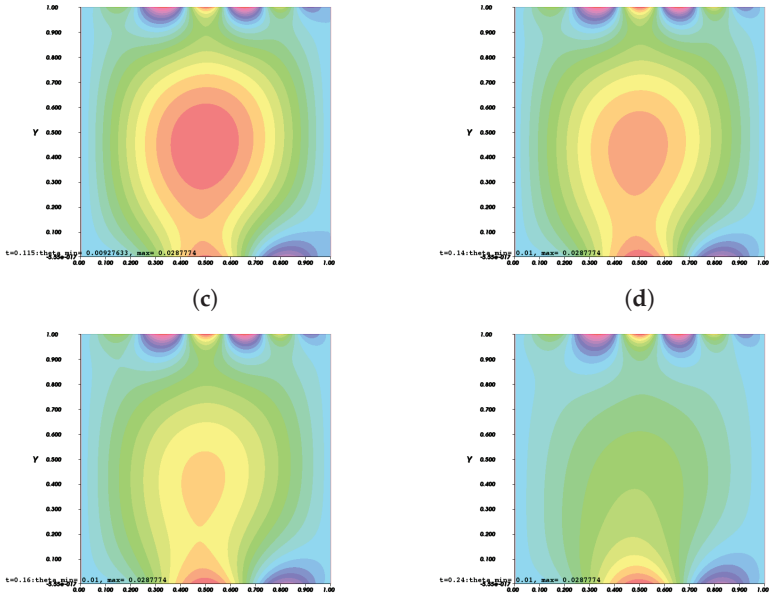

(**c**) (**d**)

(**e**) (**f**)

Figure 8. Invasion of invadopodia and cell migration from Test 1 based on (28).

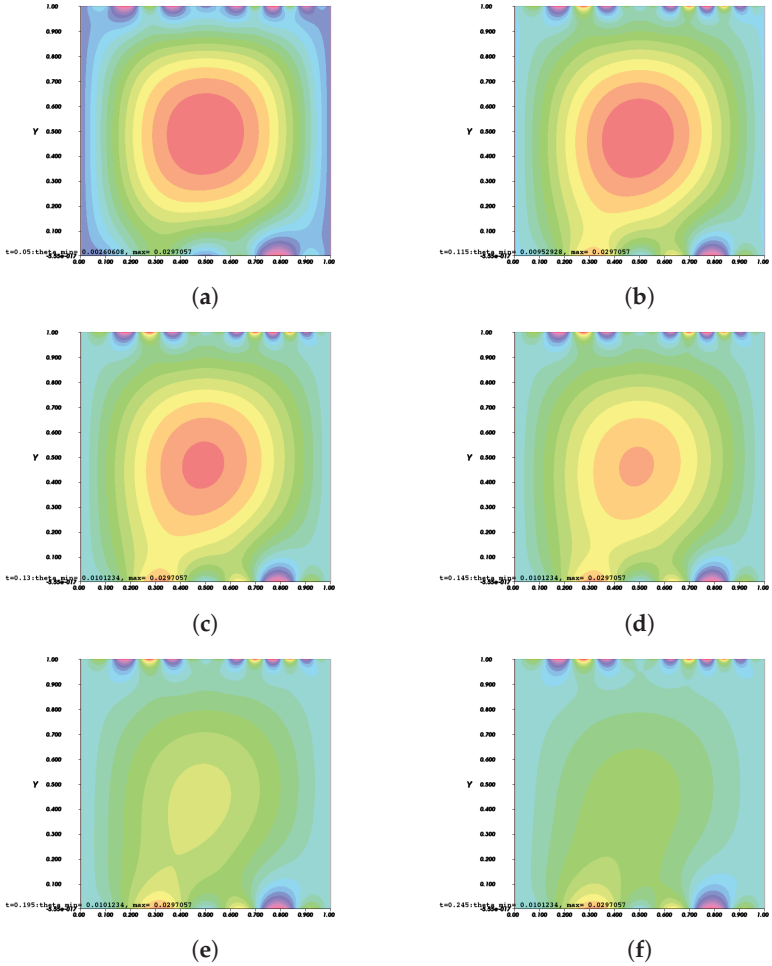

(**a**) (**b**)

(**c**) (**d**)

(**e**) (**f**)

Figure 9. Invasion of invadopodia and cell migration from Test 2 based on (28).

On the other hand, Figures 10 and 11 show the invasion of invadopodia and cell migration from Tests 1 and 2 based on (31).

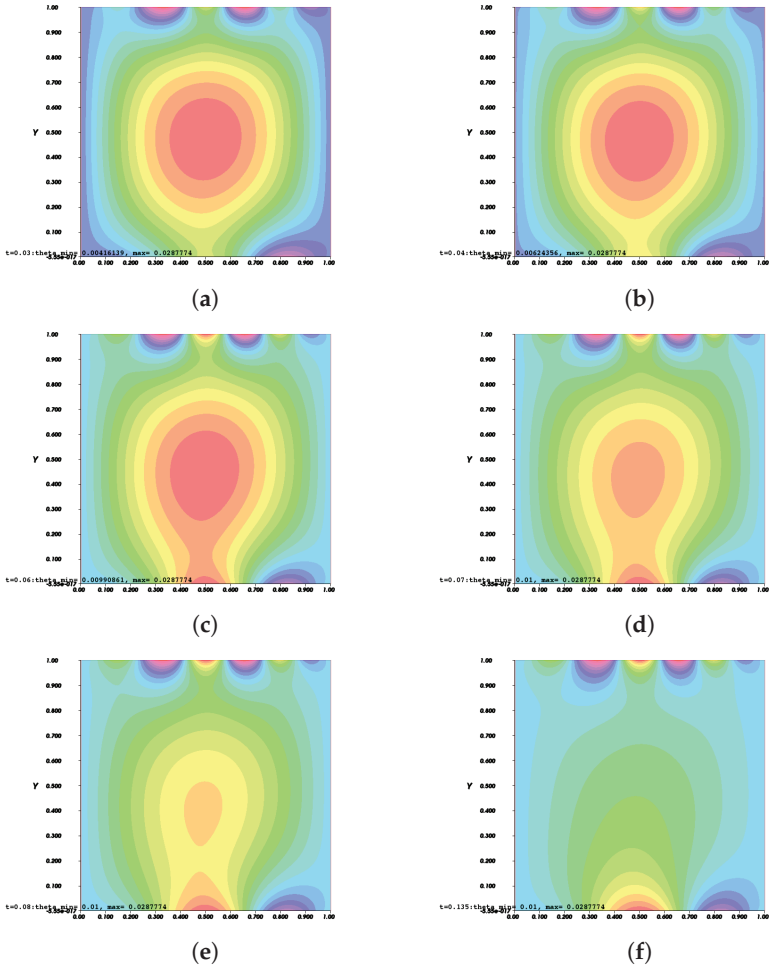

Figure 10. Invasion of invadopodia and cell migration from Test 1 based on (31).

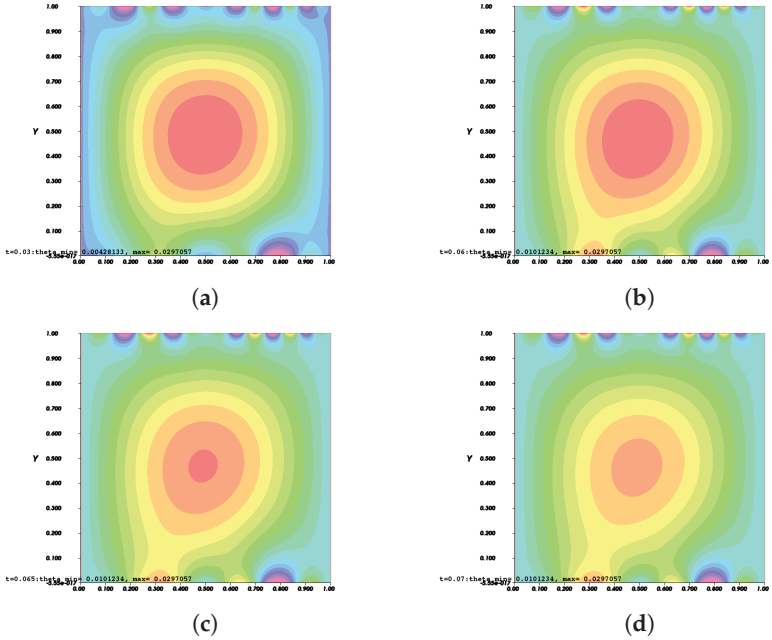

Figure 11. *Cont*.

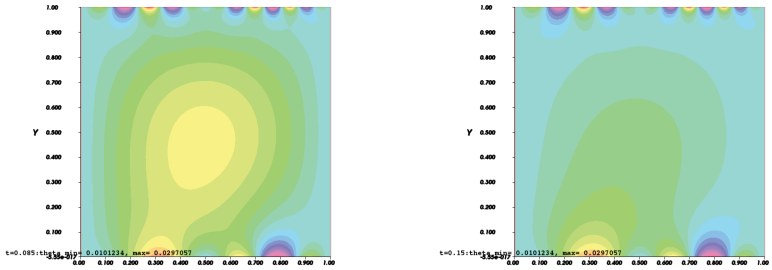

(**e**) (**f**)

Figure 11. Invasion of invadopodia and cell migration from Test 2 based on (31).

4. Discussion

Level set serves the purpose of dealing with cell membranes in order to denote the membrane interfaces when the problem is investigated as a free boundary because they are simple to execute and computationally inexpensive. The discountinuity in the level set function derivatives between two outer and inner cell interfaces that are near to one another can affect the estimation of velocity and curvature. As a result, the level set approach makes it straightforward to determine an interface's curvature and velocity in order to locate the plasma membrane interface. Therefore, we define the velocity extension to the entire domain in order to prevent singularities and instabilities as described in Section 3.

In order to enhance the simulation of invadopodia formation and also to surmount singularities and instabilities that occurred in [12] as discussed in Section 1, 3D simulations were used, resulting in Figures 6 and 7. The initial shape of a cell is depicted in Figures 6a and 7a. Figures 6a and 7b illustrate the formation of invadopodia and protrusions at the cell's boundary using Test 1 while Figures 6c and 7c used Test 2. Protrusion is caused by the membrane's displacement due to the presence of a signal gradient induced by contact of the membrane with the surrounding ECM.

As previously discussed, the authors of [12] demonstrate the existence of singularities and instabilities. On the basis of the results shown in Figures 6 and 7, both instabilities and singularities have been prevented from occurring in the simulation. This could be due to the fact that Tests 1 and 2 used a different simulation technique and set of data. The graphs for level set function, ψ for Tests 1 and 2 in Figure 12 demonstrate that the values of the level set during the deformation of the cell in both tests fluctuated.

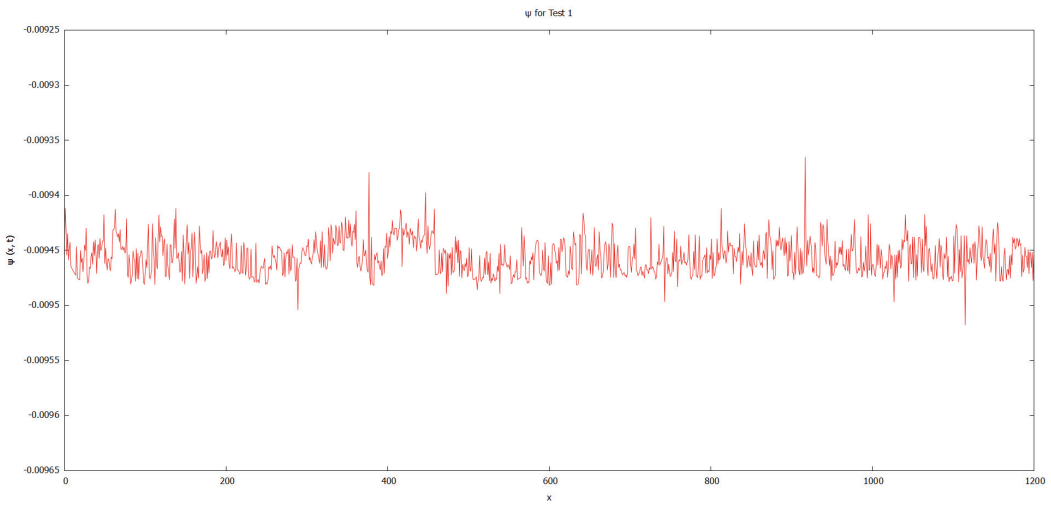

(**a**)

Figure 12. *Cont.*

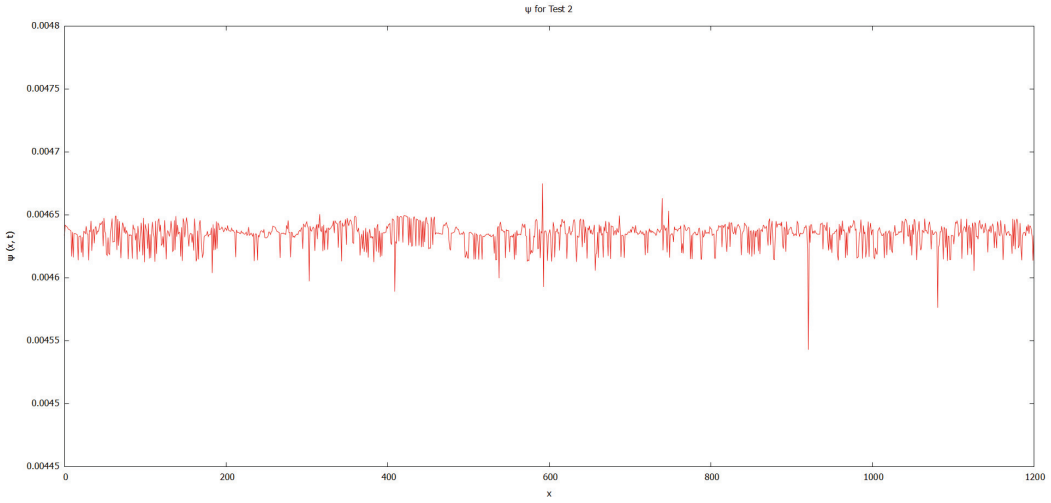

(**b**)

Figure 12. Graphs for level set function, ψ. (**a**) Test 1. (**b**) Test 2.

ECM is broken down by MT1-MMP, which also generates ligands that diffuse and attach to membrane receptors. The signal is then generated inside the cell which will spread and cause the actin molecule to polymerise. The morphology of the plasma membrane was harmed by this process. During this process, the plasma membrane begins to undergo phase transition, which can result in singularities and instabilities. Invadopodia begin to invade through the intricately patterned collagen walls in the cell's interfaces between outer and inner cells and migration occurs.

The phase field variable in the enthalpy method (phase-transition formulation) smoothly varies between two phases over a small yet numerically resolvable thickness on the diffused interface area. As a result, it offers a hazy depiction of the thinned-out membrane interface between the outer and inner cell.

Figures 8–11 depict the process of cell deformation that occurs when a normal cell undergoes mutation before it develops into a cancer cell. Invasion begins in a cancer cell after invadopodia protrude and begin to separate from the primary cell. The invasion process can be seen starting with Figure 8a and the movement of the invasive cancer cell is depicted in Figure 8b–e. These can also be seen in Figures 9a–e, Figure 10a–e, and Figure 11a–e. The interactions between the cell membrane and the surrounding ECM causing the cell to change and move, which in turn promotes the existence of ligands and activates the signal gradient. As time passes, the cell disperses to nearby regions as illustrated in Figures 8f–11f which then grows in various parts of the body.

The results of Figures 8 and 9 indicate that the phase transition of the cell membrane based on (31) is significantly faster than (28). Moreover, (31) describes why the phase-transition problem depicted in Figures 10 and 11 occurred more rapidly than in Figures 8 and 9. In (31), it is presumed that the concentration of MT1-MMP, f, embedded in the cell membrane degrades the ECM by contact and that the signal density equals the function $g(x,t)$, which also represents MT1-MMP at any time, t, at the interface based on (16), while (28) only evaluates the signal or ligand density.

When compared to [12], our findings demonstrate that phase transition occurred more slowly. The simulation results of Figures 8–11 show that as protrusion took place, the cell began to migrate through the ruptured membrane and as protrusion velocity decreased, it showed that the formation of invadopodia had stabilised. As the amount of time increases and the distance from the primary cell increases, the position of the phase-transition interface diminishes, as well as the density of the signal. Figure 13 depicts the graphs for density of signals and ligands, θ, during the cancer cell's phase transition for Tests 1 and 2, where the values fluctuated in both tests. Figure 14 displays the graphs

also for density of signals and ligands during phase transition of cancer cell, θ, but with MT1-MMP enzyme flux, g, also for Tests 1 and 2 which likewise fluctuate.

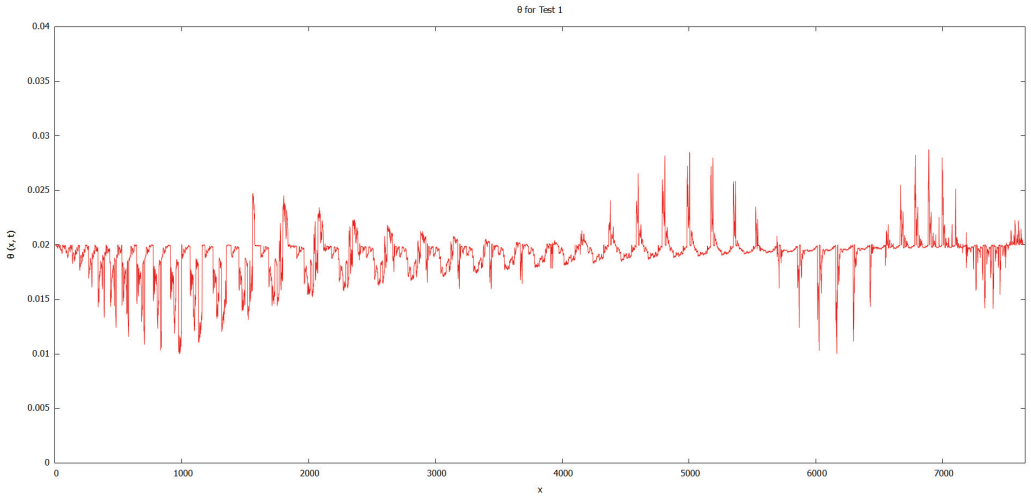

(**a**)

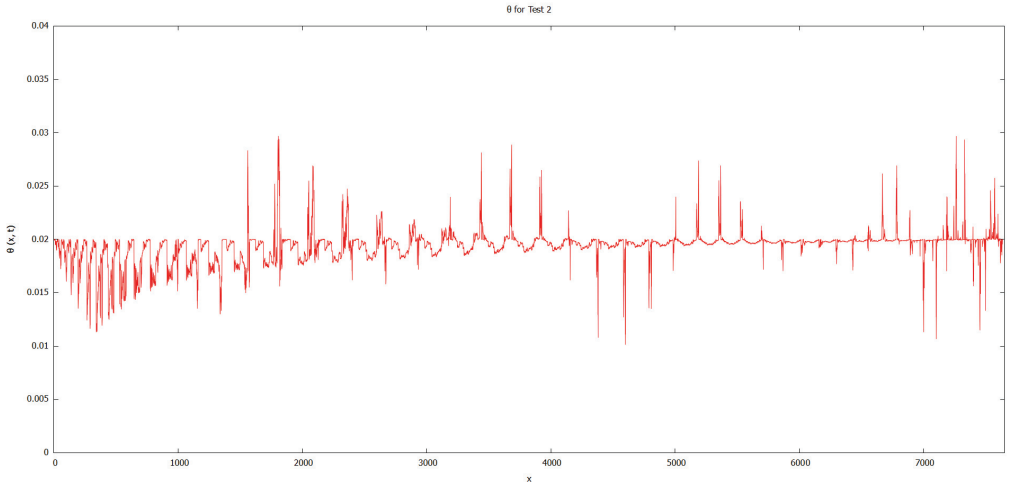

(**b**)

Figure 13. Graphs for density of signals and ligands, θ. (**a**) Test 1. (**b**) Test 2.

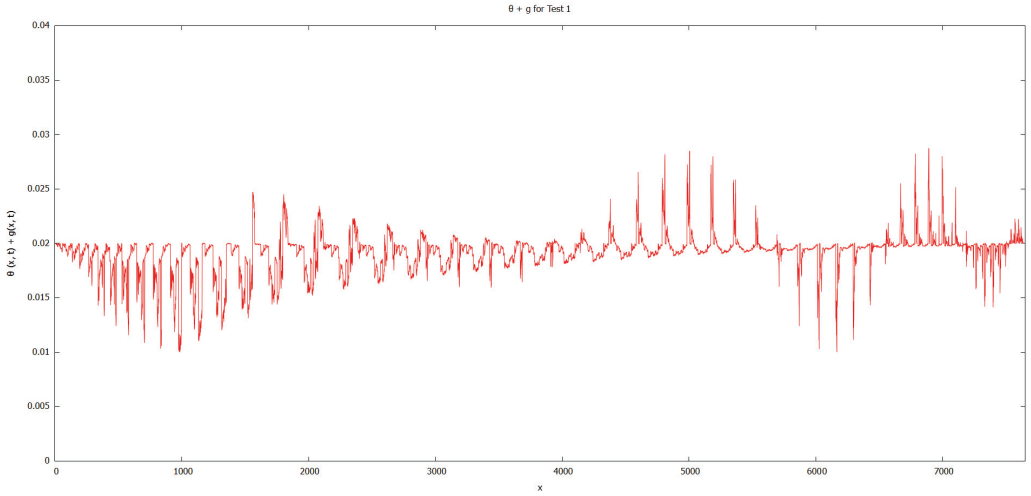

(**a**)

Figure 14. *Cont.*

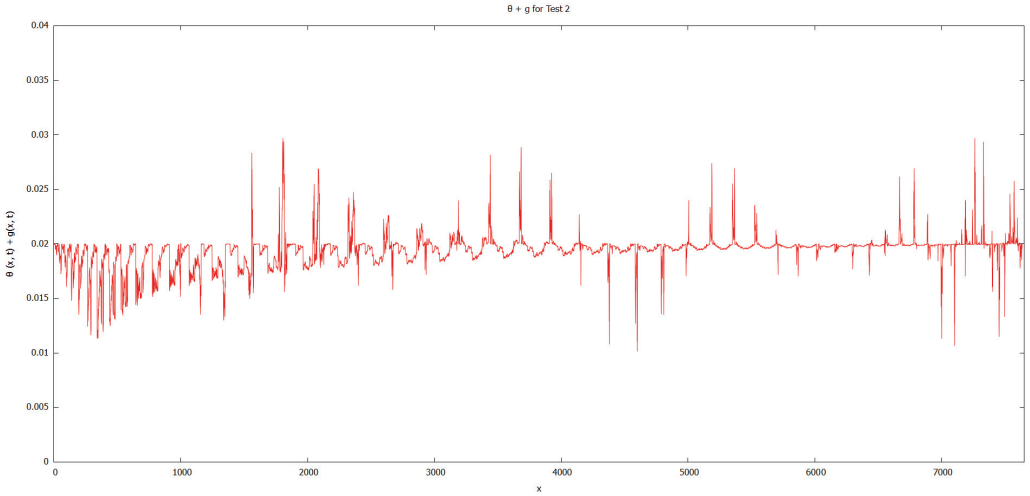

(**b**)

Figure 14. Graphs for density of signals and ligands with MT1-MMP enzyme flux, $\theta + g$. (**a**) Test 1. (**b**) Test 2.

5. Conclusions

We created a numerical method, based on the level set technique and the phase-transition formulation (enthalpy method), to address the Stefan problem of invadopodia formation. FreeFem++ and Gmsh were used to carry out all described methods. Phase-transition problems in cancer cells were created using phase-transition formulation and level set was used to determine the location of the membrane using the zero level function of ψ. The enthalpy technique was shown to be effective and precise in solving this kind of issue. Both approaches were used to mathematically resolve the deformation and invasion of cancer cells, where protrusions were caused by the presence of invadopodia and invasion was caused when the cancer cell began to disseminate to another area of the body. In addition to this, we were able to enhance the simulation outcome from [12] to a more realistic complexity for the solution to be accurate by using a different simulation technique and domain as well as a different data set for Tests 1 and 2. Singularities and instabilities were eliminated. The results that were achieved in this paper have the potential to be helpful for novel approaches or extended to other methods in the development of a more accurate numerical simulation.

Author Contributions: Methodology, T.S. and N.L.O.; software, M.A.R. and N.L.O.; writing—original draft preparation, M.A.R.; writing—review and editing, N.L.O.; supervision, N.L.O.; funding acquisition, T.S. All authors have read and agreed to the published version of the manuscript.

Funding: This work is supported partly by JST-CREST JPMJCR2022.

Data Availability Statement: No new data were created or analysed in this study. Data sharing is not applicable to this article.

Conflicts of Interest: The authors declare no conflict of interest.

Abbreviations

The following abbreviations are used in this manuscript:

BM	basement membrane
ECM	extracellular matrix
PDE	partial differential equation
ODE	ordinary differential equation
2D	two-dimensional
3D	three-dimensional

TLA	Three letter acronym
LD	Linear dichroism
FDM	finite difference method
FEM	finite element method
MMP	matrix metalloproteinases
MT1-MMP	type 1-matrix metalloproteinases

References

1. Preziosi, L. *Cancer Modelling and Simulation*; Chapman Hall/CRC Press: Boca Raton, FL, USA, 2003.
2. Hanahan, D.; Weinberg, R.A. The hallmarks of cancer. *Cell* **2000**, *100*, 57–70. [CrossRef]
3. Hanahan, D.; Weinberg, R.A. Hallmarks of cancer: The next generation. *Cell* **2011**, *144*, 646–674. [CrossRef] [PubMed]
4. Sporn, M.B. The war on cancer. *Lancet* **1996**, *347*, 1377–1381. [CrossRef] [PubMed]
5. Andasari, V.; Chaplain, M.A.J. Intracellular modelling of cell-matrix adhesion during cancer cell invasion. *Math. Mod. Nat. Phen.* **2012**, *7*, 29–48. [CrossRef]
6. Andasari, V.; Roper, R.T.; Swat, M.H.; Chaplain, M.A.J. Integrating intracellular dynamics using CompuCell3D and Bionetsolver: Applications to multiscale modelling of cancer cell growth and invasion. *PLoS ONE* **2012**, *7*, e33726. [CrossRef] [PubMed]
7. Stylli, S.S.; Kaye, A.H.; Lock, P. Invadopodia: At the cutting edge of tumour invasion. *J. Clin. Neurosci.* **2008**, *15*, 725–737. [CrossRef] [PubMed]
8. Weaver, A.M. Invadopodia. *Curr. Biol.* **2008**, *18*, R362–R364. [CrossRef]
9. Gallinato, O.; Poignard, C. Superconvergent second order Cartesian method for solving free boundary problem for invadopodia formation. *J. Comput. Phys.* **2017**, *339*, 412–431. [CrossRef]
10. Saitou, T.; Rouzimaimaiti, M.; Koshikawa, N.; Seiki, M.; Ichikawa, K.; Suzuki, T. Mathematical modeling of invadopodia formation. *J. Theo. Biol.* **2012**, *298*, 138–146. [CrossRef] [PubMed]
11. Murphy, D.A.; Courtneidge, S.A. The 'ins' and 'outs' of podosomes and invadopodia: Characteristics, formation and function. *Nat. Rev. Mol. Cell Biol.* **2011**, *12*, 413–426. [CrossRef]
12. Loling Othman, N.; Suzuki, T. Free Boundary Problem of Cell Deformation and Invasion. In Proceedings of the Methods of Mathematical Oncology: Fusion of Mathematics and Biology, Osaka, Japan, 26–28 October 2020; pp. 107–123.
13. Anderson, A.R.A.; Chaplain, M.A.J.; Newman, E.L.; Steele, R.J.C.; Thompson, A.M. Mathematical modelling of tumour invasion and metastasis. *Comput. Math. Methods Med.* **2000**, *2*, 129–154. [CrossRef]
14. Chaplain, M.A.J.; Lolas, G. Mathematical modelling of cancer invasion of tissue: Dynamic heterogeneity. *Net. Hetero. Med.* **2006**, *1*, 399–439. [CrossRef]
15. Ramis-Conde, I.; Chaplain, M.A.J.; Anderson, A.R.A. Mathematical modelling of cancer cell invasion of tissue. *Math. Comput. Modelling* **2008**, *47*, 533–545. [CrossRef]
16. Chaplain, M.A.J.; Lachowicz, M.; Szymańska, Z.; Wrzosek, D. Mathematical modelling of cancer invasion: The importance of cell–cell adhesion and cell–matrix adhesion. *Math. Models Methods Appl. Sci.* **2011**, *21*, 719–743. [CrossRef]
17. Chaplain, M.A.J.; Lolas, G. Mathematical modelling of cancer cell invasion of tissue: The role of the urokinase plasminogen activation system. *Math. Models Methods Appl. Sci.* **2005**, *15*, 1685–1734. [CrossRef]
18. Andasari, V.; Gerisch, A.; Lolas, G.; South, A.P.; Chaplain, M.A.J. Mathematical modeling of cancer cell invasion of tissue: biological insight from mathematical analysis and computational simulation. *J. Math. Biol.* **2011**, *63*, 141–171. [CrossRef]
19. Admon, M.A.B. Mathematical Modeling and Simulation in an Individual Cancer Cell Associated with Invadopodia Formation. Ph.D. Thesis, Osaka University, Suita, Japan, 2015.
20. Gallinato, O.; Ohta, M.; Poignard, C.; Suzuki, T. Free boundary problem for cell protrusion formations: Theoretical and numerical aspects. *J. Math. Biol.* **2017**, *75*, 263–307. [CrossRef]
21. Yaacob, N.; Shafie, S.; Suzuki, T.; Admon, M.A. Level set method for free boundary of invasive cancer cell using different functions of matrix metalloproteinases. *J. Phys. Conf. Ser.* **2021**, *1988*, 012020. [CrossRef]
22. Mahemuti, R.; Muhammadhaji, A.; Suzuki, T. Research on the Solution of Cell Invasion Model with Free Boundary. *Open J. Appl. Sci.* **2017**, *7*, 242. [CrossRef]
23. Crank, J. *The Mathematics of Diffusion*; Oxford University Press: Oxford, UK, 1979.
24. Groot, R.D. Second order front tracking algorithm for Stefan problem on a regular grid. *J. Comput. Phys.* **2018**, *372*, 956–971. [CrossRef]
25. Chen, S.; Merriman, B.; Osher, S.; Smereka, P. A simple level set method for solving Stefan problems. *J. Comput. Phys.* **1997**, *135*, 8–29. [CrossRef]
26. Hansen, J.P.; McDonald, I.R. *Theory of Simple Liquids: With Applications to Soft Matter*; Academic Press: Cambridge, MA, USA, 2013.
27. Hecht, F. New development in FreeFem++. *J. Numer. Math.* **2012**, *20*, 251–265. [CrossRef]
28. Geuzaine, C.; Remacle, J.F. Gmsh: A 3-D finite element mesh generator with built-in pre-and post-processing facilities. *J. Comput. Phys.* **2009**, *79*, 1309–1331. [CrossRef]

mathematics

MDPI

Article

Controlling COVID-19 Spreading: A Three-Level Algorithm

Giovanni Dieguez [1,†], Cristiane Batistela [2,†] and José R. C. Piqueira [1,*]

[1] Department of Telecommunications and Control Engineering, São Paulo, Polytechnic School, University of São Paulo, São Paulo 05508900, Brazil; giovanni.dieguez@alumni.usp.br
[2] Center for Mathematics, Computing and Cognition, Federal University of ABC, São Bernardo do Campo, São Paulo 09606070, Brazil; cristiane.batistela@ufabc.edu.br
* Correspondence: piqueira@lac.usp.br
† These authors contributed equally to this work.

Abstract: As the main methods of the coronavirus disease (COVID-19) transmission are air and physical contact, actions to mitigate and suppress its spread must be developed in order to change population dynamics and provide efficient control strategies. Here, these actions are described as a simple heuristic framework to establish public policies. Two control systems were studied: the first organized in the form of an algorithm stratified into three levels and the second as a minimization problem similar to optimal control strategies, applied to both social distancing and vaccination. The possible effects of these actions are modeled and applied to an extension of the Susceptible - Infected - Removed (SIR) compartmental model. The control system is developed, which is organized in the form of an algorithm stratified into three levels. These levels intend to represent social distancing strategies implemented by sanitary authorities around the globe, representing stronger or weaker grades of isolation intensity according to the ability of the healthcare system to cope with symptomatic individuals. The algorithm control is applied in a simulation, and the results give evidence of the effectiveness of the procedures adopted against the coronavirus. The model dynamics are analyzed and validated with simulations considering parameters obtained from epidemiological data from Brazil and Uruguay and in a more detailed way for three Brazilian states: São Paulo, Minas Gerais and Rio de Janeiro. The model was validated using cumulative data on cases and deaths. For cases of death, the results were satisfactory, while for case data, the response was reasonable, considering the possibility of adding delays or variations in parameters in the model. In addition, the effective reproduction number was proposed for the cities studied in Brazil, the result being relevant because it has a qualitative behavior similar to that published by official centers. This paper also discusses the implementation and optimization of social distancing and vaccination control strategies, considering different parameters and their effects on reducing the number of cases and deaths. Model simulations present promising results for developing strategies to attack COVID-19 dissemination.

Keywords: COVID-19; equilibrium; SIRD; social distancing; stability

MSC: 93C10; 37N35

1. Introduction

At the beginning of 2020, the epidemic of a new disease changed the history of humanity; it was responsible for a global health and economic crisis. COVID-19 is a new coronavirus progeny, SARS-CoV-2, first reported in Wuhan, China, on 31 December 2019 [1,2]. A few months later, a report published by the World Health Organization qualified the disease as a pandemic due to its prevalence worldwide [3].

Transmission of SARS-CoV-2 occurs predominantly through the physical transportation of contaminated droplets of secretions from an infected individual to an uninfected person, although the role of aerosol transmission and contaminated surface contact is currently unknown [4]. It is a disease with lower lethality when compared with its high

transmission capacity, with the spreading aggravated by the average incubation time and due to both symptomatic and asymptomatic people being able to transmit the disease [5].

The disease has several forms of manifestation, and most patients have rapid resolution, many of whom are asymptomatic. The initial symptoms are fever, cough and breathing difficulties. However, some patients with comorbidities may develop complications [6], requiring hospitalization, intensive treatment and mechanical respiratory ventilators, provoking a severe crisis in the healthcare system caused by excessive hospitalizations.

Different interventions aimed to slow the rapid evolution of the pandemic were adopted by many countries to avoid overcrowded hospitals. Strategies such as isolation of infected patients, mask-wearing, regular hand hygiene, social distancing, quarantine and total blocking of areas [7–10] were adopted worldwide.

Another public strategy may be associated with the impact of advertisements on social networks in combating the pandemic, in which it can be assumed that awareness among susceptible individuals alters collective behaviors, resulting in a reduction in the transmission of this infectious agent [11] or community awareness and global information campaigns [12].

Mathematical models are used to simulate the transmission of coronavirus and are helpful to understanding the dynamical behavior of an infection, providing tools to estimate the duration and peaks of infection outbreaks and designing efficient control strategies [13–15]. Epidemic mathematical models are present in public health literature [16,17] related to several diseases [18–26].

Macroscopic compartmental models for disease spreading that have been a field of research since the Kermack and McKendrick proposition [27–29], with a dynamic model that classifies population individuals into groups such as Susceptible - Infected - Removed (SIR) or Susceptible - Exposed - Infected - Removed (SEIR) models, could be refined by contact tracing and hospitalization strategies to explain the COVID-19 outbreak [30]. Several modifications of the SIR model [31–33] have been proposed for epidemic modeling [34–37], which have been useful to public health policy makers [38].

More complex mathematical models using the stochastic approach and estimating data based on outbreak probability have been studied for cases in Wuhan and other [39] locations. Another compartmental model proposed for case studies in India studied the dynamics of disease propagation and predicts [40] outbreaks, yet for that country, the control theory provides ideal strategies to maintain the disease outbreak [41]. Compartmental models that address mitigation strategies for the transmission of COVID-19 beyond social distancing, including blocking and closing educational institutions, are also studied in countries such as Italy [42]. There are still models that consider the influence of environmental contamination to investigate the dynamics of viral propagation [43].

Due to the urgency of COVID-19, researchers worldwide accepted the challenge of outlining mathematical models for this new epidemic. Several mathematical models have already been formulated for the population dynamics of COVID-19 in several countries [10,44–51], and pioneer methods are structured upon machine learning and statistical models, such as decision trees and linear regression [52] or even more powerful ones like artificial neural networks [53,54], showing promising results. Machine learning has also been used to assist in early detection [55] and prediction of severity [56] of COVID-19.

However, this paper considers a more classical and established approach, using the adjustment of social contact rate characterized by the control of the parameter β to mitigate COVID-19 spread. For this, a three-level controller is implemented and its relationship to social distance validated. An extension of the compartmental SIR model is considered, the Susceptible–Infected–Removed–Dead (SIRD) model, and the method is inspired by how control theory can help us reduce COVID-19 propagation [57].

This article's main motivation is the study of strategies to control the spread of the SARS-CoV-2 virus and, for that, it considers public policies based on social distancing and vaccination. This work is validated with cumulative data on cases and deaths from some

regions. In addition, the basal reproduction number and the effective reproduction number are calculated and compared with data from the COVID-19 observatory.

Finally, the implementation and optimization of these strategies is discussed, considering different parameters and their effects in reducing the number of cases and deaths to indicate public policies concerning the health system.

The remainder of this paper is ordered as follows: In Section 2, the equations and hypothesis of the model are presented. In Section 3, the analysis of model dynamics is exhibited, the equilibrium points are determined, and the basic reproduction rate R_0 for the SIRD model is defined and analyzed with two simulations. Then, in Section 4, the model is studied for the sake of establishing a baseline for the controller, with parameters derived from Brazil and Uruguay. Section 5 presents the validation for the proposed model with more detailed data for three Brazilian states. Finally, Section 6 outlines the controller, and its effectiveness is investigated for a hypothetical scenario, followed by the control strategy results in Section 7 and the more detailed control analysis for the states of São Paulo, Minas Gerais and Riode Janeiro in Section 8. The conclusions are shown at the end, in Section 9. All simulations are performed with MATLAB Simulink [58].

2. Model Formulation

The proposed model is a modification of the original SIR compartmental model [59], including a dead population compartment, here called the Susceptible - Infected - Removed - Dead (SIRD) model, shown in Figure 1. The model does not account for natural births and deaths, as the Dead are only due to complications caused by coronavirus infection.

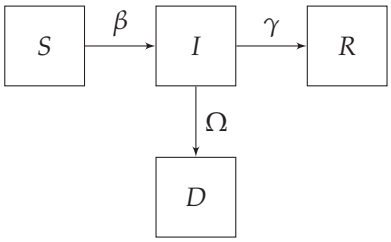

Figure 1. SIRD model.

Model parameters are described in Table 1. β is the average number of contacts that result in contamination, per unit of time; γ is the recovery rate, i.e., the rate at which individuals leave the infected compartment after recovering. Consequently, γ^{-1} represents the recovery time [60]. Additionally, Ω is the fraction of the infected population that dies per unit of time (mortality rate).

Table 1. Model parameters.

Parameter	Parameter Description
β	Average contact rate.
γ^{-1}	Mean infectious period.
Ω	Mortality rate.

As can be observed, the model presents some simplifications:

- A recovered individual should acquire immunity and does not return to the susceptible compartment. Hence, they become "Removed" ("R" from SIRD);
- Parameters β, γ and Ω are considered to be constants, despite depending on individual behavior, healthcare availability and age.

Under the described conditions, the model dynamics can be written as

$$\begin{cases} \dot{S} &= -\dfrac{\beta SI}{N}, \\ \dot{I} &= \dfrac{\beta SI}{N} - (\gamma + \Omega)I, \\ \dot{R} &= \gamma I, \\ \dot{D} &= \Omega I. \end{cases} \tag{1}$$

with $N = S(t) + I(t) + R(t) + D(t)$ and $\dot{S}(t) + \dot{I}(t) + \dot{R}(t) + \dot{D}(t) = 0$.

As natural births and deaths are not taken into account, the total number of individuals in the population is considered to be constant, and the dynamics of the dead compartment can be written as a function of the other compartments:

$$\begin{cases} D = N - S - I - R, \\ \dot{D} = -(\dot{S} + \dot{I} + \dot{R}). \end{cases} \tag{2}$$

Furthermore, the recovered compartment is dependent on the susceptible and infected populations:

$$\dot{R} = -\frac{\gamma}{\gamma + \Omega}(\dot{S} + \dot{I}). \tag{3}$$

Therefore, the system dynamics can be rewritten without the removed and dead variables, without any loss of generality:

$$\begin{cases} \dot{S} &= -\dfrac{\beta SI}{N}, \\ \dot{I} &= \dfrac{\beta SI}{N} - (\gamma + \Omega)I. \end{cases} \tag{4}$$

3. System Dynamics Analysis

3.1. Equilibrium Conditions

For the proposed SIRD model, equilibrium points can be obtained by applying the conditions $\dot{S} = 0$ and $\dot{I} = 0$. By doing so, it can be concluded that every point of the form $(S^*, 0)$ is an equilibrium point.

Equilibria at $I = 0$ are called disease-free, as opposed to equilibria at $I \neq 0$, which are called endemic [61].

3.2. Equilibrium Points Classification

In order to analyze the local stability of these points, the Hartman–Grobman theorem is applied [62], and the general Jacobian (J) is constructed.

For $(S, I) = (S^*, 0)$, the Jacobian is reduced to

$$J(S^*, 0) = \begin{bmatrix} 0 & -\dfrac{\beta S^*}{N} \\ 0 & \dfrac{\beta S^*}{N} - (\gamma + \Omega) \end{bmatrix}. \tag{5}$$

Hence, the eigenvalue set for the equilibrium points can be found by

$$\lambda(\lambda - \frac{\beta S^*}{N} + \gamma + \Omega) = 0, \tag{6}$$

Which gives

$$(0, \frac{\beta S^*}{N} - (\gamma + \Omega)); \tag{7}$$

as the eigenvalue set. Considering that one of the eigenvalues is equal to zero, it is worth noticing that the eigenvalue set obtained from the equilibrium points allows a local stability analysis with three possibilities:

- If $\frac{\beta S^*}{N} - (\gamma + \Omega) > 0 \Rightarrow$ these fixed points are unstable [62]; so, there will be a growth in cases for a small perturbation.
- If $\frac{\beta S^*}{N} - (\gamma + \Omega) < 0 \Rightarrow$ the center manifold theorem must be applied in order to classify the stability condition.

Consequently, to proceed with the equilibrium stability analysis, all points satisfying $\frac{\beta S^*}{N} - (\gamma + \Omega) < 0$ and $S^* \geqslant 0$ are studied by applying the center manifold theorem.

Considering $S^* > 0$, a new parameter $\tau > 0$ is introduced in order to translate the system so that the point ($S^* = \tau$,0) is the origin (0,0) of the new system. This is performed because the center manifold theorem only refers to neighborhoods of the origin of the corresponding analyzed system. Consequently, the rewritten system, with $Z = S - S^*$, can be written as follows:

$$\begin{cases} \dot{Z} &= -\frac{\beta(Z+\tau)I}{N}, \\ \dot{I} &= \frac{\beta(Z+\tau)I}{N} - (\gamma + \Omega)I. \end{cases} \tag{8}$$

That is, studying the system (4) around (τ,0) is the same as studying the new system (8) around (0,0). Nevertheless, the rewritten system does not possess the same physical interpretation as the SIRD model. In addition, substitute parameters are introduced,

$$\begin{cases} \phi &= \frac{\beta}{N}, \\ \alpha &= \gamma + \Omega, \end{cases} \tag{9}$$

in order to remove nonessential parameters regarding the interpretation of the stability condition. Then,

$$\begin{cases} \dot{Z} &= -\phi(Z+\tau)I, \\ \dot{I} &= \phi(Z+\tau)I - \alpha I. \end{cases} \tag{10}$$

Additionally, it is necessary to transform (10) into the form (A1), as shown in Appendix A, by changing the basis into a basis of eigenvectors. Consequently,

$$\begin{cases} \dot{u} = -(\frac{\phi^3\tau^2}{(\alpha-\phi\tau)^2} - \frac{\phi^2\tau}{\alpha-\phi\tau})v^2 - (\phi + \frac{\phi^2\tau}{\alpha-\phi\tau})uv, \\ \dot{v} = (\phi\tau - \alpha)v + \phi uv + \frac{\phi^2\tau}{\alpha-\phi\tau}v^2. \end{cases} \tag{11}$$

Therefore,

$$\begin{cases} A = [0], \\ B = [\phi\tau - \alpha], \\ f(u,v) = -(\frac{\phi^3\tau^2}{(\alpha-\phi\tau)^2} - \frac{\phi^2\tau}{\alpha-\phi\tau})v^2 - (\phi + \frac{\phi^2\tau}{\alpha-\phi\tau})uv, \\ g(u,v) = \phi uv + \frac{\phi^2\tau}{\alpha-\phi\tau}v^2. \end{cases} \tag{12}$$

To find $h(u)$, as Appendix A shows, it is necessary to consider that the coordinates of any point in the center manifold must satisfy the conditions

$$\begin{cases} y = h(x), \\ |x| < \delta, \\ h(0) = 0, \\ Dh(0) = \dot{h}(0) = 0, \end{cases} \tag{13}$$

from (A2), which substituting on (A1), gives

$$\begin{cases} \dot{h}(u)[Au + f(u, h(u))] = Bh(u) + g(u, h(u)) \\ \dot{h}(u)[Au + f(u, h(u))] - Bh(u) - g(u, h(u)) = 0. \end{cases} \iff \tag{14}$$

Now, after substituting (12) (with $v = h(u)$) into (14), it can be seen that $h(u) = 0$ is a solution to the partial differential Equation (14). Then, the vector field restricted to the center manifold is given by

$$\dot{u} = 0. \tag{15}$$

Therefore, $u = 0$ is stable in (15). Thus, Theorem A2 from Appendix A guarantees that $(Z, I) = (0, 0)$ is stable for any parameter $0 \leq \tau < \dfrac{N(\gamma + \Omega)}{\beta}$) and, consequently, $(S^*, 0)$ is stable for the same set.

To complete the stability analysis, the case with $S^* = \dfrac{N(\gamma + \Omega)}{\beta}$ is considered, i.e., the center manifold theorem [62] is applied for:

- $\dfrac{\beta S^*}{N} - (\gamma + \Omega) = 0.$

The point ($S^* = \dfrac{N(\gamma + \Omega)}{\beta}$,0) is the origin of the system (10) with parameter $\tau = \dfrac{\alpha}{\phi}$. In order to assess stability, a simulation is presented in Figure 2.

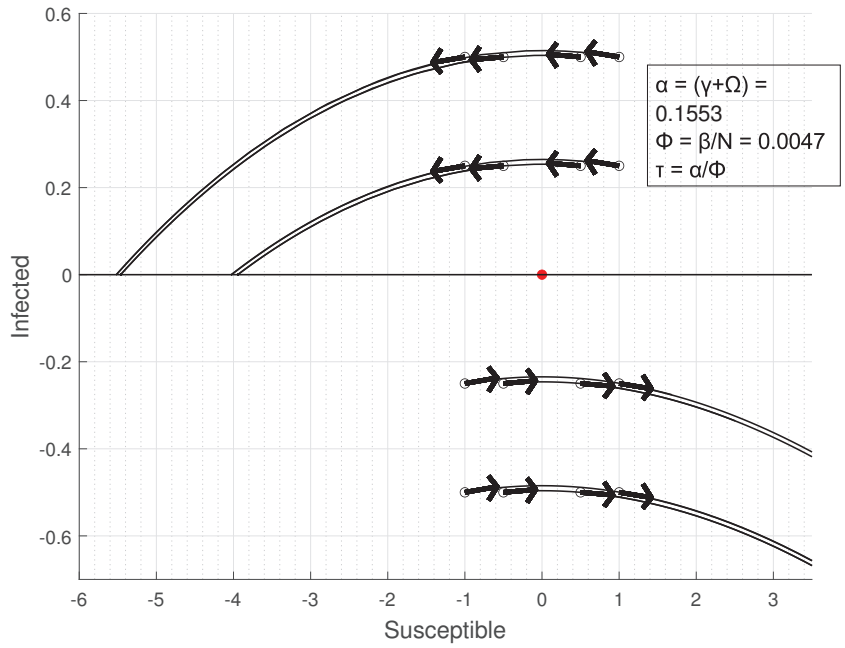

Figure 2. Simulation around the origin for $\tau = \dfrac{\alpha}{\phi}$.

As can be seen, neighborhoods close to the origin with initial values $I^* < 0$ are unstable, as the trajectories point towards negative infinite. However, the system is only defined for $I^* > 0$, considering that there can be no negative infected, although Z can be negative (as we translated the original system), and even a small disturbance would never take it to a point with $I^* < 0$. Consequently, it is a degenerated equilibrium [63].

3.3. Basic Reproduction Rate

The basic reproduction rate or R_0 is defined as the average number of secondary infections produced when one infected individual is introduced into a host population, where almost everyone is susceptible ($S \approx N$) [15,64]. For example, if the R_0 for COVID-19 in a population is 5, then each new case is expected to produce 5 secondary infections, assuming everyone around is susceptible.

Mathematically, R_0 is a threshold for stability of a disease-free equilibrium and is related to epidemic's peak and final size [61].

Looking at the equation $\dot{I}$ from (4) it can observed that, when $S \approx N$, the signal of $\dot{I}$ is defined by $\beta - (\gamma + \Omega)$.

Therefore, for the SIRD model, R_0 can be defined as

$$R_0 = \frac{\beta}{\gamma + \Omega}, \tag{16}$$

such that, when $R_0 > 1$, the equilibrium is locally unstable ($\dot{I} > 0$) but stable if $R_0 < 1$, implying $\dot{I} < 0$.

3.4. Phase Portrait for Different Values of R_0

Figures 3 and 4 show the phase portrait of the system for different values of R_0, specifically chosen to portray the only two possible outcomes.

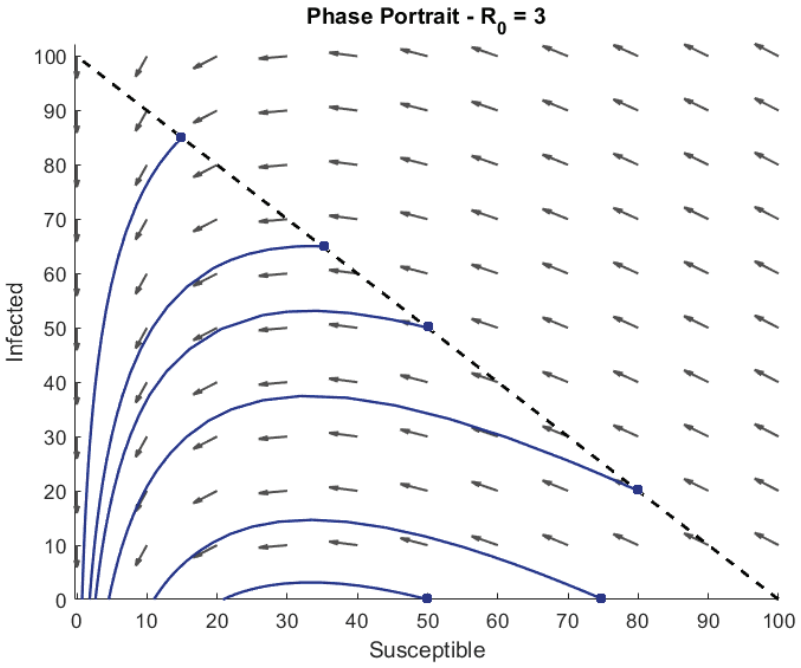

Figure 3. Phase portrait for $R_0 = 3$ (> 1).

In Figure 3, it is shown that, for $R_0 > 1$, the number of infected initially grows, but, as $\dot{S} < 0$ in that situation, at some point $\frac{S^*}{N}$ eventually becomes $< \frac{1}{R_0}$, which implies $\dot{I} < 0$, and the trajectory always ends up on the horizontal axis (I = 0). This result is known as the herd immunity value.

The interception point depends on the initial conditions. Therefore, there can be more or fewer individuals that will never become infected in the course of the epidemic (final number of susceptible at disease-free equilibrium).

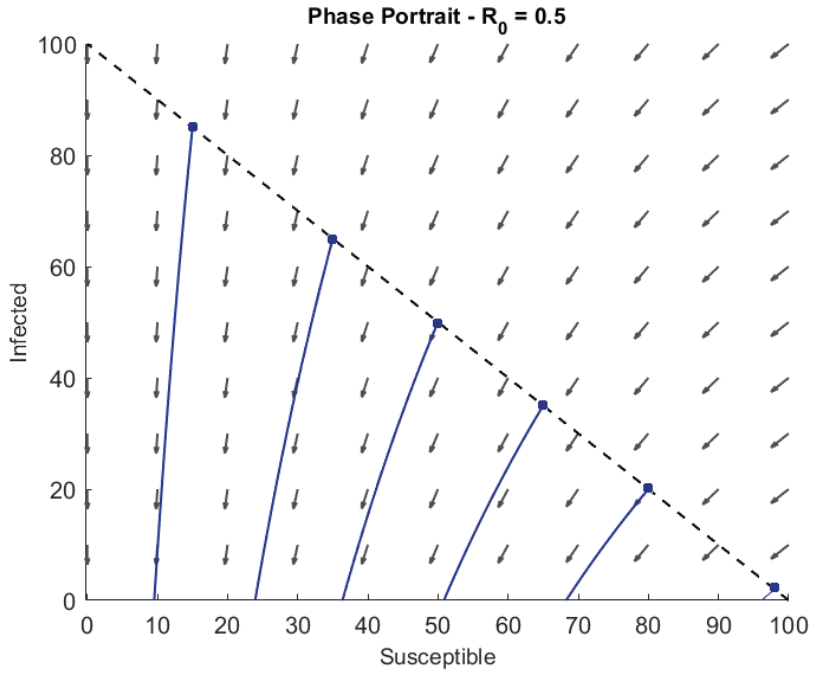

Figure 4. Phase portrait for $R_0 = 0.5 < 1$.

In Figure 4, with $R_0 < 1$, the system points toward the horizontal axis much faster, with the number of infected decreasing steeply at all times. This result is expected, as $\dot{I} < 0$ for $R_0 < 1$.

4. Case Studies and Numerical Simulations

This section presents two case studies, first with parameters derived from Brazil, followed by Uruguay. These two countries were chosen because of their different basic reproduction number, as a result of particular population dynamics concerning the contact rate β. For Brazil, R_0 is estimated to be close to 2.82 [60], and for Uruguay, R_0 is close to 1.13 [65]. These values were obtained using early infections data, as shown in Figures 5 and 6, and they are believed to present a scenario where there is no response to the pandemic, both individually or systemically.

Figures 5 and 6 show how the SIRD model compares with real data from Brazil and Uruguay in the early days of disease spread, with [66] as the data source.

The choice for the short time interval and period adopted is due to the emergence of the public strategy of social distancing, which was implemented at the beginning of the pandemic. In Figure 5, a smaller interval was also considered, since the data collected for Brazil are data for the country as a whole. As regions have socioeconomic and educational distinctions, they have different propagation dynamics and responses to mitigation strategies.

Both graphs display a good fitting for initial data, with subsequent detachment between model and data, which suggests there is a change in behavior due to the implementation and effectiveness of isolation policies or individual confinement. In Section 4.1, we use this set of parameters to simulate longer-term scenarios with no isolation that serve as a reference for evaluating the control algorithm.

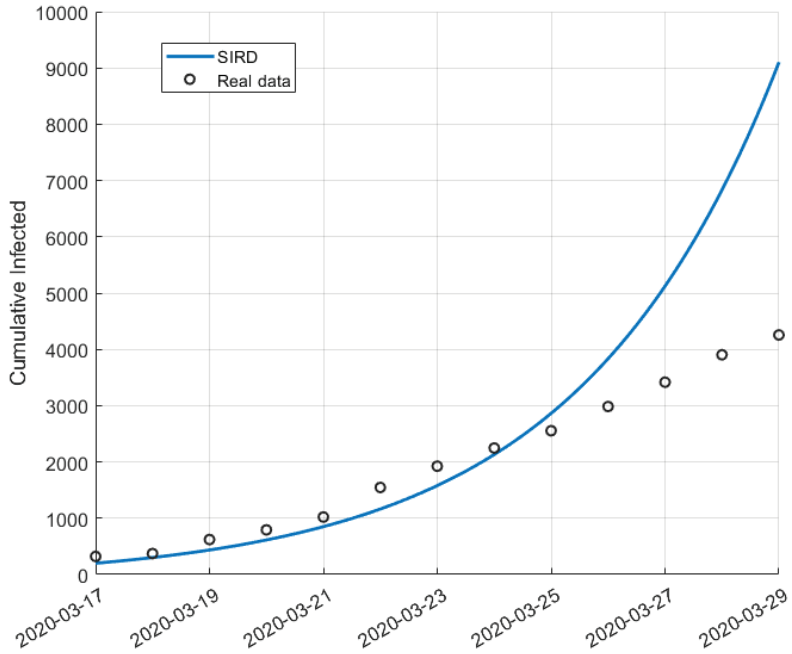

Figure 5. SIRD model validation with real data from Brazil. $R_0 = 2.82$, $\gamma = 0.1508$, $\Omega = 0.0045$.

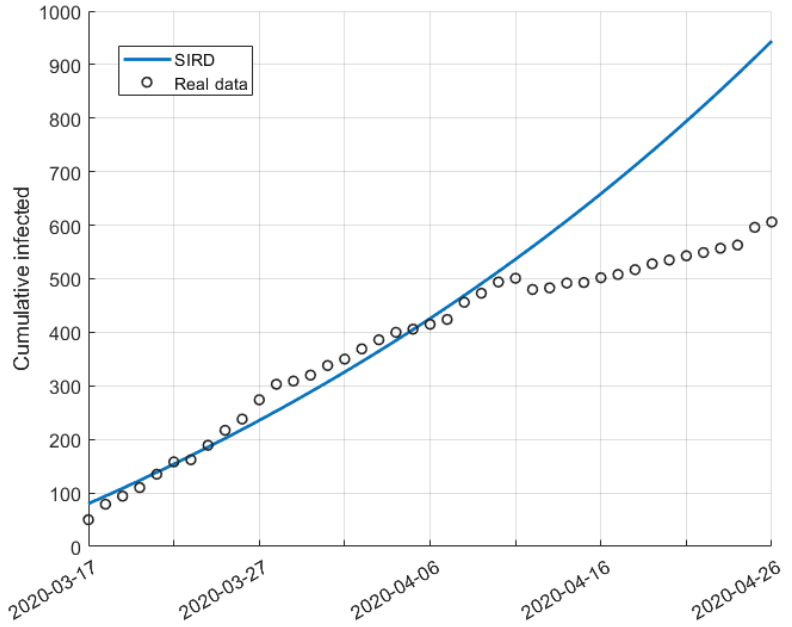

Figure 6. SIRD model validation with real data from Uruguay. $R_0 = 1.13$, $\gamma = 0.1508$, $\Omega = 0.0045$. The date 2020-04-12 presents an anomaly in the dataset, with negative new cases.

4.1. Simulation for Brazil

First, the model was simulated considering the parameters for Brazil, i.e., $N = 209.5$ million inhabitants, and $I_0 = 10$ individuals are considered, with the results shown in Figure 7.

The chosen parameters conduct a simulation for a full-blown pandemic outbreak. The last case ended about 120 days after the disease had begun being disseminated, as we can see in Figure 7B,D, which shows a high number of dead at the end, about 2.71% of the total population before the pandemic.

Figure 8 clearly shows the large proportion of the population that became infected at some point. At the end, less than 10% never became infected.

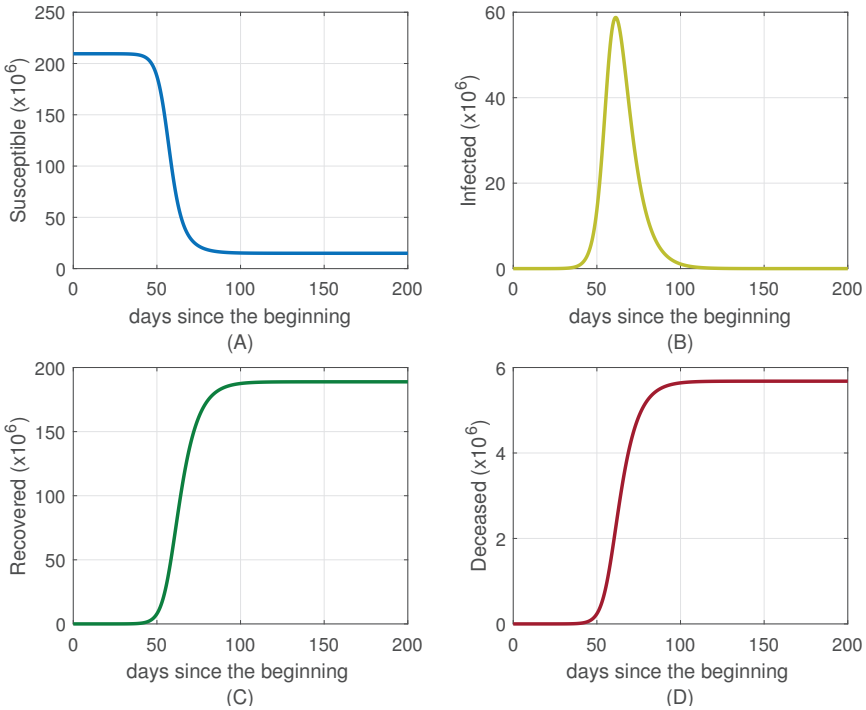

Figure 7. Brazilian case study with $R_0 = 2.82$, $\gamma = 0.1508$, $\Omega = 0.0045$. Considering: (**A**) Susceptible population; (**B**) Infected population; (**C**) Recovered population and (**D**) Deceased population.

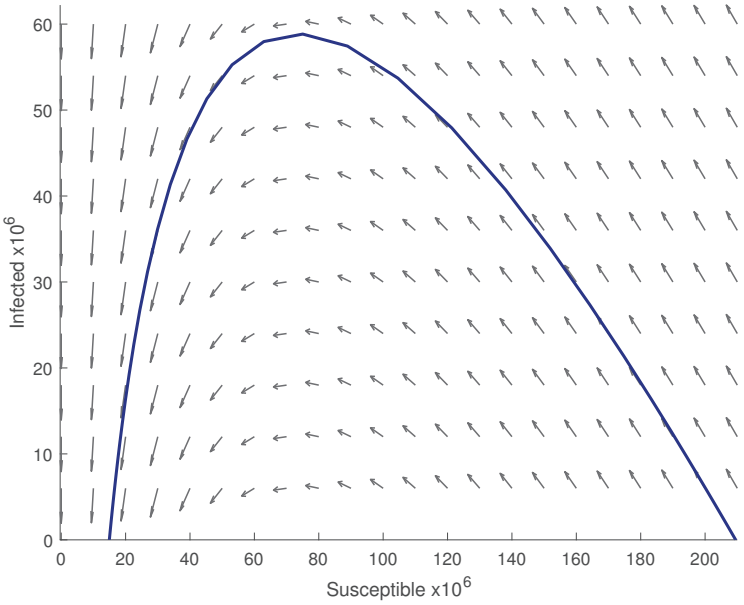

Figure 8. Phase portrait for Brazil, $R_0 = 2.82$—axis in million.

4.2. Simulation for Uruguay

The model was also simulated with parameters from Uruguay, i.e., $N = 3.45$ million inhabitants, considering $I_0 = 10$ individuals, and the results are shown in Figure 9.

As the R_0 for Uruguay is lower than Brazil's, there is a significant difference concerning the dissemination of the virus. Figure 9 shows that the pandemic lasted much longer in Uruguay than in Brazil. However, Uruguay had much fewer dead individuals in the end, only about 0.64% of the total population before the pandemic.

The low amount of individuals that ever became infected in Uruguay is highlighted in Figure 10, which is about 24% of the total population before the pandemic. Additionally, the lower number of infected individuals suggests that having a lower R_0 due to lower β

(contact rate) is a good indicator of what proportion the virus spread will achieve. This fact inspires the control algorithm used as reference for public employment polices, and it is studied in the next section.

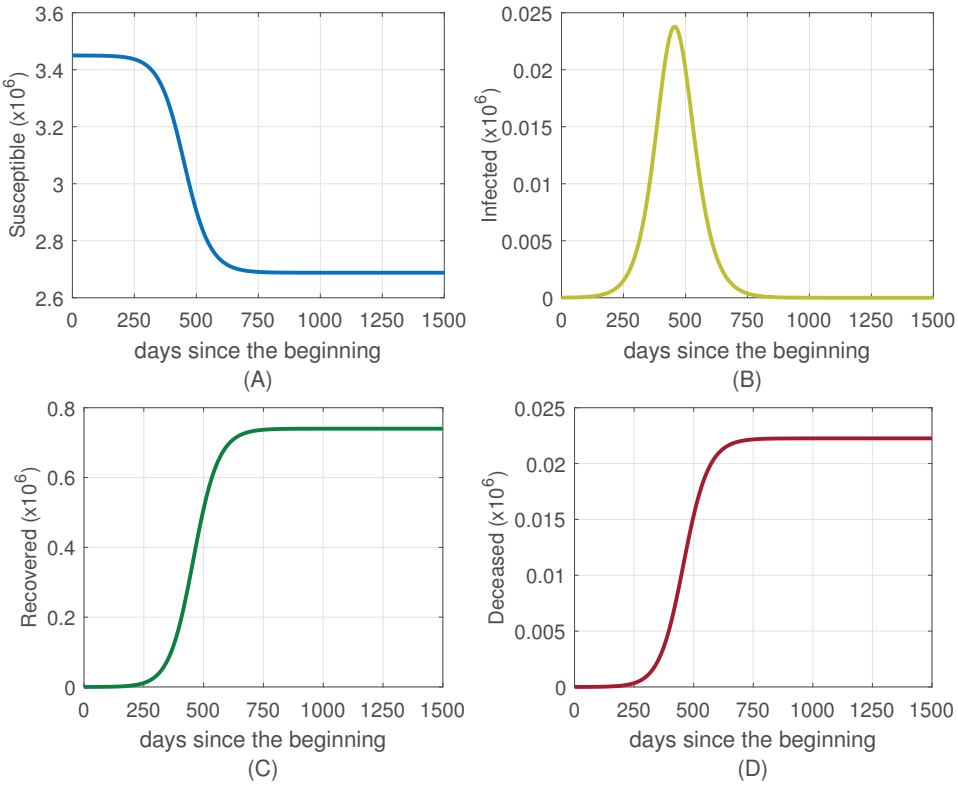

Figure 9. Uruguay case study with $R_0 = 1.13$, $\gamma = 0.1508$, $\Omega = 0.0045$. Considering: (**A**) Susceptible population; (**B**) Infected population; (**C**) Recovered population and (**D**) Deceased population.

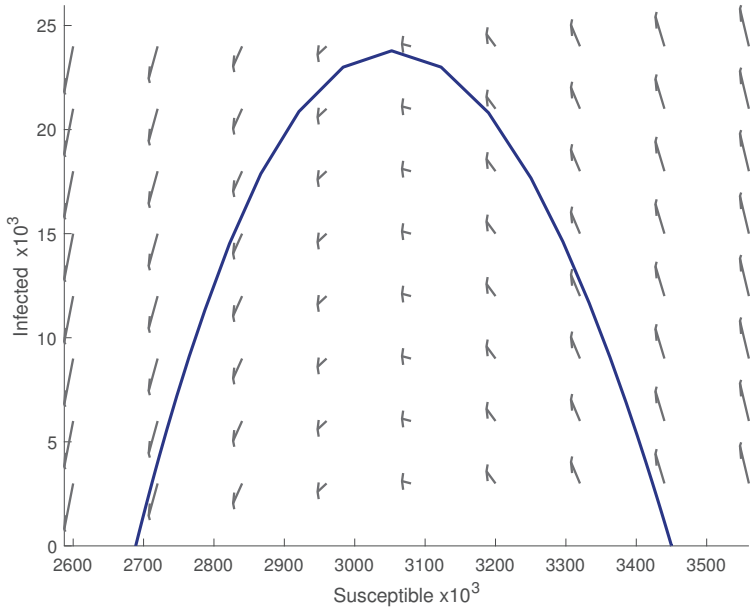

Figure 10. Phase portrait—Uruguay. $I_0 = 10$ individuals.

5. Validation for the SIRD Model

In this study, we used one year of epidemiological data from the states of São Paulo, Minas Gerais and Rio de Janeiro, starting on each state's first day of infection, to validate the SIRD model.

First, the fitting process using the parameters that generate the curve that best fits the data from the model was made using daily data. However, for this large volume of data, the minimization algorithm produced a lot of noise, or overfitting, in addition to having weekly seasonality due to irregular notification dynamics. Thus, the use of weekly data was considered more suitable.

The procedure was performed to try to minimize the functional given by Equation (17). The adopted SIRD model assumes that the parameters γ and Ω are invariant in time, while the parameter β is variable in time. So, for 52 weeks, there are 54 parameters to be estimated. The process was carried out in successive steps and, instead of performing only one minimization for the 52 weeks, minimization was performed every 15 weeks, with each step accumulating the values obtained for the previous set of weeks and calculating the values of β only for the following weeks while adjusting the values of γ and Ω. Furthermore, a regularization term was inserted in the Tiknovov regularization structure, penalizing sudden variations to produce a smoother curve.

$$min\ \theta = \tau_1 \parallel (I_t^{cum} - D_t) - (\hat{I}_t - \hat{R}_t) \parallel_2 + \tau_2 \parallel D_t - \hat{D}_t \parallel_2 + \tau_3 \parallel \Gamma B \parallel_2 . \tag{17}$$

The first term of the functional θ represents the total number of infected people since the beginning of the count, while the second term represents the total number of deaths that occurred due to the disease. Finally, the last term represents a regularization which penalizes the differences between the successive terms of β, represented by the matrix B (19), whose differences are calculated by the matrix Γ (18):

$$\Gamma = \begin{bmatrix} 1 & -1 & 0 & \cdots & 0 \\ 0 & 1 & -1 & \cdots & 0 \\ \vdots & & \ddots & & \vdots \\ 0 & \cdots & & 1 & -1 \end{bmatrix} \tag{18}$$

$$B = \begin{bmatrix} \beta_{t=0} & \beta_{t=1} & \cdots & \beta_{t=T} \end{bmatrix}^T. \tag{19}$$

In this way, better results could be obtained, as can be seen in the validations made for the states of São Paulo, Rio de Janeiro and Minas Gerais. In them, the value of R_e was calculated as described by Equation (20):

$$R_e(t) = \frac{\beta(t)}{\gamma + \Omega} \frac{S(t)}{N(t)}. \tag{20}$$

The effective reproduction number is the average number of infected individuals per infected person under existing conditions at a given time. The effective number, R_e, is the basal reproduction number, R_0 exposed to the real conditions of disease evolution. Consequently, it constantly changes, reflecting interaction between the population and the infectious agent [67,68].

The effective reproduction number R_e was estimated by finding the values that minimize the function described by Equation (18). For Equation (21), $\beta(t)$ is considered variable over time, because, due to restriction measures imposed by public policies, the transmission or contagion rate is altered, and, consequently, the key number $S(t)$ also varies according to this rate. Although $N(t)$ represents the total population and it is variable over time, for the considered interval, this constant value can be adopted.

5.1. Validation for São Paulo

For the state of São Paulo, the time-invariant parameters obtained and used can be seen in Table 2.

Table 2. Model parameters for São Paulo.

Parameter	Parameter Description	Value
γ	recovery rate	1.071
Ω	lethality of virus (mortality rate)	0.0285
N	population size	46,289,333

Where a value of 1.0701 for γ means that the average recovery period is 1.0701 weeks, and a value of 2.85% for Ω means 2.85% of infected people are killed by the virus per week.

As can be seen in Figures 11 and 12, the fit for the values of the new weekly deaths and new accumulated deaths performed well, as these were privileged through the manipulation of parameters τ_1, τ_2 and τ_3. We see that the fit for the value of new cases in Figures 13 and 14 was not as accurate as the previous fit, practically maintaining qualitative behavior.

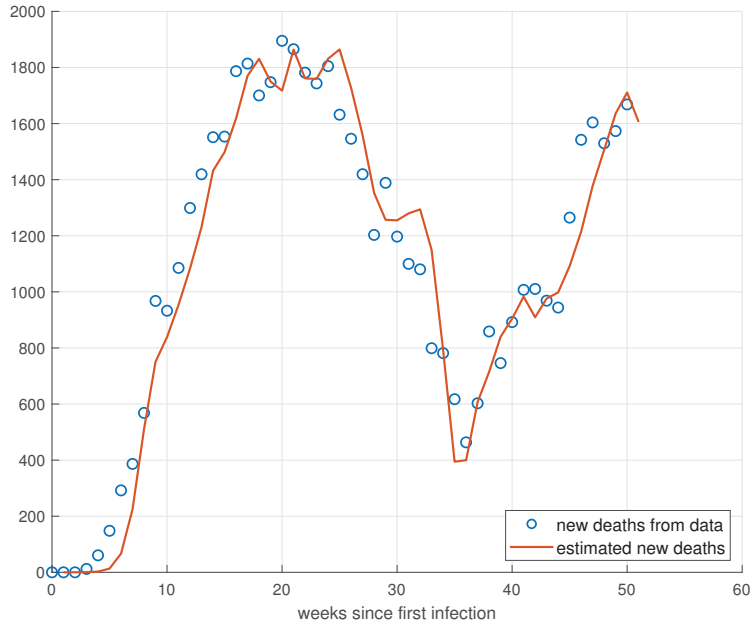

Figure 11. New weekly deaths for São Paulo.

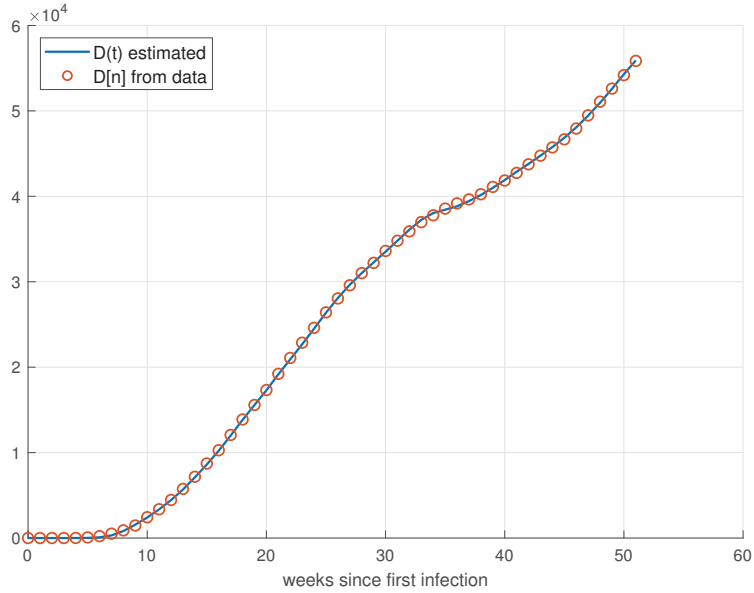

Figure 12. Accumulated deaths for São Paulo.

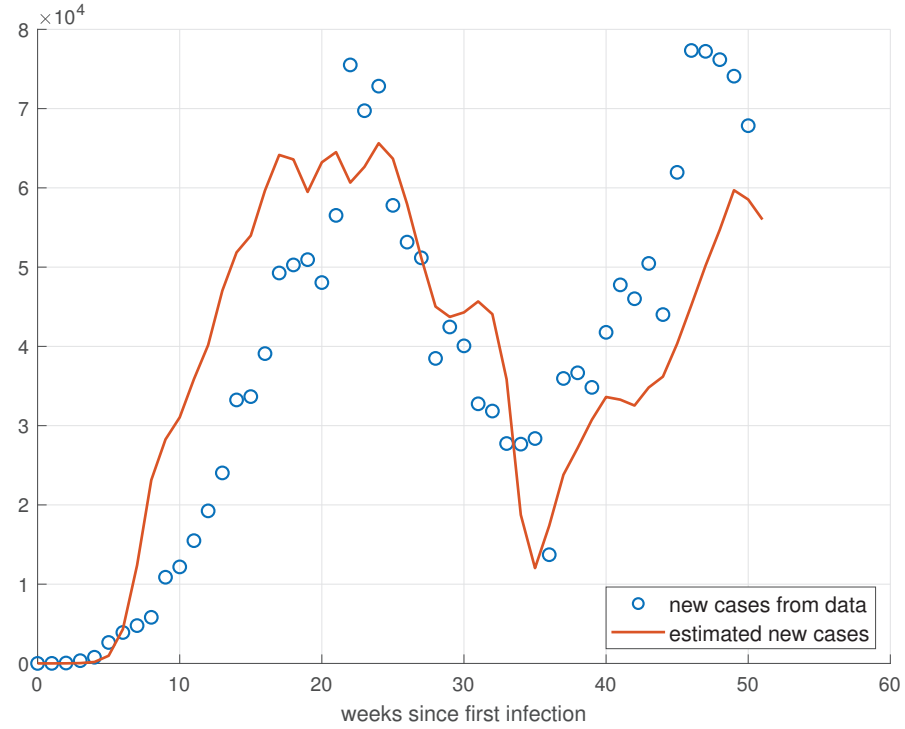

Figure 13. New cases for São Paulo.

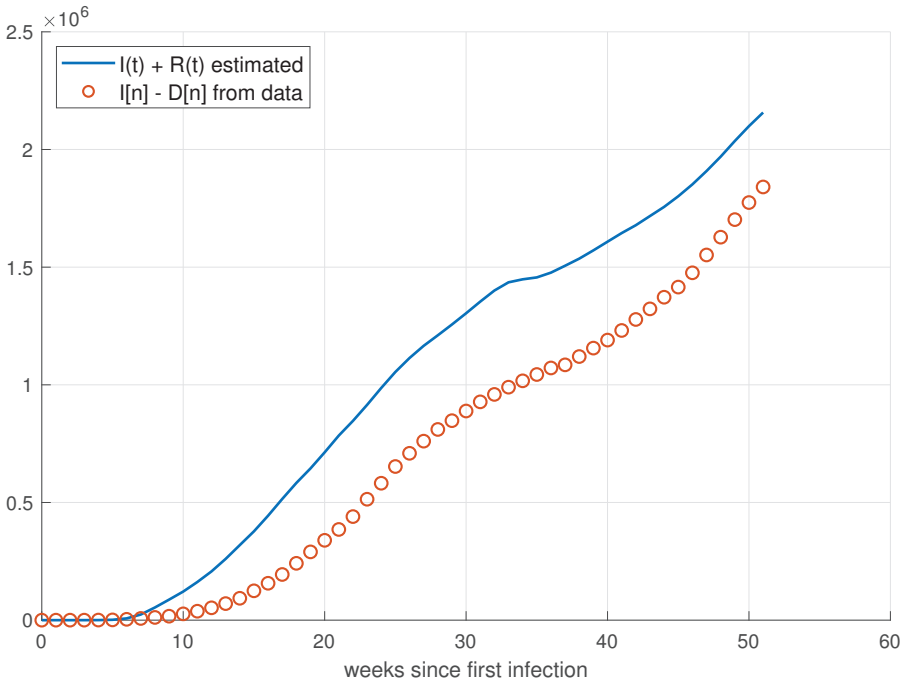

Figure 14. Accumulated cases for São Paulo.

For the graph of the effective reproduction number R_e Figure 15, it can be noted that the values were close to those obtained by the COVID-19 observatory [69], which is an independent initiative resulting from the collaboration between researchers who performed this measurement using their own methodology. There is a large divergence around 35 weeks. For the model developed in this report, the value obtained from R_e makes sense, since there was a very sharp decrease in new cases and deaths in this period.

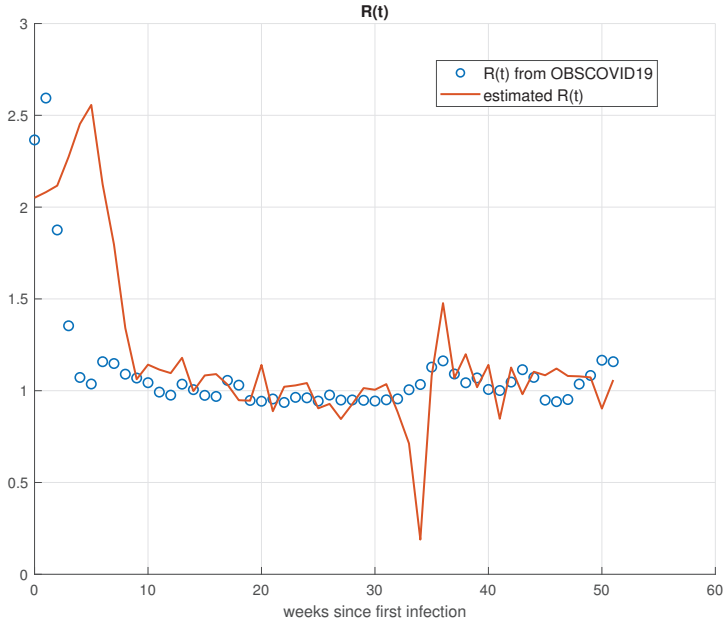

Figure 15. Comparison of effective reproduction number value for São Paulo.

5.2. Validation for Minas Gerais

The time-invariant parameters for the state of Minas Gerais can be seen in the Table 3:

Table 3. Model parameters for Minas Gerais.

Parameter	Parameter Description	Value
γ	recovery rate	0.9973
Ω	lethality of virus (mortality rate)	0.0258
N	population size	21,292,666

Here, it can be noted that the values of γ and Ω were quite close to the values obtained for São Paulo. Observing the graphs of new weekly deaths in Figure 16 and accumulated deaths in Figure 17, it can be seen that the model fit for these data had good performance, as well as for São Paulo.

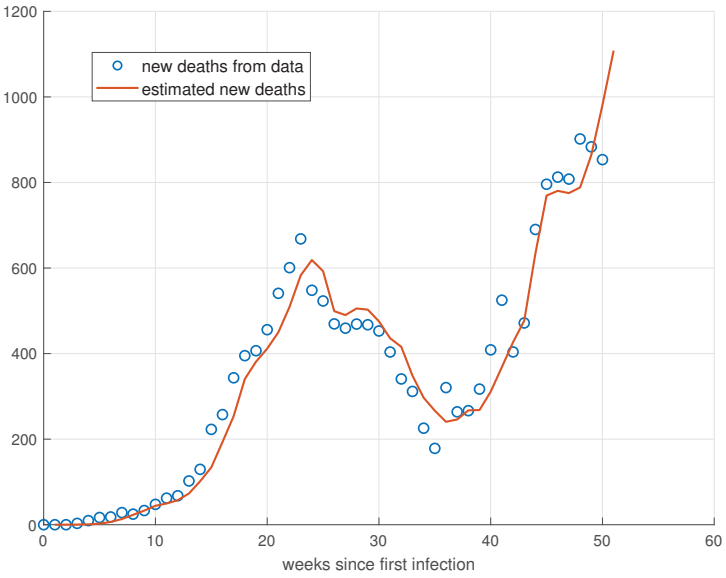

Figure 16. New weekly deaths for Minas Gerais.

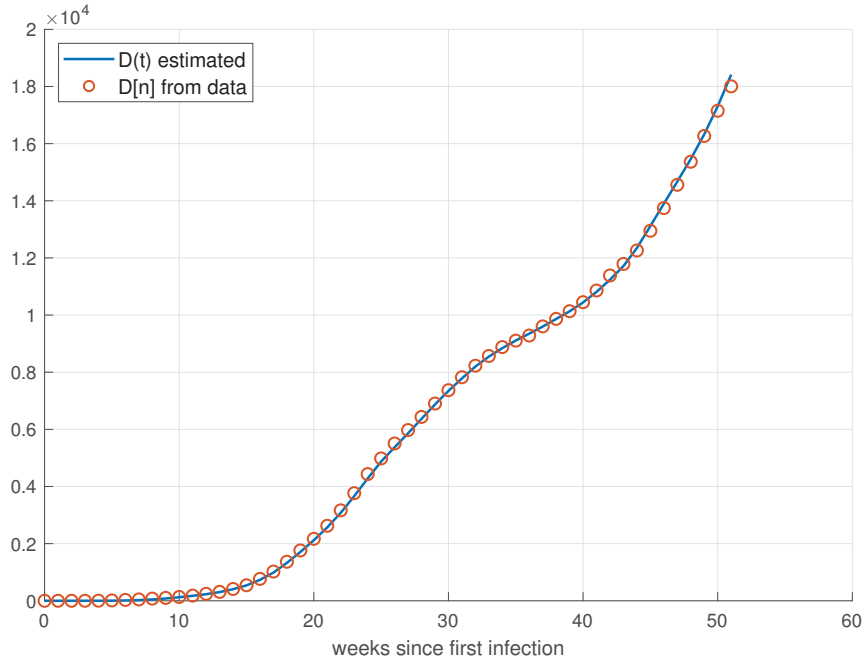

Figure 17. Accumulated deaths for Minas Gerais.

For the data of new cases in Figure 18 and accumulated cases in Figure 19, the model performed very well until around the 35th week, when it started to present a slight difference, maintaining qualitative behavior.

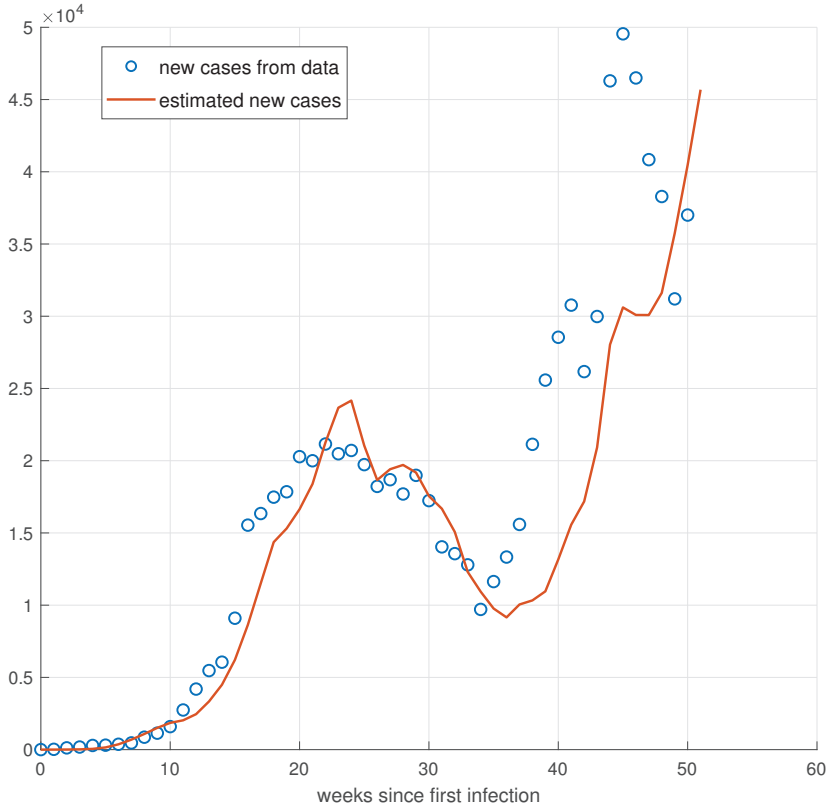

Figure 18. New cases for Minas Gerais.

For the data of R_e, it is possible to notice that there is possibly a delayed relationship between the values obtained by the model and the values obtained by the COVID-19 observatory [69], as can be seen in Figure 20.

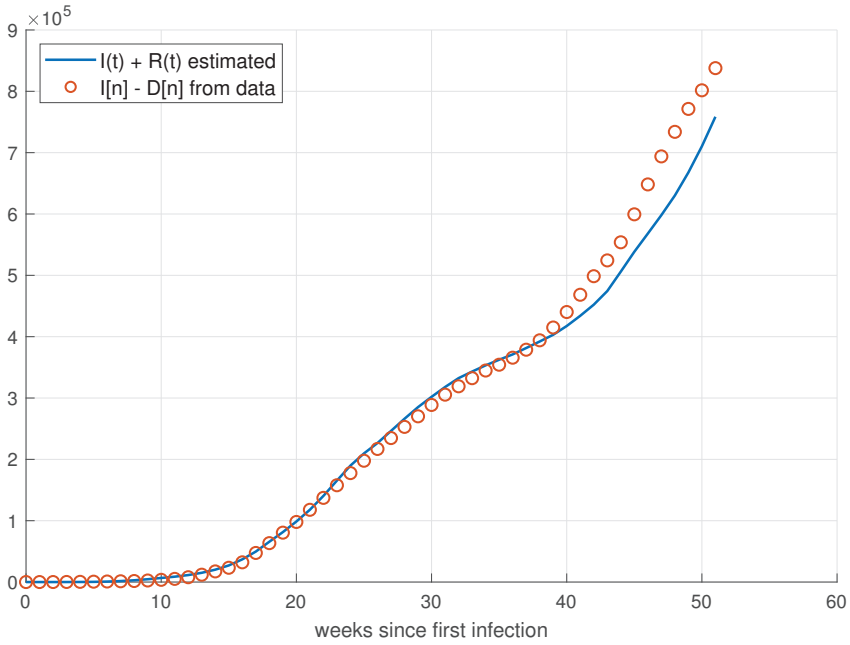

Figure 19. Accumulated cases for Minas Gerais.

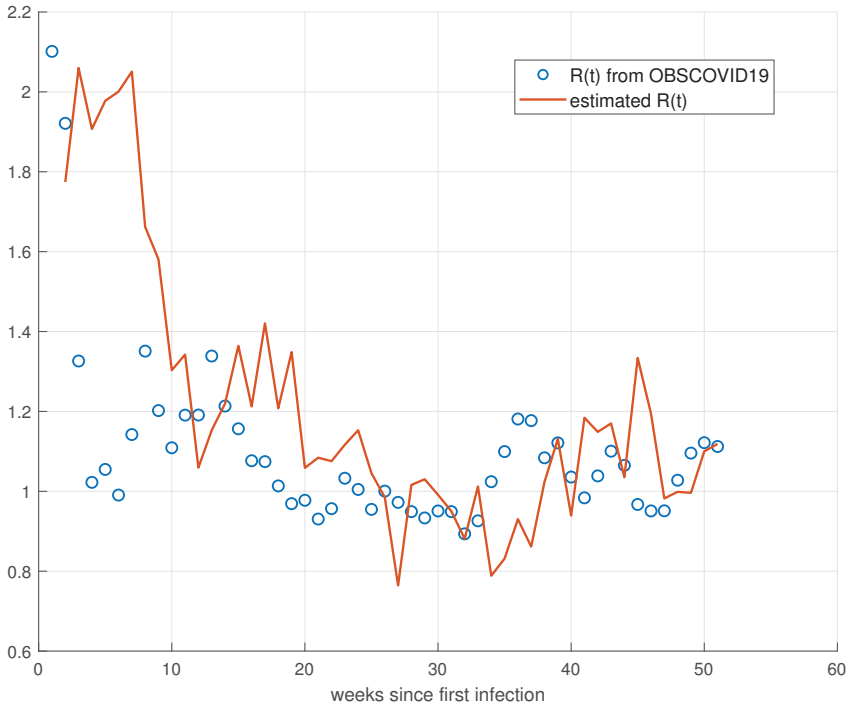

Figure 20. Comparison of effective reproduction number value for Minas Gerais.

5.3. Validation for Rio de Janeiro

For the state of Rio de Janeiro, the time-invariant parameters can be seen in Table 4.

Table 4. Model parameters for Rio de Janeiro.

Parameter	Parameter Description	Value
γ	recovery rate	0.9431
Ω	lethality of virus (mortality rate)	0.0500
N	population size	17,366,189

For the state of Rio de Janeiro, the value of Ω appears to be higher than for the other two states, while γ was close to the values found for São Paulo and Minas Gerais.

The analysis of Figures 21 and 22 shows that the fit of the model for the data of new weekly deaths and deaths accumulated in weekly reports performed well.

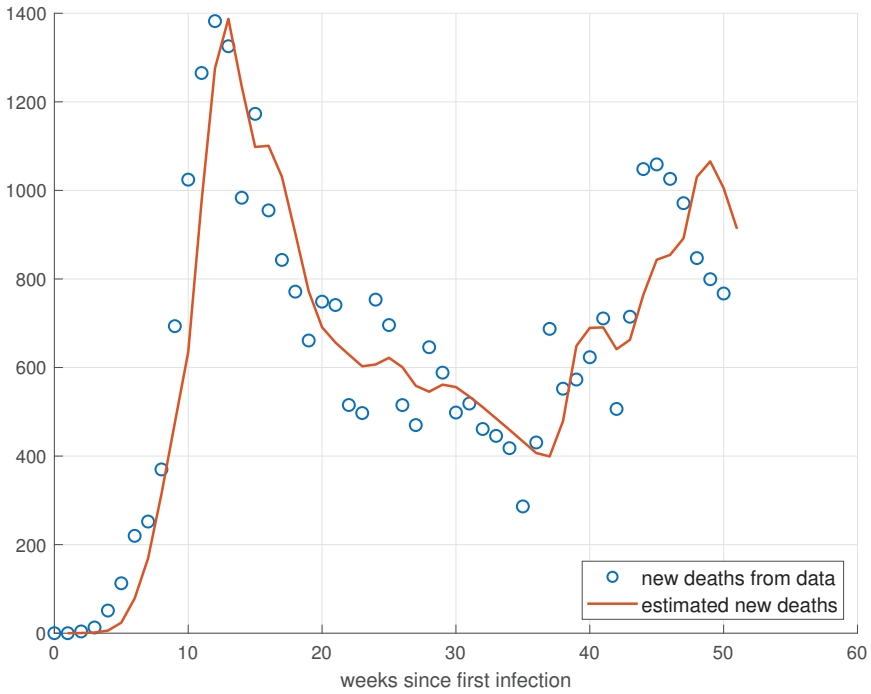

Figure 21. New weekly deaths for Rio de Janeiro.

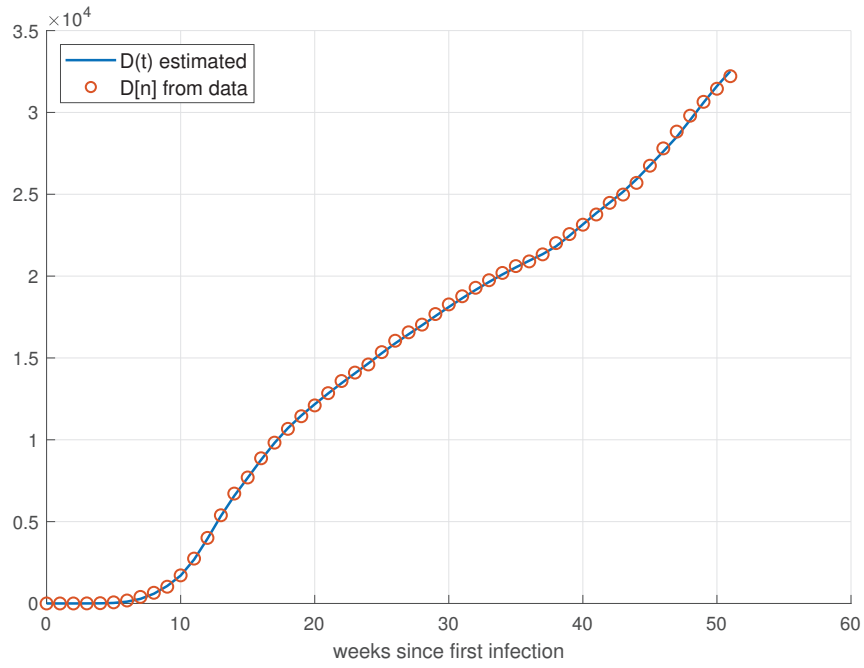

Figure 22. Accumulated deaths for Rio de Janeiro.

For the state of Rio de Janeiro, the fit for the data of new weekly cases and accumulated deaths is similar to the São Paulo fit, indicating a possible under-reporting of cases throughout the period, as shown in Figures 23 and 24.

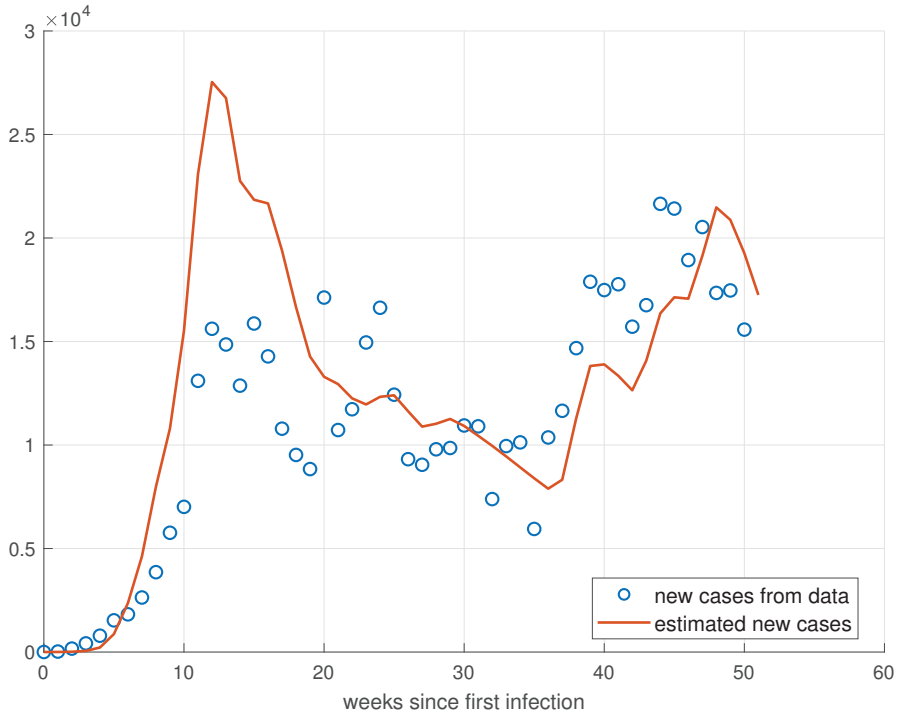

Figure 23. New cases for Rio de Janeiro.

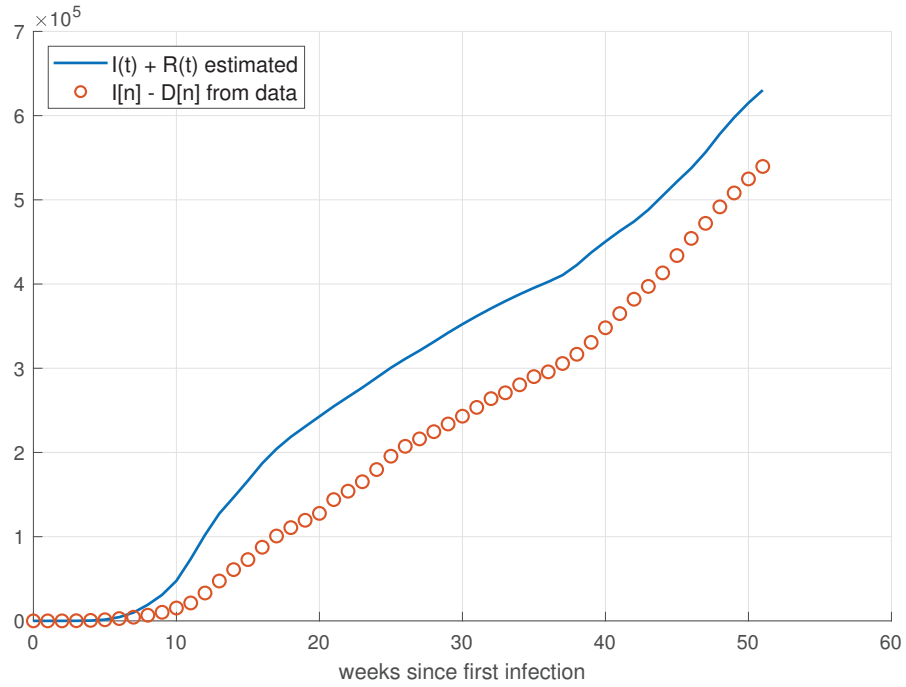

Figure 24. Accumulated cases for Rio de Janeiro.

As for both other states, the effective reproduction number appears to have some delay with respect to the number obtained by the COVID-19 observatory [69], as shown in Figure 25.

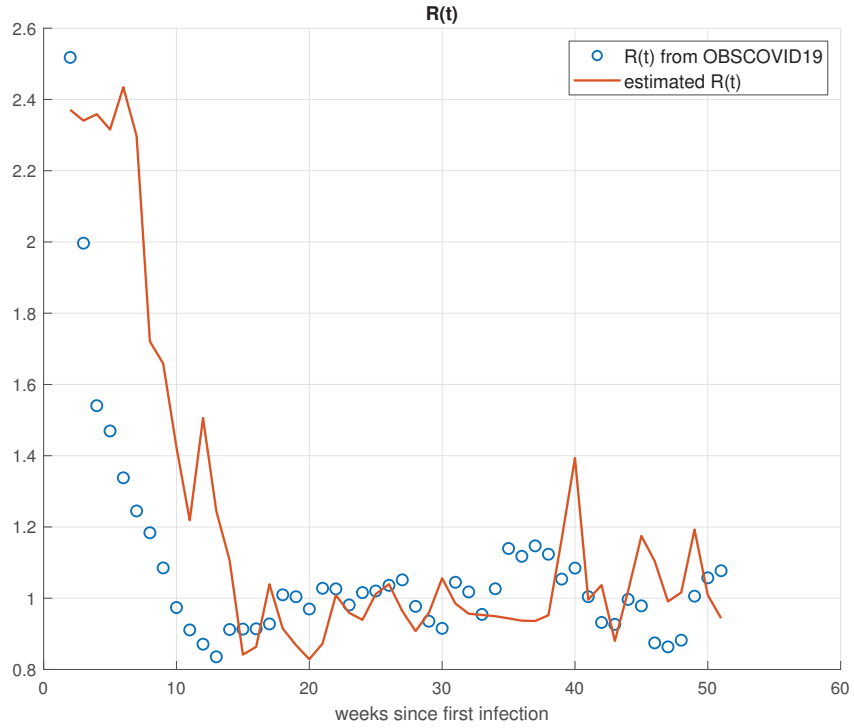

Figure 25. Comparison of effective reproduction number value for Rio de Janeiro.

6. Spread Control

Applications of control theory for epidemic diseases, including COVID-19, range from optimal control, which can be used for social distancing [70], vaccine deployment policy [71] or even a mix of isolation and a vaccination program [72], to model predictive control (MPC), which is also used for the development of social distancing [73,74] and vaccination policies [75]. However, the approach to be followed here is simpler and aims to build an algorithm explicitly programmed through feedback of state variables, similar to other heuristics [76,77] already studied.

Practical usage of the control algorithm proposed should consider the availability and uncertainty of current infection data, which are usually embedded with under-reporting and significant delays when compared with reality, especially in countries which do not have a thorough testing program organized. It should review the simplifications assumed in the model formulation in Section 2 as well, addressing the peculiarities of the disease being analyzed.

Looking forward to the future, the algorithm should address any disease that follows the same pattern of transmission of the coronavirus, that is, infections resulting from the transportation of contaminated droplets of secretions from infected individuals to susceptible ones and that suggests isolation is effective. The main difference will be the difficulty imposed by a new virus concerning the imposition of lower values of R_e, a parameter which is described in the next section. Viruses that are transmitted more easily impose a bigger challenge, as fewer contacts are needed to effectively pass the disease ahead.

Algorithm Implementation

Here, the implementation of a three-level stratified controller is studied, mitigating disease spread, aiming to maintain the demand of intensive care units (ICUs) lower than those available at all times until a vaccine is available.

As was shown, R_0 measures how the disease propagates when there are almost no infected individuals present ($S \approx N$). While R_0 provides valuable information on the viral dissemination dynamics when there is no developed immunity and information on the epidemic available, other factors begin to influence its dynamics during the course of spreading.

Therefore, the effective reproduction number R_e, which describes the average value of secondary infections as a time-dependent function, is a more appropriate parameter to be analyzed amidst an epidemic outbreak [78]. In a homogeneous population, it is simple to obtain R_e by multiplying R_0 and the susceptible proportion of the population at some instant t [79].

The idea to be developed here is to regulate R_e in order to maintain the healthcare resources at an acceptable level. The underlying mechanism is the manipulation of the contact rate of individuals β by cycling the imposition and relaxation of social distancing measures [57] as well as awareness campaigns to stimulate the adoption of individual protection procedures.

Therefore, β is no longer considered fixed but time-dependent $\beta(t)$. Contrarily, γ and Ω are still considered invariable, as treatments such as the use of remdesivir or monoclonal antibodies, both approved by the American Federal Drug Administration (FDA), are prescribed only to severe cases whereupon the patient is already hospitalized and therefore isolated [80,81] in the first case, while, in the latter, it took almost a year to be approved for emergency use [82].

Levels of the controller are decided based on the current number of patients needing an ICU. This number is defined as 5% of the current number of infected individuals, assumed as the probability of someone who becomes infected needing intensive care [83].

Each level is composed of an interval from which R_e can randomly assume any value. The interval is constructed with limits equal to $\pm 10\%$ of the measured mean value. This is performed to mimic the difficulty of imposing and tracking a precise value for R_e for diseases with only a few epidemic studies.

The stratified controller model was chosen due to being easier to implement than other forms of modeling social distancing, generally based on continuous values for R_e, which are very hard to track and impose precisely. The algorithm is also adaptable structurally speaking, as the R_e should necessarily guarantee the desired behavior according to the model. The most significant difficulties rest in creating the appropriate public policies to reach the desired R_e level.

Estimations of the economic impact of the COVID-19 pandemic are situated close to the trillion dollars figure globally [84–86], with devastating shocks on various industries, and the imposition of social distancing policies should have been, theoretically, a big part of this loss. However, there is significant evidence that quarantine is effective against not implementing containment mechanisms [87], more effective when applied early [88] and that deterioration of economic conditions preceded the introduction of isolation policies [89] or that the culprit of the COVID-19 recession is COVID-19 itself [90]. Therefore, practical usage of the three-level controller should lead to economic benefits, not to mention that saving lives should be worth the cost nevertheless.

The three-level controller is described in Table 5, with the calibration level (mitigation or suppression) related to the value of the reproduction number associated. Mitigation and suppression measures differ in whether they aim to reduce the reproduction number, R_e, to less than 1 (suppression) or to merely slow spread by reducing R_e but not to less than 1 (mitigation) [91]. Therefore, Level A can be described as mitigation strategy and Level C as a suppression one, generally called a lockdown, while Level B is situated between both.

All the actions taken at a certain point will last for a regularly chosen duration during the course of the pandemic. This is performed to reduce social and economic uncertainty as the population has time to comply.

Table 5. Description of the three-level controller.

Level	$\mathbb{E}[R_e]$	Measures Taken	Value Source	When
A	2	Self-imposed measures are stimulated in order to accelerate awareness spread. Prevention measures such as mask wearing, hand washing and self-imposed social distancing can be described as reductions in infectious output, susceptibility and contact rate, respectively [92].	As such measures stack up additively [92], a 10% efficacy for each one reduces the effective contact rate by 30%.	Intensive care unit demand is lower than 10% of the total amount available. $\frac{5I}{100} < 5$
B	1.1	Government implements social distancing measures such as reduced business hours and occupation or public spaces restrictions.	A similar R_e is obtained for the state of Sao Paulo in March 2021, when such measures where adopted [93].	Intensive care unit demand is between 10–80% of the total amount available. $5 < \frac{5I}{100} < 40$
C	0.5	Mandatory home confinement except for vital sectors workers.	Very close to the R_e obtained by Spain during adoption of lock down [94].	Intensive care unit demand is higher than 80% of the total amount available. $\frac{5I}{100} > 40$

7. Control Strategy Results

In this section, the three-level control strategy described in the former section is simulated assuming a hypothetical scenario for an isolated city in Brazil with 10 infected initial cases, a population of 100,000 inhabitants and an R_0 the same as the country's, i.e., 2.82. This number is maintained for the first 15 days to replicate initial unawareness. Brazil was chosen due to its high baseline contact rate, represented by the high value of R_0, as opposed to Uruguay. Therefore, as the number of cases and individuals in need of ICUs grow faster than the system can adapt, it represents a need for establishing isolation policies.

The number of ICUs available is considered to be 50, very close to the proportion of beds/individuals obtained for the state of São Paulo before the pandemic in 2018 [95].

The total period analyzed is one year, because this is the period assumed for the development of a vaccine, with reference to the Pfizer vaccine, which started being developed in January 2020 with the release of the SARS-CoV-2 genome [96] and initially applied in the UK at the beginning of December 2020 [97].

Three different strategies were considered: no attempt to control the disease spread; updating R_e every 30 days; and updating R_e every 21 days.

7.1. No Attempt to Control the Spread of the Disease

As expected, Figure 26 shows the potential of COVID-19 to quickly overwhelm the healthcare system, with ICU demand surpassing the availability of beds less than two months after the beginning of the pandemic. The randomness added did not result in significant differences with respect to the baseline established in Section 4.

The dynamics of free dissemination can be seen for all the compartments in the SIRD model used in Figure 27.

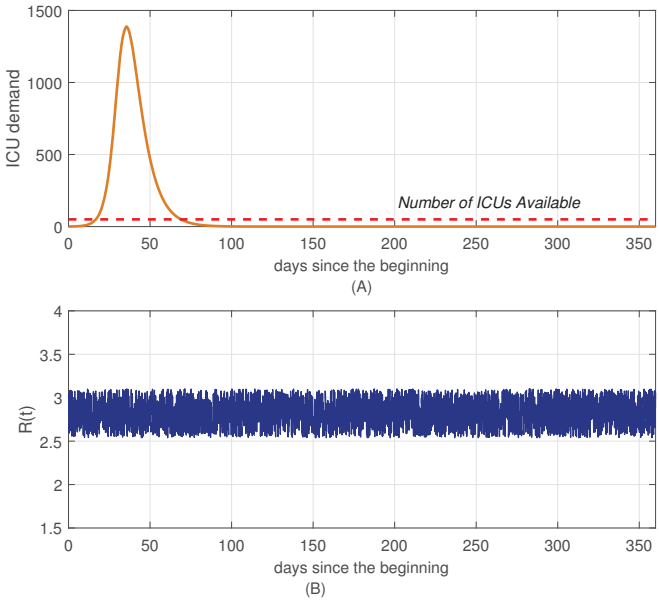

Figure 26. No control applied: (**A**) ICU demand and (**B**) $R(t)$.

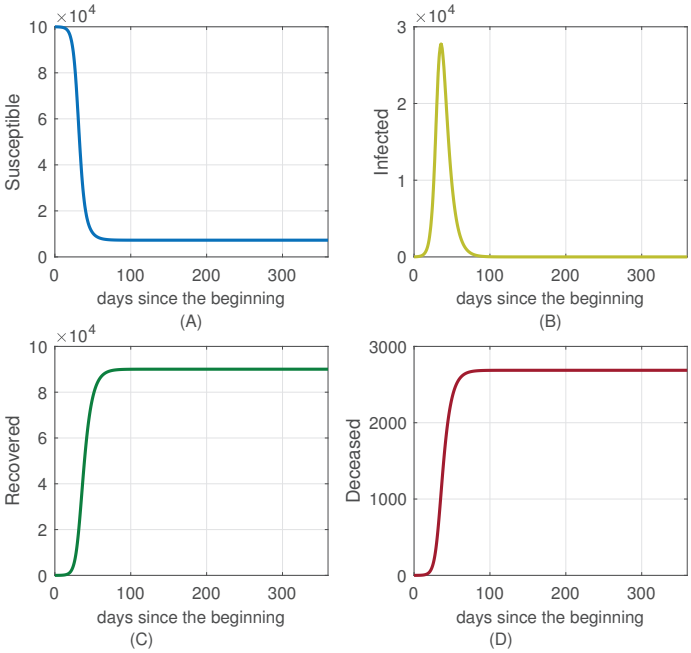

Figure 27. State variables evolution when no control is applied, considering: (**A**) Susceptible population; (**B**) Infected population; (**C**) Recovered population and (**D**) Deceased population.

7.2. Updating R_e Every 30 Days

Figure 28 displays the algorithm's performance for a 30-day interval between updates regarding the demand for ICU and shows the controlled reproductive number R_e for each cycle. It can be seen that after periods of Level C (lock-down), ICU demand went below 10% of the total number of intensive care beds available, which made the algorithm choose Level A for the following cycle.

Every time this happened, the control failed to prevent healthcare collapse, as 30 days proved to be enough time for Level A to allow a large increase in demand for ICU due to the exponential growth nature of the spread.

The improvement over the baseline was very small, as can be seen in Figure 27D, with the number of deceased at the end of the period being very close to the number of deceased at the end of the baseline.

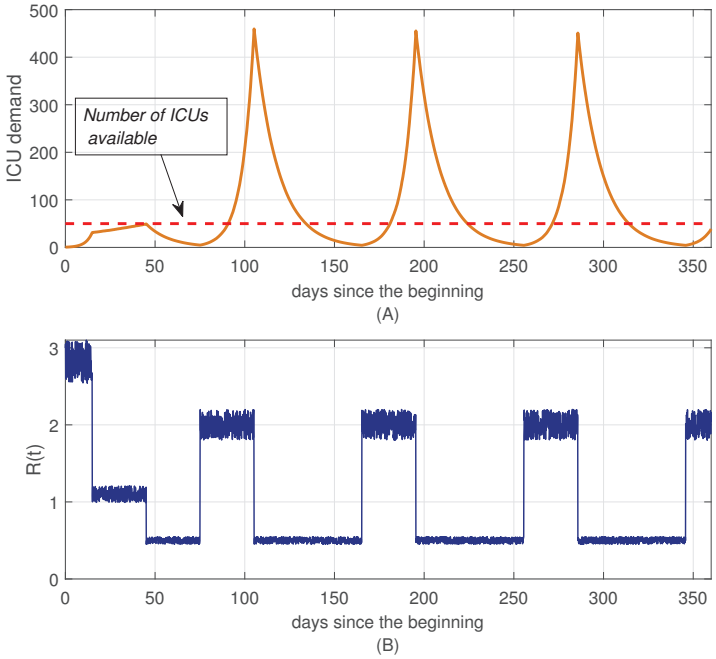

Figure 28. R_e control as measure of reducing COVID-19 spread for every 30 days, considering time evolution (**A**) ICU demand and (**B**) $R(t)$.

Figure 29 supports the effectiveness of the algorithm wiyh a 30-day cycle. Therefore, in order to prevent the ICU demand from surpassing the supply of intensive care beds, the period between updates of the algorithm is reduced, and results are shown in Section 7.3.

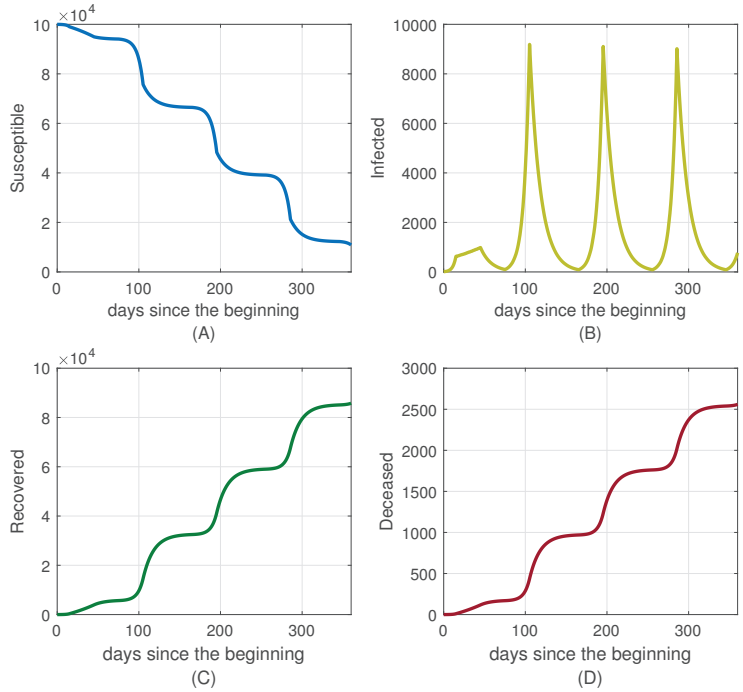

Figure 29. System state variables for algorithm with a 30-days cycle for (**A**) Susceptible population; (**B**) Infected population; (**C**) Recovered population and (**D**) Deceased population.

7.3. Updating R_e Every 21 Days

For a 21-day interval between updates, the main goal of guaranteeing appropriate care for COVID-19 patients is attained. During the 360 days of simulation, there was no instant at which the demand for intensive care units was greater than the supply, as shown in Figure 30, and there were only three periods of Level C (lock-down), allowing individuals to have greater freedom without sacrificing effectiveness.

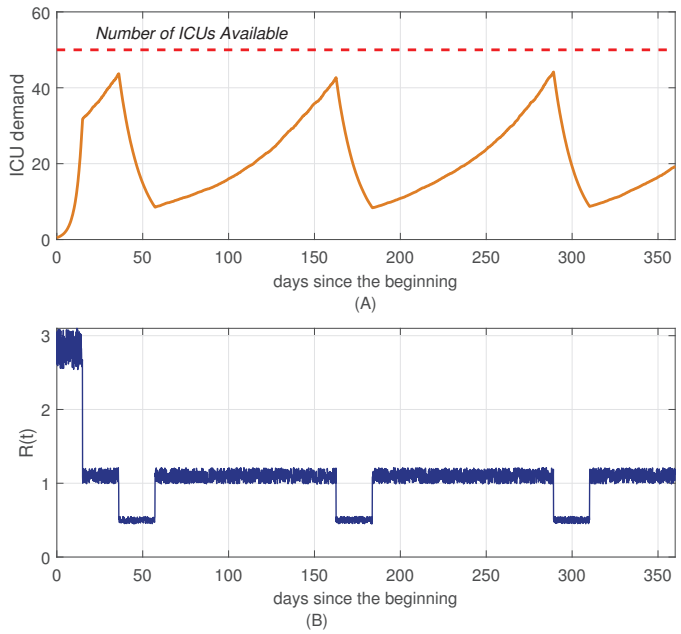

Figure 30. R_e control as measure of reducing COVID-19 spread for every 21 days considering: (**A**) ICU demand and (**B**) $R(t)$.

Figure 31 supports the effectiveness of the algorithm with a 21-day cycle, showing much fewer deaths at the end of the simulation than in simulations I (baseline) and II (30-day cycle).

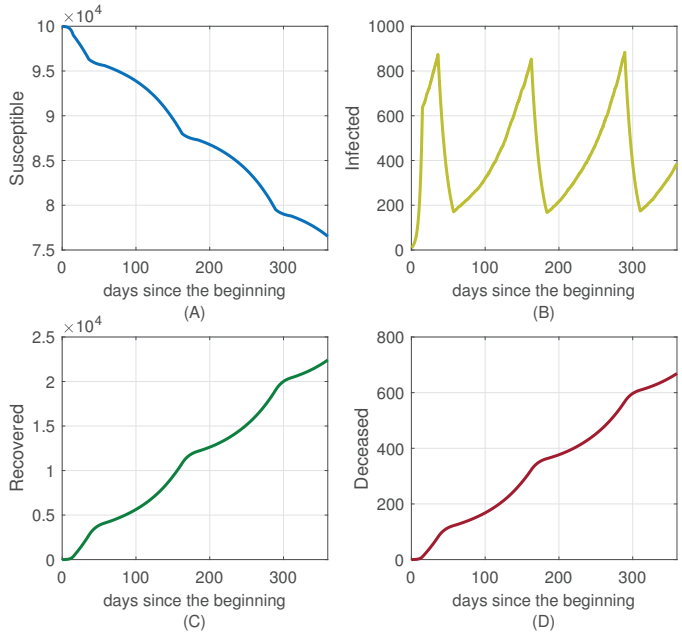

Figure 31. System state variables for algorithm with a 21-days cycle: (**A**) Susceptible population; (**B**) Infected population; (**C**) Recovered population and (**D**) Deceased population.

8. Epidemic Control

In this section, two ways of controlling the spread of the coronavirus pandemic are studied. First, a social distancing policy is applied, followed by a vaccination campaign.

8.1. Control by Social Distancing

The simulation of control by social distancing was carried out in the context described in Table 6.

Table 6. Simulation parameters for the study of epidemic control by social distancing.

Parameter	Parameter Description	Value
γ	recovery rate	1
Ω	lethality of virus (mortality rate)	0.03
N	population size	10,000,000
L	number of hospital beds available	5000
T	simulation period	52 weeks
I_0	initial number of infected	5000
R_{min}	minimum value for effective reproduction number	0.5

The values of γ and Ω adopted were based on the values obtained in the validation for São Paulo and Minas Gerais. We simulated 52 weeks, which is the amount of time it takes to develop a vaccine for the virus, with reference to the Pfizer vaccine, whose development started in January 2020 and was released in December 2020.

The initial number of infected is reasonably high to simulate a situation in which there is little information about the spread of the virus in the population studied. Additionally, a minimum value for the effective reproduction number is implemented, reflecting the highest capacity possible for public authorities to implement isolation measures in the population. This value is 0.5 and is close to the value obtained for Spain in its lockdown in 2020 [94].

The application of social distancing control was carried out by manipulating the parameter $\beta(t)$ so that the value of the effective reproduction number R_e was sufficiently low to bring about a reduction in the number of new cases and weekly deaths.

The applied control was found from the formulation of a minimization problem to find a sequence of controls represented by (22):

$$u[k] = [u(0) \;\; u(1) \;\; u(2) \;\; \ldots \;\; u(K-1)], \tag{21}$$

with the objective of minimizing the functional J (22):

$$J = \tau_1 D(t = T_f) \; - \; \tau_2 \parallel u[k] \parallel_2 \; + \tau_3 \parallel u[k] - u[k-1] \parallel_2 . \tag{22}$$

The first term of Equation (22) represents the number of accumulated deaths at the end of the period (in $t = T_f$); the second term, $u[k] = \beta[k]$, represents the control applied at instant k; and the last term represents the control differential between instant k and $k-1$. The intention behind the first term is self-explanatory: the aim is to minimize the total number of deaths at the end of the period. In contrast, a very low level of isolation has severe social and economic consequences, which is why the second term is used, which penalizes a very intense control. Finally, it is desirable that the control signal, social distancing, does not vary much from week to week to reduce future uncertainties for the population.

In addition, the restriction was imposed that at no time did the number of people in need of medical treatment exceed the number of available hospital beds, as proposed in Equation (23):

$$0.2 * I(t) \leq L \; , \; \forall t \tag{23}$$

The definition of 20% as the percentage of infected people who need hospital treatment was obtained by observing the figure and information available at the São Paulo State Health Department (https://www.saopaulo.sp.gov.br/planosp/simi/leitos/) (acessed on 20 June 2020).

Results for Social Distancing Control

As this is an optimization problem, an important factor is the choice of parameters τ_1, τ_2 and τ_3 that will drive the functional J. Variations in these parameters are related to the prioritization or penalty that gives the terms referring to the number of deaths, minimization of social distance and distance differential. Therefore, five different combinations were studied for the set (τ_1, τ_2, τ_3), with the results summarized in Table 7 and in Figure 32.

Table 7. Results obtained for the control by social distancing.

Simulation	τ_1	τ_2	τ_3	$D(t = T_f)$	$\| \beta[k] \|_2$	$\| u[k] - u[k-1] \|_2$
(I)	1	1	1	291.3530	6.2783	0.5796
(II)	1	10	1	298.4825	7.1895	2.0587
(III)	1	10	10	292.4858	6.6241	1.0437
(IV)	1	50	10	300.9959	7.0514	1.1845
(V)	1	50	50	300.4231	6.4384	0.5781
(VI)	1	100	50	319.1812	6.6833	0.9307
(VII)	1	100	100	309.0499	6.6805	0.9949
(VIII)	1	250	100	390.8686	6.9906	0.8825
(IX)	1	250	150	336.0118	6.6467	0.6248

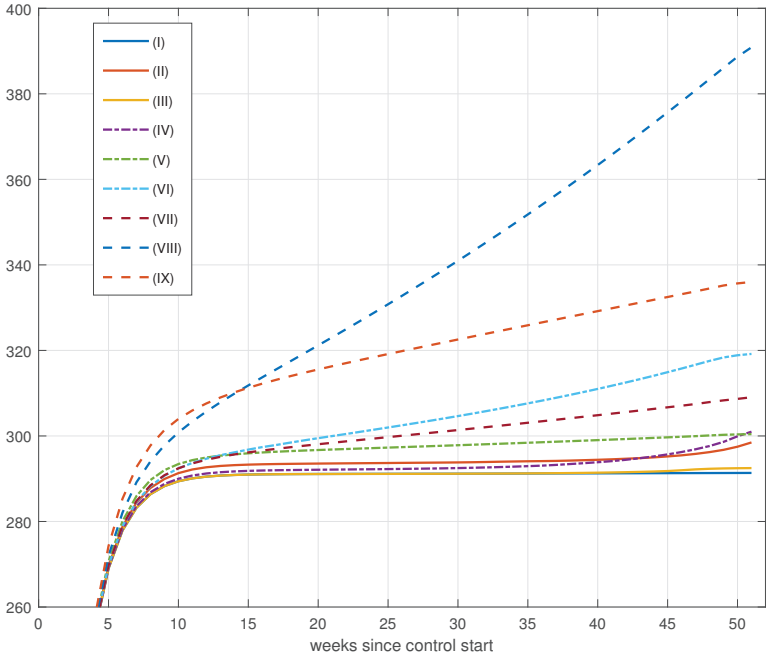

Figure 32. Comparison of the number of accumulated controller deaths due to social distancing. The first few weeks are omitted for better viewing.

It can be noted that an increase in τ_2, which is a greater prioritization of maximizing the norm of β, resulted in an increase in the number of deaths at the end of the period. Meanwhile, increases in τ_3 generally had the effect of reducing the norm of the applied controls differential, as was desired, and a reduction in the variability of R_e can be seen in the graphs below. At the same time, it produced a reduction in the number of deaths, which was unexpected.

By analyzing the graph, it is possible to notice the increase in the number of deaths accumulated in time when the value of τ_2 is increased. The effective reproduction number graphs were divided into two parts, because those in Figure 32 were very noisy, making visualization difficult. This more intense noise occurred precisely in the graphs that were associated with an increase in τ_2 without an increase in τ_3 associated.

The qualitative analysis of Figures 33 and 34 shows that there is a very intense control in the first weeks, in order to quickly reduce the number of cases to zero, as shown in Figure 35. After this period, there is a gradual release of distancing, implying a gradual increase in R_e, followed by a new constraint near the end of the period.

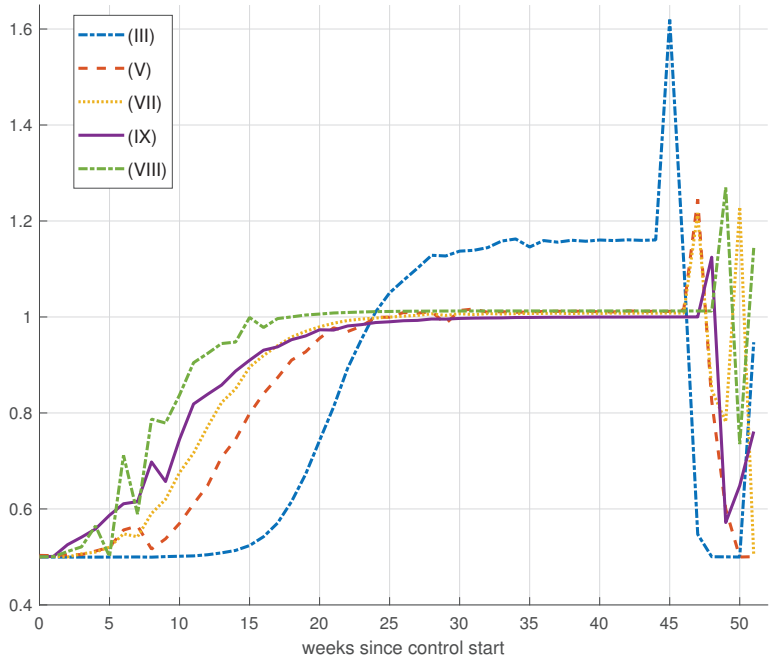

Figure 33. Comparison of the effective reproduction number of the social distancing controller for the less noisy signals.

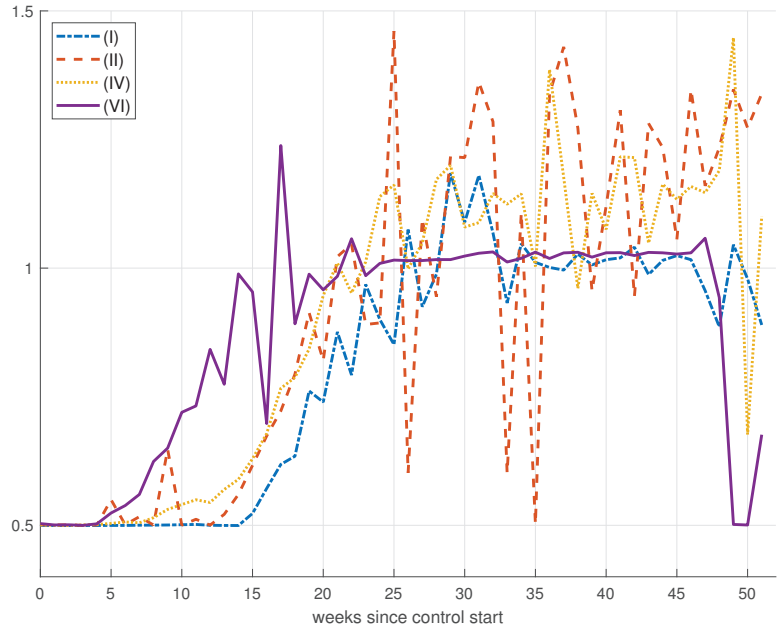

Figure 34. Comparison of the effective reproduction number of the social distancing controller for the noisier signals.

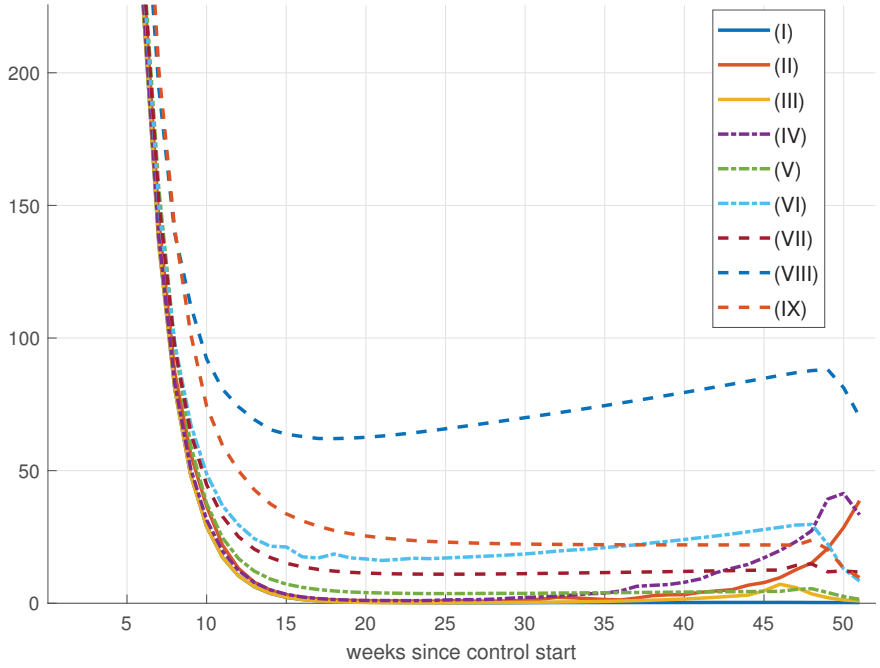

Figure 35. Number of new weekly cases for social distancing control.

A more detailed study considering social distancing as a strategy to control the spread of COVID-19 was performed in [50]. The proposed model, which consists of an alteration of the SIR model, considers the infected in two compartments: the infected being reported and the infected not reported or asymptomatic. The validation of the model is carried out for different cities in the state of São Paulo and allows the evaluation of the dynamics of disease reinfection and the relevance of social distancing as cities adhere to social isolation at different times.

8.2. Vaccination Control

To implement the vaccination control, a new term $v(t)$ was introduced in the equations that describe the system, now formulated by the set of Equation (24).

$$\begin{cases} \frac{dS(t)}{dt} &= -\frac{\beta S(t) I(t)}{N} - v(t) \\ \frac{dI(t)}{dt} &= \frac{\beta S(t) I(t)}{N} - (\gamma + \Omega) I(t) \\ \frac{dR(t)}{dt} &= \gamma I(t) + v(t) \end{cases} \tag{24}$$

The term $v(t)$ represents the number of individuals vaccinated at time t, and all parameters, β, γ and Ω, are considered constant, representing a situation in which there is no change in the behavior of the population regarding the contact rate between individuals, that is, there is no social distancing. Again, the solution to this problem is given by minimizing a functional, described by Equation (25), where we want to minimize the number of deaths while also minimizing the cost of vaccination.

$$J_{vac} \;=\; \tau_1 D(t = T_f) \;+\; \tau_2 \parallel v[k] \parallel_2 \;+ \tau_3 \parallel v[k] - v[k-1] \parallel_2 \tag{25}$$

In addition, it is desirable to minimize the vaccine immunization differential, represented by the last term of the functional, so that there is not a very sudden variation in the number of vaccines given from one week to the next.

8.2.1. Results for Vaccination Control

The simulation parameters for vaccination control can be seen in Table 8:

Table 8. Parameters for vaccination control.

Parameter	Parameter Description	Value
β	average number of contacts	2.06
γ	recovery rate	1
Ω	lethality of virus (mortality rate)	0.03
N	population size	10,000,000
L	number of hospital beds available	5000
T	simulation period	52 weeks
I_0	initial number of infected	1
v_{max}	Maximum vaccination value per instant of time	variable

Regarding the simulation for vaccination control, the number of initial infected people was reduced to simulate a condition that is still at the beginning of the spread of the disease. Also, there is no longer a minimum value for the effective reproduction number, since the value of the contact rate between individuals β is considered fixed. The value of β is fixed at $2(\gamma + \Omega)$, representing a base reproduction number value R_0 equal to 2.

A maximum value of vaccinated per time instant is established to represent scenarios in which there are limited availability of vaccines to be applied. The results obtained are compiled in Table 9.

Table 9. Results obtained for vaccination control.

Simulation	v_{max}	τ_1	τ_2	τ_3	$\mathbf{D}(t = T_f)$	$\| v[k] \|_2$	$\| v[k] - v[k-1] \|_2$
(I)	50,000	1	1	1	229,543	15,987	3943
(II)	50,000	10	1	1	198,924	210,293	14,770
(III)	50,000	50	1	1	199,421	209,570	18,477
(IV)	50,000	50	10	1	218,448	86,979	24,296
(V)	50,000	50	10	5	217,986	90,980	9120
(VI)	75,000	1	1	1	226,986	34,343	15,489
(VII)	75,000	10	1	1	189,715	259,974	24,880
(VIII)	75,000	50	1	1	183,758	294,083	40,017
(IX)	75,000	50	10	1	216,815	96,340	10,545
(X)	75,000	50	10	5	211,212	132,180	14,563
(XI)	100,000	1	1	1	228,907	21,677	7933
(XII)	100,000	10	1	1	170,477	368,702	45,626
(XIII)	100,000	50	1	1	168,307	386,925	86,353
(XIV)	100,000	50	10	1	218,549	86,186	12,683
(XV)	100,000	50	10	1	211,336	131,626	13,796

8.2.2. Effect of Increase in Weekly Vaccination

The first part of the simulations analyze the effect of increasing the limit of application of vaccines weekly. As expected, Figure 36 shows that increases in the weekly vaccination limit, when associated with an increase in the weight τ_1, which refers to the number of deaths at the end of the period, reflect a significant drop in this value.

The analysis of the weekly new cases graph reflects the same behavior. Figure 37 shows that an increase in vaccination reduces the number of new weekly cases when the weight τ_1 is increased, which prioritizes a reduction in the number of deaths in relation to the cost of administering vaccines.

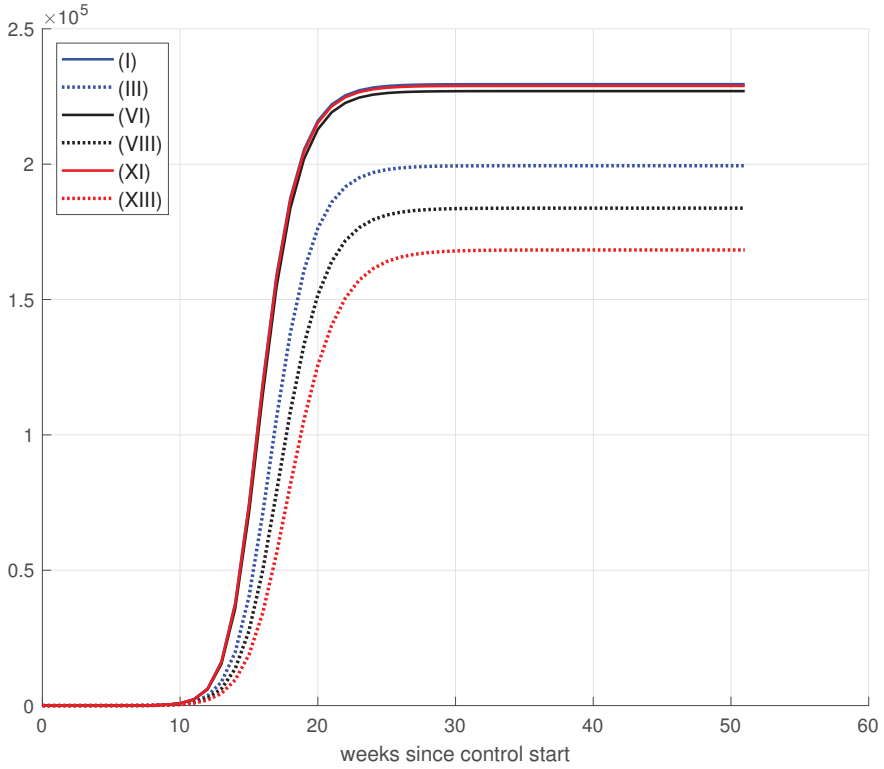

Figure 36. Comparison of the number of accumulated deaths in the vaccination control.

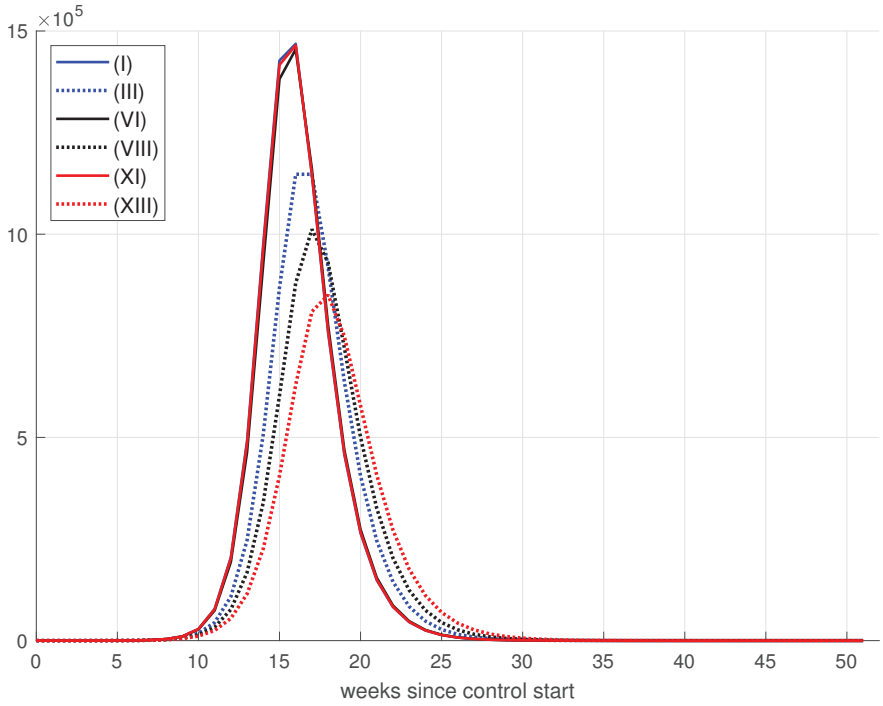

Figure 37. Comparison of the number of new cases per week in vaccination control.

Another interesting fact is that the weekly vaccination rate obtained for conditions where τ_1 is much greater than τ_2 and τ_3 is not the maximum vaccination vector at all times. It can be noted in Figure 38 that in none of the cases, the maximum vaccination for the period in 26%, 39% and 52% of the population, respectively, was reached. This is because the model assumes obtaining immunity after recovering from the disease. Therefore, individuals who were not vaccinated either died or recovered.

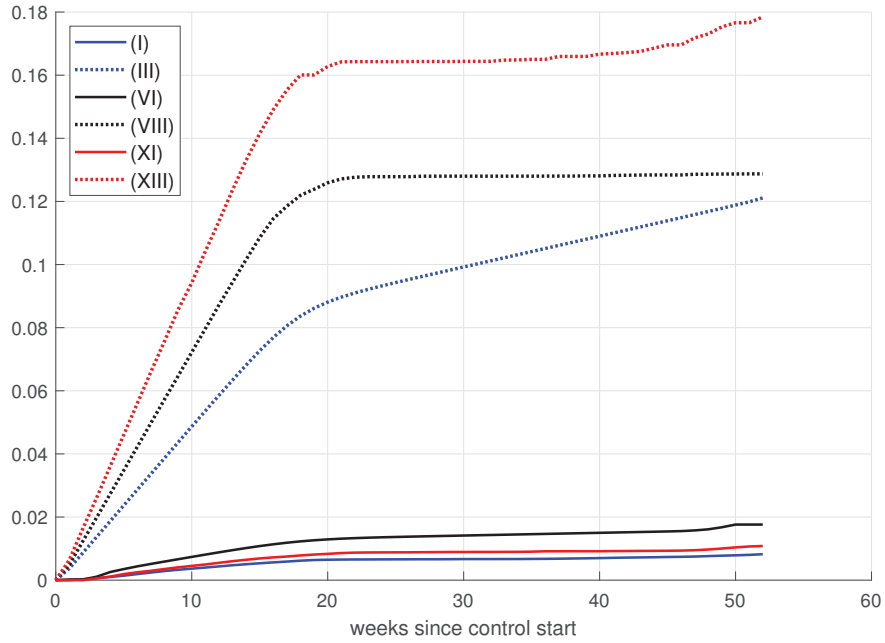

Figure 38. Comparison for the cumulative of vaccinated in the vaccination control—percentage of the initial population.

A severely negative point of the application of control only by vaccination is that the limit of the number of available hospital beds was not respected, as can be seen in Figure 39. In the tenth week, the health system collapses.

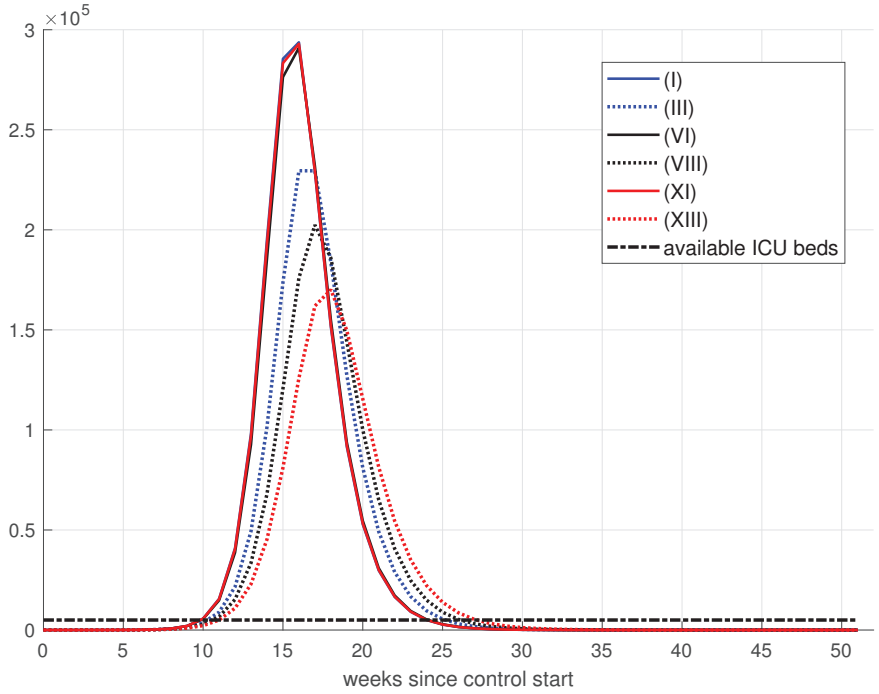

Figure 39. Comparison of the number of individuals needing hospital beds in the vaccination control.

8.2.3. Effects of Changes in Vaccination Campaign Prioritization

To highlight the policy changes when we prioritize the number of deaths over the cost of vaccination or vice versa, Figures 40–42 are presented, related to cases (VI) to (X) of the prioritization parameters. First, Figure 40 shows that the increase in τ_1 in the case (VI) pro (VII) and (VII) pro (VIII) showed a decrease in the number of accumulated deaths,

as expected; likewise, from case (VIII) to (IX), in which an increase in τ_2 is considered, the graph shows an increase in the number of accumulated deaths.

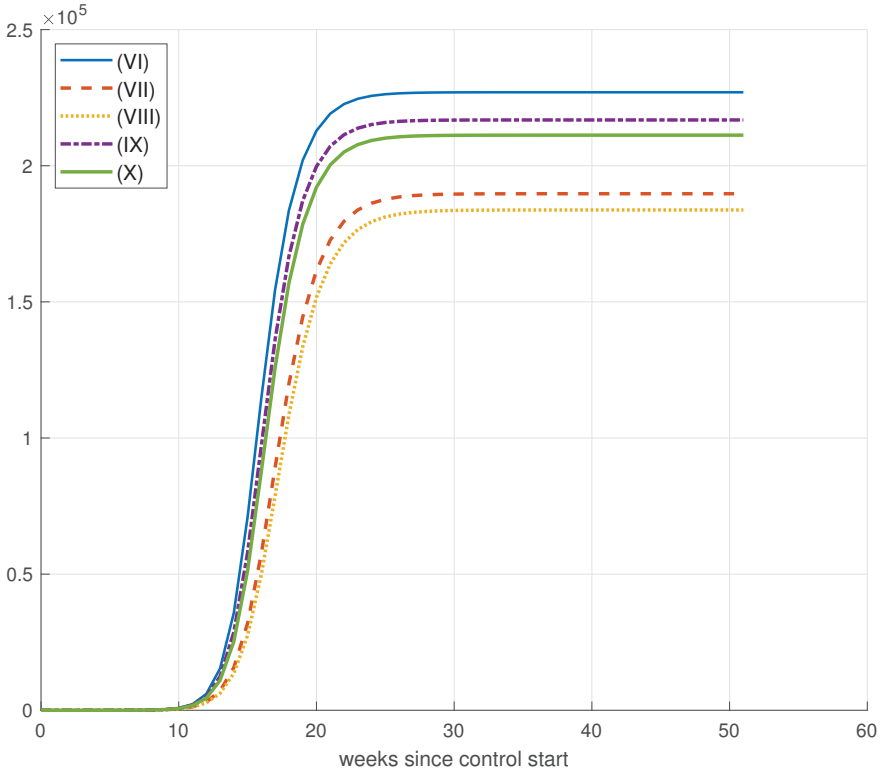

Figure 40. Comparison of the number of accumulated deaths in the vaccination control.

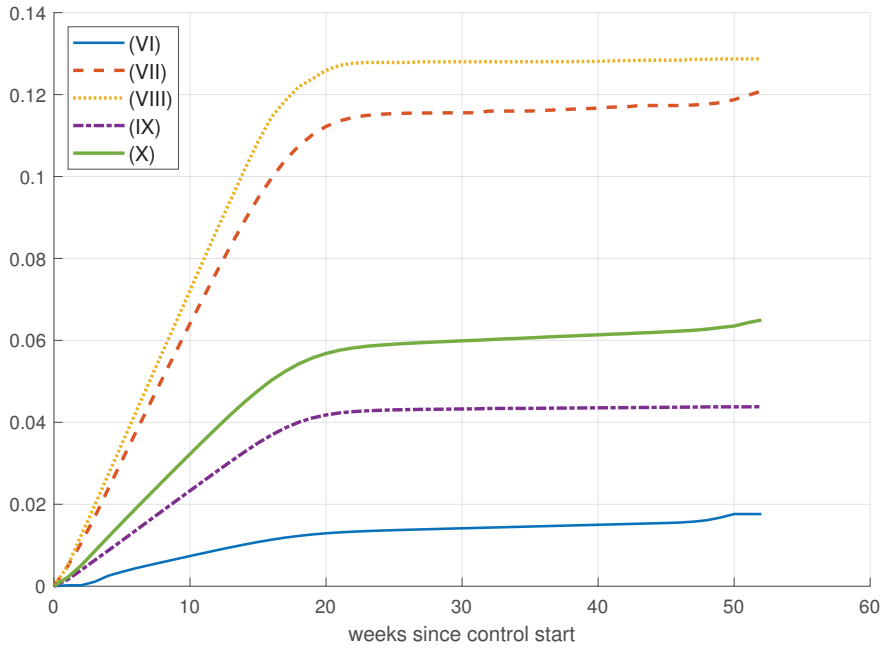

Figure 41. Comparison of the cumulative of vaccinated in the vaccination control with changes in vaccination campaign prioritization—percentage of the initial population.

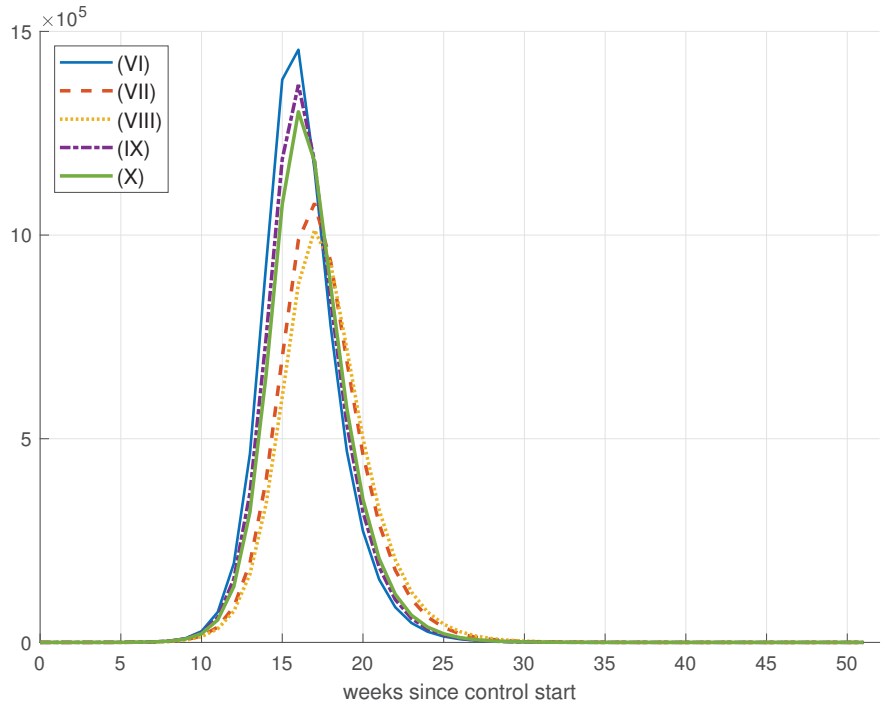

Figure 42. Comparison of the number of new cases weekly in the vaccination control.

Analogously to the case of control by social distancing, where there is a drop in the number of deaths, an increase in τ_3, which penalizes the variation in the control vector $v(t)$, also showed a drop in the number of deaths.

A more detailed study considering validation with real data of the control strategy based on vaccination was carried out in [51]. The model considers the possibility of reinfection and allows checking information on unreported infected people. The validation of the model was carried out with data from the city of São Paulo, which, due to its sociodemographic and economic difference, presents complex scenarios and can be extended to regions with the same qualitative characteristics.

9. Conclusions

Inspired by the different policies of social distances adopted by Brazil and Uruguay, showing remarkable differences concerning the results of controlling the COVID-19 epidemic, a framework for modeling and applying public policies in the form of social distancing was proposed aiming for a reduction in disease spread.

Validation of the SIRD model using cumulative case data and cumulative death data for the states of São Paulo, Minas Gerais and Rio de Janeiro proved satisfactory. For the accumulated death data, the performance was good, while for the accumulated case data, the performance was average, with advances in relation to previous results. Possibly, a better relationship between deaths and cases should be explored, such as inserting delay terms into the equations, or else considering the γ and Ω parameter variables, as we conducted with β.

Comparison of data on the effective reproduction number R_e obtained by the model with respect to the values obtained by a COVID-19 observatory showed a delay, possibly due to the difference in the methodology used. The work proposes a minimization of square errors for the developed model, while a COVID-19 observatory performed the estimate using serial intervals, defined as the time interval between the onset of illness in a primary case and the onset of illness in a secondary case [69].

Control by social distancing performed well, complying with the restrictions imposed. At all times, there was no failure of the health system. However, during the 52 weeks, the level of isolation remained intense without returning to the preisolation level. Also, con-

tinuous levels of R_e would likely be quite difficult to implement. For example, in practice, it is difficult to implement public policies with an R_e of 0.9 versus R_e of 0.95.

Meanwhile, vaccination control reduced the number of accumulated deaths at the end of the period, but it did not prevent the failure of the health system. In this way, social distancing is necessary until herd immunity is reached, the value at which a primary infection produces, on average, less than a secondary infection, which eventually leads to the extinction of the disease.

The results are satisfactory, mainly due to the good performance shown for the accumulated death data, which allowed the use of the model to apply social distancing control and vaccination control.

A three-level controller was proposed, and simulations indicate that a 21-day update strategy shows good results, preventing the healthcare system from collapsing and presenting much fewer deaths at the end of the process.

Aspects to be explored to improve the model are to consider the algorithm behavior varying R_e for each level, to have a different number of levels and to include uncertainty and delay in the observability of the number of infected cases.

Despite being an intuitively obvious conclusion, it was shown that failing to mitigate the spread of the disease is not a wise option. The algorithm with 21 days between updates presents, for example, almost 650 deaths at the end of the year, whereas doing nothing resulted in approximately 2700.

Therefore, it is possible to say that the framework outlined is a good and simple reference model to be followed when designing techniques to address COVID-19 disease spread, as well as possibly other diseases that follow the same pattern of transmission as the coronavirus.

Author Contributions: Conceptualization, C.B.; methodology, C.B. and J.R.C.P.; software, G.D.; validation, C.B.; formal analysis, J.R.C.P.; investigation, G.D.; data curation, G.D.; writing—original draft preparation, G.D. and C.B.; project administration, J.R.C.P.; funding acquisition, J.R.C.P.. All authors have read and agreed to the published version of the manuscript.

Funding: JRCP is supported by the São Paulo Research Foundation: 2022/00770-0 and the National Council for Scientific and Technological Development: 302883/2018-5.

Conflicts of Interest: The authors declare that there are no conflicts of interest regarding the publication of this article.

Appendix A

From Wiggins, 1990, p. 193 [98]. Consider vector fields of the form

$$\begin{cases} \dot{x} = Ax + f(x,y), \\ \dot{y} = By + g(x,y), \qquad (x,y) \in \mathbb{R}^c \times \mathbb{R}^s, \end{cases} \tag{A1}$$

satisfying

$$\begin{aligned} f(0,0) &= 0, \qquad Df(0,0) = 0, \\ g(0,0) &= 0, \qquad Dg(0,0) = 0, \end{aligned}$$

where A is a c $\times$ c matrix having eigenvalues with zero real parts, B is an s $\times$ s having eigenvalues with negative real part and f and g are $\mathbf{C}^r$ functions (r $\geq$ 2). Then,

Remark A1. *An invariant manifold will be called a center manifold for (A1) if it can locally be represented as*

$$W^c(0) = \{(x,y) \in \mathbb{R}^c \times \mathbb{R}^s | y = h(x), |x| < \delta, h(0) = 0, Dh(0) = 0\} \tag{A2}$$

for δ sufficiently small.

Theorem A1. *There exists a C^r center manifold for (A1). The dynamics of (A1) restricted to the center manifold is, for u sufficiently small, given by the following c-dimensional vector field*

$$\dot{u} = Au + f(u, h(u)), \qquad u \in \mathbb{R}^c. \tag{A3}$$

Theorem A2. *(i) Suppose the zero solution of (A3) is stable (asymptotically stable) (unstable); then, the zero solution of (A1) is also stable (asymptotically stable) (unstable). (ii) Suppose the zero solution of (A3) is stable. Then, if $(x(t), y(t))$ is a solution of (A1) with $(x(0), y(0))$ sufficiently small, there is a solution $u(t)$ of (A3) such that as $t \to \infty$*

$$x(t) = u(t) + \mathcal{O}(e^{-\gamma t}),$$
$$y(t) = h(u(t)) + \mathcal{O}(e^{-\gamma t}),$$

where $\gamma > 0$ is a constant.

References

1. Velavan, T.P.; Meyer, C.G. The COVID-19 epidemic. *Trop. Med. Int. Health* **2020**, *25*, 278–280. [CrossRef]
2. Wu, Z.; McGoogan, J.M. Characteristics of and important lessons from the coronavirus disease 2019 (COVID-19) outbreak in China: Summary of a report of 72 314 cases from the Chinese Center for Disease Control and Prevention. *JAMA* **2020**, *323*, 1239–1242. [CrossRef]
3. World Health Organization. *WHO Timeline-Covid-19*; WHO: Geneva, Switzerland, 2020.
4. Van Doremalen, N.; Bushmaker, T.; Morris, D.H.; Holbrook, M.G.; Gamble, A.; Williamson, B.N.; Tamin, A.; Harcourt, J.L.; Thornburg, N.J.; Gerber, S.I.; et al. Aerosol and surface stability of SARS-CoV-2 as compared with SARS-CoV-1. *N. Engl. J. Med.* **2020**, *382*, 1564–1567. [CrossRef]
5. Bai, Y.; Yao, L.; Wei, T.; Tian, F.; Jin, D.Y.; Chen, L.; Wang, M. Presumed asymptomatic carrier transmission of COVID-19. *JAMA* **2020**, *323*, 1406–1407. [CrossRef]
6. Sohrabi, C.; Alsafi, Z.; O'Neill, N.; Khan, M.; Kerwan, A.; Al-Jabir, A.; Iosifidis, C.; Agha, R. World Health Organization declares global emergency: A review of the 2019 novel coronavirus (COVID-19). *Int. J. Surg.* **2020**, *76*, 71–76. [CrossRef]
7. Singh, S.; Parmar, K.S.; Kumar, J.; Makkhan, S.J.S. Development of new hybrid model of discrete wavelet decomposition and autoregressive integrated moving average (ARIMA) models in application to one month forecast the casualties cases of COVID-19. *Chaos Solitons Fractals* **2020**, *135*, 109866. [CrossRef]
8. Prem, K.; Liu, Y.; Russell, T.W.; Kucharski, A.J.; Eggo, R.M.; Davies, N. The effect of control strategies to reduce social mixing on outcomes of the COVID-19 epidemic in Wuhan, China: A modelling study. *Lancet Public Health* **2020**, *5*, e261–e270. [CrossRef]
9. Colbourn, T. COVID-19: Extending or relaxing distancing control measures. *Lancet Public Health* **2020**, *5*, e236–e237. [CrossRef]
10. Mishra, B.K.; Keshri, A.K.; Rao, Y.S.; Mishra, B.K.; Mahato, B.; Ayesha, S.; Rukhaiyyar, B.P.; Saini, D.K.; Singh, A.K. COVID-19 created chaos across the globe: Three novel quarantine epidemic models. *Chaos Solitons Fractals* **2020**, *138*, 109928. [CrossRef]
11. Rai, R.K.; Khajanchi, S.; Tiwari, P.K.; Venturini, E.; Misra, A.K. Impact of social media advertisements on the transmission dynamics of COVID-19 pandemic in India. *J. Appl. Math. Comput.* **2020**, *68*, 19–44. [CrossRef]
12. Tiwari, P.K.; Rai, R.K.; Khajanchi, S.; Gupta, R.K.; Misra, A.K. Dynamics of coronavirus pandemic: Effects of community awareness and global information campaigns. *Eur. Phys. J. Plus* **2021**, *136*, 994. [CrossRef] [PubMed]
13. Anderson, R.M.; May, R.M. *Infectious Diseases of Humans: Dynamics and Control*; Oxford University Press: New York, NY, USA, 1992.
14. Brauer, F.; Castillo-Chavez, C. *Mathematical Models in Population Biology and Epidemiology*; Springer: New York, NY, USA, 2012.
15. Hethcote, H.W. The mathematics of infectious diseases. *Siam Rev.* **2000**, *42*, 599–653. [CrossRef]
16. Dietz, K. The first epidemic model: A historical note on PD En'ko. *Aust. J. Stattistic* **1998**, *30*, 56–65. [CrossRef]
17. Laarabi, H.; Abta, A.; Hattaf, K. Optimal control of a delayed SIRS epidemic model with vaccination and treatment. *Acta Biotheor.* **2015**, *63*, 87–97. [CrossRef]
18. Aldila, D.; Götz, T.; Soewono, E. An optimal control problem arising from a dengue disease transmission model. *Math. Biosci.* **2013**, *242*, 9–16. [CrossRef]
19. Ruan, S.; Xiao, D.; Beier, J.C. On the delayed Ross-Macdonald model for malaria transmission. *Bull. Math. Biololgy* **2008**, *70*, 1098–1114. [CrossRef]
20. Nwankwo, A.; Okuonghae, D. A mathematical model for the population dynamics of malaria with a temperature dependent control. *Differ. Equations Dyn. Syst.* **2019**, *30*, 719–748. [CrossRef]
21. Egonmwan, A.O.; Okuonghae, D. Mathematical analysis of a tuberculosis model with imperfect vaccine. *Int. J. Biomath.* **2019**, *12*, 1950073. [CrossRef]
22. Omame, A.; Okuonghae, D.; Umana, A.R.; Inyama, S.C. Analysis of a co-infection model for HPV-TB. *Appl. Math. Model.* **2020**, *77*, 881–901. [CrossRef]

23. Omame, A.; Okuonghae, D.; Inyama, S.C. A Mathematical Study of a Model for HPV with Two High-Risk Strains. In *Mathematical Modelling in Health, Social and Applied Sciences*; Springer: Singapore, 2020; pp. 107–149. [CrossRef]
24. Hattaf, K.; Yousfi, N. Optimal control of a delayed HIV infection model with immune response using an efficient numerical method. *Int. Sch. Res. Not.* **2012**, *2012*, 215124. [CrossRef]
25. Al-Khaled, K.; Yousef, M. An analytic study of the fractional order model of HIV-1 virus and CD4 + T-cells using adomian method. *Int. J. Electr. Comput. Eng.* **2021**, *11*, 1460–1468. [CrossRef]
26. Khan, M.I.; Al-Khaled, K.; Raza, A.; Khan, S.U.; Omar, J.; Galal, A.M. Mathematical and numerical model for the malaria transmission: Euler method scheme for a malarial model. *Int. J. Mod. Phys. B* **2023**, *37*, 2350158. [CrossRef]
27. Kermack, W.O.; McKendrick, A.G. A contribution to the mathematical theory of epidemics. *Proc. R. Soc. London Ser. A* **1927**, *115*, 700–721. [CrossRef]
28. Kermack, W.O.; McKendrick, A.G. Contributions to the mathematical theory of epidemics. II.—The problem of endemicity. *Proc. R. Soc. London Ser. A* **1932**, *138*, 55–83. [CrossRef]
29. Kermack, W.O.; McKendrick, A.G. Contributions to the mathematical theory of epidemics. III.—Further studies of the problem of endemicity. *Proc. R. Soc. London Ser. A* **1933**, *141*, 94–122. [CrossRef]
30. Khajanchi, S.; Sarkar, K.; Mondal, J.; Nisar, K.S.; Abdelwahab, S.F. Mathematical modeling of the COVID-19 pandemic with intervention strategies. *Results Phys.* **2021**, *25*, 104285. [CrossRef]
31. Cantó, B.; Coll, C.; Sánchez, E. Estimation of parameters in a structured SIR mode. *Adv. Differ. Equ.* **2017**, *2017*, 33. [CrossRef]
32. Ng, T.W.; Turinici, G.; Danchin, A. A double epidemic model for the SARS propagation. *BMC Infect. Dis.* **2003**, *3*, 19. [CrossRef]
33. Danca, M.F.; Kuznetsov, N. Matlab code for Lyapunov exponents of fractional-order systems. *Int. J. Bifurc. Chaos* **2018**, *28*, 1850067. [CrossRef]
34. Godio, A.; Pace, F.; Vergnano, A. SEIR modeling of the Italian epidemic of SARS-CoV-2 using computational swarm intelligence. *Int. J. Environ. Res. Public Health* **2020**, *17*, 3535. [CrossRef]
35. Lin, Q.; Zhao, S.; Gao, D.; Lou, Y.; Yang, S.; Musa, S.S.; Wang, M.H.; Cai, Y.; Wang, W.; Yang, L.; et al. A conceptual model for the coronavirus disease 2019 (COVID-19) outbreak in Wuhan, China with individual reaction and governmental action. *Int. J. Infect. Dis.* **2020**, *93*, 211–216. [CrossRef] [PubMed]
36. Piqueira, J.R.C.; Araujo, V.O. A modified epidemiological model for computer viruses. *Appl. Math. Comput.* **2009**, *213*, 355–360. [CrossRef]
37. Piqueira, J.R.C.; Batistela, C.M. Considering quarantine in the SIRA malware propagation model. *Math. Probl. Eng.* **2019**, *2019*, 6467104. [CrossRef]
38. Khajanchi, S.; Das, D.K.; Kar, T.K. Dynamics of tuberculosis transmission with exogenous reinfections and endogenous reactivation. *Phys. A Stat. Mech. Its Appl.* **2018**, *497*, 52–71. [CrossRef]
39. Kucharski, A.J.; Russell, T.W.; Diamond, C.; Liu, Y.; Edmunds, J.; Funk, S.; Eggo, R.M. Early dynamics of transmission and control of COVID-19: A mathematical modelling study. *Lancet Infect. Dis.* **2020**, *20*, 553–558. [CrossRef] [PubMed]
40. Sarkar, K.; Khajanchi, S.; Nieto, J.J. Modeling and forecasting the COVID-19 pandemic in India. *Chaos Solitons Fractals* **2020**, *139*, 110049. [CrossRef]
41. Khajanchi, S.; Sarkar, S.; Banerjee, S. Modeling the dynamics of COVID-19 pandemic with implementation of intervention strategies. *Eur. Phys. J. Plus* **2022**, *137*, 129. [CrossRef]
42. Giordano, G.; Blanchini, F.; Bruno, R.; Colaneri, P.; Di Filippo, A.; Di Matteo, A.; Colaneri, M. Modelling the COVID-19 epidemic and implementation of population-wide interventions in Italy. *Nat. Med.* **2020**, *26*, 855–860. [CrossRef]
43. Rai, R.K.; Tiwari, P.K.; Khajanchi, S. Modeling the influence of vaccination coverage on the dynamics of COVID-19 pandemic with the effect of environmental contamination. *Math. Methods Appl. Sci.* **2023**, *46*, 12425–12453. [CrossRef]
44. Mizumoto, K.; Chowell, G. Transmission potential of the novel coronavirus (COVID-19) onboard the diamond Princess Cruises Ship. *Infect. Dis. Model.* **2020**, *5*, 264–270. [CrossRef]
45. Atangana, A. Modelling the spread of COVID-19 with new fractal-fractional operators: Can the lockdown save mankind before vaccination? *Chaos Solitons Fractals* **2020**, *136*, 109860. [CrossRef]
46. Hellewell, J.; Abbott, S.; Gimma, A.; Bosse, N.I.; Jarvis, C.I.; Russell, T.W.; Munday, J.D.; Kucharski, A.J.; Edmunds, W.J. Feasibility of controlling COVID-19 outbreaks by isolation of cases and contacts. *Lancet Glob. Health* **2020**, *8*, e488–e496. [CrossRef]
47. Ivorra, B.; Ferrández, M.R.; Vela-Pérez, M.; Ramos, A.M. Mathematical modeling of the spread of the coronavirus disease 2019 (COVID-19) taking into account the undetected infections. The case of China. *Commun. Nonlinear Sci. Numer. Simul.* **2020**, *88*, 105303. [CrossRef]
48. Higazy, M. Novel fractional order SIDARTHE mathematical model of COVID-19 pandemic. *Chaos Solitons Fractals* **2020**, *138*, 110007. [CrossRef]
49. Samui, P.; Mondal, J.; Khajanchi, S. A mathematical model for COVID-19 transmission dynamics with a case study of India. *Chaos Solitons Fractals* **2020**, *140*, 110173. [CrossRef]
50. Batistela, C.M.; Correa, D.P.; Bueno, A.M.; Piqueira, J.R.C. SIRSi compartmental model for COVID-19 pandemic with immunity loss. *Chaos Solitons Fractals* **2021**, *142*, 110388. [CrossRef]
51. Batistela, C.M.; Correa, D.P.; Bueno, A.M.; Piqueira, J.R.C. SIRSi-vaccine dynamical model for the Covid-19 pandemic. *ISA Trans.* **2023**, *139*, 391–405. [CrossRef]

52. Malki, Z.; Atlam, E.S.; Ewis, A.; Dagnew, G.; Ghoneim, O.A.; Mohamed, A.A.; Abdel-Daim, M.M.; Gad, I. The COVID-19 pandemic: Prediction study based on machine learning models. *Environ. Sci. Pollut. Reserach* **2021**, *28*, 40496–40506. [CrossRef]
53. Wieczorek, M.; Siłka, J.; Połap, D.; Woźniak, M.; Damaševičius, R. Real-time neural network based predictor for cov19 virus spread. *PLoS ONE* **2020**, *15*, e0243189. [CrossRef]
54. Braga, M.B.; Fernandes, R.D.S.; Souza, G.N., Jr.; Rocha, J.E.C.D.; Dolácio, C.J.F.; Tavares, I.D.S., Jr.; Pinheiro, R.R.; Noronha, F.N.; Rodrigues, L.L.S.; Ramos, R.T.J.; et al. Artificial neural networks for short-term forecasting of cases, deaths, and hospital beds occupancy in the COVID-19 pandemic at the Brazilian Amazon. *PLoS ONE* **2021**, *16*, e0248161. [CrossRef]
55. Iwendi, C.; Mahboob, K.; Khalid, Z.; Javed, A.R.; Rizwan, M.; Ghosh, U. Classification of COVID-19 individuals using adaptive neuro-fuzzy inference system. *Multimed. Syst.* **2021**, *28*, 1223–1237. [CrossRef]
56. Iwendi, C.; Bashir, A.K.; Peshkar, A.; Sujatha, R.; Chatterjee, J.M.; Pasupuleti, S.; Mishra, R.; Pillai, S.; Jo, O. COVID-19 Patient health prediction using boosted random forest algorithm. *Front. Public Health* **2020**, *8*, 357. [CrossRef]
57. Stewart, G.; Heusden, K.; Dumont, G.A. How control theory can help us control COVID-19. *IEEE Spectr.* **2020**, *57*, 22–29. [CrossRef]
58. Moler, C.B. *Numerical Computing with MATLAB*; SIAM: Philadelphia, PA, USA, 2004.
59. Murray, J.D. *Mathematical Biology I. An Introduction*; Springer: New York, NY, USA, 2002. [CrossRef]
60. Bastos, S.B.; Cajueiro, D.O. Modeling and forecasting the early evolution of the COVID-19 pandemic in Brazil. *Sci. Rep.* **2020**, *10*, 19457. [CrossRef] [PubMed]
61. Brauer, F.; Van den Driessche, P.; Wu, J.; Allen, L.J. *Mathematical Epidemiology*; Springer: Berlin/Heidelberg, Germany, 2008. [CrossRef]
62. Guckenheimer, J.; Holmes, P. *Nonlinear Oscillations, Dynamical Systems and Bifurcation of Vector Fields*; Springer: New York, NY, USA, 1983. [CrossRef]
63. Andronov, A.A.; Vitt, A.A.; Khaikin, S.E. Theory of Oscillators, Pergamon, 1966. [CrossRef]
64. Khajanchi, S.; Bera, S.; Roy, T.K. Mathematical analysis of the global dynamics of a HTLV-I infection model, considering the role of cytotoxic T-lymphocytes. *Math. Comput. Simul.* **2021**, *180*, 354–378. [CrossRef]
65. Dutra, C. Estimate of the basic number of reproduction R0 of COVID-19 in South American countries. *Interam. J. Med. Health* **2020**, *3*, 1–7. [CrossRef]
66. Our World in Data. Coronavirus (COVID-19) Cases. 2021. Available online: https://ourworldindata.org/covid-cases (accessed on 7 September 2021).
67. Bai, Y.; Peng, Z.; Wei, F.; Jin, Z.; Wang, J.; Xu, X.; Zhang, X.; Xu, J.; Ren, Z.; Lu, B.; et al. Study on the COVID-19 epidemic in mainland China between November 2022 and January 2023, with prediction of its tendency. *J. Biosaf. Biosegurance* **2023**, *5*, 39–44. [CrossRef]
68. Wei, F.; Peng, Z.; Jin, Z.; Wang, J.; Xu, X.; Zhang, X.; Xu, J.; Ren, Z.; Bai, Y.; Wang, X.; et al. Study and prediction of the 2022 global monkeypox epidemic. *J. Biosaf. Biosegurance* **2022**, *4*, 158–162. [CrossRef]
69. Observatório COVID-19 BR. 2021. Available online: https://covid19br.github.io/ (accessed on 28 September 2021).
70. Kruse, T.; Strack, P. Optimal Control of an Epidemic Through Social Distancing. *Cowles Found Discuss.* **2020**, *3581295*, 2229. [CrossRef]
71. Jaberi-Douraki, M.; Moghadas, S.M. Optimal control of vaccination dynamics during an influenza epidemic. *Math. Biosci. Eng.* **2014**, *11*, 1045–1063. [CrossRef]
72. Hansen, E.; Day, T. Optimal control of epidemics with limited resources. *J. Math. Biol.* **2011**, *62*, 423–451. [CrossRef] [PubMed]
73. Morato, M.M.; Bastos, S.B.; Cajueiro, D.O.; Normey-Rico, J.E. An optimal predictive control strategy for COVID-19 (SARS-CoV-2) social distancing policies in Brazil. *Annu. Rev. Control* **2020**, *50*, 417–431. [CrossRef] [PubMed]
74. Köhler, J.; Schwenkel, L.; Koch, A.; Berberich, J.; Pauli, P.; Allgöwer, F. Robust and optimal predictive control of the COVID-19 outbreak. *Annu. Rev. Control* **2020**, *51*, 525–539. [CrossRef]
75. Köhler, J.; Enyioha, C.; Allgöwer, F. Dynamic resource allocation to control epidemic outbreaks a model predictive control approach. In Proceedings of the 2018 Annual American Control Conference (ACC), Milwaukee, WI, USA, 27–29 June 2018; pp. 1546–1551. [CrossRef]
76. Bin, M.; Cheung, P.Y.; Crisostomi, E.; Ferraro, P.; Lhachemi, H.; Murray-Smith, R.; Myant, C.; Parisini, T.; Shorten, R.; Stein, S.; et al. Post-lockdown abatement of COVID-19 by fast periodic switching. *PLoS Comput. Biol.* **2021**, *17*, e1008604. [CrossRef]
77. Meidan, D.; Schulmann, N.; Cohen, R.; Haber, S.; Yaniv, E.; Sarid, R.; Barzel, B. Alternating quarantine for sustainable epidemic mitigation. *Nat. Commun.* **2021**, *12*, 220. [CrossRef] [PubMed]
78. Khailaie, S.; Mitra, T.; Bandyopadhyay, A.; Schips, M.; Mascheroni, P.; Vanella, P.; Lange, B.; Binder, S.C.; Meyer-Hermann, M. Development of the reproduction number from coronavirus SARS-CoV-2 case data in Germany and implications for political measures. *BMC Med.* **2021**, *19*, 32. [CrossRef] [PubMed]
79. Garnett, G.P. Role of herd immunity in determining the effect of vaccines against sexually transmitted disease. *J. Infect. Dis.* **2005**, *191*, S97–S106. [CrossRef]
80. Centers for Disease Control and Prevention. Information for Clinicians on Investigational Therapeutics for Patients with COVID-19. 2020. Available online: https://www.cdc.gov/coronavirus/2019-ncov/hcp/therapeutic-options.html (accessed on 13 March 2021).

81. Johns Hopkins Medicine. Is the Coronavirus Treatable? 2020. Available online: https://www.hopkinsmedicine.org/health/conditions-and-diseases/coronavirus/coronavirus-treatment-whats-in-development (accessed on 5 April 2021).
82. FDA. Coronavirus (COVID-19) Update: FDA Authorizes Monoclonal Antibodies for Treatment of COVID-19. 2020. Available online: https://www.fda.gov/news-events/press-announcements/coronavirus-covid-19-update-fda-authorizes-monoclonal-antibodies-treatment-covid-19 (accessed on 7 September 2021).
83. Guan, W.J.; Ni, Z.Y.; Hu, Y.; Liang, W.H.; Ou, C.Q.; He, J.X.; Liu, L.; Shan, H.; Lei, C.L.; Hui, D.S.; et al. Clinical Characteristics of Coronavirus Disease 2019 in China. *N. Engl. J. Med.* **2020**, *382*, 1708–1720. [CrossRef]
84. COVID-19 to Slash Global Economic Output by $8.5 Trillion over Next Two Years. 2020. Available online: https://www.un.org/en/desa/covid-19-slash-global-economic-output-85-trillion-over-next-two-years (accessed on 9 September 2021).
85. Global Economy Could Lose over $4 Trillion Due to COVID-19 Impact on Tourism. 2021. Available online: https://unctad.org/news/global-economy-could-lose-over-4-trillion-due-covid-19-impact-tourism (accessed on 9 September 2021).
86. Global Economic Effects of COVID-19 (CRS Report No. R46270). Retrieved from Congressional Research Service Website. 2021. Available online: https://crsreports.congress.gov/ (accessed on 8 September 2021).
87. Gupta, A.G.; Moyer, C.A.; Stern, D.T. The economic impact of quarantine: SARS in Toronto as a case study. *J. Infect.* **2005**, *50*, 386–393. [CrossRef]
88. Demirgüç-Kunt, A.; Lokshin, M.; Torre, I. The Sooner, the Better: The Early Economic Impact of Non-Pharmaceutical Interventions During the COVID-19 Pandemic. *World Bank Policy Res. Work. Pap.* **2020**, *26*, 9257. [CrossRef]
89. Chen, S.; Igan, D.O.; Pierri, N.; Presbitero, A.F.; Soledad, M.; Peria, M. Tracking the economic impact of COVID-19 and mitigation policies in Europe and the United States. *IMF Work. Pap.* **2020**, *125*, 25. [CrossRef]
90. Aum, S.; Lee, S.Y.; Shin, Y. COVID-19 doesn't need lockdowns to destroy jobs: The effect of local outbreaks in Korea. *Labour Econ.* **2021**, *70*, 101993. [CrossRef]
91. Imperial College London. Report 9—Impact of Non-Pharmaceutical Interventions (NPIs) to Reduce COVID-19 Mortality and Healthcare Demand. 2020. Available online: https://www.imperial.ac.uk/media/imperial-college/%5Cmedicine/sph/ide/gida-fellowships/Imperial-College-COVID19-NPI-modelling-16-03-2020.pdf (accessed on 8 April 2021).
92. Teslya, A.; Pham, T.M.; Godijk, N.G.; Kretzschmar, M.E.; Bootsma, M.C.J.; Rozhnova, G. Impact of self-imposed prevention measures and short-term government-imposed social distancing on mitigating and delaying a COVID-19 epidemic: A modelling study. *PLoS Med.* **2020**, *17*, e1003166. [CrossRef] [PubMed]
93. G1. Governo de SP Avança 6 Regiões Para a Fase Amarela da Quarentena, Que Permite Funcionamento de Restaurantes até 22h. 2021. Available online: https://g1.globo.com/sp/sao-paulo/noticia/2021/02/05/governo-de-sp-avanca-6-regioes-para-a-fase-amarela-que-permite-funcionamento-do-comercio-ate-22h.ghtml (accessed on 28 March 2021).
94. Hyafil, A.; Moriña, D. Analysis of the impact of lockdown on the reproduction number of the SARS-Cov-2 in Spain. *Gac. Sanit.* **2022**, *35*, 453–458. [CrossRef] [PubMed]
95. Conselho Federal de Medicina. Medicina Intensiva no Brasil. 2018. Available online: https://portal.cfm.org.br/images/PDF/leitosdeuticapitais2018.pdf (accessed on 25 March 2021).
96. Cleve, M.I. The lightning-fast quest for COVID vaccines and what it means for other diseases. *Nature* **2021**, *589*, 16–18. [CrossRef]
97. CNN. UK Becomes First Country to Authorize Pfizer/BioNTech's COVID-19 Vaccine, First Shots Roll Out Next Week. 2020. Available online: https://edition.cnn.com/2020/12/02/uk/pfizer-coronavirus-vaccine-uk-intl-hnk/index.html (accessed on 17 April 2021).
98. Wiggins, S. *Introduction to Applied Nonlinear Dynamical Systems and Chaos*; Springer: New York, NY, USA, 1990.

mathematics

MDPI

Article

Toward Optimal Fitting Parameters for Multi-Exponential DWI Image Analysis of the Human Kidney: A Simulation Study Comparing Different Fitting Algorithms

Jonas Jasse [1,*], Hans-Joerg Wittsack [1], Thomas Andreas Thiel [1], Romans Zukovs [2], Birte Valentin [1], Gerald Antoch [1] and Alexandra Ljimani [1]

[1] Department of Diagnostic and Interventional Radiology, Medical Faculty, University Hospital Dusseldorf, Heinrich-Heine-University Dusseldorf, 40225 Dusseldorf, Germany; alexandra.ljimani@med.uni-duesseldorf.de (A.L.)
[2] Department of Haematology, Oncology and Clinical Immunology, Medical Faculty, University Hospital Dusseldorf, Heinrich-Heine-University Dusseldorf, 40225 Dusseldorf, Germany
* Correspondence: jonas.jasse@med.uni-duesseldorf.de; Tel.: +49-211-81-18044

Abstract: In DWI, multi-exponential signal analysis can be used to determine signal underlying diffusion components. However, the approach is very complex due to the inherent low SNR, the limited number of signal decay data points, and the absence of appropriate acquisition parameters and standardized analysis methods. Within the scope of this work, different methods for multi-exponential analysis of the diffusion signal in the kidney were compared. To assess the impact of fitting parameters, a simulation was conducted comparing the free non-negative (NNLS) and rigid non-linear least square (NLLS) fitting methods. The simulation demonstrated improved accuracy for NNLS in combination with area-under-curve estimation. Furthermore, the accuracy and stability of the results were further enhanced utilizing optimized parameters, namely 350 logarithmically spaced diffusion coefficients within $[0.7, 300] \times 10^{-3}$ mm^2/s and a minimal SNR of 100. The NNLS approach shows an improvement over the rigid NLLS method. This becomes apparent not only in terms of accuracy and omitting prior knowledge, but also in better representation of renal tissue physiology. By employing the determined fitting parameters, it is expected that more stable and reliable results for diffusion imaging in the kidney can be achieved. This might enable more accurate DWI results for clinical utilization.

Keywords: diffusion-weighted MRI; multi-exponential; microstructural image analysis; simulation; fitting; modelling; kidney

MSC: 92C55; 68U10; 92C50; 11L07; 92-10

1. Introduction

Diffusion-weighted MRI (DWI) is a specialized imaging technique that offers insights into the microstructure of tissue by assessing the movement of water molecules within the tissue microstructure without the need for tracer injections [1,2]. It is widely used in clinical settings to detect, characterize, and stage malignant lesions in various anatomical regions of the human body. Furthermore, DWI distinctive ability to quantify diffusion processes can be utilized to detect and characterize fibrosis and inflammation including but not limited to the abdomen. In terms of kidney applications, it enables differentiation between healthy tissue and tissue affected by renal failure, pyelonephritis, ureteral obstruction, and renal cell carcinoma [1,3,4]. A precise description of the acquired MRI signal is crucial in order to distinguish between physiological and pathological processes.

To evaluate an acquired DWI signal, multi-exponential signal analysis can be used. The conventional Intra-Voxel Incoherent Motion (IVIM) model proposes a two-compartment

model consisting of fractions related to capillary perfusion and tissue diffusion [5]. However, recent studies have indicated that bi-exponential modelling of the diffusion signal is insufficient to describe the behavior of water molecules in complex environments such as the human kidney. The kidney is composed of various structures of varying magnitudes, including dense tissue, small capillaries, and large blood vessels. This results in different diffusion environments in the renal cortex, medulla, and hilum, thus rendering a bi-exponential description insufficient [6–11]. Instead, a more appropriate approach in renal tissue involves a tri-exponential model, which encompasses the three diffusion regimes with contributions from blood flow, tubular flow, and pure tissue diffusion [7–10].

The standard method for fitting the IVIM model to the acquired renal DWI data is to perform non-linear least squares fitting (NLLS) [12] of a predefined rigid tri-exponential model. However, NLLS requires initial estimated starting values. Starting from this initial guess, the values are varied until the tri-exponential model function best fits the measured data using least squares. That way, NLLS provides a distinct unique solution for each unknown, poorly representing physiological conditions with variable value spectrums. Because NLLS requires prior knowledge regarding the number of components, its use has been limited so far. Especially in pathophysiological conditions, initial fitting values are difficult to determine and the number of diffusion compartments may vary [13]. Therefore, the recently utilized non-negative least squares fitting (NNLS) [14] approach presents an advantage, as it does not demand further specification of underlying diffusion components or specific initial starting values a priori, making it potentially superior to the NLLS algorithm. In contrast to NLLS, which requires a specific model function—in this case a tri-exponential model—to be specified, NNLS automatically determines the number and size of the exponential terms based on a specified (pseudo) continuous spectrum of exponential functions. The only assumption made, which applies to diffusion, is that the coefficients of interest should not be negative. NNLS results in a distribution of exponential terms that directly reflects the diffusion compartments of the renal tissue being studied. Therefore, NNLS has the potential to better reflect the complex characteristics of biological tissue. Nevertheless, a systematic quantitative comparison of these different signal analysis techniques and the establishment of standardized parameters for multi-exponential renal DWI investigations is missing to date.

To identify optimized fitting parameters, this study aims to compare and evaluate the NLLS and NNLS fitting approaches using an extensive multi-parametric simulation. Firstly, a synthetic multi-exponential diffusion signal was simulated, based on physiological conditions present in the human kidney. Extensive signal analysis was then performed using the introduced fitting approaches with various parameter variations. Moreover, both NLLS and NNLS were combined by using the NNLS results as initial values for the rigid non-linear fitting method (named NLLS*). In addition, the NNLS algorithm was enhanced by incorporating an area-under-curve (AUC) function to improve accuracy, referred to as NNLS_{AUC}. Afterwards, we conducted a comprehensive comparison of the results obtained from all four multi-exponential fitting techniques and derived the optimal fitting parameters. These parameters were subsequently applied to a thorough final simulation.

This study aims to determine optimized acquisition and fitting parameters by conducting a comprehensive evaluation of the NLLS and NNLS fitting approaches through extensive multi-parametric simulations based on physiological conditions present in the human kidney. Therefore, we determined a set of optimized parameters that can serve as basis for accurate analysis of real renal DWI data using multi-exponential methods.

The paper is structured as follows. Section 2 describes the mathematical model and the fitting algorithms and explains the generation of the synthetic multi-exponential signal. Next, the simulation conditions are presented in the same section, showing the parameters used and further details of the parameter variations performed. The section ends with a comprehensive description of the statistics used to evaluate the results. The results are

presented in Section 3, followed by a full discussion in Section 4. Finally, Section 5 presents the conclusions of this work.

2. Methods

2.1. Multi-Compartment Model

The diffusion signal $S(b)$ observed in the human body can generally be described as a superposition of multiple individual diffusion processes, with various diffusion coefficients resulting in a multi-exponential decay function [15]:

$$S(b_i) = \sum_{i=1}^{M} f_j e^{-b_i D_j}, \;\; j = 1, 2, \ldots, N \tag{1}$$

where b_i is the diffusion weighting b-value in mm^2/s, M is the total number of measurements i with different b-values, f_j is the amplitude of the exponential component with the diffusion coefficient D_j. In the following, f_j is denoted as the volume fraction, although this nomenclature is mathematically inaccurate due to the omission of correction for relaxation times and the exclusion of the prevailing proton density. N is the number of diffusion components. Typically, mono- or bi-exponential models are used to describe DWI data from certain organs. However, recent studies have questioned the correctness of bi-exponential fitting for the diffusion signal, particularly for renal tissue [8,9,11,16]. It appears as though a three-compartment model, considering the tubular volume fraction, is physiologically more appropriate in the context of the kidney. By applying the tri-exponential fitting model, the measured diffusion signal $S(b_i)$ can be defined as:

$$S(b_i) = \sum_{i=1}^{M} f_j e^{-b_i D_j}, \;\; j \in [1, 3] \; (tissue, tubule, blood) \tag{2}$$

The diffusion coefficient D_j can be assigned to diffusion processes in tissue, tubules, and blood. In detail, these three components relate to the restricted diffusion of water molecules in renal tissue, the pseudo-diffusion occurring inside tubules, and the pseudo-diffusion component present in blood vessels. They are often referred to as the slow, intermediate, and fast diffusion components, respectively. The same classification accounts for the three different volume fractions f_j.

The sum of all volume fractions in multi-compartment models adds up to $\sum_j^N f_j = 1$. Therefore, the diffusion signal $S(b_i)$ for a three-compartment model can be defined as:

$$S(b_i) = \sum_{i=1}^{M} f_{slow} e^{-b_i D_{slow}} + f_{inter} e^{-b_i D_{inter}} + (1 - f_{slow} - f_{inter}) e^{-b_i D_{fast}} \tag{3}$$

2.2. Non-Linear Least Square Fitting

The established tri-exponential model described in Equation (3) was incorporated into a rigid NLLS algorithm constructed around the *lsqnonlin* function of MATLAB (The Mathworks Inc., Natick, MA, USA). To fit the synthetic signal (construction details provided below), the standard trust-region algorithm [17] was employed. Initial parameter values for D, f, and boundary conditions of the non-linear fit need to be declared a priori. Hence, standard starting values and parameter ranges were chosen in accordance with literature [13], as summarized in Table 1. Following the fitting process, the NLLS algorithm produced discrete optimal values for D_j and f_j with respect to the corresponding signal input.

Table 1. Ground truth values required for the generation of synthetic multi-exponential diffusion decay data and standard simulation parameters.

Ground truth values	
Diff. coefficient blood (d_{fast})	165×10^{-3} mm^2/s
Diff. coefficient tubule (d_{inter})	5.8×10^{-3} mm^2/s
Diff. coefficient tissue (d_{slow})	1×10^{-3} mm^2/s
Vol. fraction blood (f_{fast})	0.1
Vol. fraction tubule (f_{inter})	0.3
Vol. fraction tissue (f_{slow})	0.6
Standard simulation parameters	
b-value distribution [16]	[0, 5, 10, 20, 30, 40, 50, 75, 100, 150, 200, 250, 300, 400, 525, 750]
SNR	140
Iterations	1000
Standard NNLS parameters	
M	300
D_{min}	0.7×10^{-3} mm^2/s
D_{max}	300×10^{-3} mm^2/s
Standard starting values NLLS	
Diff. coefficients	$[1.5, 30, 100] \times 10^{-3}$ mm^2/s
Volume fractions	[0.50, 0.25, 0.20]

2.3. Non-Negative Least Square Algorithm

To analyze the diffusion signal with the NNLS approach, an implementation of the algorithm of Lawson and Hanson [14] was employed. Fitting of the synthetic renal DWI data was accomplished with an in-house software based on the *lsqnonneg* MATLAB R2022a function. An advanced regularization method of NNLS using cross-validation to determine the regularization factor μ was implemented based on the open-source multi-exponential decay image analysis software *AnalyzeNNLS* (2017.05.09) from Bjarnason and Mitchell [18].

In the NNLS algorithm, the signal decay is expressed as a superposition of exponentials, similar to Equation (1) [15]:

$$y_i = \sum_{j=1}^{M} A_{ij} s_j, \;\; i = 1, \, 2, \ldots, N \tag{4}$$

with the constraint matrix A_{ij} representing the exponentials and s_j representing the corresponding amplitudes for M logarithmically spaced diffusion coefficients at N diffusion components. An inverse of A_{ij} cannot be derived due to noise contained in the signal y_i, resulting in an ill-posed problem. The NNLS algorithm is then used to minimize the minimal least squares χ^2 misfit between the measured (or simulated) and modelled data:

$$\chi^2 = min \left[\sum_{i=1}^{N} \left| \sum_{j=1}^{M} A_{ij} s_j - y_i \right|^2 \right], \tag{5}$$

while all amplitudes are implicitly defined as non-negative, stating $s_j \geq 0$ [15].

Unlike non-linear optimization methods, the NNLS algorithm does not require a priori information or an initial guess of variables to solve Equation (4). As an output, NNLS yields amplitudes for the M exponential functions for each diffusion coefficient D_j. To obtain a more physiologically realistic representation, the least-square algorithm can be adapted to

construct a continuous spectrum. By incorporating extra constraints into the matrix A_{ij}, one is able to alter the discrete character of the basic NNLS solution. By introducing the regularization term μ, Equation (5) can be adjusted accordingly [18]:

$$\chi^2 = min\left[\sum_{i=1}^{N}\left|\sum_{j=1}^{M} A_{ij}s_j - y_i\right|^2 + \mu\sum_{j=1}^{M}|s_{j+2} - 2s_{j+1} + s_j|^2\right] \quad (6)$$

The weighting factor μ serves as a smoothing constraint that affects the curvature of the NNLS solution spectrum and ensures a robust fit, determined by cross-validation. Larger μ values result in smoother distributions, satisfying the constraints at the expense of increasing misfit. For $\mu = 0$, this formula yields the least square solution χ^2_{min} from Equation (5) [18].

The outcome of the regularized NNLS fitting entails various exponential terms, which correspond to the diffusion components identified in the signal decay curve. By plotting the associated diffusion coefficients with respect to the amplitudes, distinct peaks become evident. Individual peaks can be characterized by assessing their maximum and area under curve. This allows for the derivation of the geometric mean D and volume fraction f of the contributing exponential constituents.

2.4. Combined Non-Linear and Non-Negative LS Algorithms

A unique approach was employed by combining both NNLS and NLLS methods to create a two-level analysis of the diffusion signal to overcome the starting value limitation of NLLS and thereby increase the accuracy of the fitting results. For this purpose, the NLLS algorithm utilizes the fitting results obtained by the NNLS algorithm as initial parameters, resulting in an advanced approach referred to as NLLS*.

2.5. Advanced NNLS Algorithm with AUC Constraint

In addition to the standard NNLS algorithm, we implemented an advanced fitting algorithm called NNLS_{AUC}. It is based on the same fitting results as standard NNLS and incorporates an AUC constraint following fitting. This modification aims to minimize the influence of inaccurately identified peaks and noise interferences. To achieve that, the NNLS_{AUC} technique applies adaptable interval boundaries based on estimated physiological compartment ranges for the three diffusion regimes. In cases where multiple peaks d_{ij} are encompassed by these intervals i, a weighting factor based on their respective volume fraction f_{ij} is applied to combine them into a single representative peak d_i according to Equations (7) and (8).

$$f_i = \sum_{j=1}^{n} f_{ij}, \qquad \forall\ intervals\ i \quad (7)$$

$$d_i = \sum_{j=1}^{n} \frac{d_{ij}f_{ij}}{f_i}, \quad \forall\ intervals\ i \quad (8)$$

This categorization of the diffusion spectrum requires prior knowledge of basic diffusion regime boundary parameters.

2.6. Simulation and Reconstruction

To simulate the underlying synthetic renal diffusion data, we followed the methodology outlined in Equation (3) and used the ground truth (gT) values presented in Table 1. The initial parameters used for the diffusion coefficients d and volume fractions f are based on the physiological conditions in the human kidney, considering the presence of three diffusion compartments [9,11,13]. Subsequently, the multi-exponential diffusion signals were superimposed with Gaussian noise for each b-value on a random basis, ensuring an authentic artificial signal decay with variable signal-to-noise ratio (SNR). The SNR was defined by dividing the signal at the first b-value with $b = 0$ s/mm^2 by the standard

deviation of the added noise [13,19]. For better comparison, the same simulated data were then analyzed using the different algorithms mentioned above, namely NNLS and NLLS (Figure 1). In the context of the simulation, the diffusion coefficient parameter is denoted as d in order to eliminate any potential confusion with the limits of the NNLS fitting range D_{min} or D_{max}.

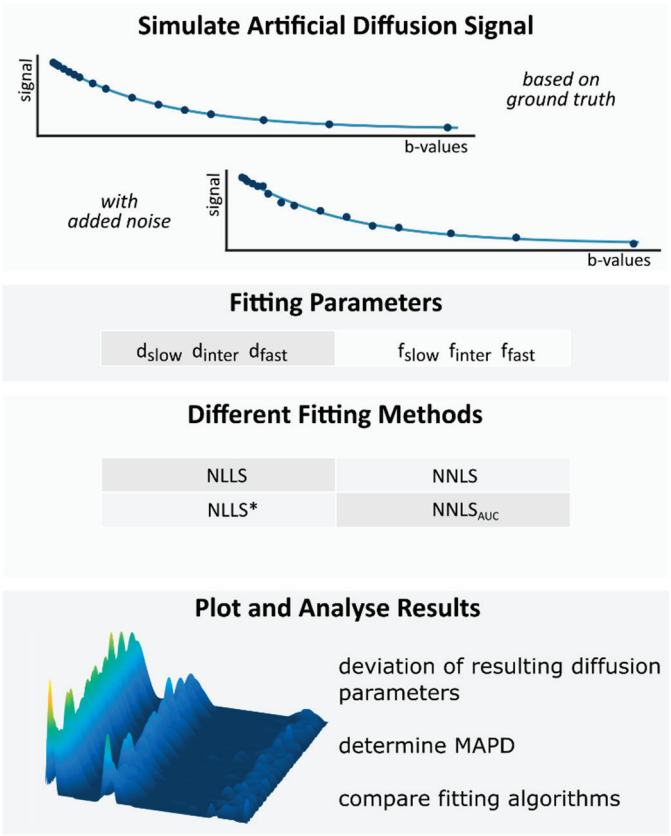

Figure 1. Simulation workflow including a list of initial parameters, the computation of synthetic signal data, the utilization of multi-exponential fitting algorithms, and the subsequent visualization and analysis of the simulation.

Values of previous works utilizing NLLS fitting were used as starting parameters [9,11,13,20,21]. The NNLS diffusion fitting range was set accordingly to encompass the entire physiologically relevant spectrum [11,13]. The total number of fitting iterations for all simulations was n = 1000.

2.7. Parameter Variation

For parameter variations, main emphasis lay on altering values within a range relevant for routine examinations of the kidneys and feasible for research imaging experiments.

The variation in SNR ranged from 50 to 600, with a primary focus on the interval between 100 and 140, including the most commonly observed SNR values of routinely acquired DWI [22,23].

In addition to the standard logarithmic distribution, other b-value compositions have been evaluated to find a suitable distribution for NNLS fitting. This work evaluates two of these other b-value compositions: an equidistant distribution and an interval distribution. The latter applies a dense concentration of b-values inside the three diffusion regimes. All b-value distributions span the same range, with b_{max} = 750.

To investigate the impact of the number of logarithmically spaced diffusion coefficients M on the NNLS fitting process, M was varied in increments of 50, resulting in a range of

100 to 600 possible exponential components for NNLS. Particular attention was devoted to the interval around M = 300, covering commonly utilized values of prior studies [11,13].

The fitting results obtained from NNLS should be self-contained from any variations made regarding the range of possible diffusion coefficients, as defined by the choice of D_{min} and D_{max}. However, altering the discrete fitting range for non-negative approaches exerts a significant influence, posing a common problem. Therefore, we compared our standard range (Table 1) to a shortened and an extended version. The shortened fitting range spans from $D_{min} = 0.9 \times 10^{-3}$ mm^2/s to $D_{max} = 200 \times 10^{-3}$ mm^2/s and the extended range encompasses values between $D_{min} = 0.5 \times 10^{-3}$ mm^2/s and $D_{max} = 500 \times 10^{-3}$ mm^2/s [11,13]. A comprehensive summary of the complete parameter variations can be found in Table 2.

Table 2. Values and sets of varied fitting parameters for NNLS.

Parameter	Variation
SNR	50, 100, 110, 120, 130, 140, 600
Equidistant b-value distribution	0, 50, 100, 150, 200, 250, 300, 350, 400, 450, 500, 550, 600, 650, 700, 750
Interval b-value distribution	0, 5, 10, 15, 20, 30, 50, 100, 150, 200, 250, 350, 450, 550, 650, 750
M	100, 200, 250, 300, 350, 400, 600
Shortened D_{min} and D_{max}	[0.8–200] $\times 10^{-3}$ mm^2/s
Extended D_{min} and D_{max}	[0.5–500] $\times 10^{-3}$ mm^2/s

2.8. Statistics

In order to compare the quality of the simulation results and depict the deviation from the gT, the Median Absolute Percentage Deviation ($MAPD$) was computed. The $MAPD$ is determined by calculating the absolute difference between the parameter estimates d and f and the gT values for all n = 1000 iterations, expressed as a percentage:

$$MAPD(x_i) = \frac{100}{gT_i} median(|x_i - gT_i|).$$

Here x_i represents one diffusion parameter estimate and gT_i the corresponding ground truth value.

To ensure more robust results, the utilization of the median was preferred to traditional mean values. This approach bypasses the strong influence of outliers, themselves heavily biased by the choice of constraint boundaries, the latter only being applicable to NNLS algorithms [21,24].

Moreover, statistical analysis was carried out using appropriate MATLAB implementations. Visualization of the data and additional statistical measures were executed using in-house developed software in R (version 4.1.3, R Foundation for Statistical Computing, Vienna, Austria).

3. Results

3.1. Evaluation of Simulated NNLS Fitting

An exemplary NNLS analysis of n = 100 signals is shown in Figure 2. This simulation was performed using standard parameters (Table 1). Three distinct peaks of the slow, intermediate, and fast component can be distinguished clearly, reflecting the three diffusion compartments employed as gT for the synthetic signal decay. Additionally, minor peaks caused by wrongly interpreted noisy signal data by the NNLS algorithm are also noticeable.

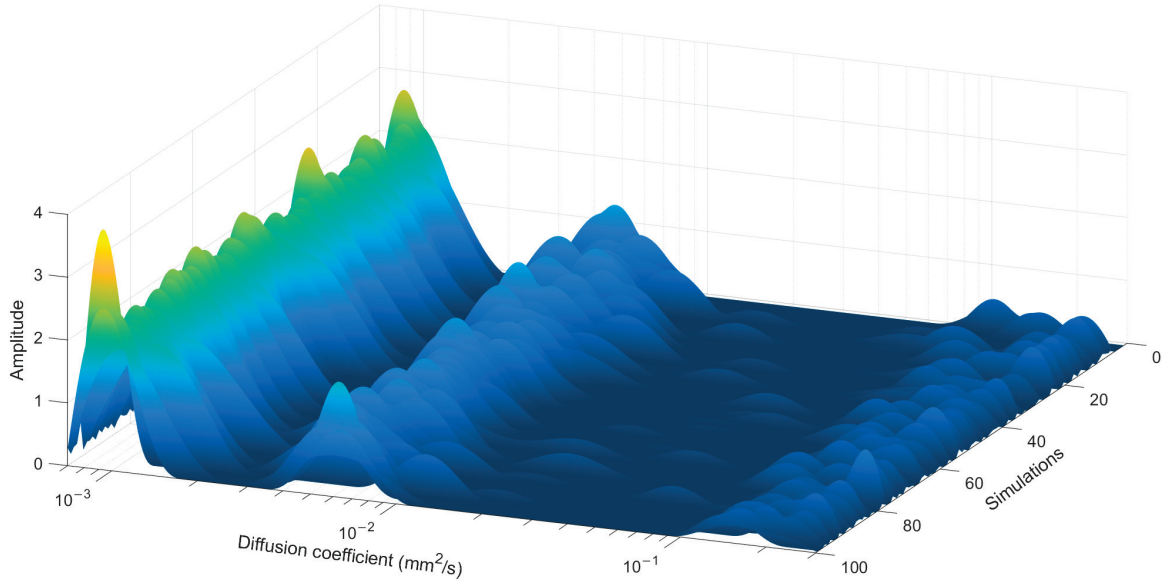

Figure 2. NNLS spectrum, representing a simulation of 100 modelled signals with an SNR of 120. Three distinctive peaks are clearly distinguishable, corresponding to the slow (**left peak**), intermediate (**middle peak**), and fast (**right peak**) components. These peaks align with the three diffusion compartments of the ground truth. Additionally, minor peaks caused by wrongly interpreted noisy signal data by the NNLS algorithm are also noticeable.

3.2. Parameter Variation

3.2.1. Signal-to-Noise Ratio

In this simulation, the SNR was varied and ranged from 50 to 600, with a primary focus on the interval between 100 and 140. The results of the simulations conducted are depicted in Figure 3A,B (for diffusion coefficients *d* and volume fractions *f*, respectively), with an optimal SNR of 600 serving as a reference. In addition to the variation in SNR, the standard simulation parameters outlined in Table 1 were employed.

The accuracy of the fitting results strongly correlates with the signal quality and, consequently, with SNR. Even in the instance of poor signal quality, with an SNR of 100 or less, differentiation of the three diffusion components remains possible with $NNLS_{AUC}$ and the standard NNLS algorithm. For the non-linear methods NLLS and NLLS*, a distinction between the slow and intermediate diffusion components can only be achieved for SNRs surpassing 130 (Figure 3). The NLLS* algorithm, up until an SNR of 600, is not capable of distinguishing the three components at any routinely achieved SNR levels.

Looking at the volume fractions (Figure 3B), the results are similar. While techniques involving non-rigid fitting possess the ability to differentiate all three compartments at SNRs of 100 and over, the results of the approaches incorporating the non-linear fitting overlap for intermediate and fast volume fractions.

In our study, NLLS methods demonstrated the highest standard derivation, particularly with respect to the slow and intermediate diffusion coefficients. Only the NNLS methods managed to distinguish all three diffusion compartments consistently.

A simplified visualization of the MAPD development with regard to increasing SNR values is illustrated in Figure A1. NLLS and NLLS* exhibit a mean MAPD of 16.46% and 18.83%, respectively. The NNLS approaches demonstrate a significantly lower average MAPD value, with plain NNLS at 12.49% and $NNLS_{AUC}$ at 10.39%. The minimum overall MAPD values concerning the routinely relevant SNR interval were observed for $NNLS_{AUC}$, reaching 9.2% at the highest SNR level of 140.

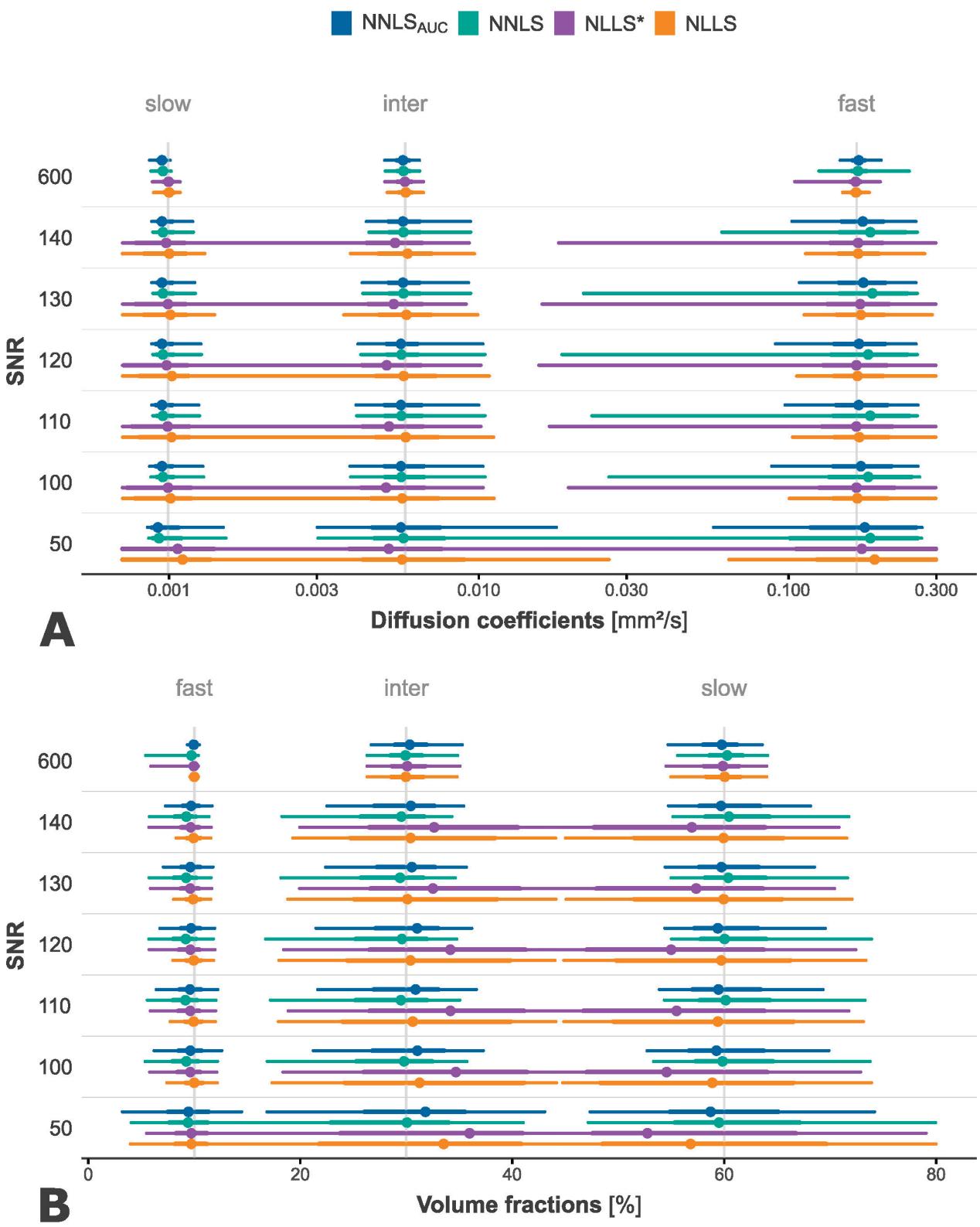

Figure 3. Simulation results for the diffusion coefficients (**A**) and volume fractions (**B**) for all SNR variations, grouped by methods. The boxplots display the median value (round dot), interquartile range (thick line), and whiskers (thin line), the latter containing 95% of the data distribution. Ground truth values are indicated by grey lines.

3.2.2. Distribution of b-Values

The evaluation of b-value distributions covers three different compositions. Figure 4 presents the findings regarding the utilized standard, equidistant, and interval distribution of b-values affecting the fitting accuracy and, consequently, the diffusion parameter estimates.

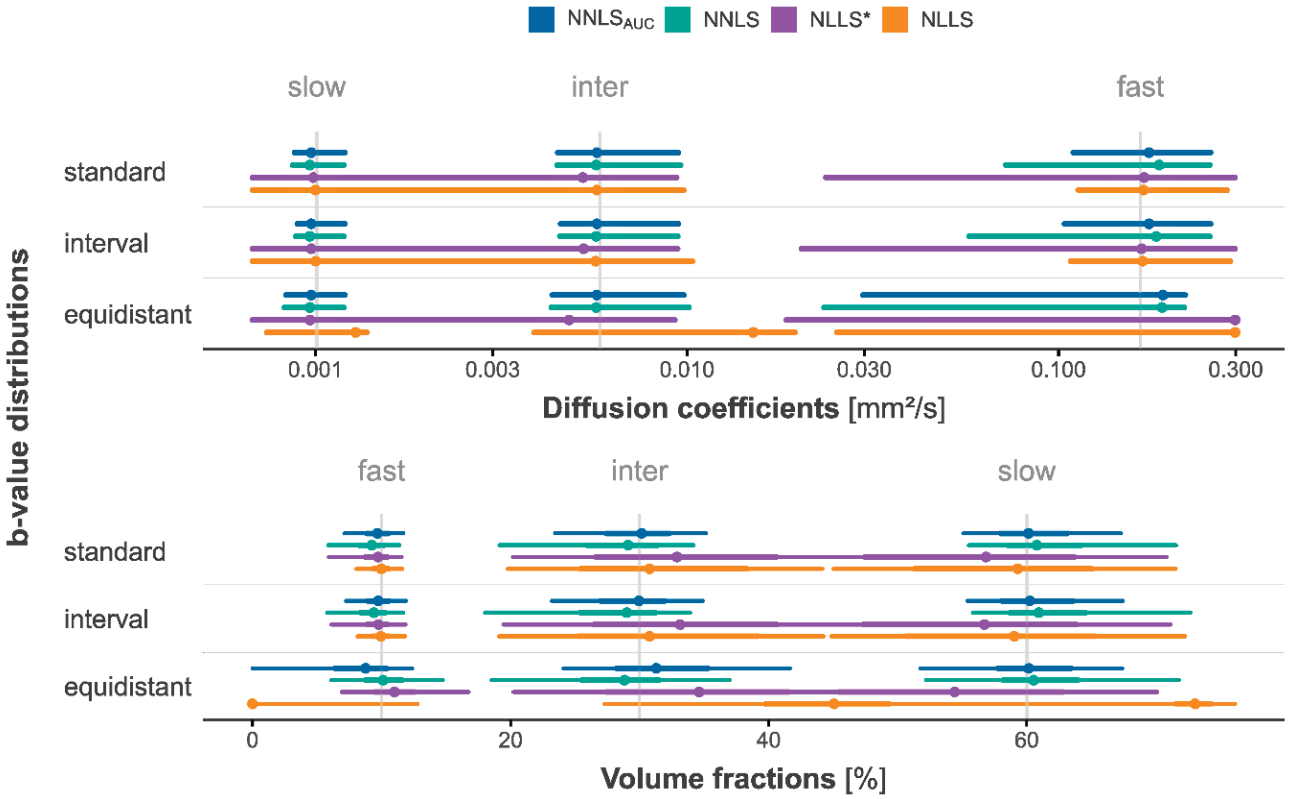

Figure 4. Simulation results of diffusion coefficients and volume fractions under variation of the b-value distribution (standard, interval, and equidistant), grouped by methods. The boxplots display the median value (round dot), interquartile range (thick line), and whiskers (thin line), the latter containing 95% of the data distribution.

A noticeable decline in accuracy can be observed when employing an equidistant distribution of b-values. Greater deviation from the gT values (12.37% mean MAPD for NNLS) across all components becomes apparent when compared to the standard distribution. However, the same is not necessarily true for the b-value composition that prioritizes the diffusion intervals. In this case, the mean MAPD for NNLS is 8.80%, slightly underperforming the standard distribution. The standard distribution, on the other hand, demonstrates the most precise results, with an average MAPD of 8.56%. In particular, the non-linear methods seem to be strongly affected by variation in the b-value distributions. In contrast, the NNLS methods exhibit more consistent results across b-value compositions.

3.2.3. Number of Logarithmically Spaced Diffusion Coefficients

For this simulation, the number of logarithmically spaced diffusion coefficients M was varied in increments of 50, resulting in a range of 100 to 600 possible exponential components for the free NNLS fitting methods. When modifying the logarithmically spaced diffusion coefficients, only NNLS and NNLS$_{AUC}$ are influenced by varying M values. Results for the diffusion coefficients are illustrated in Figure 5.

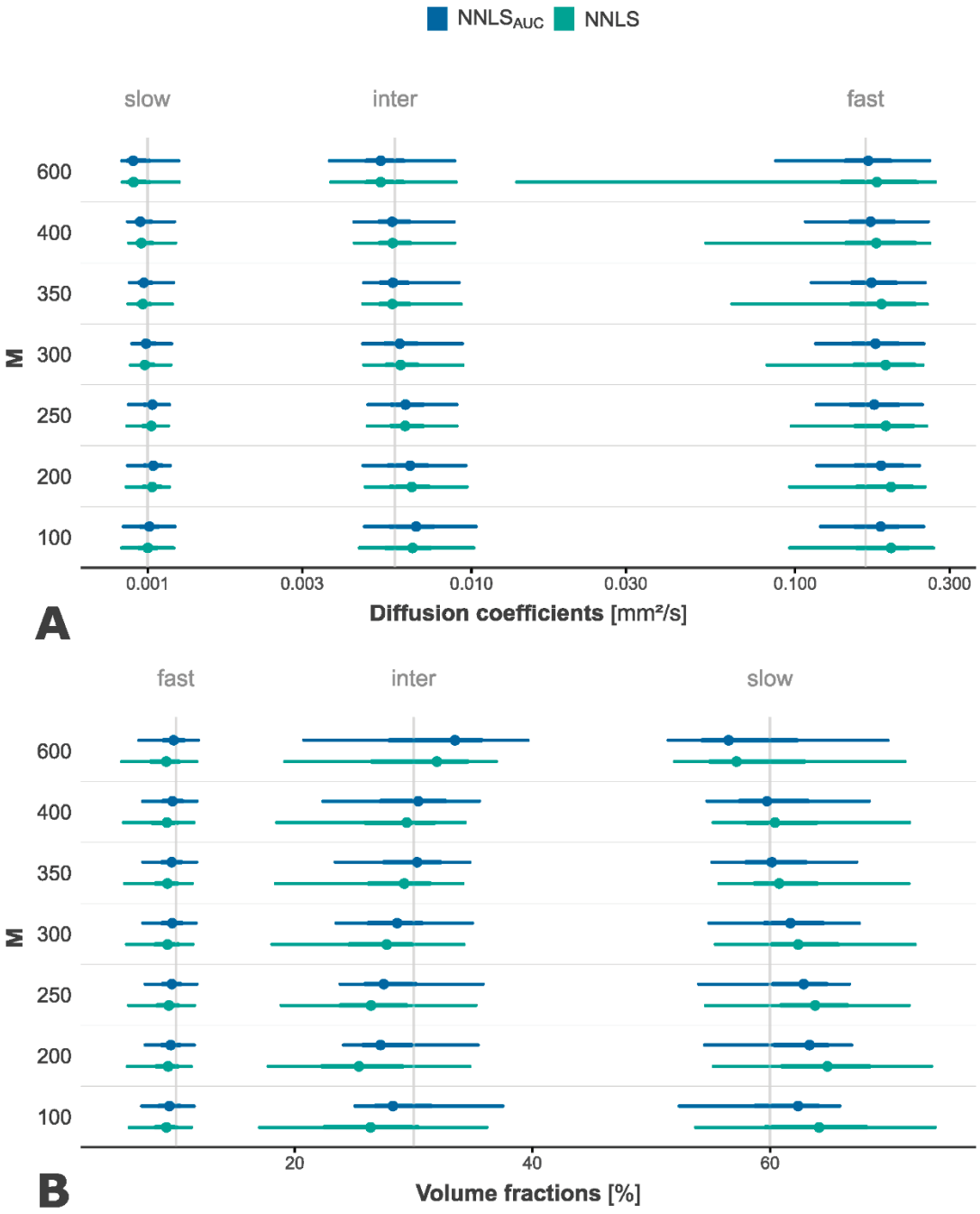

Figure 5. Simulation results for the diffusion coefficients (**A**) and volume fractions (**B**) for all variations of M, grouped by methods. The design of the boxplots is analogous to the one in prior variation figures.

Both free fitting approaches are able to distinguish the three compartments at all levels of *M*. While altering *M* only slightly affects the deviation of the results for the diffusion coefficients, it comes along with an increase in the standard derivation of the estimates for the fast component, especially in the case of NNLS. Considering f, the standard derivation remains constant, but the estimates for the intermediate and fast component vary in their derivation to the *gT*. The most accurate results are achieved when *M* is approximately 350 for NNLS and NNLS$_{AUC}$. Data for different numbers of logarithmically spaced diffusion coefficients are demonstrated in Figure A2.

The value of 350 logarithmically spaced diffusion coefficients seems most promising, with minimal deviation for both NNLS and NNLS$_{AUC}$. At $M = 350$, the total MAPD for the standard NNLS algorithm is 10.41%, decreasing to 8.36% for NNLS$_{AUC}$.

3.2.4. Diffusion Fitting Range

To investigate the impact of altering the discrete fitting range for non-negative approaches, different ranges were applied for the NNLS algorithm, namely a standard ([0.7–300] $\times$ 10^{-3} mm^2/s), a shortened ([0.9–200] $\times$ 10^{-3} mm^2/s), and an extended ([0.5–500] $\times$ 10^{-3} mm^2/s) range, as shown in Figure 6.

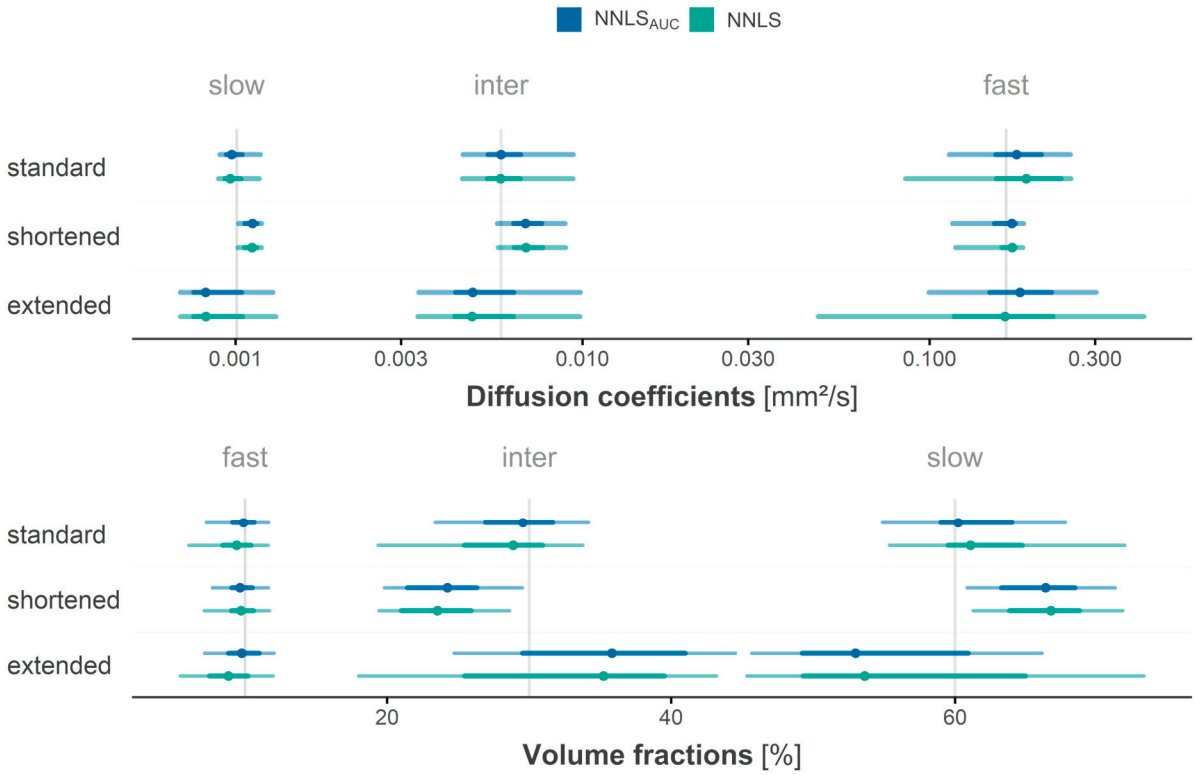

Figure 6. Simulation results of diffusion coefficients and volume fractions under variations of the diffusion fitting range, grouped by methods.

Previously used standard values for D_{min} and D_{max} produce the most accurate results, while the estimates of the shortened and extended fitting ranges deviate from the gT values. $NNLS_{AUC}$ surpasses the standard NNLS algorithm for all fitting ranges, with its total MAPD for the standard range being 8.4%. The shortened and extended ranges result in 12.31% and 18.32% deviation, respectively. The MAPD stats for standard NNLS exhibit the same tendencies but with lower accuracy.

3.3. Simulation with Optimal Simulation Parameters

For this simulation, a total of 1000 iterations were performed using the optimal parameters that have been previously evaluated. Consequently, an SNR of 140 was employed, the number of logarithmically spaced diffusion coefficients M was set to 350, and the diffusion fitting range was chosen based on the standard distribution (Table 2).

Alongside the plain NNLS algorithm, the results from $NNLS_{AUC}$, NLLS*, and standard NLLS algorithms are presented in Figure 7. The distributions of fitted values for d and f are represented by half-violin plots, while the minimalistic boxplots underneath specify the scattering by providing a visual depiction of the interquartile range (with whiskers indicated as lines and a gap in the line representing the interquartile range) and median values. The three peaks observed along the diffusion coefficient and volume fraction axis correspond to the three diffusion decay components present in the synthetic DWI signal for d and f, respectively.

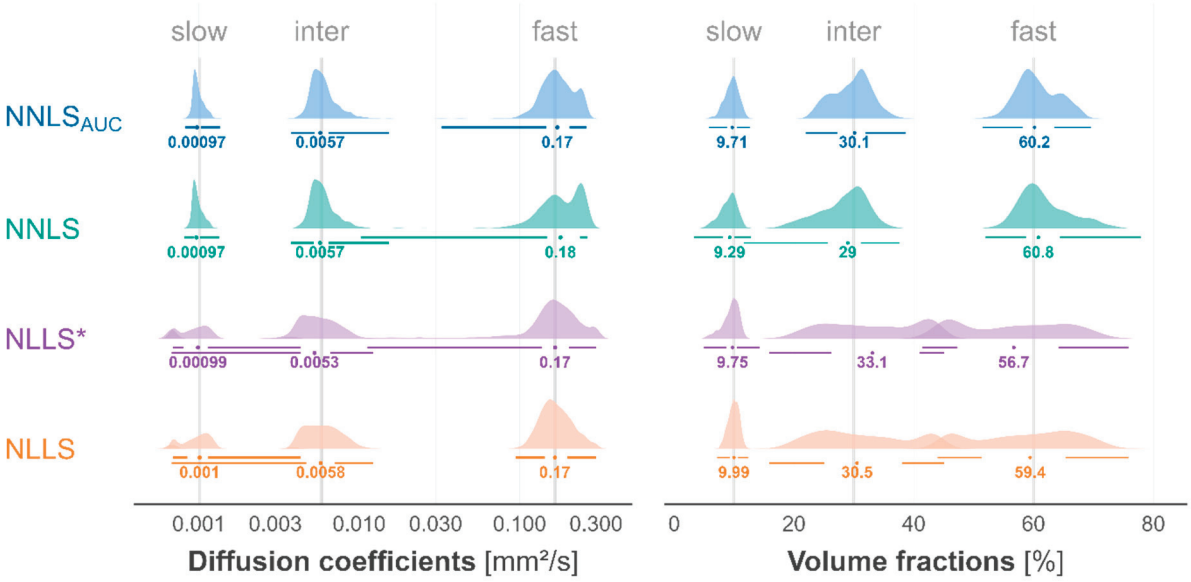

Figure 7. Simulation results of d and f grouped by methods and assigned to corresponding diffusion compartments with n = 1000 iterations. Ground truth values are indicated by grey lines. In addition to the half-violin plots representing the distribution of fitted d and f values, the minimalistic boxplots underneath specify the scattering by visualizing the associated quartile ranges and indicating the median values.

Table A1 shows the MAPD values for a simulation conducted using the previously mentioned starting values. With an average MAPD of just 10.9% for the diffusion coefficients d and 6.4% for volume fractions f, NNLS$_{AUC}$ proved to be the most accurate method with respect to gT values. Conversely, the fitting algorithms based on non-linear fitting produced the highest deviation, with an average MAPD of 16.5% and 19.2% for d along with 12.4% and 14.1% for f, in the case of NLLS and NLLS*, respectively. NNLS pre-fitting did not yield any benefits when considering the MAPD. Consequently, the results from NLLS* underperform when compared to those of the standard NLLS algorithm. As seen before, the non-linear methods encounter difficulties in differentiating the intermediate and slow components. This is evident in the significant overlaps between NLLS and NLLS*, particularly when analyzing the distribution plots. Notably, both rigid non-linear methods poorly fit the intermediate diffusion component, as indicated by the MAPD exceeding 20% for both the diffusion component and the volume fraction. For NNLS-based evaluations, on the other hand, the fast component poses the most challenges, with the highest MAPD within each parameter group reaching 25 for standard NNLS. Remarkably, NNLS$_{AUC}$ was the only method to achieve a total average deviation of less than 10%.

4. Discussion

4.1. Parameter Variations

In the present study, the NLLS and NNLS multi-exponential fitting methods were evaluated in multi-parametric simulations utilizing synthetic renal diffusion signal data. Advanced fitting algorithms based on NLLS and NNLS were implemented, and several fitting parameters were varied in order to identify the optimal parameter sets to attain the highest accuracy for the description of the renal DWI signal decay.

In existing studies, the extent of a sufficient SNR value has already been analyzed by varying the SNR with different magnitudes [13,25]. It has been found that an SNR of at least 100 is required in order to obtain reliable diffusion parameter estimates [25]. Nevertheless, a comprehensive exploration of the range of expected SNR values for in vivo DWI images is still absent. This study specifically emphasized SNR values common for DWI. As expected, a higher SNR generally results in higher output accuracy for all approaches. The NNLS

algorithms, particularly the advanced $NNLS_{AUC}$, provided more consistent results when applied to low SNR signal data. The non-linear fitting techniques exhibited limitations at SNR values below 130 and encountered difficulties with respect to the distinction of all three compartments, a phenomenon which might be due to the lack of optimal starting values for NLLS fitting. Optimization of the starting values for NLLS could improve the fitting outcomes, but this would require extensive prior work to determine the optimal parameters for individual patients, rendering it impractical for in vivo applications. NNLS methods also demonstrated less derivation at all SNR levels and proved to be the superior fitting algorithm for the SNR interval commonly encountered in routine practice.

Despite the effort to standardize DWI imaging in the kidney [26], an optimal distribution of b-values has not been established yet. Focusing on the commonly used and widely accepted b-value range of 0 to 750 s/mm^2, and considering the limitations of scan time in clinical routine, a set of 16 b-values were employed based on the findings of previous studies [10,11,13,26]. This study compared multiple b-value compositions and evaluated the impact of different distributions on fitting accuracy. Considering that low b-values are crucial for a correct and stable fit [27], and that an increased number of b-values below 100 s/mm^2 has been proved to be beneficial for fitting [10], the spacing was adjusted accordingly. Variation in b-value distributions showed superior performance with respect to the standard logarithmic composition across all different fitting approaches. The non-linear methods were greatly affected by an altered arrangement of the b-values. The equidistant distribution, in particular, compromised the fitting and parameter estimation significantly. The NNLS algorithms consistently provided stable results throughout all b-value compositions. It should further be noted that the reliability of the interval distribution may be questionable in real-world scenarios where various physiological conditions or pathologies can cause the appearance, disappearance, or shifting of different diffusion regimes within the diffusion spectrum. The study confirmed that it is crucial to cover the full b-value range, with particular attention devoted to smaller values correlating with fast diffusion motions in order to adequately represent the diffusion parameters and enable accurate fitting.

Varying the number of logarithmically spaced diffusion coefficients M for fitting in NNLS has a profound impact on the estimation of fitting parameters. When M is set to low values, similar to a very low sample rate, the ability to reliably determine the most accurate estimates is compromised. However, a very high number for M also results in divergent parameters. The choice of M is driven by a compromise between computation time and accuracy. Excessively high sample rates not only result in very long computation times, but also lead to an increased number of misinterpreted peaks in the signal data (Figure 2). If many logarithmically spaced diffusion coefficients are applied, detected regularized peaks might be split into multiple peaks. In this study, the optimal range was identified to be between 300 and 400 coefficients, with 350 providing the most accurate results for NNLS fitting techniques without a significant increase in computation time. Therefore, only in vivo data with 16 b-values in the specified standard range were considered in this study.

Furthermore, the selection of the diffusion fitting range has a significant effect on the results obtained by non-negative fitting approaches. This is a common challenge encountered in the field of multi-exponential fitting. While seeking reproducible results, it is important to avoid the expansion of the fitting range to prevent distortion of the fitting estimates. This represents a challenging task when the correct diffusion parameters of the kidney tissue are not apparent before fitting. In the current study, the $NNLS_{AUC}$ approach achieved more accurate results compared to the standard NNLS method. Among the tested diffusion ranges, neither the shortened nor the expanded intervals provided any improvements over the standard range, which spans from $D_{min} = 0.7 \times 10^{-3}$ mm^2/s to $D_{max} = 300 \times 10^{-3}$ mm^2/s.

The benefits of NNLS with varying numbers of diffusion components were not explored in this study, as Periquito et al. [13] conducted a complementary simulation approach. The study extensively investigated the impact of a varying number of diffusion components caused by pathologies such as hyperfiltration, fibrosis, and cysts. In these cases, the NNLS

algorithm was found to be superior to NLLS, as it is able to detect a fourth pathological compartment and reliably distinguish different levels of fibrosis.

4.2. Comparison of Fitting Methods

By applying optimized parameters (Table 3), the differences among the evaluated fitting algorithms become more apparent. The NNLS approaches outperformed the non-linear methods, especially owing to improved accuracy and smaller variability of the results, even though NNLS was found to incorrectly identify peaks occasionally (see Figure 2), resulting in a false fourth component that introduces bias into the results. Misfitted fourth compartments also contribute to the poor performance of NLLS*. Following the NNLS pre-fit process, the NLLS fitting was unable to effectively handle four compartments when based on a model incorporating only three diffusion coefficients, resulting in significant inaccuracies in those instances. To minimize the occurrence of misidentified compartments, further optimization is required, such as enhancement of the b-value distribution and range [13] or improvement of the quality of the acquired signal. The SNR variation demonstrates that applying NNLS to high quality signals mitigates the issue of scattering, with close to none misinterpreted signals. Thus, ensuring high signal quality for in vivo imaging, either through optimized sequence parameters or an increased number of averages, is particularly advantageous for non-negative fitting. The $NNLS_{AUC}$ method partially compensates for this limitation of the standard NNLS algorithm, including its poor performance at low SNR values, by re-evaluating the misfitted fourth compartment. This weighting approach yielded optimal results in this study. The utilization of NNLS fitting algorithms appears to be the most suitable approach for analyzing in vivo renal DWI signals. Furthermore, simulation results from this study demonstrate a significant improvement in accuracy with $NNLS_{AUC}$ as a novel fitting approach, especially when dealing with noisy image data.

Table 3. Recommended parameters for non-negative fitting.

SNR	M	D_{min}	D_{max}	b-Value Distribution
140	350	0.7×10^{-3} mm^2/s	300×10^{-3} mm^2/s	[0, 5, 10, 20, 30, 40, 50, 75, 100, 150, 200, 250, 300, 400, 525, 750]

4.3. Limitations and Outlook

It is important to note that one disadvantage of NNLS is the increased computational effort it requires. Depending on the choice of M, fitting with the NNLS algorithm takes up to 2 s per iteration. In contrast, the rigid NLLS fit is approximately 100 times faster. This discrepancy may originate from the MATLAB implementation and could potentially be addressed by employing faster programming languages and advanced implementations of the fitting algorithms. Further improvement of the code through the implementation of parallelization techniques is highly desirable to improve the computation time problem.

Bi-level optimization, as used in NLLS*, offers encouraging opportunities, but it also has limitations that need to be considered. Firstly, sensitivity to initial estimates and the risk of overfitting. While using NNLS estimates as starting points can be advantageous, the final outcome of NLLS* may still be sensitive to these initial values, making reasonably good results of the NNLS fit essential. Furthermore, the second fitting step of NLLS might not be able to improve the results significantly. Combining two fitting methods can also increase the risk of overfitting, especially when the data do not necessarily require such a complex model in the first place. This can lead to misinterpretation of the results. Additional limitations encompass the consequences of the regularization applied within the NNLS algorithm. Although regularization is necessary to enhance fitting results, it comes with miscalculation and distortion of the fitting results [19]. Given the symmetric nature of the fittings and the presence of multiple global minima, the fitting results for regularized NNLS just as NLLS may be prone to spurious minima that may not always be apparent.

Despite compensation by the high number of iterations or fitted pixels, these misfitted data points can still distort the accuracy of the outcome.

DWI data are sensitive to arbitrary diffusion processes and flowing fluids, beyond the mere presence of blood. This issue poses a challenge in the event of indiscriminate adoption of simulation parameters and may impact the quality of the fit [27]. Consequently, minor parameter adjustments may be necessary to translate the results into in vivo applications. Finally, the segmentation of the diffusion intervals for AUC calculations could potentially be adapted to accommodate other scenarios, as certain studies have assumed slightly different diffusion distributions [11,25]. The mentioned limitations, particularly their application to in vivo imaging and related adaptations, should be addressed in future studies.

The scope of this work is limited to basic least-squares approaches, not covering recent advancements in the bi-exponential IVIM model analysis which may result in improvements to multi-exponential fitting [28–30]. The application of Bayesian, neural network, and deep learning methodologies could potentially increase accuracy by identifying the distinct different diffusion components, particularly in the instance of low SNR [31]. However, these approaches have not yet been successfully tested in tri-exponential modelling. Additionally, extensive data groups are required to train neural networks, presenting a challenge to the implementation of this method due to the potential significant variances in individual patients' diffusion parameters.

5. Conclusions

To conclude, this simulation study demonstrates the advantages of free NNLS algorithms for multi-exponential fitting of renal DWI data. Modelling without an inherent number of diffusion components as in NLLS enables the reliable determination of the actual underlying diffusion compartments in the investigated tissue. NNLS provides the distribution of diffusion parameters and is less prone to inaccuracies than NLLS when compared to ground truth values.

Parameter estimates obtained through the bi-level $NNLS_{AUC}$ approach, coupled with additional area-under-curve weighting, yield further improved results and exhibit the greatest agreement with the ground truth values of this study compared to other methods. Therefore, a set of standard parameters for NNLS has been identified as a recommendation to ensure a more stable fit and reliable results for microstructural analysis of renal DWI data using multi-exponential signal analysis. The optimized fitting parameters were applied in a final systematic simulation which demonstrated the advanced accuracy of NNLS. Nevertheless, further studies are required to evaluate in vivo adaptation and assess the performance of the presented method applied to the diverse diffusion properties of human kidneys. This, especially, includes its ability to distinguish physiological and pathophysiological renal tissue, as well as its accuracy in detecting additional diffusion compartments resulting from pathologies which is of great relevance to clinical application.

Author Contributions: Conceptualization, J.J. and A.L.; methodology, J.J., A.L., H.-J.W., R.Z. and B.V.; software, J.J.; validation, J.J., A.L., B.V., R.Z. and H.-J.W.; formal analysis, all; investigation, all; resources, T.A.T. and A.L.; data curation, J.J.; writing—original draft preparation, J.J.; writing—review and editing, A.L. and T.A.T.; visualization, J.J. and T.A.T.; supervision, A.L., H.-J.W. and G.A.; project administration, A.L., G.A. and J.J.; funding acquisition, A.L. All authors have read and agreed to the published version of the manuscript.

Funding: This research received no external funding.

Data Availability Statement: The dataset is available from the corresponding author upon reasonable request.

Acknowledgments: The author of this work, Jonas Jasse, received a doctoral grant from the Jürgen-Manchot-Stiftung. A.L. was supported by an internal research grant of the local Research Committee of the Medical Faculty of Heinrich-Heine-University Düsseldorf (2020-65).

Conflicts of Interest: The authors declare no conflicts of interest.

Abbreviations

AUC	Area-Under-Curve
DWI	Diffusion-weighted Imaging
gT	Ground Truth
IVIM	Intra-voxel Incoherent Motion
MAPD	Median Absolute Percentage Deviation
NLLS	Non-Linear Least-Squares
NLLS*	Approach combining both NLLS and subsequent NNLS fitting
NNLS	Non-Negative Least-Squares
$NNLS_{AUC}$	Approach adding AUC constraint after NNLS fitting
SNR	Signal-to-Noise Ratio

Appendix A

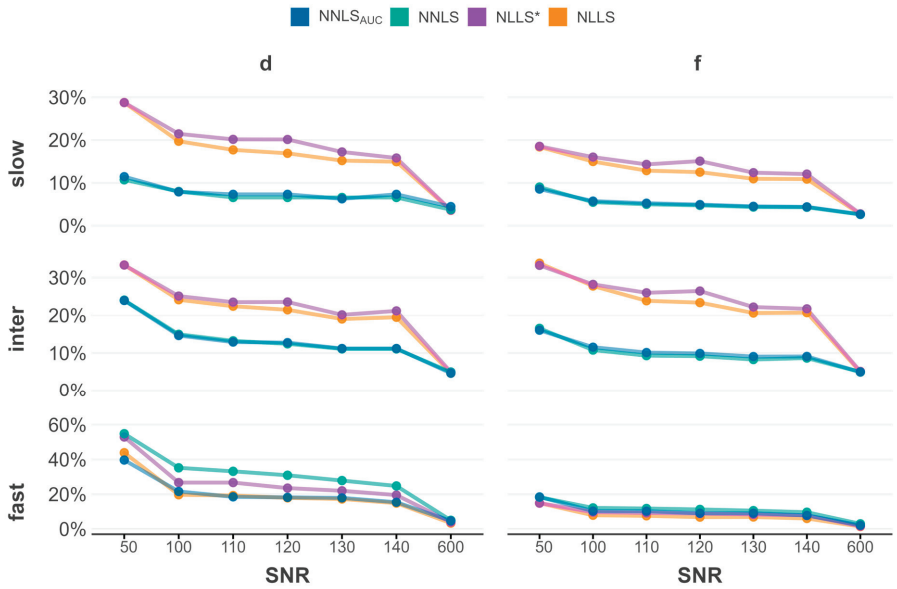

Figure A1. MAPD trend for diffusion coefficients d and volume fractions f as a function of the SNR.

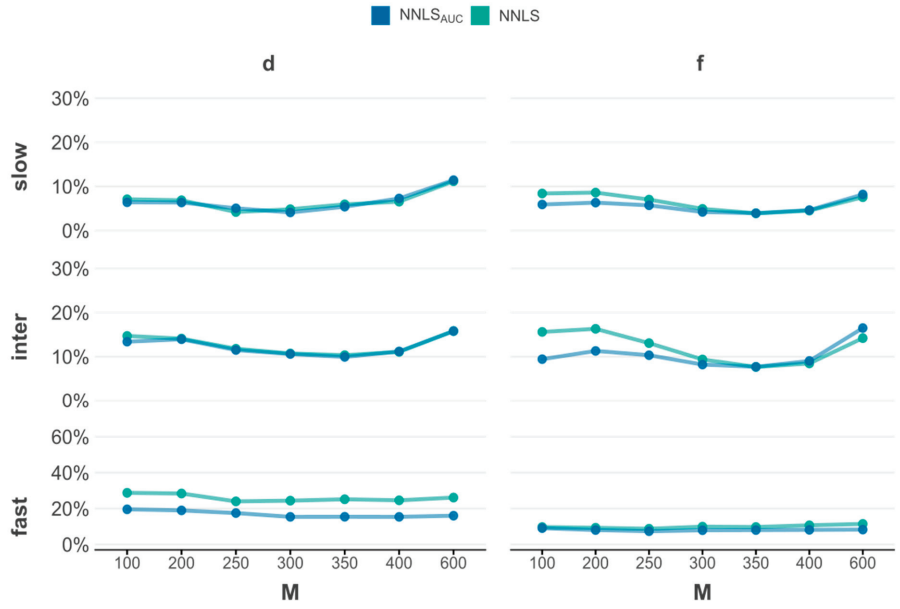

Figure A2. MAPD trend for diffusion coefficients d and volume fractions f as a function of *M*.

Table A1. MAPD for a static simulation (n = 1000) with optimal simulation parameters [in %].

Method	d_{slow}	d_{inter}	d_{fast}	Avg	f_{slow}	f_{inter}	f_{fast}	Avg	Total
$NNLS_{AUC}$	6.7	9.9	16.2	10.9	3.8	7.5	7.9	6.4	8.65
NNLS	6.4	10.3	25.0	13.9	3.9	7.6	9.9	7.1	10.50
NLLS*	15.7	22.4	19.5	19.2	12.3	22.1	8.0	14.1	16.65
NLLS	13.9	20.3	15.4	16.5	10.7	20.0	6.4	12.4	14.45

References

1. Caroli, A. Diffusion-Weighted Magnetic Resonance Imaging: Clinical Potential and Applications. *J. Clin. Med.* **2022**, *11*, 3339. [CrossRef]
2. Le Bihan, D.; Turner, R.; Douek, P.; Patronas, N. Diffusion MR imaging: Clinical applications. *AJR Am. J. Roentgenol.* **1992**, *159*, 591–599. [CrossRef] [PubMed]
3. Thoeny, H.C.; De Keyzer, F.; Oyen, R.H.; Peeters, R.R. Diffusion-weighted MR imaging of kidneys in healthy volunteers and patients with parenchymal diseases: Initial experience. *Radiology* **2005**, *235*, 911–917. [CrossRef]
4. Woo, S.; Suh, C.H.; Kim, S.Y.; Cho, J.Y.; Kim, S.H. Diagnostic Performance of DWI for Differentiating High- From Low-Grade Clear Cell Renal Cell Carcinoma: A Systematic Review and Meta-Analysis. *AJR Am. J. Roentgenol.* **2017**, *209*, W374–W381. [CrossRef] [PubMed]
5. Le Bihan, D.; Breton, E.; Lallemand, D.; Aubin, M.L.; Vignaud, J.; Laval-Jeantet, M. Separation of diffusion and perfusion in intravoxel incoherent motion MR imaging. *Radiology* **1988**, *168*, 497–505. [CrossRef] [PubMed]
6. MacKay, A.; Laule, C.; Vavasour, I.; Bjarnason, T.; Kolind, S.; Madler, B. Insights into brain microstructure from the T2 distribution. *Magn. Reson. Imaging* **2006**, *24*, 515–525. [CrossRef] [PubMed]
7. Cercueil, J.P.; Petit, J.M.; Nougaret, S.; Soyer, P.; Fohlen, A.; Pierredon-Foulongne, M.A.; Schembri, V.; Delhom, E.; Schmidt, S.; Denys, A.; et al. Intravoxel incoherent motion diffusion-weighted imaging in the liver: Comparison of mono-, bi- and tri-exponential modelling at 3.0-T. *Eur. Radiol.* **2015**, *25*, 1541–1550. [CrossRef]
8. Wurnig, M.C.; Germann, M.; Boss, A. Is there evidence for more than two diffusion components in abdominal organs?—A magnetic resonance imaging study in healthy volunteers. *NMR Biomed.* **2018**, *31*, e3852. [CrossRef]
9. van Baalen, S.; Leemans, A.; Dik, P.; Lilien, M.R.; Ten Haken, B.; Froeling, M. Intravoxel incoherent motion modeling in the kidneys: Comparison of mono-, bi-, and triexponential fit. *J. Magn. Reson. Imaging* **2017**, *46*, 228–239. [CrossRef]
10. Chevallier, O.; Wang, Y.X.J.; Guillen, K.; Pellegrinelli, J.; Cercueil, J.P.; Loffroy, R. Evidence of Tri-Exponential Decay for Liver Intravoxel Incoherent Motion MRI: A Review of Published Results and Limitations. *Diagnostics* **2021**, *11*, 379. [CrossRef]
11. Stabinska, J.; Ljimani, A.; Zollner, H.J.; Wilken, E.; Benkert, T.; Limberg, J.; Esposito, I.; Antoch, G.; Wittsack, H.J. Spectral diffusion analysis of kidney intravoxel incoherent motion MRI in healthy volunteers and patients with renal pathologies. *Magn. Reson. Med.* **2021**, *85*, 3085–3095. [CrossRef] [PubMed]
12. Marquardt, D.W. An Algorithm for Least-Squares Estimation of Nonlinear Parameters. *J. Soc. Ind. Appl. Math.* **1963**, *11*, 431–441. [CrossRef]
13. Periquito, J.; Gladytz, T.; Millward, J.; Ramos Delgado, P.; Cantow, K.; Grosenick, D.; Hummel, L.; Anger, A.; Zhao, K.; Seeliger, E.; et al. Continuous diffusion spectrum computation for diffusion-weighted magnetic resonance imaging of the kidney tubule system. *Quant. Imaging Med. Surg.* **2021**, *11*, 3098–3119. [CrossRef] [PubMed]
14. Lawson, C.L.; Hanson, R.J. *Solving Least Squares Problems*; Society for Industrial and Applied Mathematics: Philadelphia, PA, USA, 1995. [CrossRef]
15. Whittall, K.P.; MacKay, A.L. Quantitative interpretation of NMR relaxation data. *J. Magn. Reson. (1969)* **1989**, *84*, 134–152. [CrossRef]
16. van der Bel, R.; Gurney-Champion, O.J.; Froeling, M.; Stroes, E.S.G.; Nederveen, A.J.; Krediet, C.T.P. A tri-exponential model for intravoxel incoherent motion analysis of the human kidney: In silico and during pharmacological renal perfusion modulation. *Eur. J. Radiol.* **2017**, *91*, 168–174. [CrossRef]
17. Sorensen, D.C. Newton's Method with a Model Trust Region Modification. *SIAM J. Numer. Anal.* **1982**, *19*, 409–426. [CrossRef]
18. Bjarnason, T.A.; Mitchell, J.R. AnalyzeNNLS: Magnetic resonance multiexponential decay image analysis. *J. Magn. Reson.* **2010**, *206*, 200–204. [CrossRef]
19. Wiggermann, V.; Vavasour, I.M.; Kolind, S.H.; MacKay, A.L.; Helms, G.; Rauscher, A. Non-negative least squares computation for in vivo myelin mapping using simulated multi-echo spin-echo T(2) decay data. *NMR Biomed.* **2020**, *33*, e4277. [CrossRef]
20. Park, H.J.; Sung, Y.S.; Lee, S.S.; Lee, Y.; Cheong, H.; Kim, Y.J.; Lee, M.G. Intravoxel incoherent motion diffusion-weighted MRI of the abdomen: The effect of fitting algorithms on the accuracy and reliability of the parameters. *J. Magn. Reson. Imaging* **2017**, *45*, 1637–1647. [CrossRef]
21. Stabinska, J.; Zollner, H.J.; Thiel, T.A.; Wittsack, H.J.; Ljimani, A. Image downsampling expedited adaptive least-squares (IDEAL) fitting improves intravoxel incoherent motion (IVIM) analysis in the human kidney. *Magn. Reson. Med.* **2023**, *89*, 1055–1067. [CrossRef]

22. Kong, H.; Wang, C.; Gao, F.; Zhang, X.; Yang, M.; Yang, L.; Wang, X.; Zhang, J. Early assessment of acute kidney injury using targeted field of view diffusion-weighted imaging: An in vivo study. *Magn. Reson. Imaging* **2019**, *57*, 1–7. [CrossRef]
23. Zhang, G.; Sun, H.; Qian, T.; An, J.; Shi, B.; Zhou, H.; Liu, Y.; Peng, X.; Liu, Y.; Chen, L.; et al. Diffusion-weighted imaging of the kidney: Comparison between simultaneous multi-slice and integrated slice-by-slice shimming echo planar sequence. *Clin. Radiol.* **2019**, *74*, 325.e1–325.e8. [CrossRef]
24. While, P.T. A comparative simulation study of bayesian fitting approaches to intravoxel incoherent motion modeling in diffusion-weighted MRI. *Magn. Reson. Med.* **2017**, *78*, 2373–2387. [CrossRef]
25. De Luca, A.; Leemans, A.; Bertoldo, A.; Arrigoni, F.; Froeling, M. A robust deconvolution method to disentangle multiple water pools in diffusion MRI. *NMR Biomed.* **2018**, *31*, e3965. [CrossRef]
26. Ljimani, A.; Caroli, A.; Laustsen, C.; Francis, S.; Mendichovszky, I.A.; Bane, O.; Nery, F.; Sharma, K.; Pohlmann, A.; Dekkers, I.A.; et al. Consensus-based technical recommendations for clinical translation of renal diffusion-weighted MRI. *Magn. Reson. Mater. Phys. Biol. Med.* **2020**, *33*, 177–195. [CrossRef]
27. Le Bihan, D. What can we see with IVIM MRI? *Neuroimage* **2019**, *187*, 56–67. [CrossRef]
28. Gurney-Champion, O.J.; Klaassen, R.; Froeling, M.; Barbieri, S.; Stoker, J.; Engelbrecht, M.R.W.; Wilmink, J.W.; Besselink, M.G.; Bel, A.; van Laarhoven, H.W.M.; et al. Comparison of six fit algorithms for the intra-voxel incoherent motion model of diffusion-weighted magnetic resonance imaging data of pancreatic cancer patients. *PLoS ONE* **2018**, *13*, e0194590. [CrossRef] [PubMed]
29. Kaandorp, M.P.T.; Barbieri, S.; Klaassen, R.; van Laarhoven, H.W.M.; Crezee, H.; While, P.T.; Nederveen, A.J.; Gurney-Champion, O.J. Improved unsupervised physics-informed deep learning for intravoxel incoherent motion modeling and evaluation in pancreatic cancer patients. *Magn. Reson. Med.* **2021**, *86*, 2250–2265. [CrossRef] [PubMed]
30. Vidic, I.; Jerome, N.P.; Bathen, T.F.; Goa, P.E.; While, P.T. Accuracy of breast cancer lesion classification using intravoxel incoherent motion diffusion-weighted imaging is improved by the inclusion of global or local prior knowledge with bayesian methods. *J. Magn. Reson. Imaging* **2019**, *50*, 1478–1488. [CrossRef]
31. Vasylechko, S.D.; Warfield, S.K.; Afacan, O.; Kurugol, S. Self-supervised IVIM DWI parameter estimation with a physics based forward model. *Magn. Reson. Med.* **2022**, *87*, 904–914. [CrossRef] [PubMed]

mathematics

MDPI

Article

A Mathematical Perspective on the Influence of Allee Effects in Oncolytic Virotherapy

Eymard Hernández-López [1,2,*] and Jin Wang [1,*]

[1] Department of Mathematics, University of Tennessee at Chattanooga, Chattanooga, TN 37403, USA
[2] Postgraduate and Research, TecNM-TESOEM, Estado de México 56400, Mexico
* Correspondence: eymard-hernandezlopez@utc.edu (E.H.-L.); jin-wang02@utc.edu (J.W.)

Abstract: This article is concerned with the mathematical modeling of cancer virotherapy, emphasizing the impact of Allee effects on tumor cell growth. We propose a modeling framework that describes the complex interaction between tumor cells and oncolytic viruses. The efficacy of this therapy against cancer is mathematically investigated. The analysis involves linear and logistic growth scenarios coupled with different Allee effects, including weak, strong, and hyper Allee forms. Critical points are identified, and their existence and stability are analyzed using dynamical system theories and bifurcation techniques. Also, bifurcation diagrams and numerical simulations are utilized to verify and extend analytical results. It is observed that Allee effects significantly influence the stability of the system and the conditions necessary for tumor control and eradication.

Keywords: dynamical systems; tumor eradication; virotherapy; bifurcation diagrams; Hopf bifurcation; logistic growth; allee effects

MSC: 92-10; 34D20; 34C23

1. Introduction

Virotherapy, an emerging strategy in cancer treatment, uses oncolytic viruses to infect and destroy tumor cells while sparing healthy tissues. With the ability to cause tumor destruction through cancer-selective viruses based on various genetic mechanisms and delivery techniques, this therapeutic approach has gained attention as a promising complement or alternative to conventional treatment strategies such as chemotherapy and radiation therapy. However, there are several challenges currently associated with virotherapy that may limit its application in cancer treatment [1–4]. In particular, the interaction between oncolytic viruses and cancer cells within the tumor microenvironment is not well understood at present.

Tumor cells exhibit complex growth patterns inside the human body that may involve linear and nonlinear dynamics. Meanwhile, the Allee effect, a phenomenon observed initially in ecology that describes how populations of macroorganisms [5–8] or microorganisms [9,10] exhibit reduced growth rates at low densities, also potentially plays a crucial role in cancer development [11–13]. Like populations in ecosystems, the Allee effect in tumor cells suggests that cell cooperation is key to their growth and cancer proliferation at low densities. Understanding this mechanism would help in proposing new approaches to disrupt cell communication and cooperation by preventing the critical population from growing efficiently. In this sense, tumor cells have limited growth due to a lack of sufficient autocrine signals, as there is evidence of dependence on the concentration of autocrine growth factors produced by themselves [14–17]. Growth factors may be platelet-derived

growth factor PDGF. Normal cells need to receive signals from their environment to grow; however, tumor cells may produce both ligands and receptors, thus creating an autocrine loop [18].

Several studies have noted that the Allee effect may also influence cancer recurrence after treatment, pointing out that they can proliferate even at this stage, reaching their critical density more quickly. This may be due to the ability of tumor cells to manipulate their environment through autocrine cycling or as in the process of secretion of tumor TAF Angiogenesis Factor, which eventually activates endothelial cells to obtain nutrients through mini-vascularizations; this angiogenesis phenomenon could increase the capacity of tumor growth rates [19]. Given that normal cells have a different growth rate compared to cancer cells [20,21], understanding the cooperative behavior of cancer cells, similar to the Allee effect in tumor recurrence, could contribute to the design of therapies, in this case by modulating endothelial cell migration, anti-angiogenesis treatment in tumors, or anti-autocrine treatments [22–25].

Such complex tumor cell growth dynamics, coupled with the spread and replication of oncolytic viruses and the host–virus interaction, will directly impact the outcome of virotherapy. Mathematical modeling offers a powerful theoretical tool to understand the rich dynamics involved in tumor virotherapy, allowing a meaningful prediction of the efficacy of treatment and the optimization of key parameters [2,4,26–32]. Cancer modeling and simulation have advanced rapidly over the last few decades, showing a strong potential to quantify tumor dynamics and guide therapeutic development in oncology, including in diagnosis, treatment, and tumor management. In particular, the development of mathematical models allows the exploration of complex cellular–viral dynamics and the evaluation of fundamental strategies to control tumor growth through viral infection [31,33–37]. This research area may integrate mathematical biology with promising clinical applications, utilizing concepts and modeling techniques from other fields such as epidemiology (for viral infection) and ecology (for population growth and Allee effects) [7,38,39]. Recent modeling studies, for example, have combined differential equations and stochastic rules to capture the interactions between tumor cells, oncolytic viruses, and immune responses [40,41]. Furthermore, incorporating Allee effects into oncology models could demonstrate how population thresholds affect tumor stability and dynamic transitions and allow the exploration of different scenarios in virotherapy towards tumor eradication.

The present paper proposes a theoretical framework based on ordinary differential equations that incorporates multiple types of Allee effects (weak, strong, and hyper) and different patterns of tumor cell growth dynamics (linear and logistic). We plan to investigate the various scenarios involved in tumor–virus interactions thoroughly. The models representing these different scenarios are analyzed from the perspective of bifurcations, allowing the identification of critical conditions for the stability of equilibrium points and the occurrence of periodic oscillations. This study could provide quantitative tools to guide therapeutic design in controlling tumor growth by viruses.

This paper is organized as follows. Section 2 presents the general modeling framework. Sections 3 and 4 analyze linear and logistic growth patterns, respectively, each coupled with multiple types of Allee effects. Section 5 is devoted to bifurcation diagrams and numerical simulation results, followed by a discussion in Section 6. Finally, conclusions are drawn in Section 7.

2. Base Model

We propose a modeling framework that describes the interaction between normal tumor cells (denoted by T), infected tumor cells (denoted by I), and virions (denoted by V). These variables capture the key dynamics of the system, which aims to model the use of

oncolytic viruses as an antitumor therapy with the goal of promoting tumor eradication in the patient.

In the following, we present a set of differential equations that describe these interactions between tumor cells and viruses, while incorporating fundamental parameters related to cancer dynamics and therapeutic effects of the viruses.

$$\begin{aligned} T' &= \lambda g(T)A(T,\alpha,\omega) - \beta TV, \\ I' &= \beta TV - \mu I, \\ V' &= pI - \delta V, \end{aligned} \tag{1}$$

where the parameter λ is the rate at which new tumor cells are generated, β is the cell-virus contact rate, μ is the lysis rate of infected tumor cells, p is the viral replication rate, and δ is the viral removal rate. The function $g(T)$ represents the growth of the tumor cell population, which will include linear and logistic growth patterns in our study. Meanwhile, the function $A(T,\alpha,\omega)$ represents the Allee effects, where we will discuss the weak, strong, and hyper Allee effects separately. The initial conditions of the system (1) are $T(0) \geq 0$, $I(0) \geq 0$, and $V(0) \geq 0$.

In the analysis presented below, we will discuss different forms of the functions $g(T)$ and $A(T,\alpha,\omega)$ that will represent the coupling of various growth dynamics and Allee effects. Specifically, we will analyze the linear growth model in Section 3 and the logistic growth model in Section 4. We will pay more attention to the logistic growth dynamics, which may be more realistic than the linear growth in that a carrying capacity for the tumor cells is incorporated. The analytic work will provide a foundation for the comparison in Section 5 concerning bifurcation diagrams and numerical continuation results. Figure 1 summarizes the functional forms of the growth dynamics and Allee effects analyzed in this work, as well as their connections to the bifurcation diagrams in Section 5. Furthermore, we emphasize that the Allee effects discussed throughout this paper will take various types and will be interpreted in a broad sense [11].

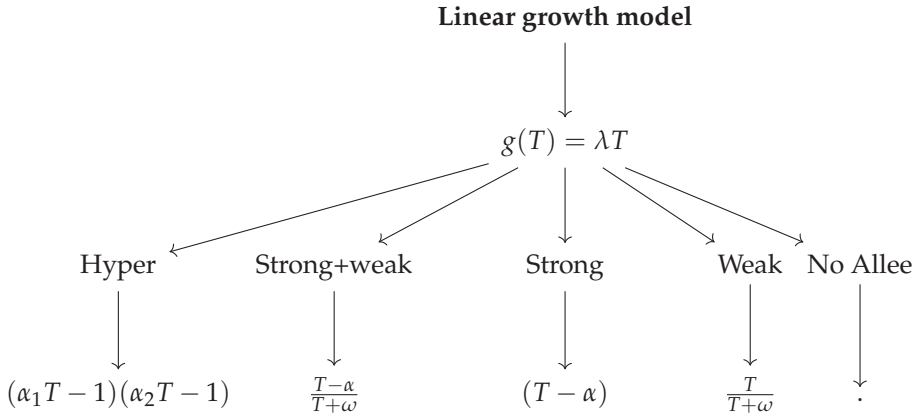

Figure 1. *Cont.*

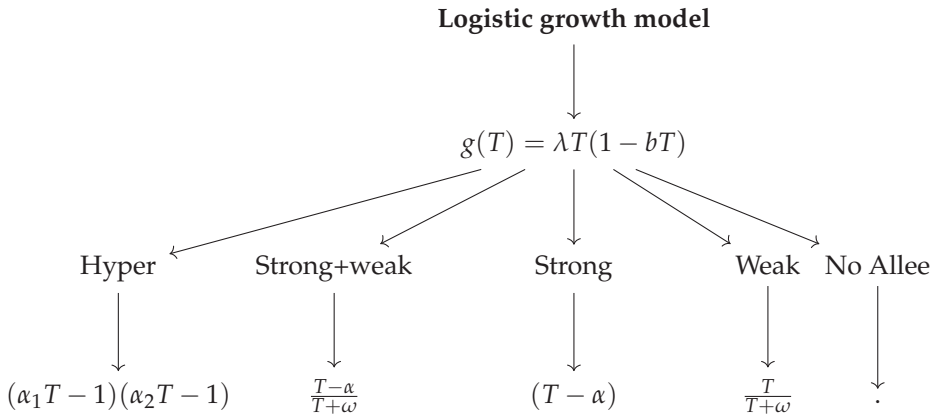

Figure 1. Functional forms of the Allee effect, with references to the corresponding bifurcation diagrams.

3. Linear Growth Model

3.1. Linear Growth with Weak and Strong Allee Effects

We examine a scenario that includes both Allee effects, as the sole consideration of the strong Allee effect produces dynamics similar to those observed when both effects are included simultaneously. This similarity is clearly illustrated in the bifurcation diagrams presented in Section 5.

So, we will consider the following system.

$$\begin{aligned} T' &= \lambda T A(T, \alpha, \omega) - \beta T V, \\ I' &= \beta T V - \mu I, \\ V' &= pI - \delta V, \end{aligned} \tag{2}$$

where the term $A(T, \alpha, \omega) = (T - \alpha)/(T + \omega)$ represents the weak and strong Allee effects simultaneously. Note that the case with weak Allee effect recovers when $\alpha = 0$. If we calculate the critical points, we obtain the trivial one $(0, 0, 0)$, the free disease critical point for the strong Allee effect α, $P_{l\alpha} = (\alpha, 0, 0)$, and the endemic point given by

$$P_{le_2} = \left(\frac{\delta\mu}{p\beta}, \frac{\delta^2\lambda(\delta\mu - p\alpha\beta)}{p\beta(\delta\mu + p\beta\omega)}, \frac{\lambda(\delta\mu - p\alpha\beta)}{p\beta(\delta\mu + p\beta\omega)} \right).$$

To evaluate the ability of a disease to spread within a population, it is essential to determine the basic reproductive number, R_α. This parameter represents the average number of secondary cases an infection will generate during its infectious stage in a fully susceptible population. In models that incorporate the Allee effect, especially when a strong Allee effect is considered, the disease dynamics may present different behaviors compared to traditional models without this effect and even with a weak Allee effect.

By calculating the critical points of the system with the weak and strong Allee effect simultaneously, we have identified the critical point $(\alpha, 0, 0)$, where α denotes the level of the strong Allee effect. This critical point is particularly interesting as it represents an equilibrium in the system where population dynamics and disease spread interact significantly [42]. This point suggests specific conditions under which the tumor cell population infected by the virus can stabilize or extinguish.

Next, we will calculate the term R_α for this model, considering the level of the Allee effect defined by α. This calculation will allow us to analyze the stability of the critical point and better understand how the Allee effect influences the virus's ability to be sustained in the tumor cell population. Using the next-generation matrix method [43], we obtain

$$F = \begin{pmatrix} 0 & \alpha\beta \\ p & 0 \end{pmatrix}, \qquad V = \begin{pmatrix} \mu & 0 \\ 0 & \delta \end{pmatrix}$$

and the basic reproductive number of the virus for system (2) for the strong Allee effect is given by

$$R_\alpha = \rho(FV^{-1}) = \sqrt{\frac{p\alpha\beta}{\delta\mu}}, \tag{3}$$

or

$$R_\alpha^2 = \frac{p\alpha\beta}{\delta\mu}.$$

Note: In the base system (1), the basic reproductive number R_α corresponds to $R_{T*} = \frac{\beta p T^*}{\mu\delta}$, depending on the first component of the critical point T^*. Suppose that the basic virus reproduction number R_{T^*} is less than 1 at the beginning of the infection. In that case, each virus-infected cancer cell produces, on average, fewer than one new infected cancer cell. Therefore, viral infection cannot spread within the cancer cell population, and the tumor returns to an uninfected state, leading to tumor persistence and eventual proliferation. However, if the basic reproduction number R_{T^*} is greater than 1, at the beginning of the infection, each cancer cell infected by the virus produces, on average, more than one new infected cancer cell. The basic reproduction number is directly proportional to the level of the Allee effect, indicating that a higher Allee effect leads to a higher reproduction number, and consequently a more significant number of infected cancer cells, which would reduce the overall cancer cell population.

If we use this number at the endemic critical point P_{le_2} we find that

$$P_{le_2} = \left(\frac{\alpha}{R_\alpha^2}, -\frac{\left(R_\alpha^2 - 1\right)\alpha^2\lambda}{R_\alpha^4\mu(\alpha + R_\alpha^2\omega)}, -\frac{\left(R_\alpha^2 - 1\right)\alpha^3\lambda}{R_\alpha^2\beta(\alpha + R_\alpha^2\omega)} \right), \tag{4}$$

where the condition of existence is $0 < R_\alpha^2 < 1$.

Once we have incorporated the strong and weak Allee effects in the system and determined the basic reproduction number R_α based on the disease-free critical point using the parameter α associated with the strong Allee effect, we proceed to analyze the behavior at the endemic point. In particular, we will explore a stability change by analyzing the Hopf bifurcation. The strong Allee effect α implies the existence of a minimum population threshold necessary to avoid extinction, while the weak Allee effect ω suggests that individual growth rate increases with population density without necessarily requiring a critical threshold.

In this analysis, we illustrate the conditions under which a Hopf bifurcation occurs in such a base system, with different Allee effects and, in this case, the linear population growth term. Subsequently, we will consider the logistic growth case. Also, this analysis will allow a better understanding of the transitions between steady state and oscillatory dynamics, providing a more complete picture of how Allee's effects affect the stability and variability of the cancer cell populations in the system. By identifying these critical points, we seek to establish the key parameters that facilitate the emergence of sustained population cycles. This is fundamental for designing therapeutic strategies for considering virus-mediated tumor cell infection as an alternative to conventional treatments, which are also affected by Allee effects.

Theorem 1. *Consider the system given by (2). The following set*

$$H = \left\{ (\lambda, \varsigma_{l_{WS_1}}, \varsigma_{l_{WS_2}}, R_\alpha^2) \mid \varsigma_{l_{WS_1}}\lambda - \varsigma_{l_{WS_2}}^2 = 0 \right\}, \tag{5}$$

contains the symmetric-saddles and Hopf bifurcations in the point P_{le_2} (4), where

$$\begin{array}{rcl} \varsigma_{l_{WS_1}} & = & \alpha(\delta+\mu)(\alpha^2+R_\alpha^6\omega-(\alpha+2)R_\alpha^4\omega+\alpha R_\alpha^2(-\alpha+\omega-1))^2 \\ \varsigma_{l_{WS_2}} & = & R_\alpha^2(\alpha+R_\alpha^2\omega)^2(-\alpha^2(\delta^2+\ \delta\mu+\mu^2)+R_\alpha^6\omega(-(\delta+\mu)^2) \\ & + & R_\alpha^4\omega((\alpha+2)\delta^2+(\alpha+4)\delta\mu+(\alpha+2)\mu^2)+\alpha R_\alpha^2(\delta^2(\alpha-\omega+1) \\ & + & \delta\mu(\alpha-\omega+2)+\mu^2(\alpha-\omega+1))) \end{array} \tag{6}$$

Proof. Taking the endemic point P_{le_2} (4) and evaluating the Jacobian matrix A, in terms of parameters, we can then calculate its characteristic polynomial similar to Equation (7). Associated with A, this is

$$p(\psi) = a_0\psi^3 + a_1\psi^2 + a_2\psi + a_3, \tag{7}$$

in terms of the trace, the sum of all second-order diagonal minors of A are denoted by SimA, and the determinant of the matrix A, where $a_0 = 1$, $a_1 = -TrA$, $a_2 = \text{Sim}A$, and $a_3 = -DetA$. Then, we calculate the parameters a_1, a_2, and a_3. We look for conditions where the $(a_1a_2 - a_3) = 0$ and we obtain the following set of parameters (5). □

Next, we calculate the stability region for the endemic point P_{le_2} (4) in the model (2).

Proposition 1. *Let $0 < R_\alpha^2 < 1$ and $\varsigma_{l_{WS_1}}\lambda < \varsigma_{l_{WS_2}}^2$, and then the endemic critical point P_{le_2} (4) of a system (2) is locally asymptotically stable.*

Proof. According to the Hurwitz stability [44], P_{le_2} (4) should be local asymptotically stable if $a_1, a_2, a_3 > 0$ and $a_1a_2 - a_3 > 0$. First, we calculate the Jacobian matrix of the system evaluated at P_{le_2} (4). From this matrix, we derive the characteristic polynomial and obtain the coefficients of the Hurwitz matrix, denoted as a_1, a_2, and a_3. In this analysis, we consider the symmetric-saddle and Hopf bifurcations, incorporating a parameter ϵ, such that

$$\lambda := \epsilon\frac{\varsigma_{l_{WS_2}}^2}{\varsigma_{l_{WS_1}}}, \tag{8}$$

if we evaluate in $(a_1a_2 - a_3)$, then we find

$$(a_1a_2 - a_3) = \epsilon(\epsilon-1)\frac{\varsigma_{l_{WS_2}}^2}{\varsigma_{l_{WS_1}}}. \tag{9}$$

If $\epsilon = 1$, the we have the Hopf bifurcation, but if $\epsilon > 1$ then $(a_1a_2 - a_3) > 0$ for $a_1, a_2, a_3 > 0$. For all, P_{le_2} (4) is locally asymptotically stable under $0 < R_\alpha^2 < 1$ and $\varsigma_{l_{WS_1}}\lambda < \epsilon\varsigma_{l_{WS_2}}^2$, with $\epsilon > 1$. □

Theorem 1 and Proposition 1 show that for the values of the basic reproduction number $R_\alpha < 1$, the existence of the endemic critical point, the system presents stability and instability; in instability, the population collapses to the trivial critical point, which is stable. On the other hand, stability may be associated with some level of cancer cells or with a cycle of co-existence through the Hopf bifurcation. Figures 2 and 3, shows this behavior, where the blue curve represents the projection of the hypersurface of Hopf bifurcations (5), by fixing the parameter values and varying the basic number reproductive term R_α.

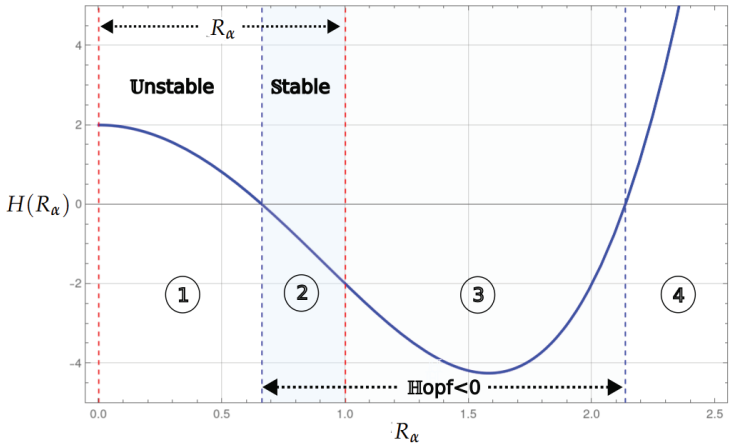

Figure 2. The bifurcation diagram corresponds to the model with linear growth and a strong Allee effect. The blue curve represents a projection of the Hopf hyperparametric set as a function of R_α.

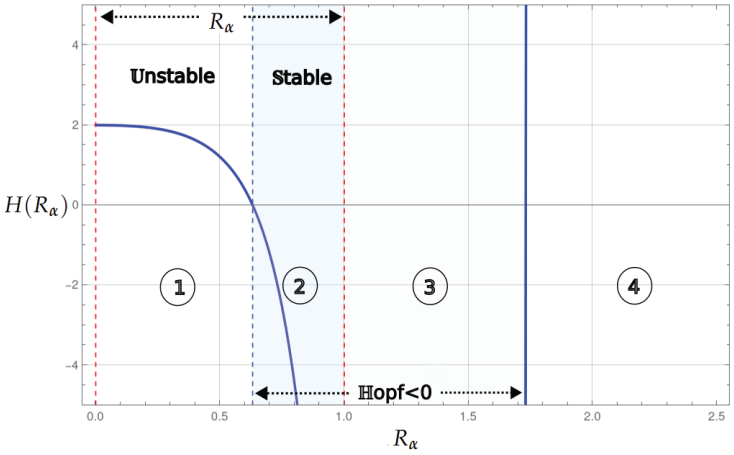

Figure 3. The bifurcation diagram corresponds to the model with linear growth and both weak and strong Allee effects (2). The blue curve represents a projection of the Hopf hyperparametric set (5) as a function of R_α.

3.2. Linear Growth with Hyper Allee Effect

In the last part of this section, we address the case of the hyper Allee effect model in a linear growth context see Figure 4. The Allee effect, which describes a positive relationship between population density and growth rate, is fundamental to understanding complex dynamics such as virus-infected tumor cells. By integrating a hyper Allee effect into a linear growth model, we analyze the conditions that lead to endemic point stability. Let

$$\begin{aligned} T' &= \lambda TA(T,\alpha_1,\alpha_2) - \beta TV, \\ I' &= \beta TV - \mu I, \\ V' &= pI - \delta V, \end{aligned} \tag{10}$$

where the term $A(T,\alpha_1,\alpha_2) = (\alpha_1 T - 1)(\alpha_2 T - 1)$ represents the hyper Allee effect, with $\alpha_1 < \alpha_2$. If we calculate the critical points, then we have the trivial $(0,0,0)$, two critical points for free disease $(1/\alpha_1, 0, 0)$, $(1/\alpha_2, 0, 0)$, and one endemic critical point

$$P_{le_H} = \left(\frac{\delta\mu}{p\beta}, \frac{\delta^2\lambda\mu(p\beta - \alpha_1\delta\mu)(p\beta - \alpha_2\delta\mu)}{p^4\beta^4}, \frac{\delta\lambda\mu(p\beta - \alpha_1\delta\mu)(p\beta - \alpha_2\delta\mu)}{p^3\beta^4} \right).$$

Analogously to the calculation of R_α (3) thought R_{T*}, we perform the calculation for infection-free points $(1/\alpha_1, 0, 0)$ and $(1/\alpha_2, 0, 0)$, and we obtain

$$\begin{aligned} R^2_{l\alpha_1} &= \frac{p\beta}{\alpha_1 \delta \mu} \\ R^2_{l\alpha_2} &= \frac{p\beta}{\alpha_2 \delta \mu} \end{aligned} \tag{11}$$

These points are now inversely related to the Allee hyper effect values α_1 and α_2. Here, we use the general structure of the basic reproduction number R_{T^*} as the infectious threshold R_{l0}. If we take the following combination of parameters $R^2_{l0} = \frac{p\beta}{\delta\mu}$, then $R_{l\alpha_1} > R_{l\alpha_2}$, with $R^2_{l\alpha_1} = R^2_{l0}(1/\alpha_1)$ and $R^2_{l\alpha_2} = R^2_{l0}(1/\alpha_2)$. Then we have the critical point P_{le_H} as

$$P_{le_H} = \left(\frac{1}{R^2_{l0}}, \frac{(R^2_{l0} - \alpha_1)(R^2_{l0} - \alpha_2)\lambda}{R^6_{l0}\mu}, \frac{(R^2_{l0} - \alpha_1)(R^2_{l0} - \alpha_2)\lambda}{R^4_{l0}\beta} \right), \tag{12}$$

the existence conditions are $0 < R_{l0} < \sqrt{\alpha_1}$ or $R_{l0} > \sqrt{\alpha_2}$. We will now study the Hopf bifurcation in this case.

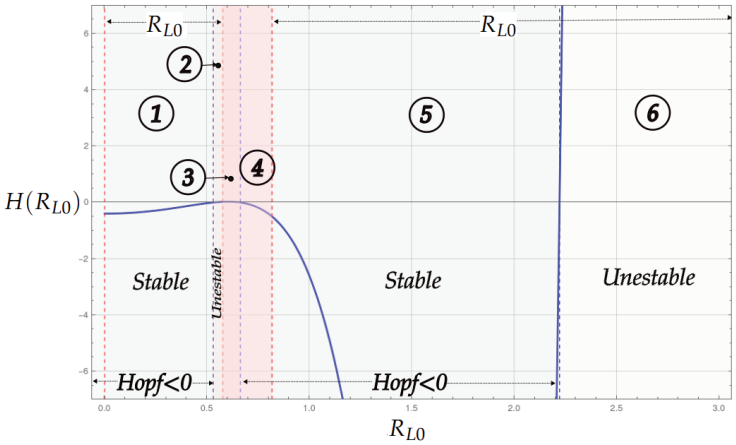

Figure 4. The bifurcation diagram corresponds to the model with linear growth and a hyper Allee effect (10). The blue curve represents a projection of the Hopf hyperparametric set (13) as a function of R_α.

Theorem 2. *Consider the system (10). The following set*

$$H_H = \left\{ (\lambda, \varsigma_{l_{H_1}}, \varsigma_{l_{H_2}}, R^2_{l0}) \mid \varsigma_{l_{H_1}} \lambda - \varsigma^2_{l_{H_2}} = 0 \right\}, \tag{13}$$

contains the symmetric-saddles and Hopf bifurcations in the point P_{le_H} (12), where

$$\begin{aligned} \varsigma_{l_{H_1}} &= (\delta + \mu)\left(R^2_{l0}(\alpha_1 + \alpha_2) - 2\alpha_1\alpha_2\right)^2 \\ \varsigma_{l_{H_2}} &= R^8_{l0}\delta\mu + R^4_{l0}\alpha_1\alpha_2(2\delta + \mu)(\delta + 2\mu) \\ &- R^6_{l0}(\alpha_1 + \alpha_2)(\delta^2 + 3\delta\mu + \mu^2) \\ R^2_{l0} &\neq \tfrac{2\alpha_1\alpha_2}{(\alpha_1 + \alpha_2)} \end{aligned} \tag{14}$$

Proof. Taking the endemic point P_{le_H} (12) and evaluating the Jacobian matrix A, in terms of parameters, then we calculate its characteristic polynomial similar to Equation (7), and we calculate the parameters a_1, a_2, and a_3 as in the Hurwitz matrix H. We obtain the set of parameters (13), when looking for conditions where $(a_1 a_2 - a_3) = 0$. □

Proposition 2. *Let* $0 < R_{l0}^2 < \alpha_1$ *or* $R_{l0}^2 > \alpha_2$ *and* $\varsigma_{l_{H_1}}\lambda < \varsigma_{l_{H_2}}^2$, *and then the endemic critical point* P_{le_H} *(12) of a system (10), is locally asymptotically stable.*

Proof. Following the proof of the weak and strong Allee case, using the Hopf bifurcation set and a parameter ϵ, we obtain the coefficients of the Hurwitz matrix, denoted as a_1, a_2, and a_3. Also, we considers the symmetric-saddle and Hopf bifurcations from (13), such that

$$\lambda := \epsilon \frac{\varsigma_{l_{H_2}}^2}{\varsigma_{l_{H_1}}}, \tag{15}$$

if we evaluate in $(a_1a_2 - a_3)$, then we obtain

$$(a_1a_2 - a_3) = \epsilon(\epsilon - 1)\frac{\varsigma_{l_{H_2}}^2}{\varsigma_{l_{H_1}}}. \tag{16}$$

The critical point P_{le_2} (12) is locally asymptotically stable under $0 < R_{l0}^2 < \alpha_1$ or $R_{l0}^2 > \alpha_2$ and $\varsigma_{l_{H_1}}\lambda < \epsilon\varsigma_{l_{H_2}}^2$, with $\epsilon > 1$. □

Theorem 2 and Proposition 2 analyze the case in which the endemic critical point is stable, and its existence is divided into two regions depending on R_{l0}. If $R_{l0} < \sqrt{\alpha_1}$, the endemic critical point can be stable or unstable. Stability occurs at a certain level of infected cancer cells or through limit cycles caused by the presence of a Hopf bifurcation. In the case where $R_{l0} > \sqrt{\alpha_2}$, the region of stability and instability is determined by the Hopf bifurcation, where, in a neighborhood, infected tumor cells coexist in a limit cycle. The bifurcation diagram shows larger instability regions for $R_{l0} > \sqrt{\alpha_2}$. This suggests a higher number of infected cancer cells and, eventually, tumor shrinkage in the presence of a high hyper Allee value α_2.

This section examined the linear population growth model incorporating weak, strong, and weak with their combinations and hyper Allee effects. This analysis shows how these effects significantly influence population dynamics and stability of virus-infected tumor cells. The bifurcation diagrams presented in Section 5 illustrate the different cases and critical points that emerge under different configurations of the Allee effect parameters. The following section will review the logistic growth case and explore how the Allee effects affect this model, which will allow us to compare the dynamics obtained under different population growth assumptions, enriching our understanding of the conditions that favor stability and, if so, its eventual application in the effective control of tumor populations.

4. Logistic Growth Model

This section will consider the base model (1) with logistic growth. Following the approach of the previous Section 3, we analyze only representative cases of the model dynamics. For example, in that section, we examined the model with linear growth under the weak Allee effect since its dynamics do not show significant differences compared to the case without such an effect. Similarly, the case of the model that simultaneously includes weak and strong Allee effects is similar to the case where only a strong Allee effect is considered. To verify these observations, one can perform the corresponding calculations or consult the associated typical diagrams, as shown in Section 5 on bifurcation diagrams.

4.1. Logistic Growth Without Allee Effect

In order to enrich our analysis and explore the dynamics of the base system (1) more fully, we added the logistic growth model. This model incorporates the carrying capacity and is a way to model the systems more realistically compared to linear growth, where an

unbounded population is considered, which allows us to study the population dynamics of tumor cells under a limited number that depends on each patient, in this case not including the Allee effect in conjunction with this carrying capacity because we want to see the dynamic without the Allee effect. In the following, we present the system and the parameters for its analysis.

$$\begin{aligned} T' &= \lambda T(1-bT) - \beta TV, \\ I' &= \beta TV - \mu I, \\ V' &= pI - \delta V \end{aligned} \tag{17}$$

where b represents the carrying capacity of the system, that is, the maximum limit of the tumor population. If we calculate the critical points here, we obtain the trivial one $(0,0,0)$, the disease-free equilibrium point $P_0 = (T_0, I_0, V_0) = (\frac{1}{b}, 0, 0)$, and the endemic point

$$P_{ge} = \left(\frac{\delta\mu}{p\beta}, \frac{\delta\lambda(p\beta - b\delta\mu)}{(p\beta)^2}, \frac{\lambda(p\beta - b\delta\mu)}{p\beta^2} \right). \tag{18}$$

As in system (1), system (17) is equivalent to those of an SEIR epidemiological model with the assumption of a constant population size. This equivalence implies that the dynamics of these systems are also similar, and results known for the SEIR model can be straightforwardly extended to the branch of the system of (1) like the basic reproductive number, similar to that founded in R_α in the previous section. The basic reproductive number R_0 is the expected number of secondary cases produced in a susceptible population by a typical ineffective individual when the tumor cell is infectious. In this model (17), R_0 denotes the average number of new tumor cells infected by a virion during its lifetime when placed in a population of fully susceptible tumor cells.

As for $R_{T^*}\,|_{T^*=\frac{1}{b}}$ or R_α (3), using the next-generation matrix method by [43], we obtain

$$R_0^2 = \frac{p\beta}{b\delta\mu}, \tag{19}$$

If the virus's basic reproductive number is smaller than 1, then at the beginning of the infection, each virus-infected tumor cell produces, on average, less than one newly infected tumor cell. Therefore, the infection cannot spread and the system returns to an uninfected state. If $R_0 > 1$, then initially each virus-infected tumor cell produces, on average, more than one newly infected cell.

Taking into account the endemic equilibrium point P_{ge} and the basic reproductive number (19), we represent the state in which the virus is present as

$$\begin{aligned} T_{ge} &= \frac{1}{bR_0^2}, \\ I_{ge} &= (R_0^2 - 1)\frac{\lambda}{b\mu R_0^4}, \\ V_{ge} &= (R_0^2 - 1)\frac{\lambda}{\beta R_0^2}. \end{aligned}$$

The conditions of existence of this point are given by $1 < R_0^2$. On the other hand, the stability of the critical point free of infection $P_0 = (\frac{1}{b}, 0, 0)$ is as follows.

Proposition 3. *For the critical point P_0,*

1. *If $R_0 < 1$, then the three eigenvalues are real and negative.*
2. *If $R_0 = 1$, then two eigenvalues are real and negative, and one equals zero.*

3. *if $R_0 > 1$, then two eigenvalues are real and negative and one is real and positive.*

Proof. First, we take the linearization of the system at P_0 as

$$A_0 = \begin{pmatrix} -\lambda & 0 & -\frac{\beta}{b} \\ 0 & -\mu & \frac{\beta}{b} \\ 0 & p & -\delta \end{pmatrix}$$

The characteristic polynomial is

$$\begin{aligned} 0 &= \begin{vmatrix} (-\lambda-\chi) & 0 & -\frac{\beta}{b} \\ 0 & -(\mu+\chi) & \frac{\beta}{b} \\ 0 & p & -(\delta+\chi) \end{vmatrix} \\ &= -(\lambda+\chi)\left((\mu+\chi)(\delta+\chi) - \frac{p\beta}{b}\right) \\ &= -(\lambda+\chi)\left(\chi^2 + (\delta+\mu)\chi + \delta\mu - \frac{p\beta}{b}\right) \end{aligned} \tag{20}$$

The second factor can be expressed as

$$\begin{aligned} Q &= \chi^2 + (\delta+\mu)\chi + \delta\mu - \frac{p\beta}{b} \\ &= \chi^2 + (\delta+\mu)\chi + \delta\mu\left(1 - \frac{p\beta}{\delta\mu b}\right) \\ &= \chi^2 + (\delta+\mu)\chi + \delta\mu\left(1 - R_0^2\right) \end{aligned}$$

Then, the roots are

$$\chi = \frac{1}{2}\left(-(\delta+\mu) \pm \sqrt{(\delta+\mu)^2 - 4(1-R_0^2)\delta\mu}\right) \tag{21}$$

The equivalent expressions for the discriminant are

$$\begin{aligned} \Delta &= (\delta+\mu)^2 - 4(1-R_0^2)\delta\mu \\ &= \delta^2 + 2\delta\mu + \mu^2 - 4\delta\mu\left(1 - R_0^2\right) \\ &= (\delta-\mu)^2 + 4R_0^2\delta\mu \end{aligned}$$

Since the discriminant $\Delta > 0$, for any $R_0 > 0$ and positive parameters $\delta, \mu > 0$, all roots are real. For $R_0 < 1$, the discrimimant $\Delta < (\delta+\mu)^2$; therefore, both roots are negative for and $b\alpha < 1$. If $R_0 > 1$, then $\Delta > (\kappa+\delta)^2$ and one of the roots in (21) is positive. □

In the following result, we will analyze the Hopf bifurcations set as a function of admissible parameters of the system (17) at the critical point P_{ge} (18).

Theorem 3. *Consider the system of autonomous equations that model the dynamics of the tumor cell population, given by (17). The following set*

$$H = \left\{(\lambda, \Phi_{01}, \Phi_{02}, R_0^2) \mid \Phi_{01}\lambda - \Phi_{02}^2 = 0\right\}, \tag{22}$$

contains the symmetric-saddles and Hopf bifurcations in the point P_{ge}, where

$$\begin{aligned} \Phi_{01} &= (\delta+\mu) \\ \Phi_{02} &= \left((\delta^2+\mu^2)-\left(R_0^2-3\right)\delta\mu\right)R_0^2. \end{aligned} \tag{23}$$

Proof. Taking the endemic point P_{ge} and evaluating in the Jacobian matrix A, we calculate its characteristic polynomial, to calculate the coefficients of Hurwitz matrix as follows:

$$\begin{aligned} a_1 &= (\delta+\mu)+\frac{\lambda}{R_0^2} \\ a_2 &= (\delta+\mu)\frac{\lambda}{R_0^2} \\ a_3 &= (R_0^2-1)\frac{\delta\lambda\mu}{R_0^2} \end{aligned}$$

All coefficients are positive for $R_0^2 > 1$. By finding the condition for $(a_1a_2 - a_3) = 0$, we obtain the set of parameters (22). □

The Hopf bifurcation represents a transition to stability in the system. This bifurcation occurs when we move one key parameter and obtain a pair of complex conjugate eigenvalues, which can be the basic reproductive number R_0^2. If we take (7), with conditions $a_0 = 1$ and $a_1 \cdot a_2 = a_3$, then we obtain one real eigenvalue given by $\psi = -a_1$ and two conjugate complexes of eigenvalues $\psi = \pm i\sqrt{a_2}$, with $a_2 > 0$. When a_2 is the change in sing, then complex conjugate eigenvalues cross the imaginary axis and appear in the Hopf bifurcation; in this case, the change in sing is given by (22), and if $a_2 < 0$, then we have the symmetric-saddles.

These eigenvalues show a transition in the system's dynamics, in which the solutions change from unstable to oscillatory behavior; under small perturbations, the system could deviate from the cycle and move towards a different solution or a higher instability. In Section 5, we present the bifurcation diagram corresponding to the Theorem 3, which graphically illustrates some equilibrium phases in the system (17).

Analyzing the endemic equilibrium point is essential to identify regions in terms of parameters where dynamic behaviors such as stability, periodic oscillations, or critical transitions of sign change points are present. In the following, we present an analysis that characterizes this point.

Proposition 4. *Let $1 < R_0^2$ and $\Phi_{01}\lambda < \Phi_{02}^2$, and then the endemic critical point P_{ge} of the system (17) is locally asymptotically stable.*

Proof. As in the proof of Theorem 3, we calculate the coefficients of characteristic polynomial a_1, a_2, a_3 which are all positive for the existence condition of endemic critical point P_{ge}. Following the stability proof in the previous section, we define the parameter λ in terms of ϵ, but with Φ_{01} and Φ_{02}. If we evaluate in $(a_1a_2 - a_3)$, we have

$$(a_1a_2 - a_3) = (\epsilon - 1)\epsilon\frac{\left(\delta^2+\mu^2-\left(R_0^2-3\right)\delta\mu\right)^2}{\delta+\mu}.$$

Then, for $\epsilon > 1$, we obtain $(a_1a_2 - a_3) > 0$ and the critical point P_{ge} is locally asymptotically stable. □

The summary of the dynamics of the logistic growth case without the Allee effect is presented in the bifurcation diagram in Figure 5. We observed the condition of existence $R_0 > 1$ of the endemic critical point P_{ge} (18) and the Hopf curve, which is a threshold that,

in addition to determining the stability of the critical point, can exhibit limit cycles in a neighborhood of parameters. In instability, a trajectory away from the unstable endemic equilibrium may tend to the trivial stable critical point, indicating the collapse of the system, or to the stable variety of the infection-free saddle point $P_0 = (1/b, 0, 0)$, indicating the propagation of cancer cells.

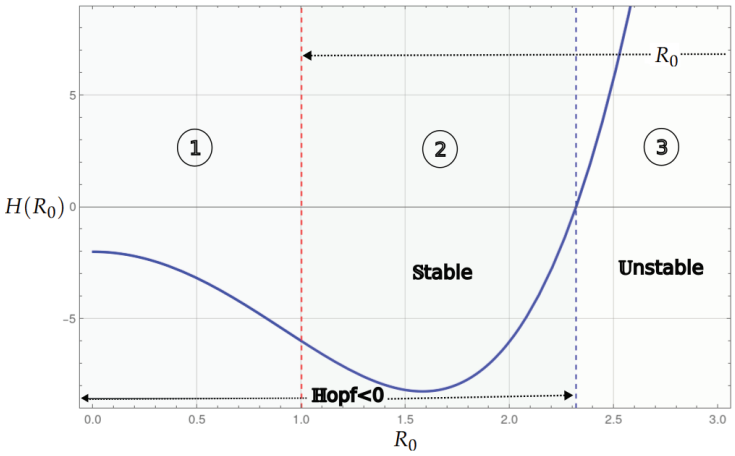

Figure 5. The bifurcation diagram corresponds to the model with logistic growth and no Allee effect (17). The blue curve represents a projection of the Hopf hyperparametric set (22) as a function of R_0.

4.2. Logistic Growth with Strong Allee Effect

This model incorporates the strong Allee effect parameter α. We present the system for its analysis in the following.

$$\begin{aligned} T' &= \lambda T(1 - bT)(T - \alpha) - \beta TV, \\ I' &= \beta TV - \mu I, \\ V' &= pI - \delta V \end{aligned} \tag{24}$$

where b represents the carrying capacity of the system, and α represents the strong Allee effect, which describes the decrease in population growth rate when tumor cell density is below a critical threshold, where we want to explore its influence on the dynamics of the system. If we calculate the critical points here, we obtain the trivial one $(0, 0, 0)$, the disease-free equilibrium point $P_{0s} = (\frac{1}{b}, 0, 0)$ in terms of the braking capacity, the disease-free equilibrium point $P_\alpha = (\alpha, 0, 0)$ in terms of the strong Allee effect, and the endemic point

$$P_{gse} = \left(\frac{\delta\mu}{p\beta}, -\frac{\delta\lambda(p\alpha\beta - \delta\mu)(p\beta - b\delta\mu)}{(p\beta)^3}, -\frac{\delta\lambda(p\alpha\beta - \delta\mu)(p\beta - b\delta\mu)}{p^2\beta 3} \right).$$

If we substitute the basic reproductive number R_0^2, from (19), because it is the same in the system (24), we obtain

$$P_{gse} = \left(\frac{1}{bR_0^2}, -(R_0^2 - 1)(\alpha b R_0^2 - 1)\frac{\lambda}{b^2\mu R_0^6}, -(R_0^2 - 1)(\alpha b R_0^2 - 1)\frac{\lambda}{b\beta R_0^4} \right),$$

in terms of R_0. Considering the critical point $P_\alpha = (\alpha, 0, 0)$, we also introduce the term R_α from (3) to represent the critical point P_{gse} as a function of the two basic reproduction numbers, R_0 and R_α, as follows.

$$P_{gse} = \left(\frac{1}{bR_0^2}, -(R_0^2 - 1)(R_\alpha^2 - 1)\frac{\lambda}{b^2\mu R_0^6}, -(R_0^2 - 1)(R_\alpha^2 - 1)\frac{\lambda}{b\beta R_0^4} \right). \tag{25}$$

The conditions of existence of this point are given by $R_\alpha^2 < 1 < R_0^2$. We observe that the basic reproductive numbers have the following relation

$$R_\alpha^2 = R_0^2 b\alpha. \tag{26}$$

Note that the stability analysis of the disease-free point P_{0s} is analogous to that performed in the previous system. However, the associated characteristic polynomial presents a modified expression, which is detailed below.

$$A_0 = \begin{pmatrix} \left(\alpha - \frac{1}{b}\right)\lambda & 0 & -\frac{\beta}{b} \\ 0 & -\mu & \frac{\beta}{b} \\ 0 & p & -\delta \end{pmatrix}$$

The characteristic polynomial is

$$\begin{aligned} 0 &= \begin{vmatrix} \left(\left(\alpha - \frac{1}{b}\right)\lambda - \chi\right) & 0 & -\frac{\beta}{b} \\ 0 & -(\mu+\chi) & \frac{\beta}{b} \\ 0 & p\gamma & -(\delta+\chi) \end{vmatrix} \\ &= \left(\left(\alpha - \frac{1}{b}\right)\lambda - \chi\right)\left((\mu+\chi)(\delta+\chi) - \frac{p\beta}{b}\right) \\ &= \left(\left(\alpha - \frac{1}{b}\right)\lambda - \chi\right)\left(\chi^2 + (\delta+\mu)\chi + \delta\mu\left(1 - R_0^2\right)\right) \end{aligned} \tag{27}$$

So, we have a Corollary from Proposition 3.

Corollary 1. *For the critical point P_0,*

1. *If $R_0 < 1$, then the three eigenvalues are real and negative.*
2. *If $R_0 = 1$, then two eigenvalues are real and negative, and one equals zero.*
3. *if $R_0 > 1$, then two eigenvalues are real and negative and one is real and positive.*

In the following result, we will analyze the Hopf bifurcations set as a function of admissible parameters of the system (24) at the critical point P_{gse} (25).

Theorem 4. *Consider the system given by (24). The following set*

$$H = \left\{(\lambda, \Phi_{s1}, \Phi_{s2}, R_0^2) \mid \Phi_{s1}\lambda - \Phi_{s2}^2 = 0\right\}, \tag{28}$$

contains the symmetric-saddles and Hopf bifurcations in the point P_{gse}, where

$$\begin{aligned} \Phi_{s1} &= \Delta_{R_{0,\alpha}}^2(\delta+\mu) \\ \Phi_{s2} &= \delta\mu\left(R_0^2\left(\alpha b\left(R_0^2-3\right)-3\right)+5\right) - \Delta_{R_{0,\alpha}}\left(\delta^2+\mu^2\right) \\ \Delta_{R_{0,\alpha}} &:= R_0^2(1+\alpha b) - 2. \end{aligned} \tag{29}$$

Proof. Take the endemic point P_{gse} and evaluate the Jacobian matrix A to look for conditions where the (TrA Sim$A$) minus the determinant $DetA$ are zero. Using the resulting polynomials Pol_0 as in [45,46], we obtain the set of parameters (28). □

The predicted result confirms the existence of a Hopf bifurcation in the system (24). This result indicates the emergence of periodic orbits near the analyzed equilibrium point, which introduces oscillatory dynamics into the model. Next, we explore the stability of the equilibrium point, which will allow us to identify the conditions under which stability exists.

Proposition 5. *Let* $1 < R_0^2 < 2/(1+b\alpha)$ *and* $\Phi_{s1}\lambda < \Phi_{s2}^2$, *and then the endemic critical point* P_{gse} *of a system (24) is locally asymptotically stable.*

Proof. The linearization of the system (24) at P_{gse} is given by

$$A_1 = \begin{pmatrix} \frac{\lambda\left(\left(R_0^2-1\right)+\left(R_\alpha^2-1\right)\right)}{bR_0^4} & 0 & -\frac{\beta}{bR_0^2} \\ -\frac{\lambda\left(R_0^2-1\right)\left(R_\alpha^2-1\right)}{bR_0^4} & -\mu & \frac{\beta}{bR_0^2} \\ 0 & p & -\delta \end{pmatrix}$$

The characteristic polynomial associated with A_1 is

$$p(\psi) = a_0\psi^3 + a_1\psi^2 + a_2\psi + a_3, \tag{30}$$

in terms of the trace, the sum of all second-order diagonal minors of A_1 denoted by SimA_1, and the determinant of the matrix A_1, where $a_0 = 1$, $a_1 = -TrA_1$, $a_2 = \mathrm{Sim}A_1$, and $a_3 = -DetA_1$. Specifically

$$\begin{aligned} a_0 &= 1, \\ a_1 &= (\delta+\mu) - \lambda\frac{\left(R_0^2-1\right)+\left(R_\alpha^2-1\right)}{bR_0^4}, \\ a_2 &= -\lambda(\delta+\mu)\frac{\left(R_0^2-1\right)+\left(R_\alpha^2-1\right)}{bR_0^4}, \\ a_3 &= (\lambda\delta\mu)\frac{\left(R_0^2-1\right)\left(1-R_\alpha^2\right)}{bR_0^4}. \end{aligned}$$

The Hurwitz matrix associated with $p(\psi)$ is given by

$$H(p) = \begin{pmatrix} a_1 & a_3 & 0 \\ a_0 & a_2 & 0 \\ 0 & a_1 & a_3 \end{pmatrix}$$

according to the Hurwitz stability [44], P_{gse} is locally asymptotically stable if $a_1, a_2, a_3 > 0$ and $a_1a_2 - a_3 > 0$. Under the conditions of the existence of the endemic point P_{gse}, $R_\alpha^2 < 1 < R_0^2$ or equivalently $1 < R_0^2 < 1/(b\alpha)$. It follows that

$$\begin{aligned} \Delta_{R_{0,\alpha}} &:= (R_0^2-1) + (R_\alpha^2-1) \\ &= R_0^2(1+b\alpha) - 2 < 0, \\ \text{or} \quad & 1 < R_0^2 < \frac{2}{1+b\alpha}. \end{aligned}$$

So $a_1 > 0$ with $1 < R_0^2 < 2/(1+b\alpha)$ or when $R_0^2 \geq 2/(1+b\alpha)$ with $(\delta+\mu) > \lambda\Delta_{R_{0,\alpha}}$. Also, the coefficient a_2 is positive with $1 < R_0^2 < 2/(1+b\alpha)$. It holds that $a_3 > 0$ for $R_\alpha^2 < 1 < R_0^2$ or equivalently $1 < R_0^2 < 1/(b\alpha)$. As we can see,

$$-(\delta+\mu)\Delta_{R_{0,\alpha}}\left((\delta+\mu) - \frac{\lambda\Delta_{R_{0,\alpha}}}{bR_0^2}\right) > 0,$$

in $1 < R_0^2 < 2/(1+b\alpha)$ and

$$\left(R_0^2-1\right)\left(1-R_\alpha^2\right) > 0,$$

in $1 < R_0^2 < 1/(b\alpha)$, then

$$\left[-(\delta+\mu)\Delta_{R_{0,\alpha}}\left((\delta+\mu)-\frac{\lambda\Delta_{R_{0,\alpha}}}{bR_0^2}\right)+\left(R_0^2-1\right)\left(1-R_\alpha^2\right)\delta\mu\right]>0,$$

for $1 < R_0^2 < 2/(1+b\alpha)$. Which implies that $a_1a_2 - a_3 > 0$. On the other hand, taking (28) we have

$$\lambda = \epsilon\frac{\Phi_{s2}^2}{\Phi_{s1}},$$

with $\epsilon > 0$ and $\Phi_{s1} > 0$. When we evaluate the last expression in $(a_1a_2 - a_3)$ we obtain

$$(a_1a_2 - a_3) = (\epsilon - 1)\epsilon\frac{\Phi_{s2}^2}{\Phi_{s1}}.$$

In this case, if $\epsilon = 1$, then we have $a_1a_2 - a_3 = 0$, which is equivalent to the Hopf condition, but if $\epsilon > 1$, also, $a_1a_2 - a_3 > 0$. For all, P_{gse} is stable when $1 < R_0^2 < 2/(1+b\alpha)$ and $\lambda\Phi_{s1} < \Phi_{s2}^2$. □

The bifurcation diagram in Figure 6 shows the dynamics when there is logistic growth and a strong Allee effect. The interval of existence of the critical point P_{gse} is determined by the red dotted vertical lines determined by $1 < R_0^2 < 2/(1+b\alpha)$, and in this case the point can be stable or unstable bounded by the Hopf bifurcation (blue curve). There may be endemic equilibrium or latent cancer, and there may also be escape from cancer; in this case, the infection-free point is P_{0s}.

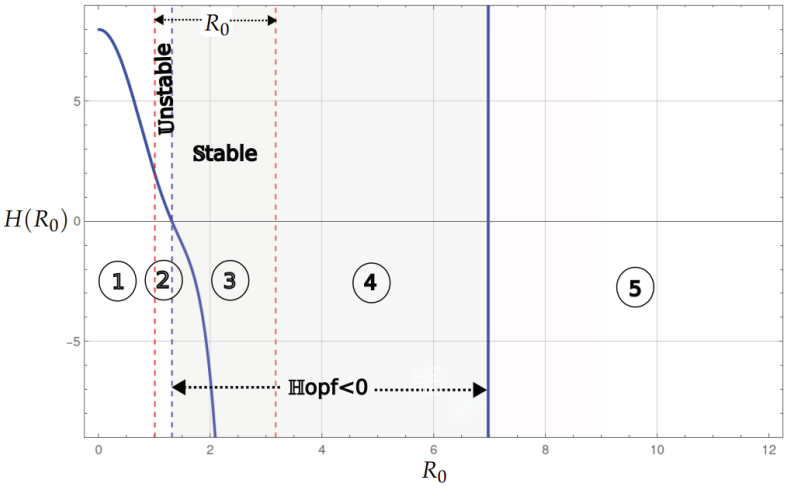

Figure 6. The bifurcation diagram corresponds to the model with logistic growth and strong Allee effect (24). The blue curve represents a projection of the Hopf hyperparametric set (28) as a function of R_0.

4.3. Logistic Growth with Hyper Allee Effect

In this model, the population experiences two thresholds: one below, which tends to extinction, and another above, which again tends to extinction. The growth rate becomes negative at very low population sizes and high population sizes, with a positive growth rate only within a specific intermediate range. We present a mathematical representation

with the hyper Allee effect by modifying the logistic growth model with additional terms that create a region of bi-stability.

$$\begin{aligned} T' &= \lambda T(1-bT)(\alpha_1 T-1)(\alpha_2 T-1)-\beta TV, \\ I' &= \beta TV-\mu I, \\ V' &= pI-\delta V, \end{aligned} \tag{31}$$

where b is the carrying capacity α_1 and α_2 are the two critical threshold with ($b < \alpha_1 < \alpha_2$). The other parameters remain the same as in the base system (1).

As in the previous case with the strong Allee effect, we take the basic reproductive number from (19) for the critical point $(\frac{1}{b},0,0)$. For the critical point $P_{\alpha_1} = (\frac{1}{\alpha_1},0,0)$, we obtain $R_{\alpha_1} = \sqrt{\frac{p\beta}{\alpha_1\delta\mu}}$. In addition to the critical point $P_{\alpha_2} = (\frac{1}{\alpha_2},0,0)$, we obtain $R_{\alpha_2} = \sqrt{\frac{p\beta}{\alpha_2\delta\mu}}$, which are expressions similar to (11). Then,

$$\begin{aligned} R^2_{\alpha_1} &= R^2_0\tfrac{b}{\alpha_1}, \\ R^2_{\alpha_2} &= R^2_0\tfrac{b}{\alpha_2}. \end{aligned} \tag{32}$$

Note that for $b < \alpha_1 < \alpha_2$, then $R^2_{\alpha_2} < R^2_{\alpha_1} < R^2_0$.

In this analysis, we first focus on the stability of the disease-free critical points: $P_b = (1/b,0,0)$, $(1/\alpha_1,0,0)$, and $(1/\alpha_2,0,0)$. These points represent states in which infected tumor cells and virions are absent while infection-free tumor cells remain in equilibrium. While b denotes the system's carrying capacity, the α_1 and α_2 correspond to hyper Allee effects on tumor cell dynamics.

Stability analysis of these points is essential to understand how system parameters, particularly the carrying capacity and Allee effects, influence the eradication or persistence of viral infection. We then performed a linear stability study, evaluating the zero solutions of the characteristic polynomial associated with these points.

Proposition 6. *For the following critical points P_b, P_{α_1}, and P_{α_2}, we have the following.*

1. *If $R_0 < 1$ or $R_{\alpha_2} < 1$, then the three eigenvalues are real negative. If $R_{\alpha_1} < 1$, then two eigenvalues are negative real, and one is positive real.*
2. *If $R_0 = 1$ or $R_{\alpha_2} = 1$, then two eigenvalues are negative real, and one equals zero. If $R_{\alpha_1} = 1$, then one eigenvalue is positive, one negative, and one zero.*
3. *If $R_0 > 1$ or $R_{\alpha_2} > 1$, then two eigenvalues are negative real, and one is positive real. If $R_{\alpha_1} > 1$, then two eigenvalues are real positive and one is real and negative.*

Proof. The discriminant for each point P_0, P_{α_1}, P_{α_2}, with its corresponding third eigenvalue, is as follows.

$$\begin{aligned} \Delta_b &= (\delta-\mu)^2+4R^2_0\delta\mu, \quad -\frac{(b-\alpha_1)(b-\alpha_2)}{b} < 0, \\ \Delta_{\alpha_1} &= (\delta-\mu)^2+4R^2_{\alpha_1}\delta\mu, \quad \frac{(b-\alpha_1)(\alpha_1-\alpha_2)}{\alpha_1^2} > 0, \\ \Delta_{\alpha_2} &= (\delta-\mu)^2+4R^2_{\alpha_2}\delta\mu, \quad \frac{(b-\alpha_2)(\alpha_2-\alpha_1)}{\alpha_1^2} < 0, \end{aligned}$$

with $0 < b < \alpha_1 < \alpha_2$. The analysis is analogous to the proof of Proposition 3. □

After analyzing the stability of disease-free points, we focus on the endemic point, where infected tumor cells and virions coexist in equilibrium with infection-free tumor cells. This critical point is particularly interesting, as its analysis may reveal other dynamic

behaviors such as periodic oscillations through a Hopf bifurcation. The endemic point in the system (31) is $P_{eH} = (T_{eH}, I_{eH}, V_{eH})$, and in particular

$$\begin{aligned} T_{eH} &= \left(\frac{1}{b}\right)\frac{1}{R_0^2}, \\ I_{eH} &= \left(\frac{\lambda}{b\mu}\right)\frac{\left(R_0^2-1\right)\left(R_{\alpha_1}^2-1\right)\left(R_{\alpha_2}^2-1\right)}{R_0^2 R_{\alpha_1}^2 R_{\alpha_2}^2}, \\ V_{eH} &= \left(\frac{\lambda}{\beta}\right)\frac{\left(R_0^2-1\right)\left(R_{\alpha_1}^2-1\right)\left(R_{\alpha_2}^2-1\right)}{R_0^2 R_{\alpha_1}^2 R_{\alpha_2}^2}. \end{aligned} \tag{33}$$

The existence conditions for the point are two main cases $1 < R_0^2 < \alpha_1/b$ or $R_0^2 > \alpha_2/b$.

Following the model approach with a strong Allee effect, we will examine the Hopf bifurcations considering their dependence on the reproductive number (19) and the parameters (32) at the critical point P_{eH} (33).

Theorem 5. *Consider the system (31) and the critical point P_{eH} (33). The following set*

$$H_{Hyper} = \left\{\left(b, \alpha_1, \alpha_2, \delta, , \lambda, \mu, R_0^2, \Phi_1, \Phi_2\right) \mid \lambda\Phi_1 - \Phi_2 = 0\right\}, \tag{34}$$

contains the symmetric-saddles and Hopf bifurcations, with

$$\begin{aligned} \Phi_1 &= (\delta+\mu)(b^2R_0^4 + b(R_0^2-2)R_0^2(\alpha_1+\alpha_2) + \alpha_1\alpha_2(3-2R_0^2))^2 \\ \Phi_2 &= b^2R_0^4(-\delta^2-\mu^2+\delta\mu(R_0^2-3)) - bR_0^2(\alpha_1+\alpha_2)(\delta^2(R_0^2-2) \\ &+ \delta\mu(3R_0^2-5) + \mu^2(R_0^2-2)) + \alpha_1\alpha_2(\delta^2(2R_0^2-3) + \delta\mu(5R_0^2-7) \\ &+ \mu^2(2R_0^2-3))b^2R_0^6. \end{aligned} \tag{35}$$

Proof. Taking the endemic point P_{eH} (33), sufficient conditions are sought for the Hopf bifurcation, and the analysis is analogous to the proof of Theorem 4 to obtain the expression (34). □

Once the existence of a Hopf bifurcation is confirmed, we will analyze the stability of the endemic point and determine the conditions under which it is stable or unstable.

Proposition 7. *Let $1 < R_0^2 < \alpha_1/b$ or $R_0^2 > \alpha_2/b$ be the condition of existence of the endemic critical point P_{eH} (33), and then it is stable, where $\lambda\Phi_1 < \Phi_2^2$ as in (34).*

Proof. By linearizing the system (31) and obtaining the Jacobian matrix A, its characteristic polynomial $P(\psi)_H$, and the coefficients a_{1_H}, a_{2_H}, and a_{3_H} at the point P_{eH} (33) we obtain the following.

$$\begin{aligned} a_{1_H} &= \left(3R_0^2-4\right)R_{\alpha_1}^2R_{\alpha_2}^2\alpha_1\alpha_2\lambda \\ &+ \left(3-2R_0^2\right)bR_0^2R_{\alpha_1}^2R_{\alpha_2}^2(\alpha_1+\alpha_2)\lambda \\ &- \left(\left(R_{\alpha_1}^2\left(1+R_{\alpha_2}^2\right)\right) + \left(R_{\alpha_2}^2-1\right)\right)b^2R_0^4\lambda \\ &- \left(R_{\alpha_1}^2\left(R_{\alpha_2}^2(\delta+\mu)-\lambda\right) - \left(R_{\alpha_2}^2-1\right)\lambda\right)R_0^6b^2. \\ a_{2_H} &= \left(\left(R_0^2-1\right)\left(1-R_{\alpha_1}^2\right) + \left((1-R_0^2)+R_{\alpha_1^2}\right)R_{\alpha_2^2}\right)(\delta+\mu)\lambda \\ &+ \left(4-3R_0^2\right)R_{\alpha_1}^2R_{\alpha_2}\alpha_1\alpha_2(\delta+\mu)\lambda \\ &+ \left(2R_0^2-3\right)R_0^2R_{\alpha_1}^2R_{\alpha_2}b(\alpha_1+\alpha_2)(\delta+\mu)\lambda \\ a_{3_H} &= \left(R_0^2-1\right)\left(R_{\alpha_1}^2-1\right)\left(R_{\alpha_2}^2-1\right)R_0^6b^3\delta\mu. \end{aligned}$$

To prove the stability of P_{eH} (33), we need to check that $\left(a_{1_H}a_{2_H} - a_{3_H}\right)) > 0$. If we use (34), let ϵ such that

$$\lambda = \epsilon\frac{\Phi_2^2}{\Phi_1}, \tag{36}$$

and we obtain

$$\left(a_{1_H}a_{2_H} - a_{3_H}\right) = \epsilon(\epsilon - 1)\frac{\Phi_2^2}{\Phi_1}.$$

If $\epsilon = 0$, then $\lambda = 0$ is not a positive range value. If $\epsilon = 1$, then we recover the set (34) and we have $\left(a_{1_H}a_{2_H} - a_{3_H}\right) = 0$. In the case of $\epsilon > 1$ we have $\left(a_{1_H}a_{2_H} - a_{3_H}\right) > 0$, so P_{eH} (33) is stable when

$$\lambda\Phi_1 = \Phi_2^2 < \epsilon\Phi_2^2,$$

for $1 < R_0^2 < \alpha_1/b$ or $R_0^2 > \alpha_2/b$, and $a_{1H}, a_{2H}, a_{3H} > 0$. □

For the Allee hyper effect, we have two threshold values, which satisfy $b < \alpha_1 < \alpha_2$; there are levels $R_{\alpha_2} < R_{\alpha_1} < R_0$ that largely determine the dynamics of the system with logistic growth. Theorem 5 and Proposition 7 determine the stability of the system, as seen in the bifurcation diagram in Figure 7, for the conditions of existence of the endemic critical point $1 < R_0 < \alpha_1/b$ or $R_0^2 > \alpha_2/b$, indicated by the vertical red dashed lines. In both intervals, one can distinguish between stability and instability through the Hopf bifurcation curve in blue. There are cycles in a neighborhood where the Hopf curve is zero, which determines latency in cancer. In addition, the population can be highly endemic with a high level of R_0, as seen in Region 5 of the bifurcation diagram.

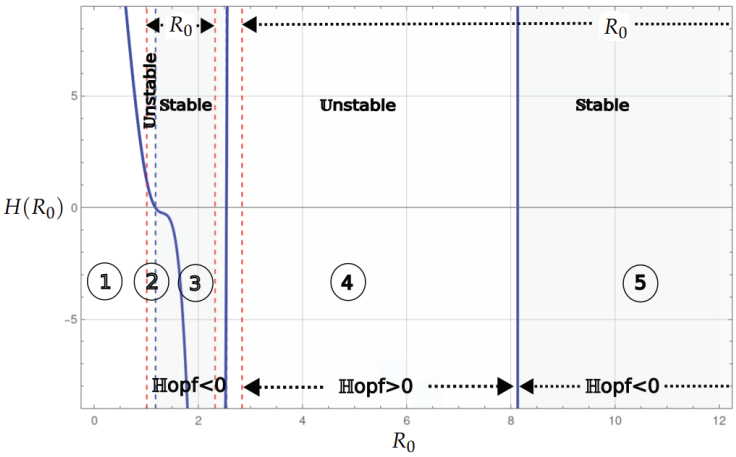

Figure 7. The bifurcation diagram corresponds to the model with logistic growth and the hyper Allee effect (31). The blue curve represents a projection of the Hopf hyperparametric set (34) as a function of R_0.

5. Bifurcation Diagrams and Numerical Results

Using bifurcation diagrams and numerical continuation techniques complements the qualitative analysis of system dynamics. These methods allow us to visualize how the variation of critical parameters, in this case, the basic reproductive numbers, affects the existence and stability of equilibrium points and periodic solutions of the model. The bifurcation diagrams offer a graphical representation of dynamics in the system, such as Hopf bifurcations, which enable us to find some changes in the stability of critical points, providing a global perspective on the behavior of the system. In turn, numerical continuation allows us to trace these solutions over multiple parametric values, facilitating the identification of regions of stability, instability, or complex oscillations.

5.1. Bifurcation Diagrams

In the following, we present the diagrams obtained from the analytical results of the previous two sections.

Figure 2 shows the bifurcation diagram corresponding to the system, which incorporates linear growth with a strong Allee effect. The bifurcation parameter considered is R_α from (3). In the upper part of the diagram, the existence interval of the critical endemic point, defined by $0 < R_\alpha < 1$, is shown, delimited by two dashed red vertical lines. The curve in blue corresponds to the Hopf bifurcation, marking a transition of stability.

The regions identified in the diagram are as follows; Region 1 corresponds to the interval where the endemic point exists but is unstable, and Region 2 represents the interval where the endemic point exists and is stable. Region 3 is associated with the region where the Hopf curve takes negative values; however, the values associated with the endemic critical point are not biologically admissible, while in the last region in the Figure 2, the Hopf curve takes positive values and has no biological interpretation in the model's context.

Figure 3 shows the bifurcation diagram for the case where the model simultaneously considers linear growth with the strong and weak Allee effects. These regions of stability are separated by the blue dashed vertical line, which marks the transition of the Hopf curve from positive to negative values.

Figure 4 shows the bifurcation diagram for the system with linear growth and hyperbolic Allee effects. A prominent feature of this model is the presence of two regions of existence for the endemic point, which are delimited by red-dashed vertical lines. The blue-dashed vertical lines represent the transition of the Hopf curve from positive to negative values. When the Hopf curve is below the horizontal axis, there may be stability at the endemic point. The regions identified in the diagram are as follows: In Region 1, the existence of the endemic point is seen as the Hopf curve is negative, and the endemic point is stable. In Region 2, the Hopf is positive, and then the endemic point is unstable. The endemic point does not exist in Regions 3 and 4. Regions 5 and 6 are stable and unstable.

Figure 5 shows the bifurcation diagram for the logistic growth system without the Allee effect. Region 1 corresponds to the case where the endemic point is absent. Region 2 is the stable region where the endemic point exists, and the values of the Hopf curve are negative. Finally, Region 3 shows the values for R_0 where the endemic point is unstable.

Figure 8, similar to the previous case, shows the bifurcation diagram for the system with logistic growth and a weak Allee effect. Region 1 corresponds to the case in which the endemic point is not present. Region 2 is the stable region, where the endemic point exists and the values of the Hopf curve are negative. Finally, Region 3 shows the values for R_0, where the endemic point is unstable. The Allee effect benefits the stable equilibrium point.

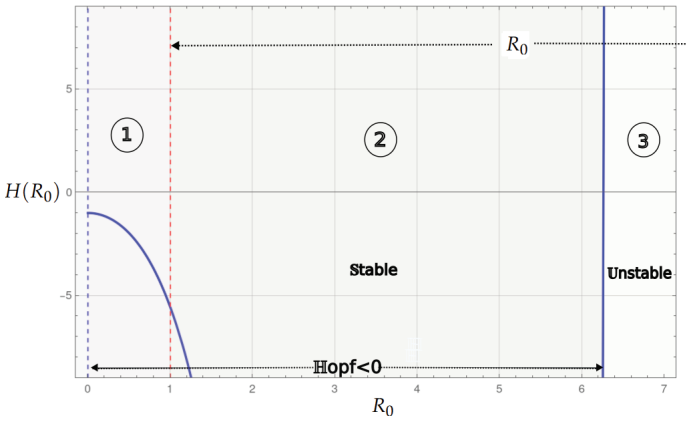

Figure 8. The bifurcation diagram corresponds to the model with logistic growth and weak Allee effect. The blue curve represents a projection of the Hopf hyperparametric set as a function of R_0.

Figure 9 shows the bifurcation diagram for the system with logistic growth and simultaneous weak and strong Allee effects. Region 1 corresponds to the case of the nonexistence of the endemic point. Region 2 is the region where the endemic point is unstable. Region 3 shows the values for R_0, where the endemic point is stable. Region 4 is the region where the endemic point does not exist, although the Hopf curve has negative values. In Region 5, there is also no biological interpretation.

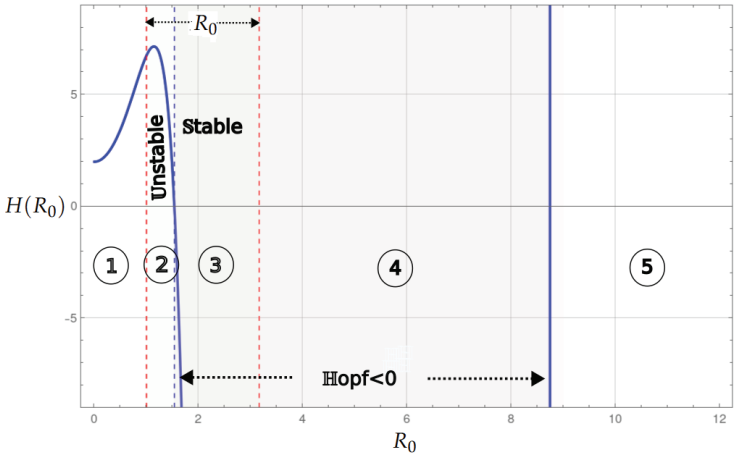

Figure 9. The bifurcation diagram corresponds to the model with logistic growth and both weak and strong Allee effects. The blue curve represents a projection of the Hopf hyperparametric set as a function of R_0.

Figure 6, similar to the previous case, shows the bifurcation diagram for the system with logistic growth, but only with the strong Allee effect. Region 1 corresponds to the case of the nonexistence of the endemic point. Region 2 is the region where the endemic point exists and is unstable, and Region 3 shows the values for R_0, where the endemic point exists and is stable. Region 4 is the region where the endemic point does not exist, although the Hopf curve has negative values, and in Region 5, there is no biological interpretation. Figure 7 shows the bifurcation diagram for the model with logistic growth and the Allee hyper effect. There is no endemic point in Region 1 and in the region between 3 and 4. In Regions 2 and 4, the endemic point is unstable, while in Regions 3 and 5, it is stable.

5.2. Numerical Continuation

Figure 10 shows the numerical continuation, performed in MATLAB (24.1.0.2653294)-MATCONT (7.1) [47], of the critical points in terms of the parameters β and μ. The initial values used for numerical continuation are $\lambda = 1$, $b = 1/4$, $\alpha_1 = 1/2$, $\alpha_2 = 3/4$, $p = 1$, $\delta = 1$, $\beta = 0.3$, $\mu = 1$. On the other hand, Figure 11 presents the projection of the Hopf curve, defined in (34), in terms of the exact parameters β and μ. The latter plot is equivalent to the bifurcation diagram presented in Figure 7, with clear correspondences between the highlighted elements; Branch 1, marked in orange in Figure 11, corresponds to the first dashed vertical line in Figure 7 and is in condition $R_0^2 = 1$. Branch 2, represented by the green straight line in Figure 11, is associated with the second dashed vertical line in Figure 7 (from left to right), corresponding to condition $R_0 < \alpha_1/b$. The red line in Figure 11 represents the third red dashed vertical line in Figure 7, defined by condition $R_0^2 > \alpha_2/b$. The Hopf projection in blue in Figure 11 is given by Equation (34) and describes the stability transitions through the parameters β and μ. In this context, Figure 10 provides a numerical representation equivalent to Figure 11, which consistently supports the analytical results obtained previously.

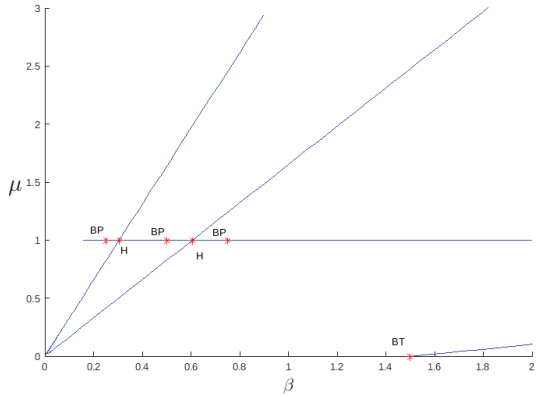

Figure 10. Numerical continuation in MATLAB (24.1.0.2653294)-MATCONT (7.1) of the bifurcation diagram for the model with logistic growth and hyper Allee effect. The blue horizontal line is a continuation through critical endemic points. The *BPs* (Branch Points) mark changes in the solution structure, determining the existence by sign changes in some components of the endemic equilibrium (33). The H points represent Hopf bifurcations (34), indicated by the diagonal lines as a function of the parameters (β, μ). Finally, BT corresponds to a Bogdanov–Takens bifurcation, with no oncological interpretation due to its negative μ component.

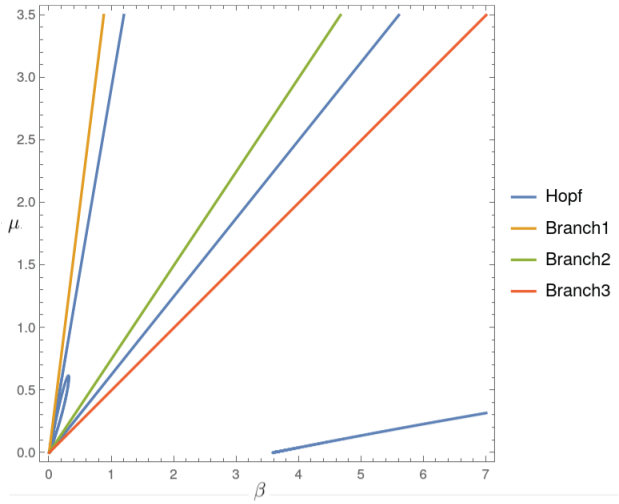

Figure 11. The projection of the analytical sets in the bifurcation diagram corresponds to the model with logistic growth and the hyper Allee effect.

Figures 12–15 present the numerical solution of a stable endemic point for different values of weak and strong Allee effects in the logistic growth model. These points were selected using the parameters corresponding to stability in the bifurcation diagram shown in Figures 5–7. The numerical continuation confirms the stability of the endemic point under the specific conditions of this region, supporting the analytical results and the bifurcation diagrams previously discussed. This representation highlights how the parametric configurations within this region allow steady-state to be achieved in the dynamical system. On the other hand, Figure 16 shows a case of stability under the Allee hyper effect. Each of these levels of the cancer cell population persists without being completely extinguished. The figure shows that the initial conditions determine the long-term population level. In this case, to reach the high population level, the initial conditions must be in a small neighborhood of the highest stable population level, while for the low population level, the initial conditions can take a larger set of values. The figure shows that an initial condition close to the carrying capacity is governed by the lowest stable level, not the

highest level, as expected. Under these parameter values, the basic reproductive number is $R_0 = 1.10547$, corresponding to Region 3 in the bifurcation diagram 7.

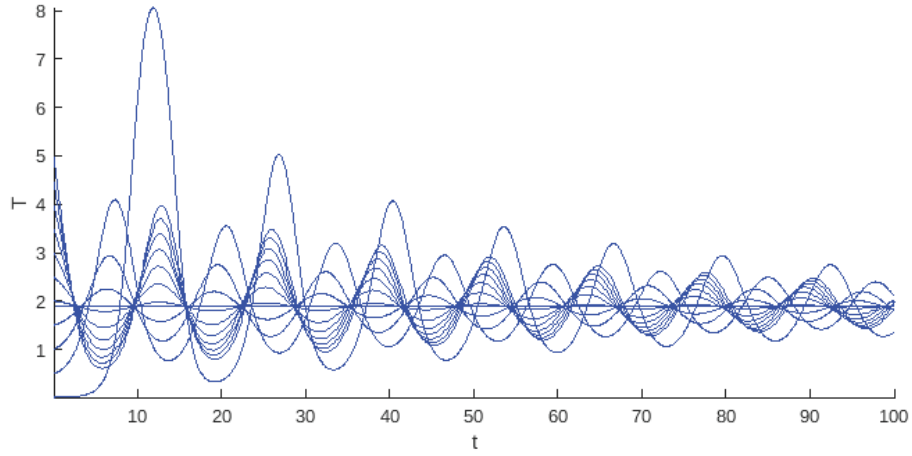

Figure 12. The numerical solution of a stable endemic point corresponds to the model with logistic growth and no Allee effect, where the different curves represent different initial conditions. Parameter values: $\lambda = 1, b = 1/10, \alpha = 0, \omega = 0, \beta = 0.2657, \mu = 0.5, p = 1$, and $\delta = 1$.

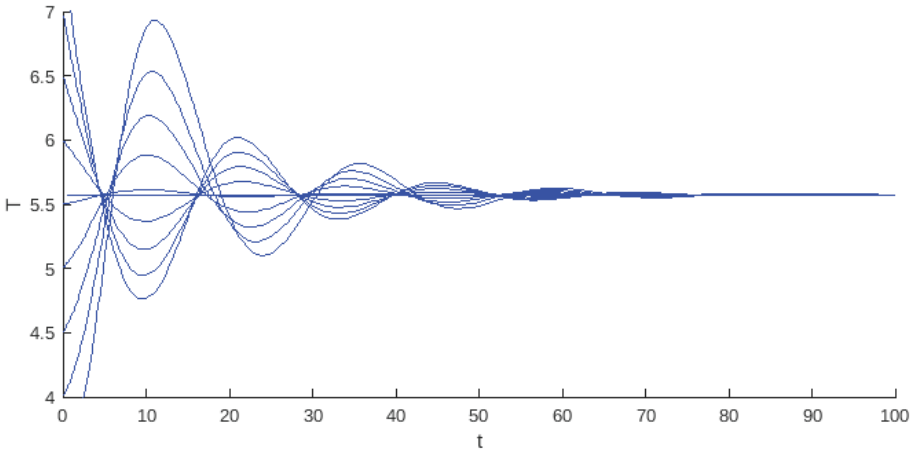

Figure 13. Numerical solution of a stable endemic point corresponds to the model with logistic growth and with weak Allee effect, with different curves corresponding to different initial conditions. Parameter values: $\lambda = 1, b = 1/10, \alpha = 0, \omega = 5, \beta = 0.0897, \mu = 0.5, p = 1$, and $\delta = 1$.

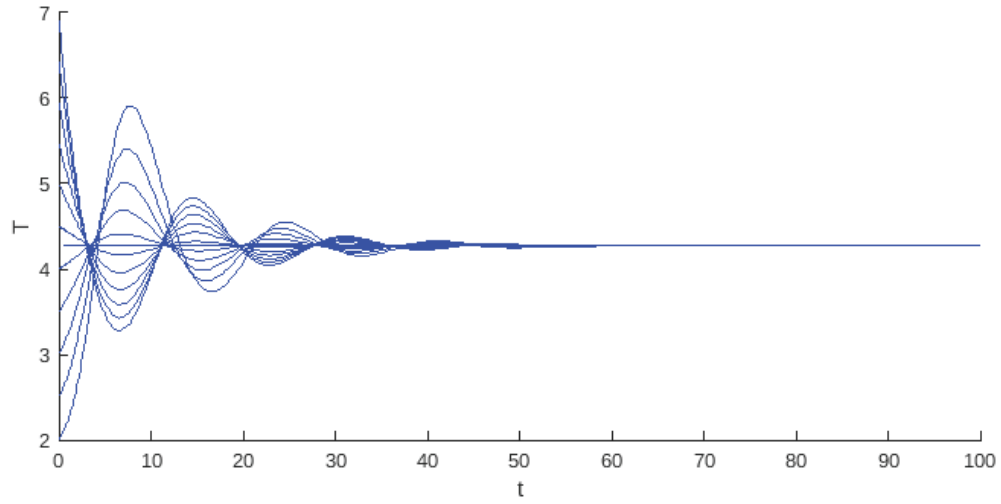

Figure 14. The numerical solution of a stable endemic point corresponds to model (24) with logistic growth and a strong Allee effect, where different curves correspond to different initial conditions. Parameter values: $\lambda = 1, b = 1/10, \alpha = 0.5, \omega = 0, \beta = 0.117, \mu = 0.5, p = 1$, and $\delta = 1$.

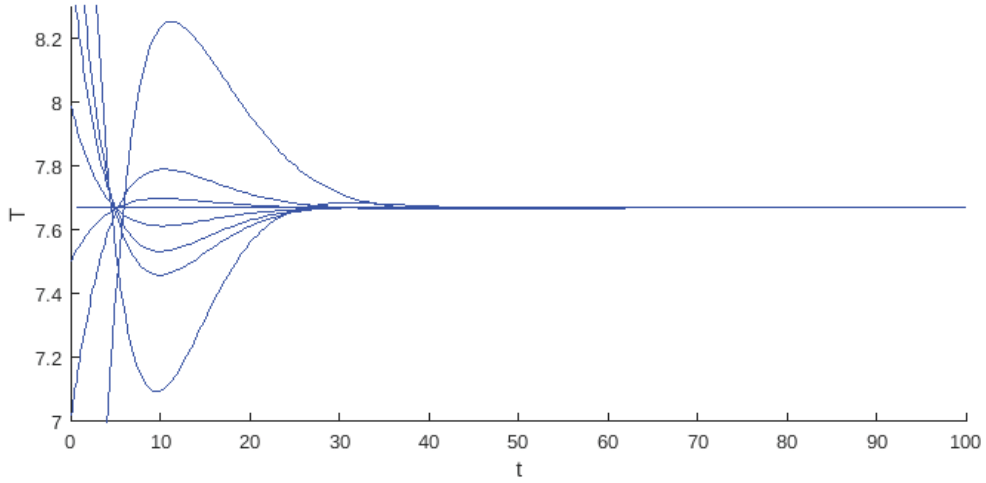

Figure 15. The numerical solution of a stable endemic point corresponds to the model with logistic growth, with both weak and strong Allee effects, where different curves correspond to different initial conditions. Parameter values $\lambda = 1, b = 1/10, \alpha = 0.5, \omega = 5, \beta = 0.0652, \mu = 0.5, p = 1$, and $\delta = 1$.

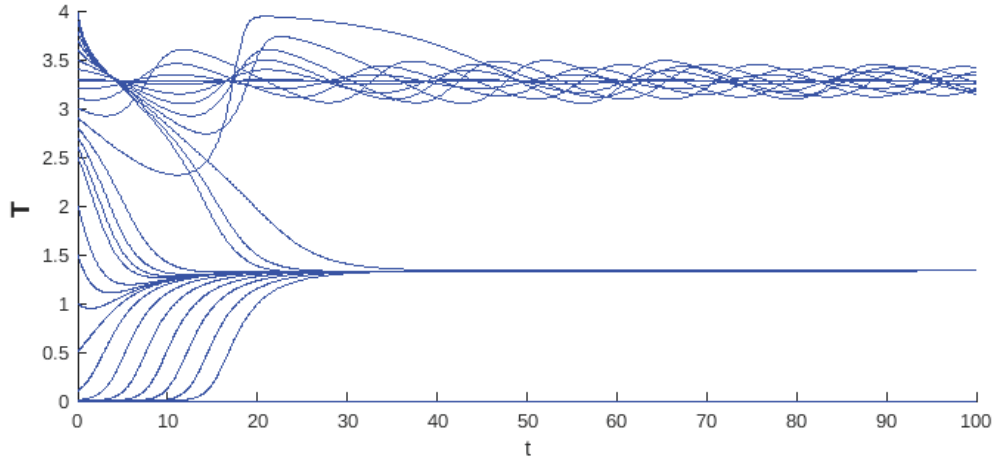

Figure 16. The numerical solution of endemic stability corresponds to the model (31) with logistic growth and the hyper Allee effect, where different curves correspond to different initial conditions. Parameter values: $\lambda = 1, b = 1/4, \alpha_1 = 1/2, \alpha_2 = 3/4, \beta = 0.30551595923505, \mu = 1, p = 1$, and $\delta = 1$.

6. Discussion

In the base model (1) with linear growth, we note that the system cannot adequately capture the stability of the critical points by not considering more complex or realistic situations, such as Allee effects. In particular, without integrating the Allee effects or considering only a weak Allee effect, the critical point of the endemic becomes unstable. However, with a strong Allee effect, the dynamic changes. This term generates a change in the stability of the endemic critical point, accompanied by a Hopf bifurcation. This bifurcation gives rise to limit cycles, adding complexity to the system dynamics. This pattern of stability change and bifurcation is preserved even when considering strong and weak Allee effects simultaneously (2), which underlines the robustness of these dynamics in the context of the model. When we incorporate the hyperbolic Allee effect, new characteristics are introduced to the system. This type of effect defines two critical levels, α_1 and α_2, which determine the existence of the endemic critical point and amplify the range of stability when $\alpha_1 < \alpha_2$. In this particular case (10), in the limit of $\alpha_2 \to \alpha_1$, the model once again reduces to the strong Allee effect, confirming the consistency of the mathematical framework.

The logistic growth model provides a more realistic situation of tumor dynamics by incorporating the carrying capacity of the system, a factor important in biological contexts where resources are limited. From the outset, this model presents richer dynamics compared to the linear case, since even without Allee effects, a change in stability is observed through a Hopf bifurcation (Figure 5). When a weak Allee effect is incorporated, the Hopf bifurcation that gives rise to the stability change of the endemic critical point is preserved. On the other hand, the stability region for this point becomes larger, as can be seen in Figure 8. Then, the weak Allee effect provides stability with many conditions without significantly altering the transitions of dynamics in the system. In the presence of a strong Allee effect, or when strong and weak Allee effects are considered simultaneously, the existence of the endemic critical point is reduced. This may be attributed to the imposition of a survival threshold for tumor cells, which limits their viability at low densities. Despite this reduction in the existence of the endemic point, the stability change is maintained by a Hopf bifurcation (Figures 6 and 9). The case with the hyperbolic Allee effect (Figure 6) introduces a markedly different dynamic. Here, a wider range is observed for both the existence of the endemic critical point and its stability.

The analysis results highlight the key role of the carrying capacity and the Allee effect in the dynamics of the system, particularly in stabilizing the critical endemic point. The carrying capacity defines a range of stability in the system for values of the basic reproduction number $1 < R_0^2 < \chi$, where χ is determined by the threshold associated with the Hopf bifurcation. This range indicates that, under controlled conditions, the system can maintain a stable equilibrium without complete tumor eradication. The Allee effect, on the other hand, reduces the existence of a critical endemic point for $1 < R_0^2 < 1/(b\alpha)$ levels, promoting the propagation of the virus and consequently reducing the population of cancer cells. This phenomenon suggests that the Allee effect may act as a regulatory mechanism that favors tumor control through viral propagation. In the case of the hyper Allee effect, the endemic point persists in an extended range for $1 < R_0^2 < \alpha_1/b$, further facilitating the virus's spread. When $R_0^2 > \alpha_2/b$, as observed in Region 5 (Figure 7), the dynamics indicate a possible drastic reduction in the tumor population. This region could represent a favorable scenario for antitumor therapies, as it combines effective virus propagation with a significant impact on cancer cell reduction.

The weak Allee effect explored in this study is observed to facilitate the stability of the endemic critical point, expanding the stability region without significantly altering the dynamic transitions of the system, meaning that a low density of virus-infected tumor cells could still allow cancer proliferation, but with lower efficiency. However, the strong Allee effect with logistic growth indicates that if the number of infected tumor cells is insufficient, the viral infection does not spread effectively, leading to tumor eradication. However, if the cell density exceeds the threshold, the tumor may persist or grow, as shown in Figure 6. When the weak and strong Allee effects are combined, the existence of the endemic critical point can be limited. In fact, in these observed cases, the limitation is very marked depending on the basic reproductive number (see Figures 3 and 9).

In Allee, the hyper effect is a more extreme case, where there are two critical thresholds, α_1 and α_2, a lower one, below which the tumor population collapses, and an upper one, which defines a steady state in which the tumor can persist. This effect suggests that the virus could be more effective in eliminating cancer if the cell population is kept within certain limits, $R_0^2 > \alpha_2/b$. In this region, where the number of infected cells is high, there is a reduction in the tumor population, which could represent an advantage for oncolytic therapies.

This study is theoretical and hypothetical, as its primary objective was to explore the dynamics through bifurcations rather than fitting specific experimental data

at this stage. However, experimental studies in cancer have empirically verified its behavior [14,16,48–53], supporting the relevance of incorporating different types of Allee effects into mathematical models, such as the one presented here, in the context of population dynamics under oncolytic virotherapy. Other papers support the idea, with experimental data showing that cancer can be modeled, including Allee effects. For example, in [48], in his discussion section paragraph 6, they include the case of the hyper Allee effect. At the same time, the works [12,13,15,54] show that populations at low densities cannot proliferate as easily, according to an Allee effect in cancer. Other references supporting the use of Allee effects in the epidemiology model are listed in Table 1. This study can be extended in future research by calibrating the model with experimental data.

Table 1. Results for different models, growth types, Allee effects, ranges of R_0, and relevant references for Allee effects.

Model+Growth	**Allee Effect**	**Range R_0**	**Hopf**	**References**
Model 1 Linear	None	N/A	No	[15,55]
Model 2 Linear	Weak	N/A	No	[15,55]
Model 3 Linear	Strong	$0 < R_\alpha^2 < 1$	Yes	[13,15,55]
Model 4 Linear (2)	Weak + Strong	$0 < R_\alpha^2 < 1$	Yes (5)	[13,15,55]
Model 5 Linear (10)	Hyper	$0 < R_0^2 < 1/\alpha_2$ or $R_0^2 > 1/\alpha_1$	Yes (13)	[12,13,15,48,54]
Model 6 Logistic (17)	None	$R_0^2 > 1$	Yes (22)	[15]
Model 7 Logistic	Weak	$R_0^2 > 1$	Yes	[12,14,15,50,56]
Model 8 Logistic (24)	Strong	$R_\alpha^2 < 1 < R_0^2$	Yes (28)	[12,14,15,50,56]
Model 9 Logistic	Weak+Strong	$1 < R_0^2 < 1/(b\alpha)$	Yes	[12,14,15,50,56]
Model 10 Logistic (31)	Hyper	$1 < R_0^2 < \alpha_1/b$ or $R_0^2 > \alpha_2/b$	Yes (34)	[12,13,15,48,54]

The weak Allee effect typically describes the situation in which the population is small and still able to grow. In the base model (1) we addressed, this effect allows the virus to infect and control tumor growth without necessarily eradicating it completely. The strong Allee effect needs to overcome a population level to avoid extinction, which in this context means that the tumor cell population is sufficiently high to avoid extinction. The combined effects mean that the tumor can reach a dormant state with viruses or be eliminated if the population is small enough, so the relatively high stable critical point in Figure 15 is observed. The most complex case of the Allee effect is hyper since two parameters are needed to determine the complex dynamics of the system. In the case of instability, if the population is below the first parameter $1/\alpha_2$, then the tumor would be eradicated; if the population is above the second threshold $1/\alpha_1$, it can proliferate and the tumor grows uncontrollably, but in the case of stability, for the basic reproductive number R_0 with values that are associated with negative Hopf curves such as Regions 3 or 5 in Figure 7, the Allee hyper-threshold values would cause endemic bistability as in Figure 16.

7. Conclusions

Our exploration of modeling in oncological virotherapy includes an epidemiology model with linear and logistic growth, with different Allee effects to observe their behavior in the dynamics of interaction with viruses. There are different modeling approaches, such as models with fractional operators, as is the case of [26], which, without considering the Allee effect, obtains complex dynamics but presents problems in analyzing stability. On the other hand, [4] discusses different modeling approaches in virology, including spatio-temporal models with PDE, epidemiology models, and variants of these. However, they do not include any Allee effect. In works such as [29–31], the authors thoroughly

study partial derivative modeling for oncological virotherapy modeling, where they couple tumor growth with cell–virus–immunity interaction; they also do not include the Allee effect. In [32], they consider an epidemiological model with the Allee effect, but have not yet done this in cancer. On the other hand, works such as [28,57–59], are conceptually closer to our approach to analyzing dynamics and stability, but also do not include the Allee effect.

Through theoretical analysis and bifurcation diagrams, critical conditions that determine the existence and stability of equilibrium points and periodic oscillations through Hopf bifurcations have been identified. The results highlight that first, the inclusion of the Allee effect, whether weak, strong, or hyper, significantly alters the dynamics of the system. In particular, strong and hyper effects introduce critical population thresholds that influence tumor eradication or persistence. The bifurcation diagrams we provide in this work are tools for identifying regions of stability and instability and help us understand dynamic transitions between disease-free and endemic states. In addition, when we incorporate logistic growth, we obtain differences in dynamics versus the linear growth model. In addition, we can observe that the different Allee effects affect the stability of the base model, too. All these combinations of factors should allow us to design viral cancer therapies with strategies based on critical parameters such as reproduction rates, Allee effects, and carrying capacity.

Our main contribution lies in the inclusion of different Allee effects using an epidemiological modeling approach for tumor–virus–immunity interactions, where we have analyzed their impact on the conditions of the existence of endemic critical points as well as their stability and bifurcation properties. Future research could extend this analysis to more complex models, including spatial heterogeneity, variability in the immune response, or treatment combination, and allow us to validate results with real data and fit the parameters of the system.

Author Contributions: Conceptualization, J.W.; Formal analysis, E.H.-L.; Investigation, E.H.-L. and J.W.; Methodology, E.H.-L. and J.W.; Project administration, J.W.; Software, E.H.-L.; Supervision, J.W.; Validation, E.H.-L. and J.W.; Visualization, E.H.-L.; Writing—original draft, E.H.-L. and J.W.; Writing—review and editing, E.H.-L. and J.W. All authors have read and agreed to the published version of the manuscript

Funding: J.W. was partially supported by the National Institutes of Health under grant number 1R15GM152943.

Data Availability Statement: The original contributions presented in this study are included in the article. Further inquiries can be directed to the corresponding author(s).

Acknowledgments: E.H.-L. acknowledges administrative and technical support from UTC and TecNM. The authors thank the three anonymous reviewers for their comments, which have improved the quality of the original manuscript.

Conflicts of Interest: The authors declare no conflicts of interest. The funders had no role in the design of the study; in the collection, analyses, or interpretation of data; in the writing of the manuscript; or in the decision to publish the results

References

1. Chen, L.; Zuo, M.; Zhou, Q.; Wang, Y. Oncolytic virotherapy in cancer treatment: Challenges and optimization prospects. *Front. Immunol.* **2023**, *14*, 1308890. [CrossRef] [PubMed]
2. Davis, J.J.; Fang, B. Oncolytic virotherapy for cancer treatment: Challenges and solutions. *J. Gene Med.* **2005**, *7*, 1380–1389. [CrossRef]

3. Goradel, N.H.; Baker, A.T.; Arashkia, A.; Ebrahimi, N.; Ghorghanlu, S.; Negahdari, B. Oncolytic virotherapy: Challenges and solutions. *Curr. Probl. Cancer* **2021**, *45*, 100639. [CrossRef] [PubMed]
4. Heidbuechel, J.P.; Abate-Daga, D.; Engeland, C.E.; Enderling, H. Mathematical modeling of oncolytic virotherapy. *Oncolytic Viruses* **2020**, *2058*, 307–320.
5. Elliott, K.; Elliott, K.; Betini, G.; Norris, D. Fear creates an Allee effect: Experimental evidence from seasonal populations. *Proc. R. Soc. Biol. Sci.* **2017**, *284*, 20170878. [CrossRef] [PubMed]
6. Kramer, A.; Drake, J. Experimental demonstration of population extinction due to a predator-driven Allee effect. *J. Anim. Ecol.* **2010**, *79*, 633–639. [CrossRef] [PubMed]
7. Luque, G.; Giraud, T.; Franck, C. Allee effects in ants. *J. Anim. Ecol.* **2013**, *82*, 956–965. [CrossRef] [PubMed]
8. Mironova, E.; Gopko, M.; Pasternak, A.; Mikheev, V.; Taskinen, J. Allee effect in a manipulative parasite within poikilothermic host under temperature change. *Parasitology* **2021**, *149*, 35–43. [CrossRef]
9. Kaul, R.; Kramer, A.; Dobbs, F.; Drake, J. Experimental demonstration of an Allee effect in mi-crobial populations. *Biol. Lett.* **2016**, *12*, 20160070. [CrossRef]
10. Ohkawa, H.; Takatsuka, C.; Kawano, T. Hidden Allee effect in photosynthetic organisms. *Commun. Integr. Biol.* **2020**, *13*, 119–127. [CrossRef]
11. Courchamp, F.; Berec, L.; Gascoigne, J. *Allee Effects in Ecology and Conservation*; Oxford Academic: Oxford, UK, 2008.
12. Fadai, N.T.; Simpson, M.J. Population dynamics with threshold effects give rise to a diverse family of Allee effects. *Bull. Math. Biol.* **2020**, *82*, 74. [CrossRef] [PubMed]
13. Fadai, N.T.; Johnston, S.T.; Simpson, M.J. Unpacking the Allee effect: Determining individual-level mechanisms that drive global population dynamics. *Proc. R. Soc. A* **2020**, *476*, 20200350. [CrossRef]
14. Gerlee, P.; Altrock, P.M.; Malik, A.; Krona, C.; Nelander, S. Autocrine signaling can explain the emergence of Allee effects in cancer cell populations. *PLoS Comput. Biol.* **2022**, *18*, e1009844. [CrossRef] [PubMed]
15. Johnson, K.E.; Howard, G.; Mo, W.; Strasser, M.K.; Lima, E.A.; Huang, S.; Brock, A. Cancer cell population growth kinetics at low densities deviate from the exponential growth model and suggest an Allee effect. *PLoS Biol.* **2019**, *17*, e3000399. [CrossRef]
16. Neufeld, Z.; Von Witt, W.; Lakatos, D.; Wang, J.; Hegedűs, B.; Czirók, A. The role of Allee effect in modelling post resection recurrence of glioblastoma. *PLoS Comput. Biol.* **2017**, *13*, e1005818. [CrossRef]
17. Ungefroren, H. Autocrine TGF-β in Cancer: Review of the Literature and Caveats in Experimental Analysis. *Int. J. Mol. Sci.* **2021**, *22*, 977. [CrossRef] [PubMed]
18. Uhrbom, L.; Hesselager, G.; Ostman, A.; Nistér, M.; Westermark, B. Dependence of autocrine growth factor stimulation in platelet-derived growth factor-B-induced mouse brain tumor cells. *Int. J. Cancer* **2000**, *85*, 398–406. [CrossRef]
19. Azimzade, Y.; Saberi, A.; Gatenby, R. Superlinear growth reveals the Allee effect in tumors. *Phys. Rev. E* **2021**, *103*, 042405. [CrossRef] [PubMed]
20. Browder, T.M.; Dunbar, C.E.; Nienhuis, A.W. Private and public autocrine loops in neoplastic cells. *Cancer Cells* **1989**, *1*, 9–17. [PubMed]
21. Shvartsman, S.; Hagan, M.; Yacoub, A.; Dent, P.; Wiley, H.; Lauffenburger, D. Autocrine loops with positive feedback enable context-dependent cell signaling. *Am. J. Physiol. Cell Physiol.* **2002**, *282*, C545–C559. [CrossRef]
22. Butera, G.; Pacchiana, R.; Donadelli, M. Autocrine mechanisms of cancer chemoresistance. In *Seminars in Cell & Developmental Biology*; Academic Press: Cambridge, MA, USA, 2018; Volume 78, pp. 3–12.
23. Garcia-Miranda, A.; Montes-Alvarado, J.B.; Sarmiento-Salinas, F.L.; Vallejo-Ruiz, V.; Castañeda-Saucedo, E.; Navarro-Tito, N.; Maycotte, P. Regulation of mitochondrial me-tabolism by autophagy supports leptin-induced cell migration. *Sci. Rep.* **2024**, *14*, 1408. [CrossRef] [PubMed]
24. Ronca, R.; Benkheil, M.; Mitola, S.; Struyf, S.; Liekens, S. Tumor angiogenesis revisited: Regulators and clinical implications. *Med. Res. Rev.* **2017**, *37*, 1231–1274. [CrossRef] [PubMed]
25. Shojaei, F. Anti-angiogenesis therapy in cancer: Current challenges and future perspectives. *Cancer Lett.* **2012**, *320*, 130–137. [CrossRef] [PubMed]
26. Alam, M.M.; Chowdhury, S.M.E.K.; Chowdhury, J.T.; Hasan, M.M.; Ullah, M.A.; Ahmed, S.F. Tumor treatment with chemo-virotherapy and MEK inhibitor: A mathematical model of Caputo fractional differential operator. *Alex. Eng. J.* **2023**, *71*, 173–183. [CrossRef]
27. Biesecker, M.; Kimn, J.H.; Lu, H.; Dingli, D.; Bajzer, Ž. Optimi-zation of virotherapy for cancer. *Bull. Math. Biol.* **2010**, *72*, 469–489. [CrossRef] [PubMed]
28. Buonomo, B.; Della Marca, R.; Rionero, S. Oscillation thresholds via the novel MBR method with application to oncolytic virotherapy. *Nonlinear Anal. Model. Control* **2022**, *27*, 948–963. [CrossRef]
29. Glaschke, S.; Dobrovolny, H.M. Spatiotemporal spread of oncolytic virus in a heterogeneous cell population. *Comput. Biol. Med.* **2024**, *183*, 109235. [CrossRef] [PubMed]

30. Pooladv, P.; Yun, C.; Yoon, A.; Kim, P.; Frascoli, F. The role of viral infectivity in oncolytic virotherapy outcomes: A mathematical study. *Math. Biosci.* **2020**, *334*, 108520. [CrossRef]
31. Timalsina, A.; Tian, J.P.; Wang, J. Mathematical and compu-tational modeling of tumor virotherapy with mediated immunity. *Bull. Math. Biol.* **2017**, *79*, 1736–1758. [CrossRef] [PubMed]
32. Yang, C.; Wang, J. On the intrinsic dynamics of bacteria in waterborne infections. *Math. Biosci.* **2018**, *296*, 71–81. [CrossRef] [PubMed]
33. Friedman, A.; Tian, J.P.; Fulci, G.; Chiocca, E.A.; Wang, J. Glioma virotherapy: Effects of innate immune suppression and increased viral replication capacity. *Cancer Res.* **2005**, *66*, 2314–2319. [CrossRef]
34. Komarova, N.L.; Wodarz, D. ODE models for oncolytic virus dynamics. *J. Theor. Biol.* **2010**, *263*, 530–543. [CrossRef] [PubMed]
35. Tian, J.P. The replicability of oncolytic virus: Defining conditions on tumor virotherapy. *Math. Biosci. Eng.* **2011**, *8*, 841–860.
36. Wodarz, D. Viruses as antitumor weapons: Defining conditions for tumor remission. *Cancer Res.* **2001**, *61*, 3501–3507. [PubMed]
37. Wu, J.T.; Kirn, D.H.; Wein, L.M. Analysis of a three-way race between tumor growth, a replication-competent virus, and an immune response. *Bull. Math. Biol.* **2004**, *66*, 605–625. [CrossRef] [PubMed]
38. Allee, W.C.; Bowen, E.S. Studies in animal aggregations: Mass protection against colloidal silver among goldfishes. *J. Exp. Zool.* **1932**, *61*, 185–207. [CrossRef]
39. Kramer, A.M.; Dennis, B.; Liebhold, A.M.; Drake, J.M. The evidence for Allee effects. *Popul. Ecol.* **2009**, *51*, 341–354. [CrossRef]
40. Jenner, A.L.; Yun, C.O.; Kim, P.S.; Coster, A.C. Mathematical modelling of the interaction between cancer cells and an oncolytic virus: Insights into the effects of treatment protocols. *Bull. Math. Biol.* **2018**, *80*, 1615–1629. [CrossRef] [PubMed]
41. Ramaj, T.; Zou, X. On the treatment of melanoma: A mathe-matical model of oncolytic virotherapy. *Math. Biosci.* **2023**, *365*, 109073. [CrossRef]
42. van den Driessche, P. Reproduction numbers of infectious disease models. *Infect. Dis. Model.* **2017**, *2*, 288–303. [CrossRef] [PubMed]
43. Van den Driessche, P.; Watmough, J. Reproduction numbers and sub-threshold endemic equilibria for compartmental models of disease transmission. *Math. Biosci.* **2002**, *180*, 29–48. [CrossRef]
44. Hinrichsen, D.; Pritchard, A.J. *Mathematical Systems Theory I: Modelling, State Space Analysis, Stability and Robustness*; Springer: Berlin/Heidelberg, Germany, 2005; pp. 337–340.
45. Chtcherba, A.D.; Kapur, D. Constructing Sylvest-er-type resultant matrices using the Dixon formulation. *J. Symb. Comput.* **2004**, *38*, 777–814. [CrossRef]
46. Delgado, J.; Hernández–López, E.; Hernández–Martínez, L.I. Bautin bifurcation in a minimal model of immunoediting. *Discret. Contin. Dyn. Syst.-B* **2020**, *25*, 1397–1414. [CrossRef]
47. Dhooge, A.; Govaerts, W.; Kuznetsov, Y.A. MATCONT: A MATLAB package for numerical bifurcation analysis of ODEs. *ACM Trans. Math. Softw.* **2003**, *29*, 141–164. [CrossRef]
48. Böttger, K.; Hatzikirou, H.; Voss-Böhme, A.; Cavalcanti-Adam, E.A.; Herrero, M.A.; Deutsch, A. An Emerging Allee Effect Is Critical for Tumor Initiation and Persistence. *PLoS Comput. Biol.* **2015**, *11*, e1004366. [CrossRef]
49. Compton, Z.; Mallo, D.; Maley, C. Stronger Together: Cancer Clones Cooperate to Alleviate Growth Barriers in Critical Cancer Progression Transitions. *Cancer Res.* **2023**, *83*, 4013–4014. [CrossRef] [PubMed]
50. Delitala, M.; Ferraro, M. Is the Allee effect relevant in cancer evolution and therapy? *Aims Math.* **2020**, *5*, 7649–7660. [CrossRef]
51. Hershey, B.; Barozzi, S.; Orsenigo, F.; Pompei, S.; Iannelli, F.; Kamrad, S.; Matafora, V.; Pisati, F.; Calabrese, L.; Fragale, G.; et al. Clonal cooperation through soluble metabolite exchange facilitates metastatic outgrowth by modulating Allee effect. *Sci. Adv.* **2023**, *9*, eadh4184. [CrossRef] [PubMed]
52. Muir, E.; Lajeunesse, M.; Kramer, A. The magnitude of Allee effects varies across Allee mechanisms, but not taxonomic groups. *Oikos* **2024**, *2024*, e10386. [CrossRef]
53. Strobl, M.; Tadele, D.; Maltas, J.; Barker-Clarke, R.; Dinh, M.; Scott, J. Abstract A023: Integrating mathematical modeling and in vitro experiments to measure ecological interactions in cancer. *Cancer Res.* **2024**, *84*, A023. [CrossRef]
54. Silva, J.; De Morais, R.; Silva, I.; Adimy, M.; Mancera, P. A mathematical model for treatment of papillary thyroid cancer using the allee effect. *J. Biol. Syst.* **2020**, *28*, 701–718. [CrossRef]
55. Hernández-López, E.; Núñez-López, M.; Capistrán, M. Stochastic dynamics between the immune system and cancer cells with Allee effect and immunotherapy. *J. Biol. Syst.* **2023**, *31*, 1125–1146. [CrossRef]
56. Hernández-López, E.; Núñez-López, M. Bifurcations in a Cancer and Immune Model with Allee Effect. *Int. J. Bifurc. Chaos* **2021**, *31*, 2130039. [CrossRef]
57. Guo, Y.; Niu, B.; Tian, J. Backward Hopf bifurcation in a mathematical model for oncolytic virotherapy with the infection delay and innate immune effects. *J. Biol. Dyn.* **2019**, *13*, 733–748. [CrossRef] [PubMed]

58. Li, H.; Liu, X.; Yan, R.; Liu, C. Hopf bifurcation analysis of a tumor virotherapy model with two time delays. *Phys. A—Stat. Mech. Its Appl.* **2020**, *553*, 124266. [CrossRef]
59. Nono, M.; Ngouonkadi, E.; Bowong, S.; Fotsin, H. Hopf and backward bifurcations induced by immune effectors in a cancer oncolytic virotherapy dynamics. *Int. J. Dyn. Control* **2020**, *9*, 840–861. [CrossRef]

MDPI AG
Grosspeteranlage 5
4052 Basel
Switzerland
Tel.: +41 61 683 77 34

Mathematics Editorial Office
E-mail: mathematics@mdpi.com
www.mdpi.com/journal/mathematics

Academic Open
Access Publishing

mdpi.com

ISBN 978-3-7258-4648-1